GFRP-REINFORCED CONCRETE EXTERIOR BEAM-COLUMN JOINTS SUBJECTED TO SEISMIC LOADING

by

MOHAMED HASSANEIN MOHAMED HASABALLA

A Thesis submitted to the Faculty of Graduate Studies of
The University of Manitoba
in partial fulfillment of the requirements of the degree of

DOCTOR OF PHILOSOPHY

Department of Civil Engineering
University of Manitoba
Winnipeg, Manitoba, Canada

Copyright © 2014 by Mohamed H. M. Hasaballa

ABSTRACT

Glass fibre-reinforced polymer (GFRP) reinforcement is used in reinforced concrete (RC) infrastructure such as parking garages and bridges to avoid steel corrosion problems. The behaviour of GFRP reinforcement under seismic loading in RC frame structures has not been widely investigated. Moment resistant frames alone or combined with shear walls are commonly used as Seismic Force Resisting Systems (SFRS). The seismic behaviour of beam-column joints significantly influences the response of the SFRS. Therefore, both the design and detailing of the beam-column joints are critical to secure a satisfactory seismic performance of these structures. However, the current Canadian FRP design codes (*CSA* 2012, *CSA* 2006) have no considerable seismic provisions, if any, due to lack of data and research in this area. Such lack of information does not allow for adequate designs and subsequently limits the implementation of FRP reinforcement as a non-corrodible and sustainable reinforcement in new construction. Therefore, it deemed necessary to track areas of ambiguity and lack of knowledge to provide design provisions and detailing guidelines.

This study investigated the seismic behaviour of the GFRP-RC exterior beam-column joints. The study consisted of an experimental phase, in which ten full-scale T-shaped GFRP-RC specimens were constructed and tested to failure, and an analytical phase using finite element modelling (FEM). Specimens in the experimental phase were divided into two series of specimens, (I) and (II). Series (I) had four specimens designed to investigate the anchorage detailing of beam longitudinal reinforcement inside the joint. The main variables in Series (I) specimens were the anchorage type (using either bent

bars or headed bars) and the reinforcement surface condition (using either deformed/ribbed bars or sand-coated bars). Series (II) had six specimens reinforced with GFRP bars and stirrups. The main objective of Series (II) was to evaluate the shear capacity of the joint. The main variables were the shear stress level in the joint ($0.70\sqrt{f'_c}$, $0.85\sqrt{f'_c}$, and $1.0\sqrt{f'_c}$) and the concrete strength (30 MPa and 60 MPa).

In the analytical phase, a commercial FEM software (ATENA-3D) was used to run a parametric study that investigated the influence of the presence of lateral beams, axial load on the column, applied shear stresses in the joint, and the concrete strength. The efficiency and accuracy of the FEM was verified against the experimental results obtained from the experimental phase before conducting the parametric study.

Test results showed that the performance of the specimens reinforced with GFRP headed bars was comparable to their counterparts reinforced with bent bars up to 4.0% drift ratio. The difference in the reinforcement surface conditions had insignificant influence on the overall behaviour. Moreover, it was concluded that the shear capacity of GFRP-RC beam-column joints is $0.85\sqrt{f'_c}$. Furthermore, an evaluation of the relevant seismic provisions in the CSA/S806-12 (*CSA* 2012) was carried out and some recommendations were proposed for consideration in the future updates of the CSA/S806-12.

ACKNOWLEDGMENTS

In the name of ALLAH

The author would like to express his deepest and sincere gratitude to his supervisor Dr. Ehab El-Salakawy, Professor of Civil Engineering and Canada Research Chair in Durability and Modernization of Civil Structures. Their guidance and continuous encouragement throughout the course of this research is tremendously appreciated. In addition, the author expresses his gratitude to his colleagues for their support during all work stages.

The financial support provided by the University of Manitoba through the UMGF award and by the Natural Science and Engineering Research Council of Canada (NSERC) through Discovery and Canada Research Chairs programs is gratefully acknowledged. Also, The GFRP reinforcement generously provided by Schoeck Canada Inc. is greatly appreciated. Many thanks to Chad Klowak, P.Eng, Lab Manager, and the technical staff in the McQuade Heavy Structures Laboratory at the University of Manitoba for their technical assistance during the construction and testing of the specimens.

Finally, I would like to thank my parents and my grandmother for their invaluable efforts and support. Special thanks to my beloved wife “Randa” for her endless support and patience throughout this significant part of our life. Thank you all, without your sincere support I would not be here to make this achievement.

Mohamed Hasaballa

TABLE OF CONTENTS

LIST OF FIGURES

LIST OF TABLES

CHAPTER 1

INTRODUCTION

1.1 BACKGROUND

Concrete structures are normally reinforced with pre-stressed and non-pre-stressed steel. The steel reinforcement is initially protected against corrosion by the alkalinity of the concrete which usually results in durable and serviceable construction. Reinforced concrete (RC) structures subjected to aggressive environments such as marine structures, bridges, overpasses, and parking garages represent a considerable percentage of the infrastructures located in North America; especially in Canada. Under these aggressive conditions, cracking and reduction of concrete alkalinity result in corrosion of reinforcing steel. The Corrosion of steel reinforcement ultimately causes concrete deterioration and loss of capacity, serviceability and structural integrity. Many alternatives are used to overcome the steel corrosion problem such as increasing concrete cover, improving the impermeability of concrete, epoxy coating protection of reinforcement, and steel galvanization. However, none of these procedures has proven to be an effective or economical long-term solution for the steel corrosion. The phenomenally high cost associated with the repair and restoration of deteriorated structures has attracted the attention towards an effective solution that has come recently into the spotlight, which is the use of the non-corrodible fibre reinforced polymers (FRPs) as reinforcement for concrete structures.

The FRP materials offer more advantages than conventional black steel reinforcement. The non-corrodible nature even in harsh chemical environments, electrical and magnetic non-conductivity, and higher tensile strength are prime examples for the many advantages the FRP reinforcement introduces to the construction industry. However, FRPs have perfect linear-elastic behaviour until failure with relatively low modulus of elasticity (50 - 65 GPa for glass FRP "GFRP" and 110 - 140 MPa for carbon FRP "CFRP") compared to steel (200 GPa), which exhibits yielding plateau. Moreover, they have different bond-to-concrete behaviour and low strength under compressive stresses. Accordingly, experimental investigations have been running to verify the behaviour of different concrete elements reinforced with FRPs. Research studies in the past two decades were involved in studying the behaviour of individual FRP-reinforced concrete elements such as simply-supported beams and slabs, and recently continuous beams and columns. However, very few researches have been conducting the integral performance of FRP-reinforced concrete frames especially those subjected to seismic forces.

The successful performance of any RC structure is influenced by the proper design of its structural elements under different combinations of loading including dead loads, live loads, wind loads, seismic loads, etc. Design of structures under seismic forces is adequately covered for concrete structures reinforced with steel; however, it is still under investigation for concrete structures reinforced with FRP materials. The CSA/A23.3-04 (*CSA* 2004) concept: "*All the structural elements in a seismic force resisting frame should have a sufficient reserve capacity to ensure that the chosen-energy dissipating mechanisms are maintained in the selected locations without the formation of any*

additional mechanisms through the deformations that can occur" may be also applied to the FRP-reinforced concrete structures.

1.2 PROBLEM DEFINITION

Shear walls and moment resisting frames are commonly used to resist seismic loads. Moment resisting frames can resist seismic loads applied on moderate and low rise buildings which include bridges, overpasses, and parking garages in low-to-moderate seismic zones. The demand for shear walls increases in high-rise buildings especially those in high-seismic zones. However, the presence of shear walls does not completely eliminate that portion of the seismic loads which is carried by the adjoining frame members through their seismically induced deformations. The seismic behaviour of beam-column connections (joints) significantly influences the earthquake response of moment-resisting frame structures. For example, the CSA/A23.3-04 (Clause 21.12) requires a minimum level of ductility and strength for all structural members subjected to seismic deformations even if they are not considered part of the seismic force resisting system. The integrity of the whole frame is undermined if the "joints", where its members are connected, fail. Therefore, both the design and detailing of the beam-column joints are critical to secure a satisfactory seismic performance of these structures.

Contrary to steel reinforcement, the GFRP reinforcement has no yielding plateau and behaves in an elastic manner up to failure (Fig. 1.1). Therefore, the concrete structures internally reinforced with FRP bars are not as ductile as their counterparts reinforced with steel.

Despite the fact that FRP does not yield, FRP-RC elements show substantial deflection prior to failure. This explains the concept of *deformability* adopted by *Jaeger et al.* (1997) which is the corresponding term to ductility in steel-reinforced concrete structures. This deformability controls the energy dissipation of seismic force. The amount of dissipated energy is represented by the area under the moment-curvature relationship for the structural elements. As far as the deformability increased, more seismic energy is dissipated by the structure.

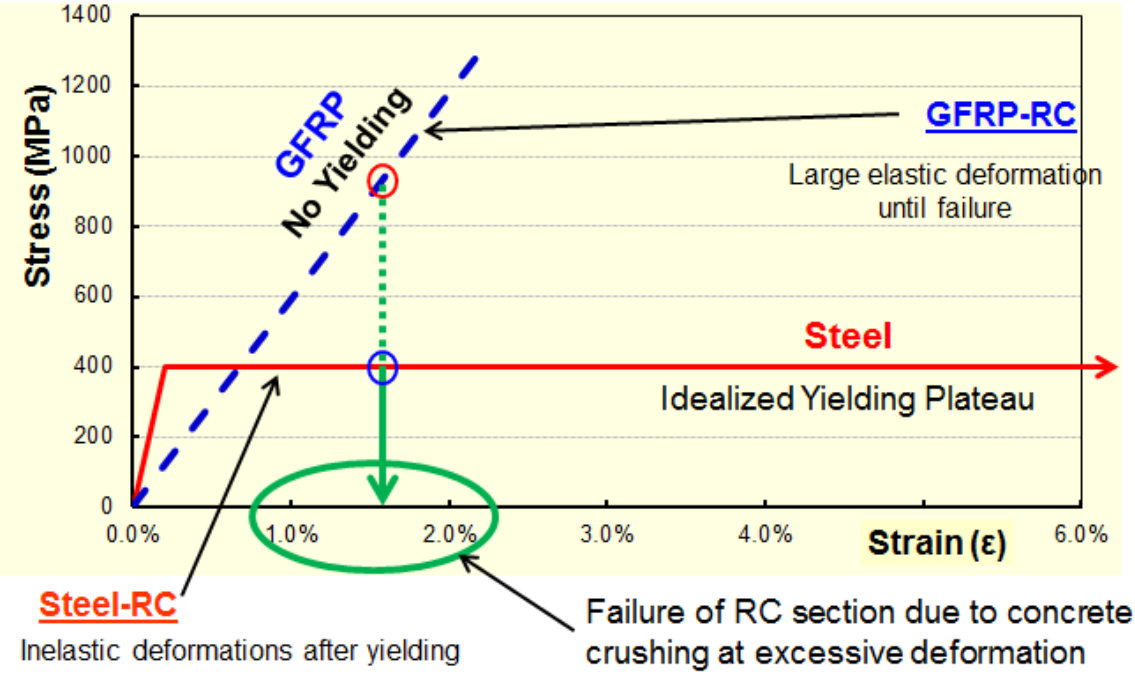

Figure 1.1: Stress-strain relationship for GFRP and steel reinforcement

It is well established that the flexural behaviour of an RC section is influenced by the tensile behaviour of the reinforcement. Experimental studies (*Ehsani and Wight* 1985, *Abdel-Fattah and Wight* 1987, *Abrams* 1987, *Nehdi et al.* 2010) on steel-RC sections subjected to flexure under simulated seismic loading showed that the failure of section is

eventually approached at higher drift ratios due to gradual crushing of concrete in the compression zone associated with high tensile strains in the steel reinforcement with strain values between 1% and 2% as shown in Figure 1.1. Regarding the GFRP reinforcement, it has a lower modulus of elasticity when compared to steel; however, with a higher strength in the range of twice to triple the yielding stress of steel (i.e. large strain value until failure) as shown in Figure 1.1. Therefore, it is thought that this combination of high strength and large strains till failure allows the GFRP reinforced concrete frames to dissipate a reasonable level of seismic force while behaving elastically up to failure. In addition, the elastic behaviour of the GFRP reinforced elements reduces the permanent concrete damage (deformation) of the structure following a seismic event.

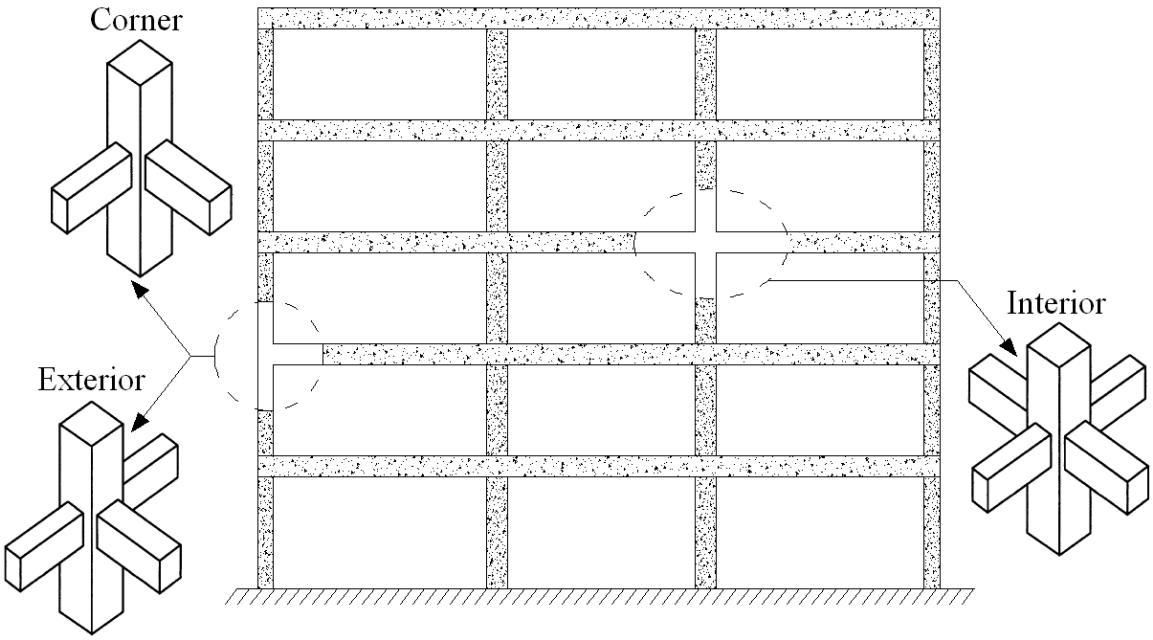

Figure 1.2: Geometry-based classification of beam-column joints

Moment-resistant RC frames are constructed from beams and columns monolithically connected through what so called the "beam-column connection" or simply the "joint". As per the ACI 352R-02 report (*ACI-ASCE* 2002), beam-column joints are classified based on the geometry into interior, exterior, and corner as shown in Figure 1.2.

One of the most critical zones in moment-resistant frames is the exterior joint due to the unsymmetrical loading and boundary conditions as well as the restraints associated with providing limited anchorage length to the beam longitudinal reinforcement in the joint. As a common practice in case of exterior beam-column joints reinforced with conventional steel, top and bottom beam longitudinal reinforcement are usually bent inside the joint to enhance their anchorage and prevent slippage. Moreover, using headed bars is also a viable alternative of 90-degree hooked bars in joints. In case of GFRP reinforcement, some restrictions still apply when using bent bars. The current manufacturing process of GFRP bent bars limits the size and length of a bent bar as well as the tensile strength, which is reduced by up to 50% at the bend location (*ACI* 2006) compared to the pultruded straight bars. On the other hand, the performance of GFRP headed-bars in beam-column joints has not been investigated yet. Therefore, the influence of the beam reinforcement detailing within the joint on the ultimate capacity and performance of the beam-column joints needs to be investigated in RC frames subjected to seismic loading.

Moreover, the current FRP design codes and guidelines (*CSA* 2012; *ACI* 2006; *ISIS Canada* 2007; *CSA* 2006) have no considerable seismic provisions, if any, due to lack of

data and research in this area. The research studies (*Ehsani and Whght* 1985, *Ehsani and Alameddine* 1991) in steel-RC frames resisting seismic loading had reported that when flexural strength ratio is maintained at a minimum value of 1.4, the joint shear stress and the confinement level of the joint are both shown to be key factors in achieving adequate strength and ductility of the joint. Yet, the current Canadian code CSA/S806-12 (*CSA* 2012) provides no limitation regarding the shear stress applied to the joint where high shear stress leads to failure of the joint and jeopardizes the integrity and stability of the whole structure. Clause 12.7 in the CSA/S806-12 allows using FRP stirrups for confining concrete columns in seismic regions and calculates the required reinforcement amount in Equation 12-4. However, it neither explicitly details this reinforcement amount to be provided in the joint nor specifies the shear capacity of the joint when the calculated amount is provided. The lack of such information not only limits implementing the FRP reinforcement in new constructions but also jeopardizes the safety of the structure. Therefore, it is deemed necessary to investigate the use of GFRP reinforcement in RC frames resisting earthquake loading.

1.3 SCOPE OF WORK

The seismic behaviour of RC frames can be investigated through testing both exterior/corner and interior beam-column joints. In exterior beam-column joints, the behaviour is deemed to be critical to the reinforcement detailing. Also, the classified large-strain-until-failure characteristic of GFRP bars is thought to be effective in moment resisting frames. In addition, due to the lower cost of GFRP bars compared to other FRP types (carbon and aramid); they are more attractive to the construction industry.

Moreover, GFRP-RC elements have different bond and stress-strain behaviour when compared to those reinforced with steel. Considering all the aforementioned factors; this study is scoped to investigate the seismic behaviour of GFRP-RC beam-column joints. Test prototypes represent beam-column connections isolated from an end bay between the assumed points of contra-flexure located at the mid-height and mid-span of the column and the beam, respectively. Test prototypes will be tested under reversed cycles of lateral loading to simulate seismic events.

1.4 RESEARCH OBJECTIVES

To obtain better understanding of the behaviour of FRP-reinforced concrete frames subjected to earthquake loading, this research focuses on studying seismic behaviour of beam-column joints totally reinforced with GFRP bars and stirrups for flexure as well as for shear resistance. Therefore, the objectives of this research are:

- Investigate the influence of anchorage type of beam longitudinal reinforcement using either bent bars or headed bars.
- Assess the effect of transverse reinforcement material using either steel or GFRP stirrups.
- Study the influence of different concrete strength using high and normal strength concrete.
- Evaluate the shear capacity of GFRP-RC beam-column joints under seismic loads.
- Provide design recommendations to predict the capacity and the structural performance of concrete beam-column connections totally reinforced with GFRP bars and stirrups.

1.5 WORK METHODOLOGY

This research consists of two phases; experimental phase and analytical phase. The research starts first with the experimental phase which includes construction and testing of ten full-size beam-column joint prototypes. Each prototype represents an exterior joint isolated from an end bay of a multi-storey structure between the assumed points of contra flexure located at the mid-height and mid-span of the column and the beam, respectively. Reversed lateral quasi-static cyclic loads are applied directly at the beam tip simulating seismic loading.

The analytical phase has two stages. The first stage consists of building a finite element model (FEM) to analyze and predict the behaviour of the GFRP reinforced beam-column joints using a commercial software package, ATENA-3D (*Cervenka and Niewald* 2005, *Cervenka* et al. 2012). The efficiency and accuracy of the FEM in this stage is verified against the experimental results obtained from the experimental phase. In the second stage of the analytical phase, the verified FEM is used to conduct a parametric study on four key parameters that are known to affect the behaviour of the beam-column joints; namely, the geometry of the joint (presence of lateral beams), axial load on the column, applied shear stresses in the joint, and the concrete strength.

CHAPTER 2

LITERATURE REVIEW

2.1 BACKGROUND

Investigating the behaviour of steel RC beam-column joints has attracted many researchers in the past four decades due to its critical influence on the overall behaviour of RC moment-resisting frames subjected to lateral forces. However, no to very limited research exists on such connections when they are totally reinforced with FRP reinforcement. Early studies by *Hanson and Connor* (1967) on steel-RC beam-column joints indicated that large inelastic deformation limits of individual members allow the entire structure to endure severe ground motion while dissipating significant levels of seismic energy. Beam-column connections had been investigated by other researchers mainly in the United States, Canada, Japan and New Zealand. The results of these studies were used by the *ACI-ASCE Committee 352*, Joints and Connections in Monolithic Concrete Structures, to develop its first design guidelines in 1976 (*ACI-ASCE Committee 352*, 1976).

These guidelines were based on the assumption that the concrete and transverse reinforcement in the joint act collectively to resist the shear forces in the joint. However, these guidelines, in many cases, lead the connections to be congested and difficult to construct. After releasing the first report by *ACI-ASCE Committee 352* (1976), more researchers had been involved in studying the behaviour of the beam-column connections

under cyclic loading taking into consideration all possible parameters that can affect their behaviour.

The following sections present a summary of the main concepts and behaviour of steel reinforced beam-column joints along with a literature review, and then followed by a brief overview of FRP materials and their important properties and characteristics related to their usage as reinforcement in various concrete elements.

2.2 RESEARCH ON STEEL REINFORCED BEAM-COLUMN JOINTS

This section presents a summary of some main parameters that affect the behaviour of exterior beam-column joints subjected to earthquake loading.

2.2.1 Influence of Joint Shear Stress and Flexural Strength Ratio

Ehsani and Wight, (1985-a) displayed the experimental results of six exterior reinforced concrete beam-column joints subjected to reversed-cyclic loading. The studied parameters in this research were the flexural strength ratio, the percentage of transverse reinforcement used within the joint and the shear stress in the joint as a function of $\sqrt{f_c'}$, where f_c' is strength of concrete inside the joint. Test results were compared with the recommendations of the *ASCE-ACI committee 352* available at that time (*ACI-ASCE-352* 1985). The dimensions of the beams were in the range of 1060 to 1525 mm long, 260 or 300 mm wide and 480 mm deep, while the column measured 2210 mm long with a 300 or 340 mm square section. Reversed lateral quasi-static cyclic loads were applied directly

at the beam tip simulating seismic loading. The specimens were tested where the column was positioned in the horizontal direction while the beam was in the vertical direction.

It was observed that the flexural strength ratio affects the location of the plastic hinges. For specimens with flexural strength ratio slightly greater than 1.0, the plastic hinge formed in the beam but spread into the joint and most of the damage was concentrated in the joint. This resulted in significant deterioration of bar anchorage and led to the pullout of the beam longitudinal steel and slippage of the column longitudinal bars, which reduced the load-carrying capacity and stiffness of the specimen as well. While, for specimens with flexural strength ratio considerably greater than 1.0, the cracks were distributed more in to the beam and away from the joint. Also for specimens which had a joint shear stress of $1.18\sqrt{f_c'}$, the load carrying capacity deteriorated after the first cycle of loading. It was concluded that:

- The flexural strength ratio should not be less than 1.4 to avoid formation of hinges at joints, larger flexural strength ratios improve the behaviour of the connections,
- The maximum shear stress in joints should not exceed 1.0 $\sqrt{f_c'}$ MPa to reduce excessive joint damage, column bar slippage, and beam bar pullout,
- Specimens that had minor slippage and bar pullout showed a very good overall behaviour in the later cycles,
- When the first two recommendations are met, additional transverse reinforcement doesn't enhance the behaviour of the specimens.

Moreover, the influence of flexural strength ratio and joint shear stress was studied by *Durrani and Wight* (1985), *Ehsani and Wight* (1985-b), *Ehsani and Alameddine* (1991).

Test results were in good agreement and similar conclusions to those listed above were drawn.

2.2.2 Effect of Transverse Beams and Slabs

Ehsani and Wight (1985-b) studied the behaviour of exterior beam-column joints taking into account the effect of transverse beams and slabs. The investigated variables were the flexural strength ratio, the percentage of transverse reinforcement used within the joint, and shear stress in the joint as a function of $\sqrt{f_c'}$. Six exterior beam-column joints were constructed and tested. Tested specimens were designed to have flexural strength ratios of 1.1, 1.5 and 2.0 assuming the flexural contribution of only the first two longitudinal slab reinforcement bars adjacent to the main beam. The design shear stress varied between $0.83\sqrt{f_c'}$ and $1.16\sqrt{f_c'}$ MPa. Beams and columns had the same dimensions and loading history described previously by *Ehsani and Wight*, (1985-a). The slabs, attached to the beams, measured 1015 mm in width and 100 mm in depth. Tests showed that not only the first two longitudinal bars yielded, as assumed by the authors, but all the slab longitudinal reinforcement around the joint yielded. Consequently, the original design flexural strength ratios were recalculated and then reduced to be 0.88, 1.16, and 1.58, respectively.

In specimens where the flexural strength ratios were less than 1.0, plastic hinges were formed in the upper column near the slab and crushing of concrete appeared in the column. Moreover, the plastic hinge was formed in the joint for the specimen with a flexural strength ratio slightly larger than 1.0 and relatively high joint shear stresses

($1.16\sqrt{f_c'}$ MPa). For specimens that had the same flexural strength ratio (slightly larger than 1.0) but lower joint shear stresses ($0.83\sqrt{f_c'}$ MPa), the flexural cracks extended into the beam for a distance of approximately twice the depth of the beam from the face of the column.

The behaviour of the test specimens in this study was compared to their counterparts without slabs or transverse beams from a previous study (*Ehsani and Wight* 1985-a). For the specimens with transverse beams and slabs, the hysteresis diagrams demonstrated unequal pinching during the positive and negative half-cycles of loading. This was primarily due to the presence of flexural cracks at the bottom of the main beam near the column, which remained opened through the test due to the flexural contribution of the slab reinforcement at the top of the beam. Furthermore, transverse beams and slabs provided additional confinement to the joint. This geometric confinement improved the overall behaviour significantly compared to similar specimens without transverse beams and slab.

The *Conclusions* were as follows;

- A flexural strength ratio of a value not less than 1.20 was recommended to ensure formation of flexural hinges in the beams
- The behaviour was improved by the presence of transverse beams which increased the confinement of the joint core.

- Increasing joint transverse reinforcement did not improve the behaviour of the joints with transverse slabs and beams as it did for the specimens that had no transverse beams and slabs.
- The presence of transverse beams helped eliminate the beam bar pullout, however, slippage of column longitudinal reinforcement was observed in specimens with and without transverse beams and slabs.

2.2.3 Effect of Loading Rate

Chung and Shah (1989) investigated the effect of cyclic loading rate, shear span-to-depth ratio, and stirrup spacing on the bond performance of exterior steel reinforced beam-column joints. Twelve anchorage-bond specimens were constructed and tested to study the effect of cyclic loading rate on a bar embedded in reinforced concrete. Each specimen represented a horizontal cantilever beam attached to a reinforced concrete block. The concrete block was subjected to axial load in the vertical direction. Test results included the mode of failure, energy dissipation, stiffness degradation, and bond stress distributions along the bar.

Then the outcomes of these tests were verified by testing three identical beam-column joints. The first one was tested under monotonic loading to determine the yield displacement of the beam; the second one was tested under cyclic loading at a frequency of 0.0025 Hz (slow-rate), while the third specimen was tested at a frequency of 1.0 Hz (fast-rate). It was observed that the maximum load-carrying capacity was quiet higher for the fast-rate loaded specimen. However, the damage rate resulted by the cyclic loading

was higher for the faster rate of loading. This was observed by the measurements of stiffness and natural frequency obtained from the free vibration test conducted after each loading stage. It was concluded that:

- Specimens which were subjected to faster rates of loading failed as a result of early fracture of steel bars. This was induced by stress concentration caused by improved bond strength at faster rates of loading.
- During higher rates of loading, fewer and wider cracks were observed at column face. In contrast, more widely-distributed cracks were observed in the beam at the slower rates of loading.
- Specimens with stirrup spacing of $d/2$ (where d is the beam depth) were significantly influenced by the loading rate. A brittle mode of failure was observed at fast rate of loading compared to a ductile mode of failure for slow rate loading specimens. On the other hand, specimens with stirrup spacing of $d/4$ were not influenced by the loading rate.

2.2.4 Effect of Detailing Scheme

Hakuto et al. (2000) studied the influence of reinforcement detailing on seismic behaviour of exterior and interior beam-column joints. For the exterior beam-column joints, specimens had shear reinforcement less than what was required by the *ACI 318-95* (1995) and *NZS 3101:1995* (1995) in both of the beam and the joint. Two identical prototypes were tested, the longitudinal beam bars in one of the specimens were anchored by bending the hooks out of the joint core while in the other specimen the longitudinal bars were anchored into the joint core as specified by the *ACI 318-95*. The beam

measured 1525 mm long, 300 mm wide and 500 mm deep, while the column measured 2900 mm long with a 460 mm square section. Reversed lateral quasi-static cyclic loads were applied directly at the column top end simulating seismic loading. The column was positioned in the vertical direction while the beam was in the horizontal direction.

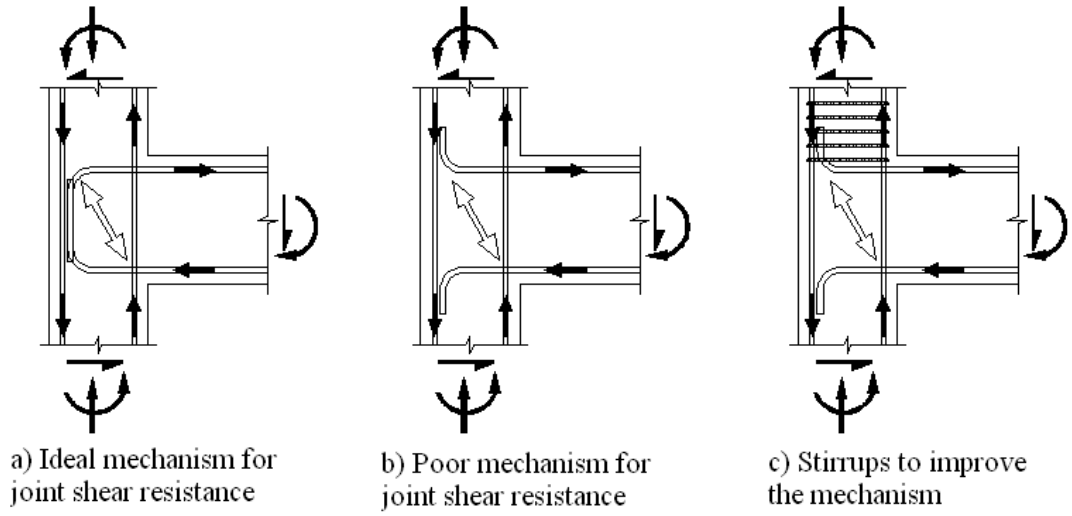

Figure 2.1: Mechanism for joint shear resistance (Reproduced from *Hakuto et al.* 2000)

This study considered the bearing stresses at the bend to act as a node in a strut-and-tie model where the diagonal compression strut acts against the beam reinforcement as shown in Figure 2.1(a). On the other hand, the detail shown in Figure 2.1(b) does not provide an effective node point at the top of the diagonal strut to achieve a stable strut and tie model. When an adequate amount of confinement is provided in the column above the joint core, the missing strut node is introduced to resist the horizontal component of force from the compression strut as shown in Figure 2.1(c).

During testing the specimen with the anchorage out of the joint core, it was observed that the beam hook was not effective in carrying the diagonal compression strut, which pushed against the longitudinal column steel leading to wide splitting-cracks along the column. It was concluded that the performance is improved significantly when the hooks of the beam bars are bent into the joint core.

Murty et al. (2003) studied the effect of different reinforcement details in beams and joints on the seismic behaviour of exterior beam-column joints. Four different anchorage details of beam longitudinal reinforcement and three details of transverse reinforcement in the joint core were investigated, as shown in Figures 2.2, and 2.3, respectively. Twelve half-scale exterior beam-column joints were constructed and tested. The beam measured 1150 mm long, 200 mm wide and 400 mm deep, while the column measured 1500 mm long with a 200 mm wide and 250 mm deep. The flexure strength ratio was kept constant at a value of 1.65. Test specimens were rotated 90 degrees such that the column member was in the horizontal position and the beam member in the vertical position, as shown in Figure 2.2. Reversed cyclic displacements were applied directly at the beam end simulating seismic loading.

Tests showed that joint transverse reinforcement has a significant influence on the post-cracking response of the specimens. The use of hairclip-type reinforcement, fully anchored in the beam, worked as additional longitudinal reinforcement in the beam. This helped shifting the plastic hinge in the beam away from the face of the column. Furthermore, it was concluded that the use of standard hook with hairclip-type transverse

reinforcement is recommended because of its ease in construction and can be used for frames in low seismic regions where the demand for high ductility is not required.

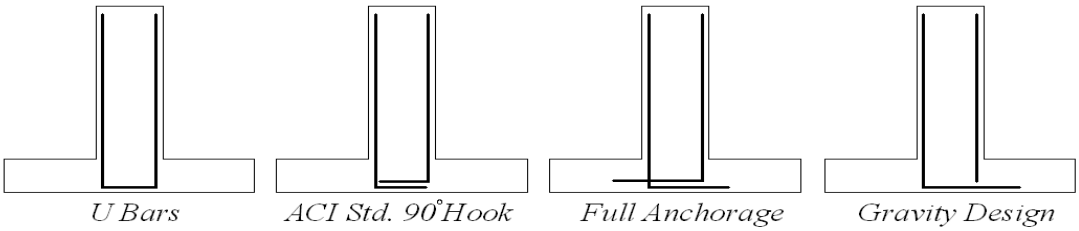

Figure 2.2: Longitudinal beam anchorage details (Reproduced from *Murty et al.* 2003)

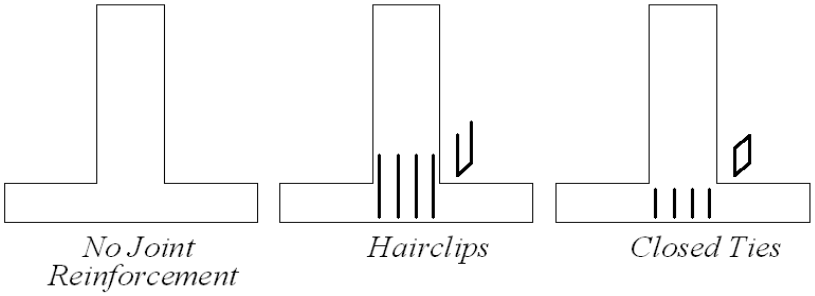

Figure 2.3: Joint details (Reproduced from *Murty et al.* 2003)

Wallace et al. (1998) studied the seismic behaviour of beam-column joints where headed bars were used as beam longitudinal reinforcement. The objective was to address the anchorage and detailing requirements for using headed reinforcement in both type (1) and (2) joints. Test parameters were the type of the joint (type 1 or 2), and anchoring details of beam longitudinal reinforcement in the joint (i.e. Headed bars and 90-degree bent bars). The experimental program included two exterior beam-column joints and five corner (knee) beam-column joints. Side stub-beams were used to represent the three-dimensional effect of transverse beams on the exterior joints. No loading was applied on stubs.

They concluded that specimens reinforced with headed bars exhibited similar behaviour to that observed in specimens reinforced using 90-degree hooked longitudinal bars. The researchers recommended a minimum anchorage length of twelve times bar diameter for headed bars of diameters 16 and 25 mm. Also, the transverse reinforcement provided in the joint should be positioned in-line with the headed bar to restrain heads from pushing the concrete cover out. In corner (knee) joints, horizontal shear stresses should be kept below $0.5\sqrt{f_c'}$ to guarantee stable behaviour of the joint.

2.2.5 Effect of Concrete Strength

The influence of using high strength concrete in seismic regions was studied by *Ehsani et al.* (1987). The study consisted of five full-scale beam-column specimens. Four specimens constructed using high strength concrete of $f_c' = 66$ MPa. Test results were compared to one of the specimens in *Ehsani and Wight*, (1985-a) constructed using normal-strength concrete of $f_c' = 44$ MPa. The flexural strength ratios of test specimens were in the range between 1.41 and up to 1.9. The primary variable for the high strength concrete specimens was the joint shear stress which had a range of $0.63\sqrt{f_c'}$ to $1.07\sqrt{f_c'}$ MPa. Tests results showed that specimens with low joint shear stresses ($0.63\sqrt{f_c'}$) failed due to flexural hinging in the beam. However for the specimen with high joint shear stress ($1.07\sqrt{f_c'}$), it exhibited joint shear failure. Also, a limited strain hardening in the beam longitudinal reinforcement was observed although the flexural strength ratio was as high as 1.67.

The study concluded that:

- The maximum allowable joint shear stress should be $0.87\sqrt{f_c'}$ when high strength concrete of $f_c' = 66$ MPa was used in exterior beam column joints.
- A combination of the flexural strength ratio and joint shear stresses determined the mode of failure rather than the flexural strength ratio only.
- High joint shear stresses resulted in a significant reduction of the energy absorption even in the presence of high flexural strength ratio.
- Specimens with high flexural strength ratio and low joint shear stresses exhibited buckling of compression reinforcement in the beam plastic hinge at very large drifts.

Ehsani and Alameddine (1991) studied the behaviour of exterior beam-column connections constructed with high strength concrete. The objectives were to evaluate the shear capacity of Type-2 joints and to check the feasibility of reducing the joint confinement required by the *ACI-ASCE 352* (1985) while ensuring a ductile behaviour. The variables were, 1) concrete compressive strength (56, 74 and 94 MPa); 2) joint shear stress (7.6 and 9.7 MPa); and 3) the degree of joint confinement in terms of transverse reinforcement ratio (1.2% and 1.8%). Twelve full-scale beam-column specimens were casted and tested.

The flexural strength ratio was kept constant at a minimum value of 1.4 for all specimens. Test results showed that specimens with low shear level and high joint confinement were able to develop the ultimate capacities. However, specimens with higher concrete

strength showed relatively higher loss of load-carrying capacity than those with lower strength. This indicates that higher strength concrete needs more confinement. Other specimens with high joint shear stress (9.7 MPa) and/or low joint confinement suffered greater strength loss and lower ductility. The study concluded that:

- The amount of transverse reinforcement required by the ACI-ASCE 352 committee was practically impossible in case when high strength concrete was used.
- Higher strength concrete requires more confinement due to its brittle nature. Therefore, the required amount of transverse reinforcement for joint confinement should be a function of the flexural strength ratio, joint shear stress, and the compressive strength of the concrete.

2.3 FRP BARS AS REINFORCEMENT FOR CONCRETE STRUCTURES

In the past two decades, FRPs have proven to be a promising alternative material for reinforcement of concrete structures. FRP materials have non-corrodible and non-magnetic nature. Therefore, they can be used in reinforced-concrete structures to eliminate the corrosion problem associated with the conventional reinforcing steel. The following section provides a brief overview of FRP materials and some of their important properties and characteristics related to their application as reinforcement in concrete.

2.3.1 Characteristics of FRP Reinforcement

Originally, FRP materials were used successfully in aerospace, marine and automotive sectors. Their positive properties and the significant reduction in their materials and

manufacturing costs helped the widespread of the FRP materials in civil engineering applications. FRP's are increasingly being used in civil infrastructure in several forms such as; reinforcing bars and tendons in new structures, wraps and laminates for strengthening of existing structures, composite bridge decks, and composite structural sections. To stay within the scope of this research, the following section will only focus on the FRP materials in the form of internal reinforcing bars.

2.3.1.1 *Constituents*

FRP reinforcement is composed of high strength continuous fibres embedded in a polymer matrix in addition to some fillers and additives. Fibres are in very small diameters and are responsible to provide mechanical strength and stiffness to the composite, while the polymer matrix (resin) has comparatively poor mechanical properties. Fibres are oriented in the longitudinal direction of the bars which is the direction of the primary loads.

(a) Types of fibers

Aramid, Carbon, and Glass fibres are the most commonly used types of fibres (*Mallick* 1988). Aramid fibres are classified as highly oriented organic fibres. They offer good mechanical properties at a low density with the added advantage of toughness or impact resistance. They are characterized as having reasonably high tensile strength (1310 MPa) Aramid composites have poor compressive strength and a medium unidirectional tensile modulus of 83 GPa which is approximately 50% higher than that of glass, and a very low density (1380 Kg/m^3) if compared to glass and carbon. Aramid fibres are resistant to

organic solvents, fuels, and lubricants. Dry aramid fibres are tough and have been used as cables or ropes, and frequently used in ballistic applications.

Concerning with Carbon fibres, they are available with a wide range of tensile moduli starting from 145 GPa (Carbon AS-4) up to more than 500 GPa. In general, the low-modulus fibres have lower specific gravities, lower cost, higher tensile strengths, and higher tensile strains to failure than the high-modulus fibres. The advantages of Carbon fibres with respect to its mechanical and physical properties are their exceptionally high tensile strength-weight ratios as well as tensile modulus-weight ratios, very low coefficient of thermal expansion, and high fatigue strength. On the other hand, the disadvantages are their low impact resistance, high electrical conductivity, and Carbon fibres are not easily wet by resins; particularly the higher modulus fibres.

Glass fibres are available in 4 types, E-glass for high electrical insulating properties, S-glass for high strength, ECR glass for improved acid resistance and acid resistance (AR glass). The average tensile strength of glass fibres ranges between approximately 1.00 and 2.00 GPa (1.75 GPa for S-glass type and 1.1 GPa for E-glass type). The tensile strength of glass fibres is reduced in the presence of water or under sustained loads (creep). The tensile strength degradation is also increased as the surface flaws grow under cyclic and fatigue loads. The tensile modulus of glass fibres ranges between 70 to 90 GPa. Glass fibres are sensitive to abrasion and corrosion due to alkaline solutions, and are considered generally a good impact resistant fibre. Specific gravity of glass fibres are approximately 2500 kg/m^3.

(b) Types of resins

The primary function of the resin is to transfer the load through shear stresses that develop at the fibre-matrix interface, provides lateral support for fibres against buckling and it is also important for the environmental protection of the fibres (*Hollaway and Head* 2001). Thermosetting resin and thermoplastic resins are two types of resins that are used in fibrous composites manufacturing. Thermosetting resins are typically used for structural applications as they are heat cured and cannot be deformed upon curing. Contrary, thermoplastic resins soften to viscous liquids when heated and can be deformed upon curing.

Generally, the factors that influence the selection of a specific resin are:

- Impregnation processing method which depends on viscosity and pot life of resin during impregnation, wet-ability to filaments, processing and/or curing temperatures and pressure, shrinkage during curing, toxicity, and shelf life for pre-impregnation.
- Adhesion levels between the resins and the fibres, impregnated in, to transfer stresses between fibres (i.e. inter-laminar shear as well as in-plane shear properties).
- Mechanical properties (i.e. elongation, thermal stability, and notch toughness) that controls the ability of resins to protect the surface of the fibres from mechanical abrasion.
- Durability and chemical resistance against attacking environments.

2.3.1.2 *Manufacturing*

Several techniques are used to produce FRP composites. The shape of the final product depends on the adopted manufacturing process. FRP bars are produced using the pultrusion technique. In this method continuous strands of the fibres are pulled from spools of fibres to be impregnated in the resin. Once they are saturated with resin, they are pulled through a heated die at which they can be formed and heat-cured as shown in Figure 2.4. Surface treatment of bars is essentially applied to ensure strong bond with concrete. The FRP bar surface-treatment could be in the form of spirals or sand coating. After curing and surface treatment, FRP bars are then cut to the required length. FRP bars are produced in different diameters and surfaces. The product diameter normally ranges from 6 mm to 25 mm.

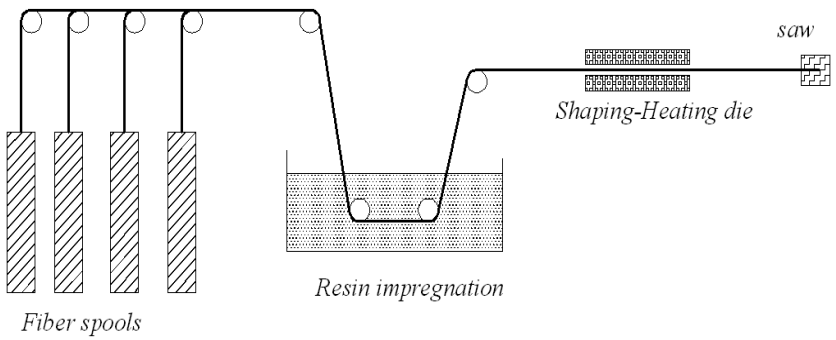

Figure 2.4: Schematic diagram for the Pultrusion manufacturing process

2.3.1.3 *Physical properties*

The density of FRP bars is considerably less than of the steel bars (i.e. one-sixth to one-fourth that of steel), as shown in Table 2.1. FRP bars have different thermal expansion in the longitudinal and transverse directions. The longitudinal coefficient of thermal

expansion is governed by the type of fibre as shown in Table 2.2, while the transverse coefficient of thermal expansion is dominated by the type of resin (*ACI* 2006).

Table 2.1: Typical densities of reinforcing bars (Reproduced from *ACI* 2006)

Type	Steel	GFRP	CFRP	AFRP
Density (kg/m^3)	7900	1250 to 2100	1500 to 1600	1250 to 1400

Table 2.2: Typical coefficients of thermal expansion for reinforcing bars (Reproduced from *ACI* 2006)

Direction	CTE × 10^{-6} / ^{0}C			
	Steel	GFRP	CFRP	AFRP
Longitudinal, α_L	11.7	6.0 to 10.0	- 9.0 to 0.0	- 6 to - 2
Transverse, α_T	11.7	21.0 to 23.0	74.0 to 104.0	60.0 to 80.0

2.3.1.4 *Mechanical properties*

The stress-strain relationship of the unidirectional FRP bars is linear elastic up to failure as shown in Figure 2.5. FRP materials do not exhibit yielding behaviour like the conventional steel does. FRP bars have higher strengths than the conventional steel; however, they have less stiffness than the steel bars have. Contrary, FRP bars have low compressive strength due to buckling of fibres.

The characteristic properties of FRP bars are variable. They depend mainly on the type and the volumetric ratio of fibre in the composite, the type of resin, and quality control during the manufacturing process. Accordingly, the manufacturer has the ability to control the properties of the product, as shown in Table 2.3. Except for FRP bars with a thermoplastic resin, FRP bars cannot be bent or reshaped after manufacturing. FRP bars

can be bent in forms of stirrups or bent bars while manufacturing, however, a strength reduction of 40 to 50% relative to the tensile strength of a straight bar is expected in the bent bars.

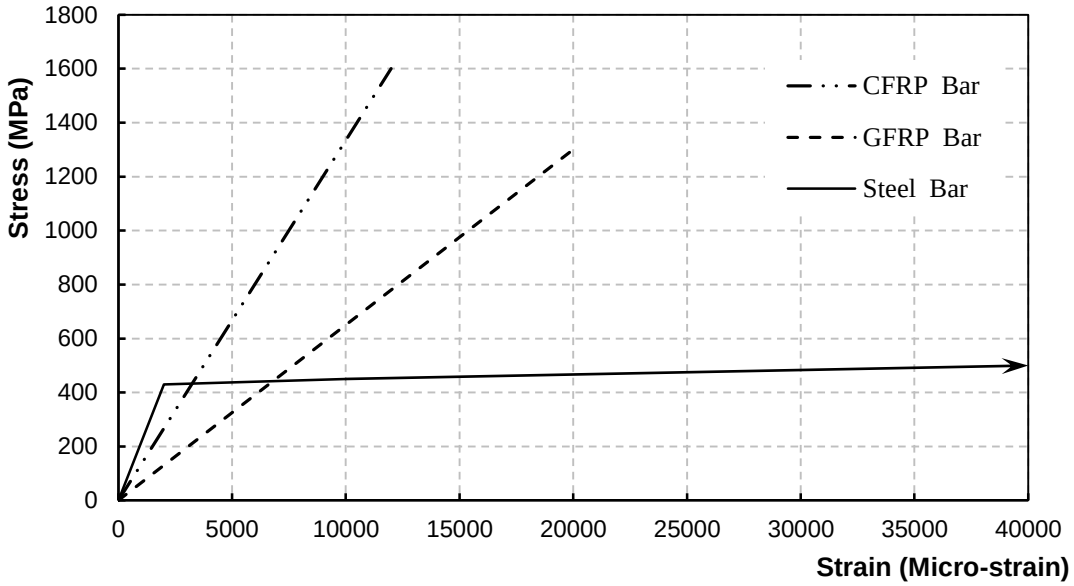

Figure 2.5: Stress–strain curve for reinforcing materials

The bond behaviour of FRP bars is affected by the manufacturing process, which controls the bar surface, mechanical properties, environmental conditions, and the design force. Bond force is transferred between the bar and the surrounding concrete by the chemical bond, frictional resistance against slip and mechanical interlock due to irregularity of the bar interface (*ACI* 2006). These differences in behaviour between FRP and steel reinforcement are reflected on the behaviour of reinforced concrete members; and therefore, they should be considered in the design of FRP reinforced concrete members.

Table 2.3: Mechanical properties of FRP bars (*ISIS Canada* 2007, *Pultrall Inc.* 2014, *Schoeck Canada Inc.* 2014)

	Trade name	Tensile strength (MPa)	Modulus of Elasticity (GPa)	Ultimate tensile strain
Carbon Fibre	V-ROD	1596.0	120.0	0.013
	Aslan	2068.0	124.0	0.017
	Leadline	2250.0	147.0	0.015
	NEFMAC	1200.0	100.0	0.012
Glass Fibre	V-ROD LM	940	42.5	0.021
	V-ROD HM	1200	62.6	0.0189
	Aslan	690	40.8	0.017
	NEFMAC	600	30	0.020
	COMBAR	1100	60	0.018

2.3.1.5 *Durability of FRP reinforcing bars*

High alkalinity of concrete (pH of approximately 12.5 to 13.5) raises durability concerns regarding the use of FRP reinforcement in concrete. Many durability studies have been conducted to determine the strength and stiffness reduction due to natural ageing of FRP bars under service environments. In these studies, accelerated ageing tests and field evaluation of existing structures were both used to evaluate the long-term behaviour of FRP reinforcement. Debaiky et al. (2006) reported that the results from accelerated test procedures should be interpreted cautiously since the conditioning environments to promote accelerated deterioration are often unrealistic when compared with the actual environment in the field. Mufti et al. (2007) conducted field evaluation study on five in-service bridges located across Canada and constructed with GFRP bars and grids. The study concluded that there were no signs of degradation of the GFRP reinforcement in the

concrete in existing structures exposed to natural environmental conditions for duration of five to eight years.

The behaviour of beam-column joints reinforced with GFRP bars and stirrups requires a solid background on the behaviour of FRP reinforced elements under axial, flexure, and shear stresses. Accordingly, the following section represents a literature review on beams and columns reinforced with FRP bars in longitudinal and transverse directions

2.3.2 Shear Strength of Concrete Beams Reinforced with FRP Stirrups

Shehata et al. (2000) presented the results of the experimental program conducted at the University of Manitoba to examine the structural performance of FRP stirrups. The objective of the study was to provide design guidelines for the use of CFRP and GFRP stirrups as shear reinforcement for concrete structures. The program had forty two panel specimens using CFRP, GFRP, and steel stirrups to study the bend effect on the strength of the stirrups in addition to ten reinforced concrete beams reinforced with CFRP, GFRP, and steel stirrups. The outcomes were as follows;

- A minimum bend radius not less than the greater of four times the effective bar diameter d_e or 50 mm was recommended for FRP stirrups in order to achieve a stirrup capacity of at least 50% of the strength parallel to the fibres, while using a tail length of $6d_e$ or 70 mm, whichever is greater,
- The strength at the bend of FRP stirrups should be taken as 40% of the strength parallel to the fibres,

- A proposed design procedure for predicting shear capacity of concrete beams reinforced with FRP stirrups was recommended for design code implementation at that time.

El-Sayed et al. (2007) conducted an experimental research to develop new CFRP stirrups as shear reinforcement for concrete members. The study focused on the reduction in the strength due to bending the FRP bar as well as the tail length extended beyond the bent portion. The research program consisted of two phases, the first phase investigated the mechanical properties of the stirrups, and the second one investigated the effect of stirrup diameter, embedment length (l_d), and anchorage of stirrups embedded in concrete. Afterwards two full-scale concrete beams were constructed and tested to study the behaviour of the CFRP stirrups in concrete beams. It was concluded that:

- The strength at the bend location was approximately 39% of the strength of the straight portion parallel to the fibre,
- Increasing the embedment length from $5d_b$ to $20d_b$ approximately doubled the stirrup capacity; where d_b is the bar diameter,
- No considerable increase in stirrup capacity was observed when increasing the tail length more than $6d_b$ and the lower bound capacity of bent part was found to be 45% of the ultimate longitudinal tensile strength of the straight portion,
- The stirrup size has insignificant effect on the performance of the stirrups,
- The performance of the stirrups in beam tests until failure fulfilled the design requirements of the available codes and guideline at this time.

Ahmed et al. (2008) investigated the shear performance of concrete beams reinforced with carbon FRP stirrups compared to those reinforced with steel stirrups. Test prototypes were designed according to CSA/S6-06 (*CSA* 2006). It was observed that the beam reinforced with CFRP stirrups had smaller crack widths at all loading stages despite that the CFRP stirrups had lower stiffness than the used steel stirrups. It was concluded that fulfilling the design stirrup strain limit at 2500 micro-strain, as specified by the CSA/S6-06 (*CSA* 2006) leads to a very conservative prediction of shear strength of reinforced concrete sections reinforced with FRP stirrups.

Ahmed et al. (2010-a) investigated the shear performance and strength of large-scale RC beams reinforced with GFRP stirrups compared to those reinforced with steel stirrups. The study considered different shear reinforcement ratios. The authors concluded that 1) at shear failure, the inclination angle of the shear crack in concrete beams reinforced with GFRP stirrups was in good agreement with the traditional 45-degree truss model; 2) using FRP stirrups with a strength ratio of bend-to-straight portion, $f_{bend} / f_{fuv} \geq 0.6$ enables using the capacity of the straight portions of the FRP stirrups in beam specimens; 3) lower ratios of f_{bend} / f_{fuv} will cause the bend strength to govern the stirrup whatever the tensile strength of the straight portion is; 4) limiting the ultimate strain (4000 micro-strain) of the FRP stirrup as specified by the ACI 440.1R-06 (*ACI* 2006) and the CSA/S6-06 (*CSA* 2006) enables a more accurate but still conservative prediction of the shear strength of concrete members reinforced with GFRP stirrups.

Ahmed et al. (2010-b) studied the performance of both CFRP and GFRP. The study consisted of both analytical and experimental phases. The experimental phase included testing seven large-scale T-beams: Three specimens were reinforced with CFRP stirrups, another three were reinforced with GFRP stirrups, and the last one was reinforced with steel stirrups. The software, Response-2000, which implements the modified compression field theory (MCFT), was used in the parametric phase of this study. The study concluded that:

- The bend strength of FRP stirrups didn't govern the shear capacity of the beams reinforced with FRP stirrups. Corresponding to an average strain equal to 4000 micro-strain in the FRP stirrups, the stresses at the bend ranged from 7% to 42% of the bend strength. This yielded a factor of safety greater than two between the actual stresses at the bend and the bend strength of FRP stirrups,
- There was a good agreement between the analytical results and the experimental ones in terms of predicting the shear capacity, mode of failure, and average stirrup strain. However, the software overestimated the shear crack width for the beams reinforced with FRP stirrups. This is referred to the crack spacing parameters implemented in the calculation procedure.

2.3.3 FRP Reinforced Concrete Columns under both Axial and Lateral Loads

Paramanantham and Daniali (1993) studied the behaviour of concrete columns reinforced with GFRP bars. The researchers developed equations for calculating column capacities under concentric and eccentric axial loads. For concentric loading, the axial capacity of the column (P_n) can be calculated as:

$$P_n = 0.85f_c^{'}(A_g - A_f) + 0.003E_f A_f \quad [2.1]$$

For columns under eccentric loading;

$$P_n = C_c + C_f - T_f \quad [2.2]$$

Where;

The force carried by concrete, $C_c = 0.85f_c^{'}\beta_1 ab$, [2.3]

The force carried by the bars in compression $C_f = 0.5A_f\varepsilon_c^{'}E_{fc}$, [2.4]

The force carried by the bars in tension $T_f = 0.5A_f\varepsilon_t E_f$ [2.5]

Where;

$f_c^{'}$: Concrete characteristic compressive strength,

A_g: Gross cross sectional area,

A_f: Area of FRP fibres,

E_f: Tensile modulus of elasticity of FRP bars,

β_1: Ratio of depth of rectangular compression block to depth to the neutral axis,

a: depth of equivalent rectangular stress block,

b: width of compression face of the member,

$\varepsilon_c^{'}$: Compressive strain of FRP bars,

E_{fc}: Compressive modulus of elasticity of FRP bars,

ε_t: Tensile strain of FRP bars,

Alsayed et al. (1999) investigated the influence of replacing longitudinal and transverse steel reinforcement by an equal volume of GFRP reinforcement on the behaviour of rectangular concrete columns. The effect of the reinforcement type on the axial capacity and deformation of the columns was studied. The experimental program consisted of testing 15 rectangular columns under concentric axial loads. Tests showed that up to 80% of the ultimate load, columns reinforced with longitudinal steel bars and GFRP ties and those reinforced with GFRP bars and ties exhibited similar behaviour to the columns that had no reinforcement at all. However, this might be attributed to the low modulus of elasticity of GFRP ties. Columns with steel ties showed higher resistance against axial shortening. It was concluded that the axial capacity of columns were reduced by 13% when using GFRP bars instead of steel bars, while when replacing steel ties with GFRP ties the capacity was reduced by 10%. In addition, they indicated that further research is still required to investigate the effect of reinforcement type on the columns behaviour.

Grira and Saatcioglu (1999) investigated the use of both steel and CFRP grids as stirrups for confinement of columns with longitudinal steel reinforcement. Several configurations of transverse reinforcement were tested under cyclic loading. The conclusion was that columns reinforced with CFRP stirrups had a comparable performance to that of columns reinforced with steel stirrups. The authors claimed that the use of grids in general provided almost uniform distribution of the confinement pressure along the column, without congesting the reinforcement cage. It was observed that the failure of the CFRP NEFMAC^{TM} grid-based stirrups occurred at the nodes, which are the weakest point of FRP grids.

Sharbatdar (2003) studied experimentally and analytically the behaviour of full-scale square columns and rectangular beams reinforced with CFRP bars and stirrups under seismic loading. Based on characterization testing, the used CFRP bars had compression strength and modulus of elasticity of 16-21% and approximately 20% of their corresponding tensile properties, respectively. Test results showed that columns with 30% of the confinement reinforcement required by the CSA-S806-02 had a brittle behaviour shortly after 2.0% lateral drift ratio. Also, those columns showed a 50% drop in flexural capacity at 3.0% drift ratio. On the other hand, columns that had 60% of the confinement reinforcement required by CSA-S806-02 showed increased deformability with lateral drift ratio up to 3.0% associated with approximately 23% strength degradation.

In the analytical part of that study, two types of axial load-bending moment interaction diagrams for columns were constructed using the plane-section analysis of FRP reinforced sections. The first type is governed by concrete compression failure (strain of 0.0035) or tensile rupture of FRP bars, whichever occurs first. The second type accounts for the confinement effect using the recorded strain level corresponding to the ultimate moment capacity obtained during testing. It was concluded that the analytical model was in good agreement with the recorded test results and resulted in safe prediction for the column capacity under eccentric loads. It was concluded also that concrete columns reinforced with CFRP bars and stirrups can develop limited inelastic deformability equal to 2/3 of the ductility levels observed in steel reinforced concrete columns at eccentricity

level of $0.25h$ to $0.30h$, where h is the column dimension parallel to the moment direction. Moreover, it was recommended that experimental and analytical studies utilizing FRP reinforced columns under different levels of concentric and eccentric monotonic and cyclic loading are still required.

2.3.4 Behaviour of Framed Structures under Seismic Loads

The research on the behaviour of the beam-column joints reinforced with FRP bars and stirrups is still in its early stages. A pioneer study, conducted by *Fukuyama et al.* (1995), explored experimentally and analytically the seismic performance of a half-scale three-storey concrete frame reinforced with aramid reinforcement in both longitudinal and transverse directions. The objective of this study was to set a seismic design philosophy that is applicable for such structures. Consequently, it was essential to verify this philosophy experimentally and analytically. In addition, the structural characteristics of FRP-reinforced concrete frames were compared with the conventional steel-reinforced ones.

Figure 2.6 shows schematic drawings of the frame specimen. Longitudinal reinforcement ratio of the beams was 0.64% and 0.48% at the bottom and the top, respectively. A reinforcement ratio of 1.47% was kept constant for the columns in all storeys. No hooks or lap splices for main reinforcement were used. Development of beam longitudinal reinforcement at the beam ends was achieved by using 200 mm beam stubs. Spiral shear reinforcement was provided to all members to avoid shear failure. Test results showed that the frame remained almost elastic with a stable behaviour up to a drift ratio level of

2.0%, then signs of concrete crushing appeared. Behaviour of the specimen can be identified with three stages. Stage 1, up to a drift ratio of 0.50%, represents the elastic range before cracking. Stage 2, between drift ratios of 0.50% and 2.0%, represents a stable plastic behaviour due to growth of cracking in members. Stage 3, drift ratios greater than 2.0%, represents unstable performance with major reduction in stiffness due to crushing of concrete.

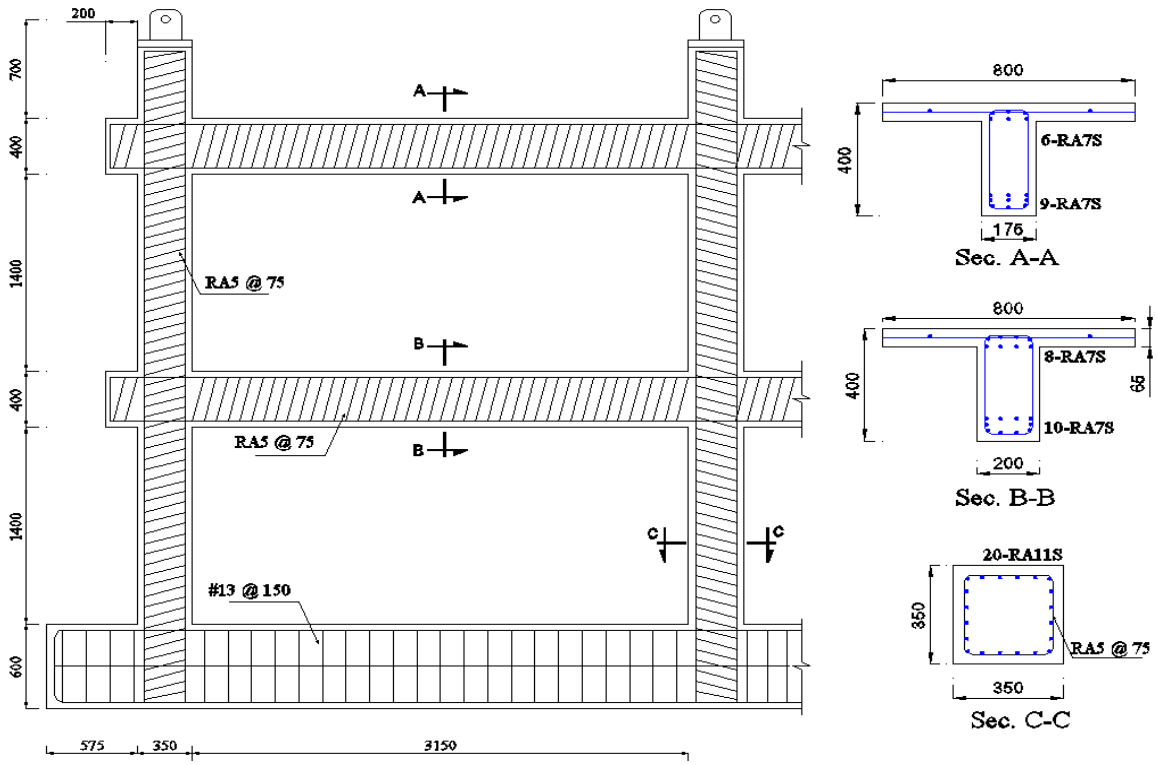

Figure 2.6: Frame details (Reproduced from *Fukuyama et al.* 1995)

The static elasto-plastic incremental method was used to analyze the load deformation relationship. The analysis overestimated the displacement probably because the joint panel deformations were ignored and the stiffness degradation ratio due to cracking was overestimated. This non-linear analysis was also performed considering the use of steel reinforcement in order to compare its results with the behaviour of the FRP reinforced

specimen. The comparison between the results of using the FRP and those of using steel reinforcement indicated that at a specific level of drift, the FRP-reinforced frame is stronger than its counterpart reinforced with steel. The researchers concluded that the small residual deformations occurred to the FRP-reinforced frame would result in minimum rehabilitation needs. Also, the investigation of the load-deformation relationship for a frame through a nonlinear incremental analysis is possible once the decay in member stiffness due to cracking and deformations of joints could be properly evaluated.

Fisher and Li (2003) adopted a new approach to avoid the formation of plastic hinges at the base of the first storey columns. The idea is based on reinforcing the column with FRP bars as longitudinal reinforcement and using the engineered cementitious composites (ECC) as a concrete mix. The reason of this combination is to utilize the relatively large flexural capacity and large deformations of FRP materials before failure to replace yielding (ductility) of steel bars. Four small-scale one-bay frames were constructed and tested. The beam measured 660 mm long, 100 mm wide and 150 mm deep, while the column height measured 635 mm with a cross section of 125 mm in depth and 100 in width. Reversal lateral displacement-controlled loading cycles were applied to the frame simulating seismic loading. The beam in all specimens was reinforced with steel bars while the column was reinforced with steel or FRP bars. The first frame was reinforced with steel bars as a control specimen. While in the second, third, and fourth frame, the column was reinforced with aramid FRP bars (AFRP), carbon FRP tendons

(CFRP), and CFRP bars, respectively. No shear reinforcement was used in these frames depending on the advanced mechanical properties of the ECC matrix (*Li* 1998).

Results showed that the steel reinforced specimen had the well-known elastic-plastic behaviour till failure at 5.0% drift ratio. For the other specimens, where column reinforced with FRP bars, cracks started first in the column member until 1.0% drift ratio then plastic hinge occurred at beam members at a range of 1.0 to 2.0% drift ratio. FRP reinforced specimens showed increasing strength with higher drift ratios till 5.0% drift ratio, however they have lower stiffness compared with steel-reinforced specimen. This is attributed to the lower modulus of elasticity of FRP materials.

It is worth to mention that the FRP reinforced frames had a residual displacement of approximately 50% of the one reinforced with steel. This is considered an advantage for FRP reinforced frames when further rehabilitation is required after surviving an earthquake event. With respect to the energy dissipation, at 2.5% drift ratio, the steel reinforced specimen dissipated an amount of energy almost 30 to 65% higher than what was dissipated by the FRP-reinforced specimens. It was concluded from this study that the effect of auto-adaptive stiffness modification might increase the period of the structure, consequently resulting in attracting lower base shear during earthquake loading. *Said and Nehdi* (2004) investigated the performance of GFRP reinforced exterior beam-column joints under cyclic reversal loads with respect to that of steel-reinforced one. Two beam-column joint prototypes were constructed and tested. The longitudinal reinforcement in the GFRP specimen was NEFMAC^{TM} G16 (201 mm^2 of cross-sectional

area), while the four-cells grid NEFMAC^{TM} G10 (77 mm^2 of cross-sectional area) was used as transverse reinforcement. The longitudinal reinforcement configuration was selected to provide the same flexural capacity of the control steel-reinforced specimen, thus inducing a comparable level of joint shear input. Test results showed that steel-reinforced specimen had approximately 23% higher total drift compared to the GFRP-reinforced specimen. Also, the dissipated energy by the steel reinforced specimen was approximately four times that dissipated by the GFRP-reinforced one. The authors concluded that to overcome the low energy dissipation of GFRP members, a combination of GFRP and steel reinforcing members may be used (i.e. outer frame members are reinforced with GFRP to address the corrosion problem, while the inner members are reinforced with steel to provide the frame with the required dissipation of energy). They also recommended that further experimental and analytical research is required to allow re-evaluation of design code provisions in order to address the low energy dissipation capacity of GFRP reinforced frames.

Sharbatdar et al. (2007) explored the seismic behaviour of three full-scale beam-column joint specimens reinforced with CFRP bars and grids as longitudinal and transverse reinforcement, respectively. The main studied parameters were the arrangement of longitudinal reinforcement and the grid spacing at the joint. Three full scale CFRP reinforced concrete beam-column joints were designed and tested. Specimens were designed according to the *CAN/CSA S806-02* (CSA 2002), *CAN/CSA A23.3-94* (CSA 1994), *CAN/CSA A23.3-04* (CSA 2004), and *ACI 440.1R-06* (ACI 2006) and the results of a previous research done by *Sharbatdar* (2003). During testing, columns were

subjected to a constant axial load of 20% of its axial capacity. Reversed cyclic loading was applied at the beam tip in order to simulate seismic loading. Test results showed that specimens had stable hysteresis behaviour up to 3.0% drift ratio followed by a gradual strength degradation caused by bar slippage and/or bar rupture. This study concluded the following:

- Specimens had a stable behaviour and remained almost elastic up to 3.0% drift ratio and the deformability of these elements is enough to suggest its ability to perform in seismic zones,
- A better deformable response of FRP reinforced concrete joints can be observed once the members are well confined and designed as over reinforced members, and
- The CSA/S806-02 requirements for column confinement showed a good agreement with the test results. No early or premature failures in the joints were observed.

Hasaballa et al. (2011) investigated the feasibility of using GFRP reinforcement in reinforced concrete structures subjected to earthquake loading. Four full-scale exterior T-shaped beam-column joint prototypes were constructed and tested under simulated seismic loading. Test parameters included the type of longitudinal and transverse reinforcement (using steel and GFRP bars) as well as the anchorage detailing of beam longitudinal reinforcement (using bent bars and straight bars). The steel reinforced specimen was the control specimen. The second specimen was reinforced with GFRP bent bars and steel stirrups. The other two specimens were totally reinforced with GFRP

bars and stirrups; however a 200-mm beam stub was added in one of them to increase the anchorage length of beam longitudinal bars. In this study, the authors proposed a design procedure for beam-column joints reinforced with GFRP bars and stirrups (Hasaballa 2009). The study concluded that:

- GFRP bars are capable of resisting tension‑compression cycles with no strength degradation.
- GFRP reinforced joints can be designed to satisfy both strength and deformability requirements of earthquake-resistant structures.
- Further investigations are required regarding the bond behaviour of the GFRP bars subjected to reversed-cyclic loading. However, if bond‑slip failure can be avoided, the GFRP reinforced joint can reach 5.0% drift capacity under reversed cyclic loading.
- The local yielding of steel reinforcement can be substituted with the large-elastic deformations exhibited by GFRP bars to reach large drift ratio.
- The steel reinforced specimen was able to dissipate energy in the order of 2 to 3 times that of the GFRP specimens
- The residual strains in the GFRP flexural reinforcement at the 4.0% drift ratio were much lower than in steel specimen. This can be beneficial in a way that the joint will regain its original shape after removing the loads, thus requiring minimum amount of repair after surviving a seismic loading event, if any.

Mady et al. (2011) studied the seismic behavior of concrete beam-column joints reinforced with GFRP bars and stirrups. Five full-scale exterior T-shaped beam-column

joint prototypes were constructed and tested under simulated seismic load conditions. The main test parameters included the types of reinforcement (steel and GFRP) and the longitudinal reinforcement ratio in terms of multiples of balanced ratio. The study concluded that:

- The tested GFRP-reinforced concrete beam-column joints reached 4.0% drift capacity safely with insignificant damage
- The low modulus of elasticity for the GFRP reinforcement led to reducing the stiffness of the tested specimens, which resulted in attracting lower forces at the same drift ratio compared to steel reinforced specimen.
- After reaching 4.0% drift ratio, the measured residual strains in the GFRP longitudinal beam reinforcement were negligible; comparing to much larger residual strains exhibited in the steel-reinforced joint. This indicates that GFRP-reinforced joints would remain functional with a minimum required amount of repair after surviving an earthquake event.
- For the GFRP-reinforced joints, as long as the joint is safe under the applied shear stresses, increasing the beam reinforcement ratio can enhance the ability of the joint to dissipate the seismic energy through utilizing the inelastic behavior of concrete.

CHAPTER 3

PROPOSED DESIGN PROCEDURE

3.1 BACKGROUND

Proper seismic performance of reinforced concrete frames is achieved when these frames have the ability to avoid a sudden collapse mechanism during strong earthquakes and absorb seismic energy through inelastic deformations. To keep the integrity of the moment resisting frames against seismic loads, the available design codes for steel reinforced concrete structures (*CSA/A23.3-04* and *ACI 318-08*) are mainly based on the following requirements;

- Seismic resisting frames should be ductile enough to dissipate the energy resulted from earthquake loads. Consequently, member confinement plays an important rule to provide the required ductility of the frame. Ductile frames can be designed for lower seismic forces.
- Strong column-weak beam design concept shall be applied to allow the formation of plastic hinges in beams rather than in the columns, as shown in Figure 3.1(a). Gravity loads are transferred to the foundations through the columns. Therefore, excessive damage to the column shall be prevented to avoid collapse due to high levels of P-Δ effect, as shown in Figure 3.1(b). Strong column-weak beam approach is achieved when the summation of columns' flexure strength is larger than the summation of the beams' flexure strength which connected to the same joint.

- The connection between the beam and the column should be kept elastic and safe against shear to ensure the integral behaviour of the frame under loading.

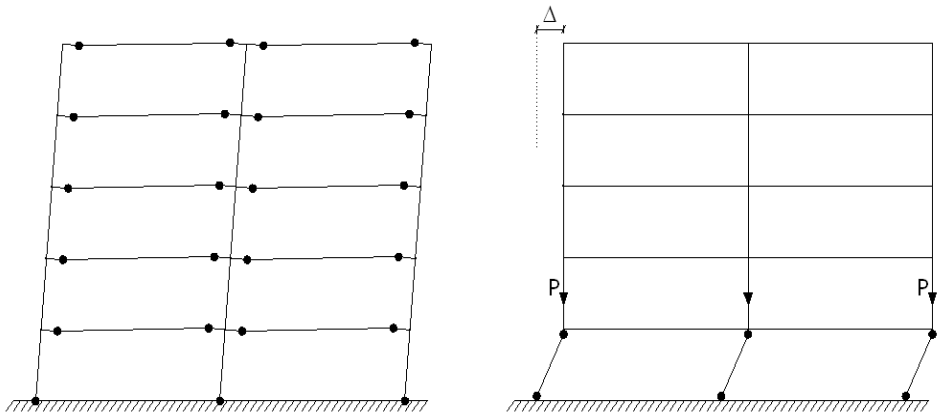

(a) Formation of plastic hinges in beams (b) Formation of plastic hinges at columns

Figure 3.1: Possible plastic hinges locations

The key to the design of ductile moment resisting frames is that the connections and columns must remain elastic throughout the load history to ensure lateral stability of the structure. If the connections or columns exhibit stiffness and/or strength deterioration with reversed cyclic loading, collapse due to P-Δ effects or to the formation of a shear-storey mechanism may be unavoidable.

Park and Paulay (1975) specified the basic requirements for a satisfactory performance of a joint in moment resisting frame as follows:

- The service load performance exhibited by the joint should be in similar quality to that of the joined members.
- The joint should safely sustain the most critical load combinations that the adjoining member could be subjected to.

- The strength of the structure should not be governed by the strength of the joint; this means that failure of the joint should not occur before formation of plastic hinges in the adjoining members.
- Ease of construction should be targeted to avoid reinforcement congestion while providing the necessary reinforcement for the joint elastic performance.

3.2 ANALYSIS OF FORCES

In 1978, *Paulay et al.* adopted an analytical model for the internal straining actions affecting the exterior beam-column joints subjected to earthquake loading. The external forces and the resulted internal actions around the joint are presented at the free body diagram shown in Figure 3.2. A rational estimation of the induced forces can be achieved using the basic static equilibrium relationships where;

$$\text{Column shear force } (V_{col}) = \frac{M_b + 0.5\, t\, V_b}{l_c} \qquad [3.1]$$

where;

M_b: Flexure moment applied at beam end,

V_b: Shear force applied at beam end,

t: Column depth,

l_c: The column height, center-to-center, between beams above and below the joint,

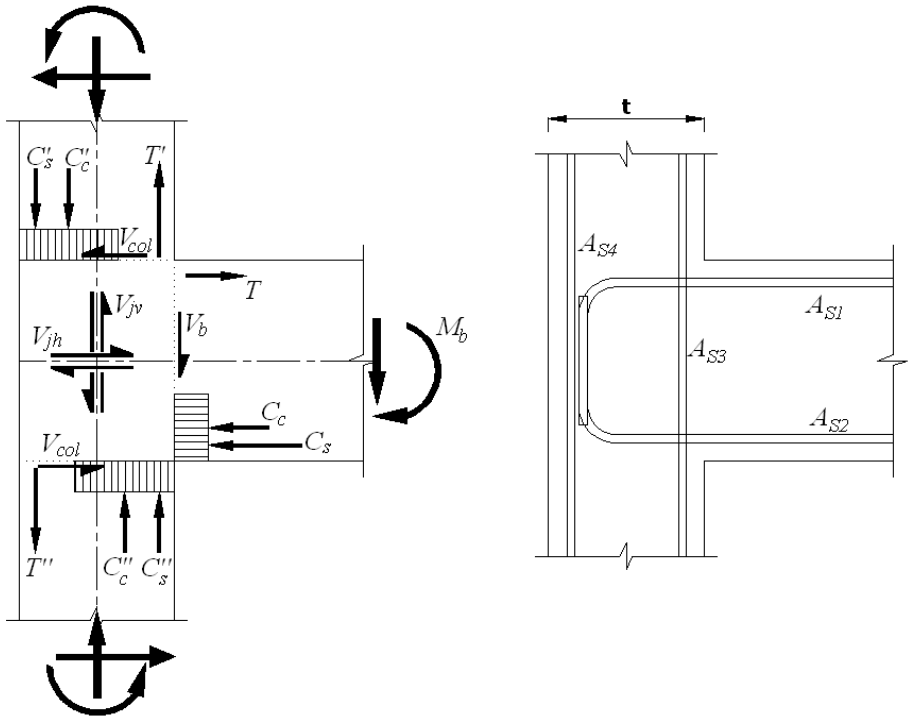

Figure 3.2: Free body diagram of an exterior beam-column joint in a multi-storey frame

(Reproduced from *Paulay et al.* 1978)

The Horizontal shear force in the joint core $(V_{jh}) = T - V_{col}$ [3.2]

Where;

T: The probable tensile force in the beam tension side which equal to $1.25\ f_y A_{s1}$.

f_y: Specified yield strength of steel reinforcement,

A_{s1}: Beam longitudinal steel reinforcement located as shown in Figure 3.2.

The vertical shear force in the joint core $(V_{jv}) = T' - T'' - V_b$ [3.3]

where;

T', T'': are the internal forces exhibited in the column as shown in Figure 3.2.

3.3 PROPOSED DESIGN PROCEDURE FOR BEAM-COLUMN JOINTS REINFORCED WITH GFRP BARS AND STIRRUPS

Type-2 beam-column joint is defined as the connection of members that are required to dissipate energy through reversals of deformation into the inelastic range and designed according to the seismic provisions. Therefore, the following section introduces a proposed design procedure for GFRP reinforced beam-column joint. This procedure was followed in designing the test specimens investigated in this study. At the time when this study started in 2010, the CSA/S806-02 (CSA 2002) has no seismic provisions for designing Type-2 beam-column joints. Due to lack of research and experimental data in this area, the current CSA/S806-12 (CSA 2012) provided only limited provisions regarding the placement of transverse reinforcement along the beams and the columns. Therefore, the proposed procedure in this chapter includes design for flexure, shear, and stability of the joint in the light of the available steel reinforced concrete design codes and FRP design guide lines, whichever is applicable. Meanwhile, the impacts of the seismic provisions implemented in the CSA/S806-12 and found to be relevant to this study are discussed in the following sections. It should be noted that this design procedure was applied to the design of test specimens as explained in Appendix A.

3.3.1 Design for Flexure

The FRP reinforcing bars under tensile forces behave in linear elastic manner up to failure. The compressive strength of FRP reinforcing bars is known to be smaller than the tensile strength and, hence, this compressive strength is often ignored in the analysis and design of FRP flexural members (*CSA* 2012 and *ACI-440* 2006). Flexural strength

relationship of FRP-RC members is determined using assumptions consistent with those applicable for steel RC members as follows:

1- Plane sections remain plane under bending, so that the strain in the concrete and reinforcement is proportional to the distance from the neutral axis (compatibility of strains);
2- The failure strain of concrete in compression is 0.0035;
3- FRPs are linear elastic up to failure;
4- Perfect bond exists between the reinforcement and the surrounding concrete;
5- The tensile strength of concrete can be neglected; and
6- Compressive strength of FRP bars is neglected.

The design for flexure according to CSA/S806-02 (*CSA* 2002), Clause 8.2.1, requires that all FRP reinforced concrete sections shall be designed in such a way that failure of the section is initiated by crushing of the concrete in the compression zone. This requirement can be waived in the current version of the CSA/S806-12 (*CSA* 2012), Clause 8.2.2, if the factored flexural resistance of the section is greater than 1.6 times the effect of the factored loads.

All concrete sections in this study were designed according to the CSA/S806-02 (*CSA* 2002), Clause 8.2.1, following the concrete crushing failure, for two reasons explained as follows:

1- At the time when this study started in 2010, the CSA/S806-02 (*CSA* 2002) was the available version and the CSA/S806-12 (*CSA* 2012) has not been released at that time.

2- The concrete crushing mode of failure provides better deformability for the concrete sections (based on the inelastic behaviour of concrete before crushing) compared to the brittle (sudden) failure due to rupture of FRP bars.

Compression failure mode occurs when the outermost fibre of concrete reaches the ultimate compressive strain for the concrete ($\mathcal{E}_{\text{cu}}$= 0.0035) before the outermost fibre of FRP reinforcement reaches its ultimate tensile strain ($\mathcal{E}_{\text{frp,u}}$). To avoid the brittle tension failure mode, the reinforcement ratio which is provided in the section (ρ_{frp}) should be larger than the balanced reinforcement ratio ($\rho_{b,frp}$). The balanced reinforcement ratio ($\rho_{b,frp}$) is the reinforcement ratio at which the concrete reaches its ultimate strain ($\mathcal{E}_{cu}$= 0.0035) simultaneously when the FRP bars reach its ultimate tensile strain ($\mathcal{E}_{frp,u}$). It can be expressed by:

$$\rho_{b,frp} = \alpha_1\beta_1 \ \frac{\phi_c}{\phi_{frp}} \ \frac{f'_c}{f_{frp,u}}\left(\frac{\varepsilon_{cu}}{\mathcal{E}_{cu}+\mathcal{E}_{frp,u}}\right) = \frac{A_{frp}}{b_w\, d} \qquad [3.16]$$

The above equation is applicable provided that placing of reinforcing bars will be no more than in one layer, otherwise each layer should be designed according to its corresponding tensile stress, where;

$\rho_{b,frp}$: FRP balanced reinforcement ratio (%)

ϕ_{frp}: FRP reinforcement resistance factor

$f_{frp,u}$: Ultimate tensile strength of FRP reinforcement

ε_{cu}: Ultimate compressive strain of concrete

$\varepsilon_{frp,u}$: Ultimate tensile strain of FRP bars

A_{frp}: Area of FRP longitudinal reinforcement

The concept of strong column-weak beam which is required in the CSA/A23.3-04 (*CSA* 2004) for steel reinforced moment resisting frames may be applied for the design of GFRP reinforced concrete moment resisting frames since the CSA/S806-02 did not address this issue. The CSA/A23.3-04 (*CSA* 2004) requires that $\sum M_{nc} \geq \sum M_{pb}$. Regarding the behaviour of GFRP bars as longitudinal flexural reinforcement, GFRP bars have linear elastic behaviour with no yielding or strain hardening as in steel reinforcement. Consequently, it can be assumed that the probable resistance of a steel reinforced beam at the CSA/A23.3-04 (*CSA* 2004) corresponds to a nominal resistance of a GFRP reinforced beam. This nominal resistance is computed based on the actual tensile stresses exhibited at the GFRP longitudinal reinforcement when a compression failure in concrete takes place. It is worth mentioning that Clause 12.7.5.1, CSA/S806-12 (*CSA* 2012) implemented the strong column-weak beam concept by requiring a flexural strength ratio greater than one. However, it does not specify how much greater than one it should be. Accordingly, the design expression for FRP frames might be:

$$\sum M_{nc} \geq \sum M_{nb} \rightarrow \text{Where } \phi_{frp} = \phi_c = 1 \qquad [3.17]$$

It is established that the axial load applied on the FRP reinforced concrete column has a significant influence on the flexural strength of its cross section (*Choo et al.* 2006). To account for the axial load effect, axial-moment interaction diagram should be established to obtain the flexure strength of the column under the specified axial load.

It should to be mentioned that neither the CSA/S806-12 (*CSA* 2012) nor the ACI-440-06 (*ACI* 2006) has guidelines for axial-moment interaction diagrams for FRP-reinforced concrete columns. The axial-moment interaction behaviour of FRP-RC columns may exhibit failure before the strength interaction reaches a pure bending condition. This failure is classified as brittle-tension failure. It happens when the outermost FRP reinforcing bars reach the ultimate strain in tension ($\varepsilon_{frp,u}$) before the outermost concrete fibre reaches the limiting strain in compression (ε_{cu}= 0.0035). FRP-RC columns are susceptible to this type of failure when low reinforcement ratios are provided. To avoid having this kind of brittle tension failure, a reinforcement ratio (ρ) larger than the balanced ratio (ρ_b) should be provided in the column.

3.3.2 Design for Shear

The design for shear is carried out according to CSA/S806-02 with some exceptions. The CSA/S806-02 (Clause 8.4.4) determines the total shear resistance of the cross section reinforced with FRP in both longitudinal and transverse directions as given in Clause 8.4.4.4 by:

$$V_r = V_c + V_{sF} \leq V_c + 0.6\lambda\phi_c\sqrt{f_c'}b_w d \qquad [3.18]$$

where;

V_r: Shear resistance of the section

V_c: Contribution of concrete in shear resistance

V_{sf}: Contribution of transverse reinforcement in shear resistance

ϕ_c: Resistance factor for concrete

λ : Factor to account for concrete density

f_c' : Specified compressive strength of concrete

b_w: Minimum effective web width

d: Distance from the extreme compression fibre to the centroid of longitudinal tension force

The contribution of concrete in shear resistance (V_c) when providing at least the minimum amount of shear reinforcement is given by:

$$V_c = 0.035\lambda\phi_c \left(f_c' \rho_w E_F \frac{V_f}{M_f} d\right)^{1/3} b_w\, d \qquad [3.19]$$

where;

ρ_w: FRP longitudinal reinforcement ratio (%)

E_F: Elastic modulus of longitudinal FRP reinforcement

V_f: factored shear force at section under consideration

M_f: factored bending moment at section under consideration

Provided that V_c does not exceed the limit of $0.2\lambda\phi_c\sqrt{f_c'}b_w d$ and shall not be taken less than $0.1\lambda\phi_c\sqrt{f_c'}b_w d$, the value ($\frac{V_f}{M_f}\ d$) should not be taken as larger than 1.0 (Clause 8.4.4.4, CSA/S806-02). It should be noted that the CSA/S806-02 is more conservative than the CSA/S806-12 with respect to the design of shear where the concrete contribution in the CSA/S806-02 is less than in Clause 8.4.4.5 in the CSA/S806-12. This in turn results in slightly larger transverse reinforcement area.

However, recent studies on GFRP reinforced beam-column joints showed a considerable amount of deformability in beam section at column face (*Hasaballa et al.* 2011, *Mady et al.* 2011). The concrete deformations in this section reduce the contribution of concrete in resisting shear forces applied on the beam section. Therefore, it is conservatively assumed no contribution of concrete in resisting shear forces in beam section (i.e. $V_c = 0$). Meanwhile, contribution of concrete can be in effect when calculating shear capacity of column section. Similar approach is also allowable by CSA/A23.3-04 for steel-reinforced beam-column joints. Accordingly, the shear force applied to the beam section is resisted by the transverse reinforcement only (V_{sF}). For shear design of beam section Equation 3.18 is proposed to be:

$$V_r = V_{sF} \qquad [3.20]$$

Then, the minimum amount of transverse reinforcement given by Clause 8.4.5.2, CSA/S806-02

$$A_{v,min} = \frac{0.3\sqrt{f_c'}\ \ b_w S}{f_{Fh}} \qquad [3.21]$$

Where;

A_v: Area of shear reinforcement perpendicular to the axis of a member within the distance *S*

S: Spacing of shear reinforcement, measured parallel to the longitudinal axis of the member

f_{Fh}: design stress of the transverse FRP reinforcement = $\phi_{frp} * f_{frp,u}$, or the stress corresponding to a strain of ***0.004*** in the FRP, or the stress corresponding to the failure of corners, hooks, bends, and laps, whichever is least.

It should be noted that the CSA/S806-12 is far less stringent in determining the minimum shear reinforcement as per Clause 8.4.5.1 which requires that

$$A_{v,min} = \frac{0.07\sqrt{f_c'}\ b_w S}{0.4 f_{Fu}} \qquad [3.22]$$

Where f_{Fu} shall not be taken greater than 1200 MPa or the stress corresponding to a strain of **0.005** in the FRP stirrups.

The comparison between Equation [3.22] and Equation [3.21] shows that the CSA/S806-02 requires minimum shear reinforcement approximately double what is required by the CSA/S806-12.

Based on the research done by *Shehata et al.* (1999), the ISIS manual No.3-2007 (*ISIS Canada* 2007) provides two expressions to calculate the strength of the stirrups based on

the stirrup configurations. Equation 10.1 in ISIS manual No.3 accounts for the radius of the bent and the embedment length as follows,

$$F_{Fh}\text{: Smaller of} \begin{cases} \left(0.4 + 0.015\frac{l_{frpd}}{d_e}\right) f_{frp,u} & [3.23] \\ \left(0.05\frac{r_b}{d_b} + 0.3\right) f_{frp,u} & [3.24] \end{cases}$$

where;

l_{frpd}: FRP stirrup tail length measured after the bent part

d_e: Effective bar diameter

r_b: Radius of bent portion of FRP stirrup

Then the contribution of the FRP shear reinforcement V_{sF} is given by Clause 8.4.4.6, CSA/S806-02

$$V_{sF} = \frac{0.4\,\phi_F\,A_v\,f_{frp,u}\,d}{S} \qquad [3.25]$$

The next step in the design is to check the confinement requirement in columns. As per CSA/S806-02, Clause 12.7, Reinforced concrete columns in seismic regions should be confined with transverse reinforcement of at least what is given by:

$$A_{Fh} = 14\, s\, h_c \frac{f_c^{'}}{f_{Fh}} \left(\frac{A_g}{A_c} - 1\right) \frac{\delta}{\sqrt{K_c}} \frac{P_f}{P_{ro}} \qquad [3.26]$$

where; $\frac{P_f}{P_{ro}} \geq 0.2$, $\left(\frac{A_g}{A_c} - 1\right) \geq 0.3$

$K_c = 0.15 \sqrt{\frac{h_c}{s} \frac{h_c}{s_l}}$ ➔ For rectilinear transverse reinforcement

where, h_c: Cross-sectional dimension of column core

A_g: Gross area of section

A_c: Cross-sectional area of the core of a compression member measured to the centreline of the perimeter hoop or spiral

δ: Design lateral drift ratio (i.e., horizontal drift / building height)

P_f: Factored axial load

P_{ro}: factored axial load resistance at zero eccentricity

K_c: Confinement coefficient

S_l: Spacing of tie legs or the spacing of grid openings in the cross-sectional plane of the column

It should be noted that the CSA/S806-12 uses similar expression to that in Equation [3.26] to calculate the transverse reinforcement required for confinement; however, it results in lower reinforcement area as discussed later in Chapter 9.

The spacing of transverse reinforcement should not exceed the limit allowed by Clause 12.7.2, CSA/S806-02 which is expressed by:

1. One-quarter of the minimum member dimension;
2. 150 mm;

3. 6 times the diameter of the smallest longitudinal bar; or
4. The requirements of Clauses 8.4.3.2 and 8.4.3.3. (i.e. shear design for sections).

It should be noted that the CSA/S806-12 adopted the same provisions regarding the maximum spacing of the transverse reinforcement as per Clause 12.7.5.2 which refers back to Clause 12.7.3.5.

3.3.3 Joint Resistance and Applied Shear Force

It is well established that the amount of transverse reinforcement in a joint should not be less than the amount provided in the column to which the joint is connected. Although CSA/S806-02, and CSA/S806-12, Clause 12.7, provide confinement provision for columns in seismic regions, however, it has no provisions to check the shear resistance of joints when this confinement provision is fulfilled. This is attributed to the lack of research and experimental data in this area. On the other hand, the CSA A23.3-04 (CSA 2004), for steel reinforced concrete, limits the factored shear resistance of joints in terms of $\sqrt{f_c'}$ as per Clause 21.5 as follows;

a. $2.2\lambda\phi_c\sqrt{f_c'}A_j$ ➔ For confined joints,
b. $1.6\lambda\phi_c\sqrt{f_c'}A_j$ ➔ For joints confined on three faces or on two opposite faces,
c. $1.3\lambda\phi_c\sqrt{f_c'}A_j$ ➔ For other joints.

Where; A_j is the Cross-sectional area of the joint, f_c' is the characteristic compressive strength of concrete.

Therefore, one of the main objectives of this study is to fill this gap in the CSA/S806 and establish an expression for the shear capacity of exterior beam-column joint that takes $\sqrt{f_c'}$ into consideration through testing specimens under different shear stress levels in the joints.

CHAPTER 4

EXPERIMENTAL PROGRAM

4.1 INTRODUCTION

Anchorage of reinforcement bars depends mainly on the surface condition of the bar as well as detailing condition at the bar end. For deformed GFRP reinforcement, anchorage is achieved by mechanical bond due to concrete bearing on ribs along the bar length. However, for sand-coated GFRP bars anchorage is achieved by means of chemical bond and frictional resistance against slip. Regarding the detailing condition of the bar end, anchorage can be achieved by means of bearing on bent portions (i.e. hooks) or even by bearing on anchorage heads attached to the far end of the bar.

Proper anchorage of beam longitudinal reinforcement is essential for reinforced concrete beam-column joints subjected to seismic loading to ensure full interaction between reinforcement and concrete. In general, reinforcement slippage in interior beam-column joints is not as critical as in exterior joints due to continuity of longitudinal reinforcement in both sides of flexural critical sections at beam ends. On the other hand, due to the discontinuity nature of the beam, exterior beam-column joints may exhibit anchorage loss of beam longitudinal reinforcement embedded in the joint when sufficient development length is not provided. In most cases, development length required for longitudinal beam reinforcement in exterior beam-column joints may be larger than the column depth required in the direction of bar development. In steel reinforced concrete frames, standard 90-degree hooks are commonly used to anchor beam longitudinal bars within an exterior

beam-column joint. However, the drawback of using this approach with FRP reinforced beam-column joints is the tensile strength reduction of FRP bent bars due to fibre bending as explained before in Chapter 2. Also in case of GFRP-headed bars the slip of end bearing-head from the bar should be considered. Accordingly, detailing of beam longitudinal bars embedded into exterior beam-column joint was investigated in this research study to achieve anchorage of beam longitudinal reinforcement.

When full anchorage of beam longitudinal reinforcement is achieved, the flexural capacity of the beam section is developed. As discussed before in Chapter 3, Section 3.2, the tensile and compressive forces developing the flexural capacity of the beam section on the column face generate horizontal shear forces in the joint (V_{jh}). As explained earlier in the literature review presented in Chapter 2, it has been well established that the structural behaviour of exterior beam-column joints is influenced by many factors. These factors importantly include, but not limited to, flexural strength ratio, ***shear stress in the joint***, confinement reinforcement in the joint, ***characteristic concrete strength***, presence of axial load on the column and geometry of the joint with respect to the attached structural members. Moreover, the Canadian codes CSA/S806-02 (*CSA* 2002) and CSA/S806-12 (*CSA* 2012) in Clause 12.7 specify the amount and placement of FRP stirrups required for confinement of columns located in seismic regions. However, due to the lack of research, it doesn't specify or evaluate the shear capacity of the beam-column joint when the joint is confined according to this clause, Clause 12.7. Accordingly, the shear capacity of exterior beam-column joints fulfilling Clause 12.7 was investigated experimentally and analytically in this research.

The experimental program includes design, construction, and testing of ten full-scale test prototypes representing an exterior joint in a multi-storey RC structure where moment resisting frames are the major seismic force resisting system. In a frame structure, during an earthquake, inertia forces are transferred from one floor to another through the columns. In most cases, columns are subjected to opposite and approximately equal horizontal forces and moments at both column ends. As a result, the points of contra-flexure occur very close to the column mid-height and at mid-span of the beams as shown in Figure 4.1. Consequently, test prototypes simulate isolated beam-column joints from an end bay between the assumed points of contra-flexure located at the mid-height and mid-span of the column and the beam, respectively as shown in Figure 4.2.

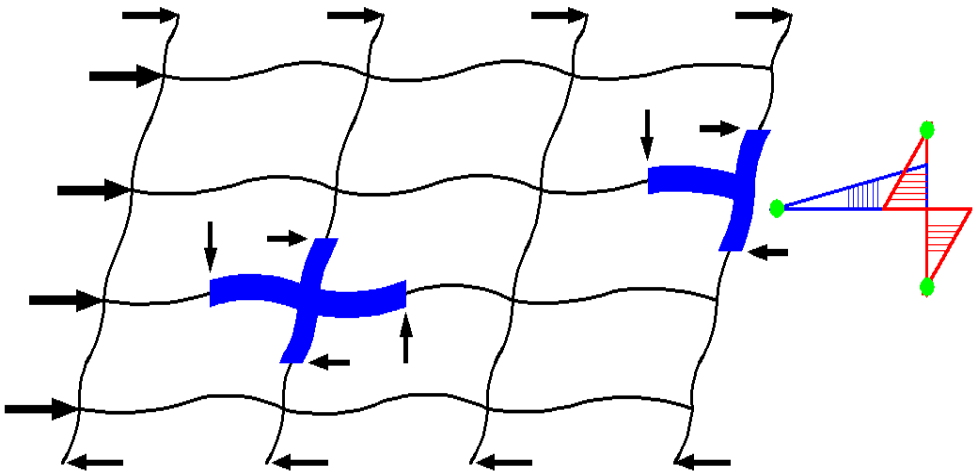

Figure 4.1: Straining actions under lateral loads

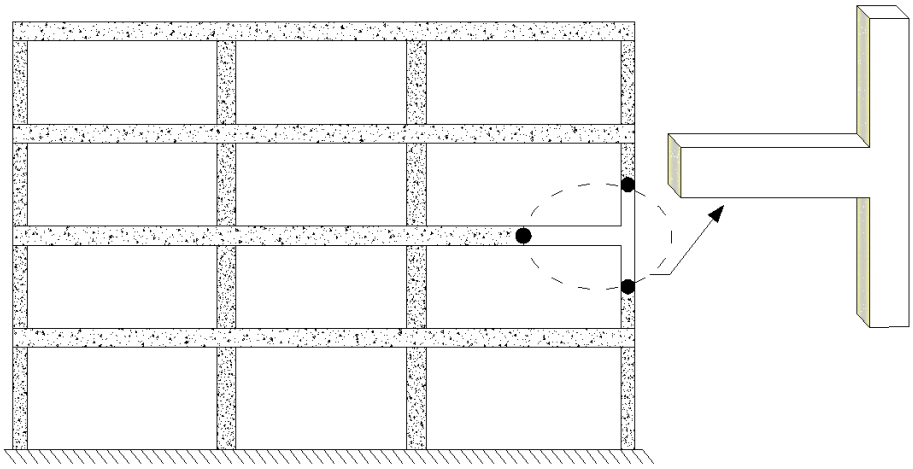

Figure 4.2: Simulated test specimen

4.2 DETAILS OF THE EXPERIMENTAL PROGRAM

The experimental phase consists of two series (I and II) to study the seismic behaviour of ten exterior beam-column joint specimens as shown in the test matrix in Figure 4.3. Series (I) was designed to study the anchorage detailing of longitudinal beam reinforcement inside the joint. Combinations of two anchorage schemes of beam longitudinal reinforcement (bent bars and headed bars) along with two different bar surface-conditions (sand-coated surface and deformed/ribbed surface) were investigated. This combination of variables resulted in four specimens (I-B-S, I-B-D, I-H-S, and I-H-D) as shown in Figure 4.3. It should be noted that 10-M steel stirrups were used as a transverse reinforcement in all Series (I) specimens.

Series (II) was designed to study the influence of concrete strength on the behaviour when the joint is subjected to various levels of shear stresses. Two different concrete strengths; normal strength (30 MPa) and high strength (60 MPa), in combination with

three different shear stress levels in joint were studied; Low shear level ($0.70\sqrt{f'_c}$), moderate shear level ($0.85\sqrt{f'_c}$), and high shear level ($1.0\sqrt{f'_c}$). Combinations of the two concrete strengths and the three shear stress levels generated six specimens as shown in Figure 4.3. These six specimens were divided into two groups based on the concrete strength; the first group consisted of three specimens (II-30-0.7, II-30-0.85, and II-30-1.0) using normal strength concrete (30-MPa) and subjected to the three shear stress levels discussed above. Similarly, the second group consisted of three specimens (II-60-0.7, II-60-0.85, and II-60-1.0) subjected to the same shear stress levels applied in the first group, while using higher concrete strength (60-MPa).

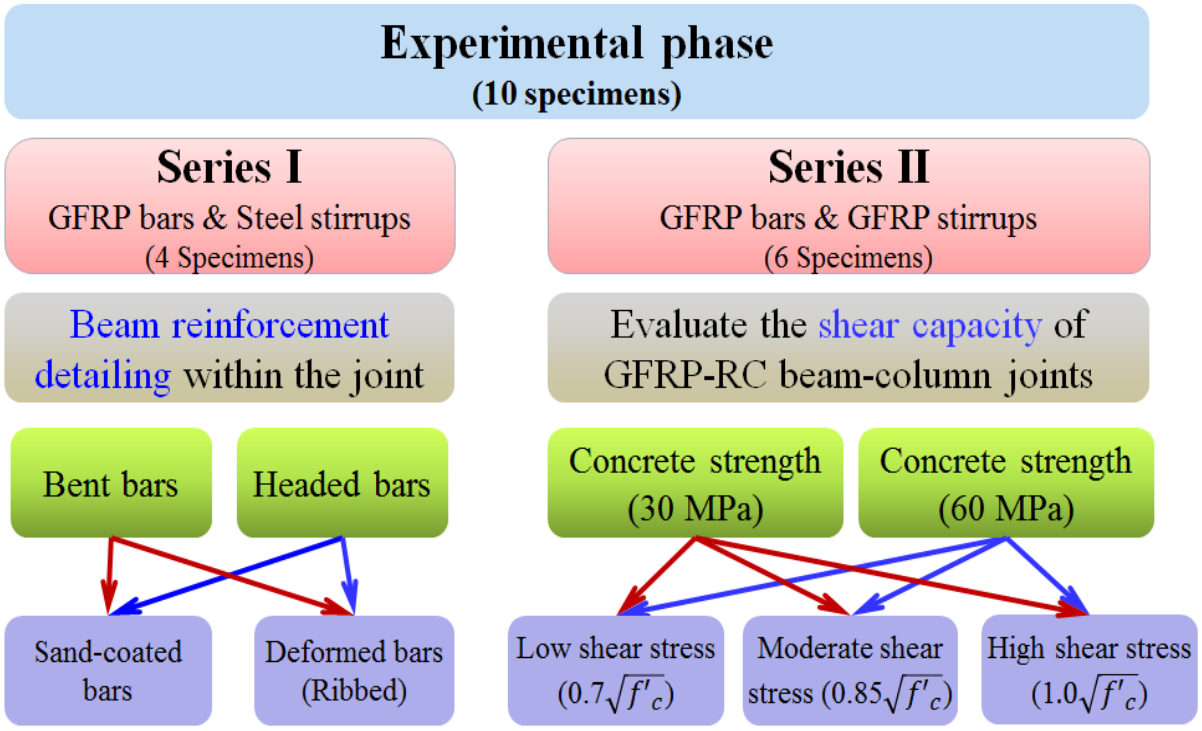

Figure 4.3: Schematic diagram for test matrix

The experimental phase of this study including design of specimens, materials, reinforcement details, construction, instrumentation, and testing procedure are discussed in the following sections.

4.2.1 Design Procedure

The design of the GFRP-reinforced concrete specimens was carried out according to the proposed design procedure discussed earlier in Chapter 3. Specimens were designed to follow the strong column-weak beam concept with a column-to-beam flexural strength ratio larger than 1.4. The deformable concrete crushing failure in the beam section near the column face was considered by providing a longitudinal reinforcement ratio, in the beam, larger than the balanced one. Detailed design calculations of two specimens are presented in Appendix A.

4.2.2 Material Properties

4.2.2.1 *Concrete*

All test specimens were constructed using normal-weight, ready-mixed concrete with a targeted 28-day concrete compressive strength of 30 and 60 MPa and a maximum aggregate size of 20 mm. All test specimens were cast and wet-cured in the laboratory for 7 days as shown in Figure 4.4. On the day of testing, the concrete compressive strength was determined based on the average value of compressive tests carried out on standard cylinders of 100 x 200 mm. The average compressive strength of the concrete on the day of testing for Series (I) and (II) specimens is shown in Tables 4.3 and 4.4, respectively.

Figure 4.4: Specimens curing in the structural laboratory

4.2.2.2 *Reinforcement*

Three types of reinforcing bars were used in this study; CSA grade 400 deformed black steel bars, deformed GFRP COMBAR™ (*Schoeck Canada Inc.* 2014) and sand-coated GFRP V-ROD™ (*Pultrall Inc.* 2014). The mechanical properties of the GFRP reinforcement were determined experimentally, as shown in Tables 4.1 and 4.2, according to CSA/S806-02 (*CSA* 2002).

Table 4.1: Mechanical properties of sand-coated bars

Configuration	Bar designation	Diameter (mm)	Area (mm^2)	Tensile strength (MPa)	Elastic Modulus (GPa)	Ultimate strain (micro-strain)
Straight	#5	15.92	198	1310	64	20470
Bent	#6	19.05	285	910	50	18200

Table 4.2: Mechanical properties of deformed/ribbed bars

Configuration	Bar designation	Diameter (mm)	Area (mm^2)	Tensile strength (MPa)	Elastic Modulus (GPa)	Ultimate strain (micro-strain)
Straight	Φ 16	16	200	1100	60	18333
Bent	Φ 20	20	314	900	45	20000

4.2.3 Test Specimens

The overall concrete dimensions of the test specimens are shown in Figure 4.5. The beam measured 2100-mm long, 350-mm wide and 450-mm deep, while the column measured 3650-mm long with a 350-mm wide and 400-mm deep. Specimens were reinforced with GFRP bars as longitudinal reinforcement for the beam and the column.

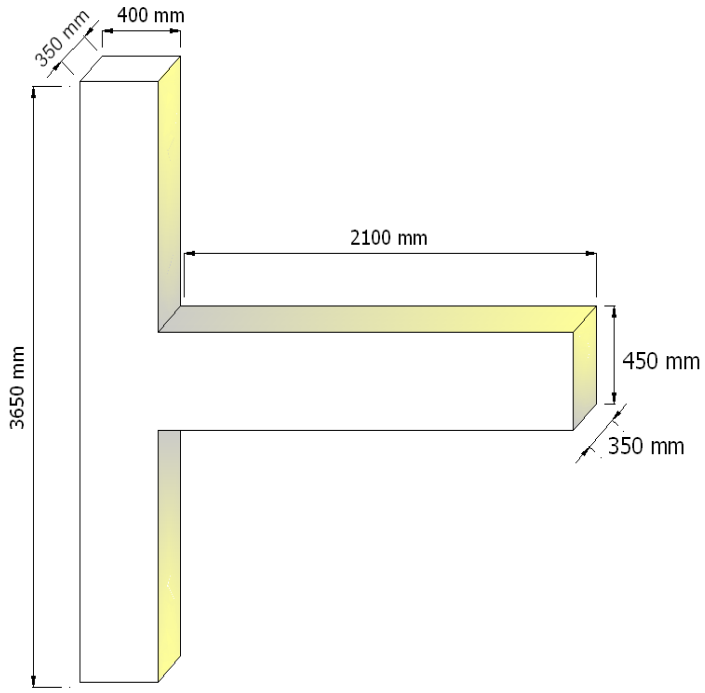

Figure 4.5: Typical concrete dimensions of test specimens

4.2.3.1 *Series (I) specimens*

Series (I) consisted of four specimens (I-B-S, I-B-D, I-H-S, and I-H-D) and was designed to study the anchorage schemes of beam longitudinal GFRP reinforcement imbedded inside the joint under seismic loads. The specimens in this series were identified where the first character stands for the series name (I); the second represents the anchorage scheme; (B) for bent bars and (H) for headed bars, while the third term represents the bar

surface-condition; (S) for sand-coated and (D) for deformed ribbed bars. For example, Specimen I-H-S belongs to Series (I), headed bars were used as beam longitudinal reinforcement, and the surface condition of the longitudinal reinforcement is sand-coated. It should be noted that specimens constructed with bent bars, namely I-B-S and I-B-D, will be collectively referred to as Specimens I-B-x; while those constructed with headed bars, namely I-H-S and I-H-D, will be collectively referred to as Specimens I-H-x. Similarly, regardless the anchorage scheme, specimens with similar bar-surface condition will be referred to as I-x-S and I-x-D.

All specimens in Series (I) were reinforced with GFRP bars as longitudinal reinforcement and steel stirrups as transverse reinforcement. The Reinforcement details and photos of Series (I) specimens are shown in Figures 4.6 and 4.7, respectively. The flexural design of the specimens was carried out according to the CSA/S806-02 (*CSA* 2002), while the required amount of transverse steel reinforcement was calculated based on CSA/A23.3-04 (*CSA* 2004). The design characteristics of Series (I) specimens are shown in Table 4.3. It should be mentioned that the values of stresses and strengths in Table 4.3 were calculated based on the values of concrete strength on the day of testing of each specimen. The reinforcement details and photos of reinforcement cages before concrete casting of specimens are shown in Figures 4.8 and 4.9, respectively.

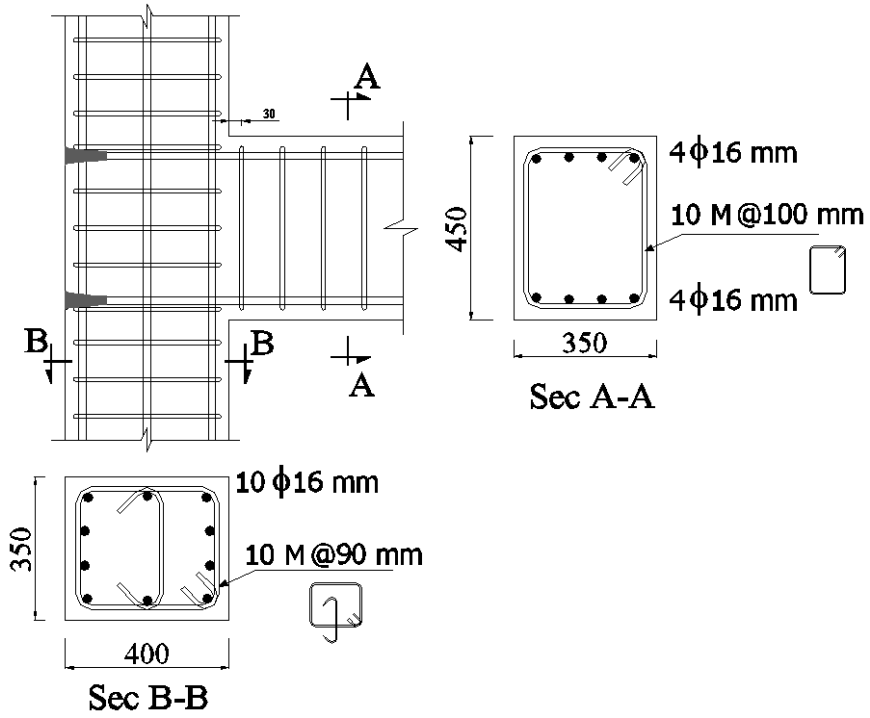

(a) Specimens I-H-D

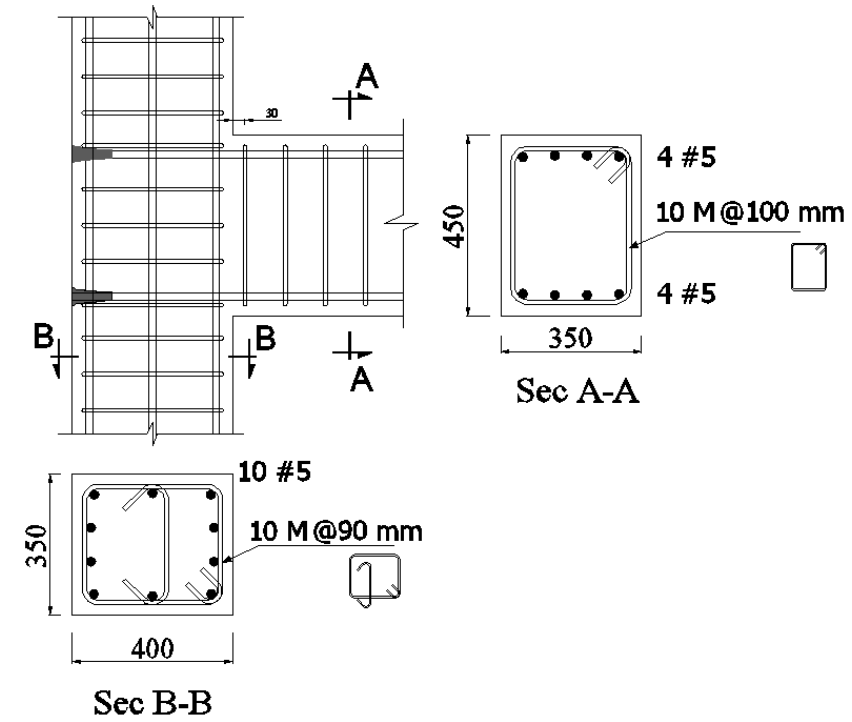

(b) Specimens I-H-S

Figure 4.6: Reinforcement details of Series (I) specimens (continued)

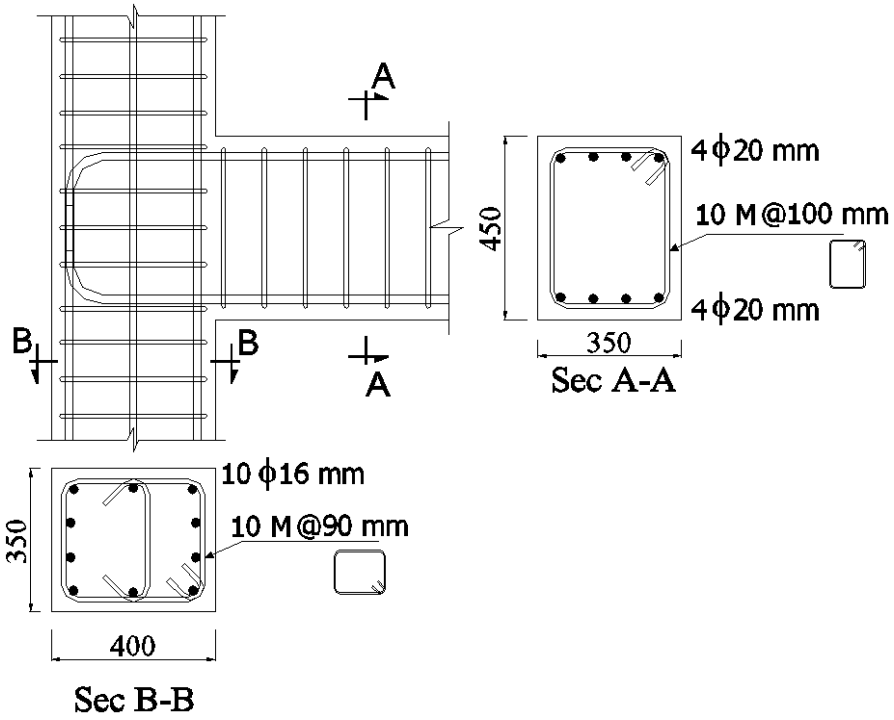

(c) Specimens I-B-D

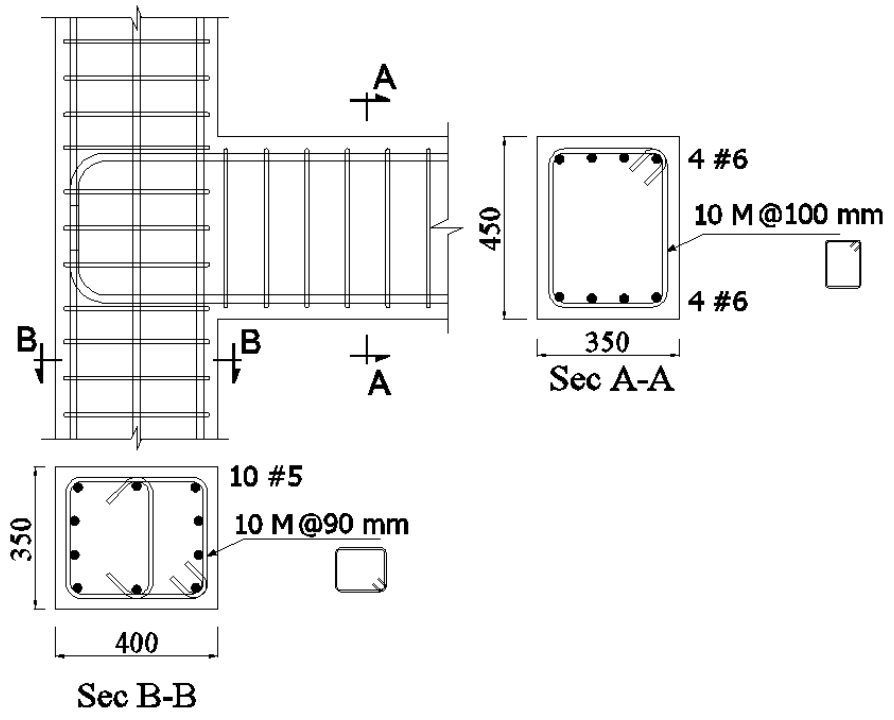

(d) Specimens I-B-S

Figure 4.6: Reinforcement details of Series (I) specimens

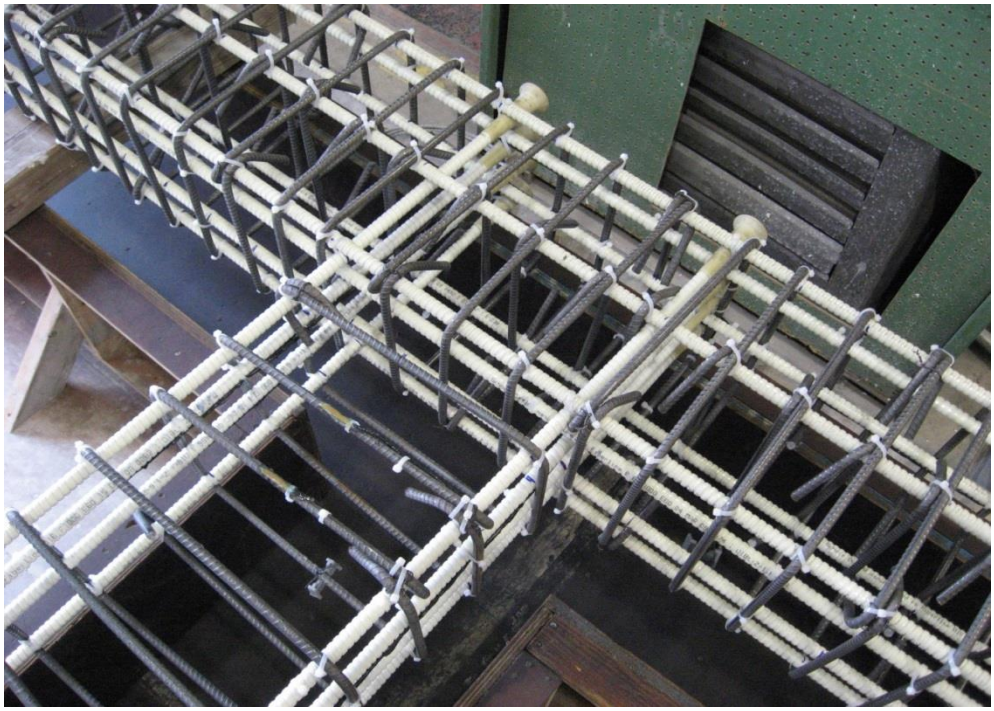

(a) Specimen I-H-D

(b) Specimen I-H-S

Figure 4.7: Photos of reinforcement configuration of Series (I) specimens (continued)

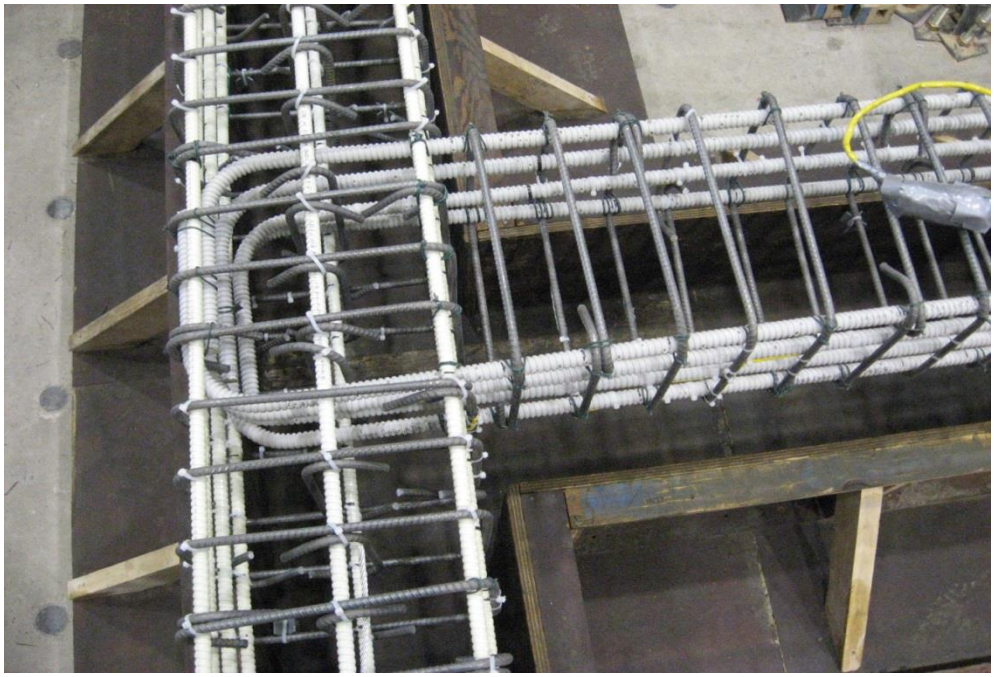

(c) Specimen I-B-D

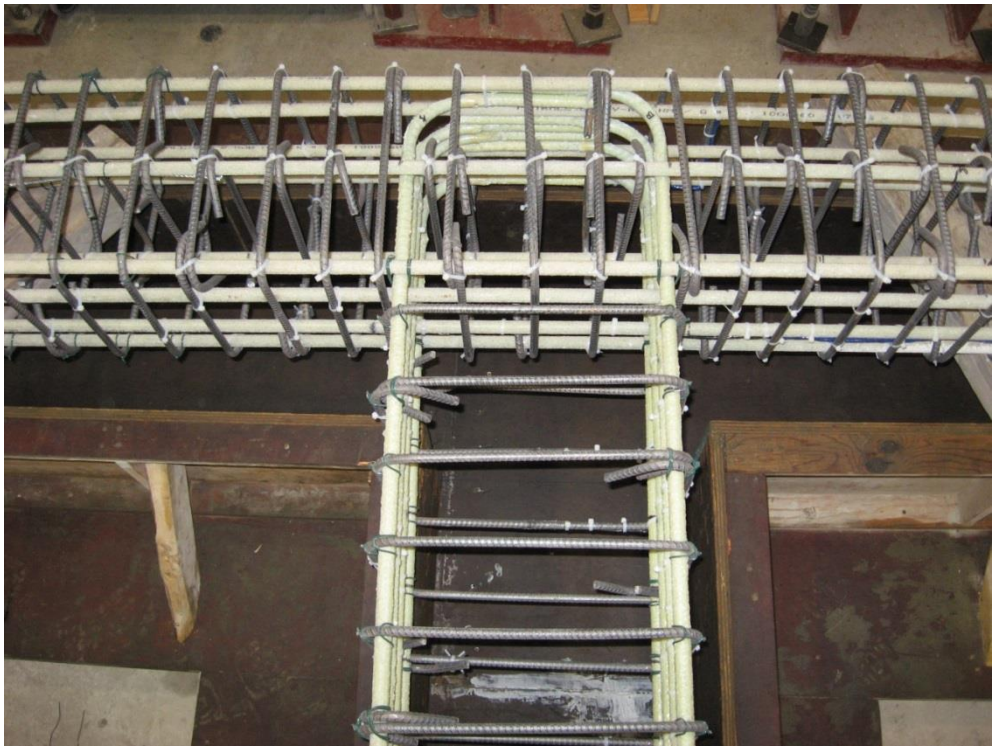

(d) Specimen I-B-S

Figure 4.7: Photos of reinforcement configuration of Series (I) specimens

Table 4.3: Design characteristics of Series (I) specimens

		Series (I)			
	Specimen ID	**I-H-D**	**I-B-D**	**I-H-S**	**I-B-S**
Beam	* No. of bars T&B	4ϕ16	4ϕ20	4ϕ16	4ϕ20
	Bar surface	Deformed		Sand coated	
	End Anchorage	Headed bars	Bent bars	Headed bars	Bent bars
	** ρ_{frp}/ρ_{bal}	1.78	2.14	1.84	1.65
	Calculated Bar stress (MPa)	800	595	937	685
	Flexural capacity (kN.m)	232	271	274	284
Column	No. of bars	10 ϕ 16		10 ϕ 16	
	Applied axial load (kN)	650		650	
	+ Flexural capacity (kN.m)	185	206	223	221
	Transverse reinforcement.	10M steel stirrup		10M steel stirrup	
	Spacing (mm)	90		90	
Overall	Flexural strength ratio	1.59	1.52	1.63	1.56
	Joint shear stress (MPa)	4.09	4.78	4.77	5.21
		$0.74\sqrt{f'_c}$	$0.79\sqrt{f'_c}$	$0.75\sqrt{f'_c}$	$0.83\sqrt{f'_c}$
	Conc. strength (MPa)	30.5	36.5	40.5	39.8
	Failure mode	Compression failure		Compression failure	

Notes:

*** No. of bars T&B:** refers to the number of bars used at each the top and bottom side of the beam, see figures of reinforcement details;

**** ρ_{frp}/ρ_{bal} :** is the ratio between the provided reinforcement ratio to the balanced reinforcement ratio;

+ Flexural capacity: is calculated using the applied axial load in the moment-axial interaction diagram of the column.

4.2.3.2 *Series (II) specimens*

Series (II) consisted of six specimens (II-30-0.70, II-30-0.85, II-30-1.0, II-60-0.7, II-60-0.85, and II-60-1.0). It was designed to study the shear capacity of the joints and the influence of concrete strength on the overall structural behaviour under seismic loading. Three different levels of shear stresses in the joint ($0.70\sqrt{f'_c}$, $0.85\sqrt{f'_c}$, and $1.0\sqrt{f'_c}$) and two concrete strengths (30 MPa and 60 MPa) were investigated. Series (II) specimens were reinforced with GFRP bars as longitudinal reinforcement and GFRP stirrups as transverse reinforcement.

The specimens in this series were identified where the first character stands for the series name (II); the second represents the concrete strength; (30) for 30 MPa concrete strength, and (60) for 60 MPa concrete strength. The third term represents the γ factor for shear stress in the joint as a multiple of $\sqrt{f'_c}$ where f'_c is the concrete strength in MPa unit. For example, Specimen II-60-0.85 is a specimen belongs to Series (II), concrete strength is 60 MPa, and the shear stress in the joint is $0.85\sqrt{f'_c}$ MPa. It should be mentioned that specimens constructed with the lower strength concrete, namely II-30-0.7, II-30-0.85, and II-30-1.0, will be referred to as Specimens II-30-xx; while those constructed with higher concrete strength namely II-60-0.70, II-60-0.85, and II-60-1.0, will be referred to as II-60-xx. Similarly, specimens subjected to the same level of shear stress in the joint will be referred to as II-xx-0.70, II-xx-0.85, and II-xx-1.0.

The design for longitudinal and transverse reinforcement was carried out according to the CSA/S806-02 (*CSA* 2002). The amount of beam longitudinal reinforcement was selected

and designed such that the tensile forces developed in the bars can apply the required level of horizontal shear stresses required to be investigated in the joint. Table 4.4 summarizes the design characteristics of each specimen in Series (II). It should be mentioned that the values of stresses and strengths in Table 4.4 were calculated based on the values of concrete strength on the day of testing. The reinforcement details and photos of cages before concrete casting of Series (II) specimens are shown in Figures 4.8 and 4.9, respectively.

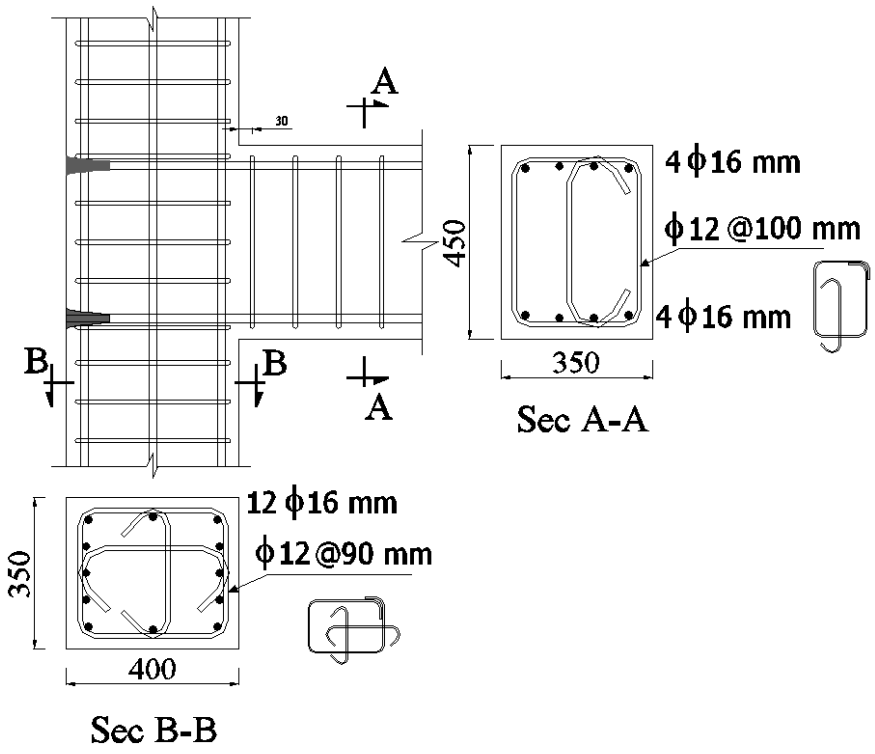

(a) Specimen II-30-0.70

Figure 4.8: Reinforcement details of Series (II) specimens (continued)

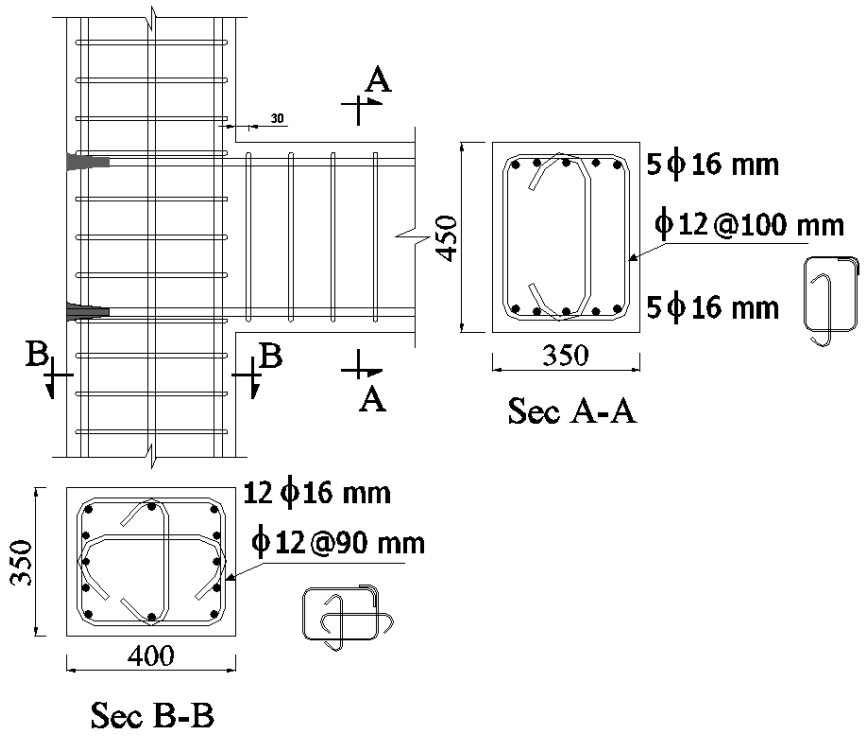

(b) Specimen II-30-0.85

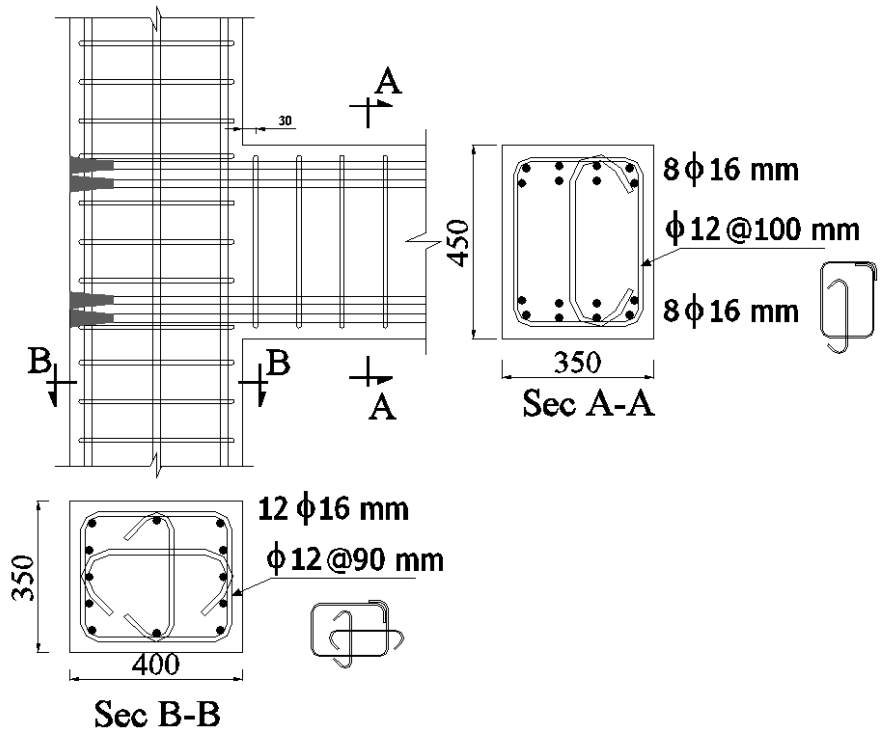

(c) Specimen II-30-1.0

Figure 4.8: Reinforcement details of Series (II) specimens (continued)

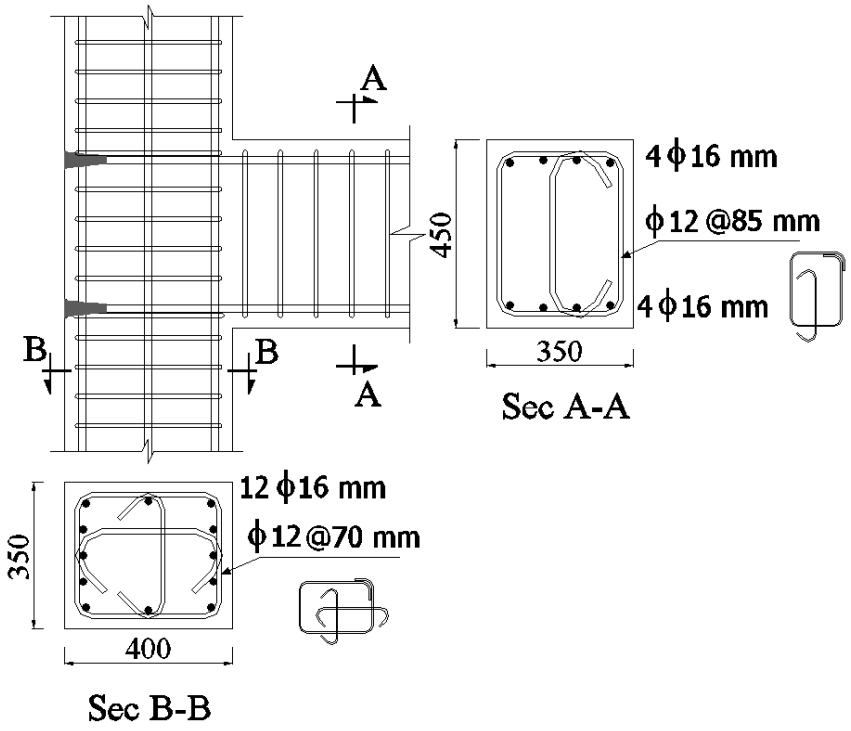

(d) Specimen II-60-0.70

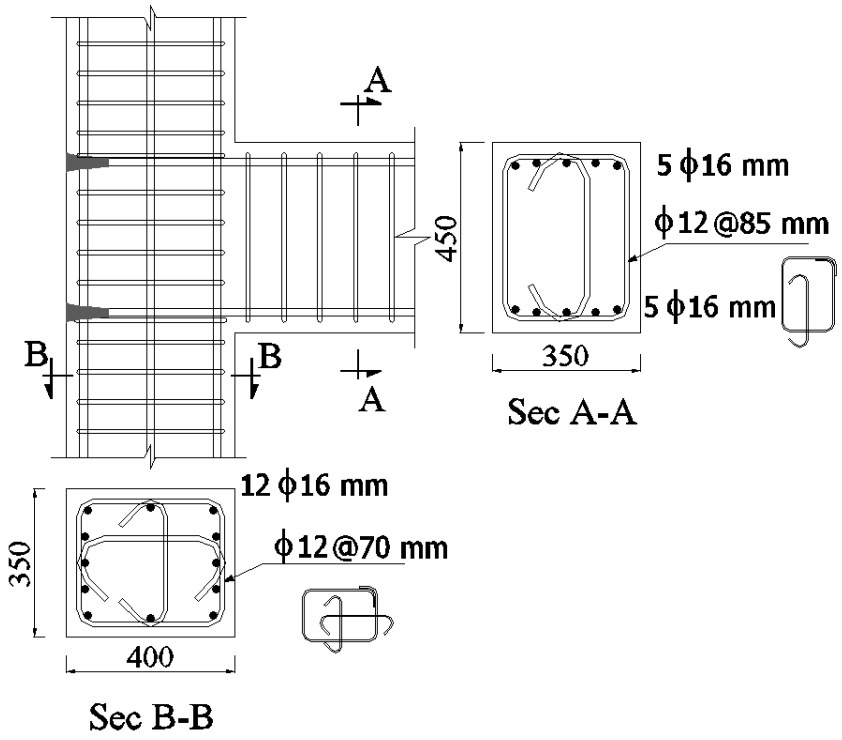

(e) Specimen II-60-0.85

Figure 4.8: Reinforcement details of Series (II) specimens (continued)

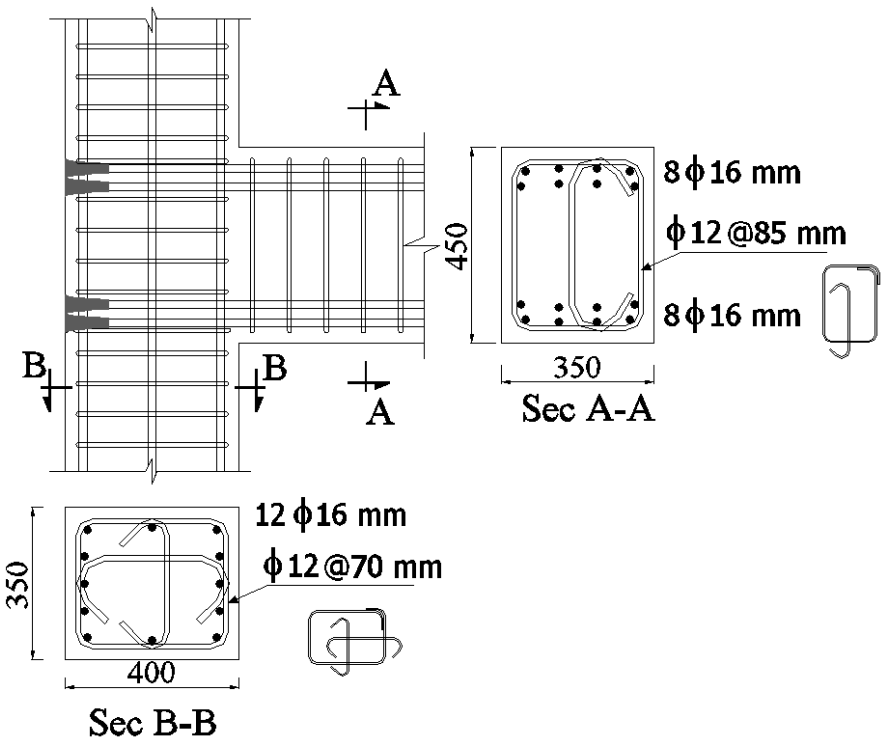

(f) Specimen II-60-1.0

Figure 4.8: Reinforcement details of Series (II) specimens

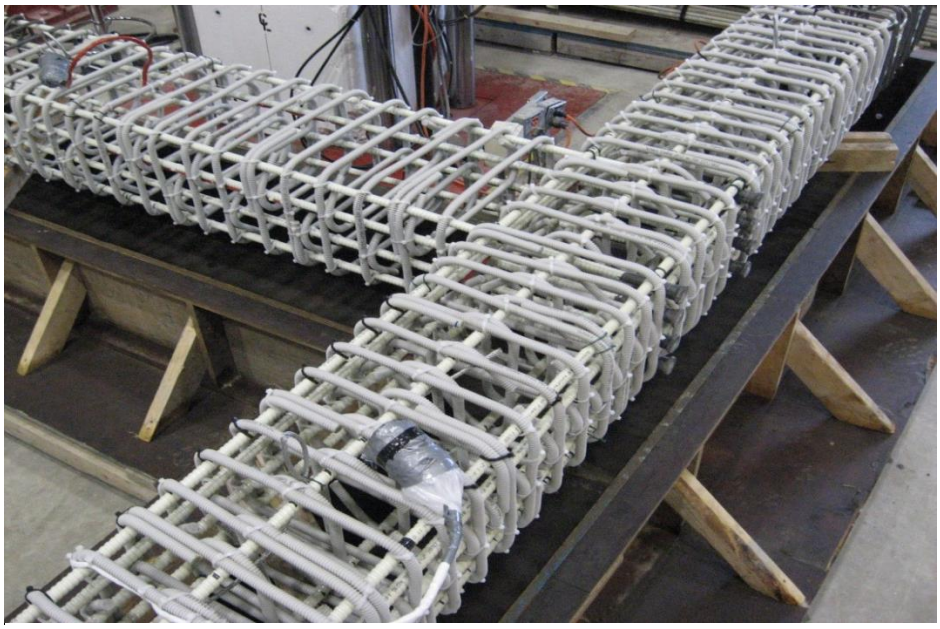

(a) Specimen II-xx-0.7

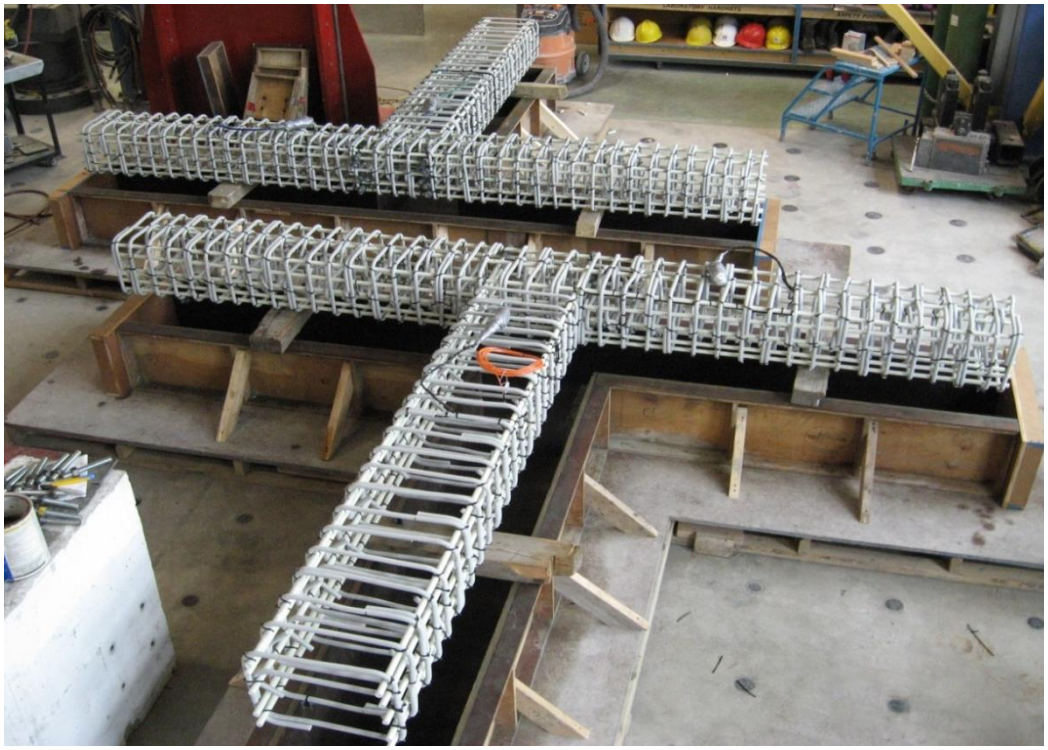

(b) Specimen II-xx-0.85 and Specimen II-xx-1.0 before concrete casting

Figure 4.9: Photos of reinforcement cages of Series (II) specimens

Table 4.4: Design characteristics of Series II specimens

		Series (II)					
	Specimen ID	**II-30-0.70**	**II-30-0.85**	**II-30-1.0**	**II-60-0.70**	**II-60-0.85**	**II-60-1.0**
Beam	* No. of bars T&B	4ϕ16	5ϕ16	8ϕ16	4ϕ16	5ϕ16	8ϕ16
	Bars configuration	one row	one row	2 rows (4+4)	one row	one row	2 rows (4+4)
	End Anchorage	Headed bar			Headed bar		
	** ρ_{frp}/ρ_{bal}	1.5	2.09	3.31	1.16	1.42	2.38
	Calculated Bar stress (MPa)	884	728	600 & 538	1008	900	712 & 643
	Flexural capacity (kN.m)	260	262	309	300	332	376
Column	No. of bars	12 ϕ 16			12 ϕ 16		
	Applied axial load (kN)	650			800		
	+ Flexural capacity (kN.m)	225	205	216	267	272	272
	Transverse reinforcement. (GFRP)	3 branches ϕ 12 mm (each direction)			3 branches ϕ 12 mm (each direction)		
	Spacing (mm)	90			70		
Overall	Flexural strength ratio	1.73	1.56	1.40	1.78	1.64	1.45
	Joint shear stress (MPa)	4.52	4.66	5.86	5.15	5.80	7.0
		$0.73\sqrt{f'_c}$	$0.82\sqrt{f'_c}$	$0.98\sqrt{f'_c}$	$0.72\sqrt{f'_c}$	$0.80\sqrt{f'_c}$	$0.97\sqrt{f'_c}$
	Conc. strength (MPa)	37.9	32.6	35.6	51.3	52.6	52.6
	Failure mode	Compression failure			Compression failure		

Notes:

* **No. of bars T&B:** refers to the number of bars used at each the top and bottom side of the beam, see figures of reinforcement details;

** ρ_{frp}/ρ_{bal} **:** is the ratio between the provided reinforcement ratio to the balanced reinforcement ratio;

+ **Flexural capacity:** is calculated using the applied axial load in the moment-axial interaction diagram of the column.

4.2.4 Test Set-up

All specimens were tested while the column was lying horizontally and the beam is standing vertically; 90-degree rotated position from the actual condition. The cyclic load was applied at the tip of the beam as shown the schematic drawing in Figure 4.10. A fully dynamic actuator, 1000 kN capacity and 500 mm stroke, was positioned horizontally against a rigid RC reaction wall. The actuator is tied to the tip of the beam to apply the simulated seismic loading scheme. Also, 1000 kN capacity hydraulic jack was positioned horizontally at one of the column ends at the centre of the column cross section. A constant axial compression force of approximately 15% of $A_c f_c'$; where A_c is the column cross-sectional area, and f_c' is the concrete strength, was applied to the column during testing.

A heavy strong reaction steel frame was pre-stressed to the strong floor at the other end of the column to sustain the column reaction against the hydraulic jack load. The two ends of the column were restrained against both vertical and horizontal displacements meanwhile their rotations were allowed (hinged boundary conditions). The column was restrained in the vertical direction over two roller supports, one at each end. Each end was tied down to the strong floor to prevent the vertical displacements. The column axial load was secured to be at the center of the cross section during the entire test through two steel hinges located between the column ends and both the hydraulic jack and reaction frame. Two heavy steel plates, 40-mm thick each, were fixed to the column faces at both ends (using steel threaded anchors embedded in concrete while casting) to prevent concentration of stresses on concrete. Photos of the test setup are shown in Figure 4.11.

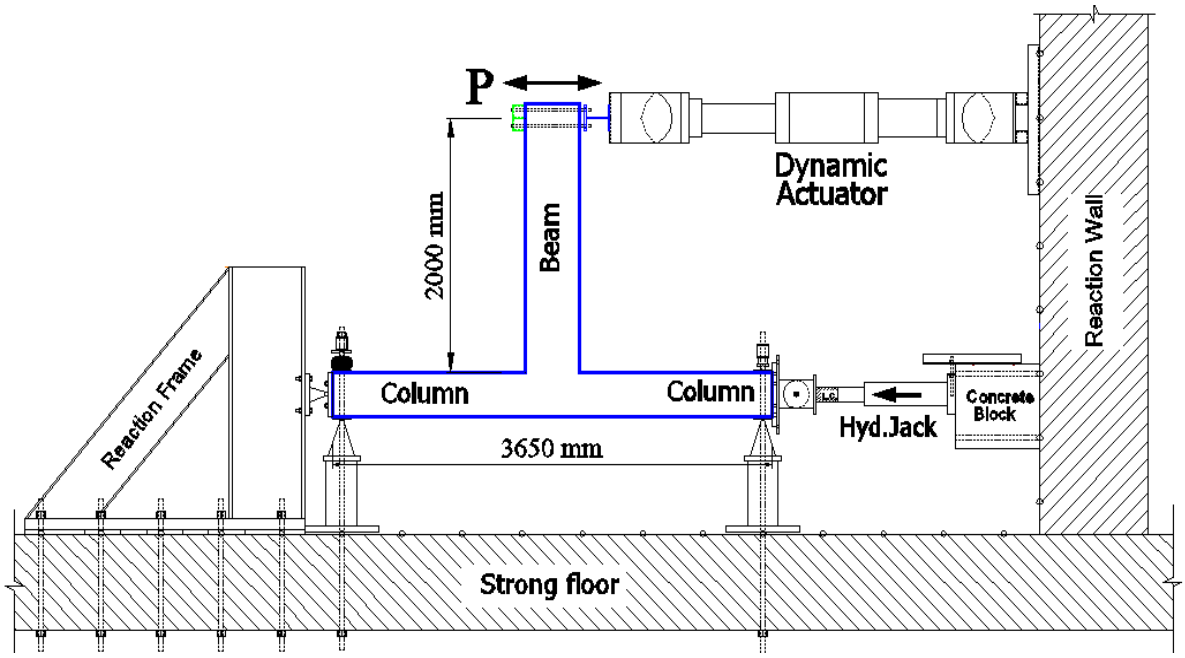

Figure 4.10: Schematic drawing for test set-up

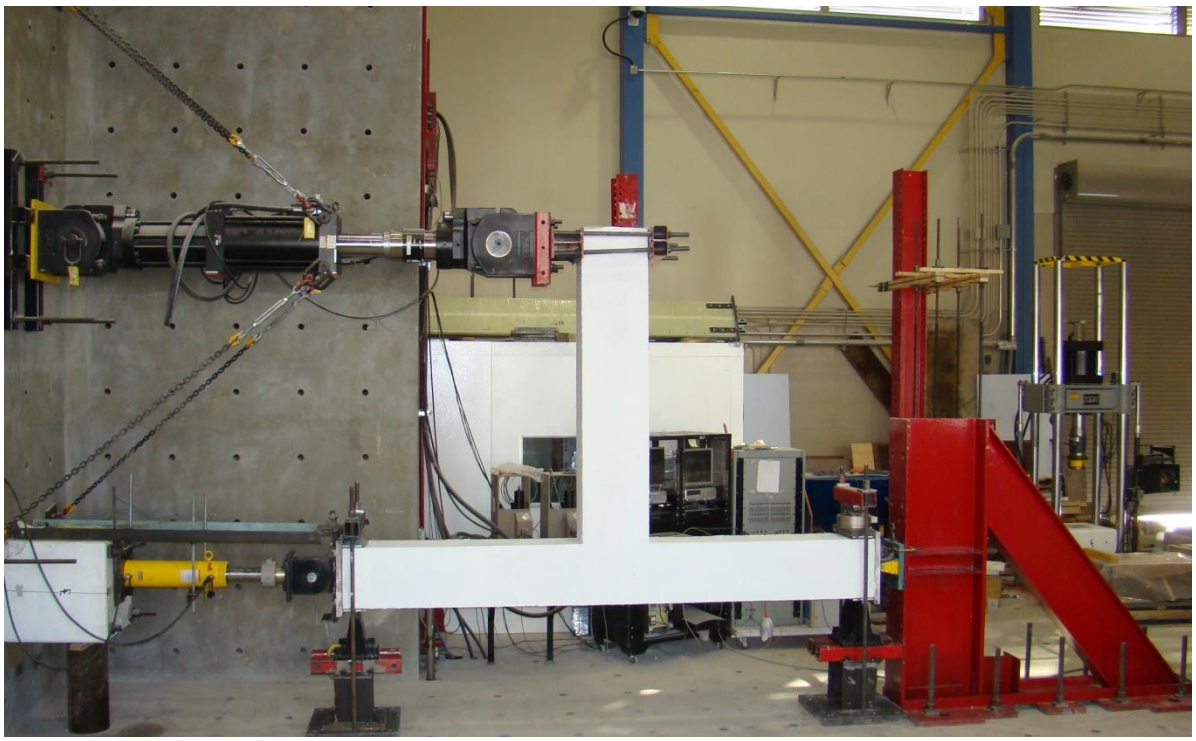

(a) Actual test setup

Figure 4.11: Photos of the used setup (continued)

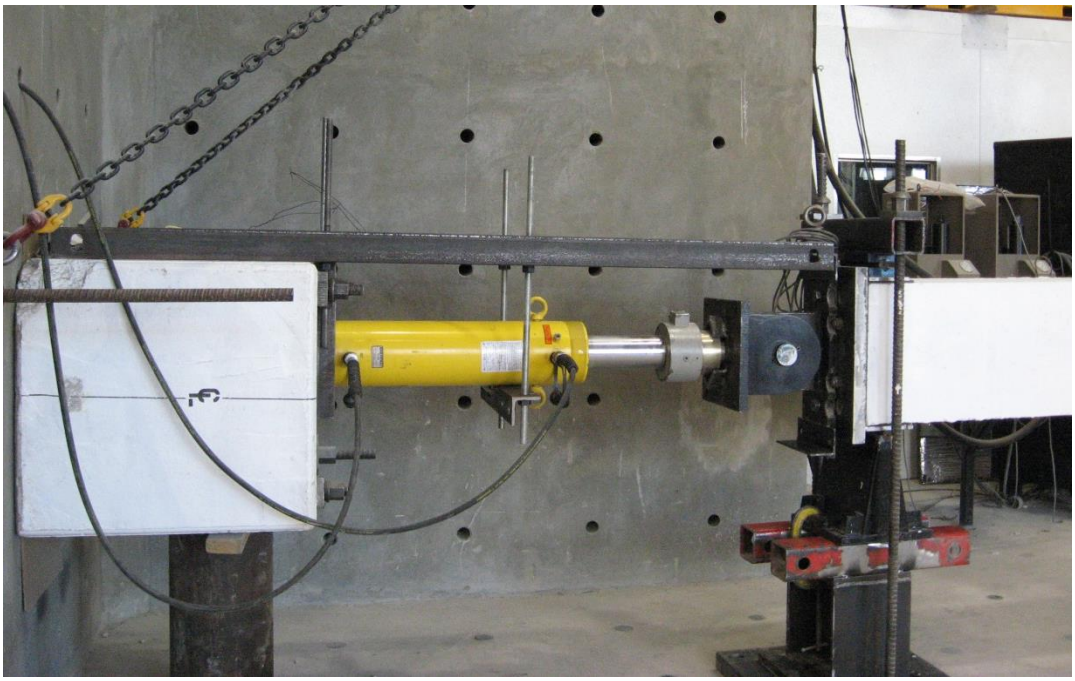

(b) Axial load application

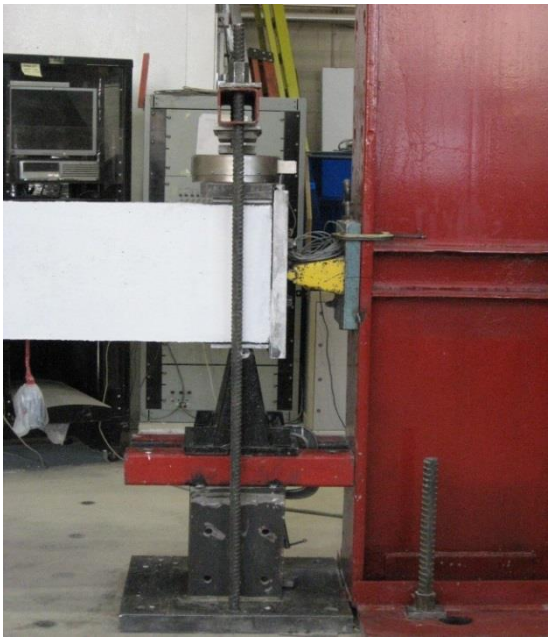

(c) Hinged boundary conditions

(d) DAQ and actuator controller

Figure 4.11: Photos of the used setup

4.2.5 Instrumentation

Instrumentations were designed to monitor the behaviour of the specimens during the test by providing a real-time recording of applied loads, displacements, and strains using a computerized DAQ system. Both internal and external instrumentation were implemented to monitor the behaviour during the test. A large number of strain gauges were mounted on longitudinal and transverse reinforcement at critical locations to detect strains during testing. Moreover, a group of load cells and linear variable displacement transducers (LVDTs) were also used to monitor the behaviour. Details of instrumentations are discussed in the following section.

4.2.5.1 *Load Cells*

Two load cells were used to measure the applied loads on the tested specimens. The first load cell was attached to the actuator to measure the applied lateral force on beam tip. The second load cell was attached to the hydraulic jack to monitor the applied axial force on column as shown before in Figure 4.11(b).

4.2.5.2 *Linear Variable Differential Transducers (LVDTs)*

When applying lateral displacement to the beam tip during testing, the exhibited drift values can be divided into four main components. These components are: (1) rotation in the anticipated beam plastic hinge zone; (2) rotation due to local slippage and large strains developed in the beam bars within the joint; (3) rotation due to overall column rotation; and (4) distortion of the joint.

A group of eight linear variable differential transducers (LVDTs) were used for rotation measurements. To measure the rotation of the beam relative to the column, a set of two LVDTs were attached vertically on both sides of the beam to the top surface of the column. The distance between those two LVDTs was set to be 500 mm as shown in Figure 4.12. During lateral displacement of the beam tip, the length of one of the LVDTs will expand while the opposite one may contract. The difference between the readings of the two LVDTs divided by their horizontal spacing (i.e. 500 mm) results in the relative rotation of the beam.

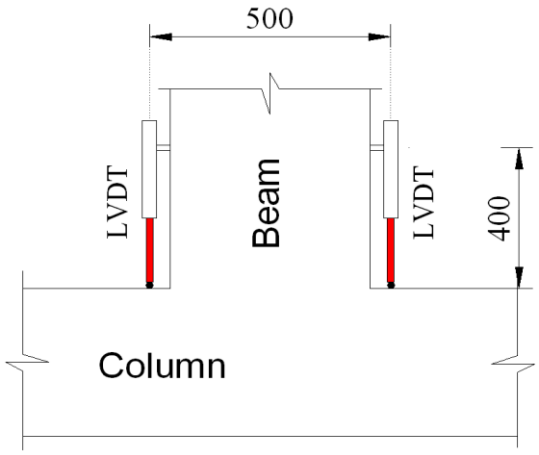

Figure 4.12: LVDT-set for measuring beam relative rotation

Also, a set of two LVDTs were attached vertically on both sides of the beam, as shown in Figure 4.13, to measure the rotation of the plastic hinge region in the beam. The distance between those two LVDTs was set to be 500 mm and the same procedure for measuring the plastic hinge rotation was followed as described previously.

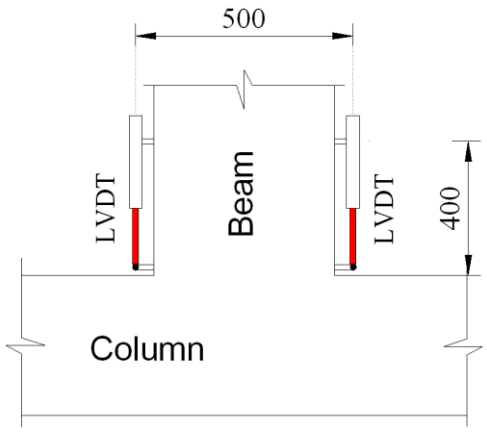

Figure 4.13: LVDT-set for measuring beam plastic hinge rotation

Rotation of column will be monitored using two vertical LVDTs spaced at a distance of 300 mm from the vertical axis of the beam as shown in Figure 4.14. The same procedure in calculating the rotation was followed as in previous sections.

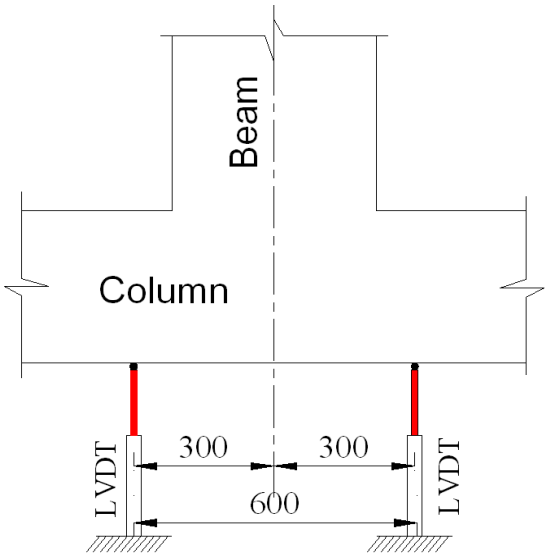

Figure 4.14: LVDT-set for measuring column rotation

In order to measure the distortion of the joint; two LVTDs are attached diagonally to the joint, as shown in Figure 4.15. The distortion value (γ) can be calculated from the LVTDs readings as shown in Figure 4.16 by substituting in the following equation:

$$\gamma = \frac{\delta - \delta'}{2l} (tan\,\alpha + cot\,\alpha) \qquad [4.1]$$

Where δ, δ': are readings of LVDTs where elongations have positive sign;

l : Initial distance between mounting rods;

α : Initial inclination of LVDTs to the horizontal.

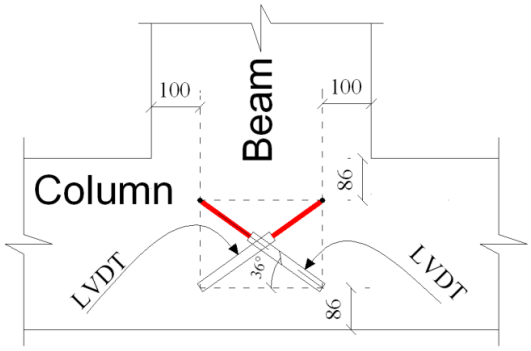

Figure 4.15: LVDT-set for measuring Joint distortion

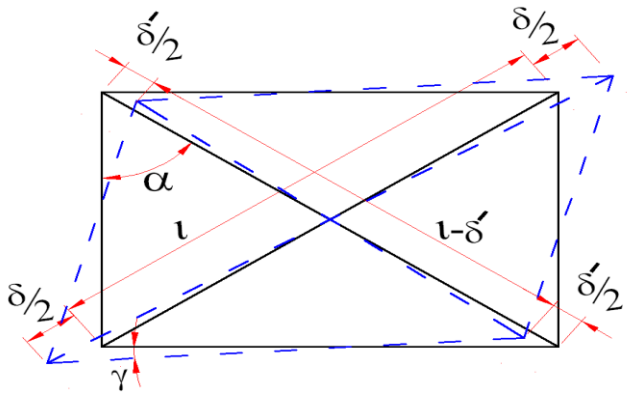

Figure 4.16: Joint distortion

Also, high accuracy (0.001 mm) LVDTs were attached to the concrete surface of the column to monitor slippage of longitudinal beam reinforcement in all test specimens reinforced with straight headed bars as shown in Figure 4.17.

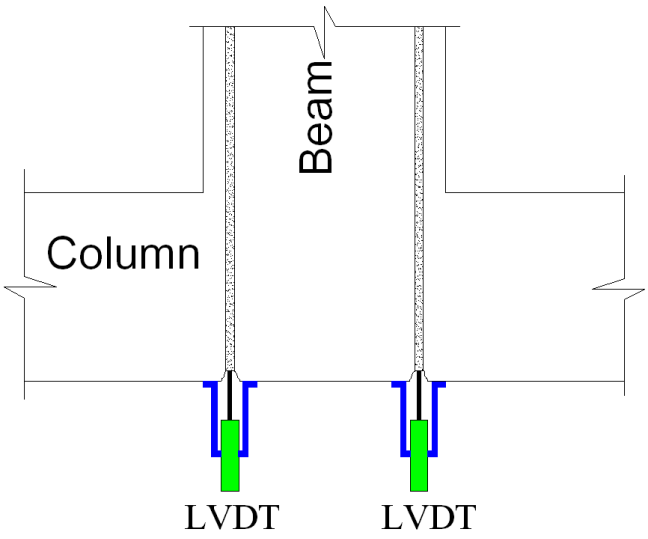

Figure 4.17: LVDTs for measuring bar slippage

4.2.5.3 *Strain Gauges*

Many strain gauges were mounted on both longitudinal and transverse reinforcement at critical locations to monitor strains induced by seismic loading. Figure 4.18 shows eleven locations of mounted strain gauges on the longitudinal bars to monitor strains due to flexural behaviour in both of the column and the beam. Developed strains in transverse reinforcement under shear stresses are monitored at eight locations where shear cracks were anticipated. Figure 4.19 shows a schematic drawing for instrumentation of strain gauges at locations at which critical strains are expected in stirrups. Although strain gauges were coated and protected, duplication of strain gauges was essential to ensure

continuous monitoring of strains in case of any damage occurs to the strain gauge while test operation.

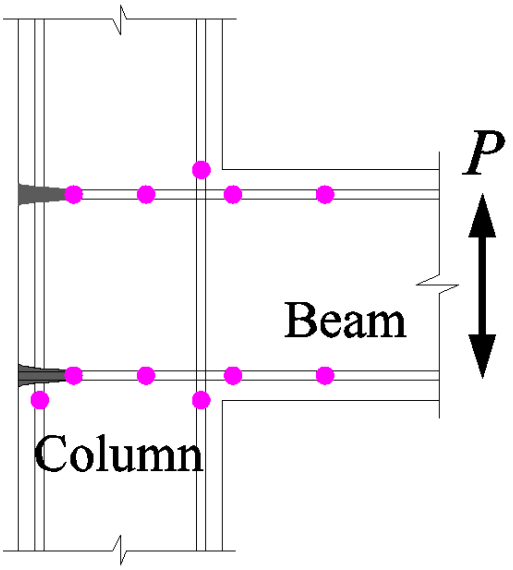

Figure 4.18: Strain gauge locations on longitudinal bars

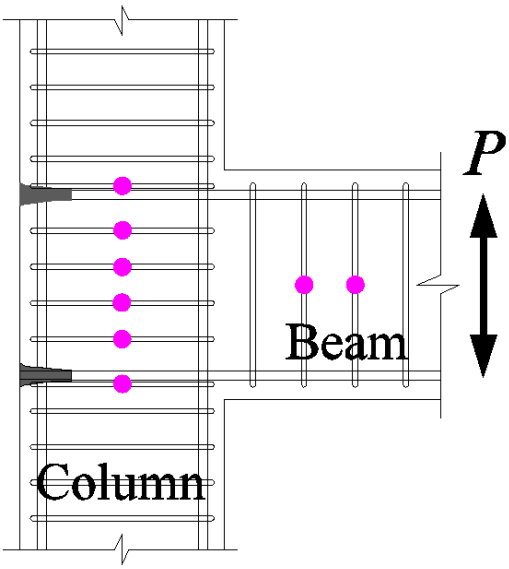

Figure 4.19: Strain gauge locations on stirrups

4.2.6 Seismic loading Scheme and Test Procedure

As reported by many researchers (*Hakuto et al.* 2000; *Ghobarah and El-Amoury* 2005, *Chun et al.* 2007), the loading process consisted of two loading phases. The first phase was carried out at a load-controlled mode, while the second phase was at a displacement-controlled mode. At the first loading phase (load-controlled), specimens were subjected to a loading cycle of amplitude equal to 25.0 kN to detect the cracking load and test the instrumentations. Then, another loading cycle represents service loading conditions (i.e. corresponding to 25.0% of the GFRP ultimate tensile strain for test specimens) was applied as shown in Figure 4.20.

As per the ACI Committee 374 report on the acceptance criteria for moment frames based on structural testing (*ACI-374.1* 2005), the second loading phase was applied under a displacement-controlled mode at a rate of 0.01 Hz, quasi-static type-loading as shown in Figure 4.21. It is simply consisted of applying a variable amplitude displacement cycles (represents increasing drift ratio) in several steps. Each step consisted of three identical (constant amplitude) displacement cycles, in order to ensure stable formation of cracking pattern.

The first step (i.e. the first three cycles) had a displacement-amplitude equal to 17.6 mm at the beam tip. This displacement was adopted from a previous study done by the researcher (*Hasaballa* 2009). It corresponds to the yielding displacement of beam longitudinal steel reinforcement (Δ_y) for a specimen reinforced with steel and had the same flexural strength characteristics of the tested specimens. According to ACI

Committee 374 report (*ACI-374.1* 2005), the ratio between the displacement amplitudes of any two consecutive seismic loading steps should be in the range of 1.25 to 1.50. Therefore, the displacement amplitude of each subsequent step was a multiplier of the yield displacement; 1.27Δ_y, 1.92 Δ_y, 2.53 Δ_y, 3.80 Δ_y, 5.07 Δ_y, and 6.30 Δ_y. The adopted loading history represented a drift ratio of values 0.8 %, 1.0 %, 1.5 %, 2.0 %, 3.0 %, 4.0 %, and 5.0 %. After certain seismic loading steps, one loading cycle with peak load equal to the service load condition was applied under a load-controlled mode in order to assess the stiffness degradation of the test prototype due to applying the prescribed seismic loading scheme, if any.

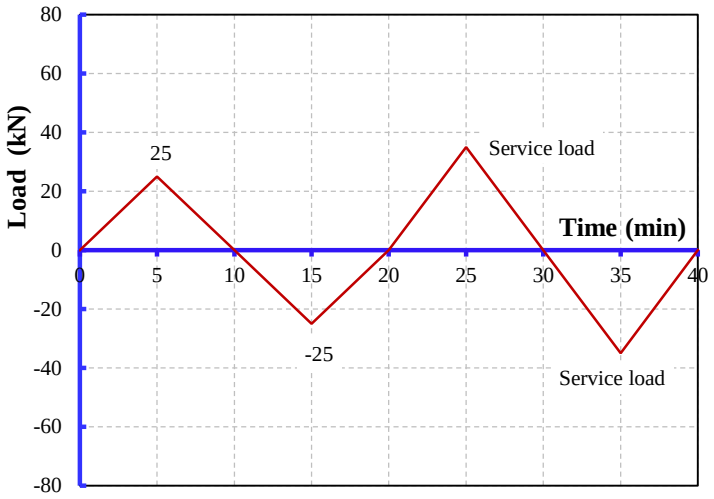

Figure 4.20: First loading phase - load-controlled mode

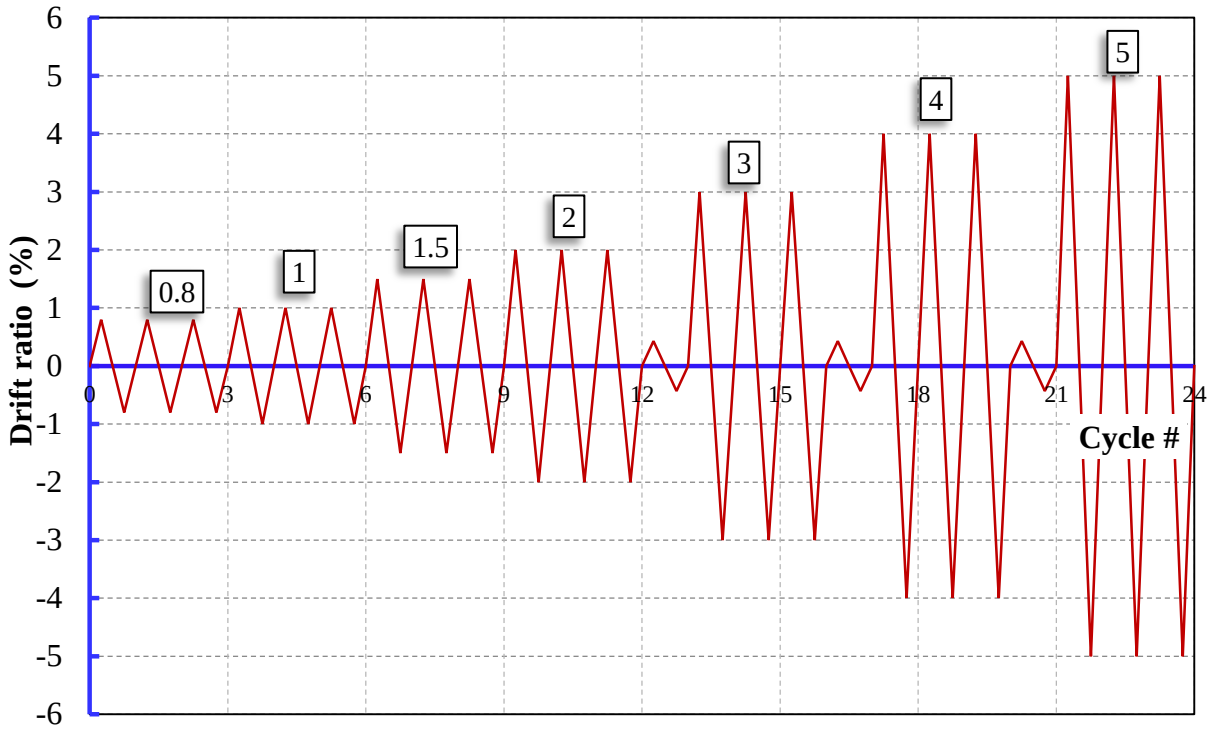

Figure 4.21: Second loading phase - displacement-controlled mode

CHAPTER 5

EXPERIMENTAL RESULTS OF SERIES (I) SPECIMENS

5.1 INTRODUCTION

This chapter presents the analysis and discussion of the experimental results of testing Series (I) specimens. This series was designed to study the anchorage detailing of longitudinal beam reinforcement inside the joint. A combination of two anchorage schemes of beam longitudinal reinforcement (bent bars and headed bars) along with two different bar surface-conditions (sand-coated surface and deformed/ribbed surface) was investigated. This combination of variables resulted in four specimens (I-B-S, I-B-D, I-H-S, and I-H-D).

It should be noted that Specimen I-B-D was reconstructed and retested. When constructed the first time, Specimen I-B-D0 was reinforced with longitudinal bent bars that are not long enough to cover the whole length of the beam due to some manufacturing restriction at the time of construction. Therefore, the beam longitudinal reinforcement was spliced within the beam length. During testing, Specimen I-B-D0 showed no consistency between the lateral load resistances in the reversed loading directions. Therefore it was decided to disregard that specimen and reconstruct it using full-length longer longitudinal bent bars that have been made available at later time. Reinforcement details and results of Specimen I-B-D0 are presented in Appendix B.

5.2 LOAD–LATERAL DRIFT RESPONSE (HYSTERETIC BEHAVIOUR)

Plots of the hysteresis diagrams which represent the relationship between the applied lateral load and the drift ratio of the beam tip are shown in Figure 5.1. The drift ratio was calculated as the ratio between the horizontal displacement of the beam end at the point of load application and the distance from the point of load application to the column centreline (i.e. 2200 mm). It should be noted that the positive values of lateral load reflect the beam lateral resistance when the actuator pushes the beam tip, while the negative values reflect the resistance in the other direction (pulling).

As shown in Figure 5.1, the measured hysteresis loops for all specimens demonstrated a typical stable elastic-linear response up to a drift ratio of 4.0%, where all specimens reached their calculated design capacity and then followed by a non-linear behaviour and lateral resistance drop in different forms for different specimens. For Specimen I-B-D, during the 5.0% loading drift and specifically at 4.6% drift ratio, the specimen experienced sudden drop in the lateral load resistance as shown in Figure 5.1(a). This drop in resistance is attributed to the slippage of the beam longitudinal headed-bars anchored in the joint due to failure of the anchorage heads attached to the end of the bars. Despite of the failure occurred in the anchorage heads, the specimen was still able to resist approximately 50.0% of its designed capacity during the rest of the 5.0% drift ratio loading cycles, dropped to 30% of the design capacity at negative side of loading.

On the other hand, Specimen I-B-D showed an increase in its lateral resistance during the 5.0% drift ratio and sustained its lateral resistance up to the first cycle of 6.0% drift ratio

as shown in Figure 5.1(b). The specimen thereafter showed a non-linear behaviour and gradual degradation of the lateral load resistance until it reached approximately 60% of its design capacity by the end of the 6.0% loading drift. The specimen showed an increase in the pinching distance from 19 kN at 3.0% drift ratio to 35 kN at 6.0% drift ratio. This is attributed to the non-linear deformation of the concrete in the beam section at column face.

Moving to the two specimens reinforced with sand-coated bars, Figure 5.1(c) shows that Specimen I-H-S was able to withstand the loading drifts up to 5.0% drift ratio with no loss of lateral resistance. During the first cycle of 6.0% loading drift, the specimen exhibited sudden drop in the lateral resistance due to failure of the anchorage heads in the joint. The lateral resistance of the specimen did not diminish completely due to this anchorage failure; however, the specimen was able to resist 60% of its design capacity by the end of the test after completing the three cycles of 6.0% loading drift.

Regarding Specimen I-B-S, Figure 5.1(d) shows that the specimen had the characteristic elastic-linear behaviour up to 4.0% drift ratio followed by a non-linear behaviour till the end of the test. After 4.0% drift ratio, the specimen continued to resist higher values of lateral loads up to the first cycle of 6.0% loading drift then a gradual degradation in the lateral resistance happened until the end of the test at 7.0% drift ratio. The non-linear behaviour of the specimen can be observed in the pinching distance which increased from 24 kN at 4.0% drift ratio to 40 kN at 7.0% drift ratio.

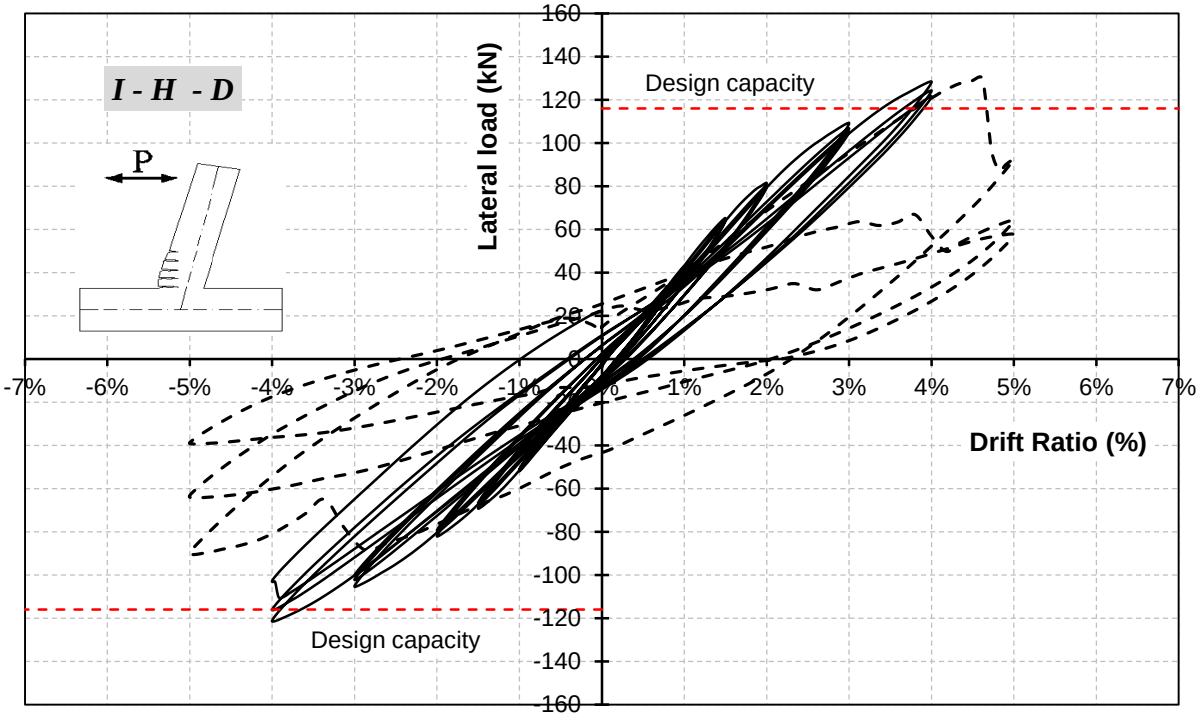

(a) Specimen I-H-D

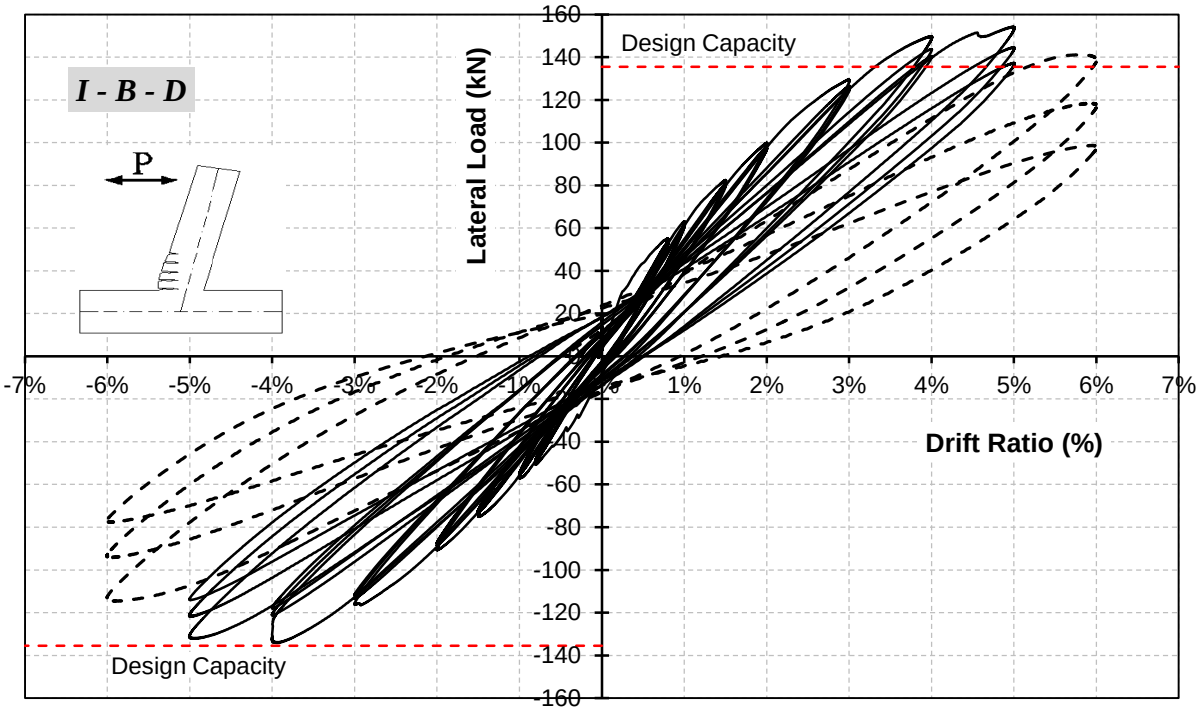

(b) Specimen I-B-D

Figure 5.1: Load-Lateral Drift relationship for Series (I) specimens (continued)

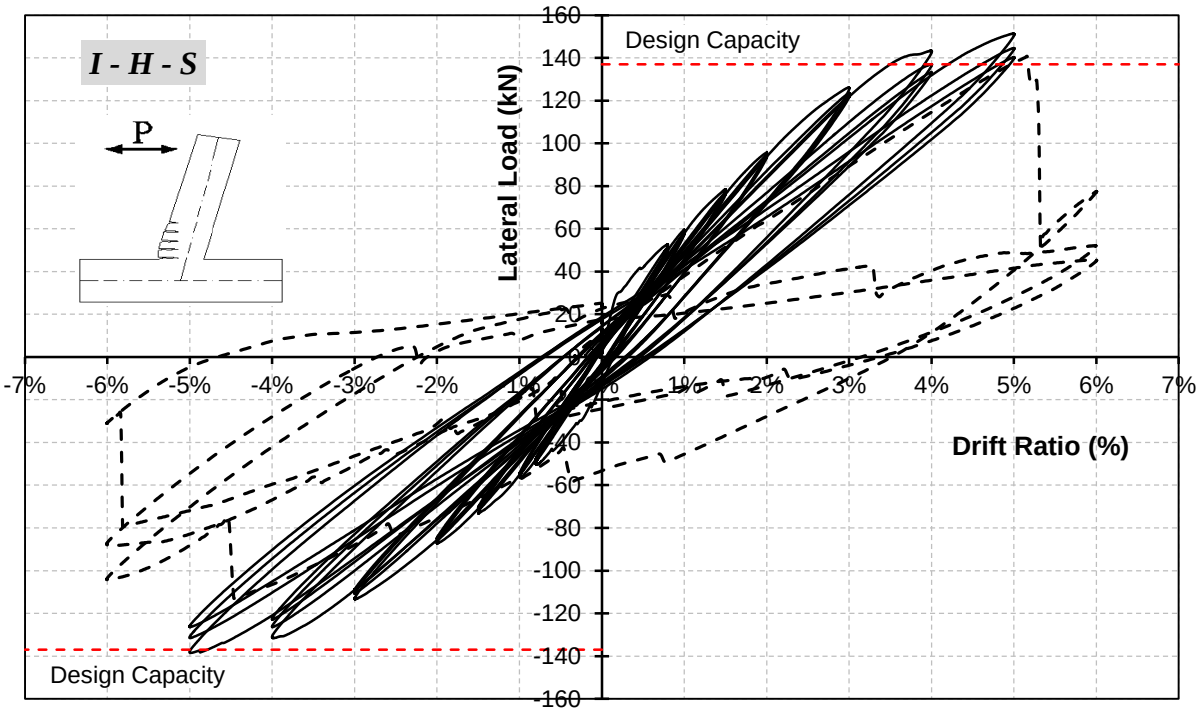

(c) Specimen I-H-S

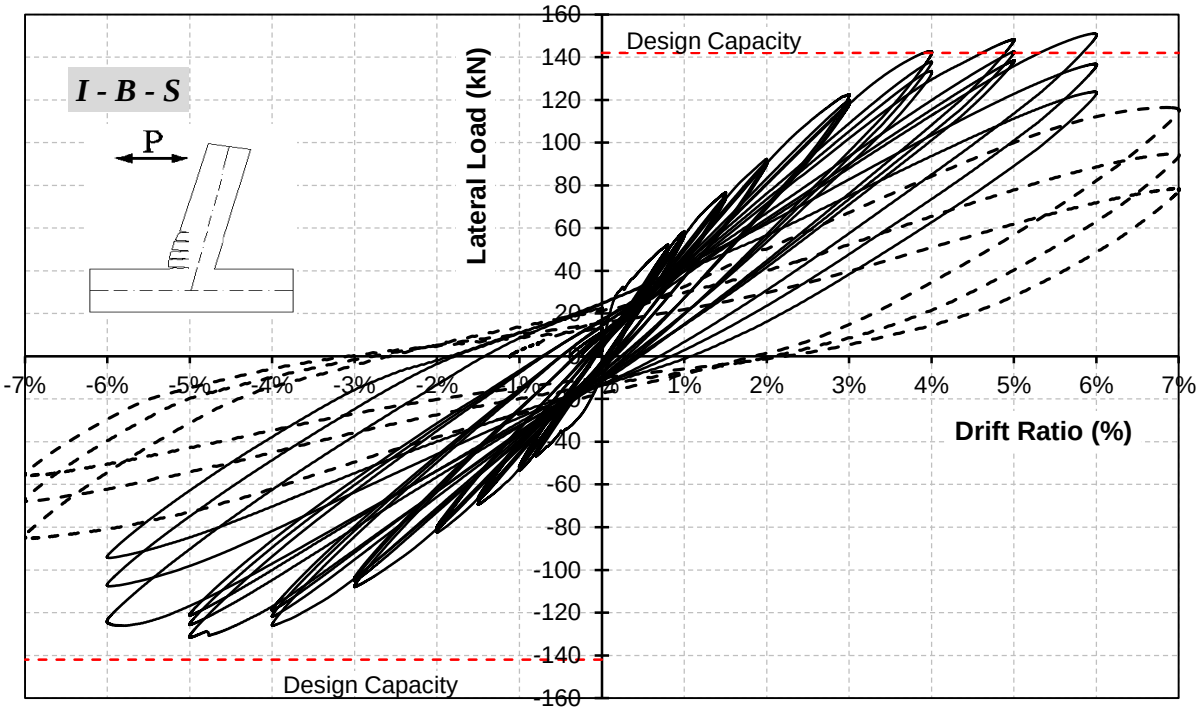

(d) Specimen I-B-S

Figure 5.1: Load-Lateral Drift relationship for Series (I) specimens

Figure 5.2 shows the normalized envelopes of load-lateral drift relationships for all Series (I) specimens. As a result of the difference in the flexural design capacity of the beam sections of the specimens, the lateral load values resisted by each specimen were normalized to the specimen's design capacity shown before in Chapter 4, Table 4.3. To evaluate the structural performance of the headed bars in comparison with the bent bars, the envelopes of specimens reinforced with deformed bars (I-x-D) are shown in Figure 5.2(a) and those reinforced with sand-coated bars (I-x-S) are shown in Figure 5.2(b). Figures 5.2(a) and (b) show that the behaviour of specimens reinforced with headed bars was identical to their counterparts reinforced with bent bars. All specimens reached or exceeded their design capacity at 4.0% drift ratio; however, specimens reinforced with headed bars experienced failure earlier than those specimens reinforced with bent bars. This is attributed to the slippage failure of the anchorage heads; however, after withstanding the design capacity. In general, it can be said that the performance of those specimens reinforced with headed bars was comparable to those reinforced with bent bars in terms of achieving the flexural design capacity.

The influence of the reinforcement surface condition, deformed and sand-coated, can be obtained from Figures 5.2(c) and (d) which show the normalized envelopes for specimens with headed bars (I-H-D and I-H-S) and those with bent bars (I-B-D and I-B-S), respectively. The figures show that specimens reinforced with deformed bars outperformed those reinforced with sand-coated bars in terms of exceeding the designed lateral load resistance. On the other hand, the specimens reinforced with deformed bars exhibited failure at earlier loading drifts compared to those reinforced with sand-coated

bars. In general, it can be noted that the reinforcement surface condition has no significant influence on the behaviour of the specimens before 4.0% drift ratio.

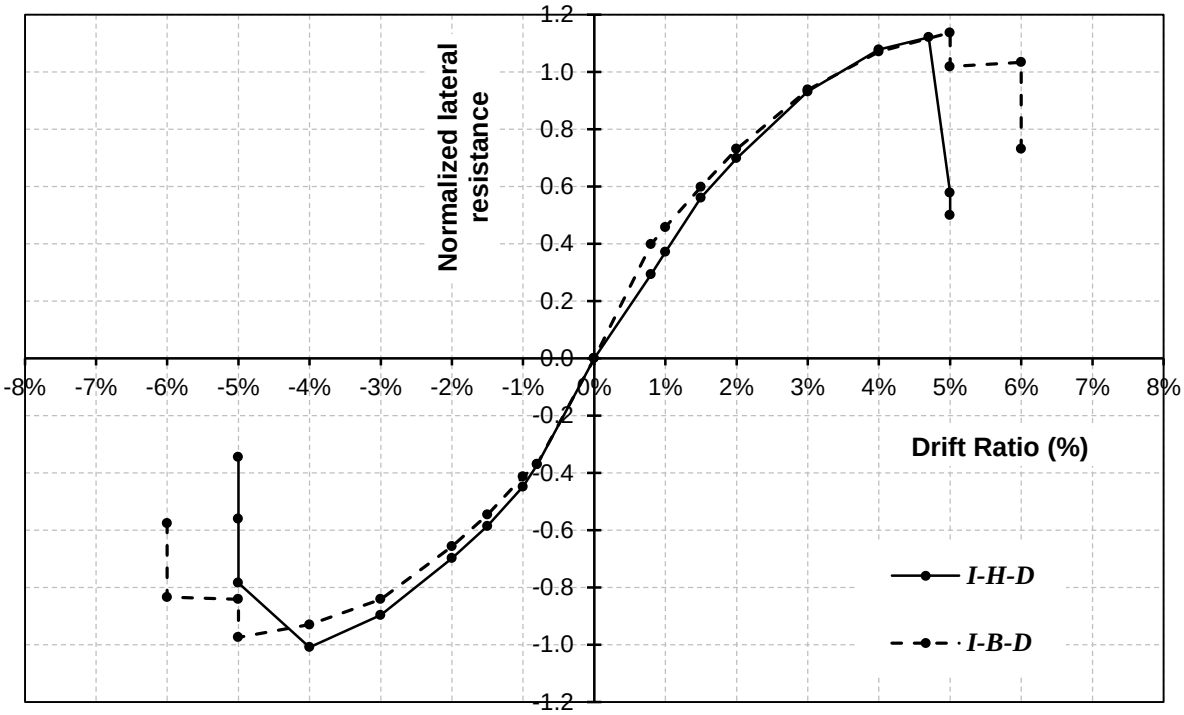

(a) Specimens I-H-D and I-B-D

Figure 5.2: Load-lateral drift relationships envelopes for Series (I) specimens (continued)

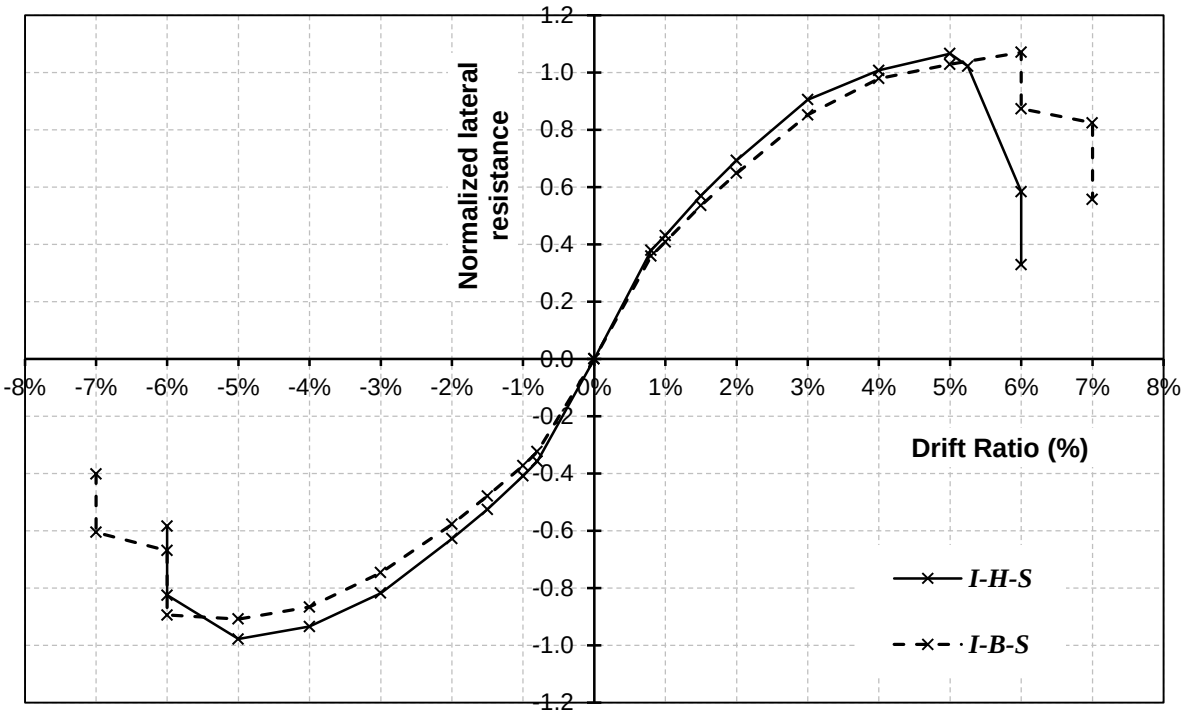

(b) Specimens I-H-S and I-B-S

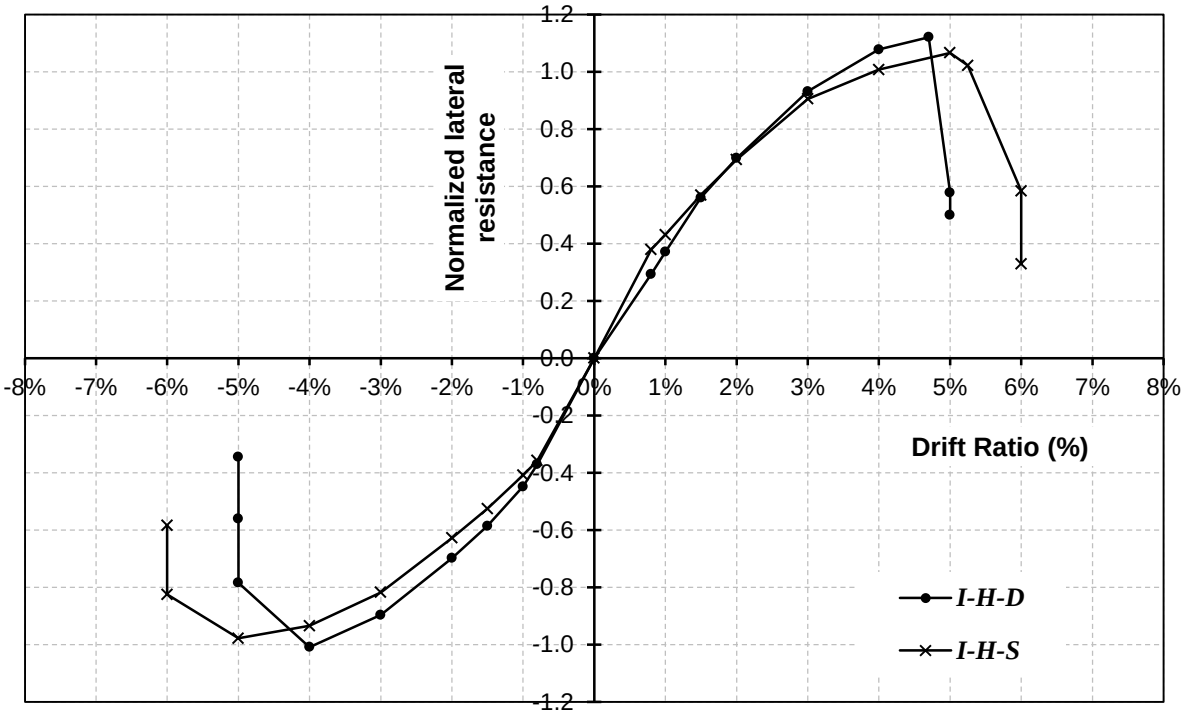

(c) Specimens I-H-D and I-H-S

Figure 5.2: Load-lateral drift relationships envelopes for Series (I) specimens (continued)

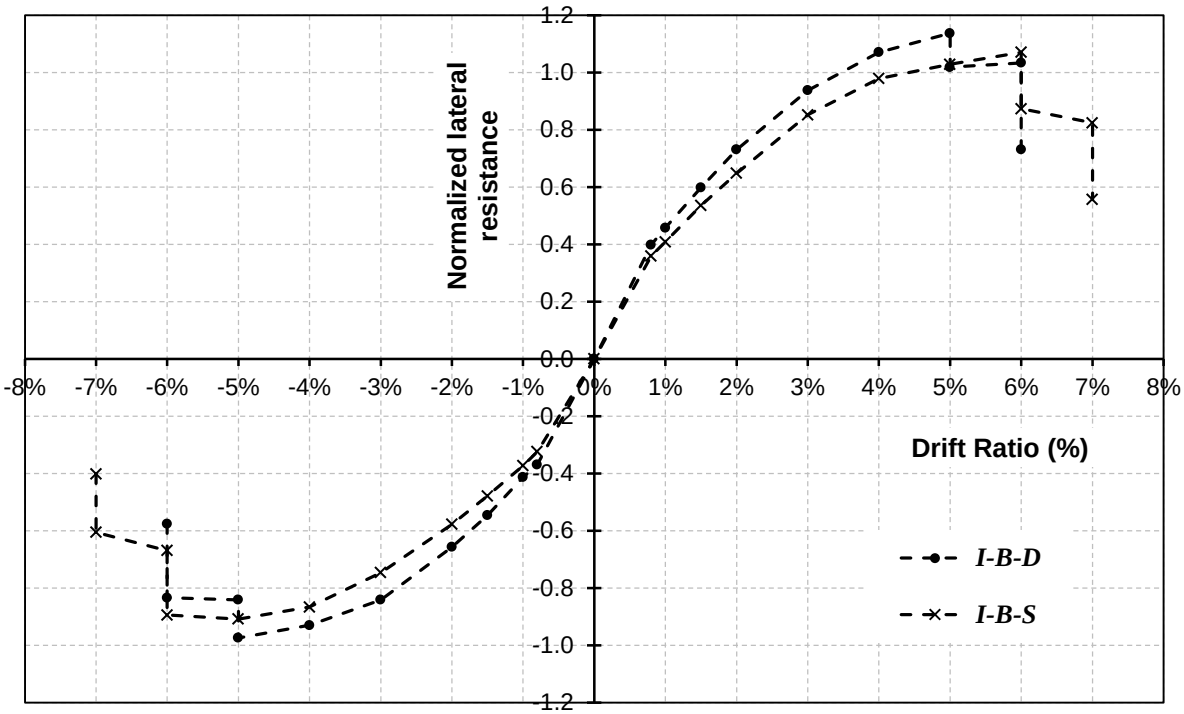

(d) Specimens I-B-D and I-B-S

Figure 5.2: Load-lateral drift relationships envelopes for Series (I) specimens

Table 5.1: Maximum lateral load resistance of Series (I) specimens with the corresponding drift ratio

Specimen	P_{design} (kN)	P_{exp} (kN)		P_{exp} / P_{design}		Drift ratio (%)
		+ve dir.	-ve dir.	+ve dir.	-ve dir.	
I-H-D	116	130	117	1.12	1.01	5.0%
I-B-D	136	154	132	1.13	0.97	5.0%
I-H-S	137	146	134	1.07	0.98	5.0%
I-B-S	142	152	127	1.07	0.90	6.0%

P_{design}: Calculated lateral load resistance considering the design flexural capacity of the beam section;
P_{exp}: Experimental lateral load resistance;
+ve dir: The value in the positive direction when the actuator pushes the beam tip;
-ve dir.: The value in the negative direction when the actuator pulls the beam tip;
Drift ratio: The drift ratio at which the maximum experimental values in the table were observed.

Evaluation of the lateral resistance of Series (I) specimens in comparison with the calculated design capacity can be obtained from Figures 5.1 and 5.2. It is observed that all test specimens in Series (I) not only achieved but also exceeded the ultimate design lateral load capacity in the positive direction of loading as shown in Table 5.1. Specimen I-H-D reached a lateral resistance that is 12% more than its design capacity at 4.0% drift ratio and maintained this level of resistance until it significantly dropped during the 5.0% loading drift due to anchorage slippage of beam longitudinal reinforcement. Regarding specimen I-B-D, it reached 94% of its design capacity at 3.0% drift ratio and continued to resist more loads until it reached a capacity that is 13% more than the design capacity. For Specimens I-H-S and I-B-S, they both exhibited 7% higher capacity than the design one. Their strength behaviour was similar to the one exhibited by Specimens I-H-D and I-B-D; however with improved capability to withstand higher drift ratios as shown in Table 5.1. It should be noted that all specimens exhibited lower resistance in the negative direction of loading (pulling) than the exhibited in the other loading direction (pushing) which is common behaviour in cyclic reversed loading. The difference in the resistance values between the two loading directions ranged from 8% to 14%.

5.3 CRACKING PATTERN AND MODE OF FAILURE

In all specimens, the formation and propagation of cracks were marked after each loading step. Damage was generally expressed by the initiation and propagation of flexural and shear cracks. Further damage and failure of specimens at the end of the tests was defined by two modes of failure; namely, 1) formation of inelastic deformability hinge in the beam associated with slippage of longitudinal reinforcement; 2) formation of inelastic

deformability hinge in the beam followed by a joint shear failure. Figures 5.3 through 5.6 show the cracking progression of specimens during testing and at failure as well. The photos presented in these figures show the same orientation of the specimens in the test setup where the column was placed in the horizontal direction and the beam in the vertical direction.

Figure 5.3 shows the cracking progression of Specimen I-H-D. flexural cracks showed on the beam surface up to a drift ratio of 1.5% as can be seen in Figures 5.3(a) to (c). Up to that level of loading, no diagonal shear cracks appeared in the joint. While increasing the lateral-displacement loading to higher drift ratios, more flexural cracks in the beams were initiated and developed up to failure. At 4.0% drift ratio, as shown in Figure 5.3 (f), failure of the concrete cover on both sides of the beam was observed, which in turn refers to the formation of inelastic deformability hinge due to concrete crushing in the beam section near the column face. This is in a good agreement with Figure 5.1(a) which shows the hysteresis loops of the specimen reaching the calculated design capacity at 4.0 % drift ratio. During the first cycle of the 5.0% drift ratio loading step, a sudden drop in the lateral loading resistance occurred as a result of anchorage slippage on both sides of beam longitudinal reinforcement. This is attributed to the bearing failure of the anchorage heads attached to the end of the longitudinal reinforcement. The slippage of the beam longitudinal reinforcement resulted in formation of a wide crack on the column face at failure as shown in Figures 5.3(h). The anchorage failure occurred in some of the bars resulted in sudden increase of tensile stresses in the adjacent bars. This in turn resulted in rupture failure of one bar as shown in Figures 5.3(j).

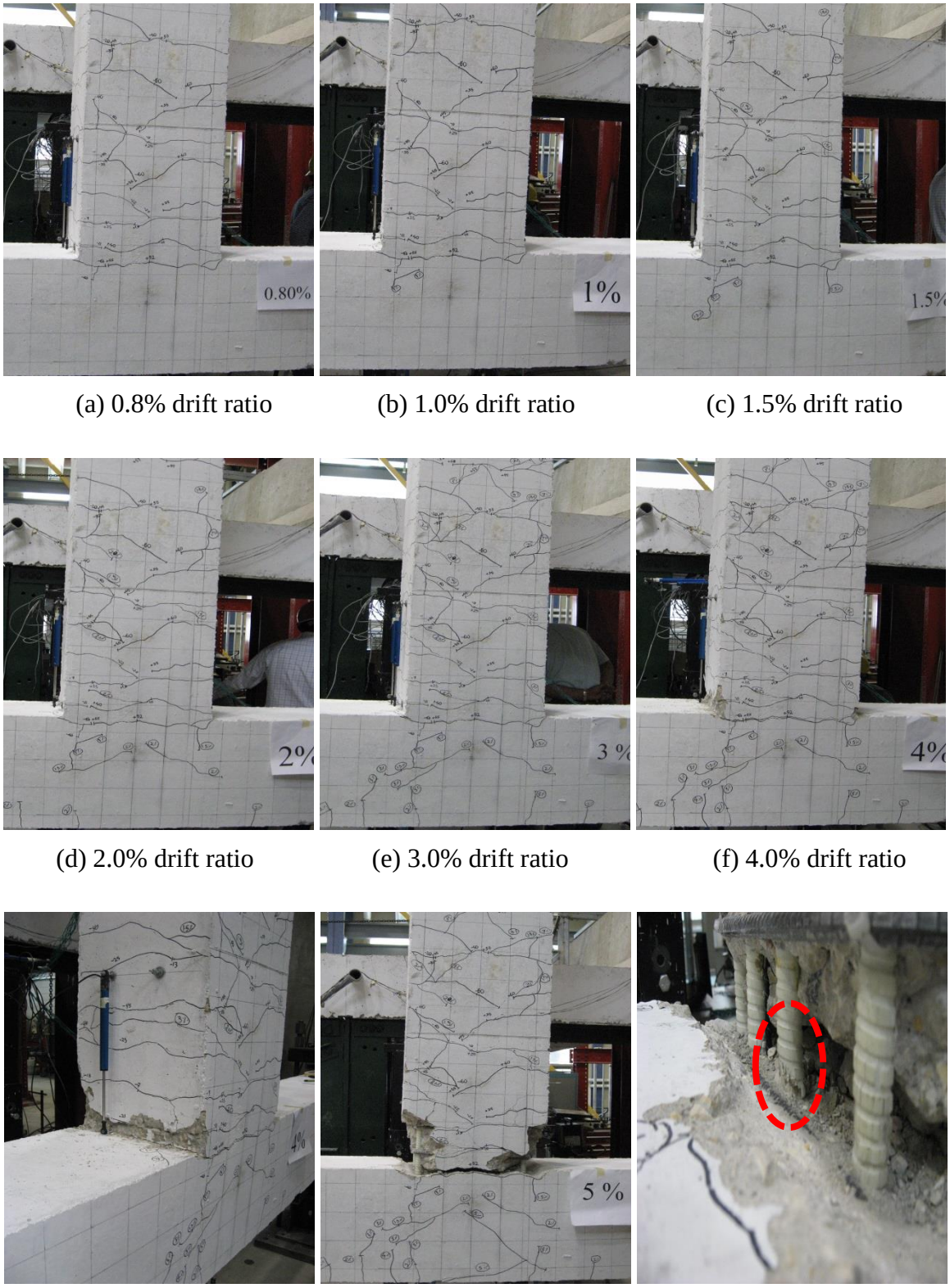

(a) 0.8% drift ratio (b) 1.0% drift ratio (c) 1.5% drift ratio

(d) 2.0% drift ratio (e) 3.0% drift ratio (f) 4.0% drift ratio

(g) 4.0% drift ratio – side view (h) 5.0% drift ratio (j) Rupture of one bar

Figure 5.3: Cracking progression of Specimen I-H-D

Regarding Specimen I-B-D, Figure 5.4 shows the cracking patterns at different loading stages. Specimen I-B-D showed a stable behaviour up to 2.0% drift ratio where flexural cracks were observed in the beam near the column face with no cracking in the joint area as shown in Figures 5.4(a) through (d). At 3.0% drift ratio, the number and propagation of flexural cracks increased in the beam. Also, minor diagonal cracks appeared in the joint.

At 4.0% drift ratio, failure of the concrete cover on both sides of the beam was observed which initiated the formation of inelastic deformability hinge due to concrete crushing in the beam section near the column face as shown in Figure 5.4(f). This is in a good agreement with Figure 5.1(b) which shows the hysteresis loops of the specimen exceeding the calculated design capacity at 4.0 % drift ratio. Formation of inelastic deformability hinge in the beam continued with increasing the lateral-displacement loading to higher drift ratios. Meanwhile, more concrete cover failed while the specimen maintained its lateral resistance through the 5.0% loading drift and until the first cycle of the 6.0% drift ratio loading. Formation of inelastic deformability hinge in the beam section extended to a distance from the column face approximately equal to the depth of the flexural reinforcement (i.e. 400 mm). After the first cycle of 6.0% drift ratio, the specimen showed degradation of lateral resistance mainly due to formation of major shear cracks in the joint as shown in Figures 5.4(h) and (j).

(a) 0.8% drift ratio (b) 1.0% drift ratio (c) 1.5% drift ratio

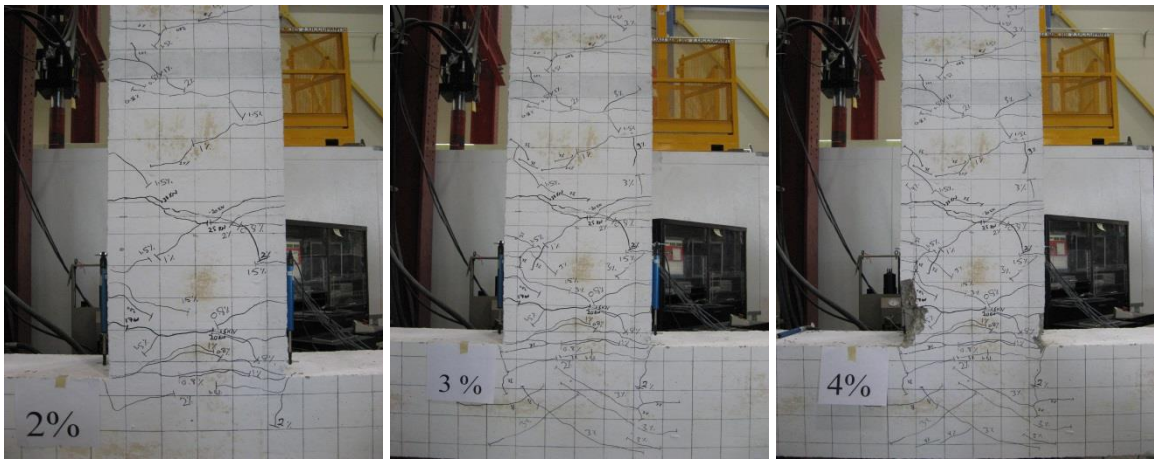

(d) 2.0% drift ratio (e) 3.0% drift ratio (f) 4.0% drift ratio

(g) 5.0% drift ratio (h) 6.0% drift ratio (j) 6.0% drift ratio - side view

Figure 5.4: Cracking progression of Specimen I-B-D

Figure 5.5 shows the cracking development of Specimen I-H-S. Development of cracks in the first stages of loading up to 2.0% drift ratio shows that the specimen exhibited similar behaviour to the one exhibited by Specimen I-H-D as shown in Figures 5.5(a) to (d). Both specimens experienced flexural cracks in the beam by increasing the loading drifts with no diagonal shear cracks appeared in the joint up to 2.0% drift ratio. Further loading resulted in increasing the number and extension of flexural cracks in the beam section and diagonal shear cracks in the joint. At 4.0% drift ratio, compression failure of concrete cover of the beam section was observed, which is in agreement with Figure 5.1(c) that shows the hysteresis loops of the specimen exceeding the calculated design capacity at 4.0 % drift ratio.

Failure of the concrete cover in the beam section continued while the specimen was resisting more lateral loads up to the first cycle of the 6.0% loading drift. At that level of loading the specimen suffered sudden drop of lateral resistance up to 40% of its design capacity due to slippage of beam longitudinal reinforcement anchored in the joint. The slippage was a result of anchorage failure of bearing heads attached to the end of the beam longitudinal reinforcement. The anchorage failure occurred at some of the bars resulted in sudden increase of tensile stresses in the adjacent bars. This in turn resulted in rupture failure of two bars as shown in Figure 5.5 (k). It should be noted that by the end of the test, the sand coating layer sheared off the GFRP reinforcement as shown clearly in Figure 5.5(k). It worth mentioning that formation of the inelastic deformability hinge in the beam section extended to a distance approximately equal to the depth of the flexural reinforcement (i.e. 400 mm) from the column face.

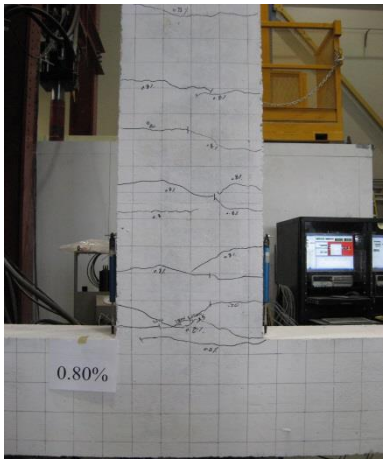

(a) 0.8% drift ratio

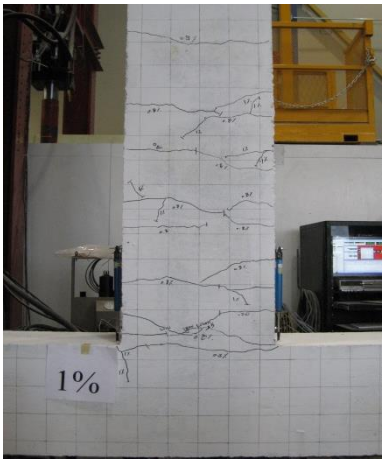

(b) 1.0% drift ratio

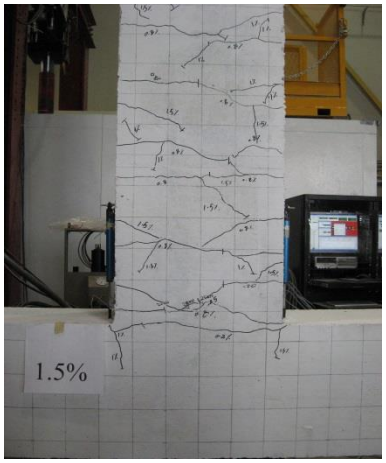

(c) 1.5% drift ratio

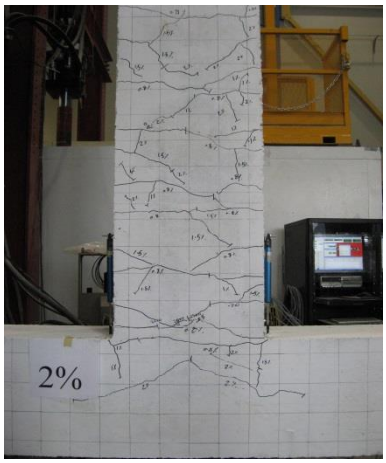

(d) 2.0% drift ratio

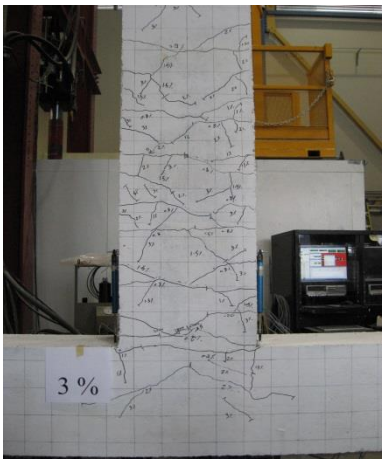

(e) 3.0% drift ratio

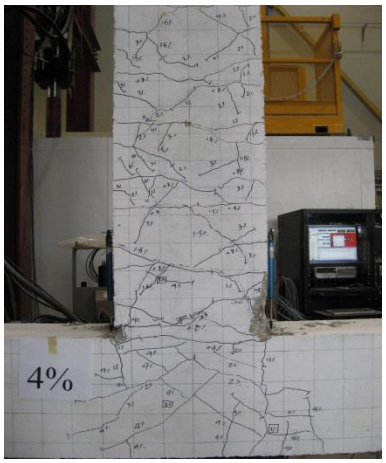

(f) 4.0% drift ratio

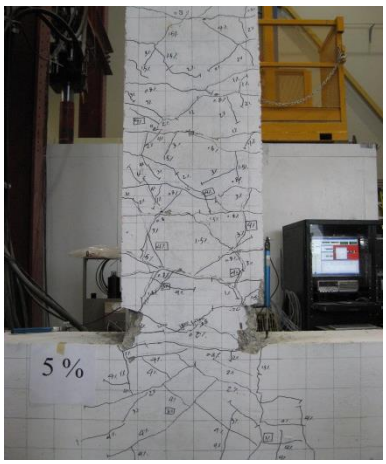

(g) 5.0% drift ratio

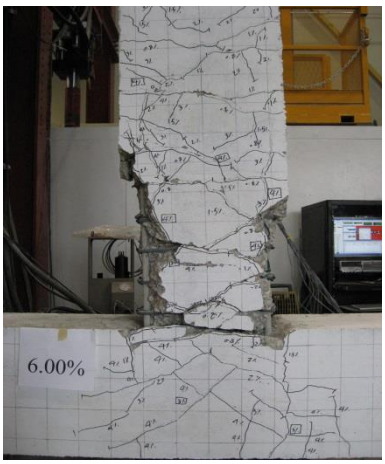

(h) 6.0% drift ratio

(j) 6.0% drift ratio - side view

Figure 5.5: Cracking progression of Specimen I-H-S (continued)

(k) Rupture of two bars and sand-coated surface shearing off

Figure 5.5: Cracking progression of Specimen I-H-S

Figure 5.6 shows the cracking pattern of Specimen I-B-S during the successive loading drifts. The specimen showed flexural cracks along the beam length with no cracking in the joint area up to 1.5% drift ratio as shown in Figures 5.6(a) through (c). At 3.0% drift ratio, the number and propagation of flexural cracks increased in the beam. Furthermore, minor diagonal cracks appeared in the joint. Failure of the concrete cover on both sides of the beam was observed at 4.0% drift ratio which initiated the formation of inelastic deformability hinge in the beam section at the column face as shown in Figure 5.6(f). Again, this is in a good agreement with Figure 5.1(d) which shows the hysteresis loops of the specimen reaching the calculated design capacity at 4.0 % drift ratio.

The development of inelastic deformability hinge in the beam continued while increasing the lateral-displacement loading to higher drift ratios; more concrete cover dropped while the specimen maintained its lateral resistance until the 6.0% loading drift. Test ended after completing the 7.0% loading drift where major diagonal shear cracks in the joint

occurred, as shown in Figure 5.6(j), and significantly affected the lateral resistance of the specimen. In general, the specimen exhibited a cracking pattern similar to the one exhibited by Specimen I-B-D; however, with more damaged concrete cover in the joint area.

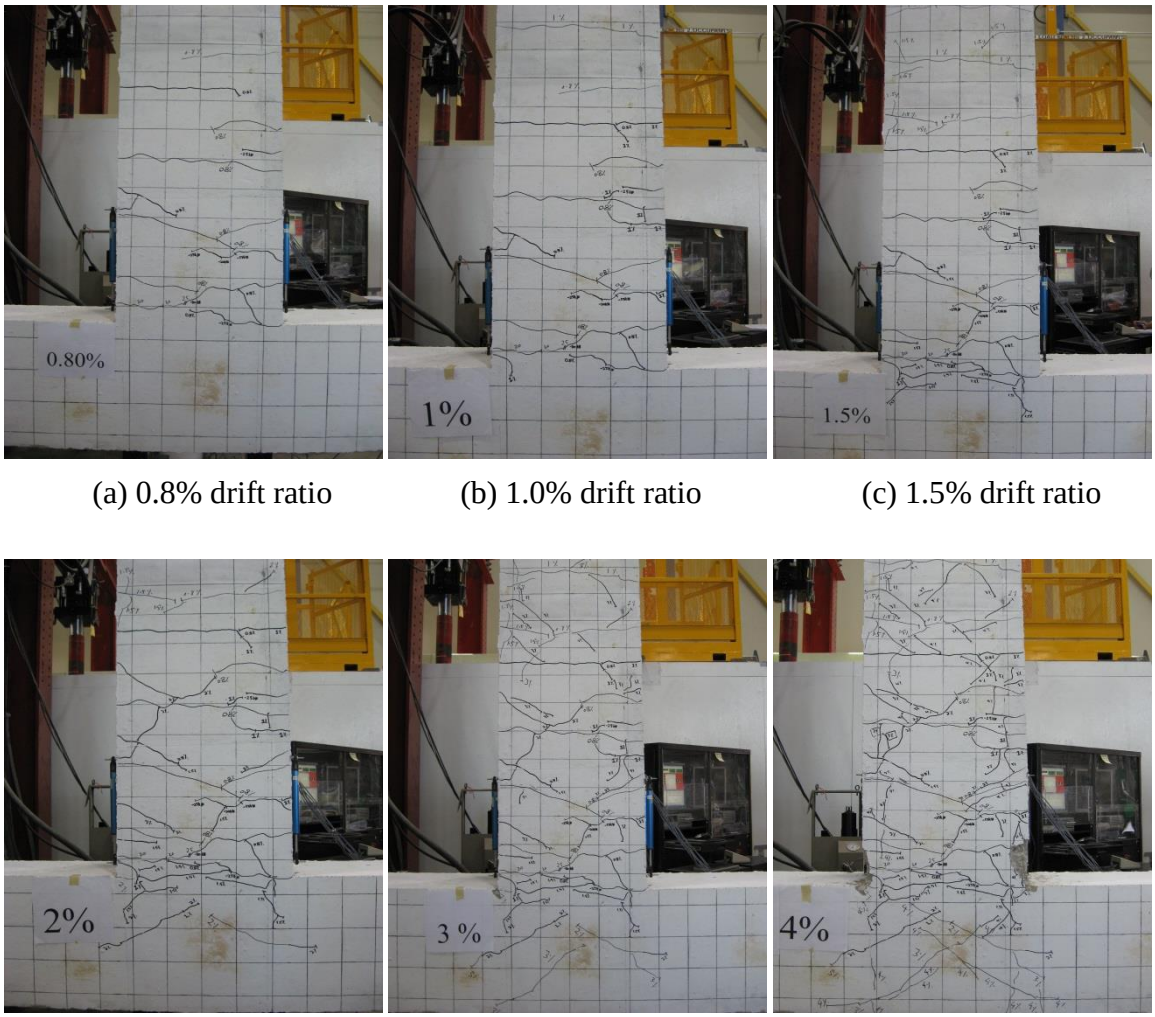

(a) 0.8% drift ratio (b) 1.0% drift ratio (c) 1.5% drift ratio

(d) 2.0% drift ratio (e) 3.0% drift ratio (f) 4.0% drift ratio

Figure 5.6: Cracking progression of Specimen I-B-S (continued)

(g) 5.0% drift ratio (h) 6.0% drift ratio (j) 7.0% drift ratio

Figure 5.6: Cracking progression of Specimen I-B-S

5.4 LATERAL DRIFT-STRAIN RELATIONSHIP

5.4.1 Developed Strains in Beam Longitudinal Reinforcement

Electrical strain gauges were mounted on the reinforcement to capture strain values at critical sections. Figure 5.7 shows the maximum recorded strains developed in beam longitudinal reinforcement at the column face for each loading drift of Series (I) test specimens. It should be noted that the strain values of the final loading stage for all specimens could not be captured because of malfunctioning of strain gauges. The figure shows that the strain values in all specimens didn't reach the ultimate strain before malfunctioning of strain gauges. All specimens exhibited the elastic-linear characteristic behaviour of the GFRP reinforcement in flexural members. Regarding Specimens I-H-D and I-H-S, Figure 5.7(a) shows that the two specimens exhibited similar values of tensile strains in the longitudinal reinforcement at the same loading drift. Similar observation is also noted for the Specimens I-B-D and I-B-S, as shown in Figure 5.7(b).

Table 5.2 shows the calculated and the experimental flexural capacities of the beam section for Series (I) specimens and the corresponding strain developed in the beam longitudinal reinforcement at the column face during the final loading drifts at 4.0%, 5.0%, and 6.0% drift ratios. Table 5.2 in conjunction with Figures 5.3(f), 5.4(f), 5.5(f), and 5.6(f) show that the calculated strain values are in good agreement with the experimental values developed at crushing of concrete in the beam sections when the calculated design flexural capacity of the beam was achieved in all specimens.

Table 5.2: Maximum strains in beam longitudinal reinforcement during testing of Series (I) specimens

Specimen	Tensile strain (micro-strain)				Moment (kN.m)			
	*Design	**Experimental			*Design	**Experimental		
		4.0%	5.0%	6.0%		4.0%	5.0%	6.0%
I-H-D	13330	12710	N/A	N/A	232	250	152	N/A
I-B-D	13225	12930	14350	15035	271	290	308	280
I-H-S	14640	13920	14730	N/A	274	276	292	160
I-B-S	13700	13730	15690	N/A	284	278	292	304

* Design values calculated using the strain compatibility when the concrete reaches an ultimate compressive strain of 0.0035

** Experimental values obtained during testing

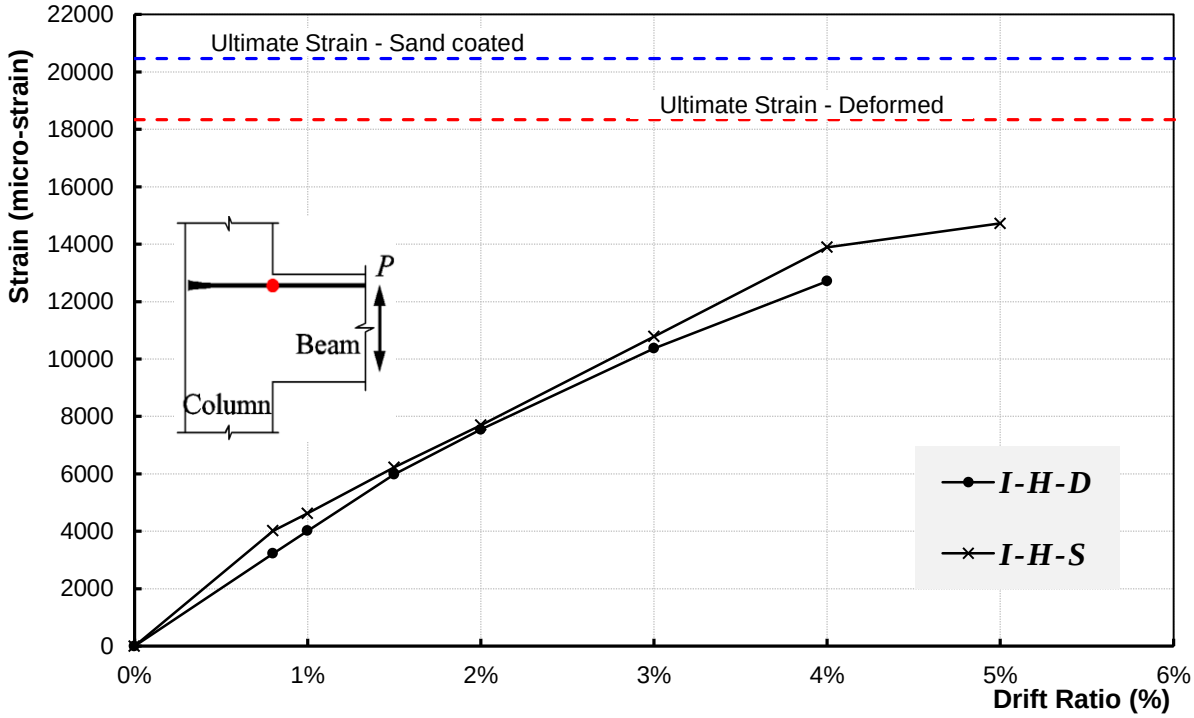

(a) Specimens I-H-D and I-H-S

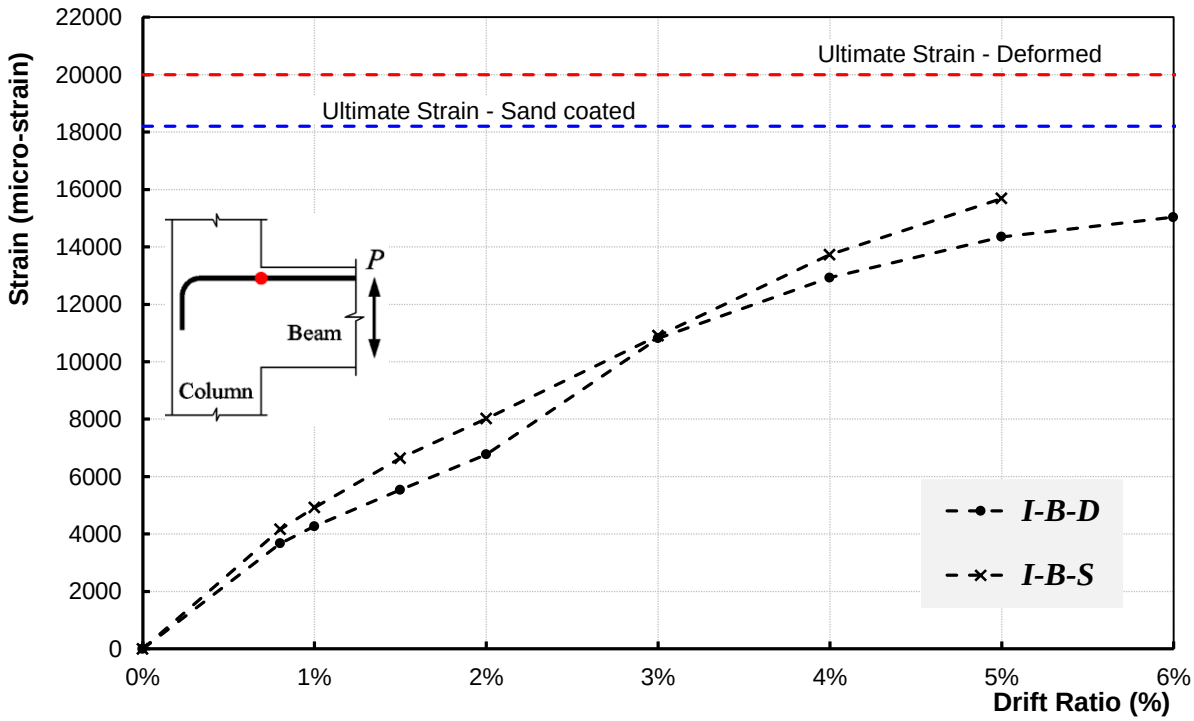

(b) Specimens I-B-D and I-B-S

Figure 5.7: Maximum strain–drift ratio relationship for beam longitudinal reinforcement

Figures 5.8(a) through (d) show the profile of the maximum tensile strains along the beam longitudinal reinforcement in the vicinity of the joint area at each loading drift. For specimens I-H-x, the figure shows the profile of the tensile strains captured by four strain gauges mounted along the beam longitudinal reinforcement at the column face, 200 mm away from the column face inside the beam (Beam side), 150 mm, and 300 mm away from the column face inside the joint (Joint side) as shown in the legend attached to Figures 5.8(a) and (c). Similarly, for specimens I-B-x, the strain profile is captured; however, the joint side had one strain gauge mounted just before the bent portion at 270 mm away from the column face as shown in Figures 5.8(b) and (d).

For Specimens I-H-D and I-H-S, the penetration of the tensile strains inside the joint was insignificant for up to 2.0% drift ratio, then started to increase with the increase of the loading drifts. The strain values at the same location; however just before the bent portion, in Specimens I-B-D and I-B-S exhibited consistent increase with increasing the drift ratio. Moreover, the readings of the strain gauge located 200 mm away from the column face in the beam are close to the maximum values recorded at the column face. This indicates that the formation of the inelastic deformability hinge length in the beam extends at least 200 mm from the column face in all specimens. The readings of the strain gauge located 300-mm away from the column face inside the joint and just before the end-bearing head were very useful to evaluate the contribution of the end-bearing heads to provide anchorage for the beam longitudinal bars as will be discussed in later section.

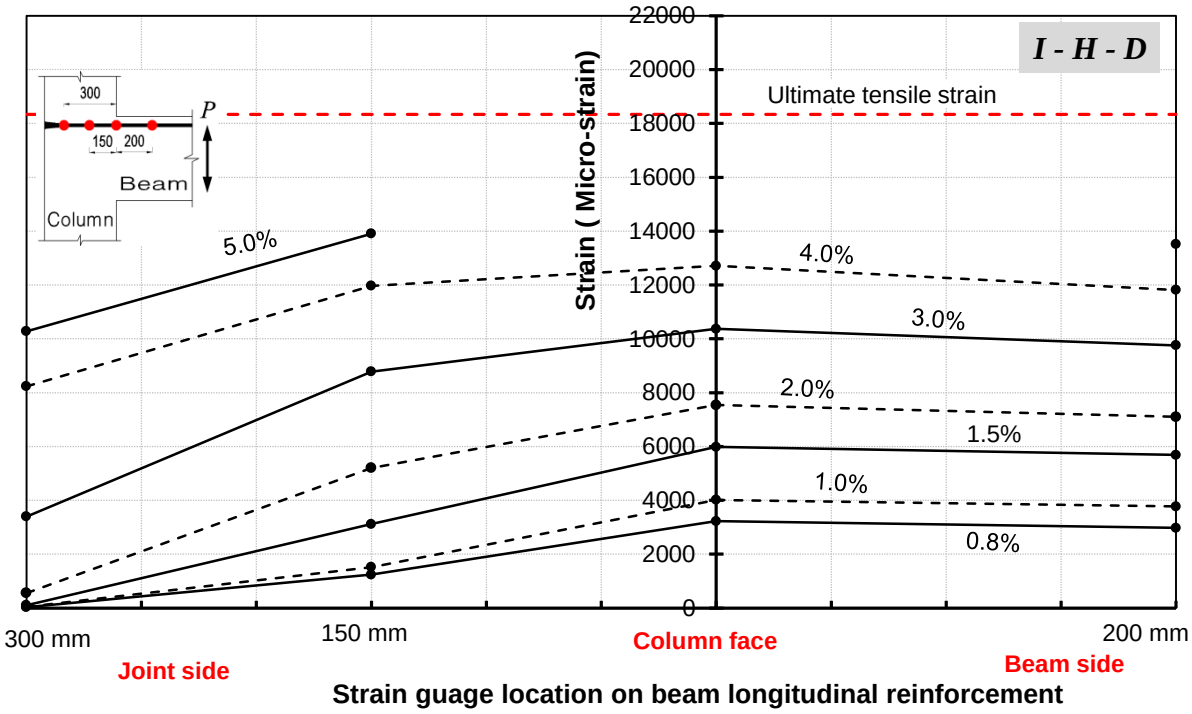

(a) Specimen I-H-D

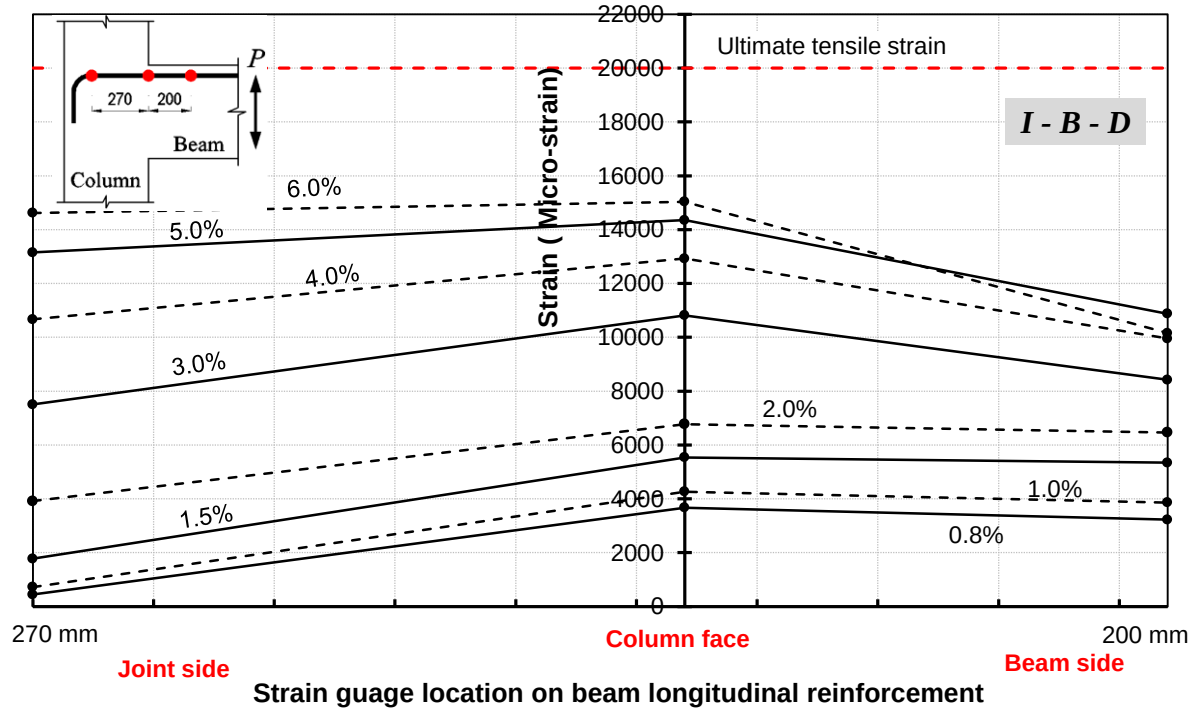

(b) Specimen I-B-D

Figure 5.8: Strain profile for beam longitudinal bars in Series (I) specimens (continued)

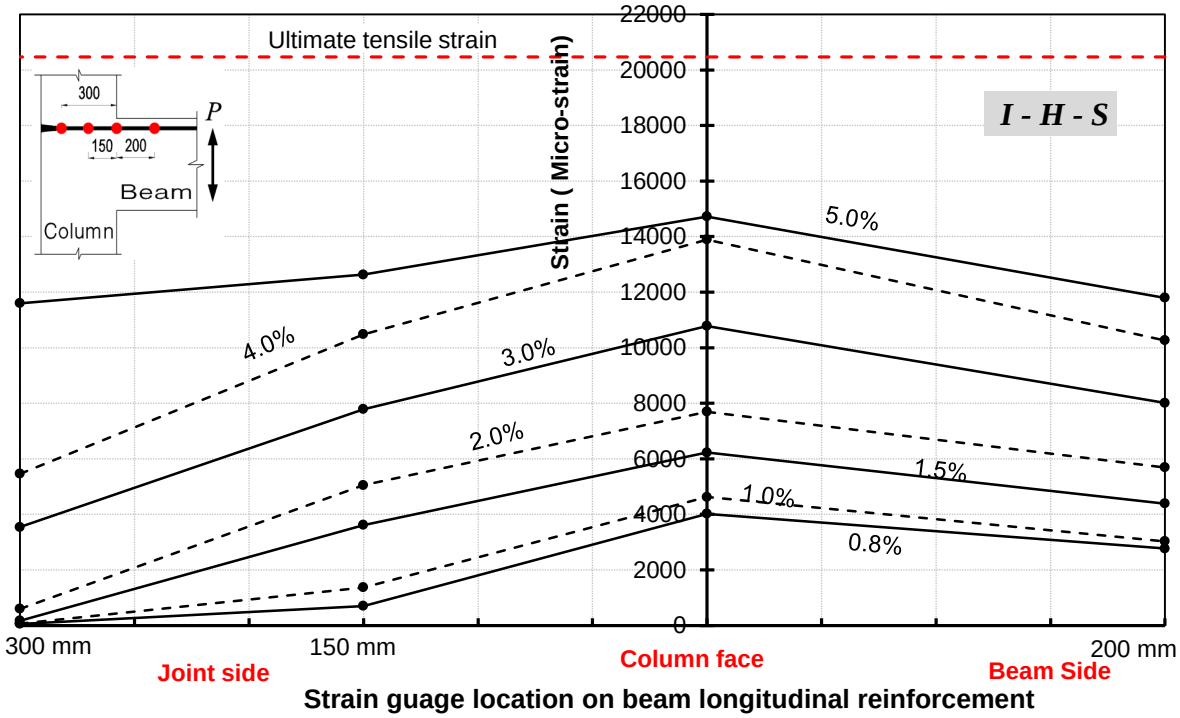

(c) Specimen I-H-S

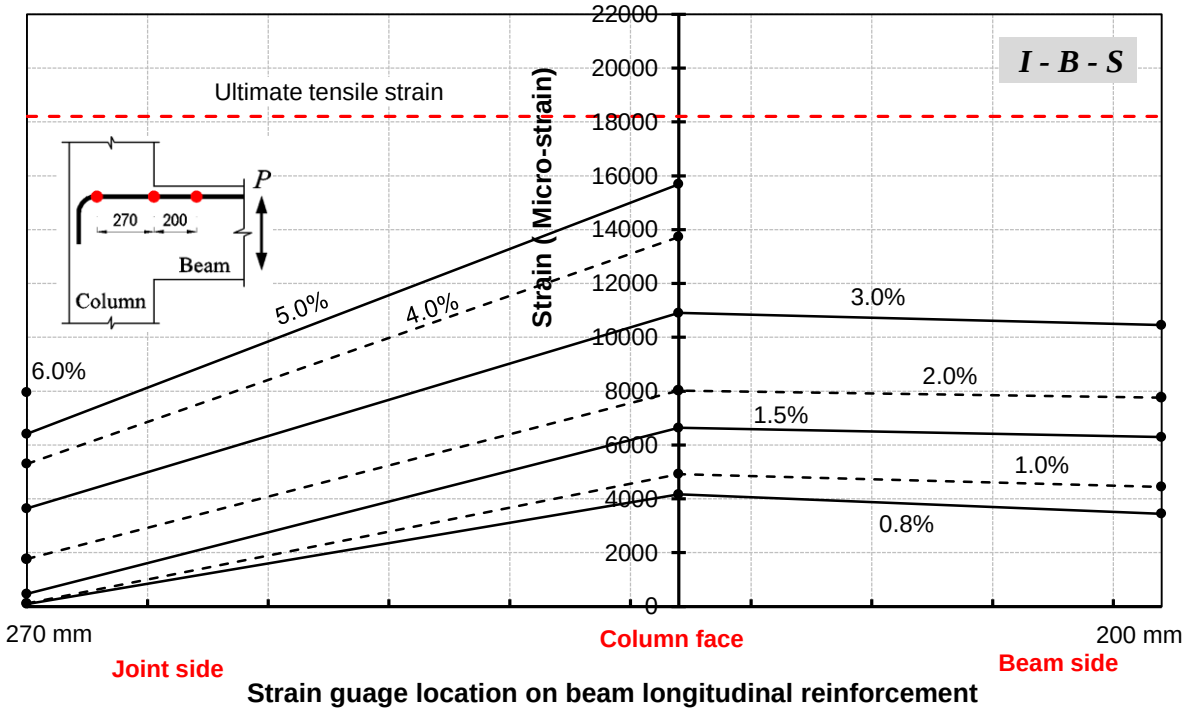

(d) Specimen I-B-S

Figure 5.8: Strain profile for beam longitudinal bars in Series (I) specimens

5.4.2 Developed Strains in Beam Transverse Reinforcement

The relationship between the maximum strains developed in the beam stirrups and the corresponding drift ratio is shown in Figure 5.9. The figure shows that the strain increases with the increase of the loading drifts until reaches a maximum value then drops down when the lateral load resistance of the specimen drops down as well. It can be noticed that none of the specimens exceeded the yielding strain of steel (2000 micro-strain). This is attributed to that the confinement requirement for the section exceeded the shear reinforcement requirements with respect to the anticipated shear force applied on the beam section.

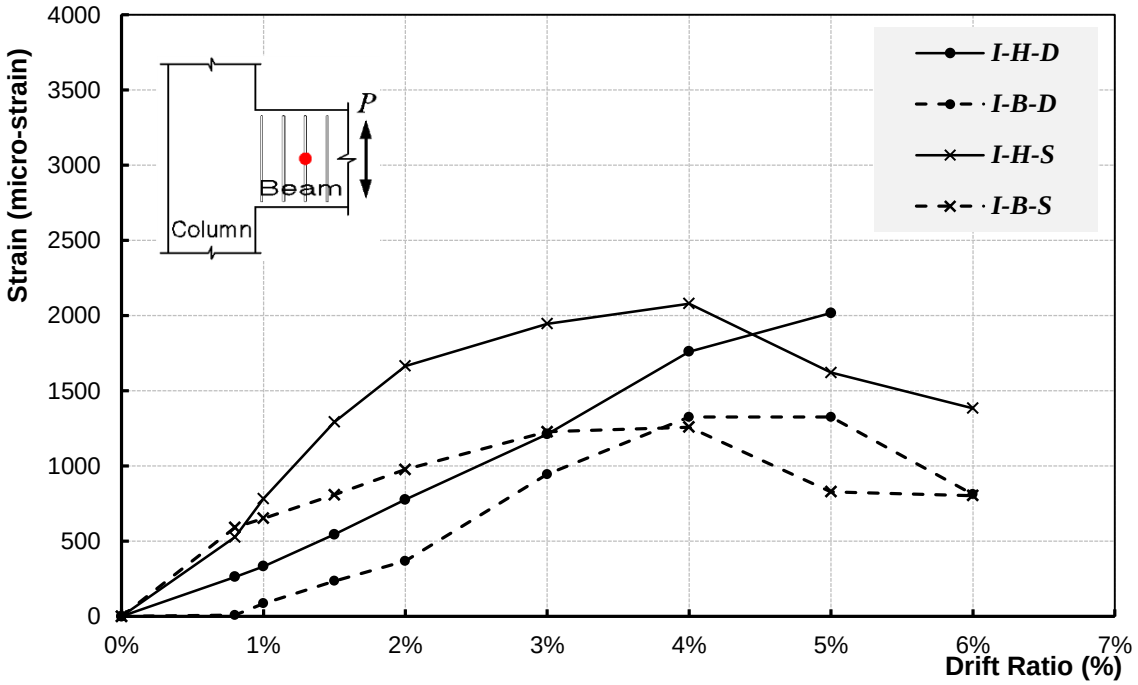

Figure 5.9: Maximum strain–drift ratio relationship for beam stirrups in Series (I) specimens

5.4.3 Developed Strains in Column Longitudinal Reinforcement

Figure 5.10 shows the relationship between the drift ratio and the maximum strains measured in the column longitudinal bar. The strain values started with negative values before applying the lateral deformation as a result of the axial compression on the column. As expected, the tensile strain values in the column were way below the ultimate tensile strain as a result of the axial load applied on the column. The highest strain values were exhibited by Specimens I-B-D and I-B-S, which experienced diagonal shear cracks in the joint. This is attributed to that the diagonal shear cracks in the joint started at the intersection of the column and the beam where the strain gauge was located as shown in the figure.

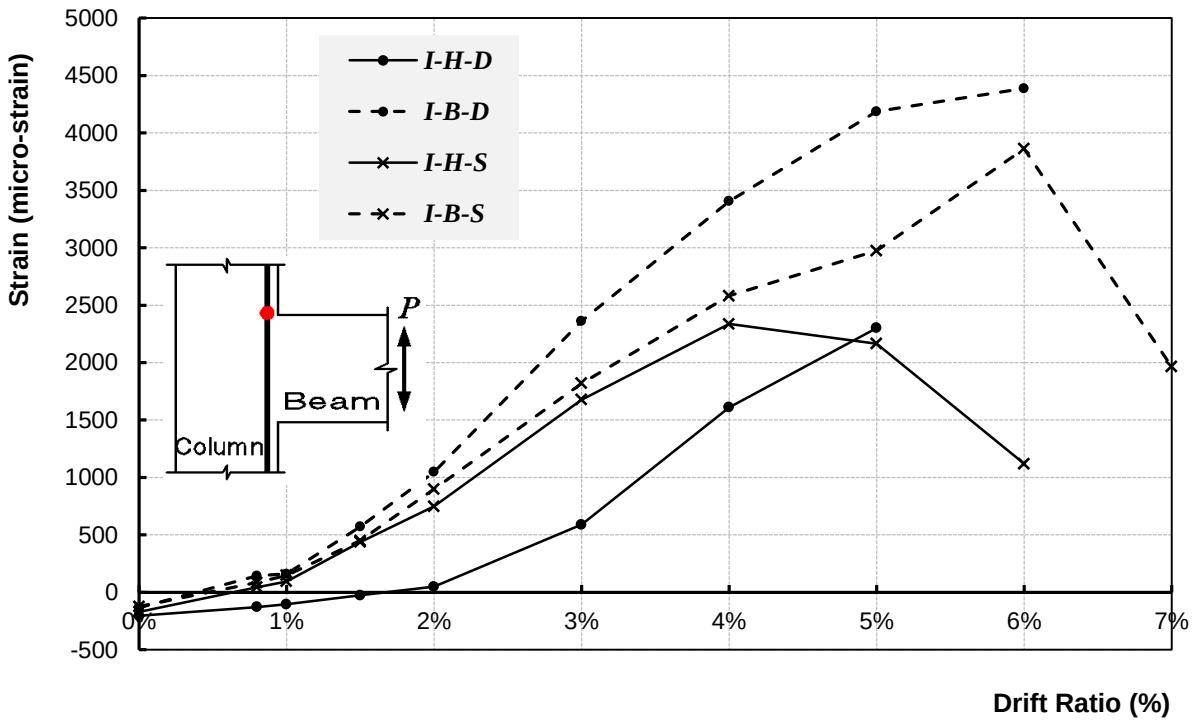

Figure 5.10: Maximum strain–drift ratio relationship for column longitudinal reinforcement in Series (I) specimens

5.4.4 Developed Strains in Joint Transverse Reinforcement

The relationship between the drift ratio and the maximum measured strain in the transverse reinforcement inside the joint is shown in Figure 5.11 for Series (I) specimens. The figure shows that the tensile strains in Specimens I-H-D and I-H-S did not exceed the yielding strain. On the other hand, the strain values in Specimens I-B-D and I-B-S approximately reached and exceeded the yielding strain at 4.0% drift ratio. This is in good agreement with the cracking pattern of the joint in these two specimens where the joint experienced wide diagonal shear cracks.

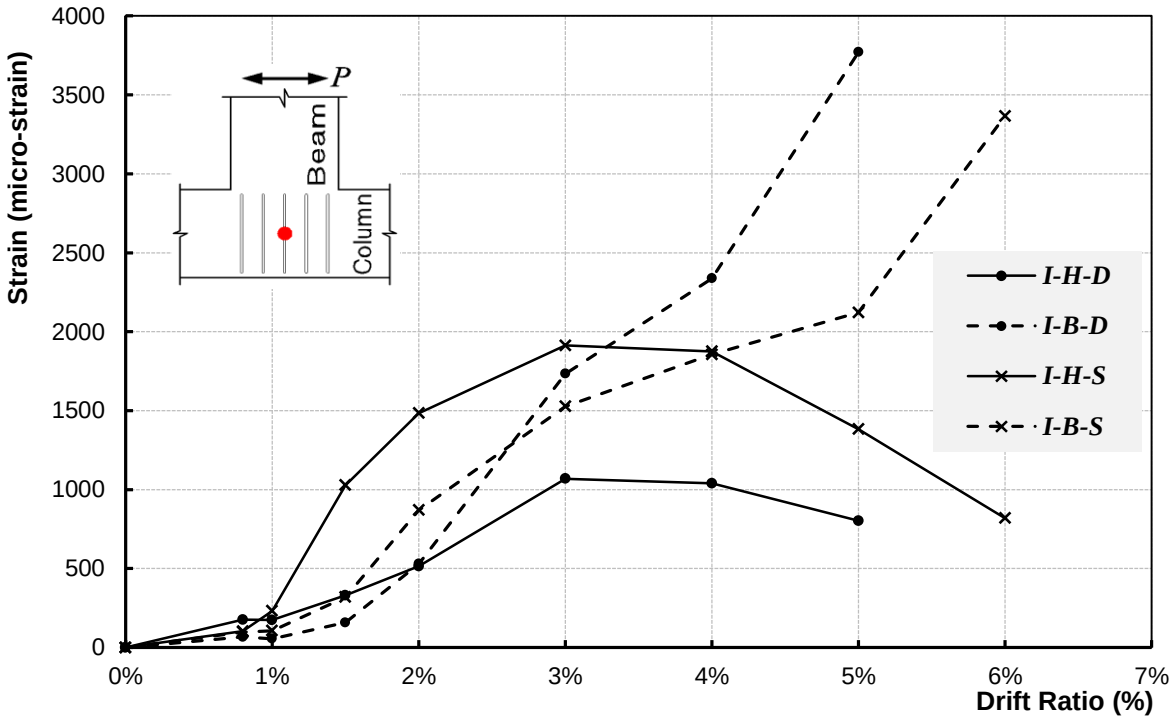

Figure 5.11: Maximum strain–drift ratio relationship for joint stirrups in Series (I) specimens

5.5 ENERGY DISSIPATION

The ability of structures to withstand severe earthquake vibrations and to perform in a satisfactory manner depends mainly on the formation of inelastic deformability hinges and their capability to absorb and dissipate seismic energy. The seismic input energy imparted to a structure is dissipated by its hysteretic behaviour. Energy dissipation is expressed in terms of the equivalent damping ratio that characterizes the shape of the hysteresis loops (*Chopra* 2000).

Figure 5.12 shows the cumulative energy dissipated by Series (I) specimens during testing for each loading drift. The cumulative energy dissipation was calculated by summation of the dissipated energy in successive load-displacement cycles. The energy dissipated by each cycle is expressed by the area that the hysteretic loop encloses in the corresponding beam tip load-displacement. From Figure 5.12(a), it is observed that all specimens dissipated the same level of energy at 4.0% drift ratio. The figure also shows that specimens, which sustained higher drift ratio, dissipated higher energy. The amount of dissipated energy after 4.0% drift ratio is significantly higher than what achieved before this limit.

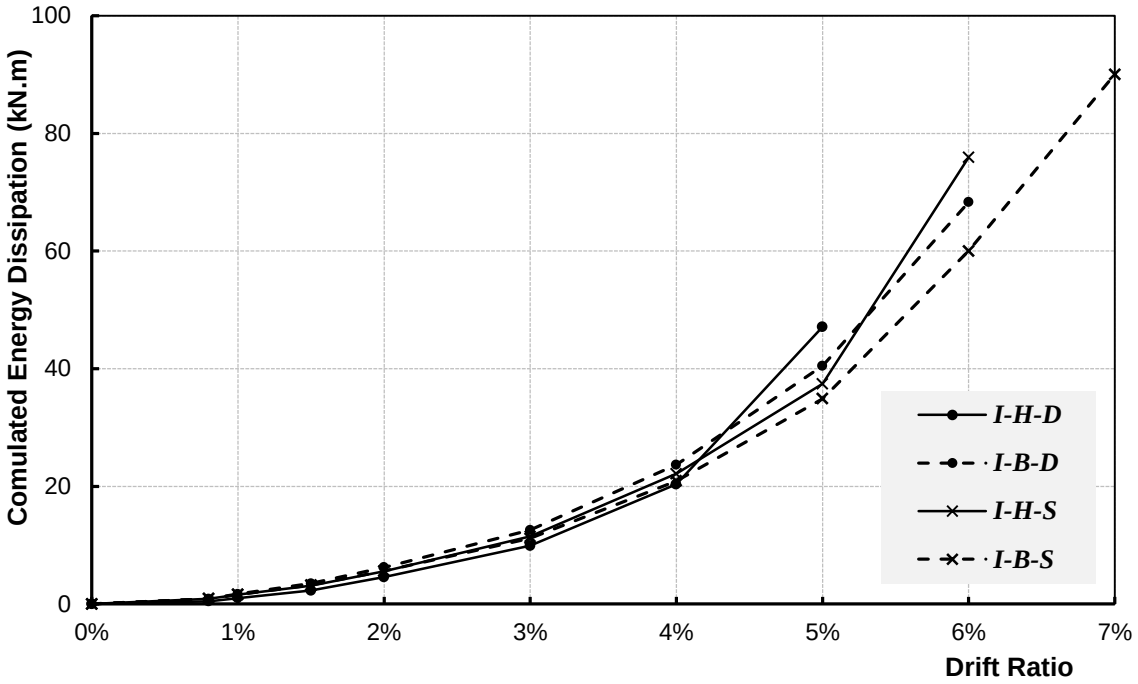

(a) Series (I) specimens

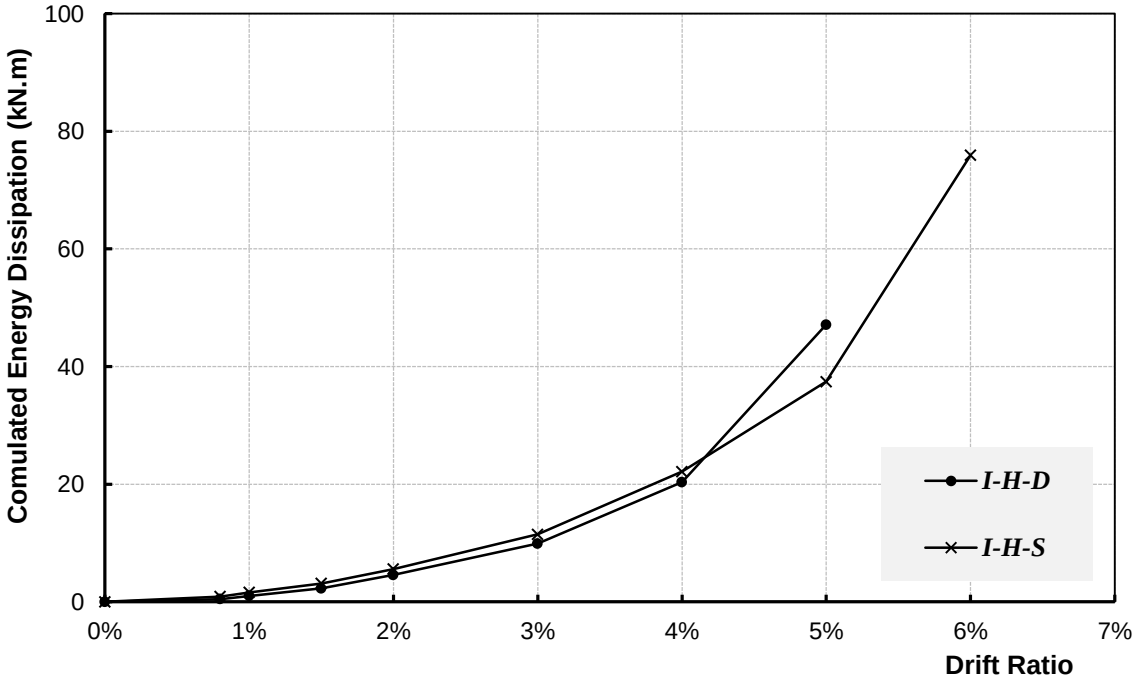

(b) Specimens I-H-D and I-H-S

Figure 5.12: Cumulative energy dissipated by Series (I) specimens (continued)

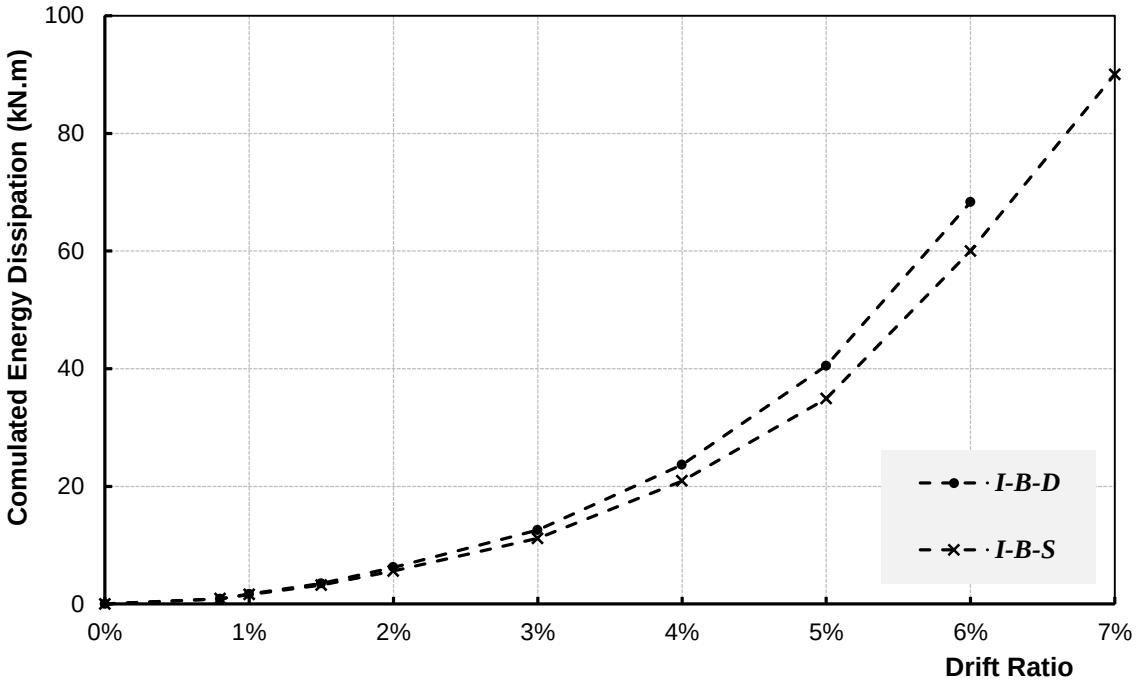

(c) Specimens I-B-D and I-B-S

Figure 5.12: Cumulative energy dissipated by Series (I) specimens

It is generally recognized that there is a strong correlation between the energy dissipated by the hysteretic action and the seismically induced level of damage. The slope of the cumulated energy dissipation-drift ratio relationship indicates the concrete damage rate due to formation of inelastic deformability hinges and/or diagonal shear failure in the joint. As shown in Figure 5.12(b), Specimens I-H-D and I-H-S had the same slope up to 4.0% then specimen I-H-D showed steeper increase in the dissipated energy at failure (5.0% drift ratio) while Specimen I-H-S experienced similar behaviour after 5.0% drift ratio. This is in agreement with the earlier discussion of the hysteretic loops and the mode of failure of the two specimens where the formation of inelastic deformability hinges and slippage (damage) started at 4.0% and 5.0% for Specimens I-H-D and I-H-S, respectively. Moreover, Specimen I-B-D, with deformed bent bars, showed slightly

higher energy dissipation than that exhibited by Specimen I-B-S with sand-coated bent bars during all levels of testing up to failure of Specimen I-B-D (6.0% drift ratio) as shown in Figure 5.12(c).

In conclusion, it is worth mentioning that both anchorage types (bent bars and headed bars) and reinforcement surface condition have no significant influence on the energy dissipation up to 4.0% drift ratio. However, specimens with bent bars sustained higher drift ratios, which resulted in higher energy dissipation, yet, at higher drift ratios.

5.6 STIFFNESS-DRIFT RELATIONSHIP

Some factors are known to influence the overall stiffness of the RC structural members; namely, the geometry of the concrete members, amount and stiffness of the reinforcement and the level of cracking. In this research study, the member geometry is not a factor since all specimens had the same concrete dimensions. This means that the concrete strength and reinforcement stiffness govern the overall stiffness of the specimens at different loading stages. Figure 5.13 shows the overall stiffness-drift ratio relationship for Series (I) specimens during testing. The stiffness was calculated using the load-lateral displacement relationship as the slope of the line connecting the two peaks of lateral load.

As shown in Figure 5.13, the range of the calculated stiffness of specimens in the un-cracked stage was approximately between 15 and 17 kN/mm. Once the specimens were subjected to the cracking load cycle, the stiffness range dropped to values approximately between 5 to 8 kN/mm due to cracks occurred in the beam section at the column face

(critical section in flexure). This shows that the stiffness in the cracked stage is approximately 33% to 50% of the original stiffness calculated based on the gross inertia of the un-cracked sections. This is in agreement with the cracked section properties of steel RC beams in the CSA/A23.3-04, Clause 21.2.5.2.1, which requires that reduced section properties shall be used as a fraction of the gross section inertia where in beams 40% of the gross inertia shall be used in the analysis to determine the straining actions and deflections of the structure. The figure also shows that the difference in concrete strength between the specimens had insignificant influence on the overall stiffness. Moreover, It is observed that the stiffness degradation after the first cyclic loading and up to failure is insignificant compared to the degradation occurred at the service stage (cracked section).

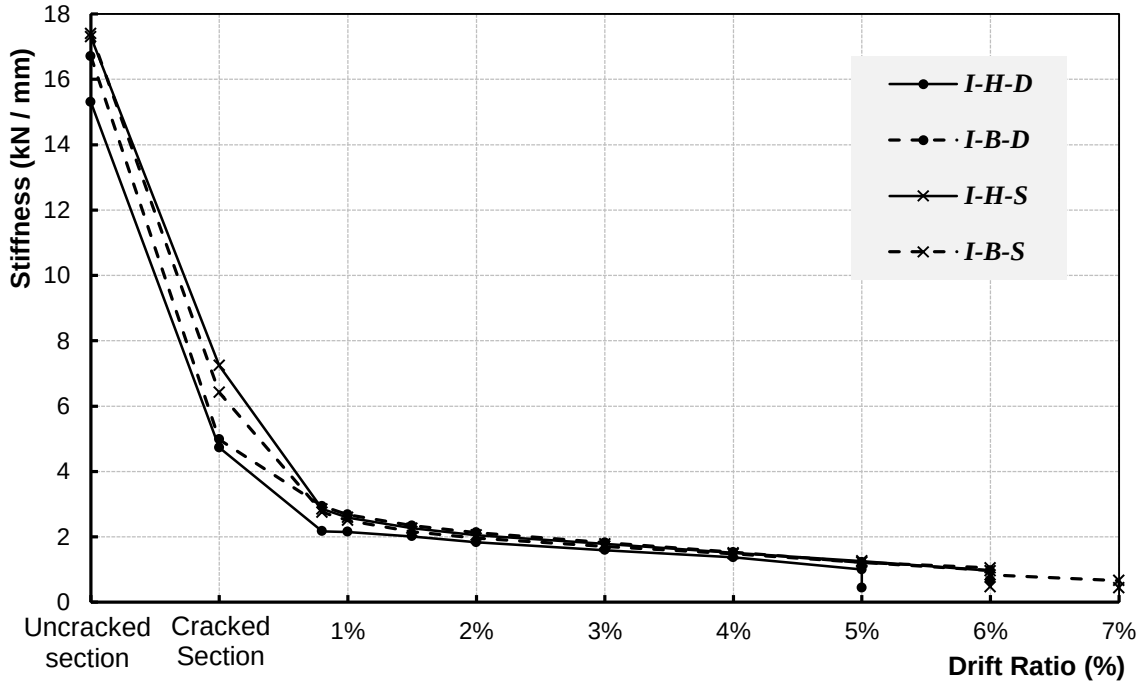

Figure 5.13: Stiffness–drift ratio relationship for Series (I) specimens

5.7 DRIFT COMPONENTS

The external instrumentation (LVDTs) in this experimental program was used to measure the main drift components. These components are: 1) development of main crack on the column face including strain penetration inside the joint; 2) rotation in the anticipated beam inelastic deformability hinge zone within a distance equal to the effective depth of the beam from the column face; and 3) distortion in the joint due to shear deformation, as shown in Figures 5.14 (a), (b), and (c), respectively. Other drift components such as column rotation, elastic flexural cracking away from the inelastic deformability hinge, and shear deformation in the beam were not considered in this study. Due to the linear-elastic behaviour of the GFRP bars, the term "plastic hinge" is not valid. However, the term "inelastic deformability hinge" is used to represent the development of large elastic tensile strains in the GFRP bars associated with the concrete reaching its ultimate compressive strain in the beam section at the column face. It should be noted that the measurement of the drift components stopped when the beam or the joint lost the concrete cover where the LVDTs were attached to.

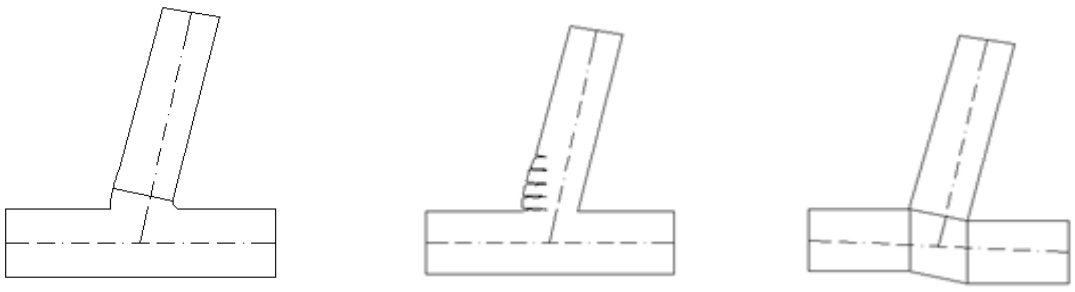

a) Main crack on column face b) inelastic deformability hinge c) Joint distortion

Figure 5.14: Major components contributing to total drift angle

Figure 5.15 shows the contribution of the major drift components (inelastic deformability hinge, main crack at column face, and joint distortion) to the overall rotation of the specimens. It should be noted that light spalling of beam concrete cover under the LVDTs fixation points in Specimens I-B-D, I-H-S, and I-B-S during testing prevented monitoring the inelastic deformability hinge rotation. However, monitoring the beam-to-column relative rotation was still applicable. Therefore, Figures 5.15(b) to (d) show the contributions of the inelastic deformability hinge and the main crack combined together in one hatched area contrary to Specimen I-H-D.

For specimen I-H-D, Figure 5.15(a) shows that the major contribution to the drift angle is attributed to the inelastic deformability hinge component where it reached 50% of the total drift angle at 0.8% drift ratio. In addition, the development of the main beam crack at the column face along with the strain penetration inside the joint (referred to as "main crack at column face" in the figures) contributed to the total drift by approximately 10% at the beginning of test to 30% at 4.0% loading drift. Collectively, the contribution of the two previous components was in the range of 60% to 65% through all levels of loading drifts up to the point where the drift instrumentation was removed after 4.0% drift ratio. The joint distortion component remained insignificant with only about 4% contribution to the total drift angle.

Similarly, for Specimens I-B-D, I-H-S, and I-B-S, the majority of the drift angle was attributed to the inelastic deformability hinge and the cracking at the column face with a contribution of approximately 60% to 65% of the exhibited drift angle. The figure shows

that the behaviour of those two specimens reinforced with headed bars, I-H-D and I-H-S, was comparable to those reinforced with bent bars, I-B-D and I-B-S. Moreover, the difference in the reinforcement surface condition does not seem to affect the rotation behaviour of the specimens since they all exhibited similar behaviour. On overall, it can be observed that the anchorage type and the reinforcement surface condition had no significant influence of the rotation of the specimens.

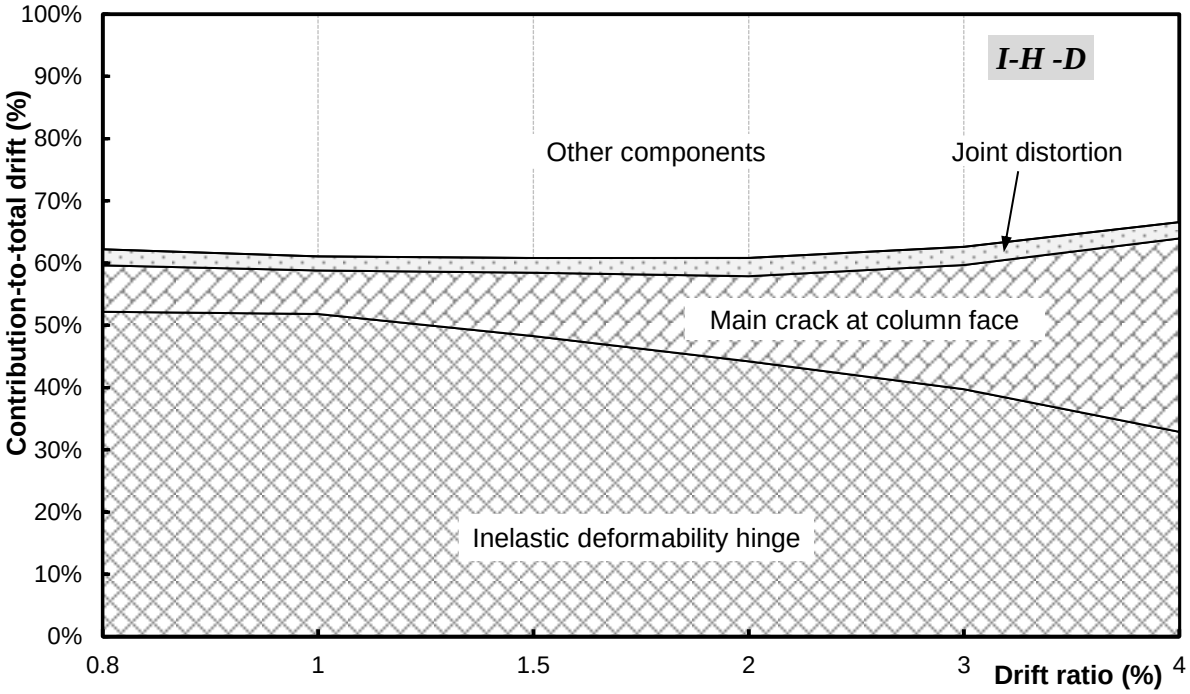

(a) Specimen I-H-D

Figure 5.15: Contributions to total drift angle for Series (I) specimens (continued)

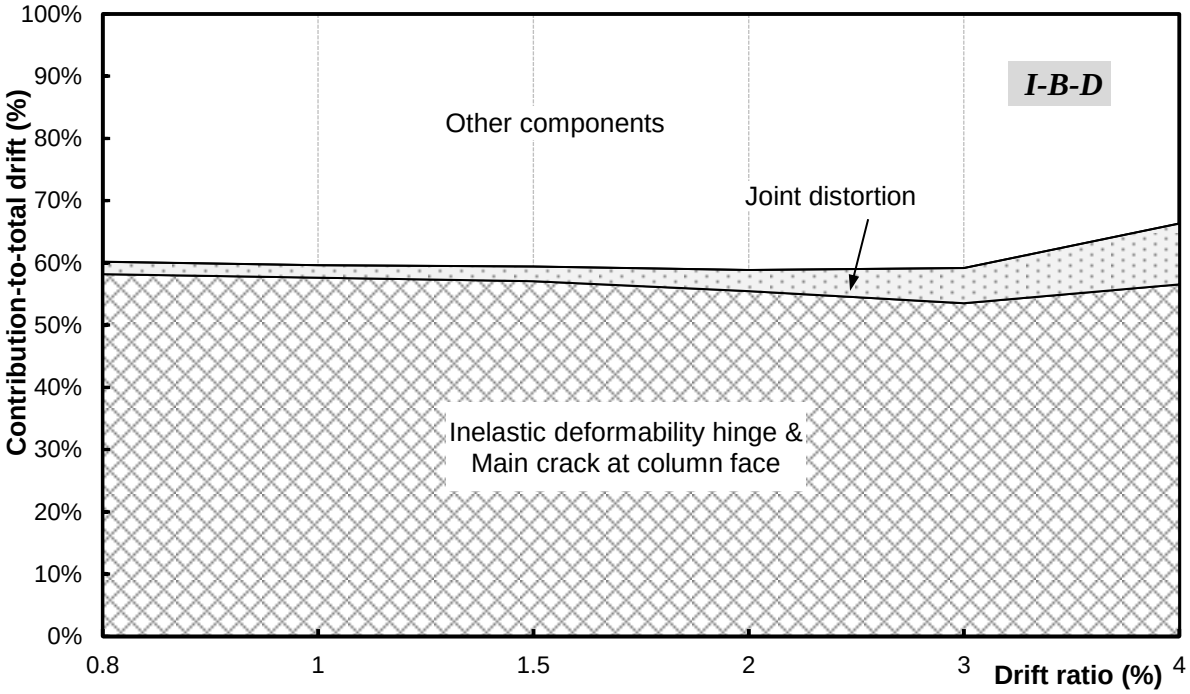

(b) Specimen I-B-D

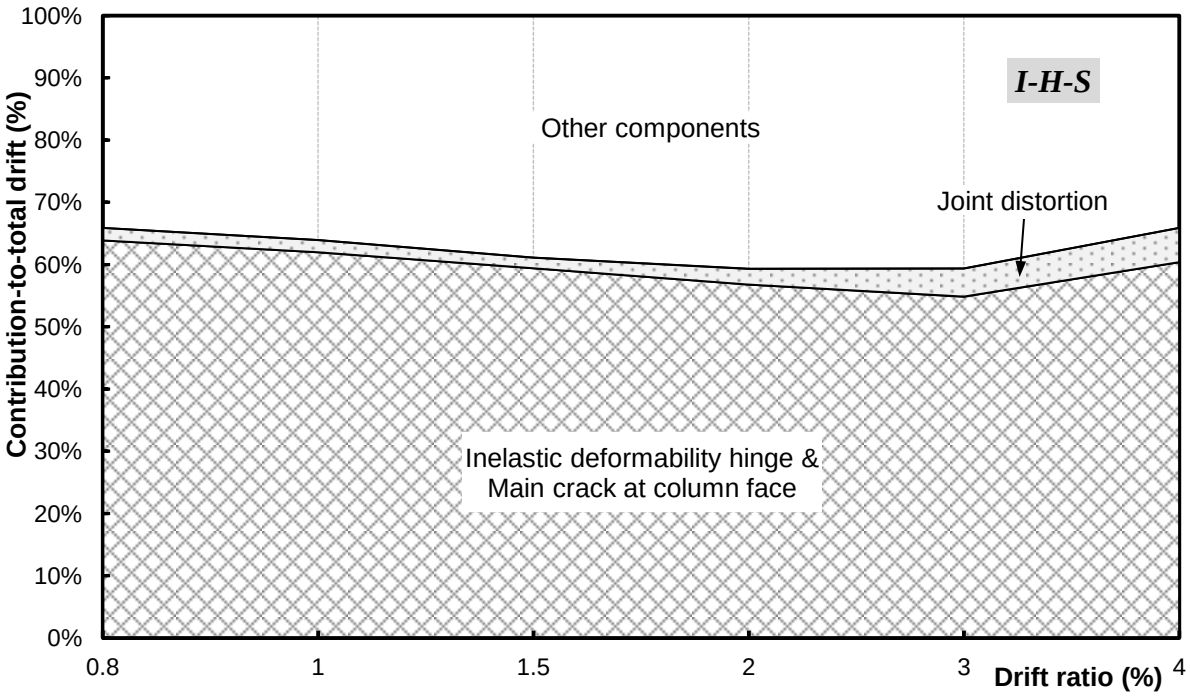

(c) Specimen I-H-S

Figure 5.15: Contributions to total drift angle for Series (I) specimens (continued)

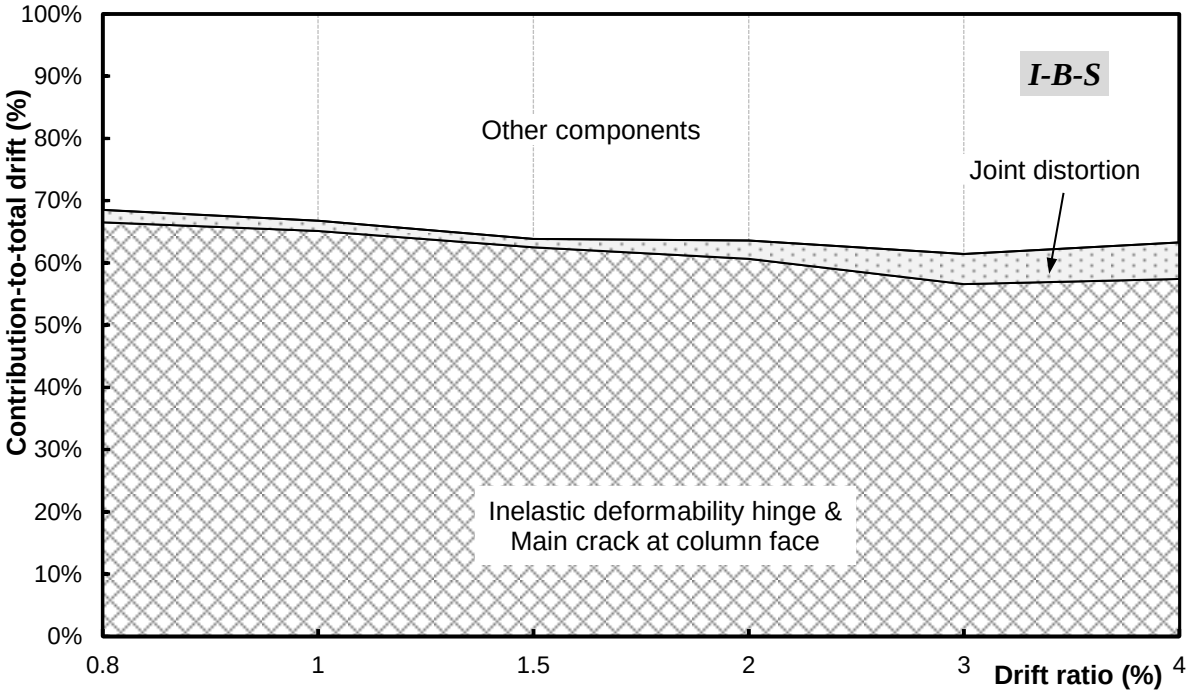

(d) Specimen I-B-S

Figure 5.15: Contributions to total drift angle for Series (I) specimens

5.8 EVALUATION OF ANCHORAGE PERFORMANCE OF GFRP HEADED BARS IN SERIES (I) SPECIMENS

As explained before in the experimental program in Chapter 4, 90-degree bent bars as well as headed bars were used as two different anchorage details for beam longitudinal reinforcement embedded into the joint in Series (I) specimens. The anchorage performance of both anchorage details is evaluated in this section.

In general, the tensile force developed in the beam longitudinal reinforcement is resisted by embedding the bar in the concrete with a depth equal to or larger than the full development length. In this case the tensile force is solely resisted by bond stresses between the reinforcement surface and the concrete. In frame elements where the depth

of the column is less than the full development length of the beam longitudinal reinforcement, an end-anchorage detail need to be implemented at the bar end either by using standard hooks or by using bearing heads. In this case, the resisting force will be a combination between the bond stresses on the available embedded length and the end-anchorage as shown in Figure 5.16 for headed and bent bars.

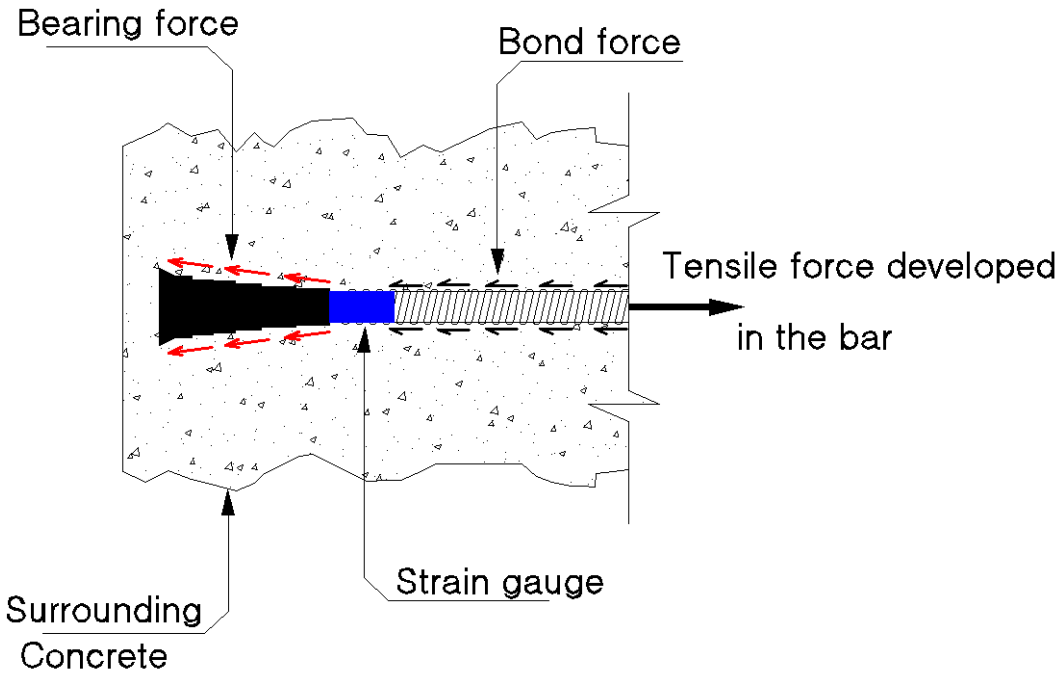

(a) Headed bar

Figure 5.16: Anchorage mechanism (continued)

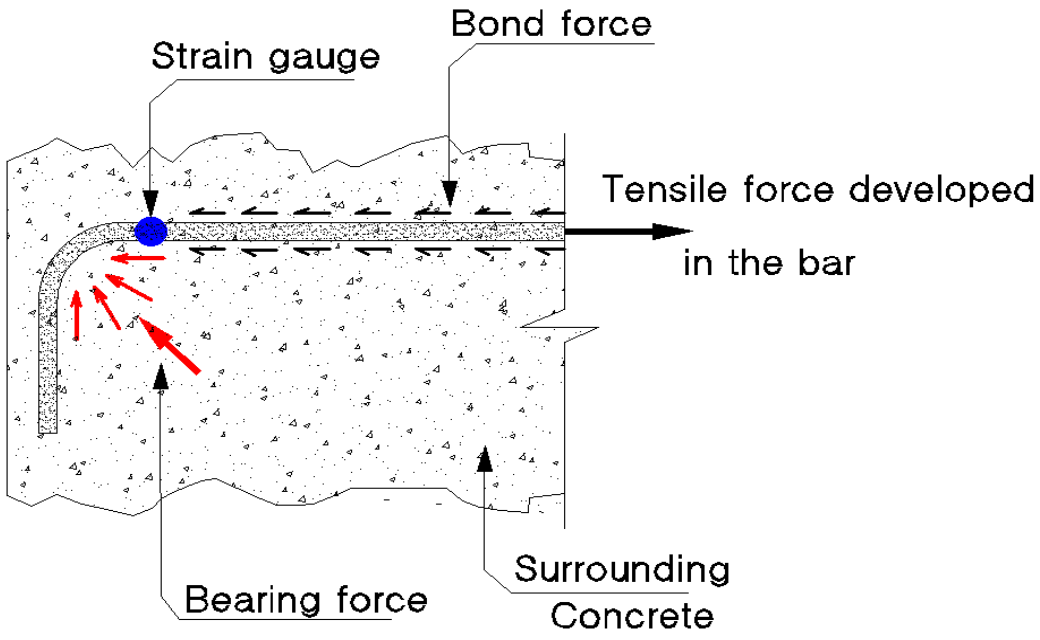

(b) Bent bar

Figure 5.16: Anchorage mechanism

To evaluate the anchorage contribution while maintaining effective bond interaction between the bars and the concrete (no bond breaker was used around the bar to eliminate the bond), a strain gauge was mounted on the rebar just before the anchorage detail (i.e. bent portion and moulded end-head) as shown before in Figure 5.16. The strain gauge in that location detects the tensile strain developed in the rebar and consequently the tensile stress resisted by the anchorage detail.

Figure 5.17 shows the relationship between the tensile stress resisted by each anchorage detail and the loading drifts for Series (I) specimens. As shown in the figure, the resisted stress increases with the increase of the loading drift as a result of the tensile force increase in the longitudinal reinforcement and gradually penetrates into the joint. As

shown in Figure 5.17(a), the maximum tensile stress resisted by the headed bars is 930 and 620 MPa in Specimens I-H-S and I-H-D, respectively. These values represent 70 and 56% of the ultimate tensile capacity of the bars used in those two specimens, respectively. Although that eventually both specimens exhibited failure due to anchorage slippage, the anchorage performance of the headed bars in both specimens was satisfactory and enabled the specimens to pass the 4.0% drift ratio safely without any signs of anchorage slippage failure.

Figure 5.17(b) shows the anchorage resistance of the 90-degree bent bars. The figure shows that Specimens I-B-D and I-B-S sustained loading drifts of 6.0% and 7.0% while the developed tensile stresses just before the bent portion reached 660 and 750 MPa, respectively. These values represent 73 and 82% of the ultimate tensile capacity of the beam longitudinal reinforcement used in these two specimens, respectively. However, it should be noted that specimens reinforced with bent bars, I-B-D and I-B-S, did not experience the anchorage-slippage mode of failure that exhibited by specimens reinforced with headed bars, I-H-D and I-H-S. Therefore, the reported values regarding Specimens I-B-D and I-B-S do not represent the maximum anchorage resistance of the 90-degree bent portions. The maximum anchorage resistance could be larger than what reported in this study since both specimens did not experience failure in the bent portions. However, the reported values can be used as a guide for the minimum anchorage resistance that can be reached by GFRP bent bars.

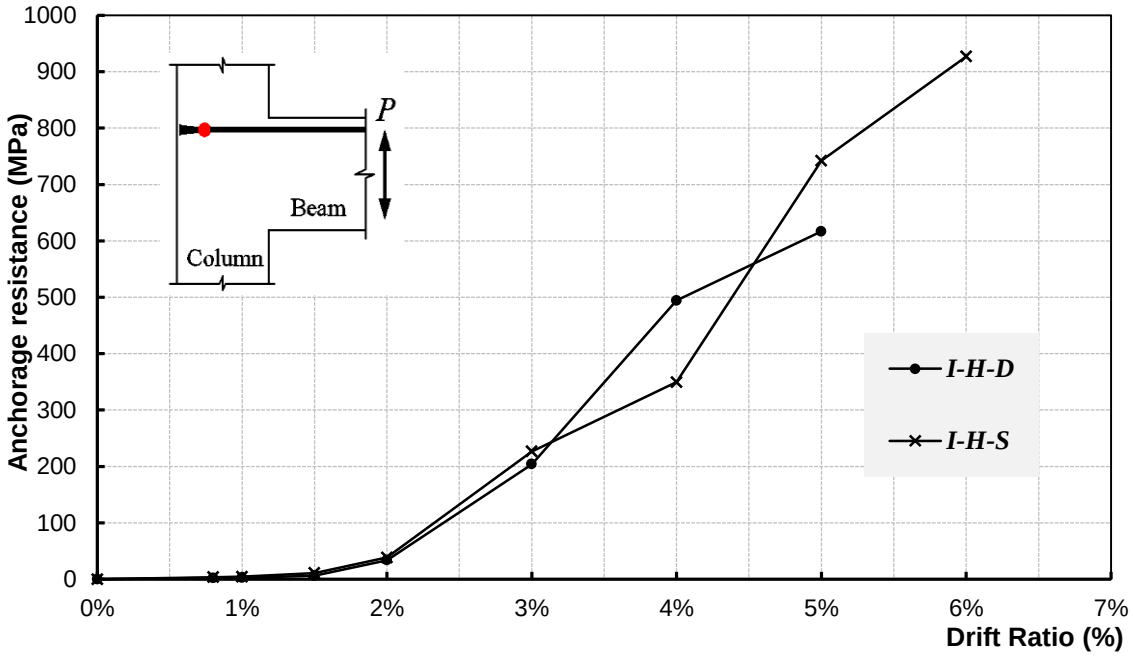

(a) Headed bar

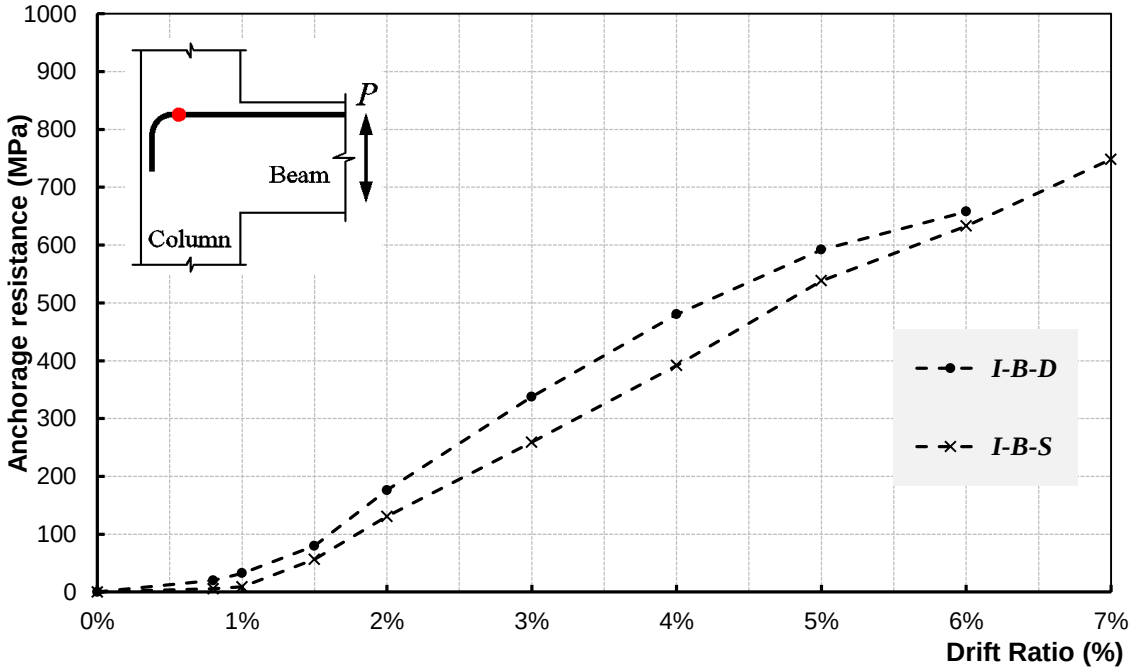

(b) Bent bars

Figure 5.17: Anchorage contribution in Series (I) specimens

In general, Figures 5.17(a) and (b) show that the anchorage performance of the headed bars was satisfactory and equivalent to the performance of the 90-degree bent bars in the sense that both anchorage details prevented the occurrence of the anchorage slippage failure before 4.0% drift ratio. Moreover, it is worth mentioning that the anchorage performance of sand-coated headed bars outperformed their counterparts with deformed surface by 50% more anchorage capacity. However, shearing-off in the sand coating around the bars was observed by the end of the test as shown in Figure 5.18(a). On the other hand, the deformed surface bars in specimen I-H-D experienced minimal damage to the deformed/ribbed surface of the bars as shown in Figure 5.18(b). Both headed bars, either with sand-coated or deformed surface, exhibited slippage failure due to failure of anchorage heads by bearing as shown in Figure 5.19.

(a) Shearing-off in sand coating on the bars

(b) Minimal damage for the deformed surface

Figure 5.18: Surface damage of beam longitudinal reinforcement in Specimens I-H-D and I-H-S

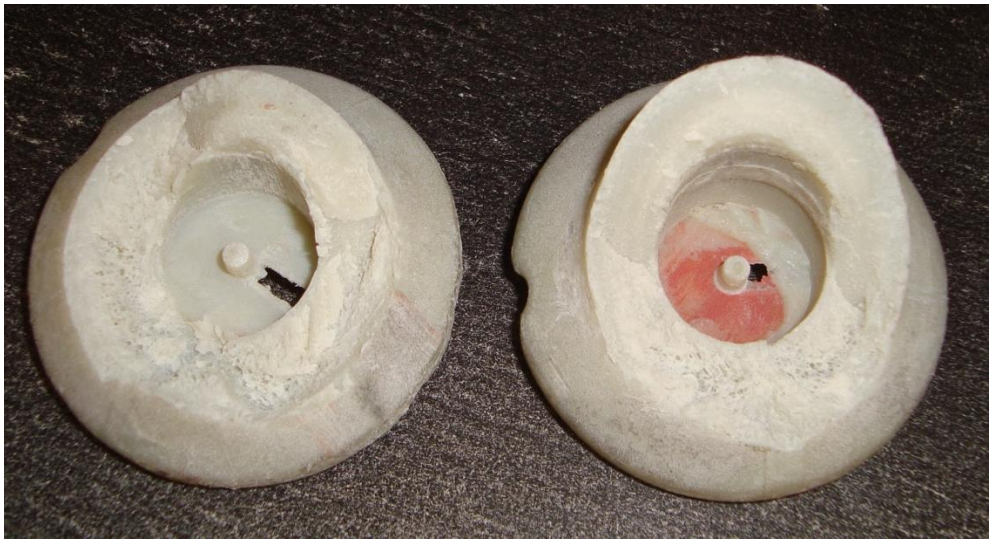

Figure 5.19: Typical bearing failure of anchorage heads in Specimens I-H-D and I-H-S

CHAPTER 6

EXPERIMENTAL RESULTS OF SERIES (II) SPECIMENS

6.1 INTRODUCTION

As explained previously in Chapter 4, Series (II) was designed to study the influence of concrete strength on the behaviour when the joint is subjected to different levels of shear stresses. Two different concrete strengths; normal strength (30 MPa) and high strength (60 MPa), in combination with three different shear stress levels in joint were studied; Low shear level ($0.70\sqrt{f'_c}$), moderate shear level ($0.85\sqrt{f'_c}$), and high shear level ($1.0\sqrt{f'_c}$). Combinations of the above concrete strengths and shear stress levels lead to six specimens (II-30-0.7, II-30-0.85, II-30-1.0, II-60-0.7, II-60-0.85, and II-60-1.0). The analysis and discussion of the experimental results for testing Series (II) specimens are presented in the following sections.

6.2 LOAD–LATERAL DRIFT RESPONSE (HYSTERETIC BEHAVIOUR)

Plots of the hysteresis diagrams which represent the relationship between the applied lateral load and the drift ratio of the beam tip are shown in Figure 6.1. The drift ratio was calculated as the ratio between the horizontal displacement of the beam end at the point of load application and the distance from the point of load application to the column centreline (i.e. 2200 mm). As shown in Figures 6.1(a), (b), and (c), the measured hysteresis loops for Specimens II-30-0.70, II-30-0.85, and II-30-1.0 demonstrated a typical stable elastic-linear response up to drift ratios of 4.0%, 4.0%, and 3.0% respectively, then followed by a non-linear behaviour and lateral-resistance drop in

different forms for the three specimens. Although Specimen II-30-1.0 showed the highest lateral load resistance, it was the first specimen to show signs of failure and failed at 5.0% drift ratio. Regarding Specimen II-30-0.70, once it reached 5.0% drift ratio a sudden drop in the lateral load resistance was observed. This drop in resistance is attributed to the slippage of the beam longitudinal headed-bars anchored in the joint due to failure of the anchorage heads attached to the end of the bars. Despite of failure of the anchorage heads, the specimen was still able to resist 50.0% of its designed capacity during the rest of the 5.0% drift ratio loading cycles till the end of the test at 6.0% drift ratio.

Contrary to Specimen II-30-0.70, Specimens II-30-0.85 and II-30-1.0 showed non-linear behaviour and gradual degradation of the lateral load resistance after reaching 4.0% drift ratio. Regarding Specimen II-30-0.85, the non-linear response started at 5.0% drift ratio. This can be shown by the increase in the pinching distance of the hysteresis loops from 23 kN at 4.0% to 45 kN at 6.0% drift ratio. This can be attributed to the non-linear deformation of the concrete in the beam and the joint. The specimen showed no loss of lateral resistance from 4.0% to the first cycle of 5.0% drift ratio then a gradual degradation of the resistance was observed during the rest of the 5.0% loading cycles until the end of the test at 6.0%. During the 5.0% drift ratio loading cycles, the specimen lost approximately 25% of its maximum resistance, while by the end of the test at 6.0% drift ratio, the specimen was able to withstand approximately 40% of its maximum resistance as shown in Figure 6.1(b). For Specimen II-30-1.0, the non-linear response started on the 4.0% drift ratio where the specimen reached the maximum resistance. The

specimen exhibited that increase in pinching distance of the hysteresis loops, however, from 24 kN at 3.0% to 50 kN at 5.0% drift ratio. It showed earlier signs of failure and lateral resistance degradation started at 4.0% drift ratio with insignificant loss of approximately 15.0% and ended by approximately 60.0% loss of the maximum resistance by the end of the test at 5.0% drift ratio as shown in Figure 6.1(c).

Regarding Specimens II-60-0.70, II-60-0.85, and II-60-1.0 constructed with higher concrete strength, the hysteretic behaviour was identical to that behaviour exhibited by Specimens II-30-0.70, II-30-0.85, and II-30-1.0, respectively; however, with achieving higher values of lateral load resistance and drift ratios. As shown in Figure 6.1(d), Specimen II-60-0.70, exhibited the typical stable elastic-linear behaviour up to 5.0% drift ratio then a sudden drop to approximately 50.0% in the lateral load resistance occurred when the specimen reached the 6.0% drift ratio. This sudden drop in lateral load resistance is similarly attributed to the failure of the anchorage heads of the beam longitudinal reinforcement embedded in the joint.

While Specimen II-60-0.70 exhibited sudden failure in the lateral load resistance at 6.0% drift ratio, Specimens II-60-0.85 and II-60-1.0 showed the elastic-linear behaviour up to 6.0% and 5.0% drift ratios, respectively, then followed by a non-linear behaviour and gradual loss of lateral resistance due to the plastic deformations occurred in the concrete. Due to the higher shear stress generated in the joint, Specimen II-60-1.0 showed earlier lateral resistance degradation at 6.0% drift ratio, as shown in Figure 6.1(f), contrary to Specimen II-60-0.85 which showed similar behaviour, however, at 7.0% drift ratio as

shown in Figure 6.1(e). The generated shear stress in the joint also influenced the non-linear behaviour of the specimens; this can be shown in Specimen II-60-1.0 by the increase in the pinching distance of the hysteresis loops from 30 kN at 5.0% to 65 kN and 75 kN at 6.0% and 7.0% drift ratio. While Specimen II-60-0.85 had increase in the pinching distance of 22.0 kN, 30.0 kN, and 75.0 kN at 5.0%, 6.0% and 7.0%, respectively.

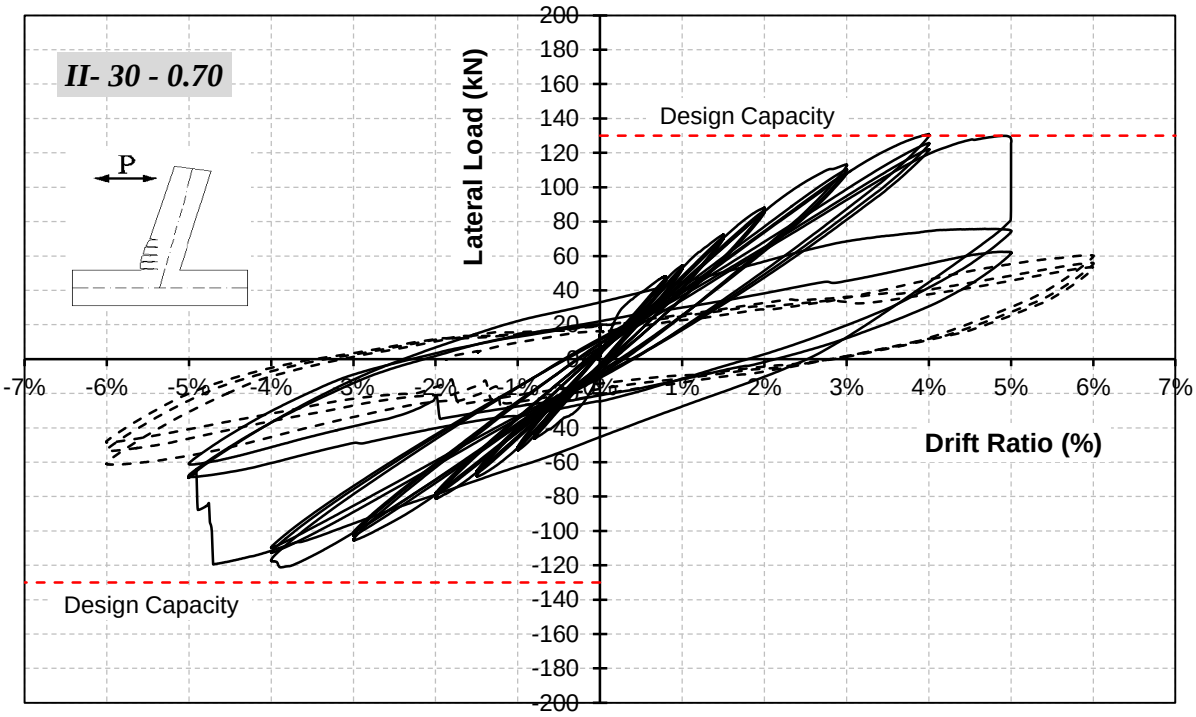

(a) Specimen II-30-0.70

Figure 6.1: Load-Lateral Drift relationship (continued)

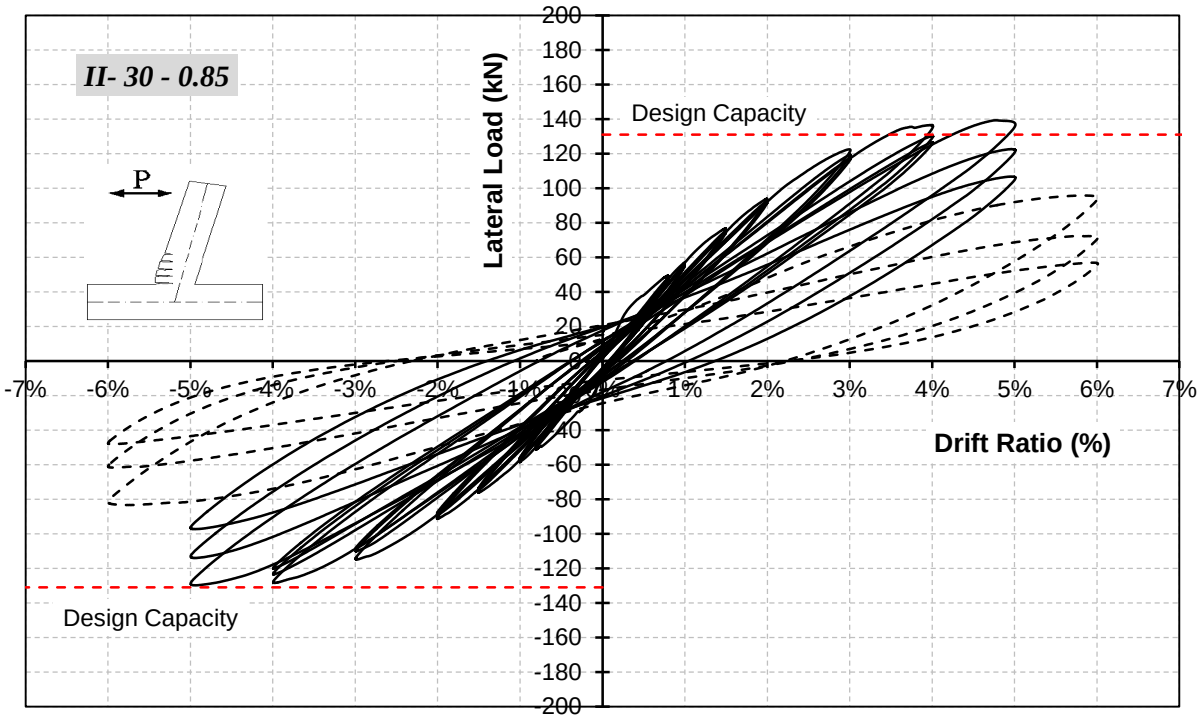

(b) Specimen II-30-0.85

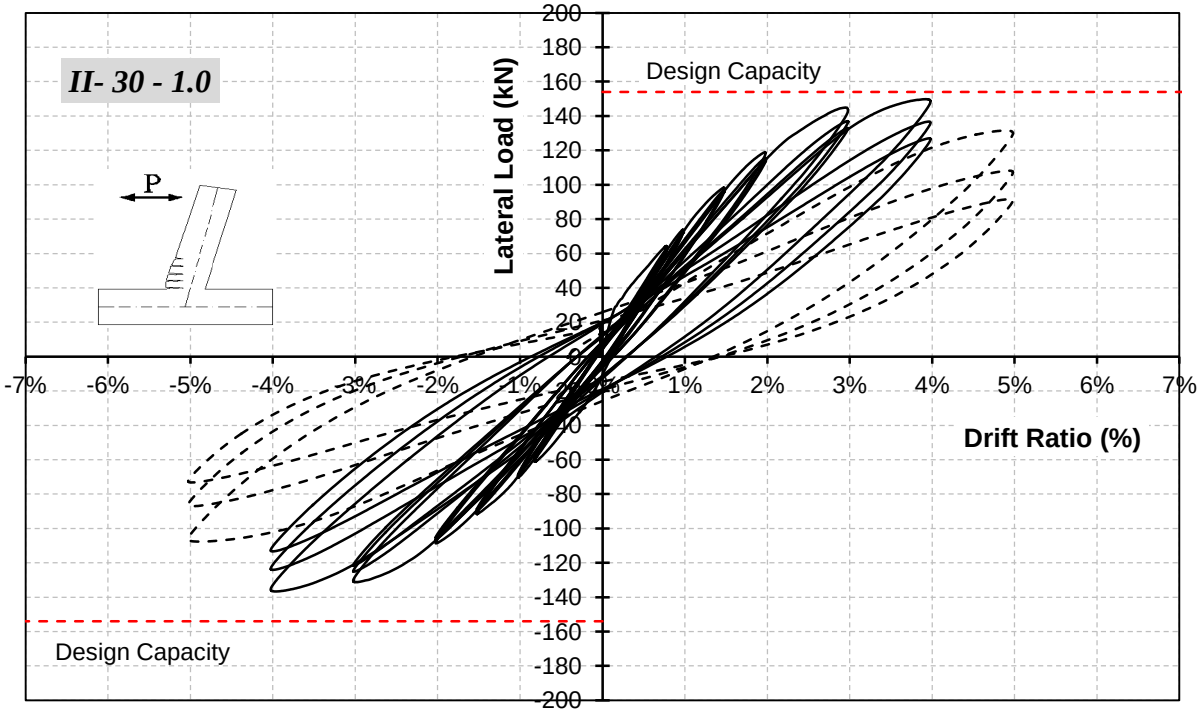

(c) Specimen II-30-1.0

Figure 6.1: Load-Lateral Drift relationship (continued)

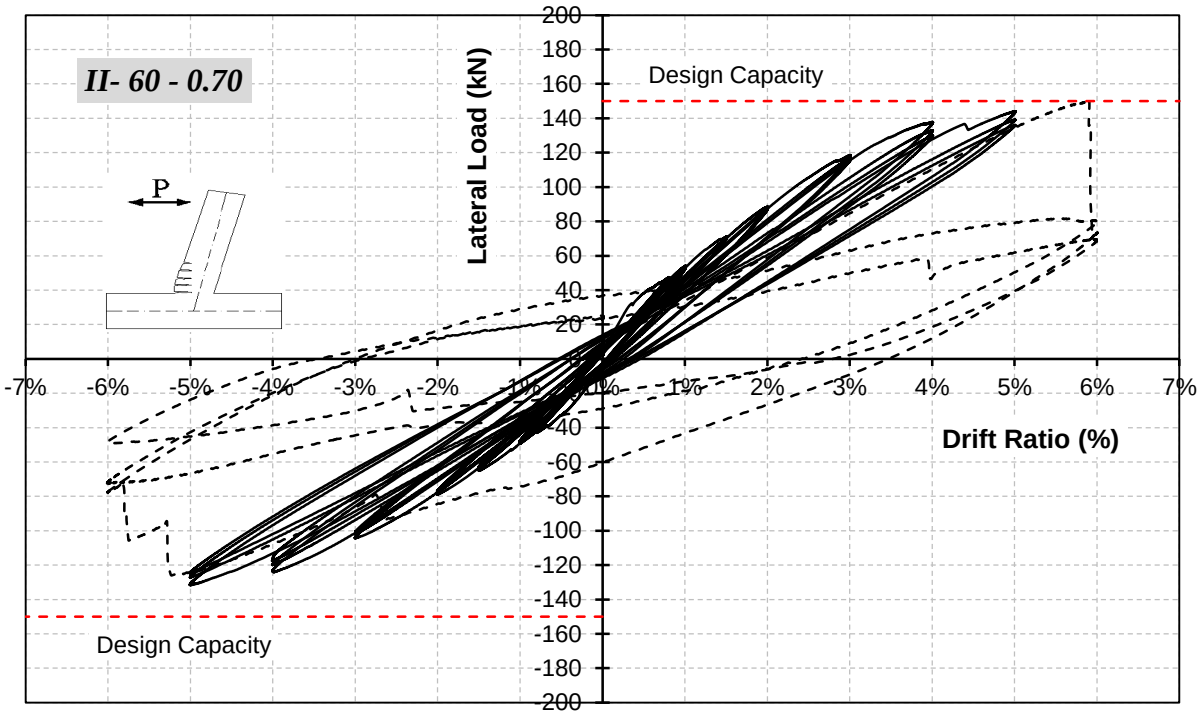

(d) Specimen II-60-0.70

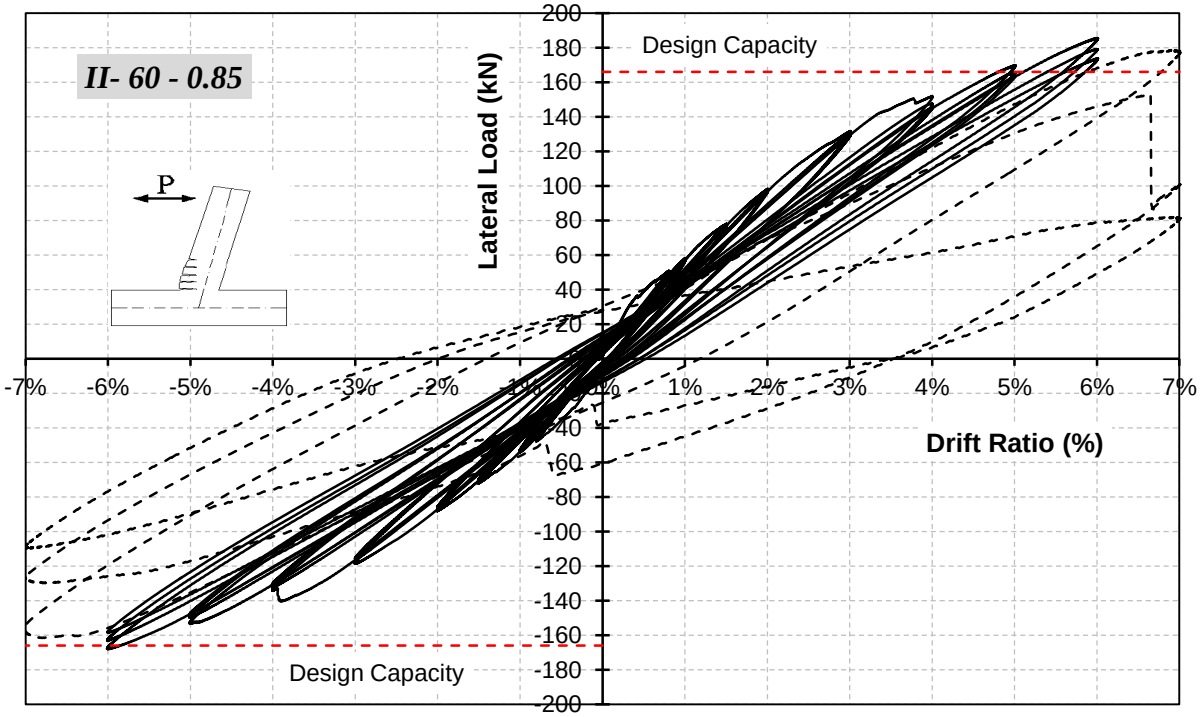

(e) Specimen II-60-0.85

Figure 6.1: Load-Lateral Drift relationship (continued)

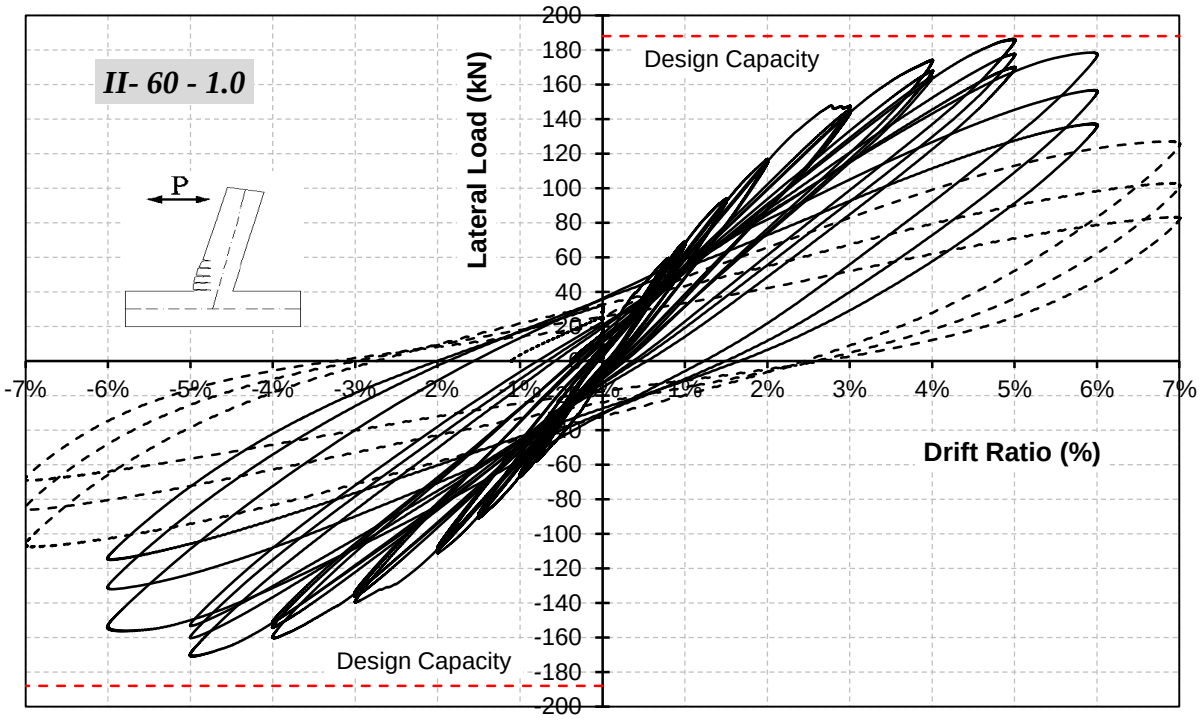

(f) Specimen II-60-1.0

Figure 6.1: Load-Lateral Drift relationship

It should be noted that test specimens in Series (II) achieved approximately the ultimate design lateral load capacity in the positive direction of loading as shown in Table 6.1. Specimen II-30-0.70 achieved its ultimate design capacity at 4.0% drift ratio and maintained this capacity in the first cycle of the next loading drift until it reached 5.0% drift ratio then a sudden drop occurred due to bar slippage.

Regarding specimen II-30-0.85, it did not only reach the ultimate design capacity, but also exceeded it by 7.0%. At 3.0% drift ratio, the specimen showed 120 kN of lateral resistance which represents 92.0% of the design capacity; then at 4.0% drift ratio, the specimen reached the ultimate design capacity (133 kN) and maintained this capacity

until the completion of the 4.0% loading drift. At 5.0% loading drift, the specimen exceeded the design capacity by 7.0% in the first cycle then the capacity showed some degradation during loading until the specimen reached 82.0% of the design capacity by the end of the 5.0% loading drift. For Specimen II-30-1.0, it barely reached 97.0% of the design capacity at first cycle of 4.0% loading drift which dropped to 82.0% by the end of the same loading drift. This is attributed to the high shear stress level developed in the joint which accelerated the failure of the specimen.

Similar behaviour exhibited by specimens II-30-xx is also observed in specimens II-60-xx with the exception that specimens II-60-xx exhibited their ultimate capacities at prolonged drift ratios. Specimens II-60-0.70 and II-60-0.85 reached and exceeded, respectively, the design capacity at 6.0% drift ratio. Specimen II-60-1.0 barely reached 96.0% of its design lateral capacity at the first cycle of 5.0% loading drift until the resistance dropped to 87.0% by the end of the 5.0% loading drift.

In general, all specimens exhibited lateral load resistance in the negative loading direction less than what exhibited in the positive loading direction. The difference between the lateral resistance in the two loading direction was observed to be between 7.0% and 15.0%. This is attributed to the fact that the compression zone of the beam section in the negative direction of loading (pulling direction) was a tension zone earlier when the section is subjected to the loading in the positive direction. It is advised that the designer should keep this in mind during the design process.

Table 6.1: Lateral load capacities of Series (II) specimens

Specimen	P_{design} (kN)	P_{exp} (kN)		P_{exp} / P_{design}		Drift ratio (%)
		+ve dir.	-ve dir.	+ve dir.	-ve dir.	
II-30-0.70	130	130	120	1.00	0.92	5.0
II-30-0.85	131	140	130	1.07	0.99	5.0
II-30-1.0	155	150	137	0.97	0.88	4.0
II-60-0.70	150	150	127	1.00	0.85	6.0
II-60-0.85	166	186	169	1.12	1.02	6.0
II-60-1.0	188	180	165	0.96	0.88	5.0

Note:
P_{exp}: Experimental lateral load resistance;
P_{design}: Calculated lateral load resistance considering the design flexural capacity of the beam section;
+ve dir: The value in the positive direction when the actuator pushes the beam tip;
-ve dir.: The value in the negative direction when the actuator pulls the beam tip;
Drift ratio: The drift ratio at which the maximum experimental values in the table were observed.

The influence of the shear stress level in the joint is presented in Figure 6.2 which shows the envelopes of the hysteretic behaviour for all specimens. As shown in Figures 6.2 (a) and (b), Specimens II-30-1.0 and II-60-1.0, which were subjected to the high shear stress level in the joint, recorded the highest value of the lateral load resistance in comparison with the other four specimens subjected to moderate and low shear stress in the joint (II-30-0.70, II-30-0.85, II-60-0.70, and II-60-0.85). This is in good agreement with the fact that both specimens had the largest longitudinal reinforcement amount in the beam (8ϕ16 each top & bottom). On the other hand, this large amount of reinforcement area increased the tensile forces applied to the joint which in turn increased the shear stress in the joint and accelerated the failure of the joint. Therefore, Specimens II-30-1.0 and II-60-1.0

exhibited earlier failure at 4.0% and 5.0% drift ratio, respectively, compared with the other four specimens as shown in Figure 6.2.

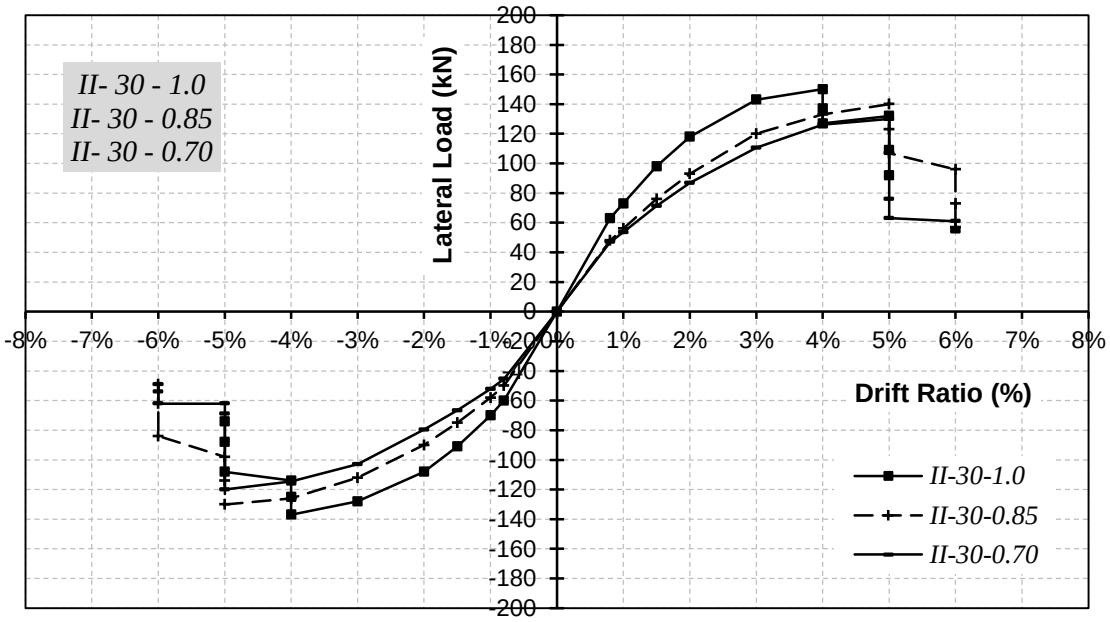

(a) Specimens II-30-0.70, II-30-0.85, and II-30-1.0

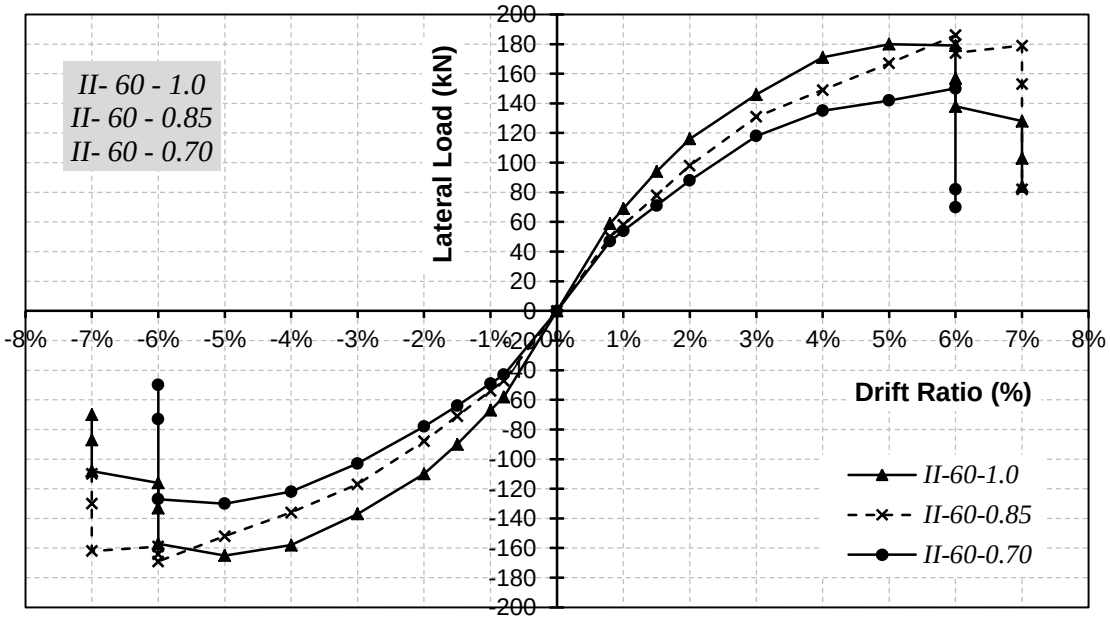

(b) Specimens II-60-0.70, II-60-0.85, and II-60-1.0

Figure 6.2: Load-Lateral Drift relationship Envelopes; Joint Shear stress

The influence of the concrete strength can be shown in Figure 6.3 where the envelope of the hysteretic behaviour is shown for each two counterpart specimens. Figure 6.3 (a) shows that Specimens II-30-0.70 and II-60-0.70 had an identical behaviour up to 3.0% drift ratio. Similar behaviour was observed from Figures 6.3 (b) and (c) comparing Specimen II-30-0.85 with II-60-0.85 and Specimen II-30-1.0 with II-60-1.0.

The concrete strength did not affect the lateral resistance significantly. For example, the increase in concrete strength of 35.0%, from 37.9 MPa in Specimen II-30-0.70 to 51.3 MPa in Specimen II-60-0.70, resulted in an increase of only 9.0% in the lateral load resistance as shown in Figure 6.3 (a). Similarly, the increase of the concrete strength of up to 60.0% resulted in an increase of 20.0% in the lateral load resistance as shown in Figures 6.3 (b) and (c). On the other hand, the concrete strength had a great influence on the drift ratio attained by each specimen. For example, approximately 50.0% and 60.0 % increase in the concrete strength resulted in an increase of the sustained drift ratio by 40.0% and 50.0%, respectively as shown in Figures 6.3 (b) and (c). This can be attributed to the fact that the design of all specimens was controlled by the compression failure of the concrete not by the rupture failure of the reinforcement. Therefore increasing the concrete strength delayed the failure of the specimens and allowed the specimens to sustain higher drift ratios.

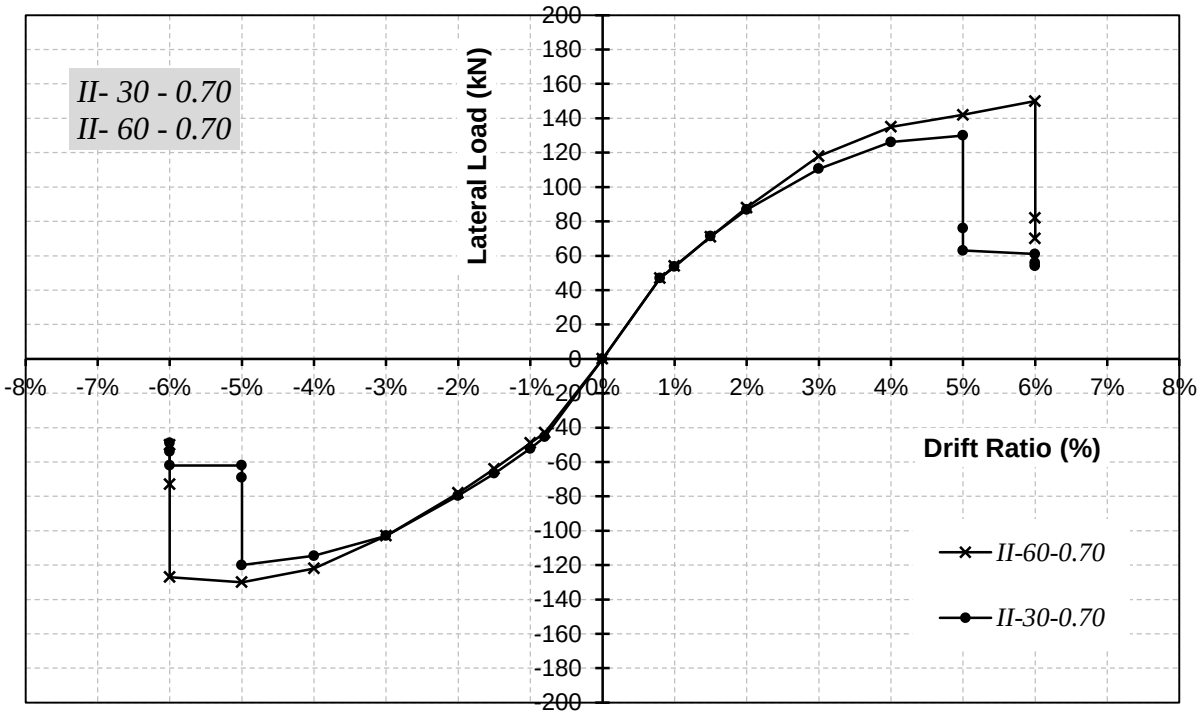

(a) Specimen II-30-0.70 versus Specimen II-60-0.70

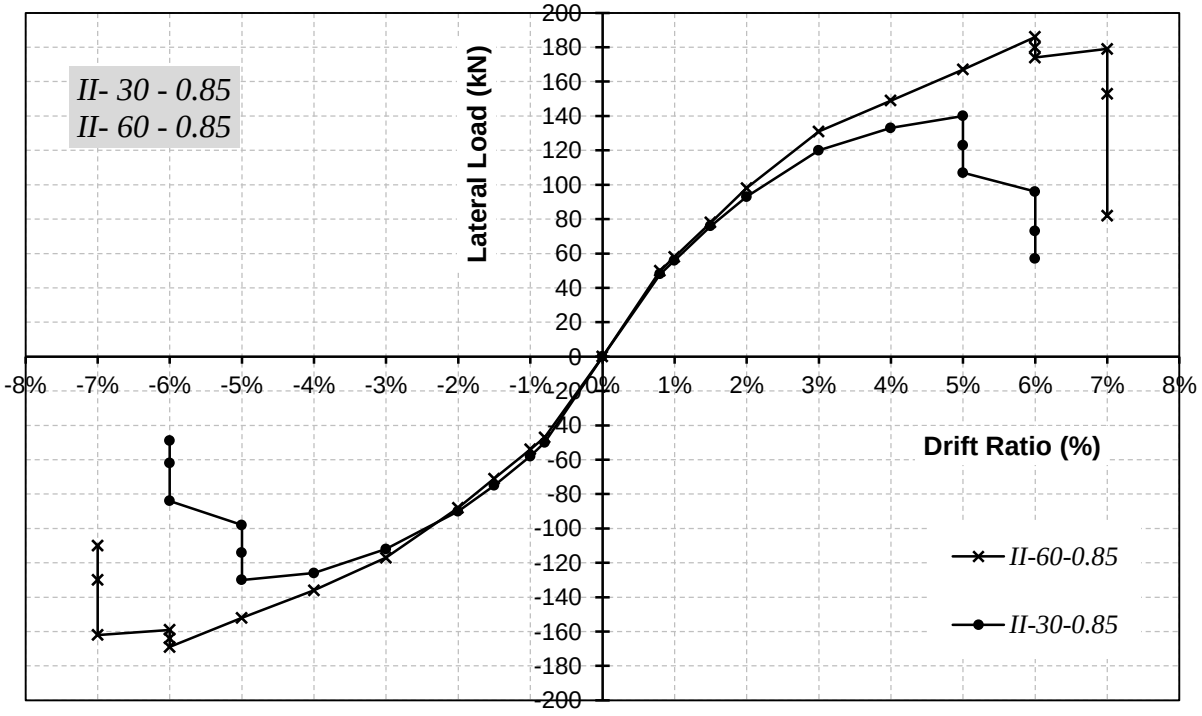

(b) Specimen II-30-0.85 versus Specimen II-60-0.85

Figure 6.3: Load-Lateral Drift relationship Envelopes; Concrete strength (continued)

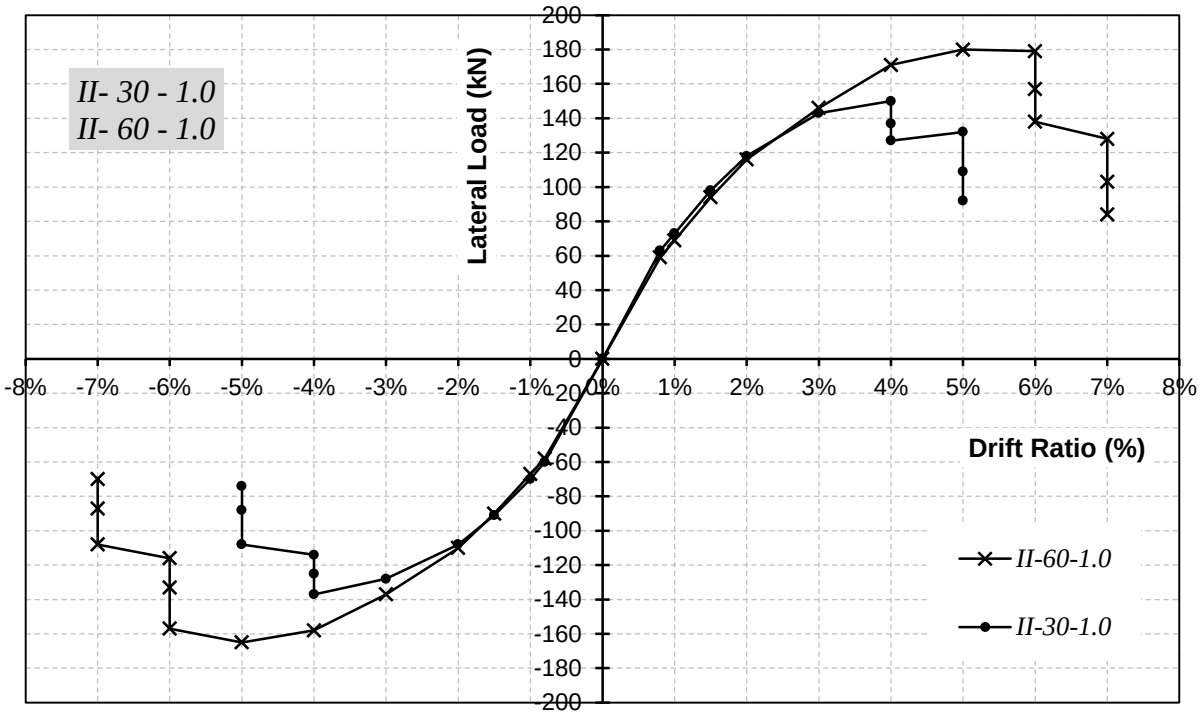

(c) Specimen II-30-1.0 versus Specimen II-60-1.0

Figure 6.3: Load-Lateral Drift relationship Envelopes; Concrete strength

6.3 CRACKING PATTERN AND MODE OF FAILURE

In all specimens, the formation and propagation of cracks were marked after each loading step. Damage was generally expressed by the initiation and propagation of flexural and shear cracking. Further damage and failure of specimens at the end of the tests was identified by three different modes of failure; namely, 1) formation of inelastic deformability hinge in the beam associated with slippage of longitudinal reinforcement; 2) simultaneous formation of inelastic deformability hinge in the beam and shear failure in the joint, and 3) diagonal shear failure in the joint. Figures 6.4 to 6.9 show the cracking progression of specimens during testing and at failure as well. The photos presented in

these figures show the same orientation of the specimens in the test setup where the column was placed in the horizontal direction and the beam in the vertical direction.

Figure 6.4 shows the cracking progression of Specimen II-30-0.70 where only flexural cracks showed on the beam surface up to a drift ratio of 1.5% as shown in Figures 6.4 (a) to (c). Up to that level of loading, no diagonal shear cracks appeared in the joint. While increasing the lateral displacement-loading to higher drift ratios, more flexural cracks in the beam were initiated and developed up to failure. At 4.0% drift ratio, as shown in Figure 6.4 (f), failure of concrete cover on both sides of the beam was observed, which in turn refers to the formation of inelastic deformability hinge due to concrete crushing in the beam section near the column face. This is in a good agreement with Figure 6.1 (a) which shows the hysteresis loops of the specimen reaching the calculated design capacity at 4.0 % drift ratio.

The concrete damage in the inelastic deformability hinge area extended to cover a distance of approximately 400 mm from the column face. During the first cycle of the 5.0% loading drift, a sudden drop in the lateral loading resistance occurred as a result of anchorage slippage on both sides of beam longitudinal reinforcement. This is attributed to the bearing failure of the anchorage heads attached to the end of the longitudinal reinforcement. The slippage of the beam longitudinal reinforcement resulted in formation of a wide crack at the column face at failure of the specimen as shown in Figures 6.4 (h) and (j).

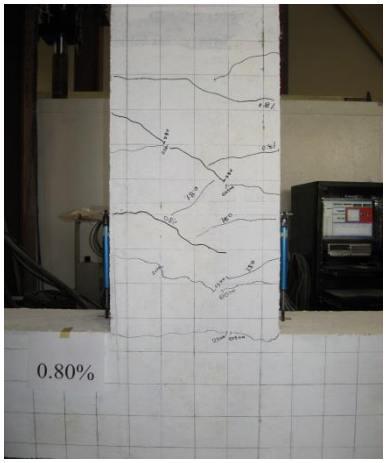

(a) 0.8% drift ratio

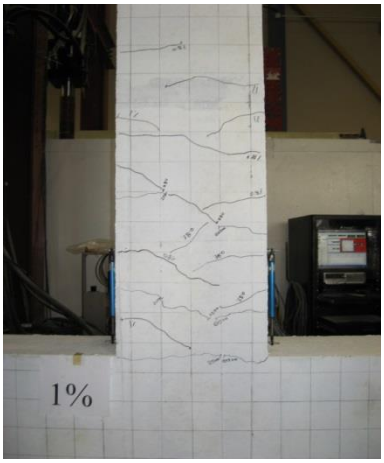

(b) 1.0% drift ratio

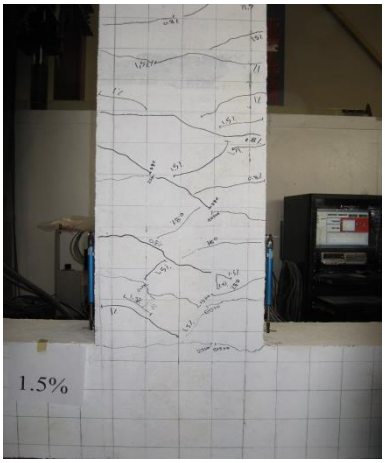

(c) 1.5% drift ratio

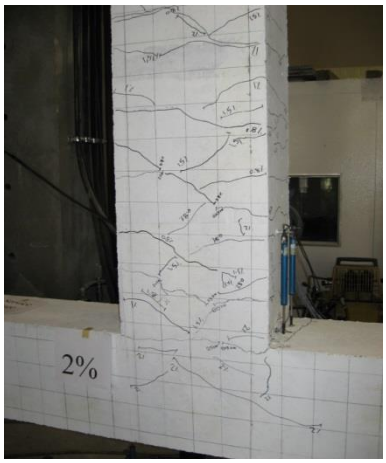

(d) 2.0% drift ratio

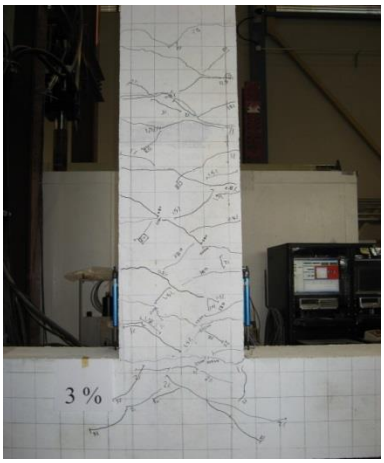

(e) 3.0% drift ratio

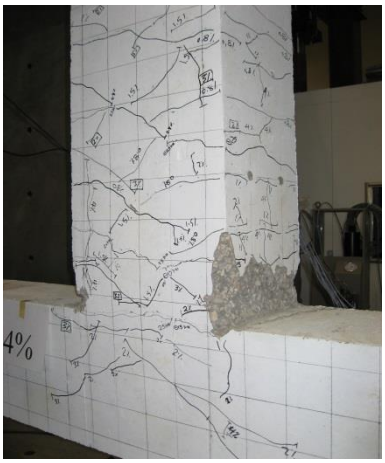

(f) 4.0% drift ratio

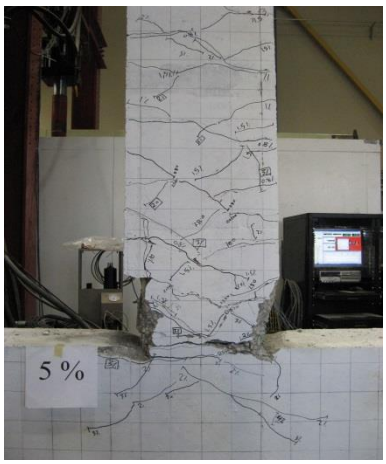

(g) 5.0% drift ratio

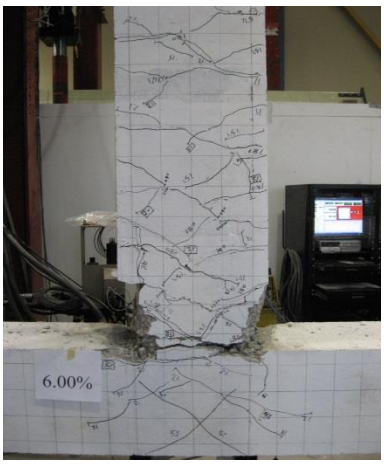

(h) 6.0% drift ratio; Failure

(j) East side at failure

Figure 6.4: Cracking progression of Specimen II-30-0.70

Regarding Specimen II-30-0.85, Figure 6.5 shows the cracking pattern of the specimen during the test. The specimen exhibited flexural cracks in the beam up to 1.0% drift ratio. Unlike Specimen II-30-0.70, diagonal shear cracks in the joint started to show earlier in Specimen II-30-0.85 at 1.5% drift ratio. Flexural cracks in the beam and diagonal shear cracks in the joint continued to show and develop during testing with the increase of loading drifts. At 4.0% drift ratio, the specimen exhibited concrete crushing failure (inelastic deformability hinge) in the beam section at the face of the column. This is also in agreement with Figure 6.1 (b) which shows the hysteresis loops of the specimen reaching the calculated design capacity at 4.0 % drift ratio. At this stage the specimen started to show signs of diagonal shear failure in the joint through intensive diagonal shear cracks in the joint.

At 5.0% drift ratio, the inelastic deformability hinge in the beam continued to develop while the specimen continued to lose more concrete cover in the beam section as a result of concrete crushing. Moreover, major diagonal shear cracks appeared in the joint and extended out of the joint into the column sides as shown in Figure 6.5 (g). By the end of the test at 6.0% drift ratio, the specimen lost the concrete cover and exhibited concrete crushing in the joint and its vicinity. Eventually, the specimen exhibited failure as a result of simultaneous formation of inelastic deformability hinge due to concrete crushing in the beam along with a diagonal shear failure in the joint, as shown in Figures 6.5 (h) and (j).

(a) 0.8% drift ratio

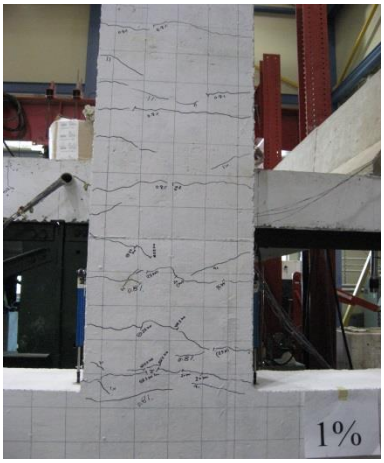

(b) 1.0% drift ratio

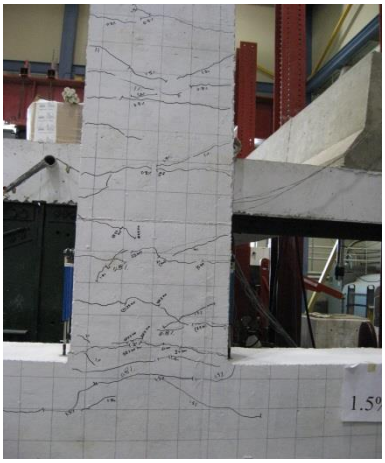

(c) 1.5% drift ratio

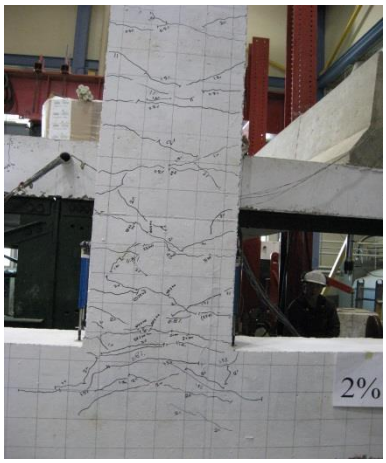

(d) 2.0% drift ratio

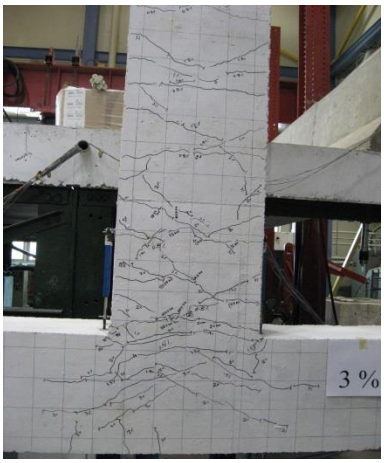

(e) 3.0% drift ratio

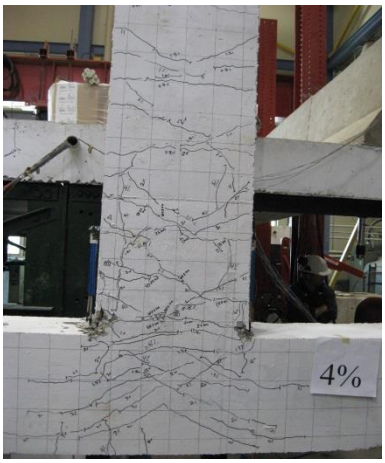

(f) 4.0% drift ratio

(g) 5.0% drift ratio

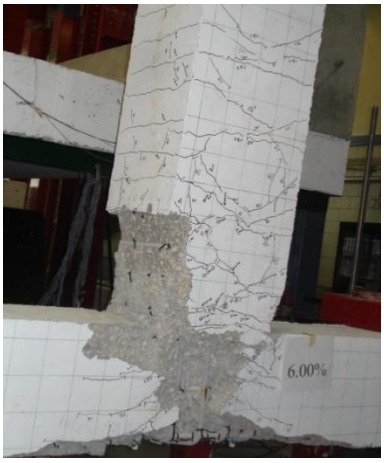

(h) 6.0% drift ratio; Failure

(j) backside at failure

Figure 6.5: Cracking progression of Specimen II-30-0.85

Figure 6.6 shows the cracking progression of Specimen II-30-1.0. The specimen exhibited flexural cracks in the beam section at the beginning of the test as shown in Figure 6.6 (a). This specimen was designed to experience the highest shear stress in the joint ($1.0\sqrt{f'_c}$); as expected, the specimen showed diagonal shear cracks in the joint at 1.0% drift ratio which is earlier than when the previous two specimens did so, as shown in Figure 6.6 (b). It is worth mentioning that the intensity of the cracks in both beam and joint for the three specimens (II-30-0.70, II-30-0.85, and II-30-1.0) at the same drift ratio is proportionally influenced by the amount of longitudinal reinforcement in the beam.

The large amount of longitudinal reinforcement provided in the beam section accelerated the formation and propagation of flexural cracks in the beam as well as the diagonal shear cracks in the joint. However, the influence of the longitudinal reinforcement amount was more significant in the joint, where major diagonal shear cracks appeared in the joint then extended out into the column sides and accompanied with loose concrete cover as shown in Figure 6.6 (f). By the end of the test at 5.0% drift ratio, the specimen exhibited a complete diagonal shear failure and crushing of concrete in the joint as shown in Figures 6.6 (g) and (h).

(a) 0.8% drift ratio

(b) 1.0% drift ratio

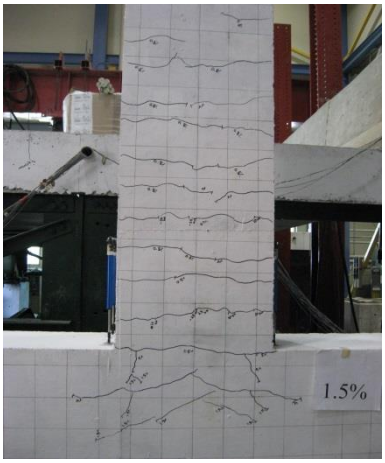

(c) 1.5% drift ratio

(d) 2.0% drift ratio

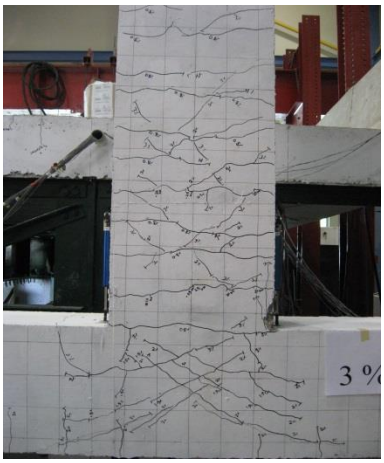

(e) 3.0% drift ratio

(f) 4.0% drift ratio

(g) 5.0% drift ratio; Failure

(h) Joint at Failure; zoom in

Figure 6.6: Cracking progression of Specimen II-30-1.0

Figure 6.7 shows the cracking sequence of Specimen II-60-0.70. The specimen exhibited only flexural cracks in the beam section with no diagonal cracks in the joint at all up to 1.5% drift ratio as shown in Figures 6.7 (a) through (c). The intensity of flexural cracks in the beam increased with the increase in loading drift ratios up to a drift ratio of 5.0%. At this stage, formation of inelastic deformability hinge in the beam section occurred at the column face due to crushing of concrete in the beam section at that location. This is in agreement with the design calculation of the specimen and with Figure 6.1 (d) which shows the hysteresis loops of the specimen reaching 95.0% of the calculated design capacity at 5.0 % drift ratio.

The concrete damage in the inelastic deformability hinge area extended over a distance of approximately 600 mm from the column face. After formation of inelastic deformability hinge at 5.0% drift ratio, the loading continued to 6.0% drift ratio when the specimen exhibited sudden drop in the lateral resistance at the first cycle of loading due to loss of anchorage of the beam longitudinal reinforcement anchored in the joint. This is attributed to the failure of the bearing heads attached to the end of the beam longitudinal reinforcement. Accordingly, the specimen exhibited the first mode of failure; formation of inelastic deformability hinge in the beam associated with slippage of longitudinal reinforcement, similar to Specimen II-30-0.70. It is worth mentioning that the joint was intact with few insignificant diagonal cracks up to the end of the test at 6.0% drift ratio.

(a) 0.8% drift ratio (b) 1.0% drift ratio (c) 1.5% drift ratio

(d) 2.0% drift ratio (e) 3.0% drift ratio (f) 4.0% drift ratio

(g) 5.0% drift ratio (h) 6.0% drift ratio; Failure (j) backside at failure

Figure 6.7: Cracking progression of Specimen II-60-0.70

As shown in Figure 6.8, Specimen II-60-0.85 showed similar trend to the previous specimen with uniform flexural cracks on the beam surface and no diagonal shear cracks in the joint up to 2.0% drift ratio. At 4.0% drift ratio, the specimen showed signs of concrete crushing in the beam section at the face of the column; these signs were rapidly developed to a clear formation of inelastic deformability hinge at 5.0% drift ratio as shown in Figures 6.8 (f) through (h). This is in a good agreement with Figure 6.1 (e) which shows the hysteresis loops of the specimen reaching the calculated design capacity at 5.0 % drift ratio.

At 6.0% drift ratio, the inelastic deformability hinge formation in the beam continued to develop by losing more concrete cover in the beam section as a result of concrete crushing; at the same time, the specimen continued to resist more lateral load and exceeded the design value by approximately 12%. At this stage, the specimen started to show signs of diagonal shear failure in the joint through major diagonal shear cracks in the joint which extended out into the column sides as shown in Figure 6.8 (j). By the end of the test at 7.0% drift ratio, the concrete cover got loose in the joint area. Eventually, the specimen exhibited failure because of simultaneous formation of inelastic deformability hinge due to concrete crushing in the beam along with a diagonal shear failure in the joint, as shown in Figures 6.8 (k) through (n).

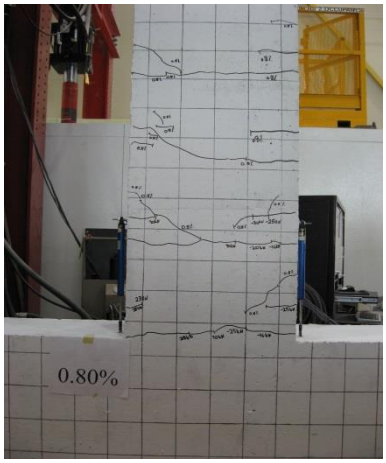

(a) 0.8% drift ratio

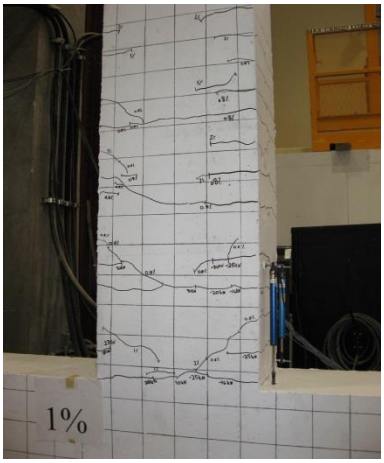

(b) 1.0% drift ratio

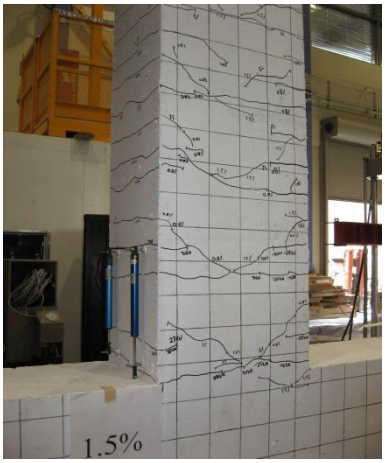

(c) 1.5% drift ratio

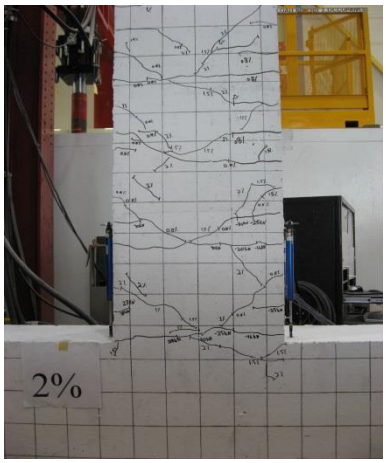

(d) 2.0% drift ratio

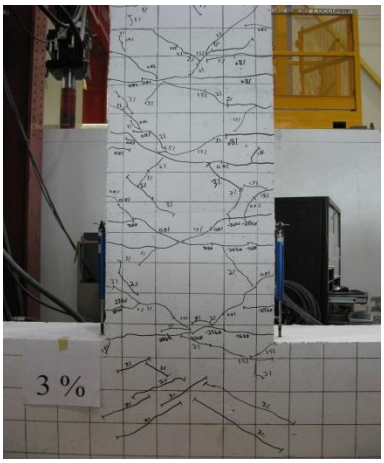

(e) 3.0% drift ratio

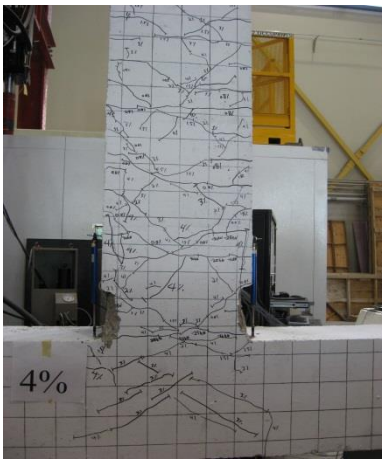

(f) 4.0% drift ratio

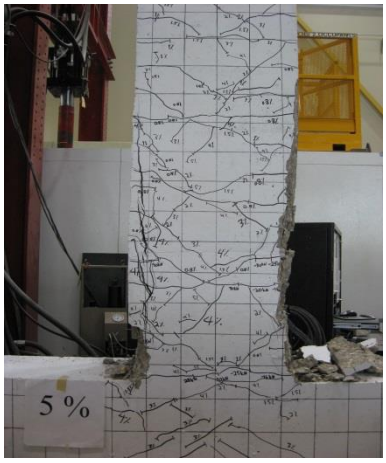

(g) 5.0% drift ratio

(h) 5.0% drift ratio; side view

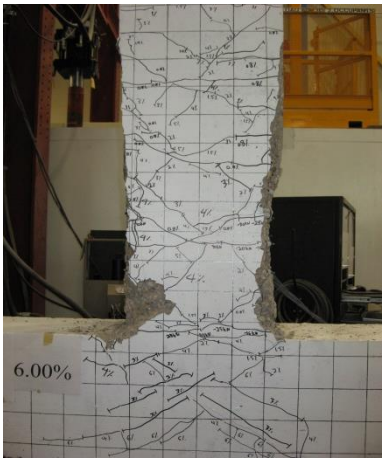

(j) 6.0% drift ratio

Figure 6.8: Cracking progression of Specimen II-60-0.85 (continued)

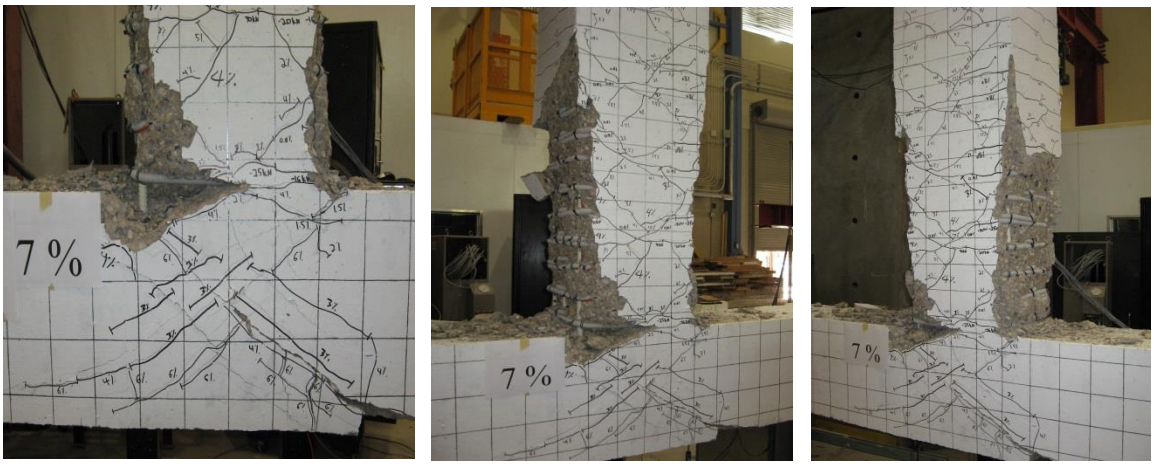

(k) 7.0% drift ratio; joint failure (m) failure east side (n) failure west side

Figure 6.8: Cracking progression of Specimen II-60-0.85

Figure 6.9 shows the cracking sequence of Specimen II-60-1.0 during testing. Only flexural cracks appeared on the beam surface at the beginning of the test up to reaching a drift ratio of 1.0% as shown in Figures 6.9 (a) and (b). Similar to Specimen II-30-1.0, Specimen II-60-1.0 was designed to experience the highest shear stress in the joint ($1.0\sqrt{f'_c}$) in order to assess the shear capacity of such joints. As expected, diagonal shear cracks in the joint appeared at 1.5% drift ratio which is earlier than when the previous two specimens did so, as shown in Figure 6.9 (c).

A similar behaviour to the one observed in Specimen II-30-1.0 was observed too in Specimen II-60-1.0; the intensity of the cracks in both beam and joint for the three specimens (II-60-0.70, II-60-0.85, and II-60-1.0) at the same drift ratio is proportionally influenced by the amount of longitudinal reinforcement in the beam. The large amount of longitudinal reinforcement provided in the beam section accelerated the formation and propagation of flexural cracks in the beam as well as the diagonal shear cracks in the

joint. However, the influence of the longitudinal reinforcement amount was more significant in the joint, where major diagonal shear cracks appeared in the joint then extended out into the column sides and accompanied with spalling of concrete cover as shown in Figure 6.9 (g). By the end of the test at 7.0% drift ratio, the specimen exhibited a complete diagonal shear failure and crushing of concrete in the joint where the concrete cover in joint area was completely damaged and spalled, as shown in Figure 6.9 (j).

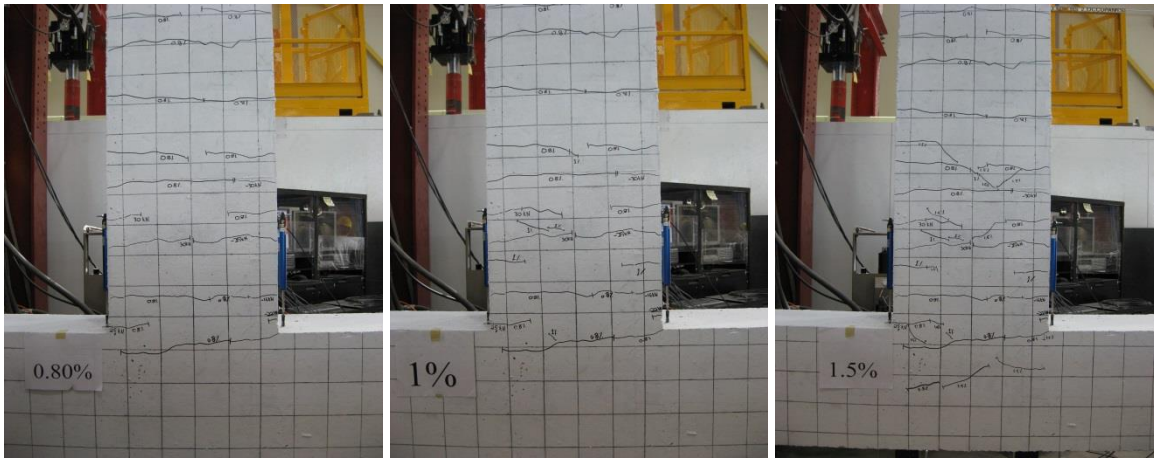

(a) 0.8% drift ratio (b) 1.0% drift ratio (c) 1.5% drift ratio

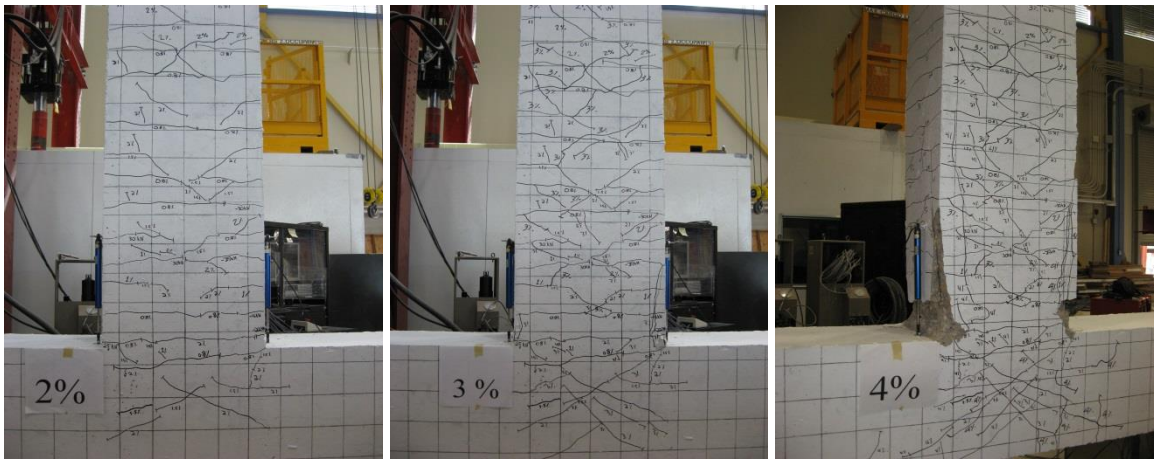

(d) 2.0% drift ratio (e) 3.0% drift ratio (f) 4.0% drift ratio

Figure 6.9: Cracking progression of Specimen II-60-1.0 (continued)

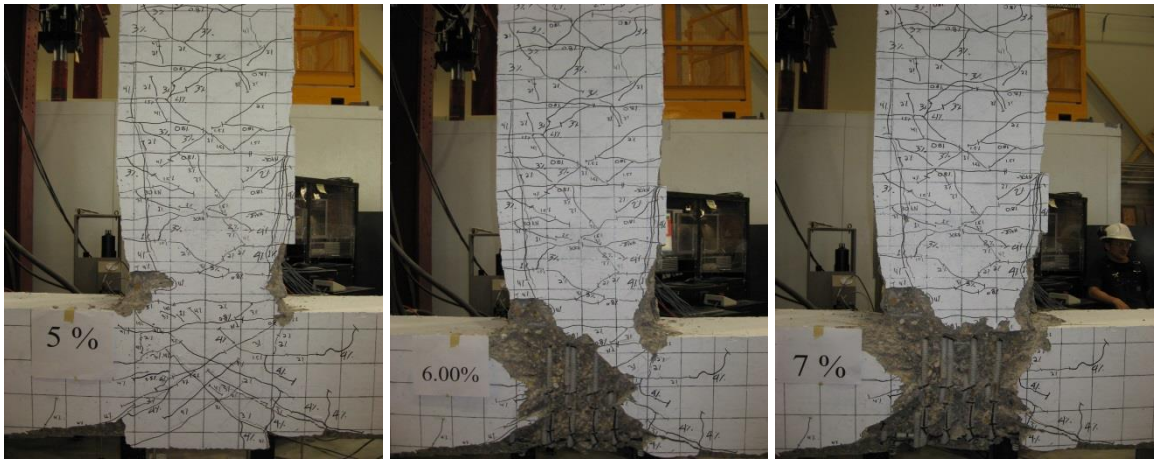

(g) 5.0% drift ratio (h) 6.0% drift ratio (j) 7.0% drift ratio; failure

Figure 6.9: Cracking progression of Specimen II-60-1.0

The influence of concrete strength on formation of beam deformations / hinges in Series (II) specimens is summarized in Figures 6.10 and 6.11. In light of the test observations, it was noticed that the beam element in each specimen experienced "*Inelastic deformability hinge*" within a distance equal to the depth of the beam reinforcement (*d*) from the column face. Due to the linear-elastic behaviour of the GFRP bars, the term "plastic hinge" does not express the actual behaviour accurately. In FRP-RC sections, excessive curvature is developed due to inelastic deformation in concrete while the GFRP reinforcement elongates in a linear-elastic fashion. Therefore, the term "*Inelastic deformability hinge*" is used to represent the development of large elastic tensile strains in the GFRP bars associated with the concrete reaching its ultimate compressive strain in the beam section at the column face.

In general, both types of specimens, II-30-xx and II-60-xx, exhibited formation of the "inelastic deformability" hinge in the beam section within a distance (*d*) from the column

face. The formation of that inelastic deformability hinge contributes significantly to the total drift angle exhibited by each specimen as discussed later in this chapter. In specimens constructed with lower concrete strength, II-30-xx, the inelastic deformability hinge in the beam takes the form of crushed concrete that starts on the left and right faces (Note: Directions are with respect to specimens orientation in the shown figures) and extends to the core forming approximately a flat surface of crushed concrete as shown in Figure 6.10. However, the formation of the inelastic deformability hinge in specimens constructed with higher concrete strength, II-60-xx, was shaped as a V-notch, as shown in Figure 6.11.

The formation of hinges in the beam section under seismic loading is influenced by the tensile behaviour of the reinforcement, concrete strength, failure characteristics of the concrete, and the applied moment on the section. Regarding the tensile behaviour of the reinforcement at large strains, steel reinforcement exhibits a yielding plastic-plateau with approximately constant stress while the concrete compression zone exhibits a non-linear behaviour, then eventually a plastic hinge forms in the section. However, the GFRP reinforcement exhibits a linear-elastic stress-strain relationship up to failure while the concrete compression zone exhibits a non-linear behaviour and eventually inelastic deformability hinge forms; in this case, the concrete deformation is the main source of plasticity in this type of joints.

Nevertheless, when the section is subjected to a bending moment, flexural cracks start from the tension side and stop at the boundary of the compression zone where the neutral

axis is located. In seismic loading, the moment direction is consistently reversed, therefore, flexural cracks form on both sides of the section and tend to intersect towards the section core. Under the same moment value, the concrete strength influences the compression zone depth and consequently the location of the neutral axis. In a lower-strength concrete, the neutral axis shifts towards the mid depth of the section because the section requires a deeper compression zone (C_1) to balance with the tensile force, as shown in Figure 6.10 (c). However, a similar section with higher concrete strength requires smaller depth of the compression zone (C_2), as shown in Figure 6.11 (d).

Moreover, specimens with higher concrete strength showed higher lateral load resistance. Higher lateral load increased the shear force on the section and, consequently, increased the inclination angle of the cracks, as shown in Figures 6.10 (b) and 6.11 (c). This in turn influenced the intersection location of the cracks.

As shown in Figure 6.11(b), the failure surface is approximately smooth and goes through the cement paste and the aggregates together, which is a characteristic of the high strength concrete, where the cement paste tends to be as strong as the aggregates. On the other hand, Figure 6.10 (a) shows a rough flat failure surface in the normal strength concrete specimens where the concrete failure forms in the cement paste surrounding the aggregates. Therefore, the concrete damage in the lower strength concrete took the form of loose aggregates surrounded by cement paste, as shown in the flat surface in Figure 6.10 (a). While in higher strength concrete, the concrete failed in form of isolated chunks of concrete as shown in the V-notch in Figures 6.11 (a) and (b).

Although the formation of the inelastic deformability hinges attributes considerably to the total drift angle exhibited by the beam, the elastic curvature of the sections about their neutral axes along the remaining beam length has also a contribution to the drift angle.

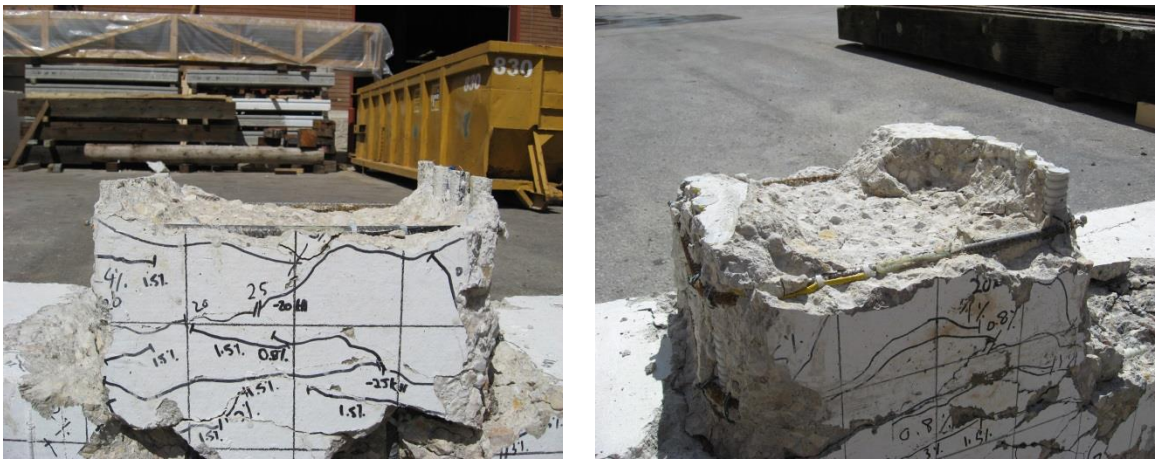

(a) Flat failure surface in beam section

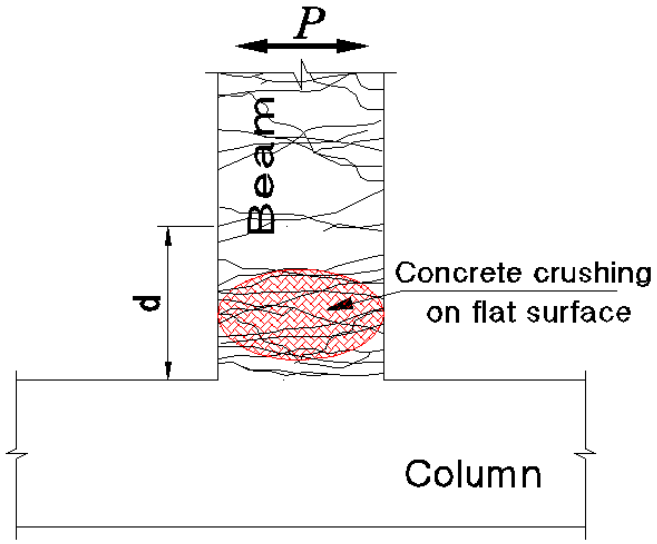

(b) Schematic drawing of cracking pattern

Figure 6.10: Inelastic deformability hinge formation as flat surfaces in specimens II-30-xx (continued)

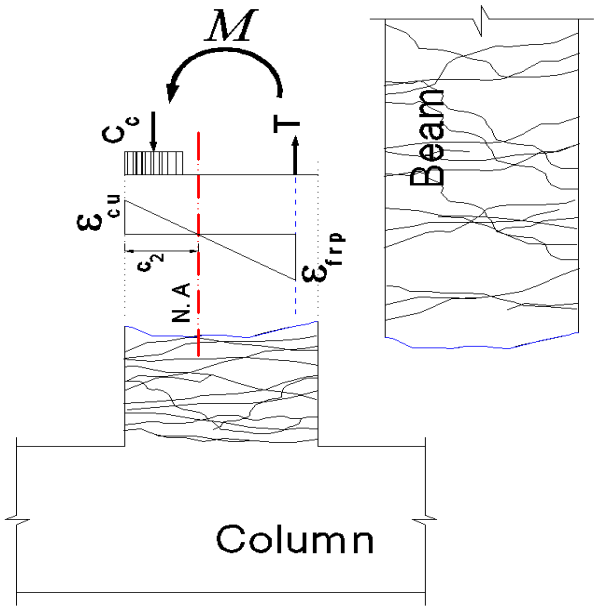

(c) Sectional analysis under flexure

Figure 6.10: Inelastic deformability hinge as flat surfaces in specimens II-30-xx

(a) Beam-to-column V-notch

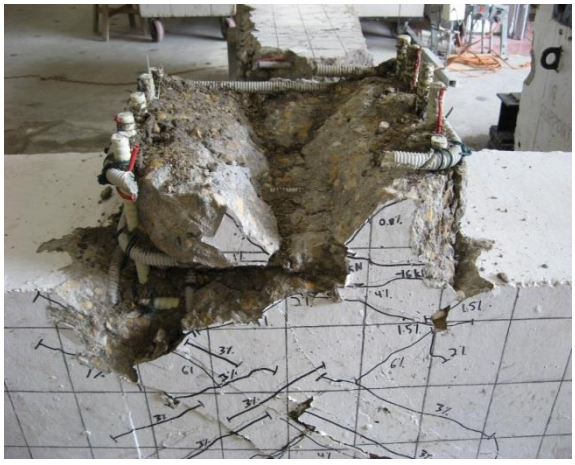

(b) Beam removed

Figure 6.11: Inelastic deformability hinge formation as a V-notch in specimens II-60-xx

(continued)

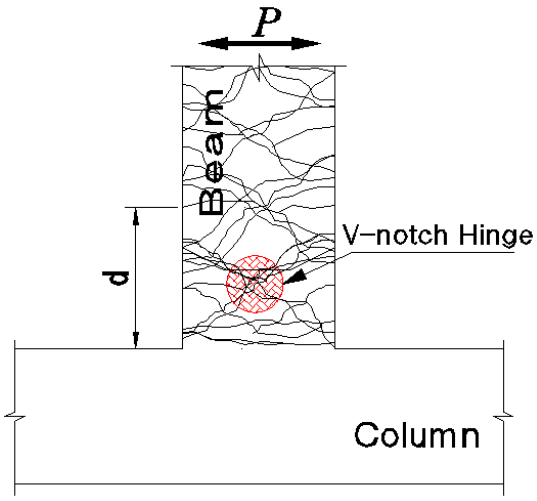

(c) Schematic drawing of cracking pattern

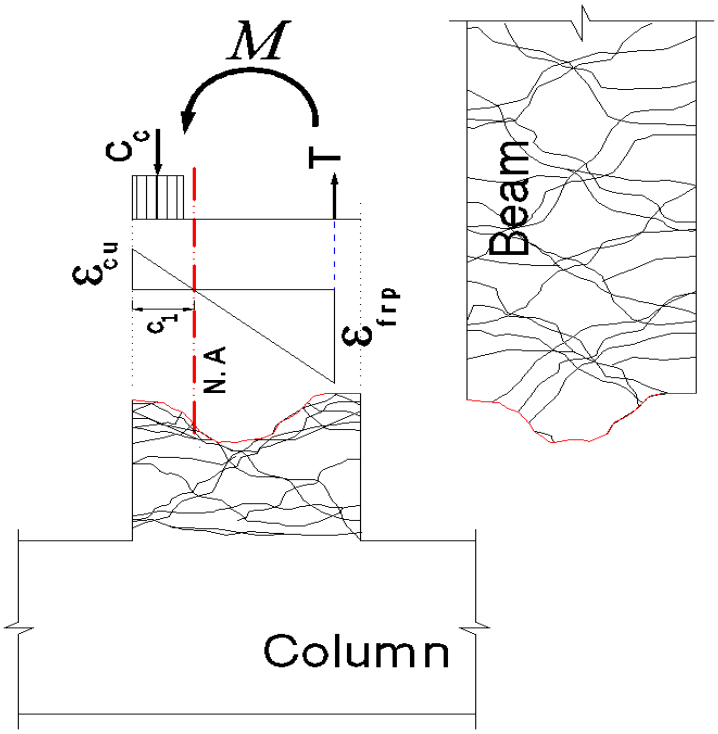

(d) Sectional analysis under flexure

Figure 6.11: Inelastic deformability hinge formation as a V-notch in specimens II-60-xx

6.4 LATERAL DRIFT-STRAIN RELATIONSHIP

6.4.1 Developed Strains in Beam Longitudinal Reinforcement

Readings of strain gauges on longitudinal reinforcement were captured by the DAQ and saved to the computer during testing to guarantee real time monitoring of test results. Figure 6.12 shows the maximum recorded strains developed in beam longitudinal reinforcement at the column face at each drift ratio loading step for Series (II) specimens. It should be noted that the maximum strains at failure of Specimens II-30-0.70 and II-60-0.85 could not be captured since the strain gauges on longitudinal reinforcing beam bars were malfunctioned before reaching the failure of the specimens.

All specimens in Figure 6.12 exhibited the well-established characteristic of GFRP reinforced elements under flexure where the strains increased in a fairly linear-elastic fashion up to failure. None of the specimens reached the ultimate tensile strain in the longitudinal reinforcement; however, the highest recorded tensile strains 18050, 17350, and 16500 micro-strain observed in Specimens II-60-0.70, II-60-0.85, and II-30-0.70, respectively, were very close to the ultimate tensile strain value (i.e 18333 micro-strain). These high strain values represent 90 % to 98 % of the ultimate tensile strain, which increases the vulnerability of these three specimens to exhibit the undesirable brittle failure by rupture of longitudinal reinforcement.

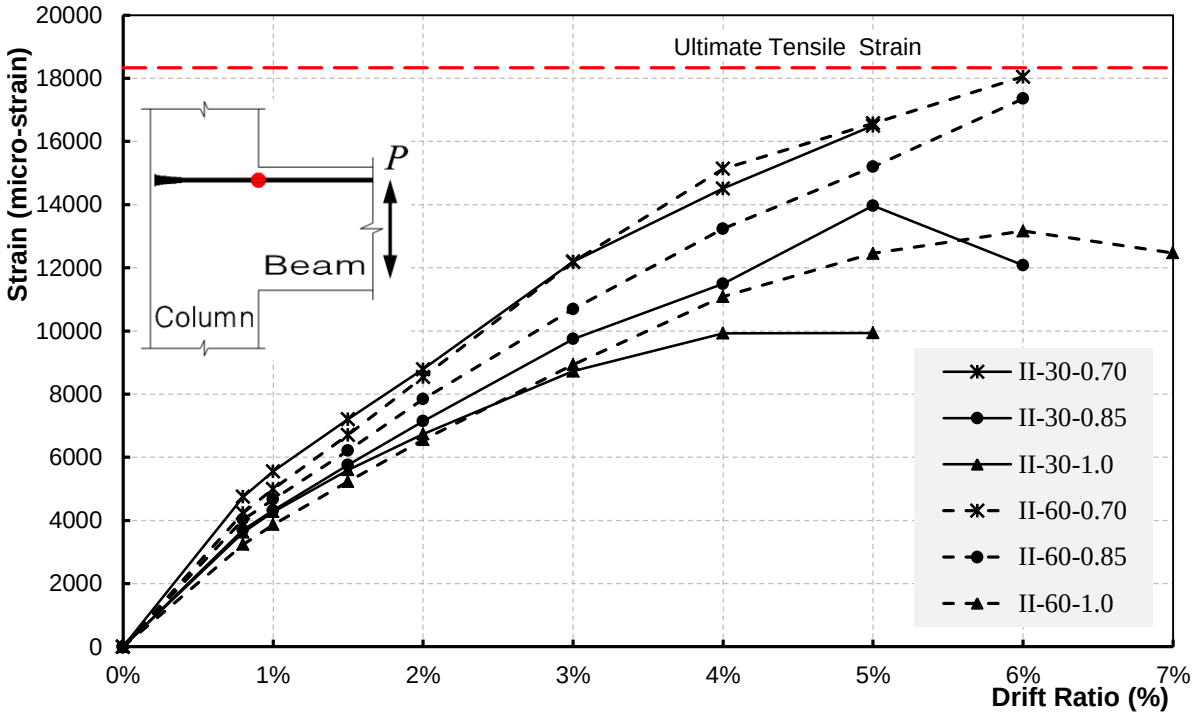

Figure 6.12: Maximum strain–drift ratio relationship for beam longitudinal reinforcement

Table 6.2: Maximum strains in beam longitudinal reinforcement during testing

Specimen	Strain (micro-strain)				Moment (kN.m)			
	*Design	**Experimental			*Design	**Experimental		
		Drift ratio				Drift ratio		
		4.0%	5.0%	6.0%		4.0%	5.0%	6.0%
II-30-0.70	14740	15220	16500	N/A	260	255	260	122
II-30-0.85	12140	12500	13970	12080	262	266	280	192
II-60-0.70	16800	15140	16580	18050	300	270	286	300
II-60-0.85	15000	13240	15200	17350	332	298	334	370

* Design values were calculated using the strain compatibility when the concrete reaches an ultimate compressive strain of 0.0035

** Experimental values recorded during testing

Table 6.2 shows the calculated and the experimental flexural capacities of the beam section for those specimens exhibited formation of inelastic deformability hinge in the beam and the corresponding strain developed in the beam longitudinal reinforcement at the column face during the final stages of testing at 4.0%, 5.0%, and 6.0% drift ratios. The table shows that Specimens II-30-0.70, II-30-0.85, II-60-0.70, and II-60-0.85 exhibited maximum strain values (16500, 13970, 18050, and17350 micro-strain, respectively) approximately 7.0% to 16.0% higher than the calculated values (14740, 12140, 16800 and 15000 micro-strain, respectively). Moreover, similar observation was noted in Series (I) specimens. This can be attributed to the linear-elastic behaviour of the GFRP bars up-to-failure combined with the characteristic of the well-confined concrete sections, especially those resisting seismic loads. Confinement of sections increases the ductility of the concrete to attain higher compressive strains. In this regards, the behaviour of GFRP-RC sections at ultimate-state under cyclic reversed loads can be described in two phases as shown in Figure 6.13.

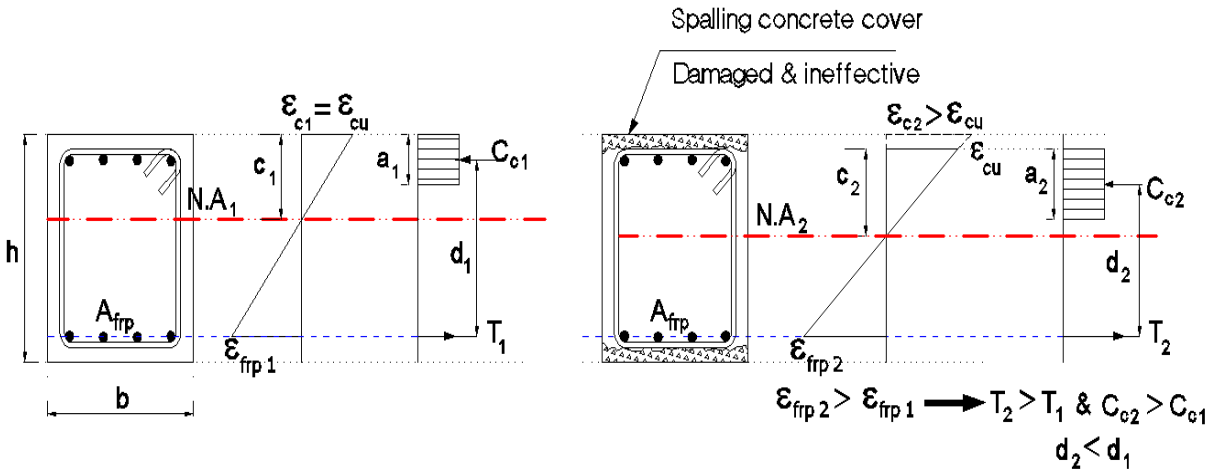

(a) Phase 1 (b) Phase 2

Figure 6.13: Strain-Compatibility of beam section at ultimate

Phase 1 develops when the outer-most fibre of the concrete reaches the ultimate compression strain ($\varepsilon_{cu} = 0.0035$); using the compatibility of strains, the strain develops in the longitudinal reinforcement is (ε_{frp1}) as shown in Figure 6.13 (a). At that time the section develops its flexural capacity (M_{r1}) at a certain drift ratio (R_1). Phase 2 starts after Phase 1 when the strain in the concrete cover exceeds the ultimate compressive strain at a drift ratio (R_2) higher than (R_1). At that time the concrete section loses its top and bottom "unconfined" concrete cover. Consequently, the effective depth of the longitudinal reinforcement decreases as shown in Figure 6.13 (b).

At a higher drift ratio (R_2), the curvature of the section increases and the section tends to attain or exceed its flexural capacity by developing the concrete compressive force (C_{c2}) into the confined concrete core (new effective geometry of the concrete), as shown in Figure 6.13 (b). The increased curvature of the section at higher drift ratios increases the strain in the GFRP reinforcement (ε_{frp2}) and consequently increases the tensile force developed in the reinforcement (T_2) due to the linear-elastic characteristic of the GFRP reinforcement. From equilibrium of forces, the increased tensile force (T_2) is balanced with the compressive force in the concrete (C_{c2}) through increasing the compression zone depth, as shown in Figure 6.13 (b). The section then develops a flexural resistance (M_{r2}) equal to the tensile force (T_2) multiplied by the effective depth (d_2). The confinement provided to the concrete core by means of close stirrups increases the ductility and integrity of the concrete core to exceed the ultimate compressive strain. The concrete section follows this behaviour until it exhibits gradual degradation in the flexural

resistance due to deterioration of concrete strength under higher strains and gradual reduction of the leverage distance (d_2).

The behaviour of the test specimens supported the explanation above. For example, the design calculations of Specimen II-60-0.70 were based on the beam section reaching the ultimate flexural capacity (300 kN.m) when the outermost fiber of concrete in the compression zone reaches the ultimate compressive strain ($\varepsilon_{cu} = 0.0035$). At 5.0% drift ratio, the specimen reached a flexural capacity (286 kN.m) approximately equal to the designed value (300 kN.m). At that time the specimen showed crushing in the beam concrete cover, as shown previously in Figure 6.7 (g), and the tensile strain in the beam longitudinal reinforcement (16580 micro-strain) was in good agreement with the calculated strains (16800 micro-strains). The calculated depth of the compression zone (a_1) at that moment is 58 mm and, consequently, the effective depth (d_1) is 371 mm.

Although at 6.0% drift ratio the specimen lost the concrete cover, it attained its flexural resistance and reached 300 kN.m again with higher curvature in the section which increased the longitudinal reinforcement strain (18050 micro-strain) to 7.0% greater than the calculated value (16800 micro-strain) before the specimen exhibited slippage of beam longitudinal reinforcement. For more explanation with meaningful numbers, it is assumed that the spalled concrete cover shown in Figure 6.13 (b) is 25 mm each. To reach the flexural capacity of 300 kN.m with a 25-mm less reinforcement depth, it requires that the confined concrete core reaching a higher compressive strain equal to 0.0045 while the tensile strain in the bar reaching 18140 micro-strain. This calculated strain value (i.e

18140 micro-strain) is in good agreement with the experimental tensile strain in Specimen II-60-0.7 at 6.0% drift ratio as shown in Table 6.2. The calculated depth of the new compression zone (a_2) is 63 mm and the effective depth (d_2) is 343 mm.

Moreover, the design calculations of Specimen II-60-0.85 are based on that the beam section reaches the ultimate flexural capacity (332 kN.m) when the concrete in the compression zone reaches the ultimate compressive strain ($\varepsilon_{cu} = 0.0035$). At 5.0% drift ratio, the specimen reached a flexural capacity (334 kN.m) equal to the design calculation value (332 kN.m). At that moment the specimen showed crushing in the concrete cover of the beam, as shown previously in Figure 6.8 (g), and the tensile strain in the beam longitudinal reinforcement (15200 micro-strain) was in good agreement with the calculated strains (15000 micro-strains). The calculated depth of the compression zone (a_1) at that moment is 63 mm and the effective depth (d_1) is 368 mm. At 6.0% drift ratio, the specimen exhibited a flexural resistance of 370 kN.m which is 11.0% larger than the calculated resistance (332 kN.m) by approaching higher curvature in the concrete section. To reach a higher flexural resistance of 370 kN.m after losing the concrete cover, the confined concrete core should reach a higher strain equal to 0.006. Accordingly, the calculated depth of the new compression zone (a_2) is 77 mm and the effective depth (d_2) is 337 mm. The calculation shows increase in the compression zone depth (a_2) and reduction of the effective depth (d_2) in Phase 2, as explained before. Consequently, it is reasonable to observe that the tensile strain in the beam longitudinal reinforcement (17350 micro-strain) exceeds the design calculated values (1500 micro-strain).

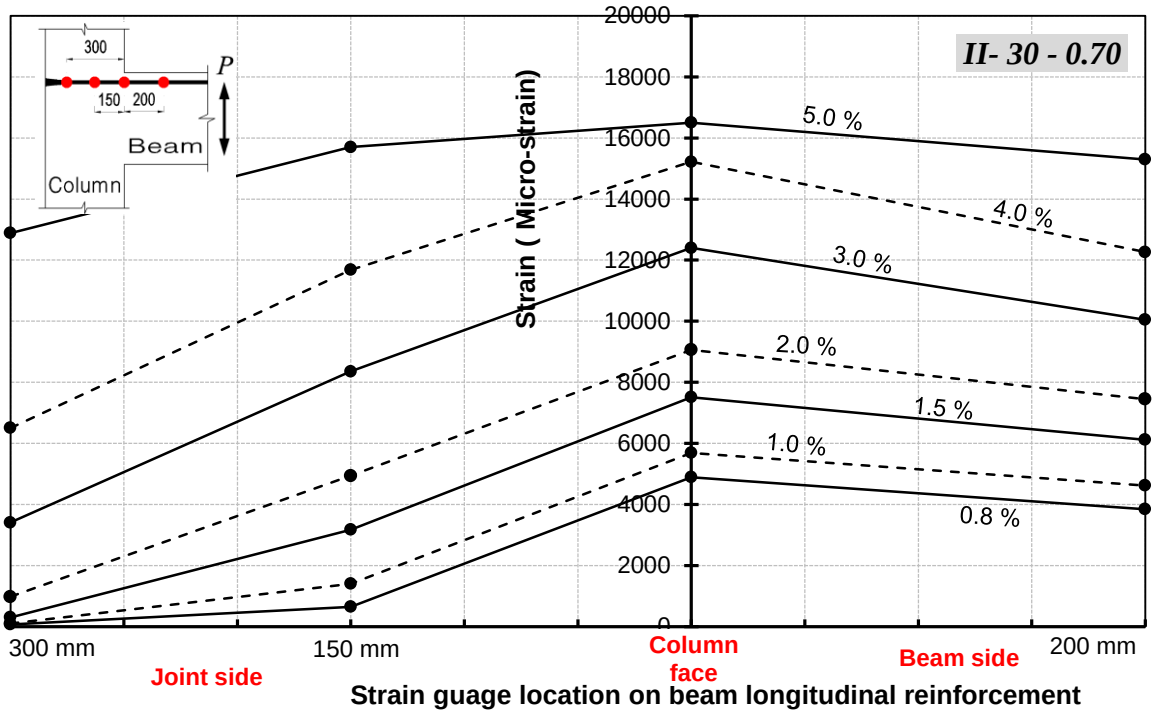

(a) Specimen II-30-0.70

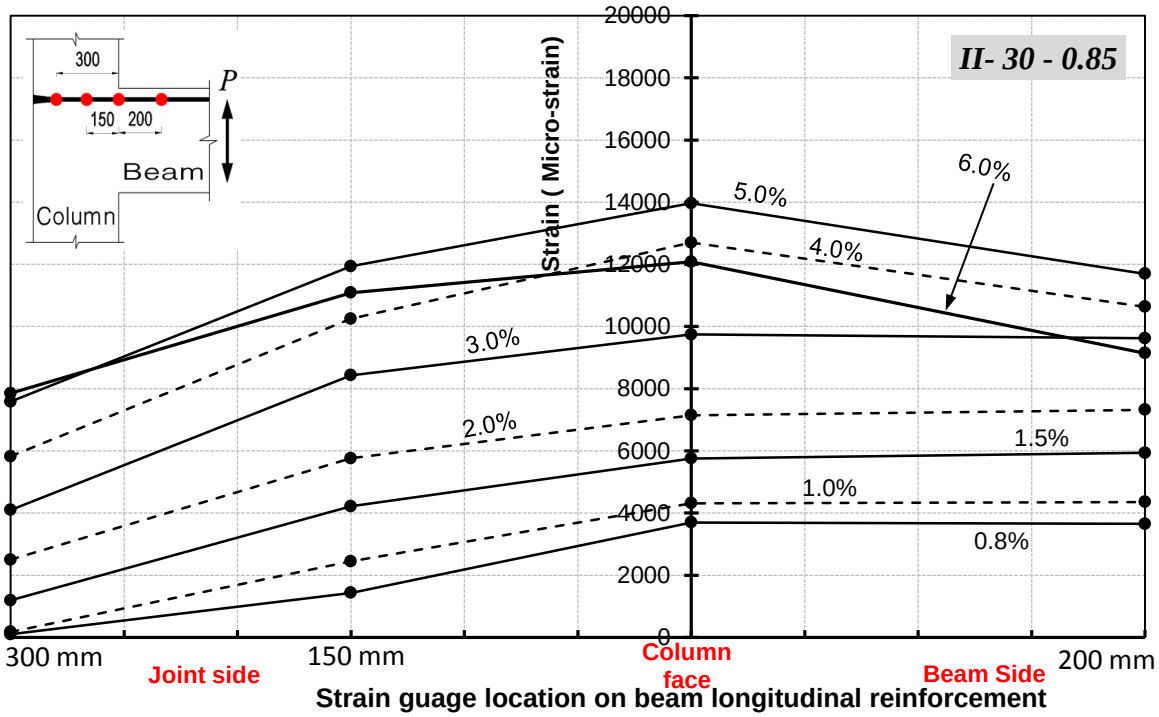

(b) Specimen II-30-0.85

Figure 6.14: Strain profile for beam longitudinal bars in Series (II) specimens (continued)

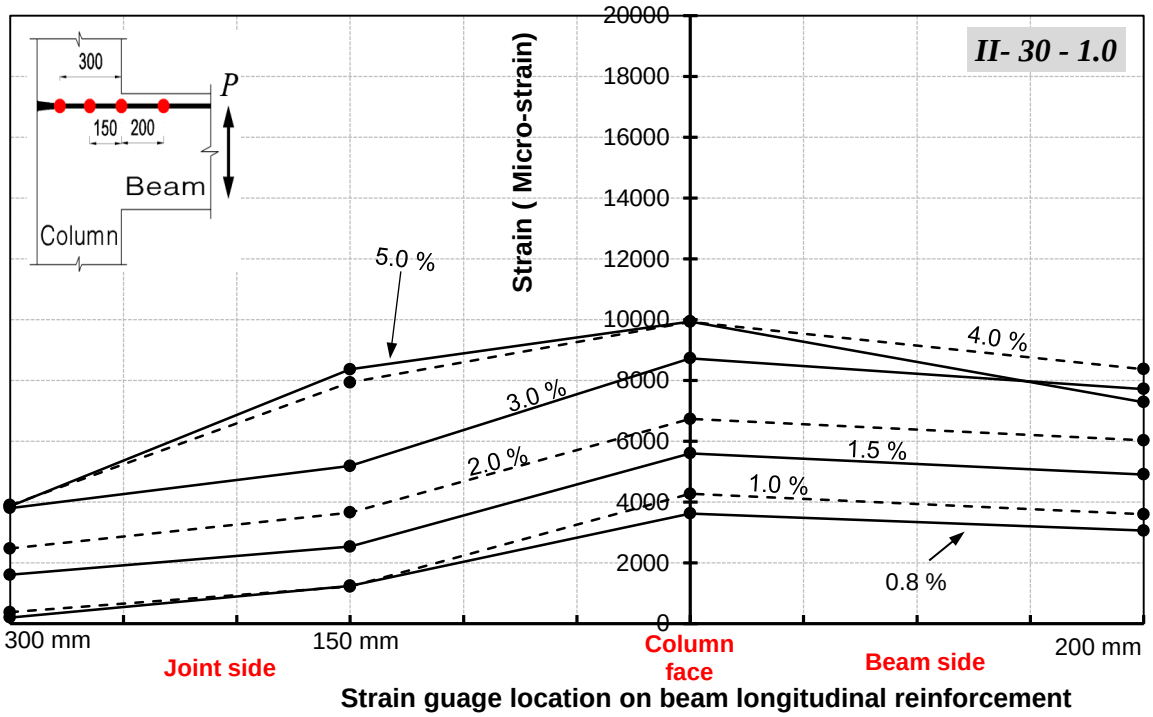

(c) Specimen II-30-1.0

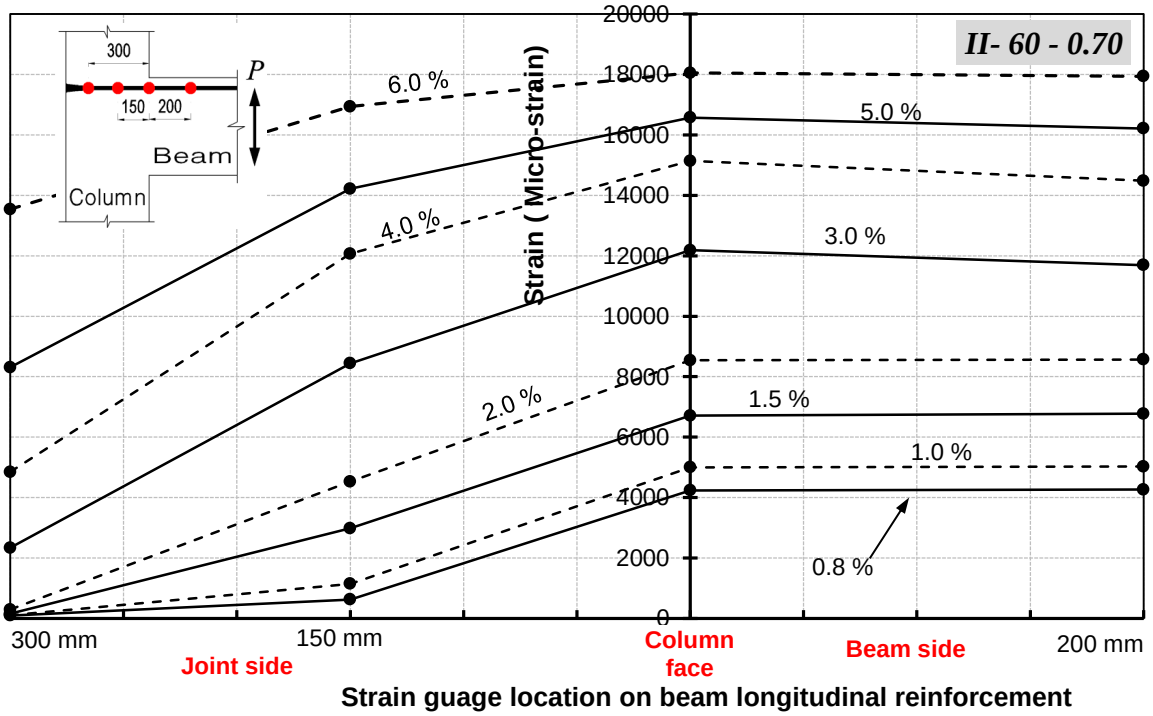

(d) Specimen II-60-0.70

Figure 6.14: Strain profile for beam longitudinal bars in Series (II) specimens (continued)

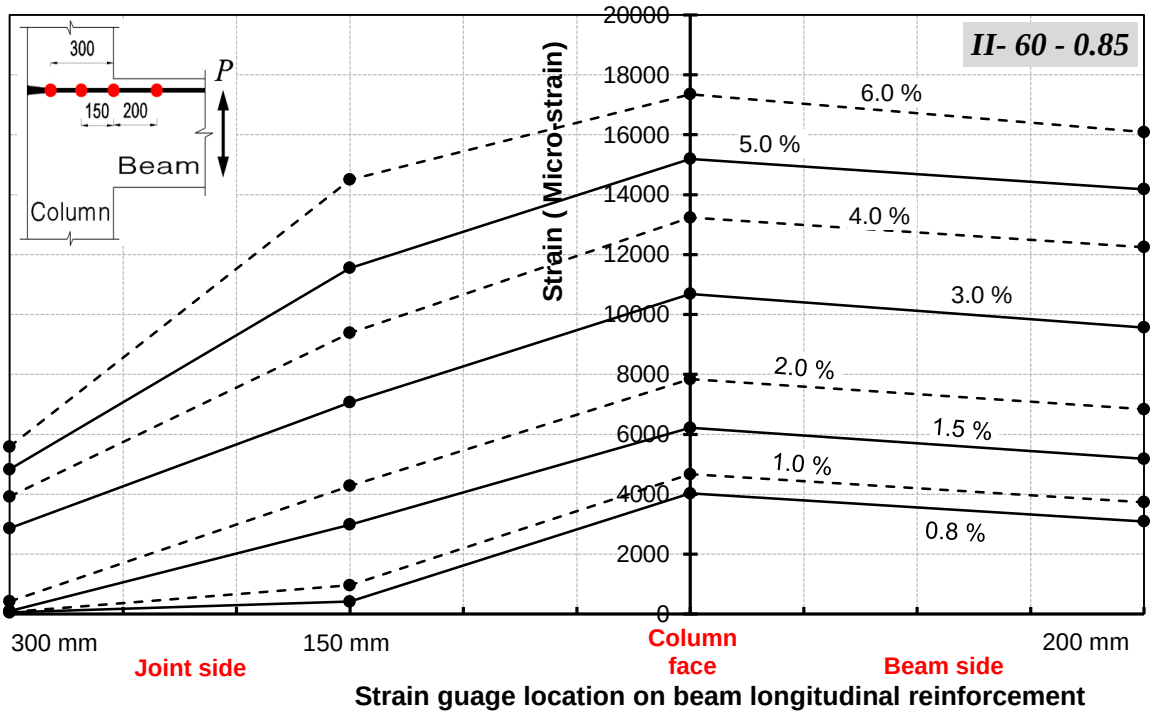

(e) Specimen II-60-0.85

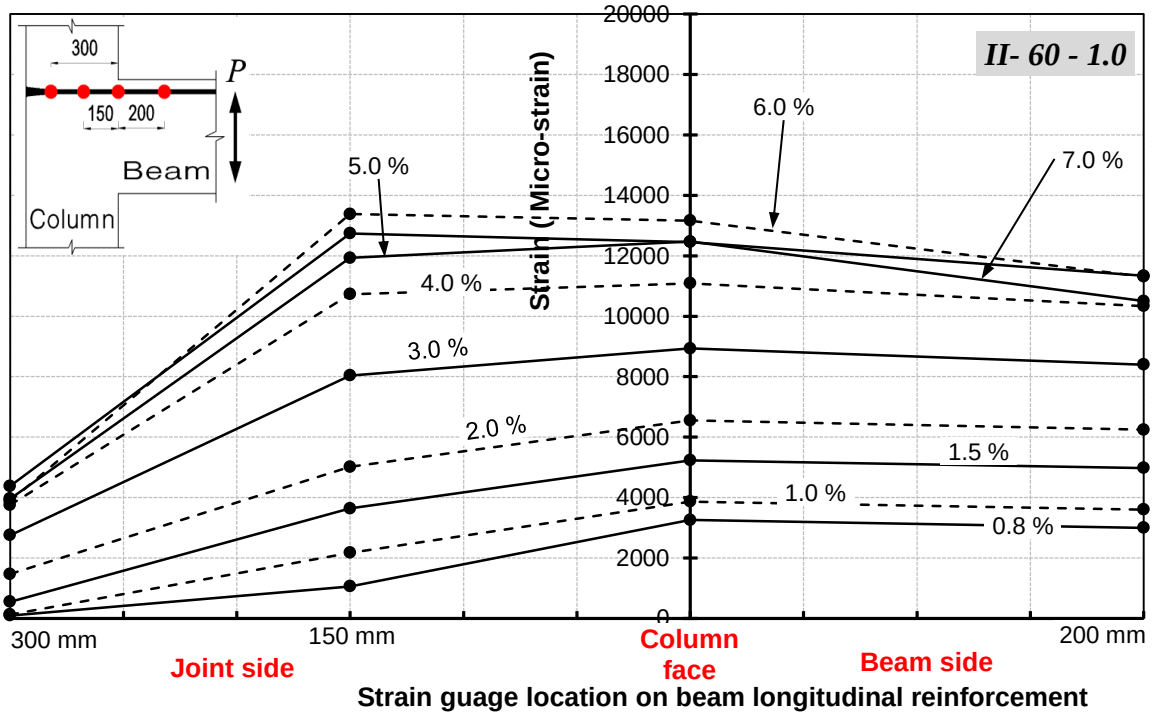

(f) Specimen II-60-1.0

Figure 6.14: Strain profile for beam longitudinal bars in Series (II) specimens

Figures 6.14 (a) through (f) show the distribution of the tensile strain along the beam longitudinal reinforcement in the vicinity of the joint area during the increasing loading drifts. Typically, the figure shows the profile of the tensile strains captured by four strain gauges mounted along the beam longitudinal reinforcement at the column face, 200 mm away from the column face inside the beam (Beam side), 150 mm, and 300 mm away from the column face inside the joint (Joint side), as shown in the legend attached to the figure. For Specimens II-30-0.70 and II-60-0.70, the strain readings increased with the increase of the drift ratio up to failure as shown in Figures 6.14 (a) and (d). Apparently, this can be observed also in Figure 6.14 (e) for Specimen II-60-0.85; however, it should be noted that Figure 6.14 (e) does not show strain readings at 7.0% drift ratio during failure of the specimen due to malfunctioning of strain gauges at that level of loading.

For Specimens II-30-0.85, II-30-1.0, and II-60-1.0, the strain values increased with the increase of loading drifts up to 5.0%, 4.0%, and 6.0%, respectively. Then these specimens exhibited a drop in the strain values in the successive loading drifts as shown in Figure 6.14 (b), (c), and (f), respectively; this is in good agreement with the hysteretic behaviour of these specimens shown previously in Figures 6.1 (b), (c), and (f) where the specimens showed reduction in lateral load resistance. Also, Figure 6.14 shows that the maximum strains during all loading drifts were highly concentrated at the column face where the section at this location is subjected to the maximum moments. It is observed that the readings of the strain gauge located 200 mm away from the column face in the beam are equal or very close to the maximum values recorded at the column face. This

indicates that the formation of the inelastic deformability hinge in the beam extends at least 200 mm from the column face in all specimens.

The penetration of the tensile strains inside the joint was insignificant for all specimens up to 1.5% drift ratio then started to increase with the increase of the loading drifts. The increase of tensile penetration inside the joint was significantly observed in Specimens II-30-0.70 and II-60-0.70 where the tensile strain at the farthest point inside the joint reached at least 75.0% of the strain developed at the column face. This is attributed to the high tensile forces developed in the beam reinforcement especially when the beam reached the maximum flexural capacity. The readings of the strain gauge located 300-mm away from the column face inside the joint and just before the end-bearing head were very useful to evaluate the contribution of the end-bearing heads to provide anchorage for the beam longitudinal bars as will be discussed later in this chapter. Although Specimens II-30-1.0 and II-60-1.0 exhibited the highest flexural resistance compared to their counterparts with similar concrete strength, they exhibited the lowest values of tensile strains at the column face. This is attributed to the larger number of longitudinal reinforcement provided in the joint which collectively resulted in higher tensile force but with lower tensile strain.

6.4.2 Developed Strains in Joint Transverse Reinforcement

The relationship between the drift ratio and the maximum measured strain in the transverse reinforcement inside the joint is shown in Figure 6.15 for Series (II) specimens. The figure also shows the allowable tensile strain limit for transverse

reinforcement, 4000 and 6000 micro-strain, set by the CSA/S806-02, Clause 12.7.1 (CSA 2002) and CSA/S806-12, Clauses 12.7.5.2, 12.7.3.3 (CSA 2012), respectively. As highlighted before, this research program started in year 2010 before publishing the CSA/S806-12; therefore, the design of the specimens was carried out according to the CSA/S806-02 which was available at that time when the program started. Accordingly, it deemed necessary for the integrity of the research to evaluate the performance based on both the current and previous standards.

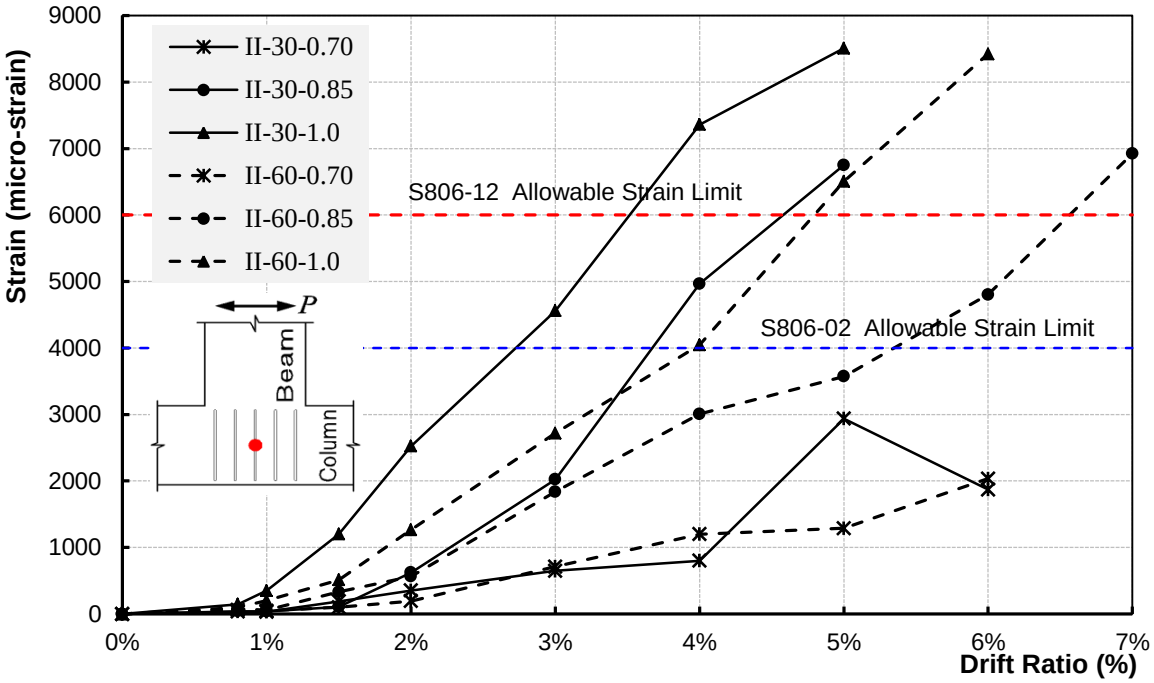

Figure 6.15: Maximum strain–drift ratio relationship for joint stirrups

Figure 6.15 shows that Specimens II-30-0.85, II-30-1.0, II-60-0.85, and II-60-1.0 exceeded the allowable strain limit set by both the CSA/S806-02 and CSA/S806-12. The aforementioned specimens exceeded the CSA/S806-02 limit at 4.0%, 3.0%, 6.0%, and 5.0% drift ratio, respectively; while the same specimens exceeded the CSA/S806-12 limit

at drift ratios 5.0%, 4.0%, 7.0%, and 5.0%, respectively. It should be noted that exceeding the allowable strain limit observed in these four specimens is in agreement with the diagonal-shear failure in the joint exhibited by these specimens. On the contrary, the maximum strains in Specimens II-30-0.70 and II-60-0.70 kept below the allowable limits until failure. This is also in agreement with the mode of failure exhibited by both specimens where the joints were intact until the end of the tests.

The maximum strain value (8500 micro-strain) in stirrups inside the joint was exhibited by Specimens II-30-1.0 and II-60-1.0. This can be attributed to that the joints in both specimens were subjected to the highest shear stress in the joint ($1.0\sqrt{f'_c}$) compared with the other four specimens in Series (II) which were subjected to lower levels of shear stress in the joint and consequently lower strains developed in the stirrups. Interestingly, Figure 6.15 shows that each two specimens subjected to the same level of shear stress in the joint exhibited the same level of strain in joint stirrups at the end of the test although that they did not fail at similar drift ratio. For example, Specimens II-30-0.85 and II-60-0.85, at failure, exhibited the same value of maximum strains in the joint of approximately 6750 and 6920 micro-strain, respectively, although Specimen II-30-0.85 failed earlier at 5.0% drift ratio while Specimen II-60-0.85 failed at 7.0% drift ratio. This indicates that reaching a tensile strain of 6000 micro-strain in the stirrups confining the joint results in diagonal shear failure in the joint.

It should be also highlighted that for each two specimens having the same level of shear stress in the joint, for example Specimens II-30-0.85 and II-60-0.85, they have different

concrete strength and consequently different transverse reinforcement since the concrete strength influences the transverse reinforcement ratio as per Clause 12.7.3.3 (Equation 12-4), CSA-S806-02. Yet, both specimens exhibited the same level of strain in the joint stirrups at the end of the test although that they did not fail at the same drift ratio. Accordingly, it is concluded that Equation 12-4 in the CSA-S806-02 accurately proportions the transverse reinforcement in the joint which results in exhibiting the same level of strains in stirrups under the same level of shear stress considering the difference in concrete strength and transverse reinforcement ratio.

Figures 6.16 (a) through (f) show the profile of the strains developed in stirrups located in the joint during testing at different loading drifts. The vertical axis in the middle of the figure shows the strain values and represents the centre line of the joint and the horizontal axis represents the stirrups location in the joint relative to the centre line of the joint. It should be mentioned that not all the loading drifts have been presented in all figures, especially for specimens exhibiting low strain values, since adding all loading drifts may reduce the clarity of the figure. This is done in a way that does not affect the conclusions drawn from the figure. For example, Figure 6.16 (a) shows the strain profile across the joint at drift ratios 1.5%, 3.0%, 4.0%, 5.0%, and 6.0%. Strains developed during the drift ratios 0.8%, 1.0% are hidden since they are insignificant and below the strain profile at 1.5% drift ratio; for 2.0% drift ratio, the strains profile is typically in between the one at 1.5% drift ratio and the one for 3.0% drift ratio.

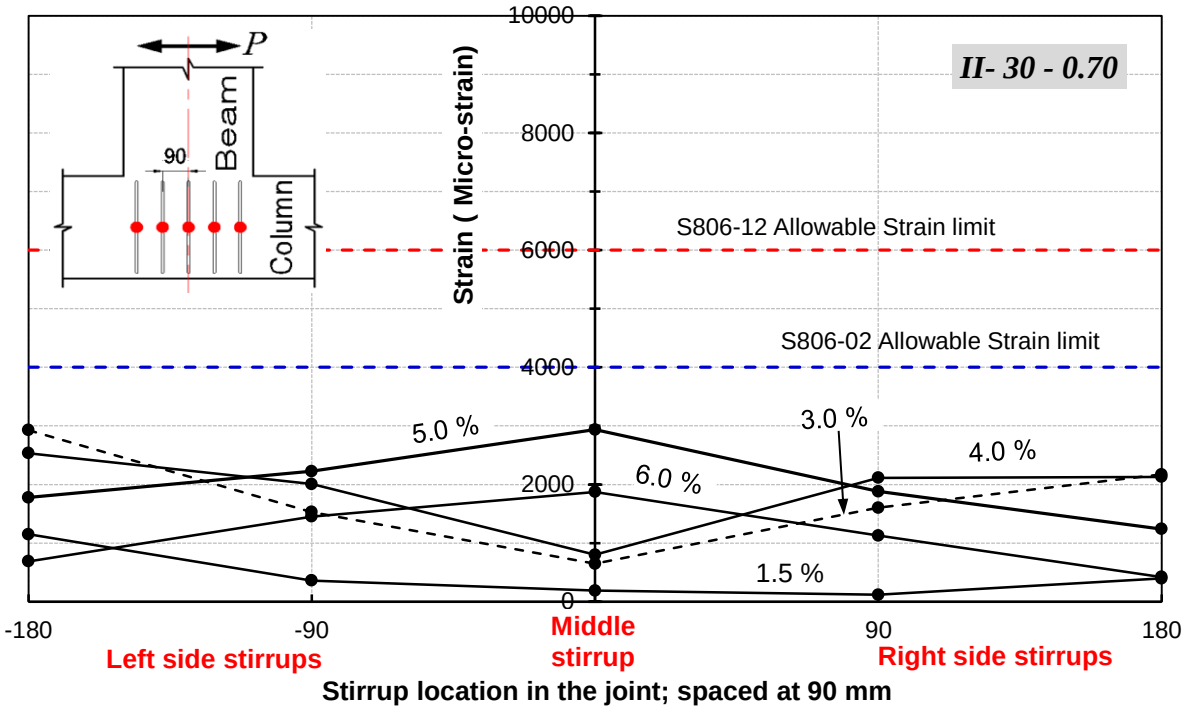

(a) Specimen II-30-0.70

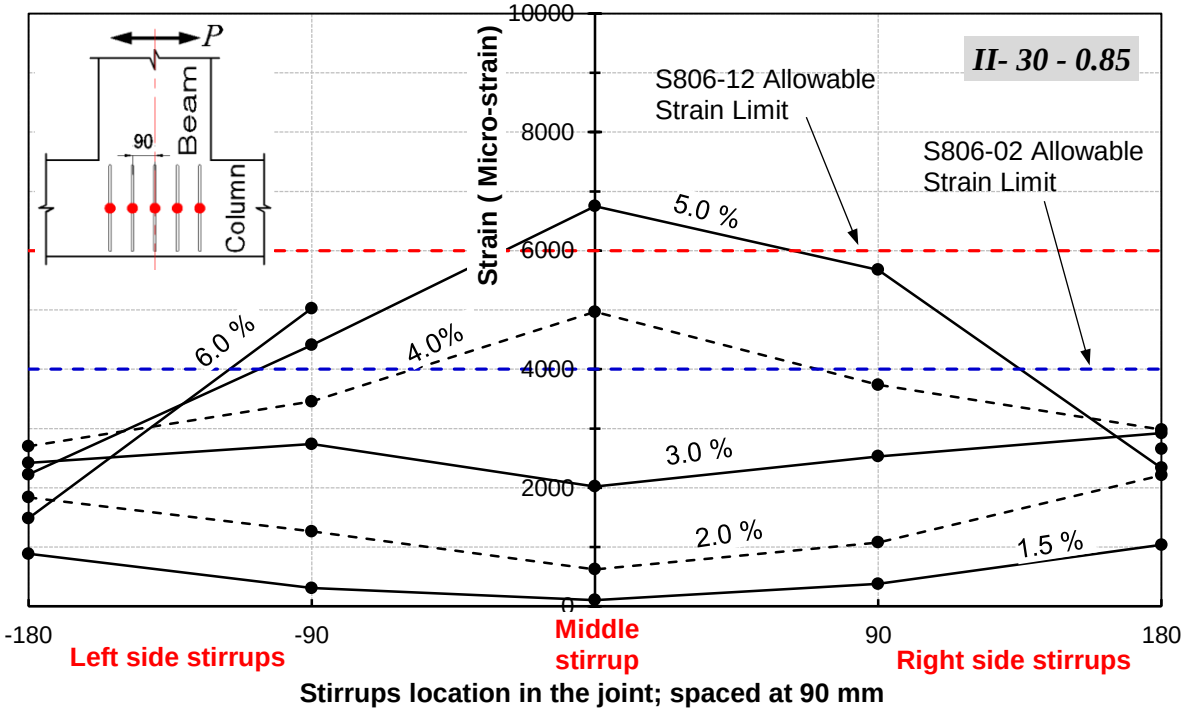

(b) Specimen II-30-0.85

Figure 6.16: Strain profile for joint stirrups in Series (II) specimens (continued)

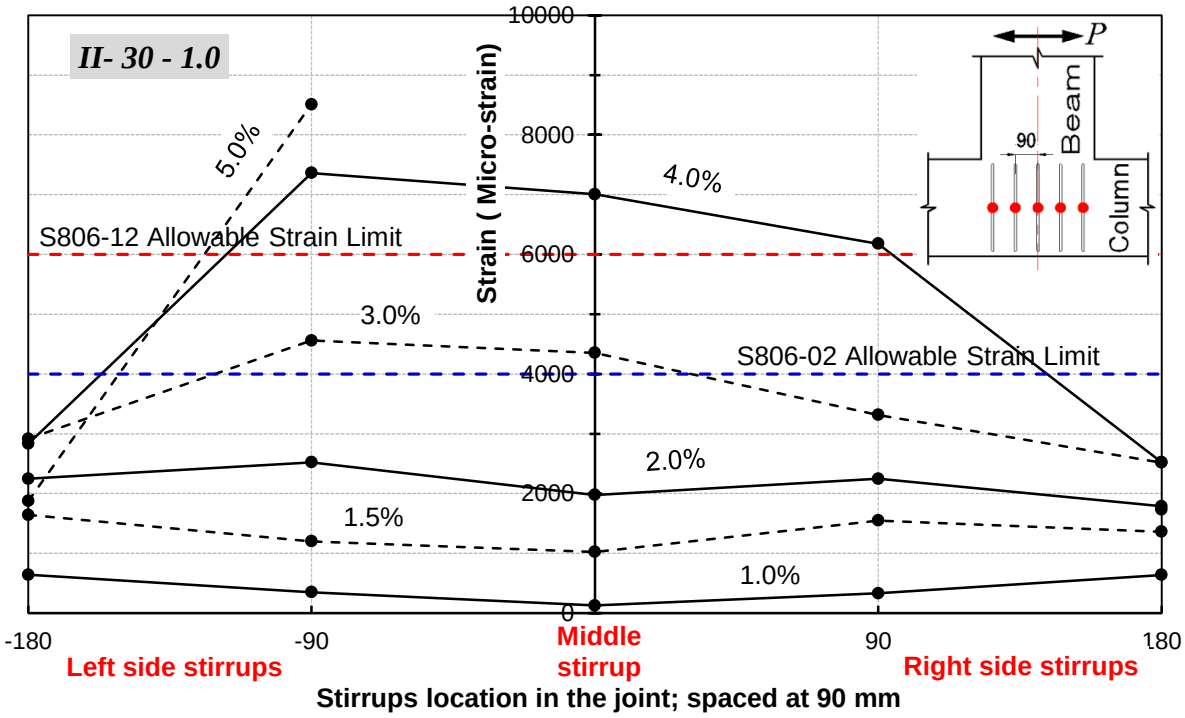

(c) Specimen II-30-1.0

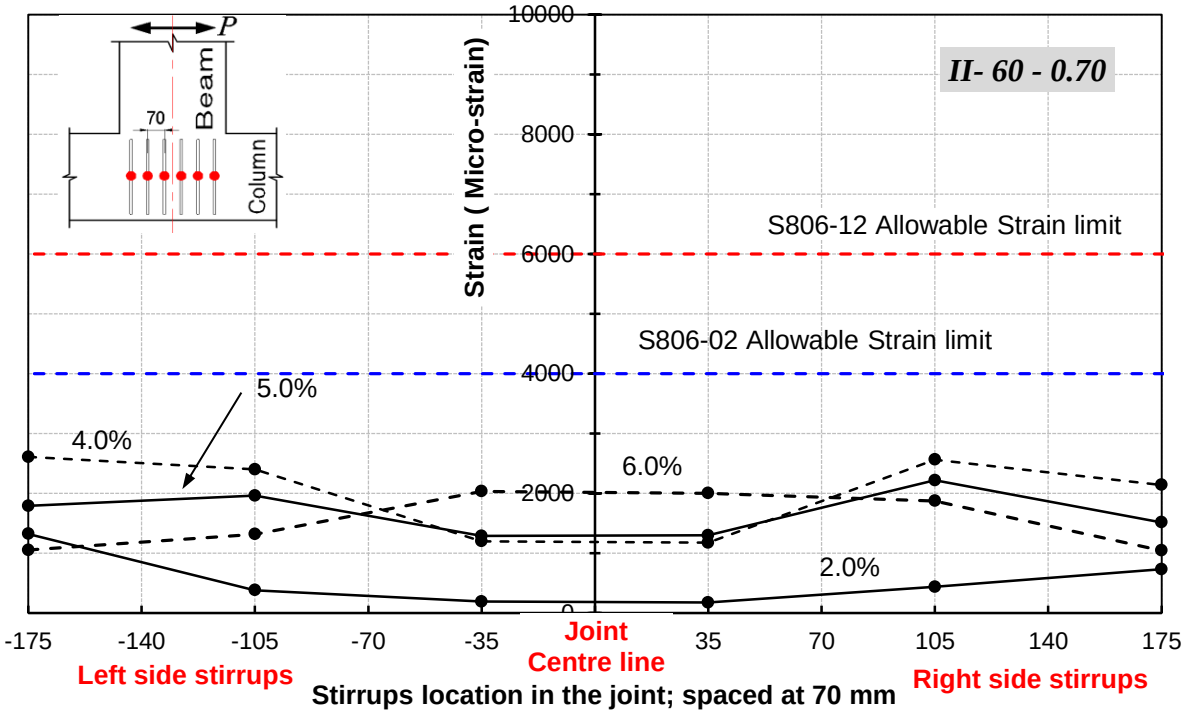

(d) Specimen II-60-0.70

Figure 6.16: Strain profile for joint stirrups in Series (II) specimens (continued)

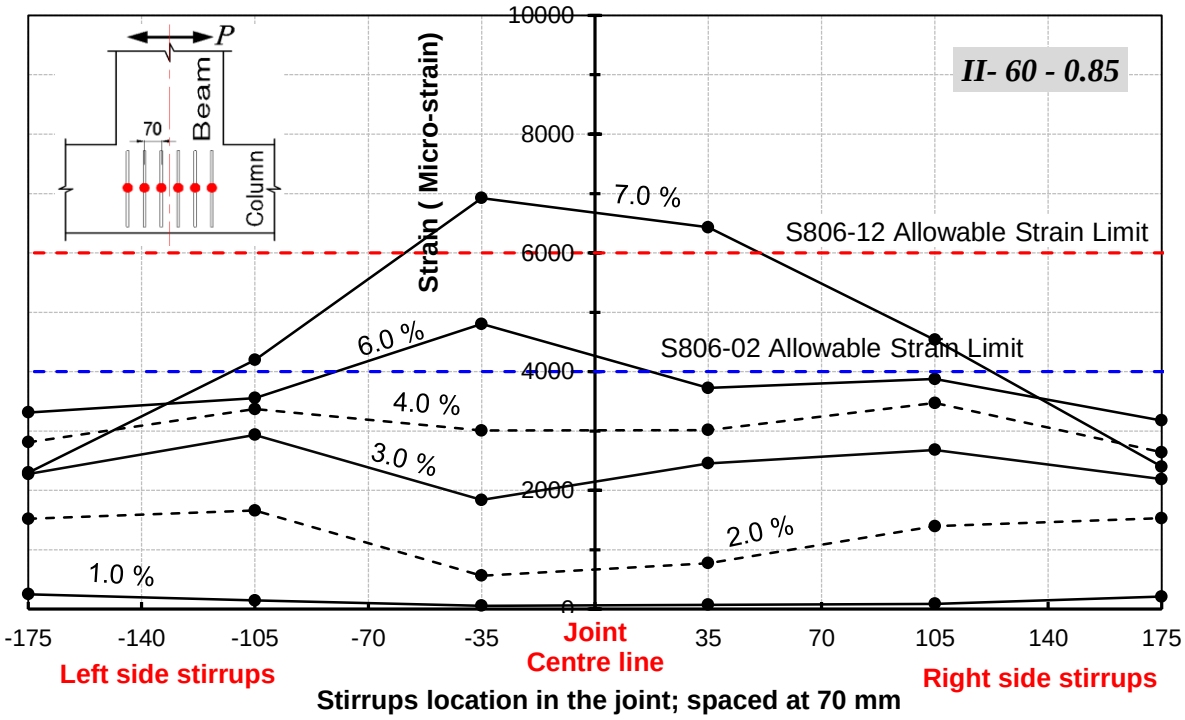

(e) Specimen II-60-0.85

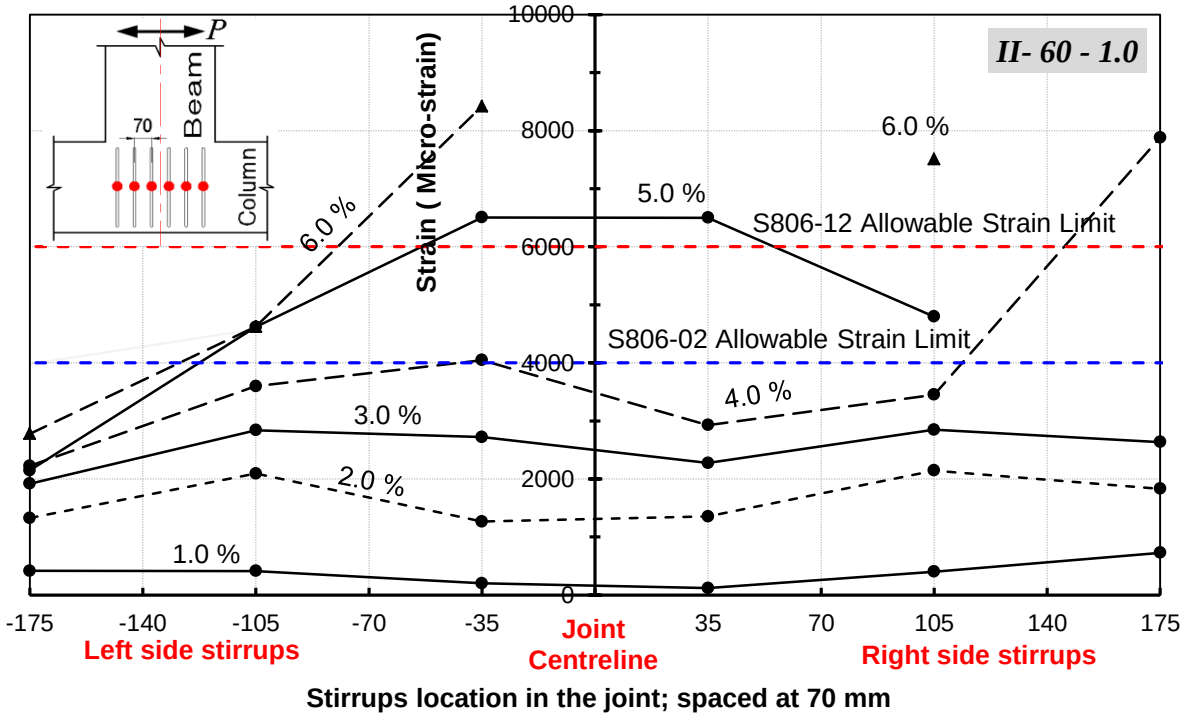

(f) Specimen II-60-1.0

Figure 6.16: Strain profile for joint stirrups in Series (II) specimens

Figure 6.16, in general, shows that the strain values increase with the increase in loading drifts as long as the specimen shows higher resistance to the lateral load and then drops when the lateral load resistance of the specimen deteriorates with the increase of the loading drifts. Specimens II-30-1.0 and II-60-1.0 showed the highest rates of developing strain in the stirrups during testing while Specimens II-30-0.70 and II-60-0.70 showed the lowest rate. This is attributed to the shear stress applied to the joint where Specimens II-30-1.0 and II-60-1.0 had the highest shear stress and Specimens II-30-0.70 and II-60-0.70 had the lowest one.

Moreover, the strain profile across the joint takes a V-shape in the early loading drifts up to a certain drift ratio with high strain values in the sides of the joint and lower values in the centre of the joint. Afterwards, the strain profile tends to invert its shape with an increase of the strain at the centre line of the joint. This is attributed to the appearance of the diagonal shear cracks which starts at the joint sides where the beam longitudinal bars are anchored and then propagates to the centre of the joint.

6.4.3 Developed Strains in Beam Transverse Reinforcement

In this research study, all specimens were designed to develop the flexural resistance of the beam section while avoiding shear failure since studying the shear failure in the beam was out of the scope of this study. The relationship between the maximum strains developed in the beam stirrups and the corresponding drift ratio is shown in Figure 6.17. Since the shear failure was not expected in the beam, only two strain-gauges were mounted on the stirrups in the anticipated inelastic deformability hinge zone. The

reported values are for the one that captured the maximum strains. It can be noticed that the strains developed in all specimens were below 3000 micro-strain. The figure shows that the strain increases with the increase of the loading drifts until reaches a maximum value then drops down when the lateral load resistance of the specimen drops down as well. None of the specimens reached the allowable stain limit in stirrups set by either the CSA/S806-02 or CSA/S806-12. This is attributed to that the confinement requirement for the section exceeded the shear reinforcement requirements.

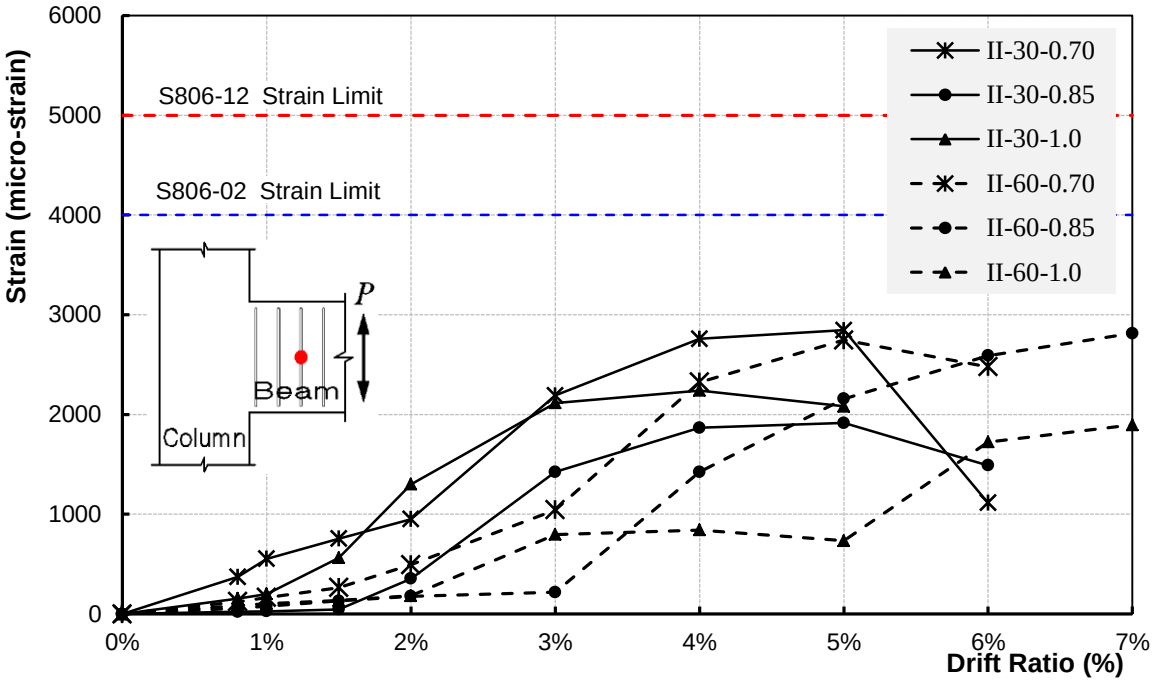

Figure 6.17: Maximum strain–drift ratio relationship for beam stirrups

6.4.4 Developed Strains in Column Longitudinal Reinforcement

Figure 6.18 shows the relationship between the drift ratio and the maximum strains measured in the column longitudinal bar. As expected the tensile strain values in the column were way below the ultimate tensile strain as a result of the axial load applied on

the column. The highest strain values were exhibited by those specimens, namely II-60-1.0 and II-30-1.0, subjected to the highest shear stress in the joint. This is attributed to that the diagonal shear cracks in the joint starts at the intersection of the column and the beam where the strain gauge is located a shown in Figure 6.18. As the shear stress increases in the joint, the diagonal crack width increases which in turn increases the tensile strain in that location.

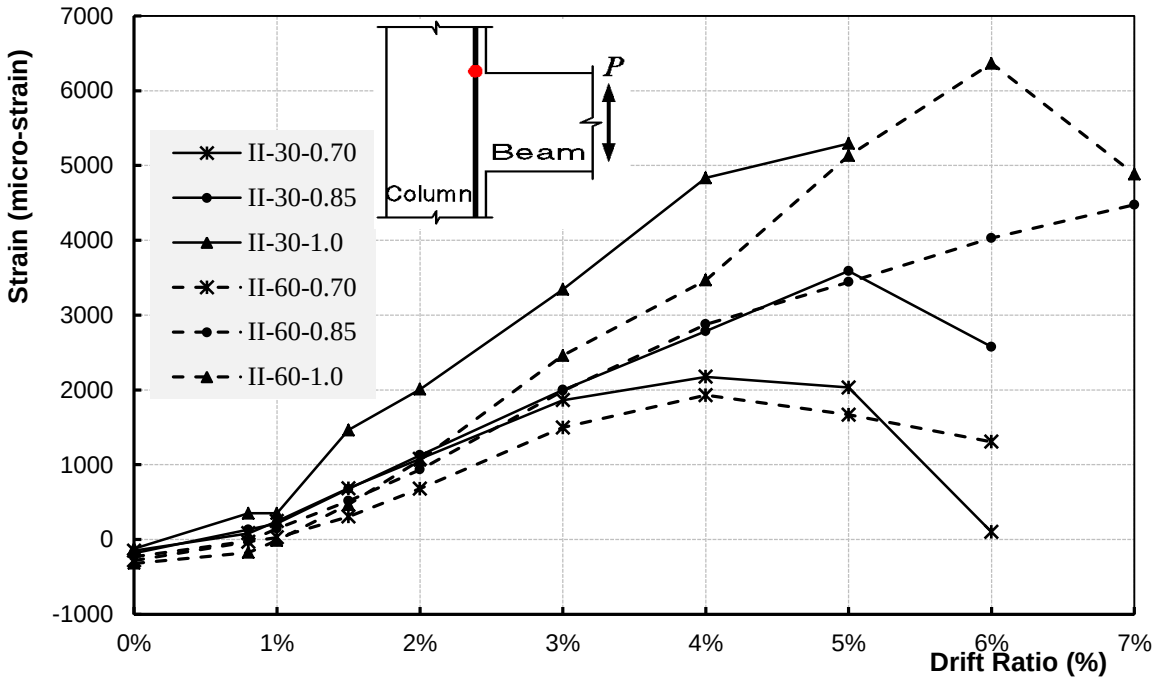

Figure 6.18: Maximum strain–drift ratio relationship for column longitudinal reinforcement

6.5 ENERGY DISSIPATION

Figure 6.19 shows the cumulative energy dissipated by Series (II) specimens during testing at each loading drift. The cumulative energy dissipation was calculated by summation of the dissipated energy in successive load-displacement cycles. The energy dissipated by each cycle is expressed by the area that the hysteretic loop encloses in the corresponding beam tip load-displacement. It is clear that all specimens experienced the same low level of the dissipated energy up to 3.0% drift ratio compared to the dissipated energy at failure of each specimen.

It is generally recognized that there is a strong correlation between the energy dissipated through the hysteretic action and the seismically induced level of damage. The slope of the cumulated energy dissipation-drift ratio relationship indicates the concrete damage rate due to formation of inelastic deformability hinges or/and diagonal shear failure in the joint. As shown in Figure 6.19 (b), Specimens II-30-0.70 and II-60-0.70 had the same slope up to 4.0% then Specimen II-30-0.70 showed significant increase in the dissipated energy at 5.0% and 6% drift ratio while Specimen II-60-0.70 experienced similar behaviour after 5.0% drift ratio. This is in agreement with the earlier discussion about the hysteretic behaviour and the mode of failure of the two specimens where the formation of inelastic deformability hinges and slippage (damage) started at 4.0% and 5.0% for Specimens II-30-0.70 and II-60-0.70, respectively.

Figures 6.19 (b) to (d) show that specimens of low concrete strength (II-30-xx) experienced higher energy dissipation than those of high concrete strength (II-60-xx) at

the same drift ratio. This is despite the fact that specimens II-60-xx showed higher lateral load resistance than specimens II-30-xx at the same loading drift as shown previously in Figures 6.3 (a) to (c). It means that the pinching of the hysteretic loops for specimens II-30-xx is wider than those of specimens II-60-xx. This is attributed to the higher ductility of the lower strength concrete compared to the higher strength concrete which is more brittle (less ductile) and loses its plasticity as the strength increases. Therefore, higher strength concrete needs more confinement (*Ehsani and Alameddine*, 1991). Although the lower energy dissipation is considered a disadvantage, on the other hand, it means that the joint regains its original shape after removing the loads, thus requiring minimum amount of repair after surviving such a loading event.

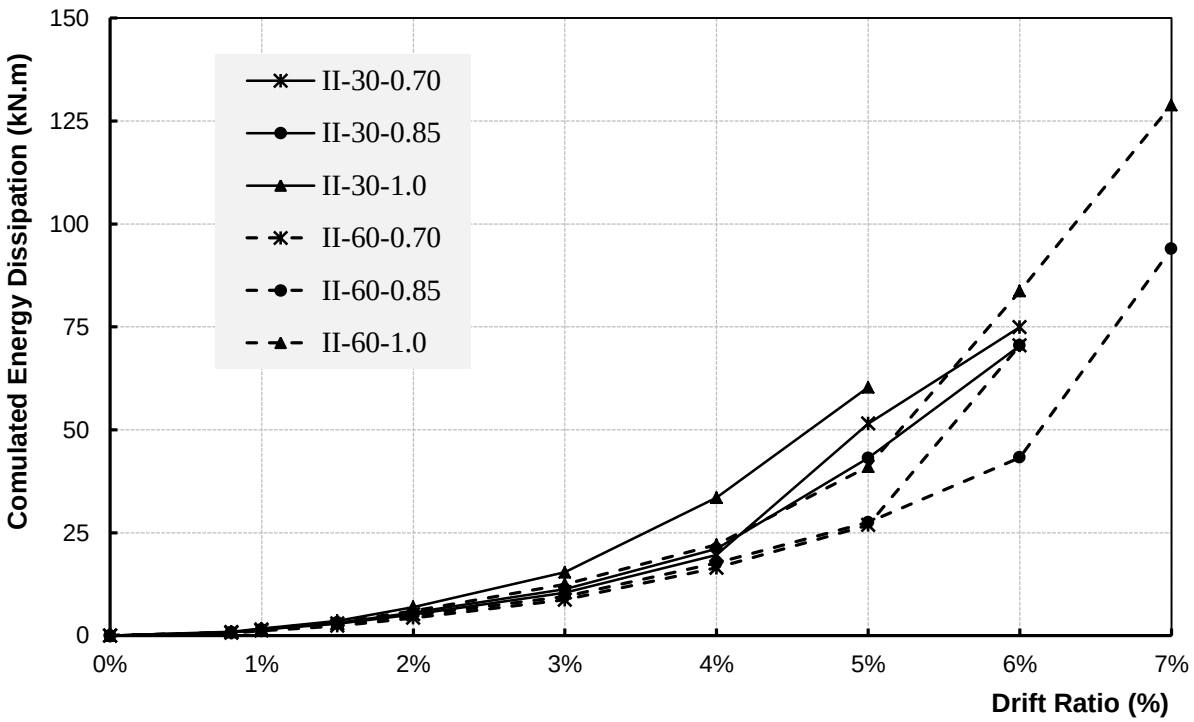

(a) Series (II) specimens

Figure 6.19: Cumulative energy dissipated by Series (II) specimens (continued)

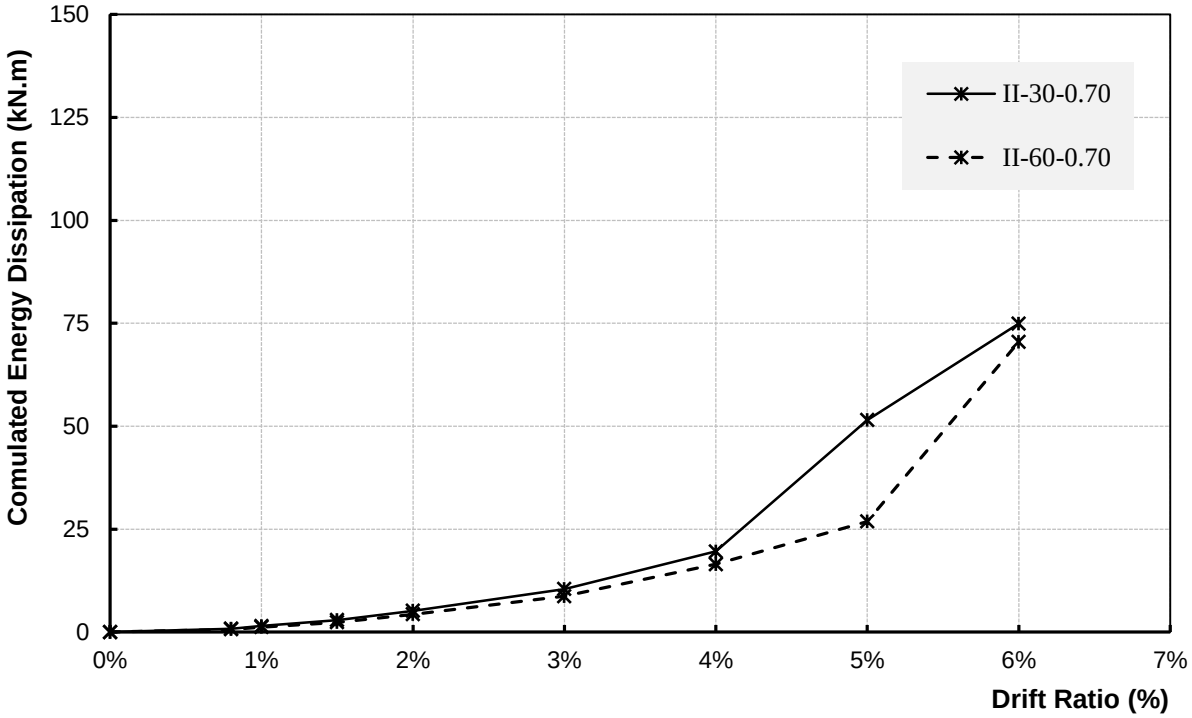

(b) Specimens II-30-0.70 and II-60-0.70

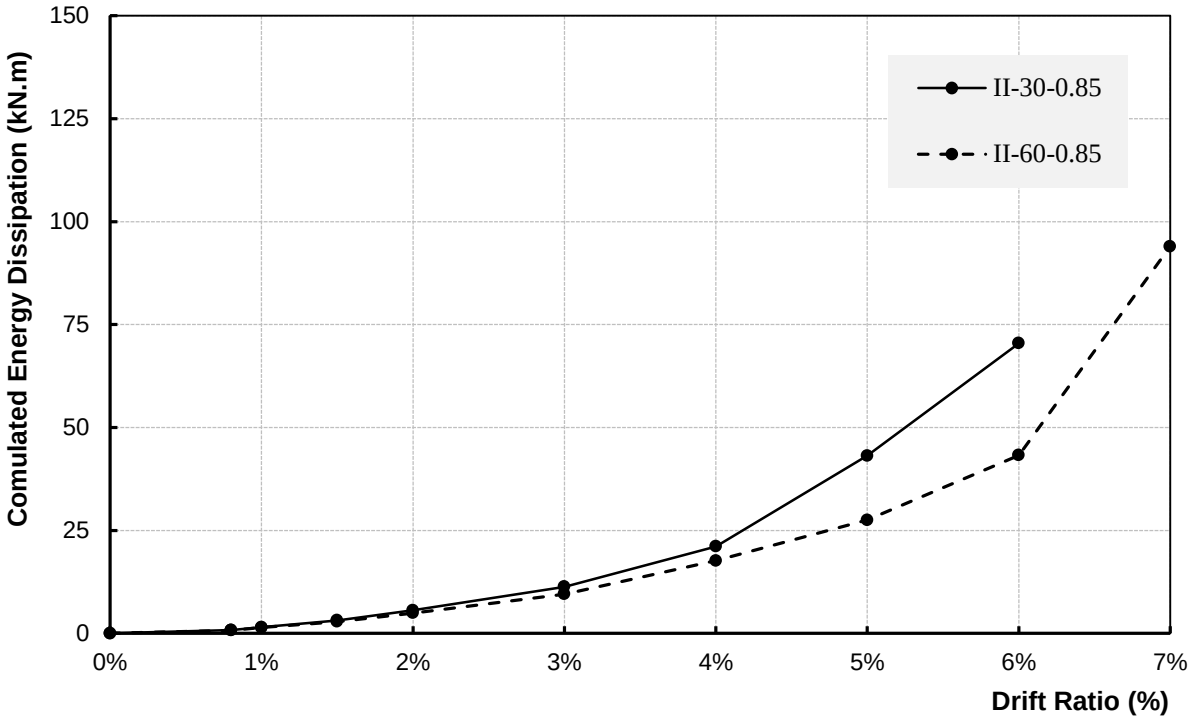

(c) Specimens II-30-0.85 and II-60-0.85

Figure 6.19: Cumulative energy dissipated by Series (II) specimens (continued)

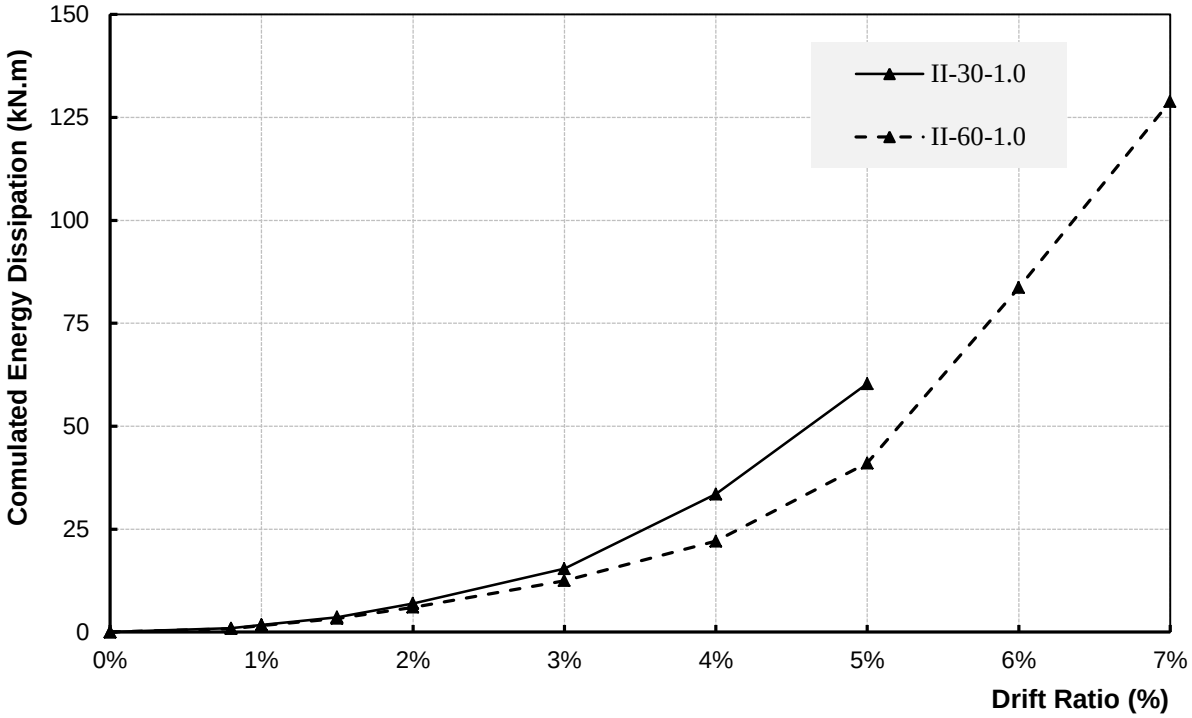

(d) Specimens II-30-1.0 and II-60-1.0

Figure 6.19: Cumulative energy dissipated by Series (II) specimens

6.6 STIFFNESS-DRIFT RELATIONSHIP

It is established that the overall stiffness of the RC structural members is influenced by the member dimensions, concrete elastic modulus, amount and stiffness of the reinforcement and the level of cracking. In this research study, the influence of the member dimensions was disregarded for all specimens since all specimens had the same concrete dimensions. Moreover, the influence of concrete elastic modulus due to differences in concrete strength accounts mainly before cracking of section. This means that the reinforcement stiffness dominates the overall stiffness of the specimens at different loading stages after cracking. Figure 6.20 shows the stiffness-drift ratio relationship for Series (II) specimens during loading drifts. Figure 6.20 (a) shows the

stiffness-drift ratio relationship for the full range of applied drift ratio starting from the un-cracked gross section to the failure of each specimen. While Figure 6.20 (b) is a magnification of the same relationship focussing on drift ratio from 1% to failure of each specimen. In Figure 6.20, the stiffness of the specimen is calculated from the load-lateral displacement relationship as the slope of the line connecting the two peaks of load.

As shown in Figure 6.20 (a) the range of calculated stiffness of specimens in the un-cracked stage was approximately between 16 and 20 kN/mm due to the differences in concrete strength. Then once the specimens are cracked, the stiffness range dropped to values approximately between 4 to 8 kN/mm due to cracks occurred in the beam section at column face (critical section in flexure). This implies that the stiffness in the cracked stage is approximately 25% to 40% of the original stiffness calculated based on the gross inertia of the un-cracked sections. This is in agreement with the cracked section properties of steel-RC beams used by the CSA/A23.3-04, Clause 21.2.5.2.1. This clause requires that reduced section properties shall be used as a fraction of the gross section inertia in the analysis to determine the straining actions and deflections of the structure, where in beams 40% of the gross inertia shall be used. The same clause also provides values of the reduced effective properties for other steel-RC structural elements such as columns, coupling beams, walls, and slab frame elements.

As shown in Figure 6.20 (b), it can be noticed that Specimens II-30-1.0 and II-60-1.0 recorded the highest stiffness among the other specimens. This is attributed to the higher reinforcement ratio in these two specimens compared with the other specimens in Series

(II). In general, specimens of lower concrete strength experienced loss of stiffness faster than those of higher concrete strength. Moreover, specimens subjected to high shear stress in the joint, II-30-1.0 and II-60-1.0, experienced loss of stiffness faster than other specimens subjected to lower shear stress in the joint.

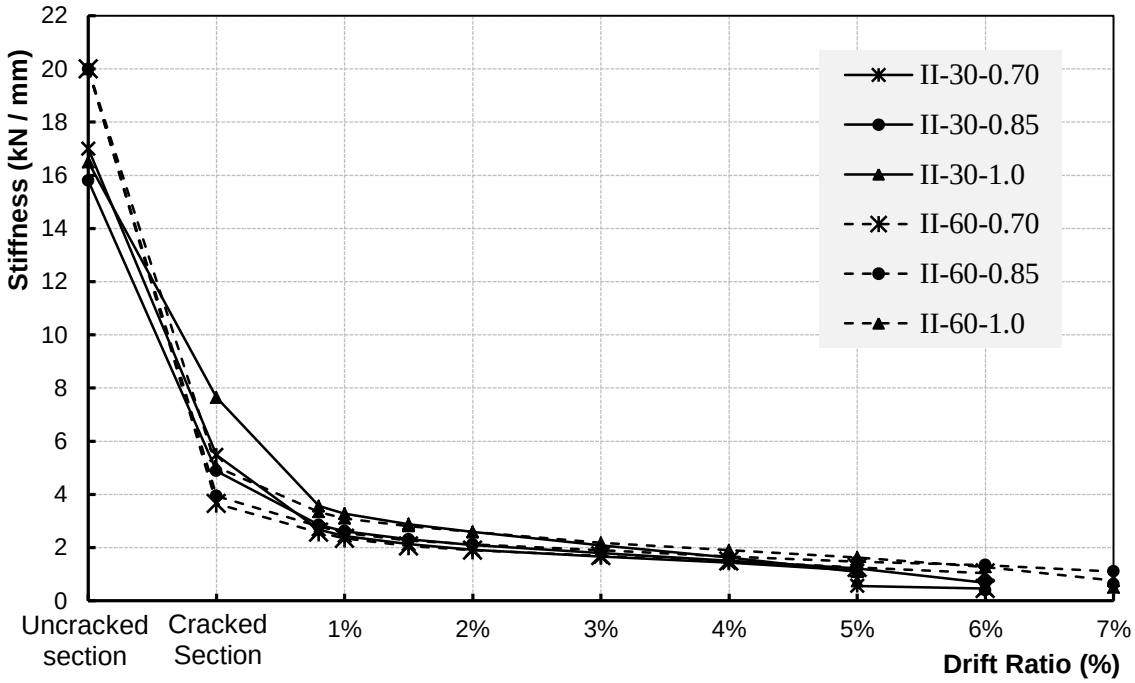

(a) Full relationship

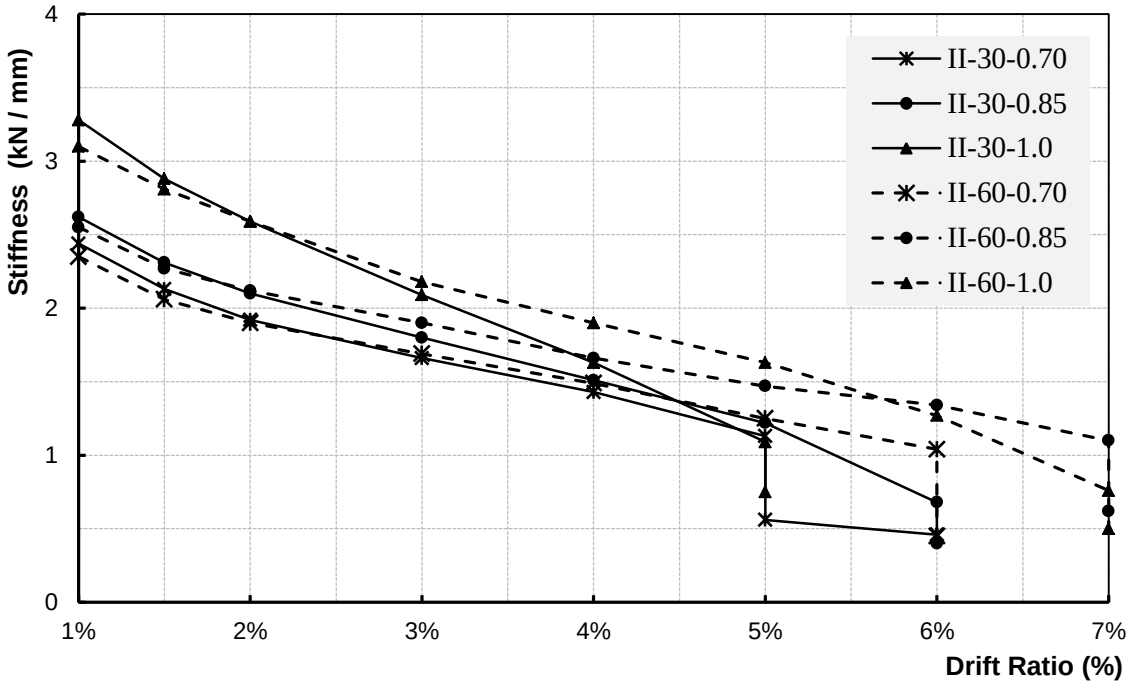

(b) Magnified chart

Figure 6.20: Stiffness–drift ratio relationship for Series (II) specimens

6.7 DRIFT COMPONENTS

As discussed before in Chapter 5, the main drift components that were measured in this study consisted of: 1) development of main crack on the column face including strain penetration inside the joint; 2) rotation in the anticipated beam inelastic deformability hinge zone within a distance equal to the effective depth of the beam from the column face; and 3) distortion in the joint due to shear deformation as shown in Figures 6.21 (a), (b), and (c), respectively. Other drift components such as column rotation, elastic flexural cracking away from the inelastic deformability hinge, and shear deformation in the beam were not considered in this study. It should be noted that the measurement of the different contributing components stopped at the loading drift when the beam or the joint lost the concrete cover where the LVDTs were attached to.

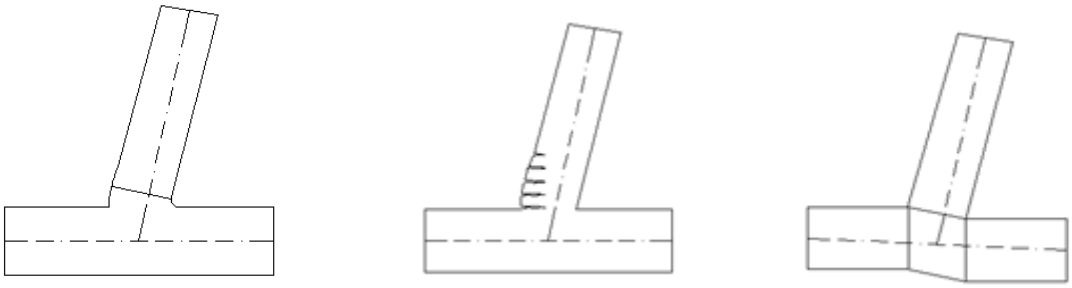

a) Main crack on column face b) Inelastic deformability hinge c) Joint distortion

Figure 6.21: Major components contributing to total drift angle

Figures 6.22 (a) through (f) show the contribution of the studied drift components to the overall rotation of the specimens. The remaining part of the curve reflects the other components which were not considered as mentioned above. The figures show that the development of main crack on the column face along with the strain penetration inside

the joint (referred to as "Main crack at column face" in the figures) contributed to the total drift by approximately 15% to 35%. Also, the formation of the inelastic deformability hinges in the specimens contributed to the total drift angle by approximately 30% to 45%. Collectively, the contribution of the previous two components was in the range of 50% to 65% through all levels of loading drifts.

It should be noted that for Specimen II-30-1.0, the LVDTs attached to the beam were removed after the 3.0% drift ratio due to concrete damage at the points where the LVDTs were attached. Similar note is applicable in Specimen II-30-0.85; however, for those LVDTs assigned to measure the deformation of the inelastic deformability hinge.

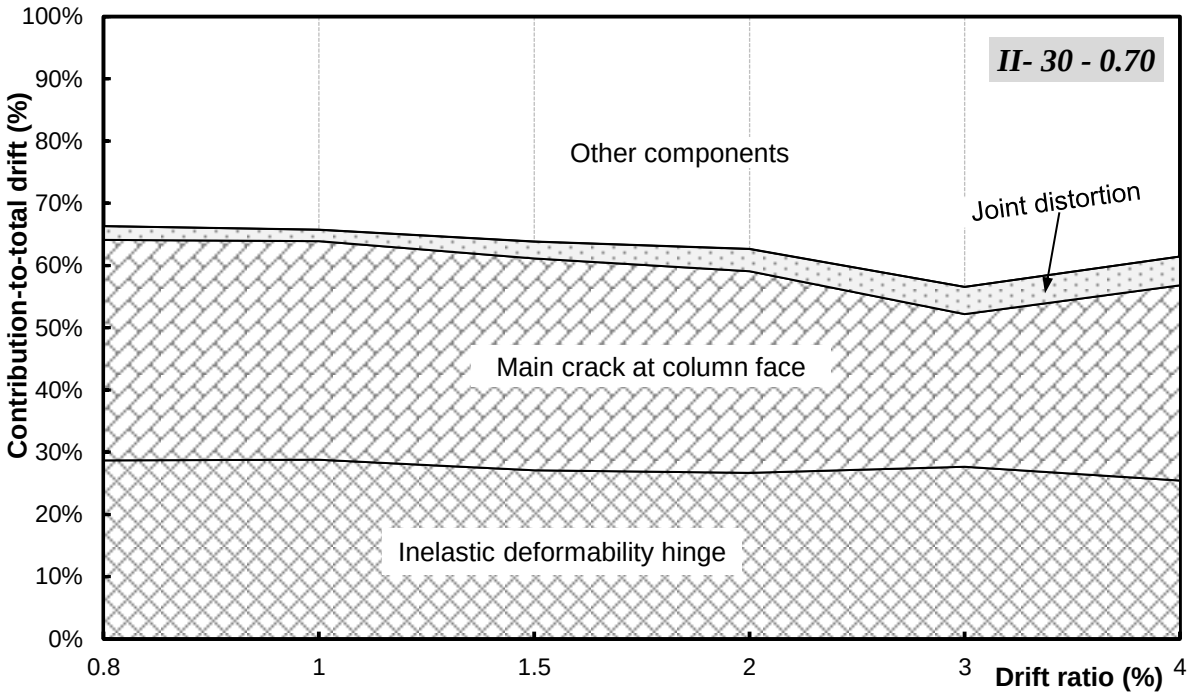

(a) Specimen II-30-0.70

Figure 6.22: Components contribution to total drift angle for Series (II) specimens

(continued)

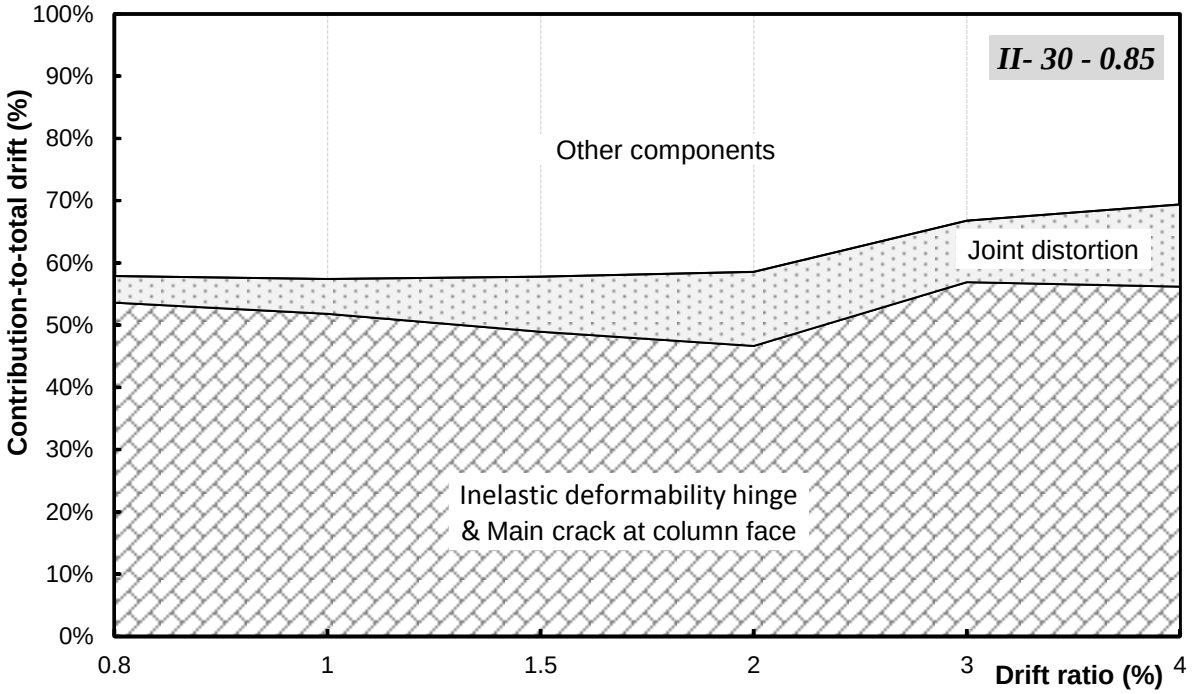

(b) Specimen II-30-0.85

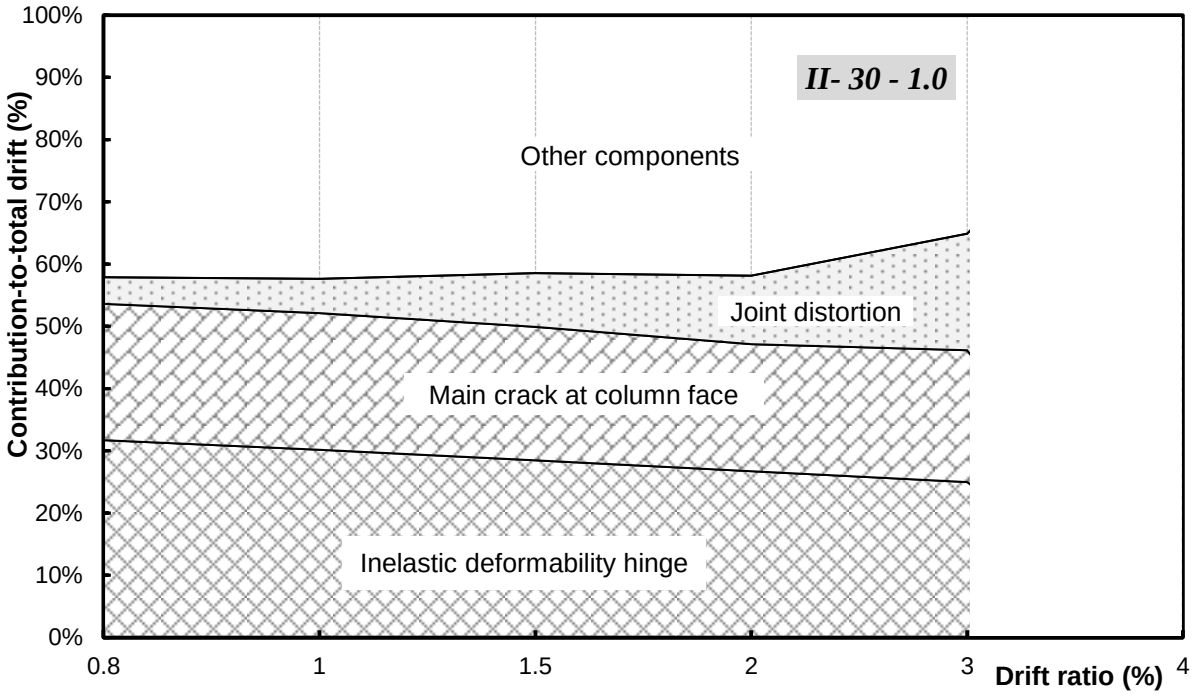

(c) Specimen II-30-1.0

Figure 6.22: Components contribution to total drift angle for Series (II) specimens (continued)

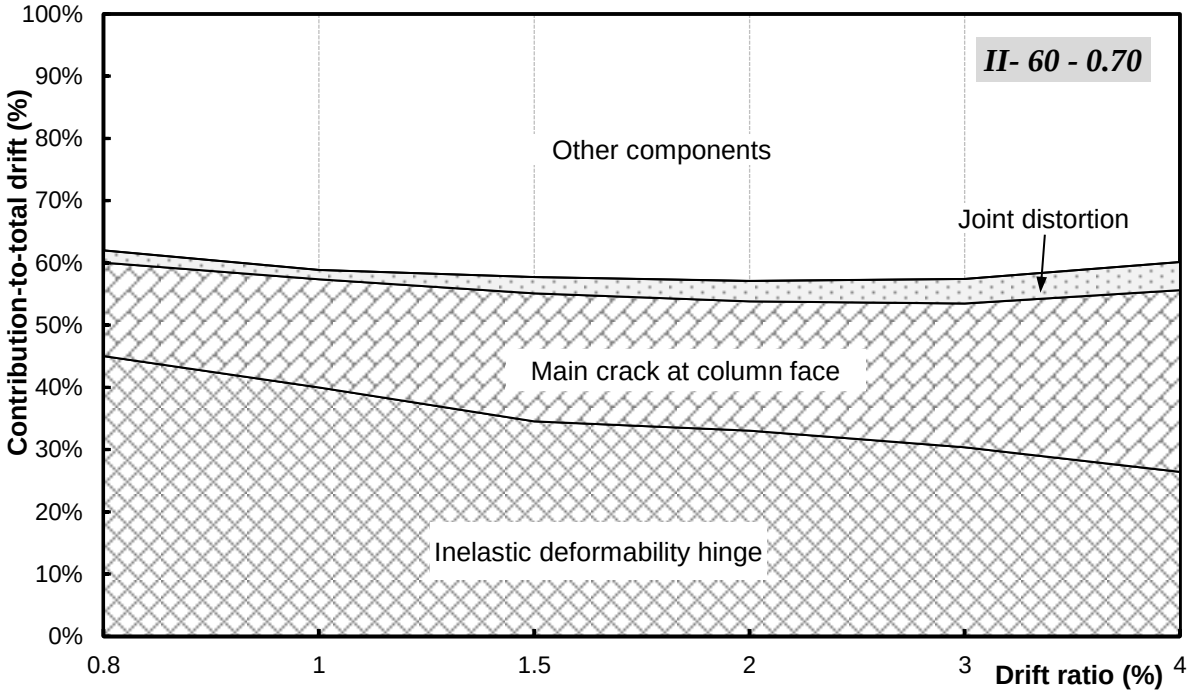

(d) Specimen II-60-0.70

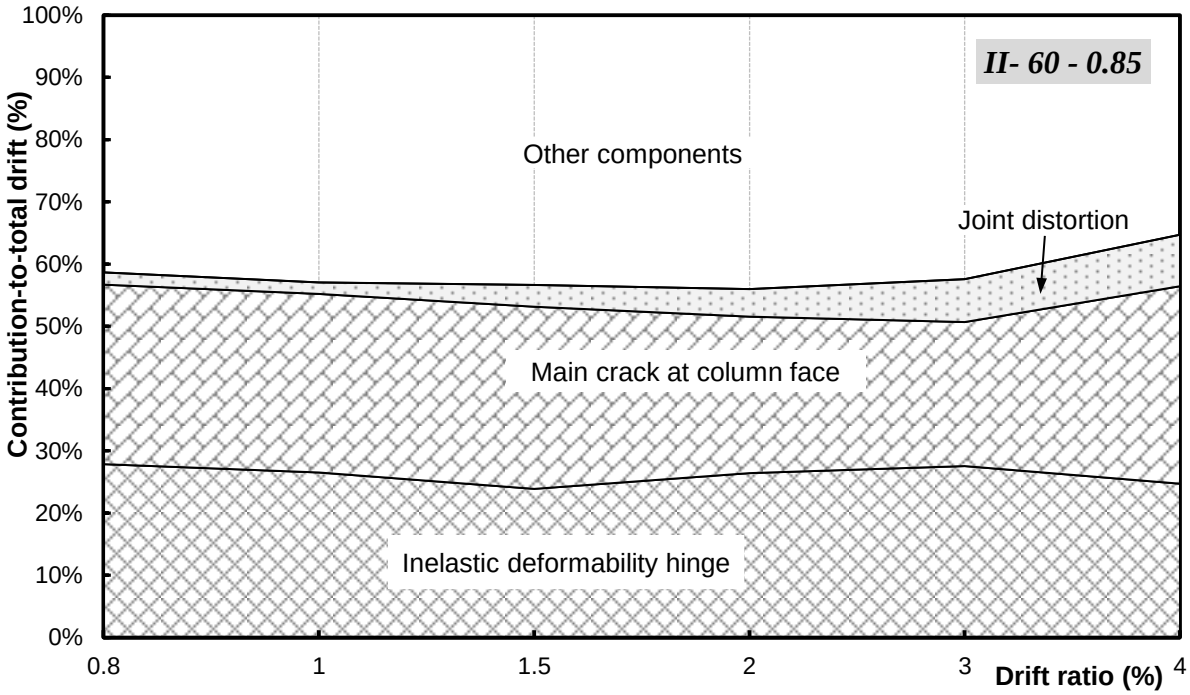

(e) Specimen II-60-0.85

Figure 6.22: Components contribution to total drift angle for Series (II) specimens (continued)

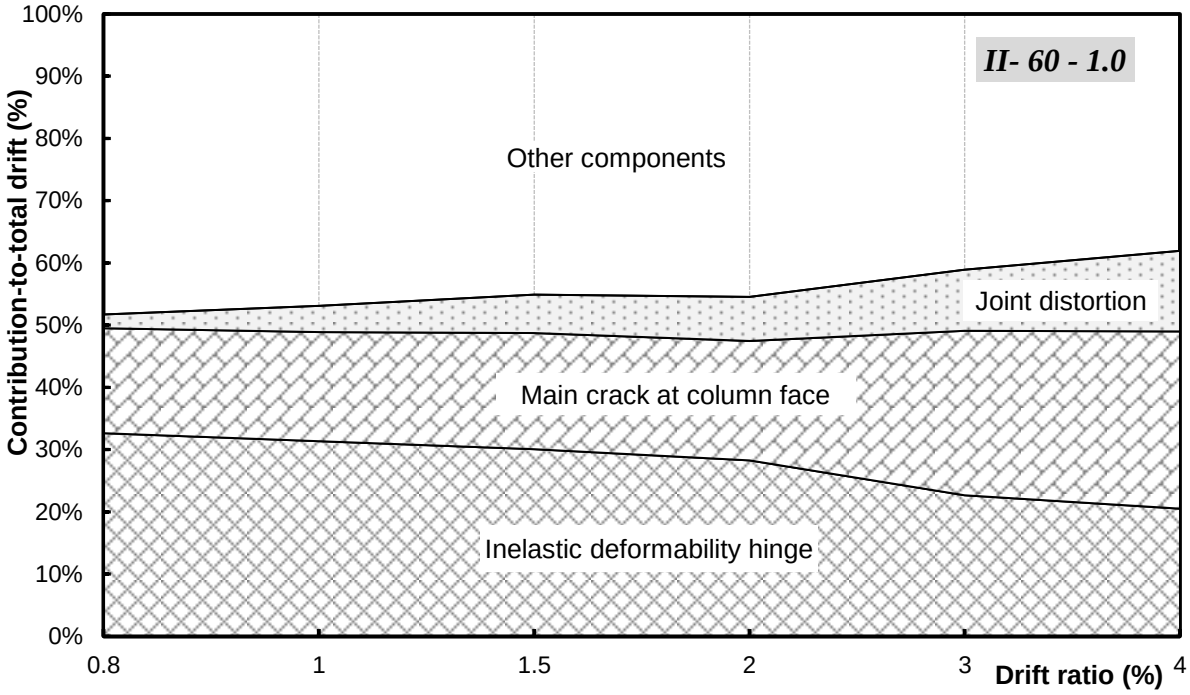

(f) Specimen II-60-1.0

Figure 6.22: Components contribution to total drift angle for Series (II) specimens

Series (II) specimens were designed to study the behaviour under different shear stress levels in the joint; therefore, evaluation of the joint distortion contribution is a good indication for shear deformation exhibited by the joints. Figures 6.22 (a) to (f) show that the shear distortion in the joint increases with the increase of loading drifts and reaches its maximum value just before the end of the test when each specimen experiences its maximum lateral load resistance. Figure 6.23 shows the contribution of the joint distortion to the drift angle at successive loading drifts during testing. The Figure shows that Specimens II-30-1.0 and II-60-1.0 subjected to the highest shear level in the joint ($1.0\sqrt{f'_c}$) recorded a significant joint distortion contribution to the total drift angle by 46% and 33%, respectively. The specimens subjected to lower shear stress in the joint

exhibited lower values of joint distortion. Furthermore, it is noticed that specimens of lower concrete strength (II-30-xx) suffered higher distortion in the joint than their counterparts of higher concrete strength (II-60-xx). This observation is in good agreement with the cracking pattern of the joints and tensile strains exhibited in the joint stirrups during testing. It is worth to mention that in RC frames resisting seismic loads, it is desirable to maintain the joint intact and in elastic condition in order maintain the stability and axial capacity of the column taking into consideration that the joint is part of that column. Therefore, it is required to limit the shear deformation in the joint to provide stability for the structure.

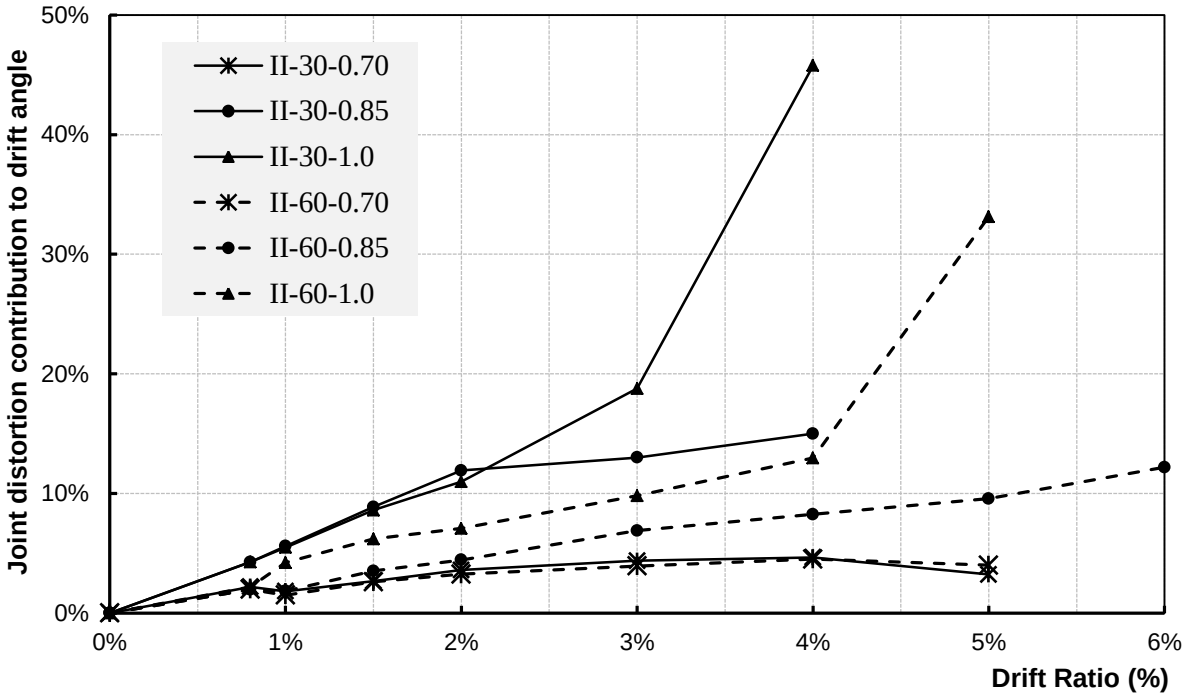

Figure 6.23: Contribution of joint distortion to total drift angle for Series (II) specimens

6.8 ANCHORAGE PERFORMANCE OF GFRP HEADED BARS

In Series (II) specimens, headed bars were used to provide anchorage for beam longitudinal bars into the joint by bearing. The anchorage contribution of the heads to resist the pull-off tensile forces developed in the beam longitudinal reinforcement at the column face was evaluated in this study. In general, the tensile force developed in the beam longitudinal reinforcement is resisted by embedding the bar in the concrete with a depth equal to or larger than the full development length. In this case, the tensile force is solely resisted by bond stresses between the reinforcement surface and the concrete. In frame elements where the depth of the column is less than the full development length, an end-anchorage detail is required either by using standard hooks or by using bearing heads. In this case the resisting force will be a combination of the bond stresses on the available bar length in contact with concrete and the end-anchorage as shown in Figure 6.24.

To evaluate the contribution of the end-bearing heads in the beam column specimens while maintaining effective bond interaction between the bar and the concrete (no bond breaker is used around the bar to eliminate the bond), a strain-gauge was mounted on the bar just before the bearing head (i.e. 300 mm away from the column face inside the joint) as shown in Figure 6.24. This strain-gauge records the tensile strain developed in the bar that to be resisted by the end-bearing head. Figure 6.25 shows the relationship between the tensile strain recorded by that strain-gauge shown in Figure 6.24 and the loading drifts for Specimens II-30-0.70 and II-60-0.70 which both exhibited slippage failure at the end of testing. As shown in Figure 6.25, the developed strain increased with the

increase of the loading drifts as a result of the tensile force increase in the longitudinal reinforcement. At the end of testing and just before failure of the bearing heads, Specimens II-30-0.70 and II-60-0.70 exhibited tensile strain values, in the bar section just before the head, approximately equal to 12000 and 13550 micro-strain, respectively. These strain values represent 65% and 74% of the ultimate tensile strain of the bar. This means that the bearing heads were capable of resisting at least 65% of the ultimate tensile strength of the longitudinal reinforcement (i.e 0.65 * 1100 = 715 MPa).

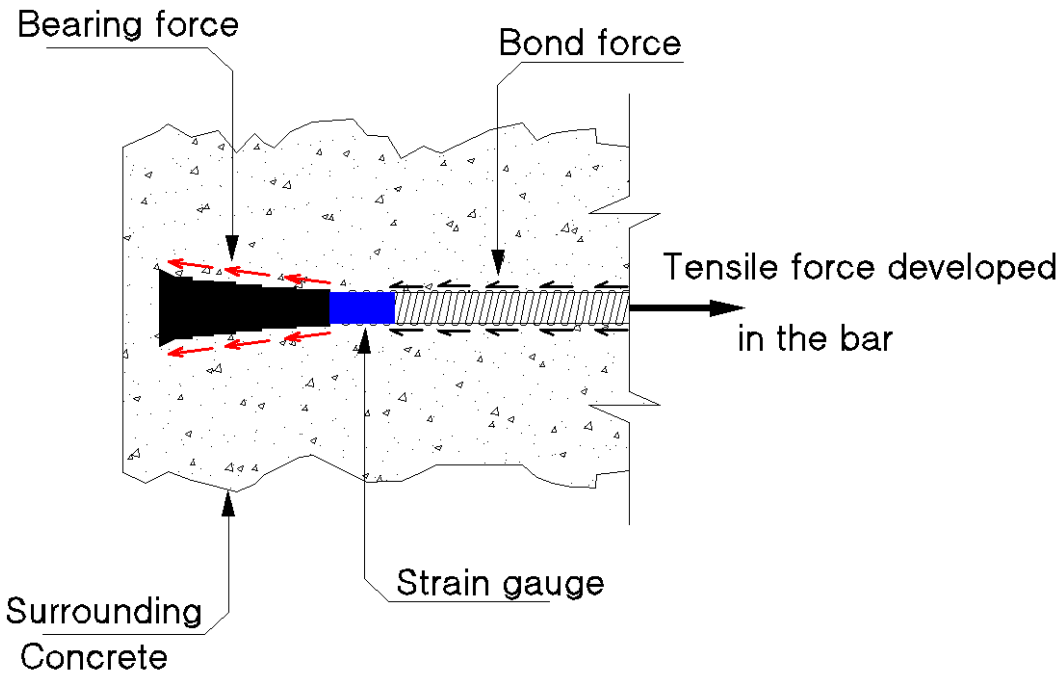

Figure 6.24: bearing resistance of beam longitudinal headed reinforcement

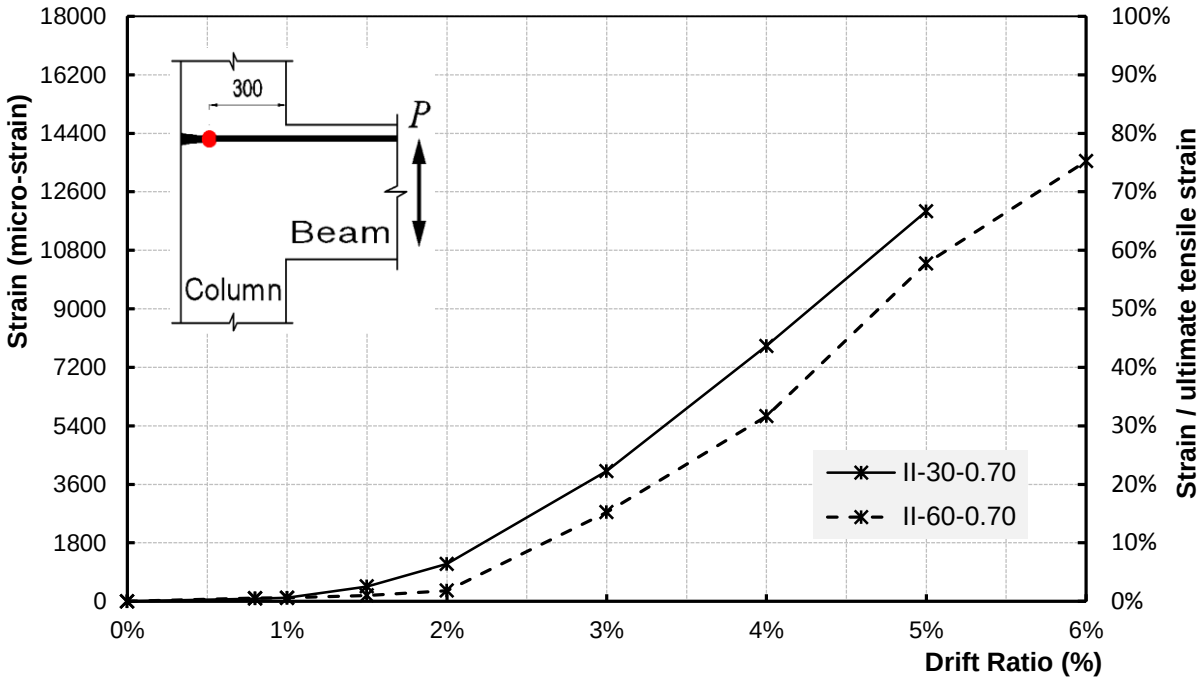

Figure 6.25: Bearing contribution of beam longitudinal headed bars in specimens II-30-0.70 and II-60-0.70

It is worth mentioning that during testing of Series (II) specimens, two modes of failure in the anchorage heads were observed as shown in Figures 6.26 and 6.27. The first mode of failure occurred due to the failure in the interface between the bar and the head due to shearing-off of the bar ribs in contact with the head, as shown in Figure 6.26 (a). Once the interface between the bar and the head failed, a sudden pullout of the bar through the concrete core of the joint occurred. This mechanism was resisted solely by the mechanical bond between the deformed surface of the bar and the concrete which in turn caused some damage to the deformed ribs along the bar surface as shown in Figure 6.26 (b). The second mode of failure occurred due to splitting of the anchorage head bearing base (i.e. end part of the largest diameter) as shown in Figure 6.27.

It should be noted that the observed modes of failure in the anchorage heads were influenced by the shear stress in the joint. In Specimens II-30-0.70 and II-60-0.70 where the joints were subjected to low shear stress ($0.70\sqrt{f'_c}$) and experienced elastic behaviour with no damage until the end of the test, the intact surrounding concrete confined the head to act integrally as one unit. While in those specimens exhibited shear diagonal failure in the joint, the surrounding cracked concrete did not provide enough confinement to the whole head to act as one unit; instead, it created a slight space around the head which resulted in concentration of bearing stresses on the head base (with the largest diameter) resulting in splitting of base as shown in Figure 6.27. After losing the head base, the anchorage of the bar was developed by a wedging mechanism resulted from the remaining conical-shaped part of the head.

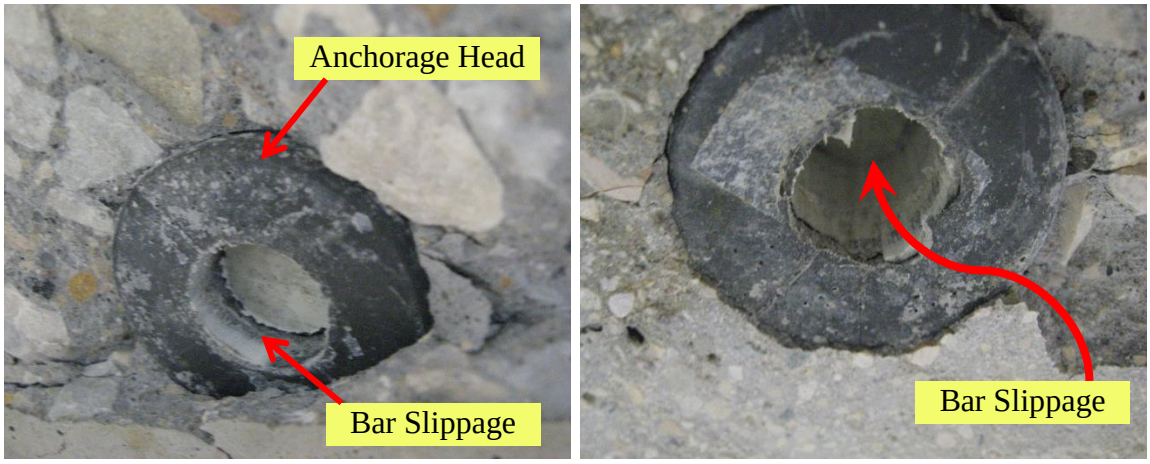

(a) Failure in the contact surface between the bar and the head

Figure 6.26: Failure of end-bearing heads in Specimens II-30-0.70 and II-60-0.70

(continued)

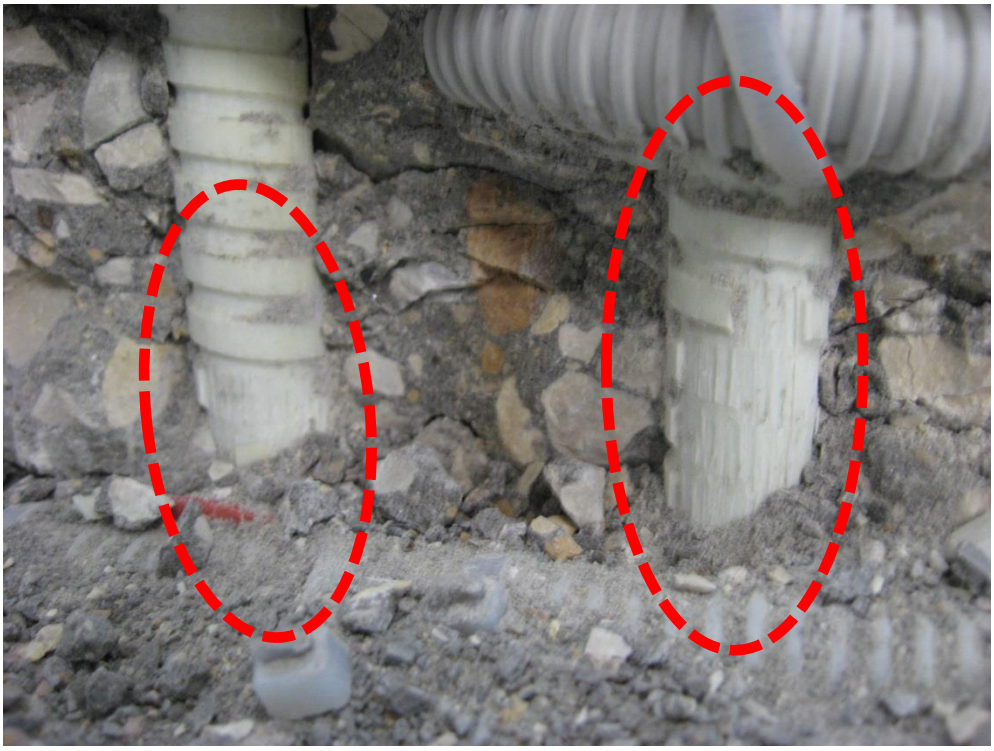

(b) Shear-off in bar ribs

Figure 6.26: Failure of end-bearing heads in Specimens II-30-0.70 and II-60-0.70

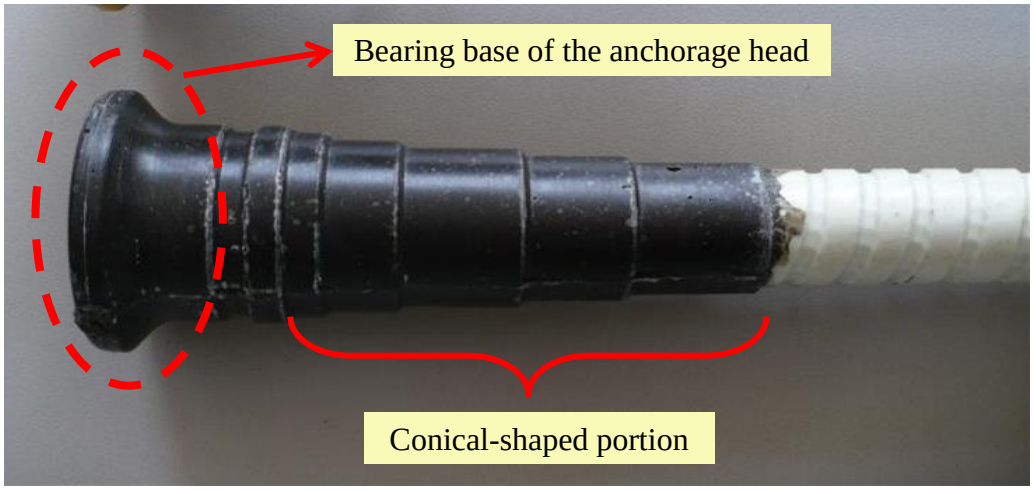

(a) Anchorage head

Figure 6.27: Failure end-bearing heads in Specimens II-30-0.85, II-30-1.0, II-60-0.85, and II-60-1.0 (continued)

(b) Loss of head base

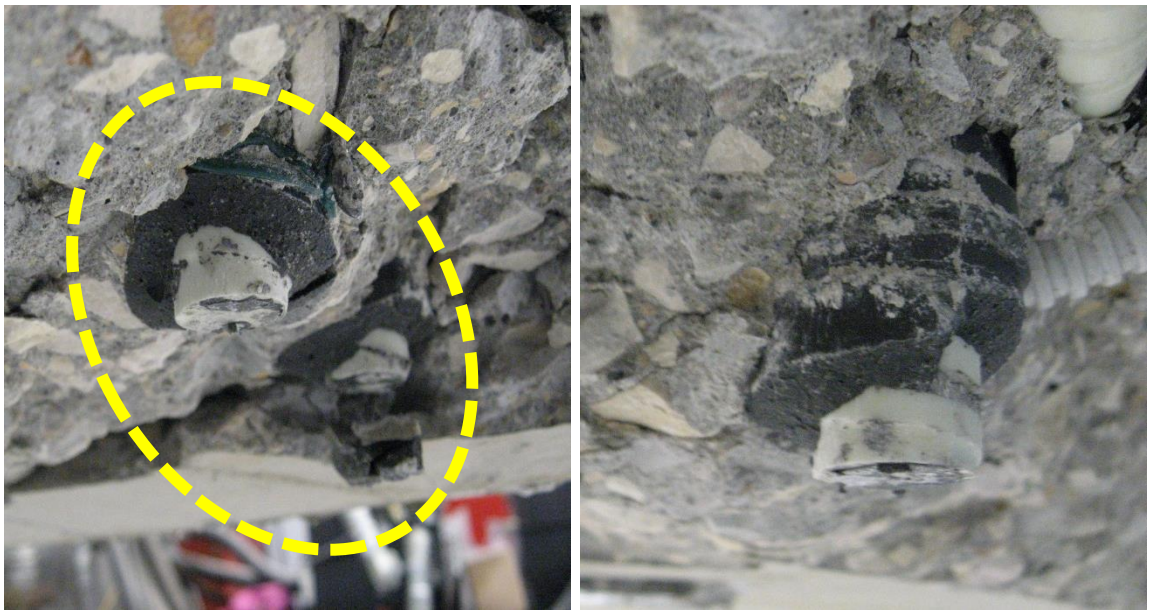

(c) Remaining part of the head attached to the bar inside the joint core

Figure 6.27: Failure end-bearing heads in Specimens II-30-0.85, II-30-1.0, II-60-0.85, and II-60-1.0

6.9 INFLUENCE OF SHEAR STRESS IN THE JOINT ON THE OVERALL BEHAVIOUR

Three different shear stress levels were tested in Series (II) specimens; $0.70\sqrt{f'_c}$, $0.85\sqrt{f'_c}$, and $1.0\sqrt{f'_c}$. In the light of the observations and results of testing Series (II) specimens, the influence of the shear stress in the joint can be summarized as follows:

1) Although Specimens II-30-1.0 and II-60-1.0 showed the highest lateral resistance compared with their counterparts with lower shear stress level in the joint, the high shear stress in the joint in these two specimens accelerated the degradation in the lateral resistance capacity and consequently the failure of the specimens as shown previously in the hysteretic behaviour figures.

2) High shear stress in the joints of Specimens II-30-1.0 and II-60-1.0 prevented both specimens to achieve the calculated lateral capacity as shown previously in Table 6.1 and to maintain their maximum lateral resistance during the successive loading drift.

3) The low shear stress in the joints exhibited by Specimens II-30-0.70 and II-60-0.70 limited the cracks and non-linear deformations in the joint which helped the joint stay in the elastic range. This in turn is reflected on maintaining the axial capacity of the column. On the contrary, the high shear stress in the joint increased the intensity and the width of the cracks in the joint which increased the permanent deformation in the concrete core of the joint.

4) Each two specimens subjected to the same level of shear stress in the joint exhibited the same level of strain in joint stirrups at the end of the test although that they did not fail at similar drift ratio.

5) Specimens II-30-1.0 and II-60-1.0 subjected to the highest shear stress in the joint exhibited the maximum values of tensile strain in the joint stirrups which exceeded the allowable strain limits in the stirrups set by the CSA/S806-02 and the CSA/S806-12.

6) Although Specimens II-30-1.0 and II-60-1.0 exhibited the highest stiffness in the early stages of loading, high shear stress in the joint accelerated the stiffness degradation of the specimens to the point that they exhibited lower stiffness at the end of the test compared to their counterparts with lower shear stress in the joint as shown previously in Figure 6.20.

7) High shear stress in the joints significantly increased the distortion of the joint which resulted in at least one third of the specimen drift angle was attributed to distortion occurred in the joint as shown in Figure 6.23.

8) The shear stress in the joint influenced the anchorage performance of the beam longitudinal GFRP headed bars embedded into the joint. The shear stress influenced the cracking pattern and the non-linear deformation in the concrete core of the joint which in turn influenced the anchorage capacity and performance of the headed bars embedded in the joint as shown previously in Figures 6.26 and 6.27.

6.10 EVALUATION OF THE STRUCTURAL BEHAVIOUR BASED ON THE ACI 374.1-05

6.10.1 Acceptance Criteria for Moment Frames Based on Structural Testing and Commentary ACI 374.1-05

The objective of the ACI 374.1-05 Standard (*ACI* 2005) is to define the minimum experimental evidence that shall be provided in order to validate the use of steel-RC moment resisting frames not satisfying the seismic provisions and requirements of Chapter 21 of ACI 318-99 (ACI 1999) for structures in regions of high seismic risk. For regions of moderate seismic risk or for structures assigned to satisfy intermediate seismic performance, less stringent provisions than those specified by this standard are appropriate. Although the ACI 374.1-05 was originally published to evaluate the structural behaviour of steel-RC frames; in the absence of such standards relevant to the FRP-RC frames, it is thought useful to use the ACI 374.1-05 as a guideline to evaluate the structural behaviour of the GFRP-RC test specimens in this program. The evaluation criteria set by the ACI 374.1-05 will be explained and discussed in order to evolve evaluation criteria that can be applied on the FRP-RC moment resisting frames and in the meantime consistent with the Canadian standards. Subsequently, the evolved evaluation criteria will be applied to each of Series (II) specimens.

6.10.2 ACI 374.1-05 Evaluation Criteria

1) Design Procedure: The ACI 374.1-05 requires that a design procedure shall have been developed for prototype frames having the generic form for which acceptance is sought and that design procedure shall be used to proportion the test modules. Regarding Series

(II) specimens reinforced with GFRP bars and stirrups, the design procedure was proposed in Chapter 3 and the design calculation of the specimens are provided in Appendix A.

2) Adequate Large Scale: The ACI 374.1-05 requires that test specimens shall have a scale large enough to represent fully the complexities and behavior of the real materials and of the load transfer mechanisms in the prototype frame. Test prototypes shall have a scale not less than one-third full size. The minimum extent of the isolated specimens shall be the distance between the contra-flexure points nearest to that joint for both beams and columns for linear elastic lateral load response of the generic moment frame. For all specimens in this experimental program, all the GFRP-RC specimens were full scale specimens.

3) Structural Integrity: The ACI 374.1-05 requires that the test results shall demonstrate the ability of the frame to retain its structural integrity and support its specified gravity loads through peak displacements equal to or exceeding storey drift ratios of 3.5%.

For the response of a structure regarding the design of seismic shear force, building codes normally specify a maximum allowable inter-storey drift. Structures which were designed to meet that drift limit, however, may experience greater drifts during an earthquake equal to the design basis earthquake. Actual drifts depend on the strength of the structure, its initial elastic stiffness, and the ductility expected for the given lateral load resisting system. Specification of suitable limiting drifts for the test modules requires

interpretation and allowance for uncertainties in the assumed ground motions and structural properties.

The rationale to set the 3.5% drift ratio as a key value in the evaluation criteria of the ACI 374.1-05 is explained in this part. In the International Building Code 2000 (*IBC*, 2000), which was available at the time when the ACI 374.1-05 was prepared, the design seismic shear force applied at the base of a building is inversely related to a response modification factor (*R*). This (*R*) factor increases in higher ductility lateral force resisting systems. To maintain the integrity of a structure that responds inelastically, the inter-storey drifts should be limited to certain values depending on hazard posed by the building and the building height.

As per the IBC-2000, for moment resisting frames which are part of a building representing a substantial hazard to human life in the event of a failure, the allowable story drift ratio is 2.0% for frames of four stories or less in height and 1.5% for frames greater than four stories in height. If the building failure does not pose a substantial hazard to human life, the corresponding drift ratios are 2.5% and 2.0%, respectively.

To compensate for the use of the (*R*) value, the IBC 2000 requires that when the design storey drift is calculated using a linear dynamic analysis, the calculated drift should be multiplied by a deflection amplification factor (C_d). That amplified design storey drift must be less than the allowable story drift set by the code. For example, in monolithic frames satisfying the requirements of 21.1 through 21.5 of ACI 318-99, C_d is assigned a

value of 5.5. However, research studies (*Uang and Maarouf*, 1993) have found that the amplified design storey drift may be too low. Alternatively, drift ratios of 8 times the IBC-calculated values (rather than 5.5) are more representative to the upper bounds of the expected drift ratios. The value of 8/5.5 times the IBC 2000 allowable drift limits results in new values on real drift ratios of 2.2% to 3.6%. Therefore, a value of 3.5% drift ratio was chosen by the ACI 374.1-05 as a conservative limit to be satisfied by the test modules. This key value of 3.5% drift ratio was adopted based on an outdated standard (IBC 2000). Therefore, another value can be calculated using the same procedure, however; in conformance with the current International Building Code 2012 (*IBC* 2012) and the current National Building code of Canada (*NBC* 2010).

The International Building Code 2012 (*IBC* 2012) requires that structures shall be designed according to the ASCE/SEI 7-10 Standard "Minimum design loads for buildings and other structures" (*ASCE 7*, 2010). The ASCE/SEI 7-10 is more stringent than the IBC 2000; it limits the storey drift ratio to 2.0%, and 1.5% in buildings of 4 stories or less categorized as Risk Category III, and IV, respectively. For buildings higher than 4 stories, the limit is 1.5%, and 1.0%, respectively. Buildings in Risk Category III are those structures which their failure could pose a substantial risk to human life with potential to cause a substantial economic impact and/or mass disruption of day-to-day civilian life in the event of failure; while Risk Category IV is for Buildings and other structures designated as essential facilities. R and C_d factors for Special reinforced concrete moment frames are 8 and 5.5, respectively, as per Table 12.2-1 in the ASCE/SEI 7-10. Therefore the modified key drift ratios that can be used to evaluate the test results

are 2.9 % and 2.2% not considering the importance factor. A value of 3.0% drift ratio can be then adopted to conform to the current American standards.

Regarding the National Building Code of Canada (NBC 2010), it requires that the largest inter-storey drift at any level not to exceed 1.0% for post-disaster buildings, and 2.0% for High Importance Category buildings as per Clause 4.1.8.13. The same clause requires that the calculated lateral deflection of the structure using a linear elastic analysis method shall be multiplied by $R_d\ R_o/\ I_E$; where R_d , R_o , and I_E are the ductility-related force modification factor, over-strength-related force modification factor, and earthquake importance factor, respectively. R_d and R_o factors can be obtained from Table 4.1.8.9 in the NBC 2010 based on the construction material and relevant code of design, and the Seismic Force Resisting System (SFRS) selected to resist the seismic forces. FRP-RC seismic force resisting systems designed according to the CSA/S806-12 are not addressed in Table 4.1.8.9 in the NBC 2010 because of the lack of research and experimental data in this field. Therefore, the CSA/S806-12 in Clauses 12.4.2.4 and 12.4.2.5 requires that R_d and R_o shall be taken equal to 1.0. Alternatively, the key value of the drift ratio required to evaluate the behaviour of the specimens can be adopted from the CSA/S806-12, Clause 12.7.5.2, which requires that the amount of transverse FRP-reinforcement in SFRS columns shall be calculated in accordance with Clauses 12.7.3.3 and 12.7.3.4 using a design drift ratio equal to 4.0% for frames subjected to high seismic actions. Accordingly, a 4.0% drift ratio (Δ) will be considered the drift level at which acceptance is sought in the evaluation of the structural behaviour of the test specimens.

4) Relative energy dissipation ratio (β): The ACI 374.1-05 requires that for cyclic loading at the given drift level at which acceptance is sought, but not less than a drift ratio of 3.5%, the relative energy dissipation ratio (β) calculated from the measured results of the third cycle between the limiting acceptance drift ratios must equal or exceed 0.125. The relative energy dissipation ratio (β) is the ratio of actual to ideal energy dissipated by test specimen during reversed cyclic loading between given drift ratio limits. The relative energy dissipation ratio concept is similar to the equivalent viscous damping concept used by Clauses 13.3.3.1 and 13.9.5.2 in the NEHRP Provisions (*NEHRP*, 1997-a) and the Commentary (*NEHRP*, 1997-b) for design and evaluation of seismically isolated structures. It can be expressed as the ratio of the area of the hysteresis loop for that cycle to the area of the circumscribing parallelograms defined by the initial stiffness during the first cycle and the peak resistance during the cycle for which the relative energy dissipation ratio is calculated as shown in Figure 6.28.

The relative energy dissipation ratio concept illustrated in Figure 6.28 is for the third cycle for the key drift ratio (Δ). As shown in the figure, the relative energy dissipation ratio (β) is equal to the ratio between the hatched cycle and the circumscribing area (A B δ_1 C D δ_2). The circumscribing area (A B δ_1 C D δ_2) consists of two parallelograms, A B δ_1 δ_2 and δ_2 δ_1 C D. The east and west sides of the parallelogram A B δ_1 δ_2 are sloped equal to the initial stiffness (K) of the first loading cycle in the positive lateral direction; the height of the side AB from the drift axes (datum) represents the peak lateral load (L_1) resisted in the positive loading direction for this cycle. Similarly, the boundaries of the

parallelogram δ_2 δ_1 C D are determined taking into consideration that the peak lateral load and the initial stiffness are different in the negative loading direction. The total area of the two parallelograms equals to $(L_1 + L_2)*(\delta_1 + \delta_2)$.

It is worth mentioning that, in a building frame as compared to a test specimen, damping is generally also provided by column hinging at the base of the frame in addition to the beam hinging. Hence, the relative energy dissipation ratios for SRFS frames will probably be greater than the values established from the test specimens. Moreover, typical relative energy dissipation ratios at 3.0% drift ratio have been reported to be 30, 17, and 10% for reinforced concrete, hybrid reinforced/pre-stressed concrete, (*Cheok et al.*, 1996), and pre-stressed concrete modules (*Stanton and Mole*, 1994; *Priestley and Tao*, 1993), respectively.

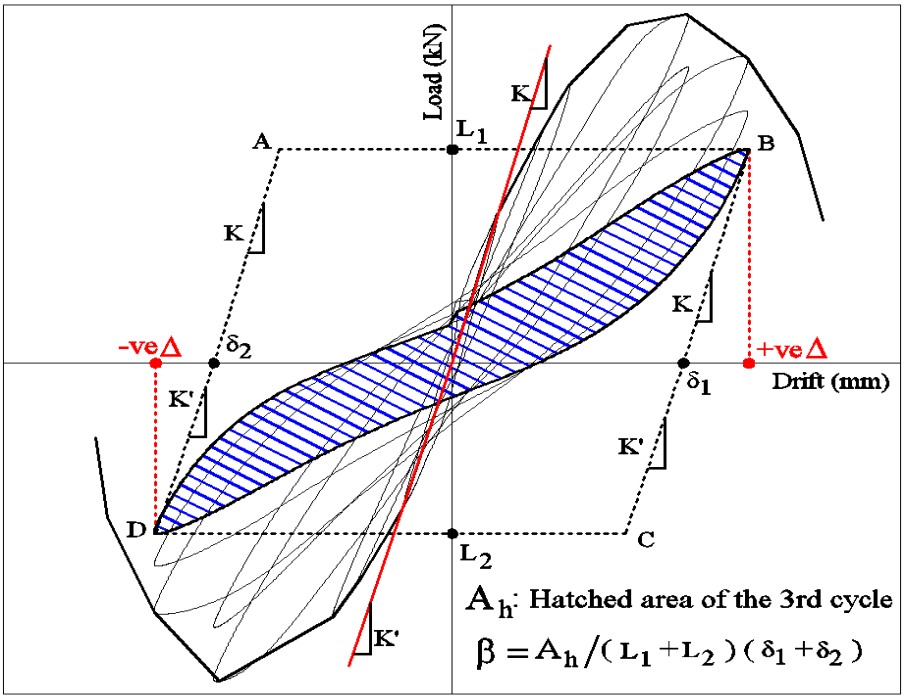

Figure 6.28: Calculation of the relative energy dissipation ratio (β)

5) Adequate Initial Stiffness: To ensure that test specimens have adequate initial stiffness, they shall have attained a lateral resistance equal to (L_n) before its drift ratio exceeds a value of (Δ_C) as shown in Figure 6.29.

Where L_n : is the nominal lateral resistance of test specimen determined using specified geometric properties of test members, specified reinforcement strength, specified compressive strength of concrete, a strain compatibility analysis for flexural moment strength, and a strength/material reduction factor (ϕ) of 1.0; and

Δ_C : is a limiting initial drift ratio consistent with the allowable storey drift limitation of the relevant building code (Δ_a); it equals to Δ_a / ϕ C_d.

To apply this condition using the NBC 2010, the allowable story drift limitation (Δ_a) is equal to 2.0% (for High-Importance Category buildings), the deflection amplification factor (C_d) will be replaced by R_d R_o/ I_E where R_d = R_o = 1.0 and I_E = 1.3, and ϕ = 0.75 for FRP reinforcement as per the CSA/S806-12, Clause 7.1.6.3. Accordingly, Δ_C will be equal to 2.0% / (0.75/1.3) = 3.5%. Of course this value (3.5%) of Δ_C is not realistic since it exceeds the NBC 2010 drift ratio limit (2.0%). This is attributed to using R_d = R_o = 1.0 as a result of that the ductility and over-strength characteristics of the FRP-RC SFRS have not yet been demonstrated due to lack of research and experimental data in this field. Therefore, in the light of the previous explanation and available limited knowledge, the limiting initial drift ratio (Δ_C) will be taken equal to 2.0%; however, more research is still required to set a more reliable value for this condition.

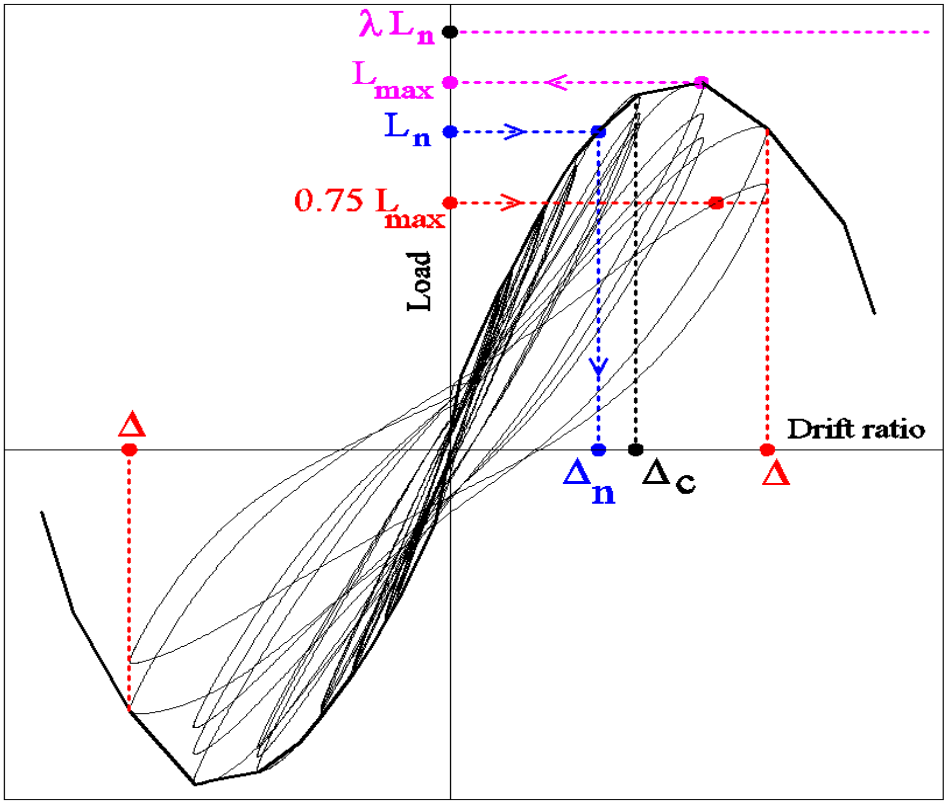

Figure 6.29: Schematic drawing for key values used in the evaluation criteria

6) Flexural Strength Ratio (λ): It also requires that those frames satisfy the strong column-weak beam action by having a flexural strength ratio (λ) [also known as column over strength factor] of at least 1.2 as required by the ACI 318-99. All of Series (II) specimens were designed so that the lowest flexural strength ratio was 1.42 as shown in Table 4.4, Chapter 4. The Seismic provisions of the CSA/S806-12, Clause 12.7.5, require that "*The sum of the factored flexural resistances of the column sections framing into a joint, accounting for axial loads, shall exceed the sum of the nominal flexural resistances of the beams framing into the same joint*". This means that the flexural strength ratio (λ) should exceed 1.0. To provide strong column-weak beam mechanism, the maximum

lateral resistance (L_n) recorded in the test shall have not exceeded ($\lambda\ L_n$), where λ is the specified over-strength factor for the test column as shown in Figure 6.29.

In light of the experimental results, it is sought that in the design of FRP-RC frames a stringent value higher than 1.0 should be used for the flexural strength ratio to achieve the strong column-weak beam action. The discussion of this recommendation is discussed later in Chapter 9.

7) Strength Degradation: this condition was set to limit the strength degradation at high drift ratios after reaching the maximum capacity (L_{max}). It requires that the peak force for a given loading direction shall have been not less than 0.75 L_{max} for the same loading direction at the drift level at which acceptance is sought (Δ), but not less than a drift ratio of 3.5%, as shown in Figure 6.29. In this study, the drift level at which acceptance is sought; (Δ) is equal to 4.0%. When strengths differ for opposite loading directions, this requirement applies independently to each direction.

8) Secant Stiffness: For cyclic loading at the drift level at which acceptance is sought, but not less than a drift ratio of 3.5%, the secant stiffness from a drift ratio of –0.35% to a drift ratio of +0.35% shall have been not less than 0.05 times the stiffness for the initial drift ratio (K) defined previously in item 5. In this study, the drift level at which acceptance is sought; (Δ) is equal to 4.0%.

6.10.3 Application of the ACI 374.1-05 Evaluation Criteria on the Test Specimens

In this section the evaluation criteria, evolved in the previous section, are applied to the six specimens of Series (II). Regarding the design procedure condition, all specimens satisfied this condition and indeed were designed according to an established design criterion as discussed before in Chapter 3. Also the specimens satisfied the adequate scale conditions as they were constructed as full scale specimens.

1) Relative energy dissipation ratio (β):

Table 6.3 shows the structural evaluation of each specimen in Series (II) with respect to the evaluation criteria discussed before. Regarding the relative energy dissipation ratio (β), the table shows that specimens II-30-xx satisfied this condition and exceeded the accepted value of 0.125 while specimens II-60-xx could not pass this value; however, they exhibited values (0.108, 0.109, 0.111) which are very close to 0.125 and the difference was insignificant. The reason for low values of relative energy dissipation ratio (β) exhibited by specimens II-60-xx is attributed to the way the inelastic deformability hinges in the beam form, as discussed before in Section 6.3. Specimens with high concrete strength tend to form the V-notch hinges with minimal concrete crushing contrary to specimens II-30-xx with low concrete strength where the flat surface hinges form with significant crushing of concrete in the vicinity of the inelastic deformability hinge. It is observed that Specimens II-30-1.0 and II-60-1.0 which were subjected to high shear stress in the joint dissipated the highest level of energy in their concrete category. This is attributed to the excessive non-linear deformation and crushing of concrete in the joint not to the formation of inelastic deformability hinges in the beams.

Moreover, it should be noted that the calculated values for the relative energy dissipation ratio (β) exhibited by Series (II) GFRP-RC specimens are in agreement with the pre-stressed concrete modules reported by Stanton and Mole (1994), and Priestley and Tao (1993). Accordingly, it can be concluded that the behaviour of the specimens with respect to the dissipation of energy is more or less satisfactory; however, steel-RC structures outperform the GFRP-RC structures by approximately 2 to 3 times.

In general, to maintain high levels of energy dissipation while benefiting from the non-corrodible nature of GFRP reinforcement, and overcome the corrosion problem of steel reinforcement, a viable solution to this issue can be the use of hybrid seismic resistant systems. In hybrid seismic resistant systems, steel RC shear walls can provide lateral load resistance and absorb the seismic energy while using GFRP-RC moment resisting frames as the main structural system to support gravity loads. The presence of steel RC shear walls does not eliminate the need of the adjoining GFRP-RC frame members to share part of the seismic loads and lateral drifts through their seismically-induced deformations. Accordingly, GFRP-RC moment resisting frames should be properly designed and detailed to resist seismic forces.

Table 6.3: Evaluation of the structural behaviour of Series (II) specimens

	Evaluation Criteria						
Specimen	Relative Energy Dissipation Ratio (β) at 4.0% drift ratio	Adequate Initial Stiffness at 2.0% drift ratio	Flexural Strength Ratio (λ)		Strength Degradation before 4.0% drift ratio	Secant Stiffness / Initial Stiffness (K)	
			Design	Experimental		+ve Loading	-ve Loading
II-30-0.70	0.134 > 0.125	Only achieved 68% L_n	1.73	1.73	Did not occur in both loading direction	0.43	0.41
II-30-0.85	0.137 > 0.125	Only achieved 71% L_n	1.56	1.46	Did not occur in both loading direction	0.46	0.43
II-30-1.0	0.228 > 0.125	Only achieved 75% L_n	1.40	1.44	Did not occur in both loading direction	0.30	0.3
II-60-0.70	0.108 < 0.125	Only achieved 60% L_n	1.78	1.78	Did not occur in both loading direction	0.5	0.5
II-60-0.85	0.109 < 0.125	Only achieved 60% L_n	1.64	1.46	Did not occur in both loading direction	0.52	0.53
II-60-1.0	0.111 < 0.125	Only achieved 62% L_n	1.45	1.51	Did not occur in both loading direction	0.55	0.53

2) Adequate initial stiffness:

For the requirement of adequate Initial Stiffness at 2.0% drift ratio, Table 6.3 shows that the specimens did not achieve the nominal capacity (L_n) before or at the 2.0% drift ratio and only achieved a range of 60% to 75% of (L_n). Apparently, the specimens did not satisfy this condition; however, a careful analysis to the maximum strain–drift ratio relationship for beam longitudinal reinforcement at the column face, Figure 6.12, shows that the specimens exhibited a strain range of approximately 6500 to 8500 micro-strain. These values of strains reflect a stress range of 400 to 527 MPa which is the same stress range that steel RC specimens would reach to achieve the nominal capacity and would have been considered satisfactory specimens. However, the issue here is that the tensile strength of GFRP reinforcement is 2 to 3 time higher than steel reinforcement. Accordingly, GFRP-RC sections have greater flexural capacity when compared to their counterparts reinforced with the similar reinforcement ratio of steel reinforcement. Therefore, the GFRP-RC specimens have reserved capacities after reaching 2.0% drift ratio, which enable them to resist seismic forces linearly with no strength degradation while increasing the loading drifts. This is attributed to the linear-elastic behaviour of the GFRP reinforcement until failure.

In light of these results, when moment resisting frames are the main SFRS, it is recommended to calculate the nominal flexural capacity of the GFRP-RC beam sections at a stress level in the GFRP longitudinal bars does not exceed 500 MPa. This recommendation is to ensure that the section will attain this capacity at or prior reaching the drift ratio limit set by the relevant code.

3) Flexural Strength Ratio (λ):

Table 6.3 shows the design and the experimental flexural strength ratio for each specimen. Specimens II-30-0.85 and II-60-0.85 which achieved higher flexural capacity in the beam showed lower experimental flexural strength ratio than the design value; contrary to specimens II-30-1.0 and II-60-1.0. Taking into consideration that none of the specimens exhibited flexural failure in the column, it is recommended to use the lowest value of the flexural strength ratios *(λ)* (i.e. 1.4), shown in Table 6.3, as a satisfactory conservative level in the design. When more research is done, a lower value may be considered then.

4) Strength Degradation:

Table 6.3 shows that all specimens did not show any strength degradation before the 4.0% drift ratio. This is attributed to the linear behaviour until failure of the GFRP reinforcement. The lateral resistance of the specimens increased with the increase of the loading drifts up to 5.0% drift ratio.

5) Secant Stiffness:

Table 6.3 shows that all specimens satisfied this condition where they showed stiffness near the zero loads that is greater than 0.05 times the initial stiffness (K) of each specimen. This is attributed to the elastic behaviour of the GFRP reinforcement, through which the specimens showed elastic behaviour with insignificant permanent deformation.

CHAPTER 7

NUMERICAL MODELLING

7.1 GENERAL

Limited number of parametric studies (*Sritharan et al.* 2000, *Sritharan* 1998, *Rashid et al.* 2000, *Li* 2003) has been carried out on steel RC beam-column joints using commercial software packages such as ABAQUS (*Hibbitt et al.*, Inc.), ANACAP (*ANATECH Research Corp.*), and ATENA-3D (*Cervenka and Niewald* 2005). These studies investigated the performance of beam-column joints reinforced with steel reinforcement. However, to investigate the essential requirements for modelling reinforced concrete structural elements with the aforementioned software packages, studies of other structural elements, such as slabs, columns, bridge girders and shear walls are indeed helpful to be considered and reviewed (*Hassan et al.* 2000, *James et al.* 2001, *Li et al.* 2005, *El-Ragaby et al.* 2005, *Seliem et al.* 2006, *Xu et al.* 2007). There was a good agreement between all these studies to use the same material library and elements for both reinforcement (steel or FRP) and concrete.

The analytical part of this study consists of two stages. The objective of the first stage is to build non-linear finite element models (FEM) that reasonably predict the behaviour of real structural elements. ATENA-3D finite element software package (Version 4.3.1) was used to build the finite element models. The finite element analysis considered both geometrical and material non-linearity. In this regards, the results obtained from the finite element analysis are verified against the results of experimental testing of full scale

beam-column joint specimens. The second stage aimed to use the verified models to conduct a parametric study on the different parameters known to affect the beam-column joints. In the following sections, detailed information about the selected materials, elements, as well as the suggested methods for connecting the reinforcement and concrete elements are discussed. However, details about ATENA-3D finite element characteristics can be found in theory and user manual of the program (*Cervenka and Niewald* 2005, *Cervenka* et al. 2012).

7.2 ATENA-3D FINITE ELEMENT MODEL

7.2.1 Concrete Material

An eight-node, 3-D solid, brick element "CCIsoBrick", is used for the three-dimensional modeling of concrete. The concrete material was modeled using the Fracture-Plastic Constitutive Model (CC3D Non-Linear Cementitious 2). It combines constitutive models for tensile (fracture) and compressive (plastic) behavior of concrete. The fracture model is based on the classical orthotropic smeared crack formulation and crack band model where the Rankine failure criterion is used for concrete cracking, exponential tensile softening, and can be used as rotated or fixed crack model. The hardening/softening plasticity model under compressive stresses is based on Menetrey-Willam failure surface (Menetrey et al. 1997). This model can be used to simulate concrete cracking and crushing under high confinement, and crack closure due to crushing in other material directions.

The Menetrey-Willam failure surface adopts the uniaxial compressive concrete test based on the experimental work of Van Mier (1986) where, in the concrete stress-strain relationship, the softening curve is linear and the elliptical ascending part as shown in Figure 7.1 and given by the following equations:

$$\sigma = f_{co} + (f_c - f_{co})\sqrt{1 - [(\varepsilon_c - \varepsilon_{eq}{}^{p})/\varepsilon_c]^2} \qquad [7.1]$$

Where $f_{co} = 2f'_t$; [7.2]

$$\varepsilon_c^p = f'_c / E \ ; \qquad [7.3]$$

$$W_d = (\varepsilon_{eq}{}^{p} - \varepsilon_c{}^{p})\, L_C \qquad [7.4]$$

Where f_{co} is the starting point of the non-linear curve, ε_c^p is the value of plastic strain at the max compressive strength, on the descending curve, shown in Figure 7.1, the equivalent plastic strain (ε_{eq}^p) is transformed into displacements through the length scale parameter (L_C).

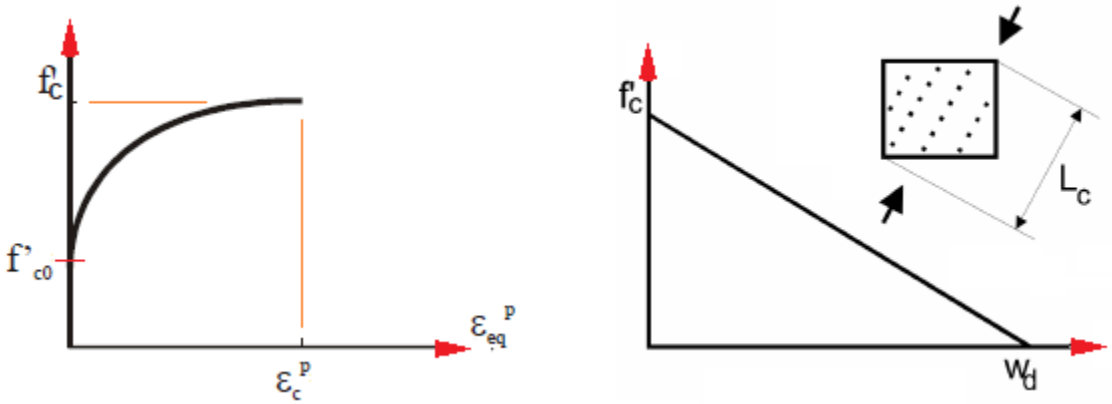

(a) Non-linear ascending part (b) Linear descending part

Figure 7.1: Van Mier compressive stress-strain relationship of concrete

It should be noted that there are additional interactions between the plasticity and fracture models that is considered by the software to properly describe the behaviour of the concrete material;

- The tensile strength of the concrete decreases after the concrete crushes;
- The compressive strength also decreases when cracking occurs in the perpendicular direction (strength-softening effect) as explained by Vechio and Collins (1986) in the compression field theory. The strength-softening of the concrete is addressed in ATENA-3D by the coefficient ($r_{c,lim}$) which was taken in this study equal to 0.9;
- The shear strength of a cracked concrete is calculated using the Modified Compression Field Theory of Vechio and Collins (1986);
- The effect of tension stiffening where cracks cannot fully develop along the section is also accounted for (i.e. contribution of cracked concrete to the tensile stiffness of reinforcing bars). Tension stiffening is simulated by specifying a factor that represents the relative limiting value of tensile contribution as a fraction of the tensile capacity of the concrete. This factor was taken in all specimens of this study equal to 0.4.

The default formulas for calculating the concrete parameters are listed in Table 7.1.

Table 7.1: Concrete characteristics as calculated by ATENA-3D

Parameter	Formula
Cylinder strength (f'_c)	$f'_c = 0.85\, f'_{cu}$
Tensile strength (f'_t)	$f'_t = 0.24\, (f'_{cu})^{2/3}$
Initial elastic modulus (E)	$E = (6000 - 15.5\, f'_{cu})\, \sqrt{f'_{cu}}$
Fracture energy (G_f)	$G_f = 0.000025\ f'_t$

Where f'_{cu} : Cube concrete strength

7.2.2 Reinforcement Materials

In ATENA-3D, the reinforcement can be modeled in two different forms: discrete and smeared. The discrete reinforcement is in the form of individual reinforcing bars which is modeled by finite truss elements. When the analysis starts, the program automatically decomposes each reinforcement bar into individual truss finite elements embedded into the generated mesh of the concrete solid elements. In this way, the bar stiffness will be included into the numerical analysis. On the other hand, the smeared reinforcement is a component of composite material and can be considered either as a single (only one-constituent) material in the element under consideration or as one of such constituents. This can be done by reinforcing a macro-element in certain directions with a specific reinforcement ratio that represents actual uniform distribution of the reinforcement in the cross section. In this study, the discrete model of reinforcement was used for longitudinal and transverse reinforcement.

The stress-strain relationship of the reinforcement materials can be in the form of either bi-linear elastic-perfectly plastic or 4-segment multi-linear. Cyclic reinforcement model is also available for use in RC elements under cyclic loading as will be discussed later.

7.2.2.1 *Steel reinforcement stress-strain relationship*

Steel reinforcement was modeled using the non-linear model established by Menegotto and Pinto (1973) for steel reinforcement subjected to cyclic-reversed loading as shown in Figure 7.2. The basic characteristics of the reinforcement were determined using a multi-linear form with yield strength of 460 MPa and an ultimate strength of 615 MPa at a strain value of 5.0%. The Elastic modulus of steel reinforcement was taken equal to 200 GPa.

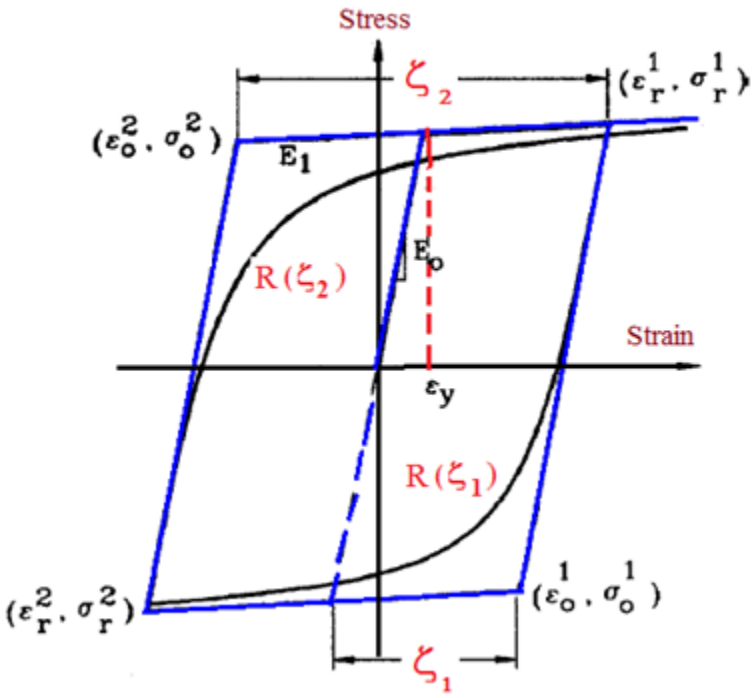

Figure 7.2: Cycling reinforcement model (Reproduced from *Menegotto and Pinto*, 1973)

7.2.2.2 *GFRP reinforcement stress-strain relationship*

It is well established that the GFRP reinforcement has elastic-linear behaviour up to failure. Consequently, the GFRP reinforcement was modeled with a linear behaviour up

to an ultimate tensile stress of 1100 MPa at an ultimate tensile strain of 1.833 % as shown in Figure 7.3.

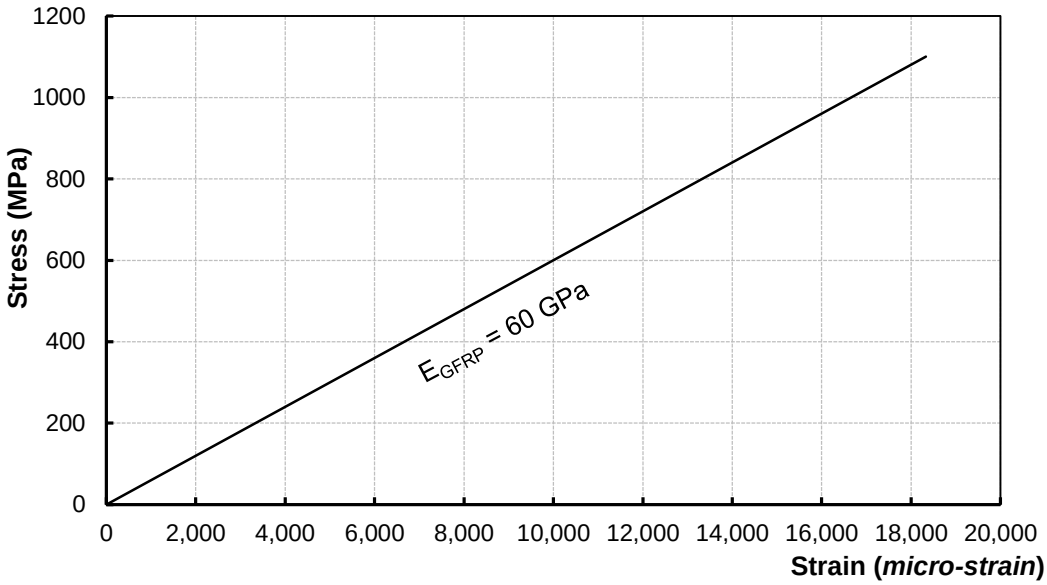

Figure 7.3: Stress-strain relationship of GFRP longitudinal reinforcement

7.2.3 Reinforcement Bond Models (Concrete-Reinforcement Interaction)

It is well established that concrete-reinforcement bond interaction plays an important role in the strength and structural integrity of the RC frames subjected to seismic loads. All current reinforced concrete design codes set minimum requirements to avoid slippage of reinforcement. In finite element modeling, it can be either assume full contact between the reinforcement and the concrete (perfect bond) or define a bond-slip relationship between the reinforcement and the surrounding concrete. The perfect-bond assumption seems to be unrealistic in case of RC elements subjected to seismic load where concrete deformations and cracks allow for partial/full slippage of reinforcing bars. In ATENA-3D both ways are implemented and available to use; however, in this study a bond-slip

relationship was used to better simulate the actual behaviour of the elements. Bond models for the used steel and GFRP reinforcement are discussed in the following sections.

7.2.3.1 *Steel reinforcement bond-slip relationship*

In ATENA-3D, two predefined bond-slip models for steel reinforcement are incorporated in the program; the CEB-FIB model code 1990 (Comité Euro-International du Béton, 1993) and Bigaj model (Bigaj, 1999). In addition to that, there is an option to input a general user-defined bond-slip model. In this study, the bond-slip relationship given by the CEB-FIB model code 1990 was used. The generated bond-slip relationship is influenced by the concrete compressive strength, reinforcement type, confinement conditions, and the quality of the surrounding concrete. The bond-slip relationship of the CEB-FIB model code 1990 is given by Equations 7.5 to 7.8 and shown in Figure 7.4.

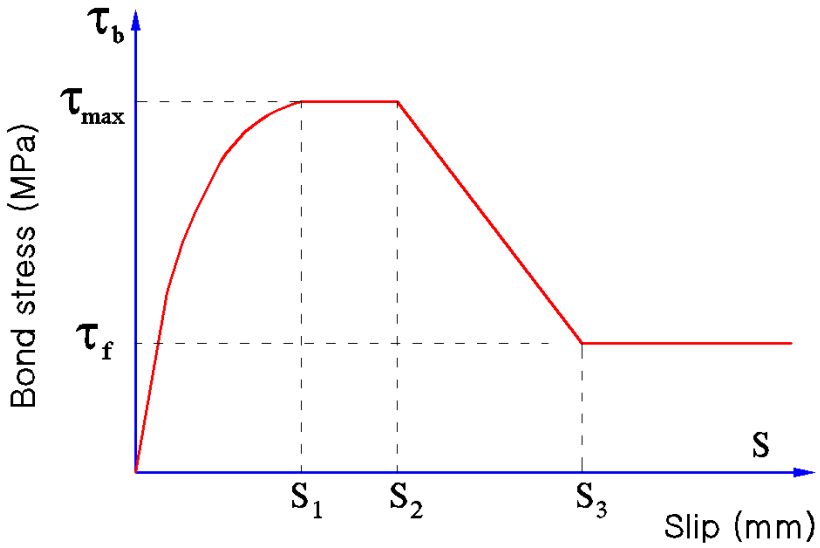

Figure 7.4: Bond-slip relationship as given in the CEB-FIB model code 1990 (Reproduced)

$$\tau_b = \tau_{max} \left(\frac{S}{S_1}\right)^{\alpha} \quad ; \ 0 \leq S \leq S_1 \qquad [7.5]$$

$$\tau_b = \tau_{max} \quad ; \ S_1 \leq S \leq S_2 \qquad [7.6]$$

$$\tau_b = \tau_{max} - \left(\tau_{max} - \tau_f\right) \left(\frac{S - S_2}{S_3 - S_2}\right) \quad ; \ S_2 \leq S \leq S_3 \qquad [7.7]$$

$$\tau_b = \tau_f \quad ; \ S > S_3 \qquad [7.8]$$

For ribbed bars embedded in good confined concrete where the bond failure is exhibited by shearing of the concrete between the ribs, values of the above mentioned parameters defining the bond-slip relationship are given in Table 7.2.

Table 7.2: definition of the parameters used in CEB-FIB 1990 bond-slip relationship

Parameter	S_1	S_2	S_3	α	τ_{max}	τ_f
Value	1.0 mm	3.0 mm	Clear rib spacing (8.0 mm)	0.4	$2.5\sqrt{f_c'}$	0.4 τ_{max}

7.2.3.2 *GFRP reinforcement bond-slip relationship*

The bond-slip relationship of the GFRP ribbed reinforcement is shown in Figure 7.5 as given by the manufacturer for concrete strength of 50 MPa. The bond-slip relationship was implemented in the program using the general user-defined bond-slip model.

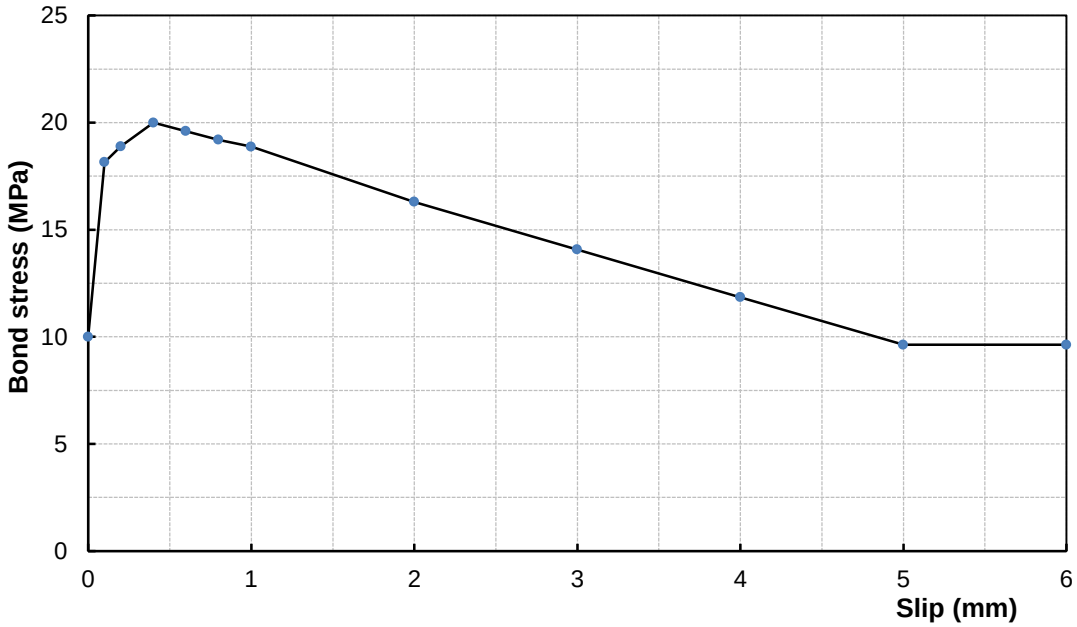

Figure 7.5: Bond-slip relationship for the GFRP ribbed longitudinal reinforcement

7.2.4 Loading and Bearing Plates

50-mm thick steel plates were used at the lines of load applications and at supports to avoid concentration of stresses on the concrete at those points since this may cause premature failure or cracking in those locations. In real cases, it is noted that the concentration of stresses rarely occurs as the supports or loads are usually applied over a certain area and never at single points. The steel plates were modeled using 3D solid elements with the 3D Elastic Isotropic material. The parameters of this material were defined with an elastic modulus of 200 GPa, Poisson's ratio of 0.3, and no yielding strength to avoid any premature failure in the steel plates.

7.2.5 Geometry and Boundary Conditions

All test specimens were modelled in ATENA-3D using the same full-scale concrete dimensions explained before in the Chapter 4 "Experimental Program" as shown in Figure 7.6. All models were created to have the beam and column lengths in X-Z plane; the width of the specimen is extended in the Y-direction. To simulate the boundary conditions of the test specimens during the experimental testing, column ends were restrained against the movement in the Z-direction to simulate roller supports at both ends, as shown in Figure 7.6, while the right support is restrained against the movement in the X-direction along the middle height of the column. In all specimens investigated in this study, the concrete macro-elements were meshed into finite elements each has a cubic shape (i.e. aspect ratio of an element equal to 1.0) with side length of 50 mm.

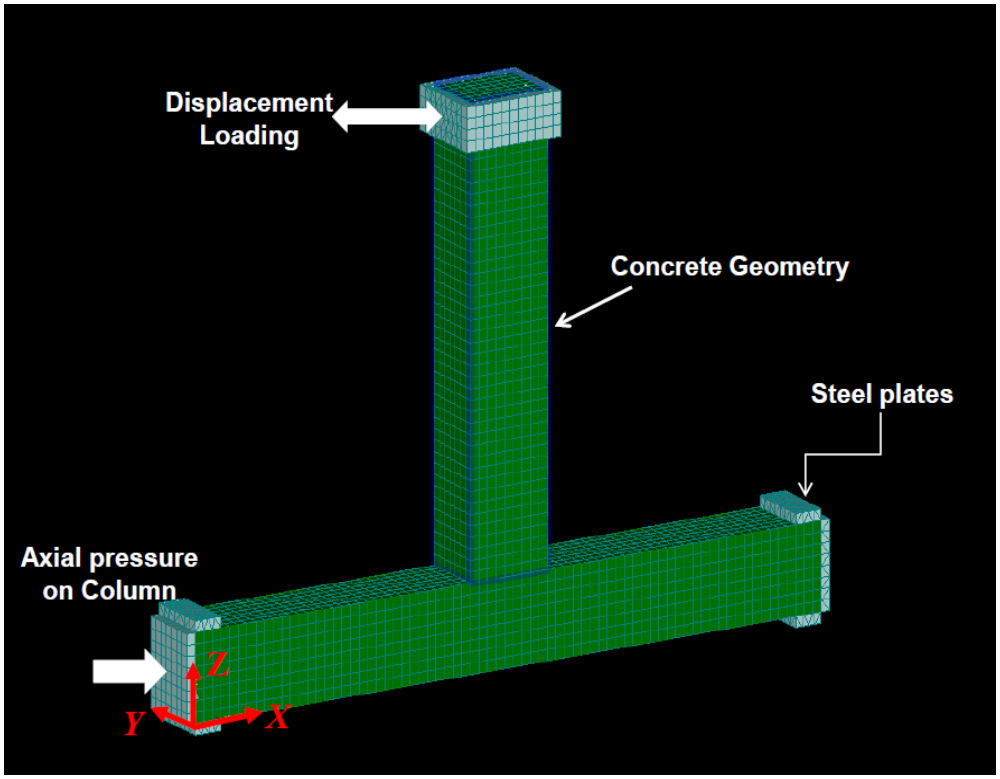

(a) Geometric model

Figure 7.6: Geometric model of beam-column joints test specimens (continued)

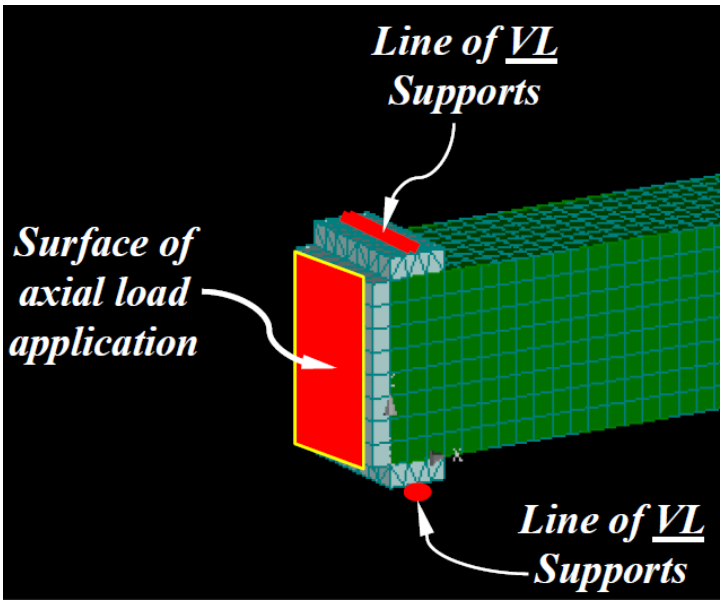

(b) Left support

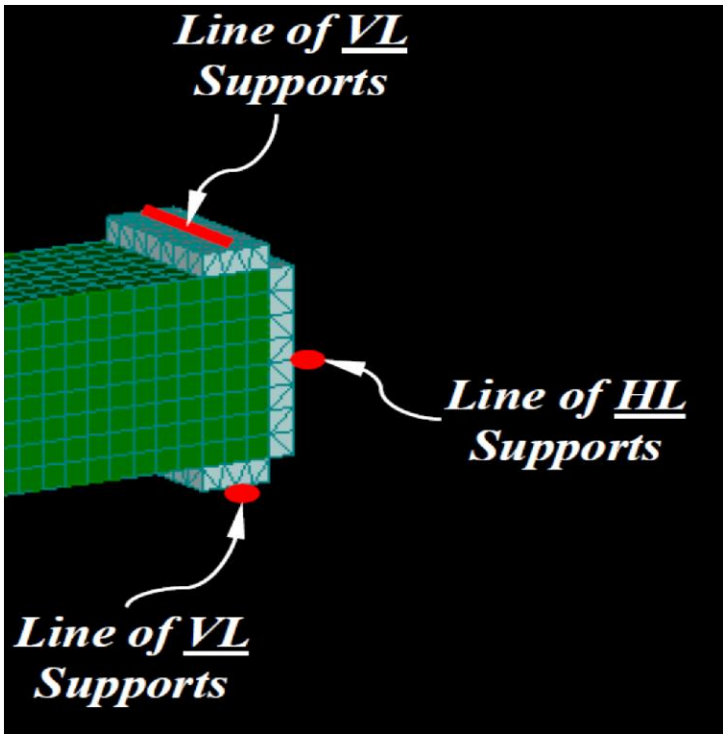

(c) Right support

Figure 7.6: Geometric model of beam-column joints test specimens

7.2.6 ATENA-3D Non-Linear Solution Parameters

ATENA-3D has the option to perform a geometric non-linear solution for the model using the concept of incremental step-by-step analysis. In this study, the axial load on the column was applied in a load-controlled mode divided into a series of 10 increments (steps) each is 10% of the assigned applied load. Then after, the lateral drift loading was applied in a displacement-controlled mode where the beam tip was programed to reach the assigned displacements in successive increments each is equal to 1.0 mm until it reaches the required displacement in each loading direction. For example, to apply the 0.8% loading drift (18.0 mm), the model was programed for the beam tip to move in the positive X-direction a series of 18 steps, each is 1.0 mm, then move back 18 steps to reach the zero displacement then continue to move 18 steps in negative X-direction then move back another 18 steps to complete a full cycle of 72 steps.

At each loading step, load iterations are performed until the convergence criteria are satisfied. After reaching the equilibrium and completion of each loading step, the stiffness matrix of the model is adjusted to reflect the non-linear changes in structural stiffness before proceeding to the next load step. In this regards, ATENA-3D adopts two methods of numerical solution, Full Newton-Raphson Method and the Arc-Length Method, with the ability to modify the solution parameters in each method. In this study, the Full Newton-Raphson Method showed faster convergence with numerical results, which were in good agreement with the experimental ones.

As mentioned before that, in nonlinear analysis, it is necessary to iterate until some convergence criterion is satisfied. There are four convergence criteria supported in ATENA-3D. The first one checks the norm of deformation changes during the last iteration whereas the second one checks the norm of the out-of-balance forces. The third one checks out-of-balance energy and the fourth checks the out-of-balanced forces in terms of maximum components. The values of the convergence limits are set by default to 0.01 or can be changed by the user (*Cervenka* et al. 2012). In this study, the default convergence limits were found satisfactory. It should be noted that the solving time for running each model was approximately between 80 and 140 hours subject to the drift ratio that each model can withstand.

7.3 FINITE ELEMENT MODEL VERIFICATION

In this section, the outputs of the finite element models were verified against the experimental results. Six specimens were selected for the verification process including two steel RC specimens (SS03-B06-J06 and S0) from two previous studies (*Mady* 2011 and *Hasaballa* 2009) and four GFRP-RC specimens from Series (II) specimens (II-30-0.75, II-30-1.0, II-60-0.75, and II-60-1.0). These specimens were selected to show the validity of the FE model for modelling both steel and GFRP-reinforced joints. Since the shear stress level in the joint is one of the main parameters in this study, it deemed necessary to validate the numerical results against the experimental ones of two steel RC specimens subjected to different shear stress in the joint and had different modes of failure. The comparison was performed with respect to the hysteretic behaviour and the strain values in the longitudinal reinforcement of the beam.

7.3.1 Specimen SS03-B06-J06

The concrete geometry, steel reinforcement details of this specimen are shown in Figure 7.7; further details about this specimen were reported by Mady (2011). The specimen had a column length and a beam length similar to those of Series (I) and Series (II) specimens in this research study; the only difference in the geometry is the column cross section as shown in Figure 7.7. It should be noted that the specimen exhibited formation of inelastic deformability hinge in the beam while the shear stress in the joint was $0.69\sqrt{f'_c}$ (3.94 MPa).

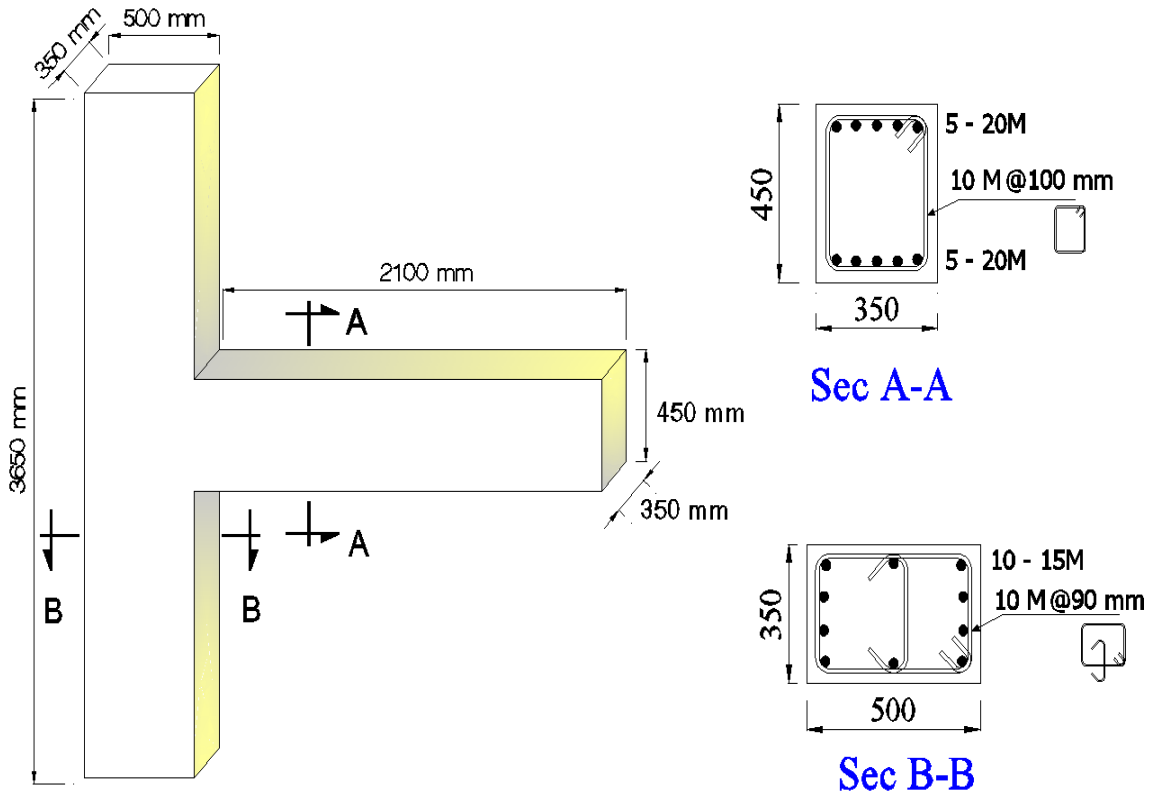

(a) Concrete dimensions and reinforcement details

Figure 7.7: Geometric and reinforcement configuration of Specimen SS03-B06-J06 with steel reinforcement (continued)

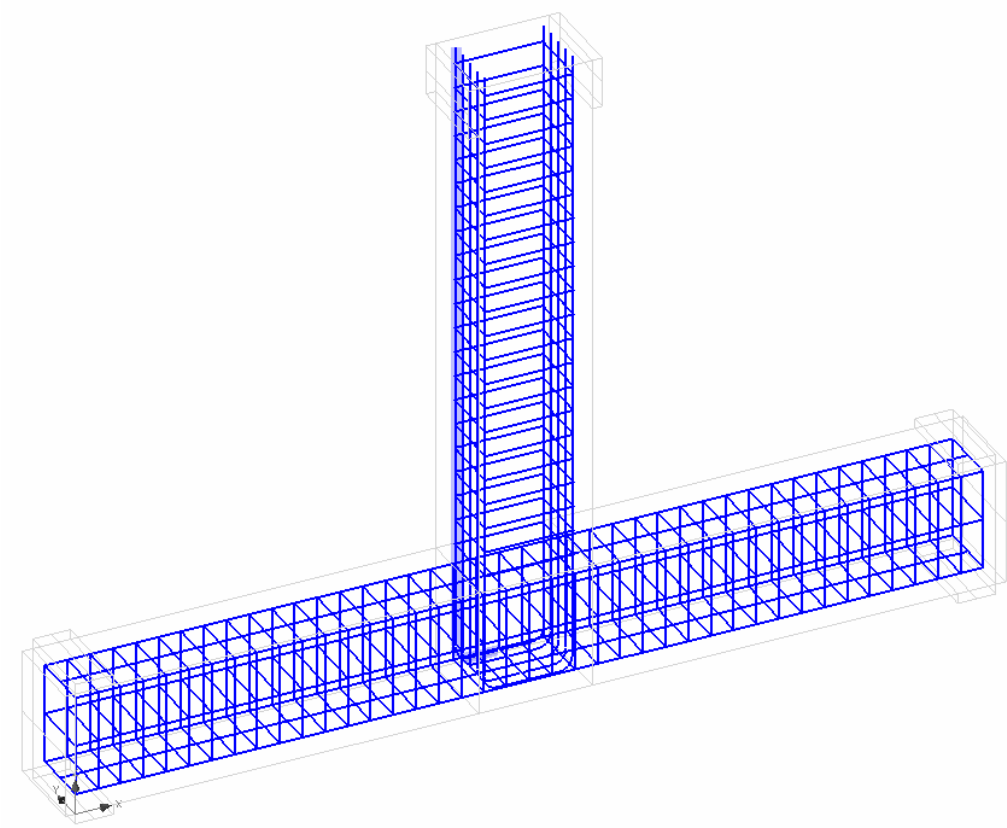

(b) Reinforcement of specimen modeled in ATENA-3D

Figure 7.7: Geometric and reinforcement configuration of Specimen SS03-B06-J06 with steel reinforcement

Figure 7.8 shows the experimental and analytical hysteretic behaviour of Specimen SS03-B06-J06. The finite element model showed a good agreement with the experimental hysteretic behaviour. A similar trend for the fat-hysteretic/cyclic behaviour for the steel reinforced specimen is also shown in the figure; however, pinching distance of the hysteretic loop is larger in the model results than in the experimental results. This is attributed to the buckling of steel reinforcement near the zero load values; this can be shown in Figure 7.8 near the horizontal axis where the experimental loop significantly changes its slope (stiffness) due to buckling of steel reinforcement in the plastic hinge

region. In the meantime, buckling of steel reinforcement under compression cannot be simulated in the finite element model.

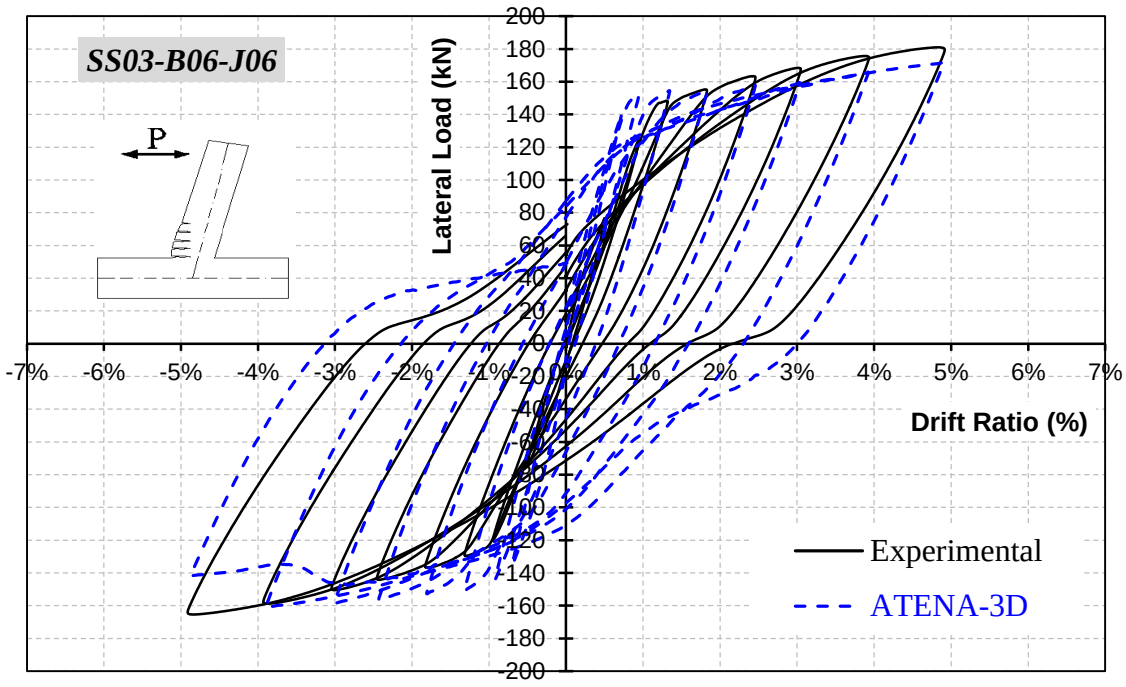

Figure 7.8: Experimental hysteretic behaviour against the analytical one of Specimen SS03-B06-J06

Figure 7.9 shows the envelope diagrams of the hysteretic behaviour of the experimental as well as the analytical results. In general, the figure shows a good agreement between the analytical and the experimental results, where the difference in load values did not exceed 10% except in the first two cycles of loading. It is clear that the stiffness of the modelled specimen in the first two loading drifts is higher than the experimental one. This is attributed to characteristic of the concrete stress-strain relationship adopted by the ATENA-3D and used in this model which assumes higher elastic modulus of the concrete before cracking.

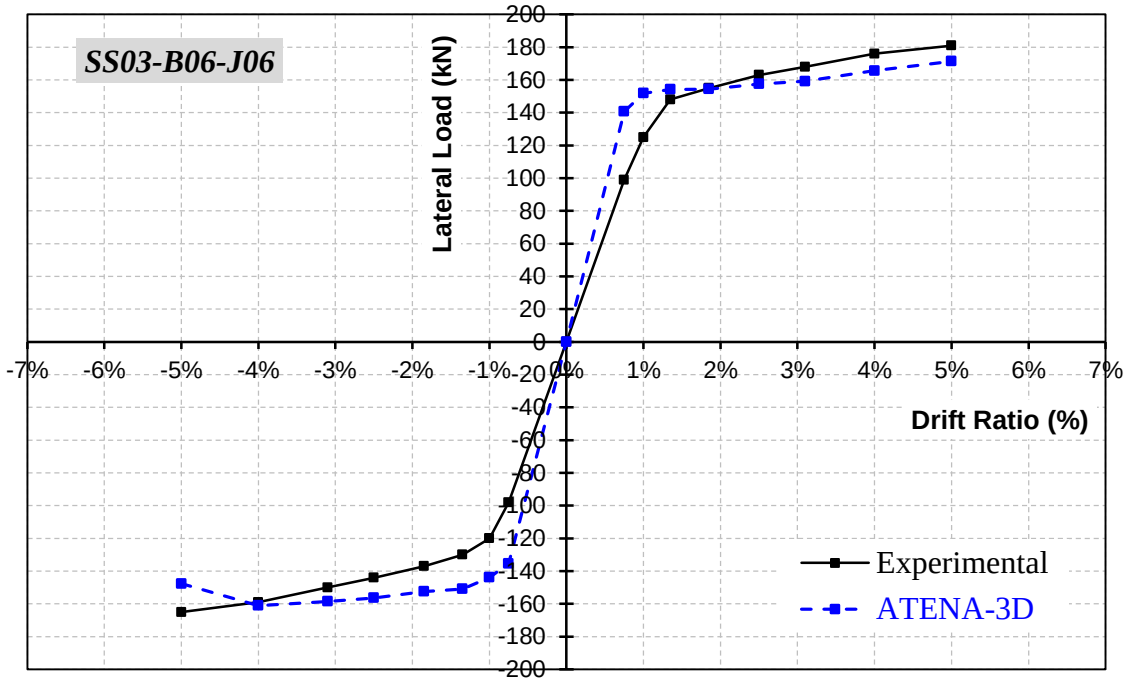

Figure 7.9: Envelopes of hysteretic behaviour for Specimen SS03-B06-J06

7.3.2 Specimen S0

The second specimen in the verification process is the steel reinforced concrete Specimen S0 which was experimentally tested by Hasaballa (2009). Figure 7.10 shows the geometry and reinforcement details of the specimen. The specimen had a column length and a beam length similar to those of Series (I) and Series (II) specimens in this research study; except that column in Specimen S0 has a smaller depth (350 mm) as shown in Figure 7.10. Experimental test results for that specimen showed that the specimen exhibited a diagonal shear failure in the joint after reaching 4.0% drift ratio where the shear stress in the joint was $1.0\sqrt{f'_c}$ (5.63 MPa).

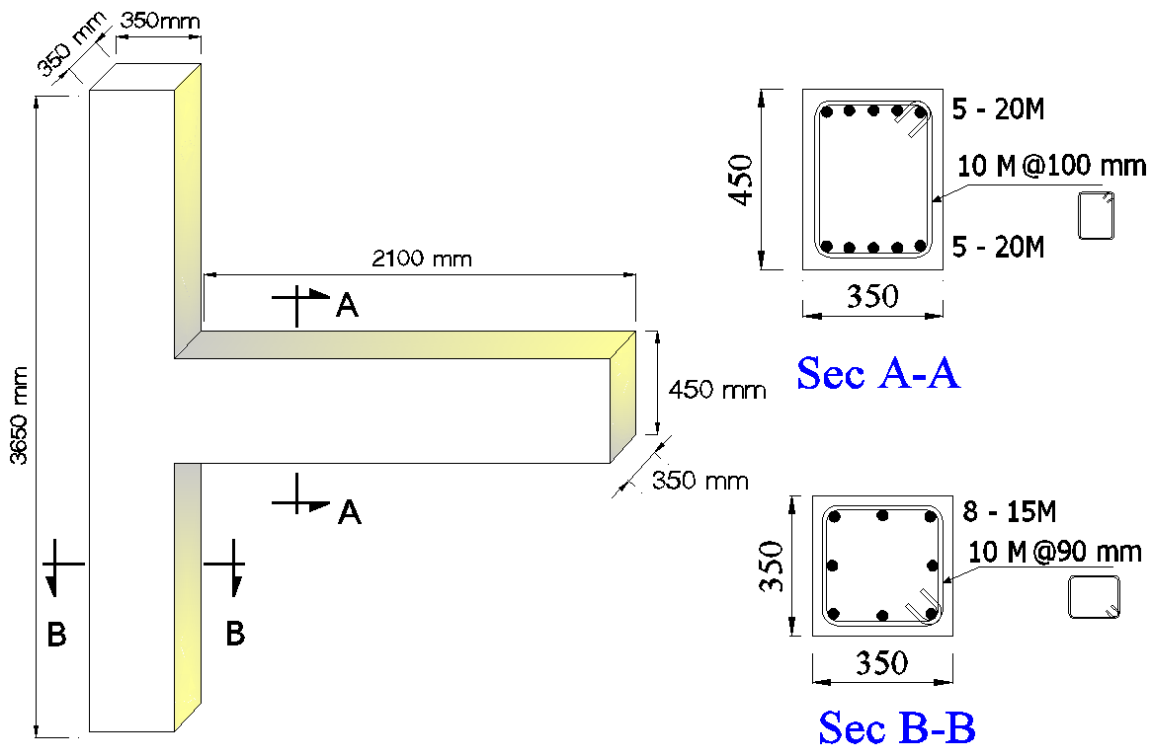

Figure 7.10: Concrete dimensions and reinforcement details of Specimen S0

Figure 7.11 shows the experimental hysteretic behaviour of Specimen S0 against the analytical one. The finite element model showed a good agreement with the experimental hysteretic behaviour. A similar trend for the fat-hysteretic/cyclic behaviour for the steel reinforced specimen is also shown in the figure. Again, the pinching distance of the hysteretic loop in the finite element model is larger than in the experimental which is attributed to the fact that the finite element model cannot simulate buckling of reinforcement as discussed earlier.

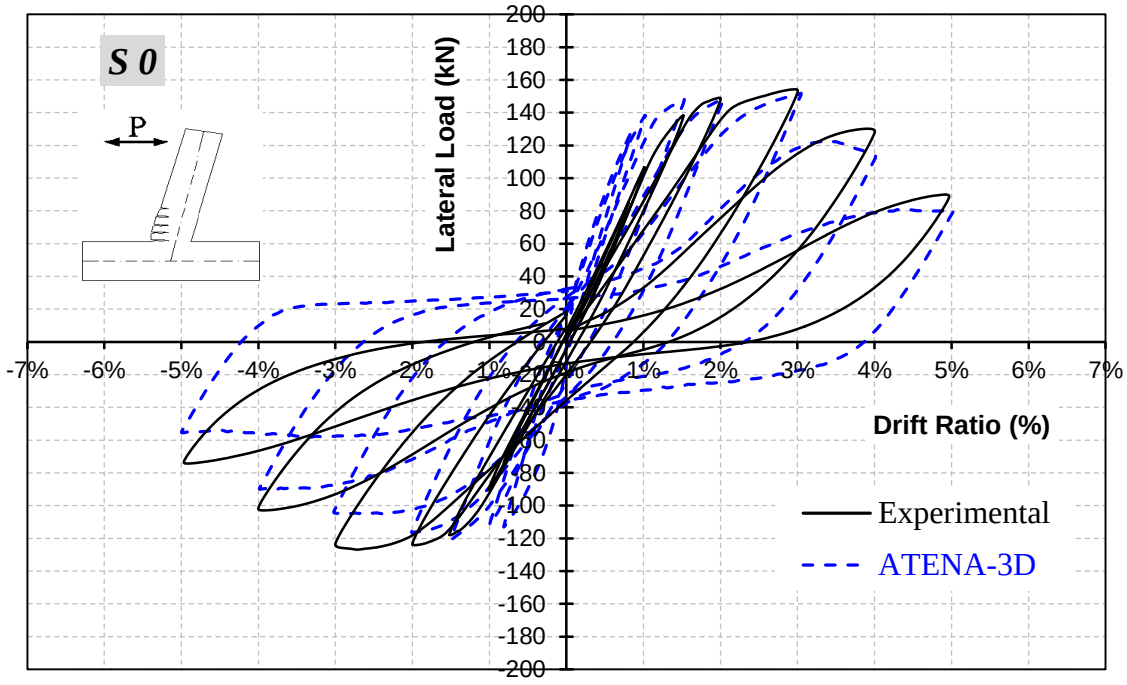

Figure 7.11: Experimental hysteretic behaviour against the analytical one of Specimen S0

Figure 7.12 shows the envelope diagrams of the hysteretic behaviours of the experimental as well as the analytical results. In general, the figure shows good agreement between the analytical and the experimental results, where the difference in load values did not exceed 10% except in the first two cycles of loading. It is clear that the stiffness of the modelled specimen in the first two loading drifts is higher than the experimental one. This is attributed to characteristic of the concrete stress-strain relationship adopted by the ATENA-3D and used in this model which assumes higher elastic modulus of the concrete before cracking.

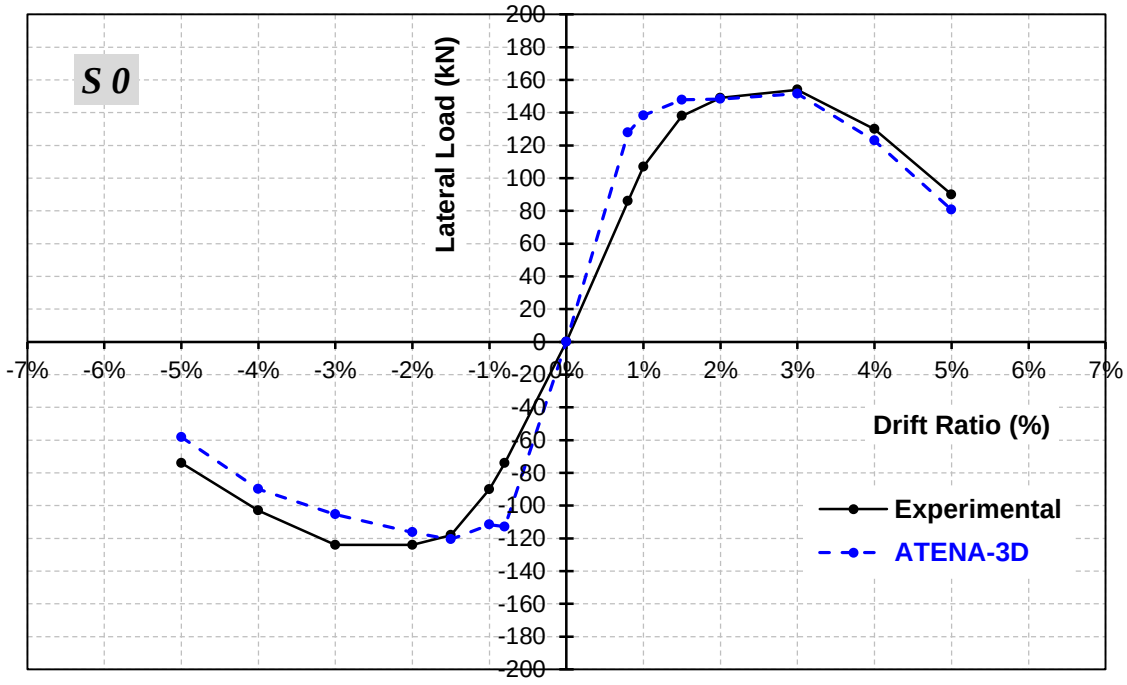

Figure 7.12: Envelopes of hysteretic behaviour for Specimen S0

7.3.3 Series (II) Specimens (II-30-0.70, II-30-1.0, II-60-0.70, and II-60-1.0)

This section presents the verification of the finite element modeling results of four specimens from Series (II), namely II-30-0.70, II-30-1.0, II-60-0.70, and II-60-1.0, against the experimental results presented previously in Chapter 6. Concrete dimensions and reinforcement details of those specimens are presented in Chapter 4. These specimens were selected for the verification process because they represent the upper and lower bounds of the concrete strength and shear stress levels in the joint investigated in this study. The results of these analytical models were compared in terms of the cracking pattern, the hysteric behaviours and their envelope, and the developed strains in the beam longitudinal reinforcement. Figure 7.13 shows the concrete stress in the Z-Z direction. Concrete stresses developed in the beam section at the column face were in agreement with the compression strength of the concrete in each specimen. The figure also shows

the cracking pattern of each specimen, where also a good agreement is observed with the experimental cracking pattern discussed before in Chapter 6.

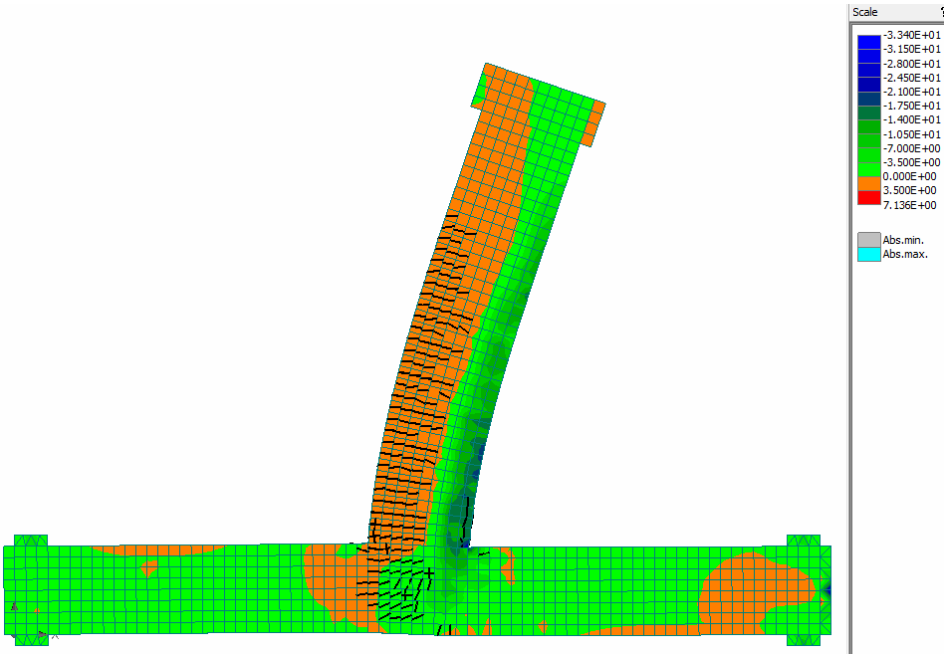

(a) II-30-0.70 at 5.0% drift ratio

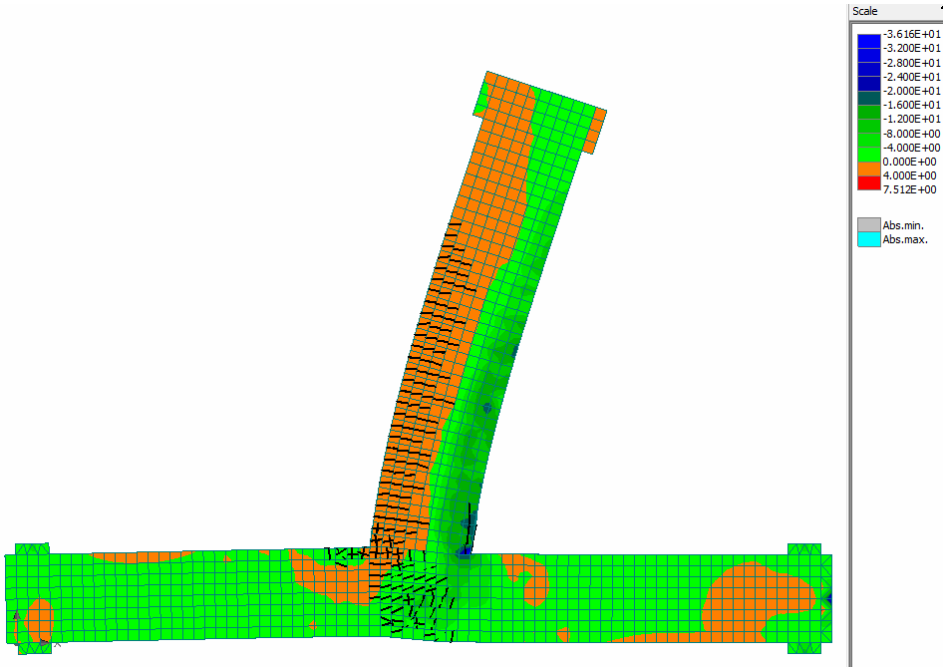

(b) II-30-1.0 at 5.0% drift ratio

Figure 7.13: Concrete stresses in the Z-Z direction and cracking pattern on deformed specimens (continued)

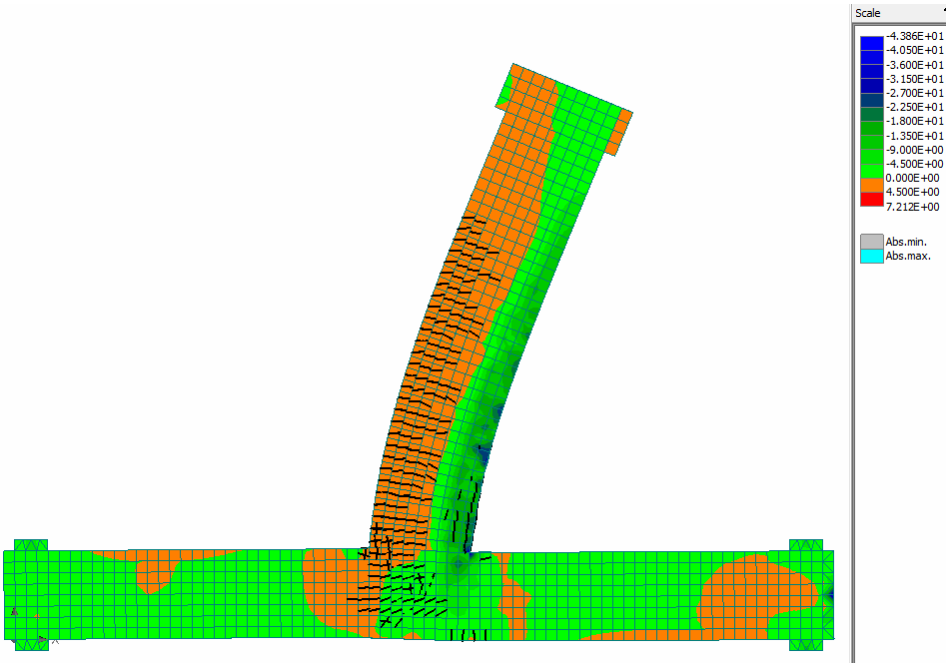

(c) II-60-0.70 at 6.0% drift ratio

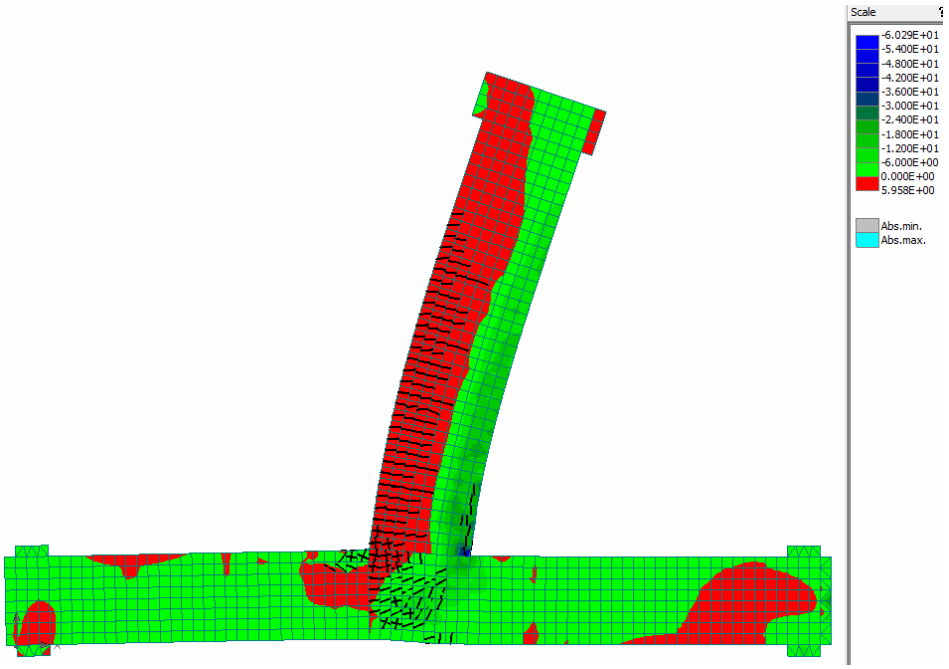

(d) II-60-1.0 at 5.0% drift ratio

Figure 7.13: Concrete stresses in the Z-Z direction and cracking pattern on deformed specimens

The lateral load-drift ratio relationships of all specimens are shown in Figure 7.14. It is clear that, in all specimens, the experimental hysteretic behaviour was in good agreement with that of the finite element model. It should be noted that the finite element model had no ability to detect the slippage of the beam longitudinal headed bars from the joint which occurred in the last loading cycles in Specimens II-30-0.70 and II-60-0.70 as shown in Figure 7.14 (a) and (c). This is attributed to the fact that the ATENA-3D had no option to add spring elements between the concrete and the reinforcement to model the anchorage capacity of the GFRP headed bars. The solution for this problem is to compare the tensile stress in the reinforcement just before the anchorage head with the anchorage capacity of the heads. When the stress in that location exceeds the anchorage capacity, the user can decide to terminate the analysis.

Moreover, it is observed that the pinching distances at the 0.0% (origin point) drift ratio in the finite element models were smaller than in the experimental results. This is due to the fact that the compression contribution of the beam longitudinal reinforcement, though it is small, could not be simulated in the model, since the software does not accept defining a compression stress-strain relationship different than the tensile stress-strain relationship of the reinforcement. Therefore, it was decided to deactivate the compression contribution of the beam longitudinal bars. The deactivation of the compression contribution leads the hysteretic loop to significantly change its slope near the zero lateral load (horizontal axis).

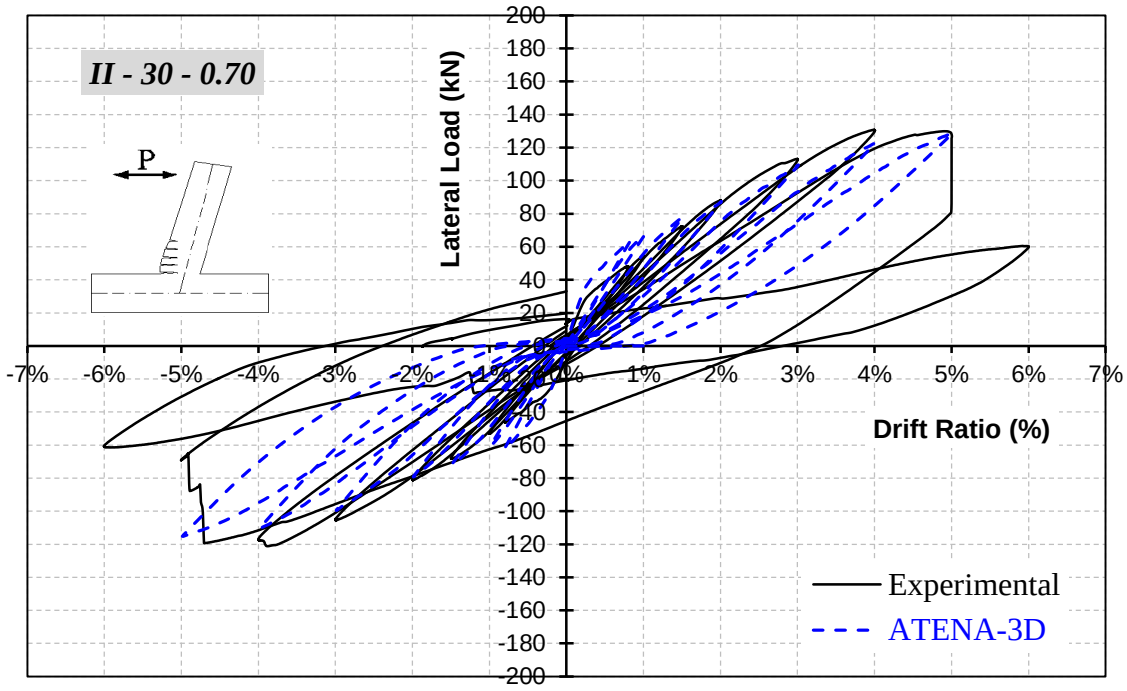

(a) Specimen II-30-0.70

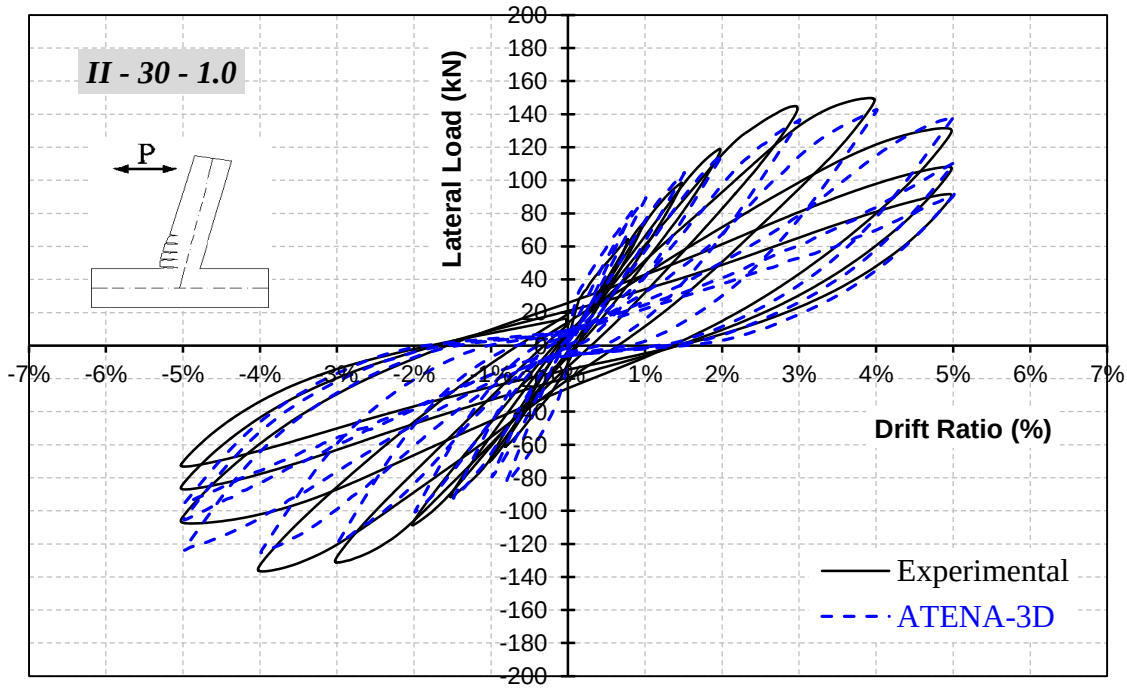

(b) Specimen II-30-1.0

Figure 7.14: Experimental hysteretic behaviour against the analytical one of Series (II) specimens (continued)

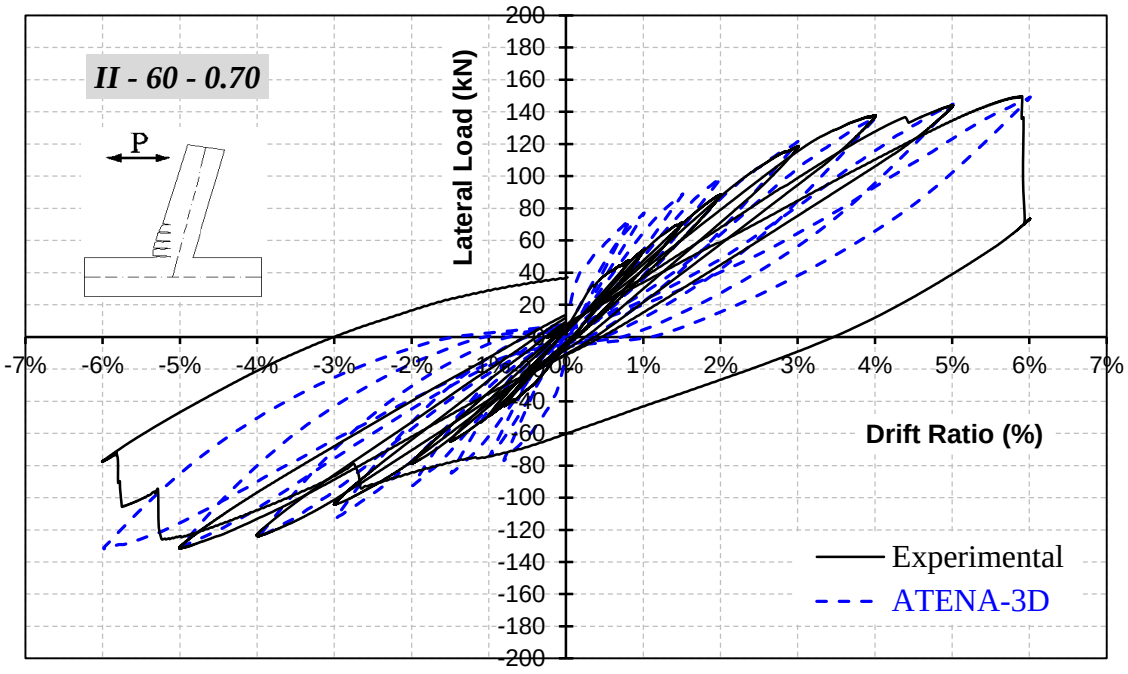

(c) Specimen II-60-0.70

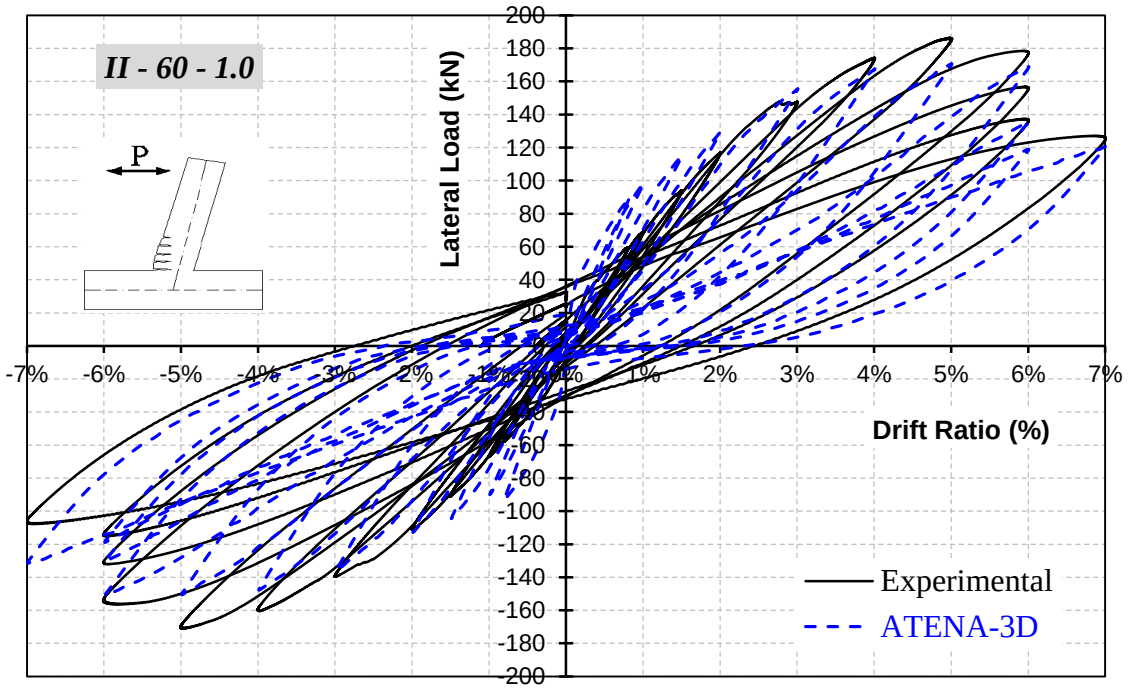

(d) Specimen II-60-1.0

Figure 7.14: Experimental hysteretic behaviour against the analytical one of Series (II) specimens

Figure 7.15 shows the envelopes of the hysteretic loops for both the analytical model and the experimental results. It is clear that the lateral load resistance of each loading cycle in the ATENA-3D models is in a good agreement with the experimental values. It is observed that the difference between the model values and the experimental load values increases only at the first two loading cycles. Similar observation was also recorded in the verification process of the steel RC specimens (SS03-B06-J06 and S0); this is also attributed to the adopted concrete model, which assumes a higher elastic modulus of the concrete. Otherwise, the difference in lateral load between the model values and the experimental ones does not exceed 10 %.

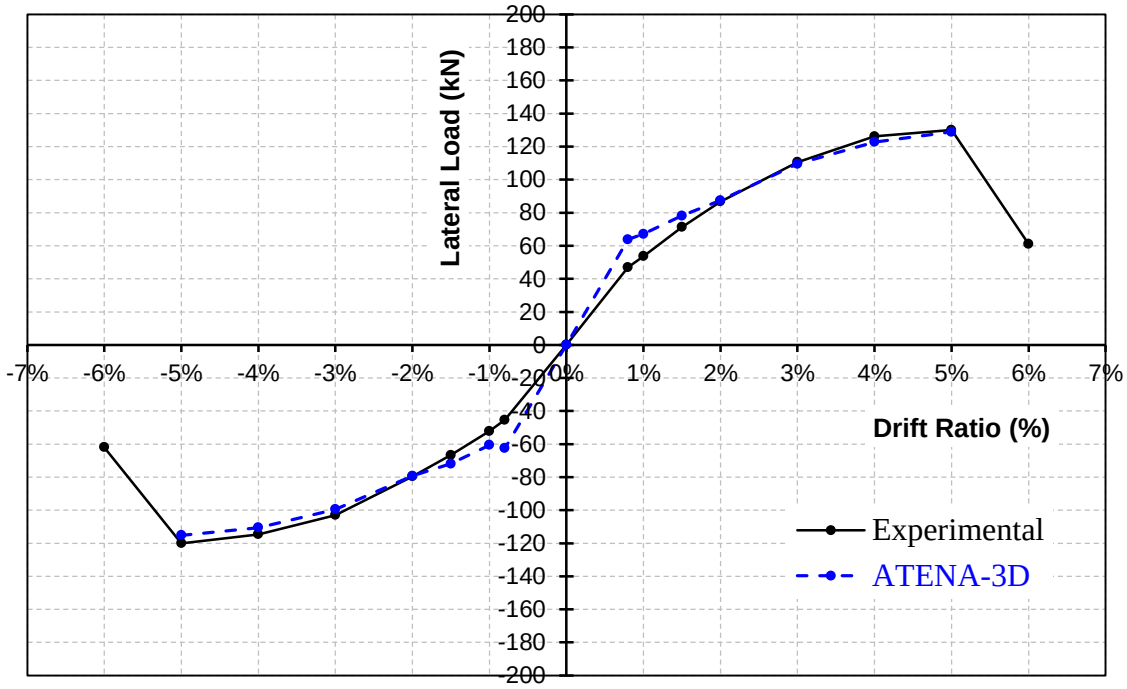

(a) Specimen II-30-0.70

Figure 7.15: Envelopes of hysteretic behaviour for Series (II) specimens (continued)

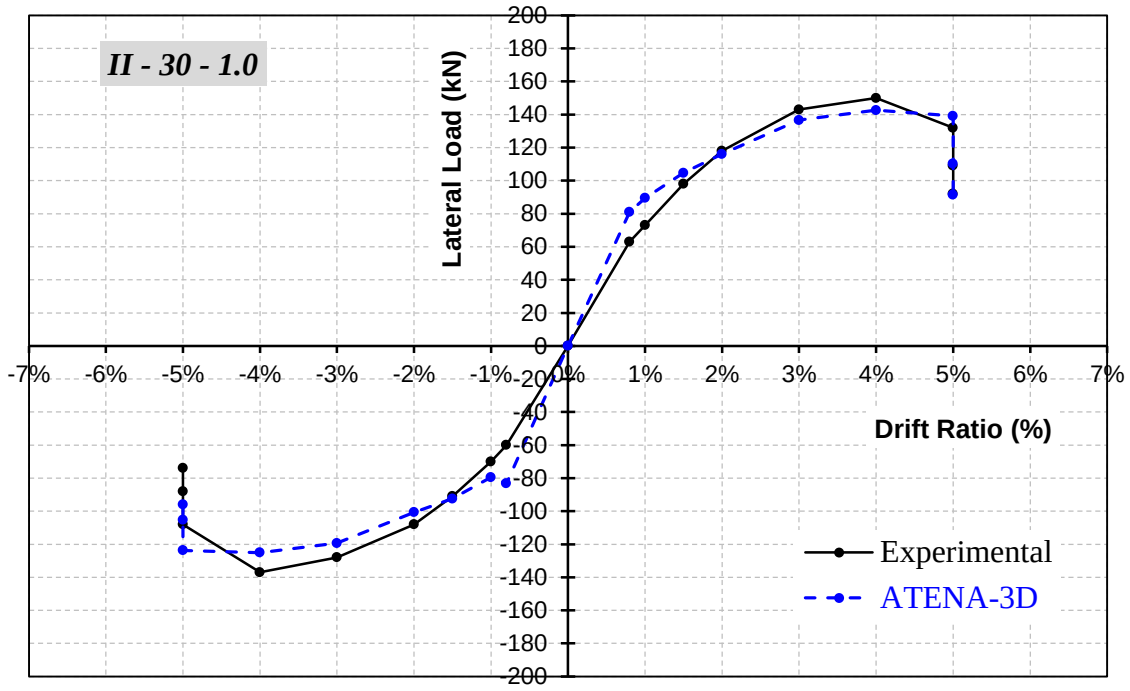

(b) Specimen II-30-1.0

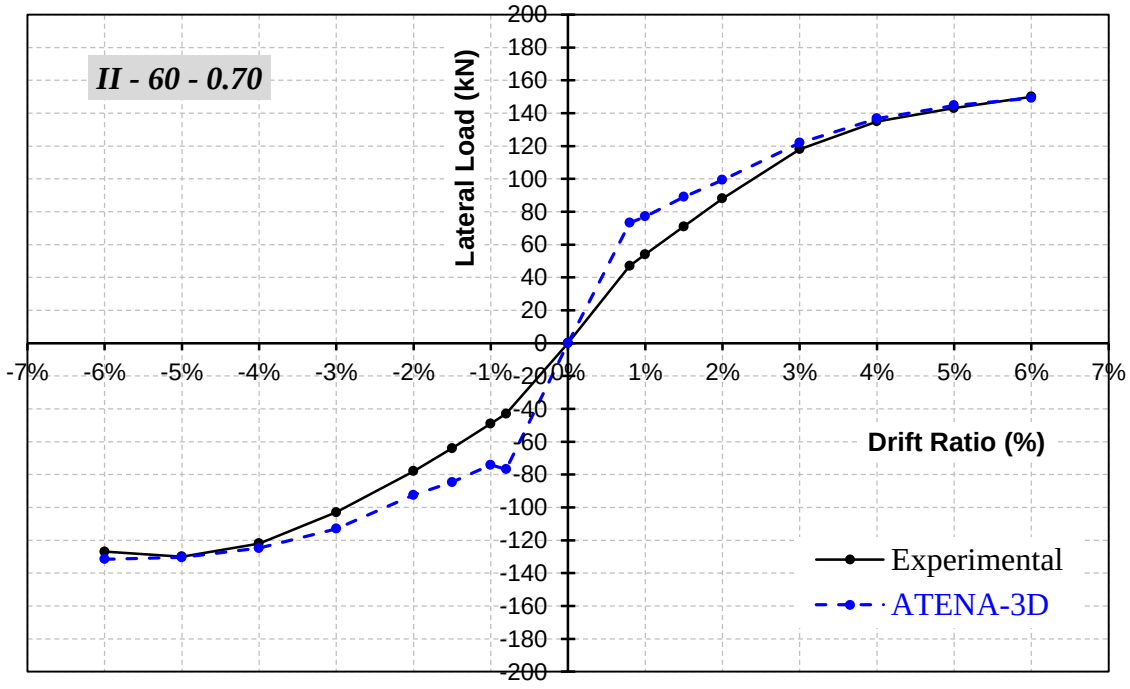

(c) Specimen II-60-0.70

Figure 7.15: Envelopes of hysteretic behaviour for Series (II) specimens (continued)

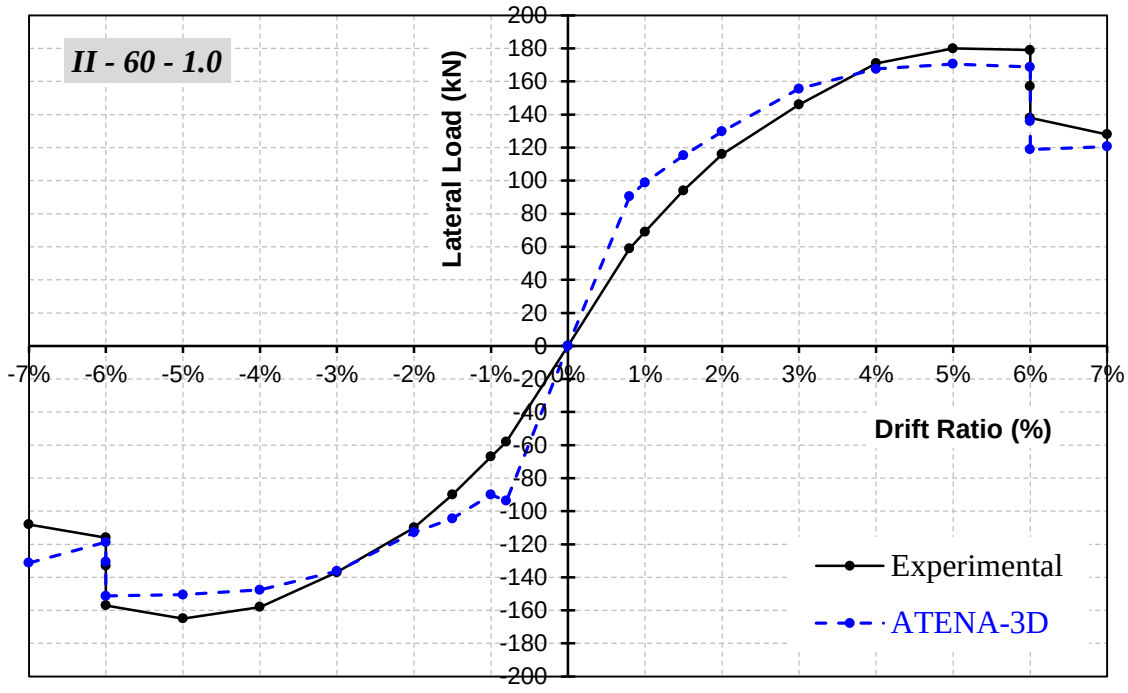

(d) Specimen II-60-1.0

Figure 7.15: Envelopes of hysteretic behaviour for Series (II) specimens

Figure 7.16 shows the tensile strain-drift ratio relationship of the beam longitudinal reinforcement for the finite element model compared to that of the experimental tests. It shows that the finite element models were able to capture similar trends of the relationship to those observed in the experimental results; however, with some deviation in the values. Up to 2.0% drift ratio, the difference in the strain values between the model and the experiment was insignificant; however, that difference reached an average of 15% in Specimens II-30-0.70 and II-30-1.0, and of 13% in Specimens II-60-0.70 and II-60-1.0 as shown in Table 7.3.

Table 7.3: Ratio between the experimental strain values to the finite element ones

drift ratio	Experimental / ATENA-3D			
	II-30-0.70	II-30-1.0	II-60-0.70	II-60-1.0
3%	1.18	1.11	1.11	1.07
4%	1.18	1.14	1.14	1.16
5%	1.20	1.09	1.12	1.20
Average	1.15		1.13	

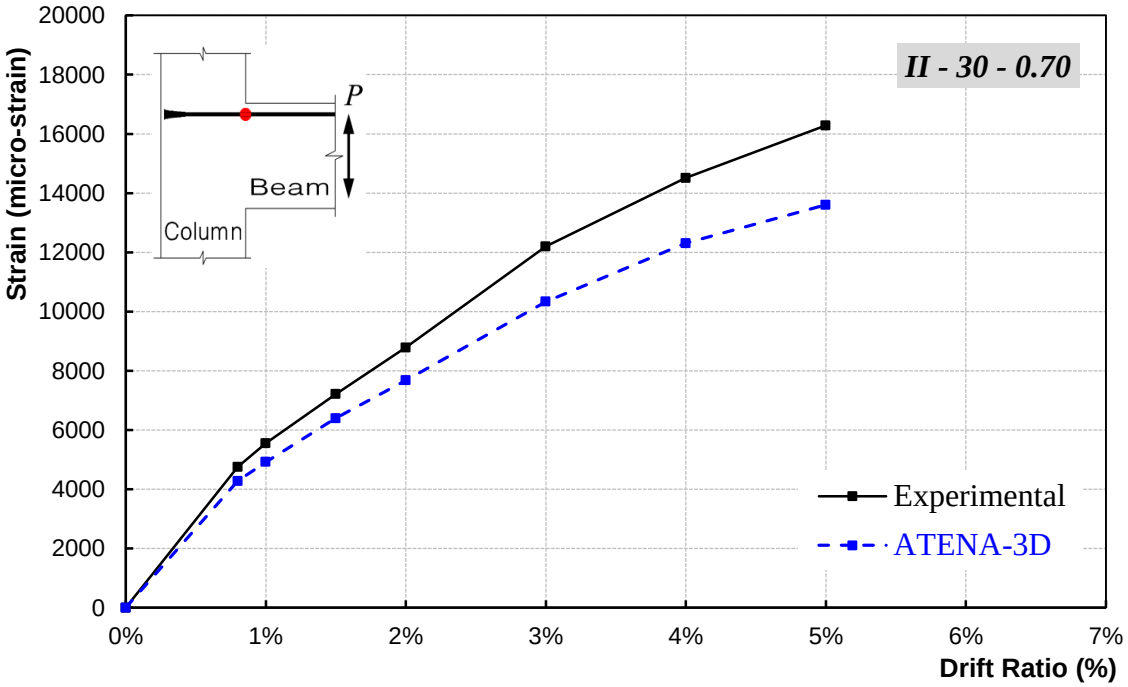

(a) Specimen II-30-0.70

Figure 7.16: Maximum strain–drift ratio relationship for beam longitudinal reinforcement

(continued)

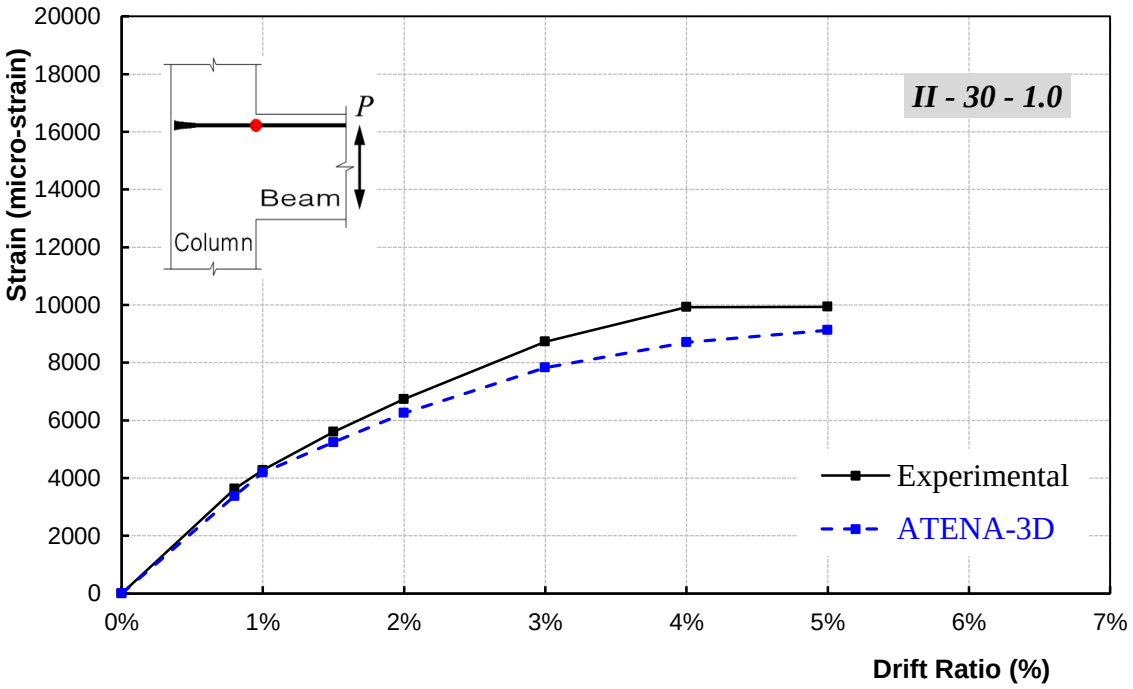

(b) Specimen II-30-1.0

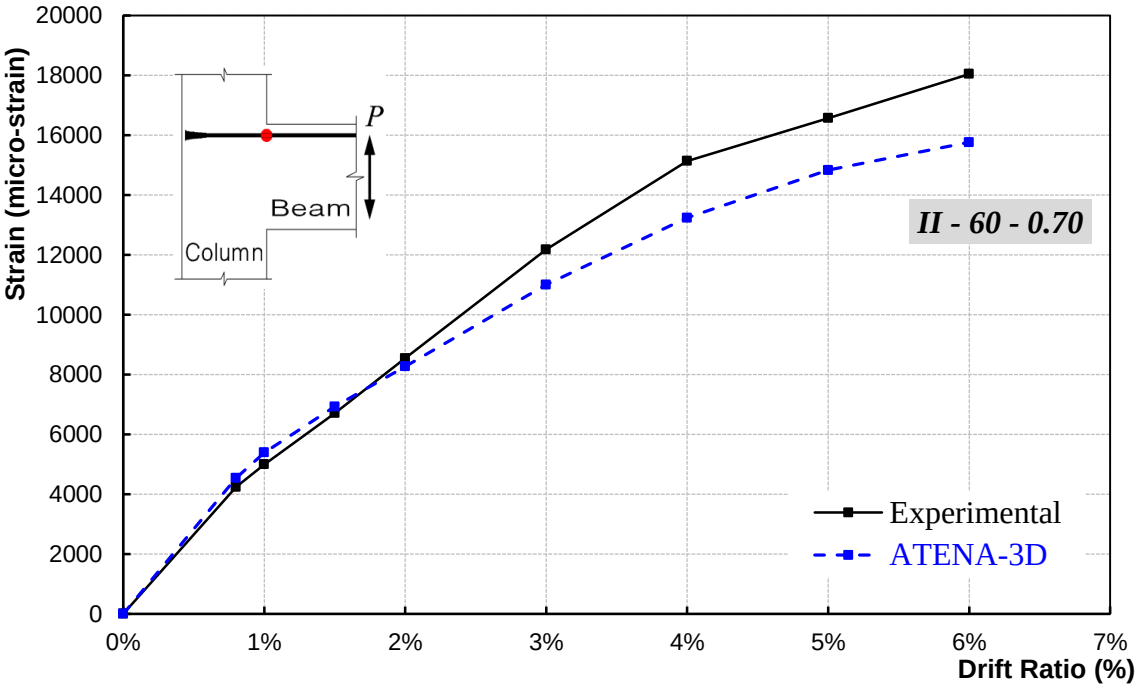

(c) Specimen II-60-0.70

Figure 7.16: Maximum strain–drift ratio relationship for beam longitudinal reinforcement (continued)

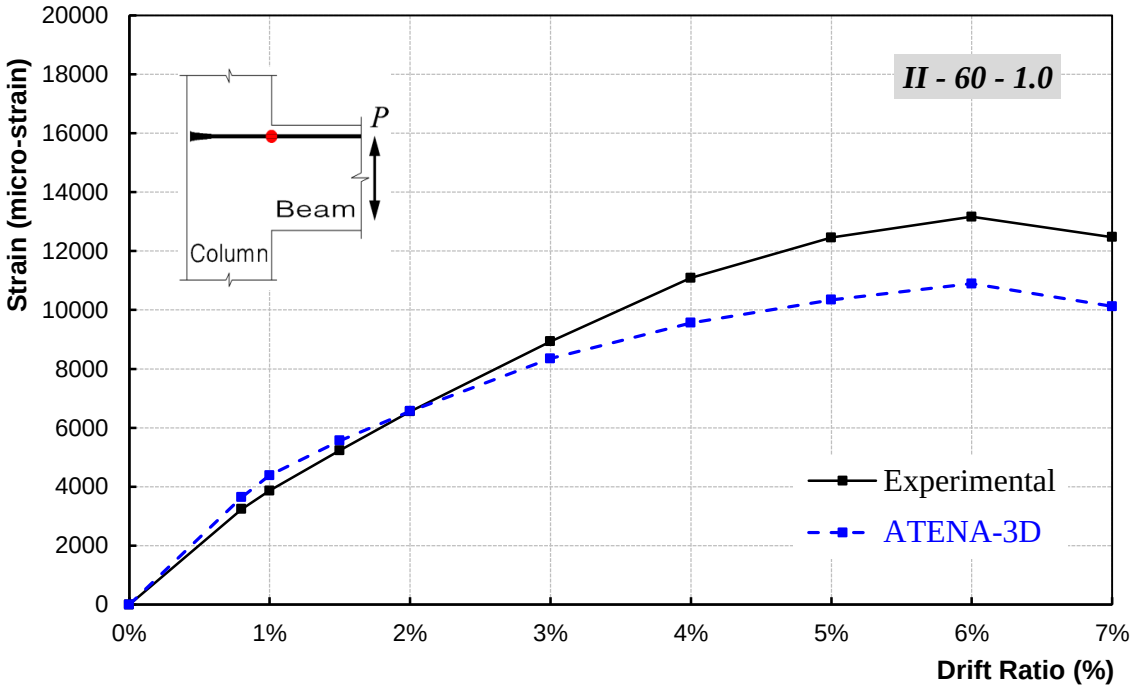

(d) Specimen II-60-1.0

Figure 7.16: Maximum strain–drift ratio relationship for beam longitudinal reinforcement

7.3.4 Remarks

It has been verified that the results of the ATENA-3D finite element modeling were in good agreement with the experimental ones. The hysteretic behaviour of the analytical models matched the experimental one in trend and lateral load resistance. ATENA-3D was able to capture the post-failure behaviour of concrete after reaching the maximum lateral resistance. On the other hand, the program was not able to detect the anchorage failure of the beam longitudinal reinforcement anchored in the joint; however, the reinforcement detailing is not in the scope of the parametric study carried out in this thesis. Up to 2.0% drift ratio, the developed strains in the analytical model showed no deviation from the experimental ones; however, at higher drift ratio the strain values need to be magnified by 15% more to match the experimental values.

Accordingly, the constructed FE model is capable of performing a parametric study to investigate the influence of some key parameters on the behaviour of FRP-reinforced beam-column joints. The results of this parametric study are shown in the next chapter.

CHAPTER 8

PARAMETRIC STUDY

8.1 GENERAL

Based on the verification process carried out in the previous chapter, reliability and confidence were established in adopting the non-linear finite element analysis using ATENA-3D for beam-column joints. The verified analytical models were employed to investigate the effect of four key parameters on the general behaviour of GFRP-RC exterior beam-column joints. The key parameters investigated in this study were identified as the concrete strength, presence of lateral beams, level of axial load applied on the column, and the influence of shear stress in the joint on the residual axial capacity of the column after surviving an earthquake event.

Figure 8.1 shows a flow chart for the test matrix used in this parametric study and the configuration of each parameter. The figure shows that the parametric study consists of four parameters; the first two parameters have sets of six specimens while the third and fourth parameters have sets of eight and nine specimens, respectively. ATENA-3D was used to perform the analysis on each configuration for the selected parameters. The identification of the specimens used in the experimental program was also adopted here in this analytical study. The loading history used in the verification of the finite element results with the experimental results, as explained in Chapter 7-Section 7.2.6, was also used in this parametric study. The following sections present the details of the finite element modeling and the studied parameters.

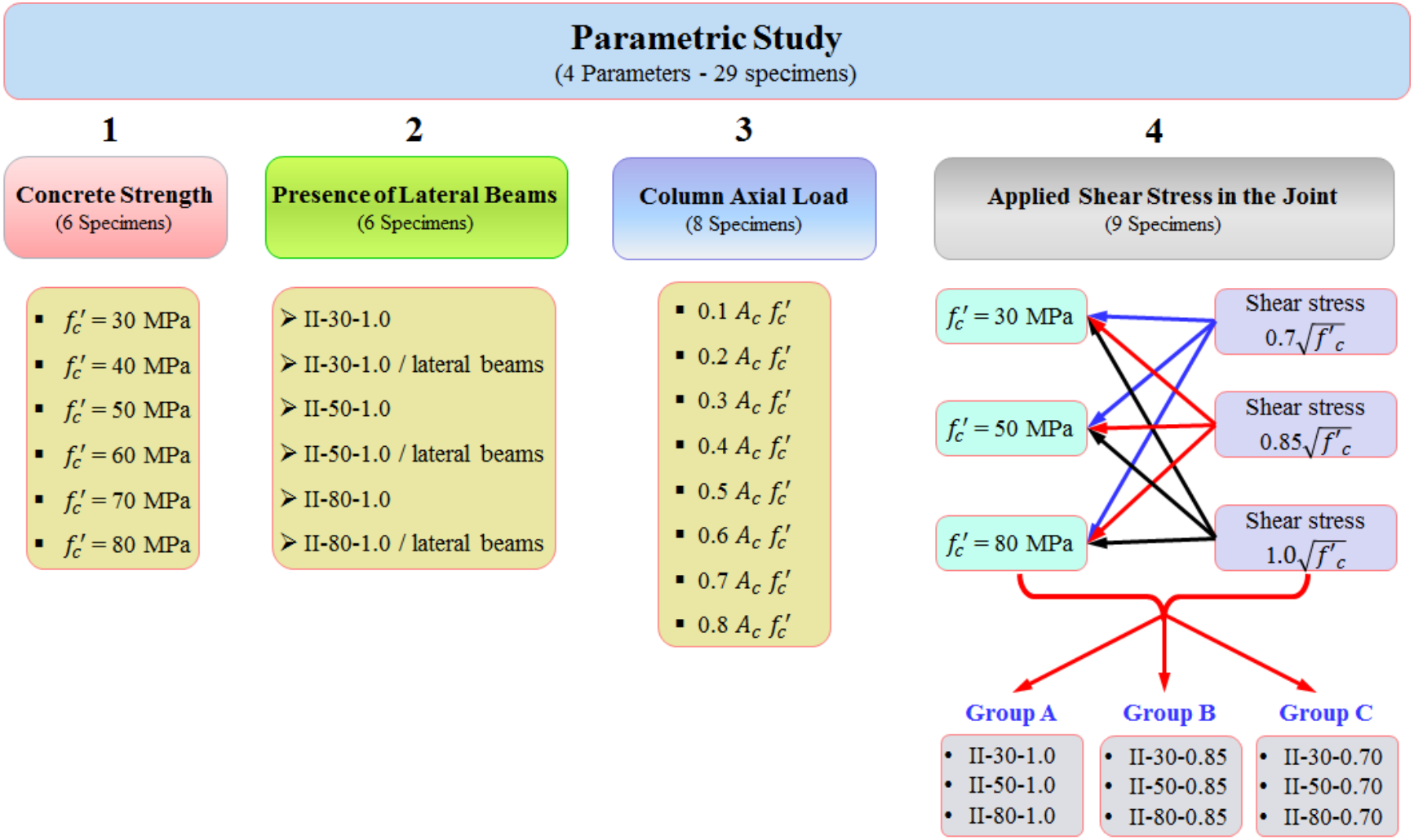

Figure 8.1: Parametric study test matrix

8.2 STUDIED PARAMETERS

8.2.1 Concrete Strength

The influence of the concrete compressive strength was investigated in this study using six different concrete strengths. As shown in Figure 8.1, the study started with a specimen of a concrete strength equal to 30 MPa and gradually increased the strength by an increment of 10 MPa in the successive specimens until a specimen with concrete strength of 80 MPa was reached. The finite element model of Specimen II-30-0.70 was used to carry out the runs. The area of the longitudinal reinforcement in the beam was increased to be 900 mm^2 instead of 800 mm^2 to ensure that a concrete crushing failure occurs in the beam section except in specimen with concrete compressive strength of 80 MPa where reinforcement rupture is expected. Table 8.1 shows the ratio between the provided longitudinal reinforcement ratio in the beam section and the balanced reinforcement ratio (ρ_{frp}/ρ_{bal}). The results of these analytical models were compared in terms of the envelope of the hysteric behaviour and the corresponding mode of failure, and the developed strains in the beam longitudinal reinforcement.

Table 8.1: Provided reinforcement ratio relative to the balanced reinforcement ratio in the beam section

Specimen	30 MPa	40 MPa	50 MPa	60 MPa	70 MPa	80 MPa
ρ_{frp}/ρ_{bal}	2.06	1.6	1.33	1.19	1.07	0.97
Mode of Failure	Concrete crushing					Bar rapture

Figure 8.2 shows the envelopes for the load-drift relationships for specimens with different concrete compressive strengths, f_c'. As expected, the specimen with the lowest concrete strength, 30 MPa, exhibited the lowest lateral resistance in both directions of loading. At 4.0% drift ratio, it was found that increasing the concrete strength from 30 to 70 MPa increased the sustained lateral load resistance by 36%. The figure also shows that specimens with lower concrete strength developed their maximum lateral resistance earlier than those with higher concrete strength. For example, specimen with 30 MPa developed its maximum lateral resistance at 4.0% drift ratio, while specimen with 70 MPa developed its maximum capacity approximately at 6.0% drift ratio and kept unchanged up to 8.0% drift ratio.

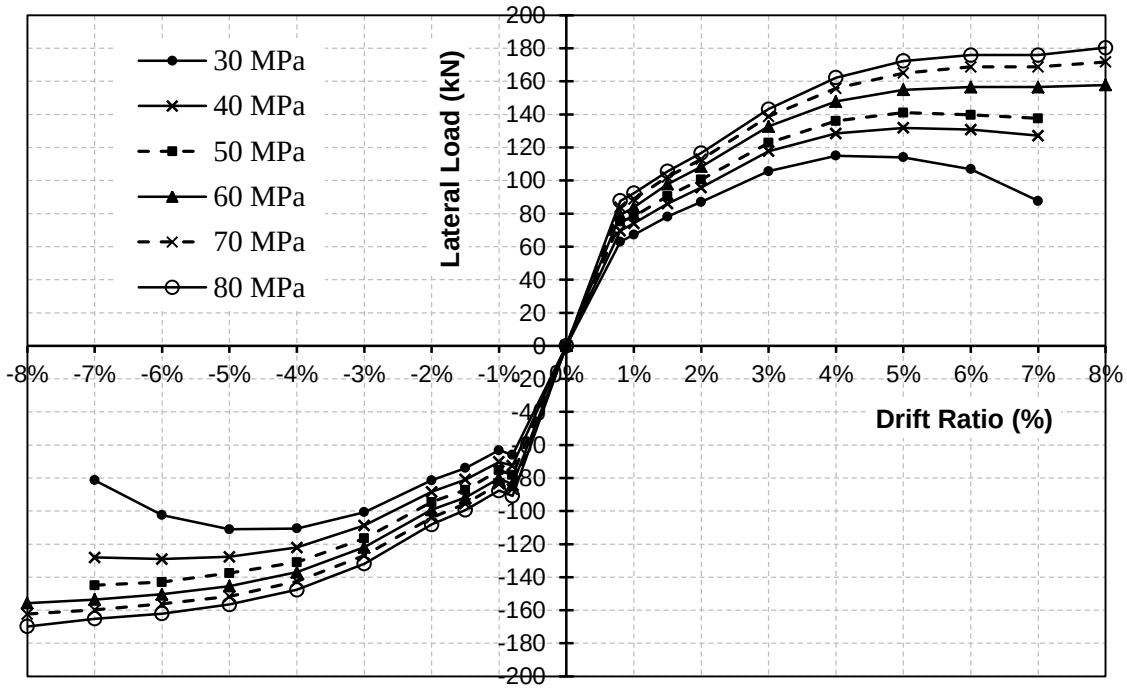

Figure 8.2: Envelopes of the hysteretic behaviour of specimens

It was concluded previously in Chapter 7 that there is a good correlation between the strain values in the analytical models and the experimental values up to 2.0% drift ratio. After the 2.0% drift ratio it was found that the strain values of the analytical models need to be magnified by 15% to match the experimental values. In Figure 8.3, where the objective of the figure is to compare the developed strains with the ultimate tensile strain, the ultimate tensile strain of the reinforcement was reduced by 15%, instead of increasing the strain values by 15% as recommended before, to keep the consistency of the obtained results after 2.0% drift ratio. For example, the obtained strain value from the analytical model of the 80MPa specimen at 6 % drift ratio is approximately 15950 micro-strain; as concluded in Chapter 7, this value should be magnified by 15% to be 18340 micro-strain. However, in Figure 8.3, the ultimate tensile strain was reduced by 15% instead of magnifying the strain value.

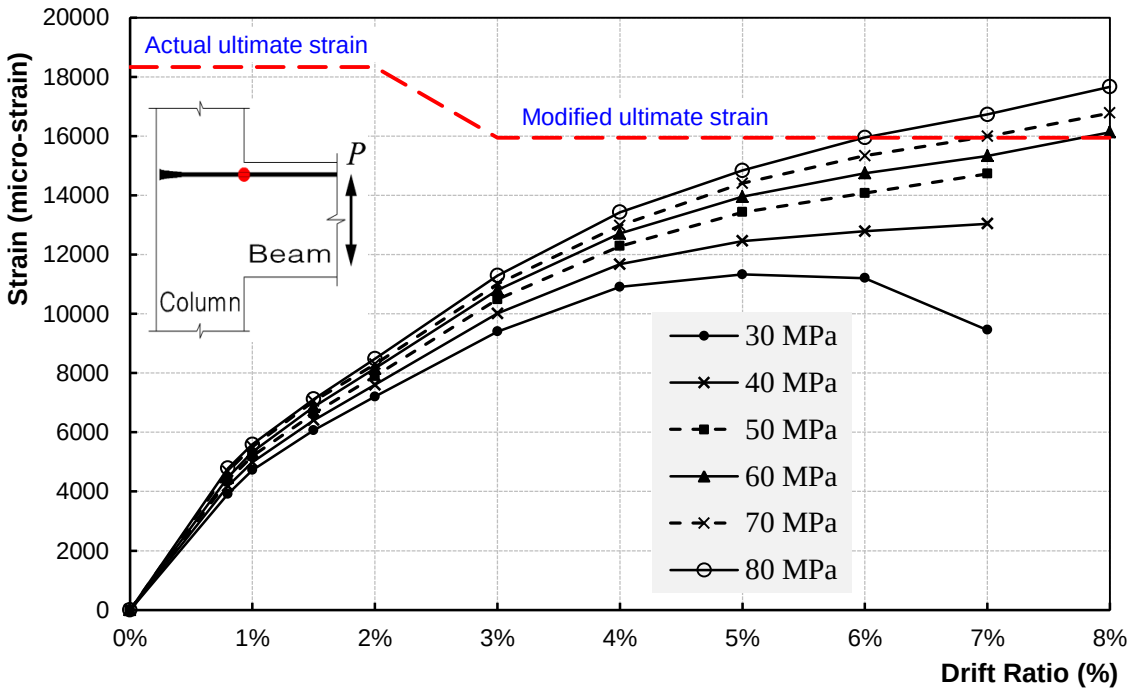

Figure 8.3: Maximum strain-drift ratio relationship for beam longitudinal reinforcement

Figure 8.3 shows a good agreement with Table 8.1; the figure shows that specimen with concrete strength of 80 MPa exhibited failure in the beam section due to rapture of reinforcement. Although the two specimens with concrete strengths of 60 MPa and 70 MPa were designed to fail by crushing of concrete in beam section, the figure shows that both specimens exhibited rupture of beam longitudinal reinforcement. However, this rupture of the longitudinal reinforcement in the 60 MPa and 70 MPa specimens occurred at 8.0% and 7.0%, respectively, which is after reaching the maximum lateral resistance (i.e. concrete compression failure) at 6.0% and 7.0% drift ratio, respectively, as shown previously in Figure 8.2. This observation supports that explanation discussed before in Chapter 6, Section 6.4.1 (Figure 6.13) in which the concrete section redistributes the stresses on the reduced dimensions of the section after spalling of concrete cover that reached the ultimate compressive strain. This is in addition to the increased ultimate compressive strain of the concrete core due to the confinement provided by the stirrups. Consequently, the section exhibited higher tensile strains in the beam longitudinal reinforcement at higher drift ratios to maintain the flexural resistance of the section. Therefore, it is recommended to set a minimum reinforcement ratio in terms of ρ_{frp}/ρ_{bal} to avoid rupture of reinforcement in higher drift ratios. This recommendation should be reflected in the future updates of the CSA/S806-12.

8.2.2 Presence of Lateral Beams

Based on the analysis and the discussion of the experimental results in Chapter 6, it was found that high shear stress level ($1.0\sqrt{f'_c}$) resulted in diagonal shear failure in the joints which accelerated the degradation and failure of the specimens. It is well established that the confinement of the joint provided by means of either transverse reinforcement or by the adjoining structural concrete members framing into the joint faces influences the behaviour of the specimens. Moreover, the number of the confined faces of the joint influences the behaviour as well. In this study, the influence of confining the joint on three faces (i.e. the presence of two lateral beams) on the overall behaviour is studied. Therefore specimens with high shear stress level in the joint were modeled to study the influence of the confinement provided by the lateral beams.

The presence of lateral beams is a parameter that could be affected by many variables such as concrete strength, shear stress in the joint, loading magnitude and direction applied to the lateral beams, and size of the lateral beams. In this study the influence of lateral beams presence is studied from the aspect of the confinement which these beams provide to the joint to affect the overall behaviour in terms of sustained lateral loads and drift ratios. In order to generate enough specimens to draw reliable conclusions, the specimens were modeled using concrete strength of 30, 50, and 80 MPa, as shown in Figure 8.1. Since the influence of the concrete strength has been already studied in Section 8.2.1, accordingly the influence of the presence of lateral beam can be evaluated in isolation of the concrete strength.

As shown in Figure 8.1, this parameter consists of six specimens (finite element models); three of them are exterior beam column joint with no lateral beams in addition to their counterparts with lateral beams as shown in Figure 8.4.

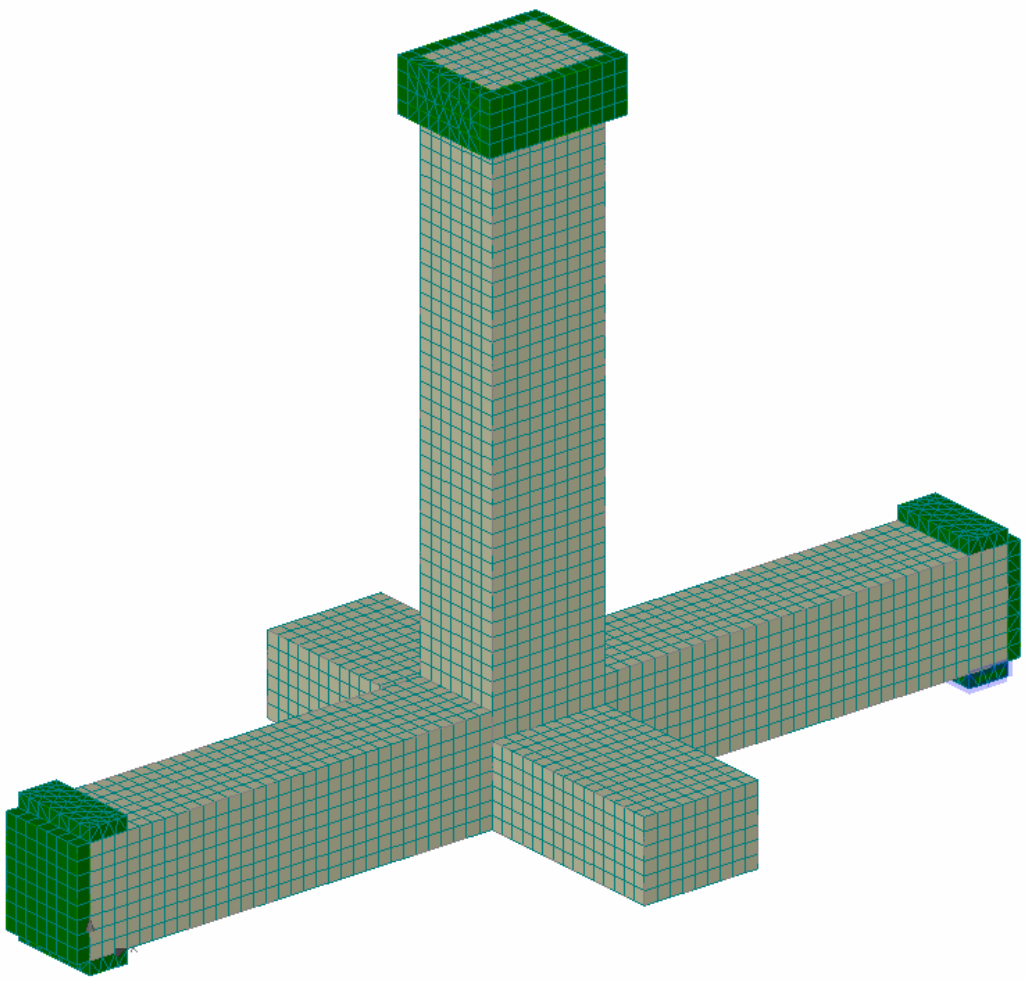

Figure 8.4: ATENA-3D finite element model for beam-column joint with lateral beams

Regarding the size of the lateral beams, it should be noted that the CSA/A23.3-04 (CSA 2004), Clause 21.5.4.1, considers a framing member to confine a joint face if at least 75% of that joint face is covered by that framing member. In absence of such clause in the CSA/S806-12 (CSA 2012), the CSA/A23.3-04 was taken as a guide in this aspect.

Therefore, the cross sectional dimensions of the lateral beams, 300-mm in width and 450-mm in depth, were selected such that it covered 75% of the joint confined faces. The length of each lateral beam was 750 mm. The lateral beams were reinforced with six GFRP bars of 16 mm diameter and 12 mm stirrups spaced at 100 mm as shown in Figure 8.5. The results of the analytical models were presented in form of the envelope of the hysteric behaviour, the developed strains in the beam longitudinal reinforcement, and the shear distortion developed in the joint.

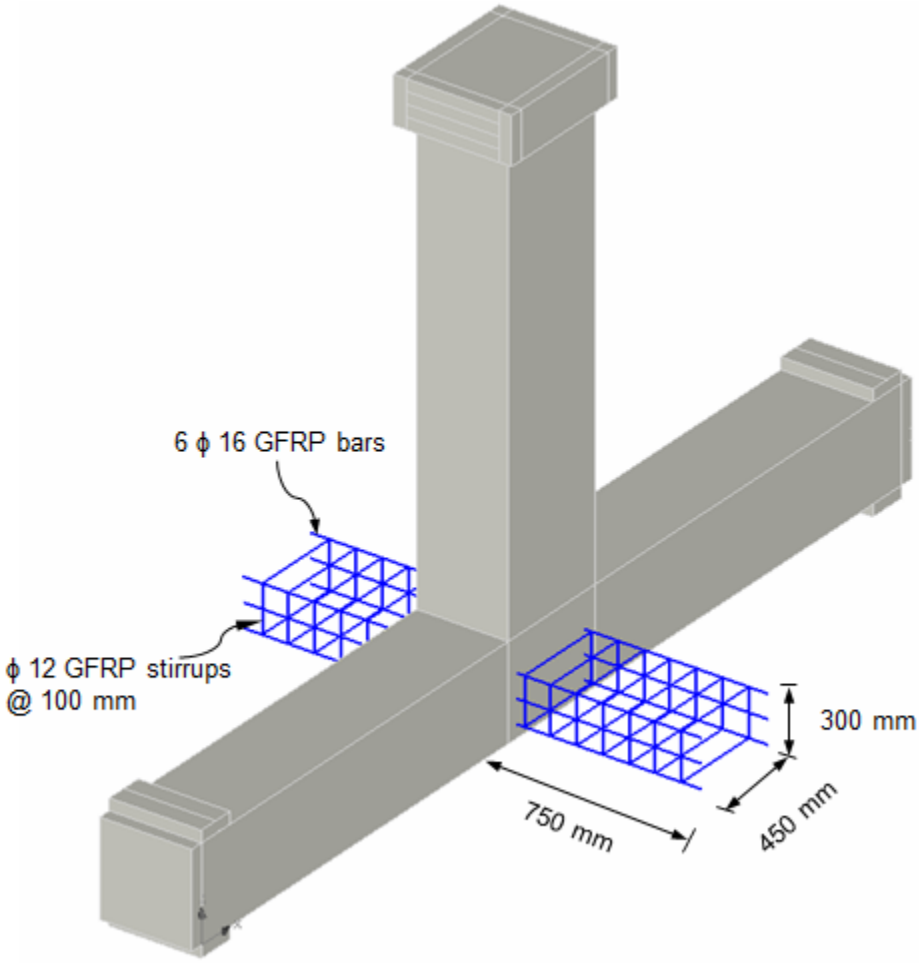

Figure 8.5: 3-D view of lateral beam reinforcement

Figure 8.6 shows the envelopes for the load-drift relationships for the six specimens. The figure shows that up to 2.0% drift ratio, there was no difference in the lateral load resistance of specimens with lateral beams compared to their counterparts without lateral beams. Afterwards, the specimens with lateral beams showed approximately 10% increase in the maximum lateral load resistance than what exhibited by their counterparts. The figure also shows that specimens with no lateral beams experienced higher rate of strength degradation than what those with lateral beams experienced. Specimens with no lateral beams experienced failure at earlier drift ratios than what their counterparts did. As expected, the concrete strength influenced the lateral load resistance of the specimens; those with higher concrete strength showed higher lateral load resistance. An increase in the concrete strength from 50 MPa to 80 MPa (60% higher) resulted in approximately 20% higher lateral load resistance.

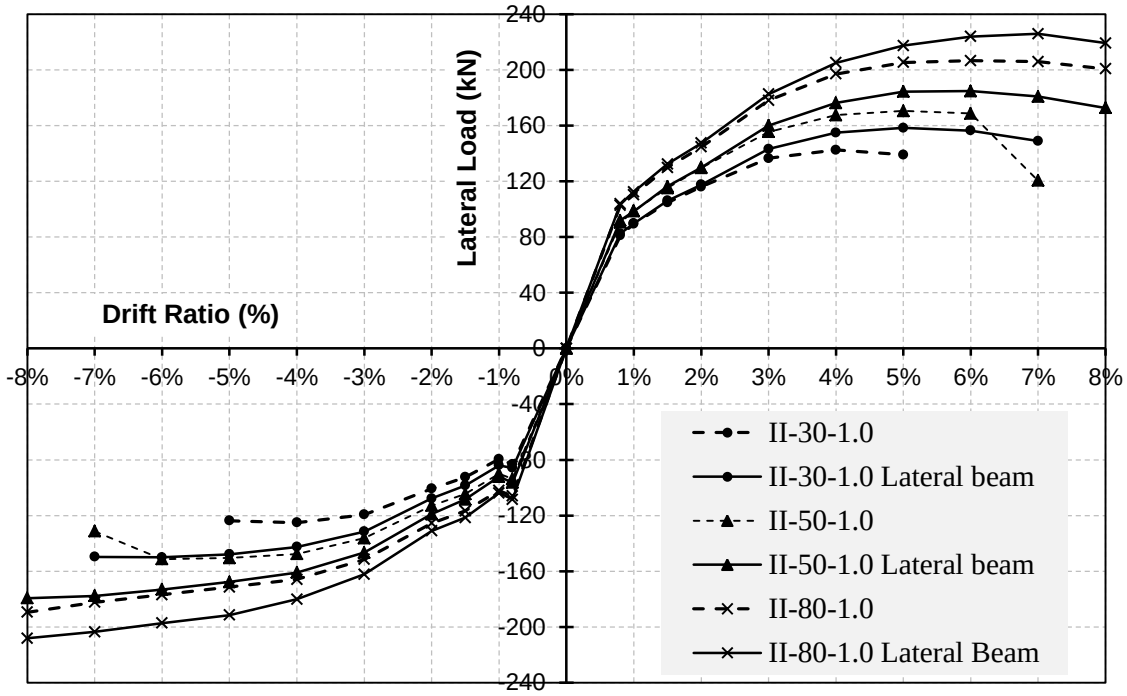

Figure 8.6: Envelopes of the hysteretic behaviour of specimens

Figure 8.7 shows the relationship between the maximum developed strains in the beam longitudinal reinforcement and the corresponding drift ratios. The figure shows that after 2.0% drift ratio, specimens with lateral beams developed tensile strains between 10% and 15% higher than those of their counterparts. This is in a good agreement with Figure 8.6 where specimens with lateral beams showed higher lateral load resistance. It should be noted that none of the specimens reached the ultimate tensile strains of the GFRP reinforcement.

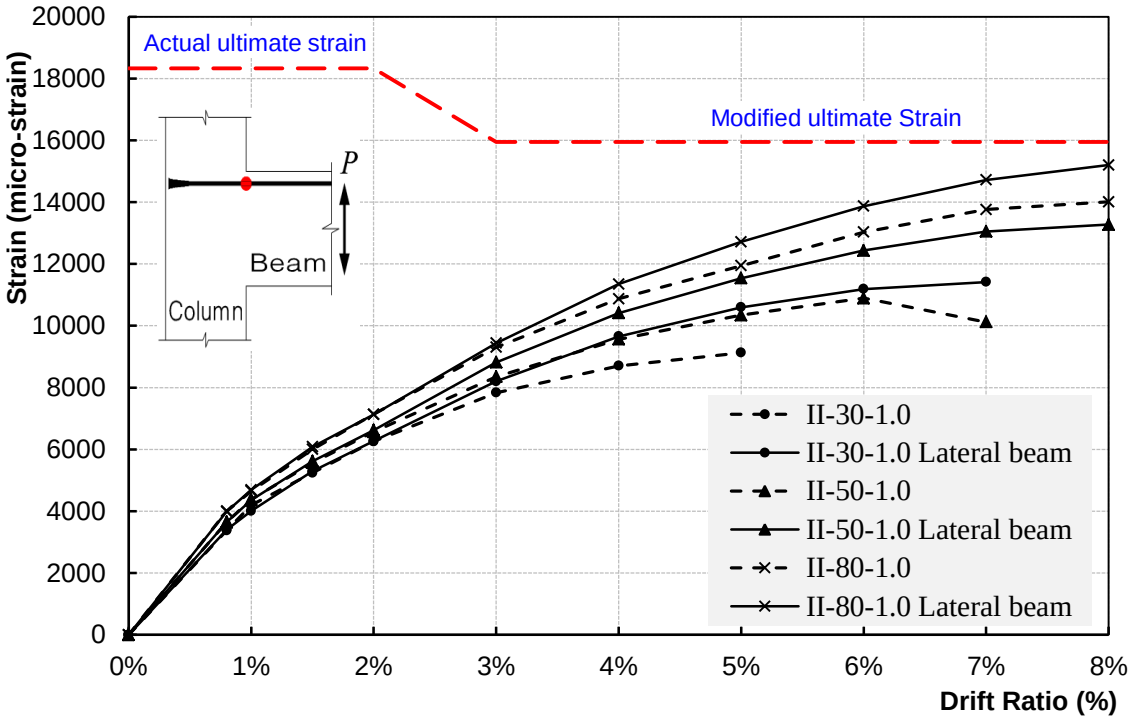

Figure 8.7: Maximum strain-drift ratio relationship for beam longitudinal reinforcement

It is well established that the shear distortion in the joint contributes to the total drift of the structure. The shear distortion is influenced by the level of confinement provided to the joint; when more confinement is applied to the joint, less distortion in the joint is

expected. Figure 8.8 shows the contribution percentage of the joint distortion to the total drift angle with the corresponding drift ratio. It is shown in the figure that specimens with no lateral beams exhibited higher shear distortion in the joint that exceeded 20% of the total drift angle after 4.0% drift ratio. At 4.0% drift ratio, the presence of the lateral beams reduced the shear distortion by 50%, 50%, and 40% in Specimens II-30-1.0, II-50-1.0, and II-80-1.0, respectively.

Moreover, concrete strength influenced the shear distortion in specimens without lateral beams, where the highest shear distortion at the same drift ratio was exhibited by Specimen II-30-1.0 with the lowest concrete strength. The increase in concrete strength reduced the shear distortion in the joint. On the other hand, the figure indicates that the influence of concrete strength in specimens with lateral beams was insignificant. This is attributed to that the influence of concrete strength can be significant in exterior joints with no lateral beams (i.e. lower shear strength) where shear diagonal failure is of concern. The confinement provided to the joint by the presence of lateral beams increased the shear capacity of joint and therefore reduced the shear distortion in the joint to the point that the influence of concrete strength was not detected.

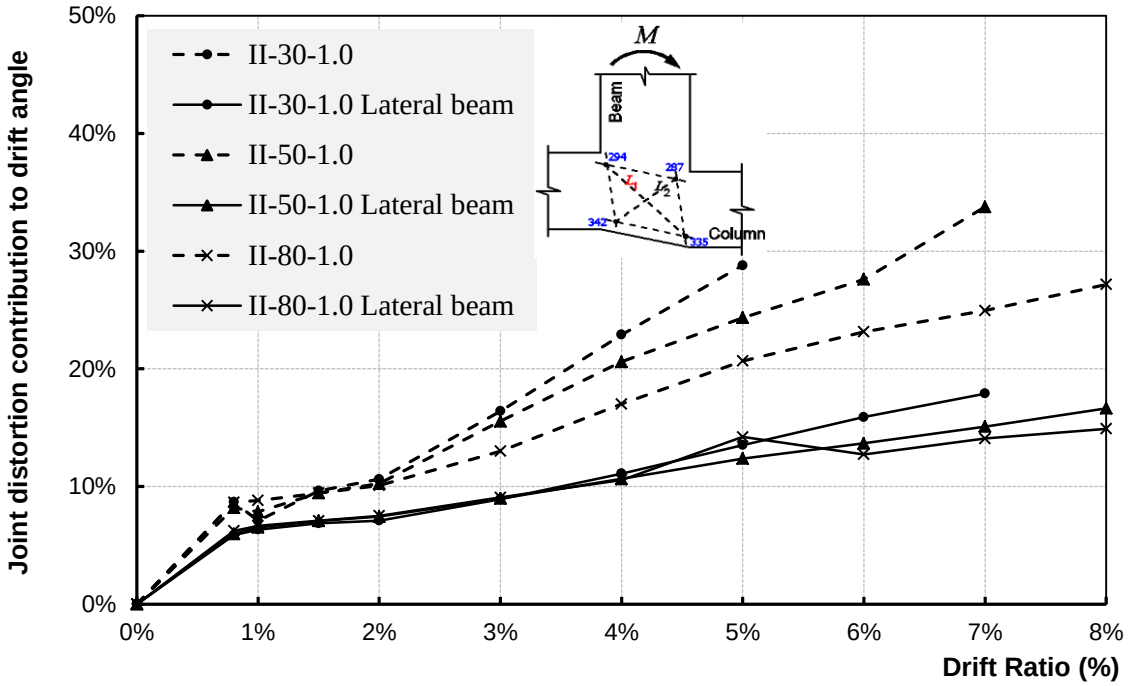

Figure 8.8: Contribution of joint distortion to total drift angle for all models

8.2.3 Axial Load Level on the Column

The level of axial load on the column influences the behaviour of beam-column joints in different aspects. It affects the flexural strength of the column cross section and consequently changes the flexural strength ratio of the beam-column joint. It also contributes to the shear capacity of the concrete along the column length. As well, it influences the shear deformation and distortion in the joint. In this study, the influence of the axial load level on the column was studied. The level of axial load was expressed as a percentage of $A_c * f_c'$, where (A_c) is the column cross-sectional area (350 mm in width by 400 mm in depth) and (f_c') is the concrete strength. A series of eight different axial load levels were applied on the column starting from 0.1 $A_c\, f_c'$ to 0.8 $A_c\, f_c'$ with an increment of 0.1 $A_c\, f_c'$ as shown previously in Figure 8.1. All specimens were modelled using a concrete strength of 50 MPa and they have identical concrete dimensions and

reinforcement details. The calculated shear stress applied on the joint was $0.85\sqrt{f'_c}$. Specimens are identified by the level of axial load applied on the column in terms of $A_c\ f'_c$. The results of the analytical models were presented in the form of the hysteric behaviour of the models and their envelopes, and the shear distortion developed in the joint.

Figure 8.9 shows the load-drift relationships for the eight specimens (finite element models). The figure shows that, at the same drift ratio, when the axial load level increases the pinching distance increases as well. This is attributed to the increase of non-linear deformations developed in the joint under higher levels of axial load. The figure also shows that specimen subjected to axial load on the column equal to 0.1 $A_c\ f'_c$ maintained its lateral load resistance at 5.0% and 6.0% drift ratios, while specimens with 0.2 $A_c\ f'_c$, 0.3 $A_c\ f'_c$, and 0.4 $A_c\ f'_c$ experienced drops in their lateral load resistance after 5.0%, 5.0%, and 4.0% drift ratio, respectively. On the contrary, specimens with 0.5 $A_c\ f'_c$ and 0.6 $A_c\ f'_c$ could not attain higher drift ratios due to failure in the joint at earlier drift ratios, while specimens with 0.7 $A_c\ f'_c$ and 0.8 $A_c\ f'_c$ exhibited earlier failure due to flexural failure in the column. Figure 8.10 shows the envelopes of the lateral load-drift relationships for all specimens. The figure shows that specimens with axial load higher than 0.3 $A_c\ f'_c$ experienced drops in their lateral capacity after 4.0% drift ratio. In other words, higher levels of axial load changed the mode of failure, accelerated the failure in the joint, and limited the ability of the specimen to sustain higher drift ratios.

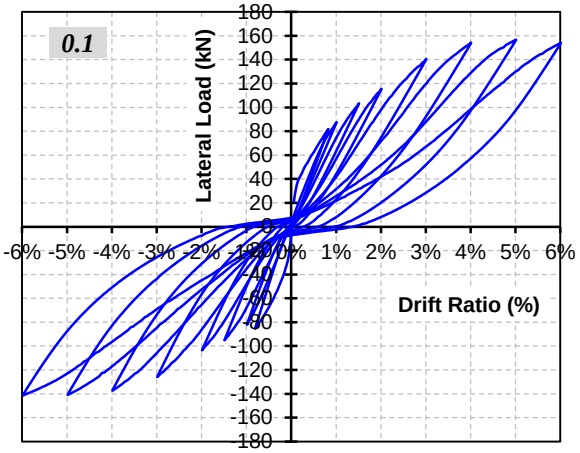

(a) 0.1 $A_c\ f_c'$

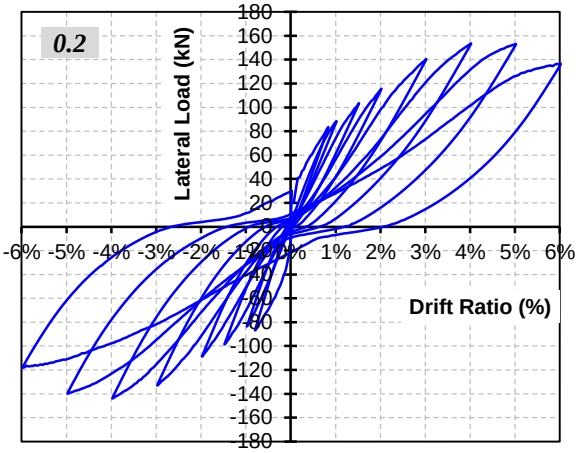

(b) 0.2 $A_c\ f_c'$

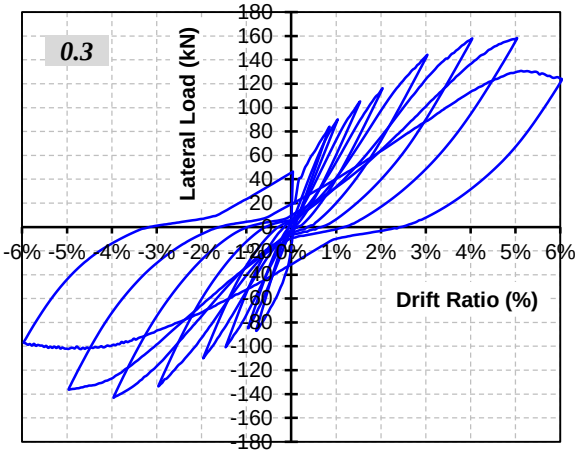

(c) 0.3 $A_c\ f_c'$

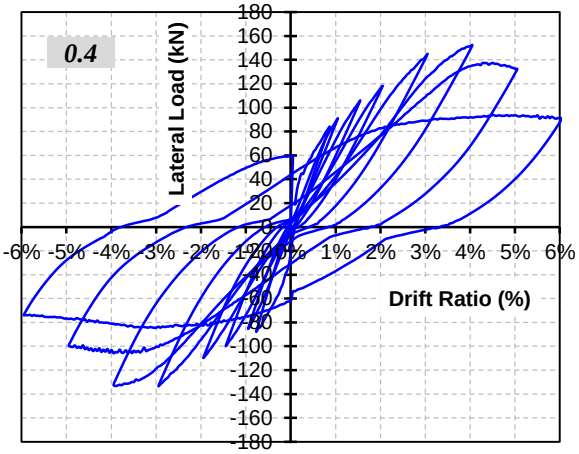

(d) 0.4 $A_c\ f_c'$

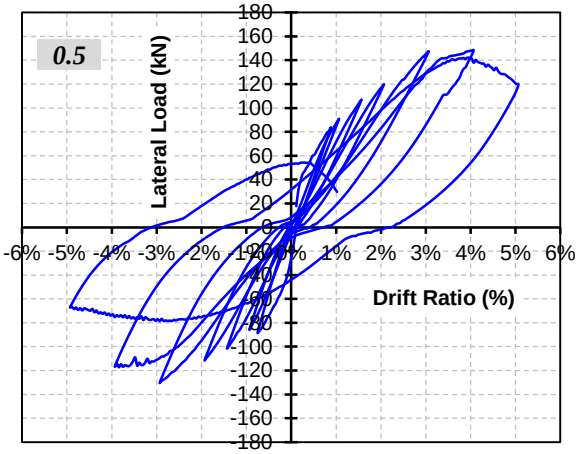

(e) 0.5 $A_c\ f_c'$

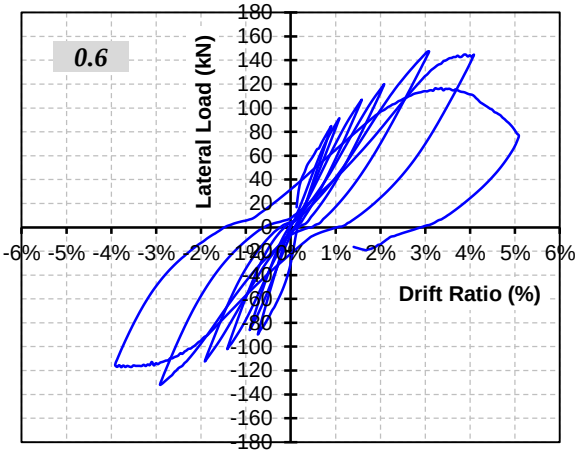

(f) 0.6 $A_c\ f_c'$

Figure 8.9: Load-Drift relationship (continued)

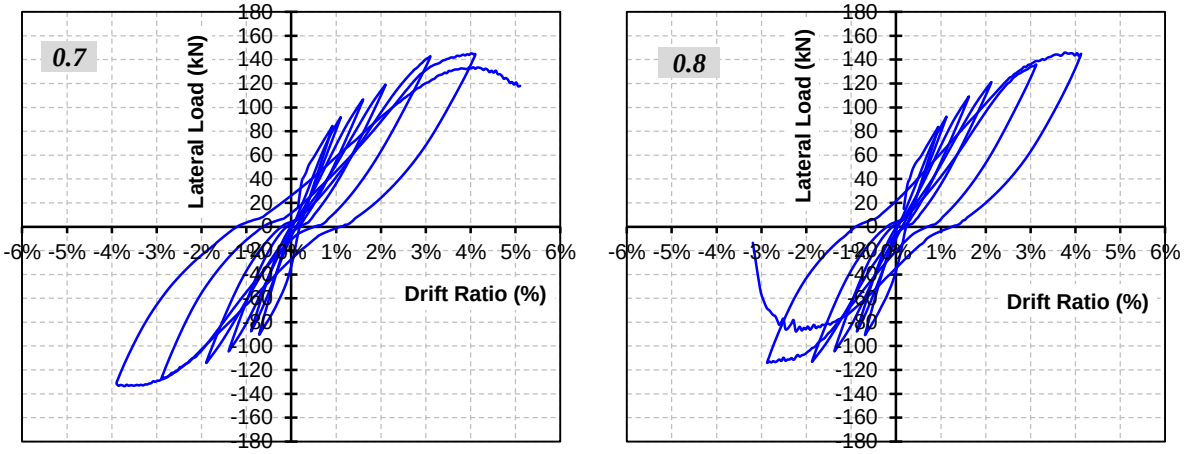

(g) 0.7 $A_c\ f_c'$ (h) 0.8 $A_c\ f_c'$

Figure 8.9: Load-Drift relationship

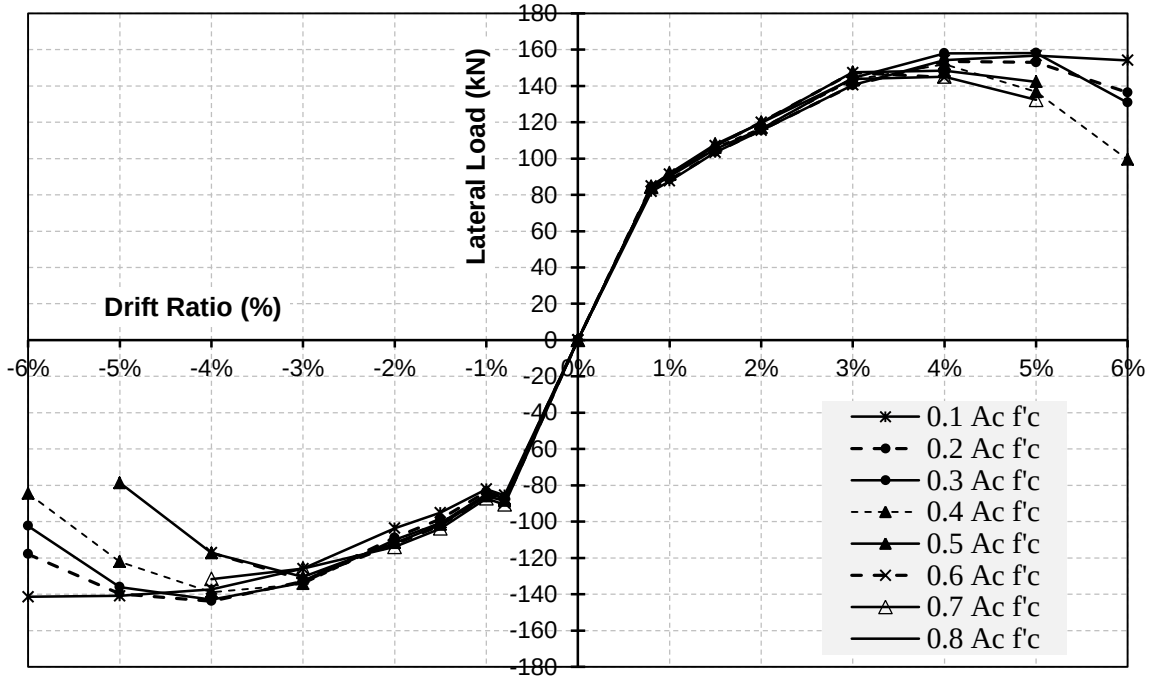

Figure 8.10: Envelopes of the hysteretic behaviour of specimens

Figure 8.11 shows the maximum lateral load resisted by the beam tip at different axial load levels on the column. The figure shows insignificant increase (approximately 3%) in the lateral load resistance by increasing the axial load up to the level of 0.3 $A_c\ f_c'$. By

increasing the axial load over 0.3 $A_c\ f_c'$, the models exhibited a drop in the lateral resistance by 10% up to an axial load level of 0.6 $A_c\ f_c'$. Finally, at axial load level of 0.8 $A_c\ f_c'$, the drop in the lateral capacity reached 15%.

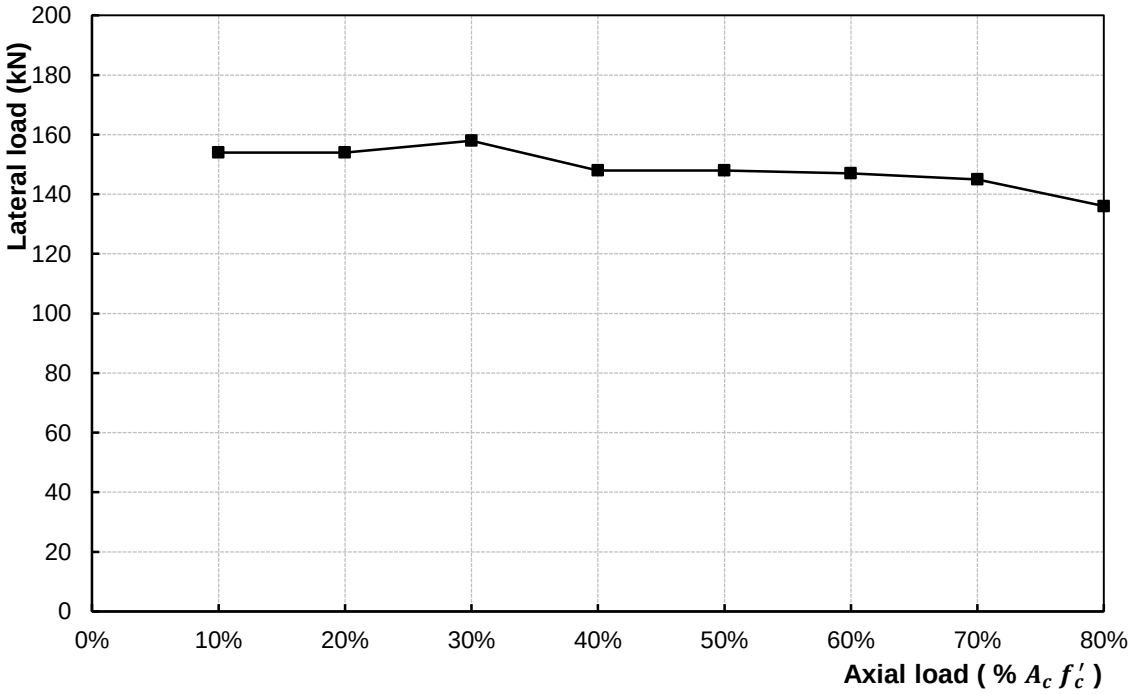

Figure 8.11: Maximum lateral load attained at different axial load levels on column

A better understanding of the influence of the axial load applied on the column cannot be accomplished without discussing the column interaction diagram shown in Figure 8.12. Therefore, it deems necessary to analyze the behaviour of each specimen in conjunction with understanding the interaction diagram. Although research in the area of FRP-RC columns is still in its early stages, the interaction diagram was calculated in accordance with the procedure reported by Choo et al. (2006).

The flexural strength ratio of a specimen can be calculated as:

$$R = (M_{rc,\,top} + M_{rc,\,bott}) \div M_{rb} \qquad [8.1]$$

Where

$M_{rc,\,top} = M_{rc,\,bott}$: Flexural capacity of the column cross-section above and below the joint. The flexural capacity of the column sections above and below the joint are assumed to be equal while neglecting the extra axial load applied on the lower part of the column from the beam;

M_{rb}: Flexural capacity of the beam cross-section which is equal to 330 kN.m;

Based on the previous definition, the equation above can be re-arranged to be:

$$R = M_{rc,\,top} \div (M_{rb} / 2) \qquad [8.2]$$

$$R = M_{rc,\,top} \div (165) \qquad [8.3]$$

This in turn defines the area on Figure 8.12 where the strong column-weak beam concept is applied and the flexural strength ratio exceeds 1.0. Accordingly, the flexural strength ratio increases by increasing the axial column loading where the column reaches the maximum flexural capacity at approximately axial level of 0.3 $A_c\ f_c'$, then it drops down by increasing the axial load level. This increase in the flexural strength ratio explains the increase in the lateral resistance reported before in Figure 8.11. Afterwards, increasing the axial level above 0.3 $A_c\ f_c'$ reduces the flexural capacity of the column and consequently the flexural strength ratio of the models.

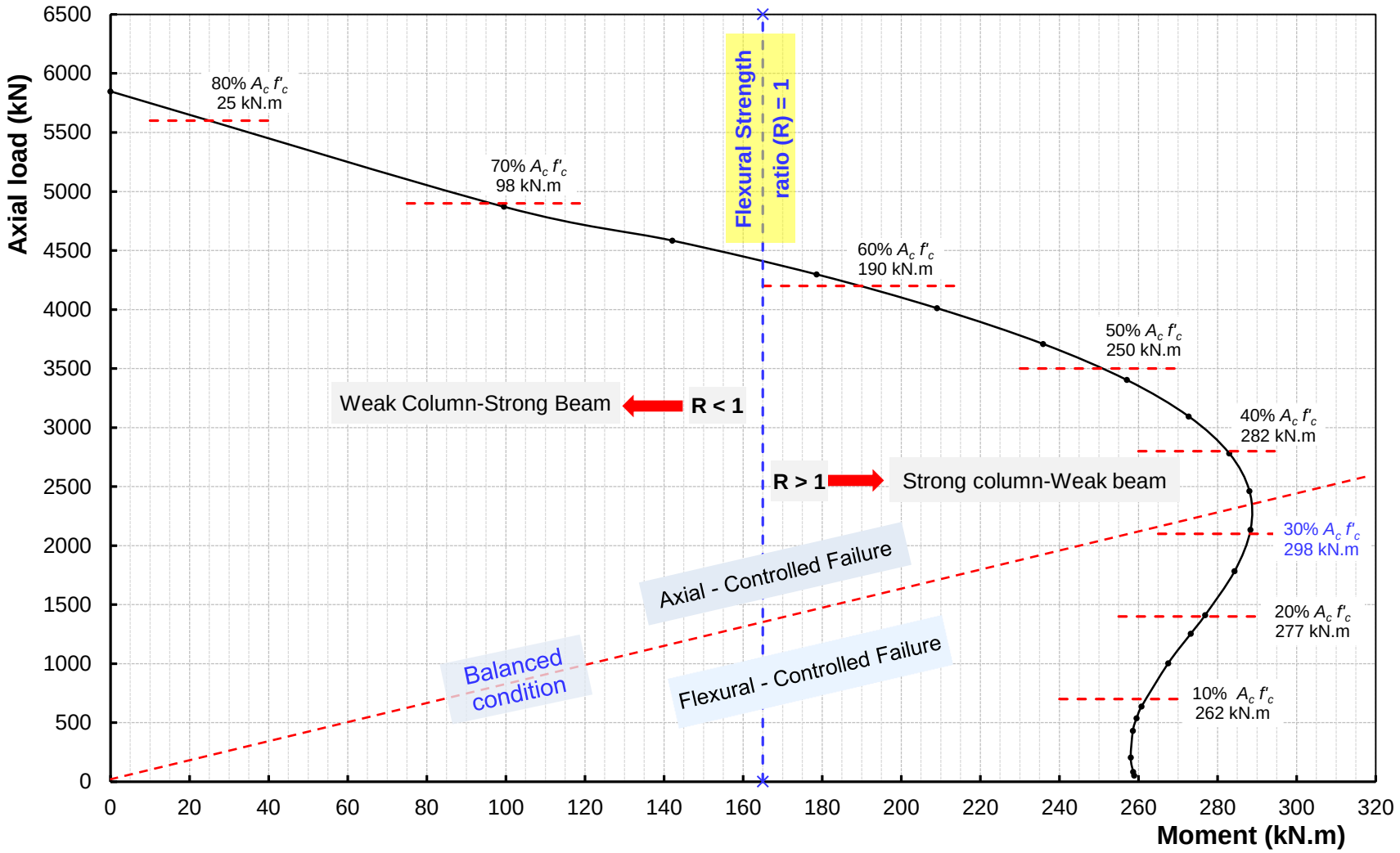

Figure 8.12: Calculated moment-axial interaction diagram of the column

Furthermore, increasing the axial load level over 0.6 $A_c\ f_c'$ shifted the behaviour from the strong column-weak beam to the weak column-strong beam as the flexural strength ratio dropped below 1.0 as shown in Figure 8.12. This is in agreement with the drop in lateral resistance of the beam tip reported before in Figure 8.11 in those models subjected to axial load level of 0.7 $A_c\ f_c'$ and 0.8 $A_c\ f_c'$. The mode of failure exhibited in those two models was flexural failure in the column cross section, as shown in Figure 8.13, where the strain in the concrete exceeded the ultimate compressive strain of the concrete.

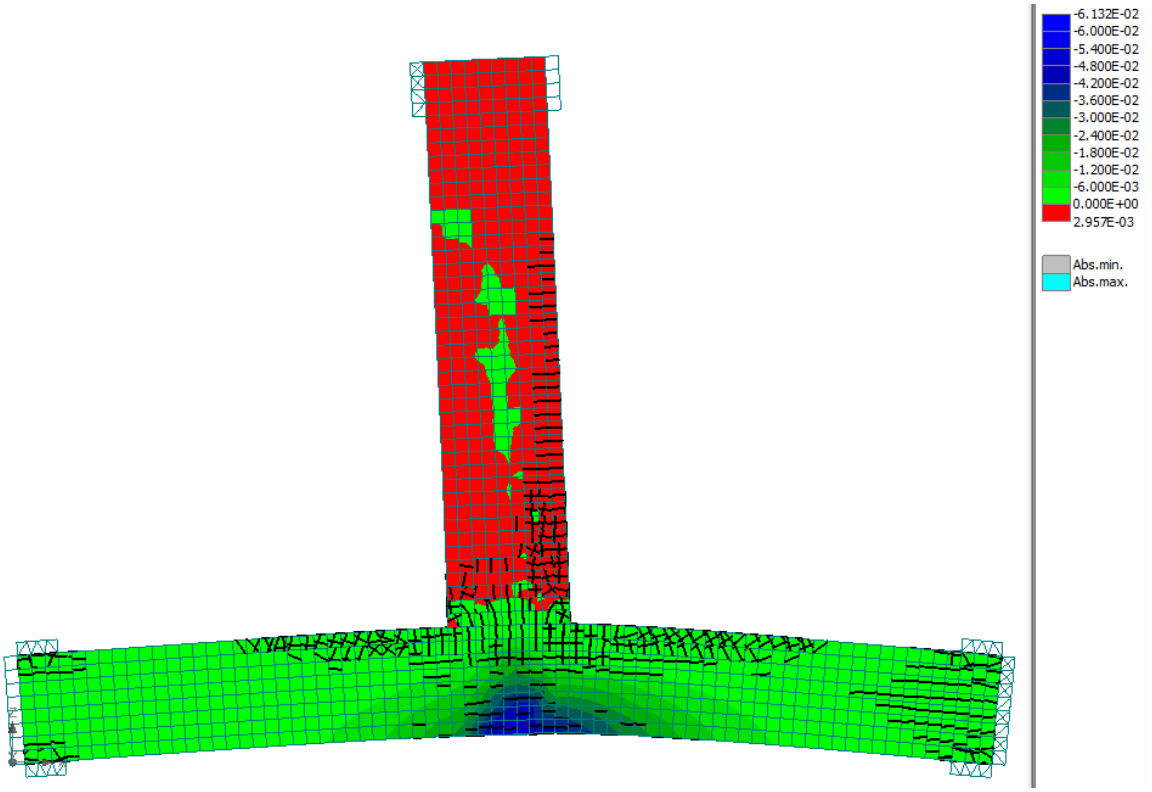

Figure 8.13: Plastic strains (X-X direction) and cracking pattern on the deformed shape of the model 0.8 $\boldsymbol{A_c\ f_c'}$ at failure

Figure 8.14 shows the contribution of the shear distortion in the joint to the total drift angle when the column is subjected to different levels of axial loading. The figure shows that increasing the axial load slightly reduces the shear distortion in the joint when the drift ratio is kept below 2.0%. At 4.0% drift ratio, the reduction in the joint distortion can be observed by increasing the axial load level up to 0.3 $A_c\ f_c'$, then the joint distortion showed no change up to an axial level of $0.5\ A_c\ f_c'$. Further increase in the column axial load increased the distortion in the joint to the point it represented more than 20% of the 4.0% drift angle. Similar behaviour is observed at 5.0% drift ratio; however, with significant increase in the joint distortion to reach up to 50% of the drifting angle at an axial load level of $0.6\ A_c\ f_c'$. It should be noted that the higher values of join shear distortion are in agreement with larger pinching distances in the hysteretic behaviour of the models, Figure 8.9, at loading drifts above 4.0% drift ratio.

The drop in the joint distortion at 4.0% and 5.0% drift ratio when the axial load level exceeds $0.6\ A_c\ f_c'$ is in good agreement with the interaction diagram of the column. It is attributed to the change of the mode of failure to be in the column rather than in the joint for those models having a flexural strength ratio less than 1.0.

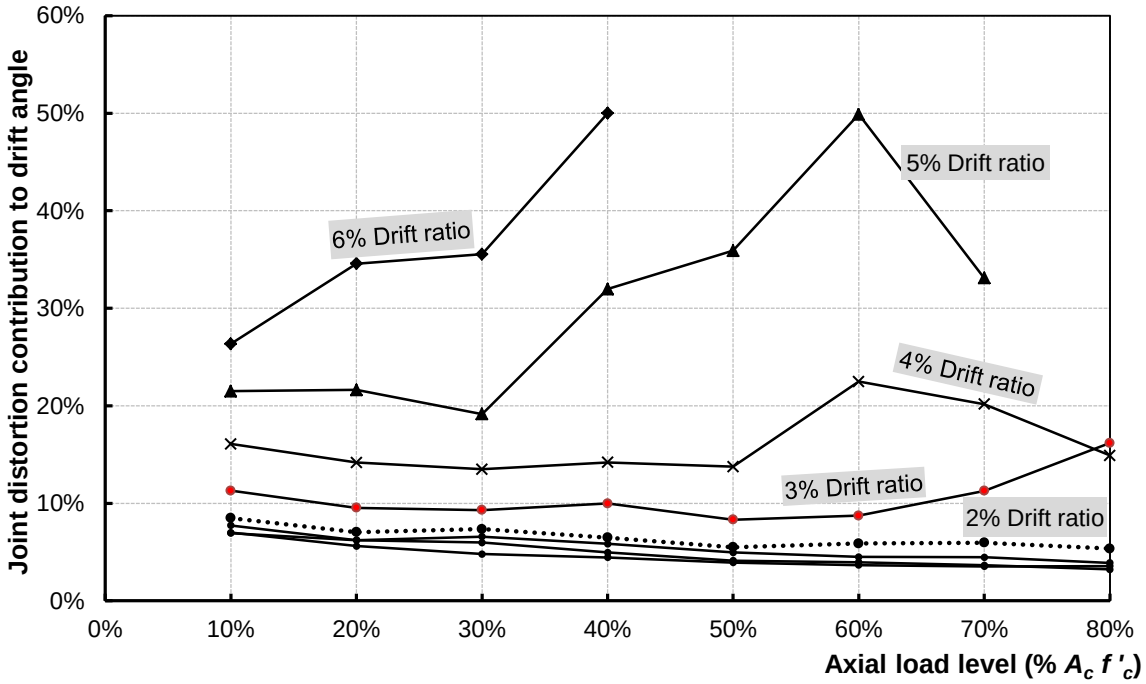

Figure 8.14: Contribution of joint distortion to total drift angle at different axial load levels

8.2.4 Applied Shear Stress in the Joint

As explained earlier in the analysis and discussion of the experimental test results, cyclic shear stress in the joint influences the degradation rate of concrete strength in the joint as a result of the development and propagation of cracks in the joint. Taking into account that the joint is part of the column, degradation of concrete inside the joint core jeopardizes the axial capacity of the column to carry the gravity loads. This in turn may lead the structure to collapse. Furthermore, the research in the field of GFRP-RC column is still in its early stages with very few research studies (*Sharbatdar* 2003, *Choo et al.* 2006, and *De Luca et al.* 2010). Therefore, it is deemed necessary to study the influence of the shear stress applied in the joint on the axial capacity of the column in exterior beam-column joint after surviving a seismic event.

Concrete strength and the level of shear stress applied in the joint are known to affect the axial degradation in the joint as a result of shear distortion. As shown in Figure 8.1, a combination of three different concrete strengths (30, 50, and 80 MPa) and three shear stress levels ($0.7\sqrt{f'_{cu}}$, $0.85\sqrt{f'_{cu}}$, and $1.0\sqrt{f'_{cu}}$) resulted in a series of nine specimens. The nine specimens were divided into three groups (A, B, and C) based on the shear stress in the joint; where concrete strength is the variable in each group. For example, Group (A) has three specimens where the joint is subjected to a constant shear stress ($1.0\sqrt{f'_{cu}}$) and the concrete strength varied from 30 MPa through 50 MPa to 80 MPa.

The methodology applied to study this parameter followed the steps below;

- Determining the original capacity of three columns under pure axial loading; the columns are typical in dimensions and reinforcement but are modeled using concrete strengths of 30, 50, and 80 MPa;
- Apply lateral drift loading up to 4.0% drift ratio on the beam-column joint specimen while the column is subjected to a constant axial load approximately equal to 0.1 $A_c\ f'_c$. The lateral loading drifts were similar to the one used in the experimental part of this study; however, only one cycle at each drift ratio was applied;
- Stop the lateral drift loading and apply axial load on the column up to failure to detect the residual capacity of the column after sustaining the lateral loading.

The results of the analytical models are presented in form of the envelope of the hysteric behaviour, the permanent shear distortion developed in the joint, axial capacity of the column after applying the simulated lateral loading history relative to the original capacity before the application of lateral load.

Figure 8.15 shows the axial load-axial shortening relationship of the typical column used in all specimens which has a cross-section of 350 mm in width and 400 mm in depth and a height of 3650 mm. Hinged boundary conditions of the column ends were used similar to those used in the verification process. The results of the ATENA-3D finite element models for the intact columns showed that the axial capacity of the column reached 4250, 6920, and 9580 kN when the concrete strength was 30, 50, and 80 MPa, respectively. It was found that the column capacity under pure "concentric" axial loading is approximately equal to 85% $A_c\ f_c'$, where (A_c) is the column cross-sectional area (350 mm in width by 400 mm in depth) and (f_c') is the concrete strength. These results are in good agreement with the experimental test results of De Luca et al. (2010) of GFRP reinforced concrete columns.

Figure 8.16 shows the permanent shear distortion deformation in the joint after the specimen sustained lateral loading drifts up to 4.0% drift ratio. The figure shows the permanent distortion in the joint increases by increasing the shear stress in the joint. Moreover, specimens modeled with lowest concrete strength (30 MPa) exhibited the highest permanent shear deformation in the joint, while those with higher concrete strength showed lower values of shear permanent deformation in the joint.

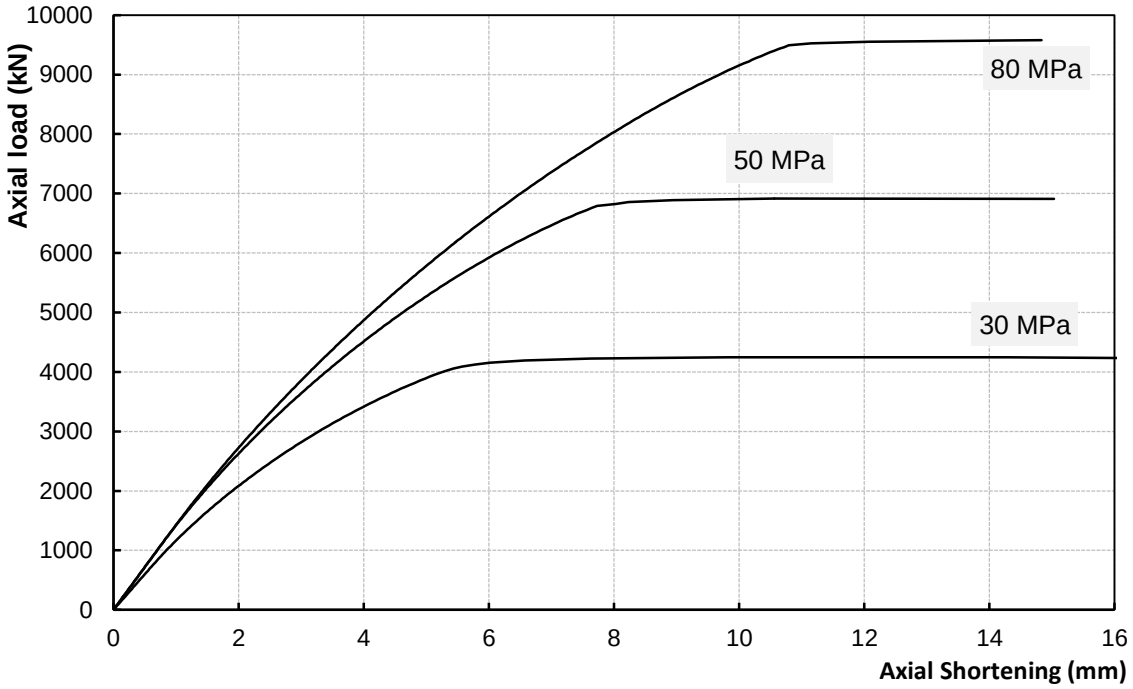

Figure 8.15: Original axial capacity of the column using different concrete strengths

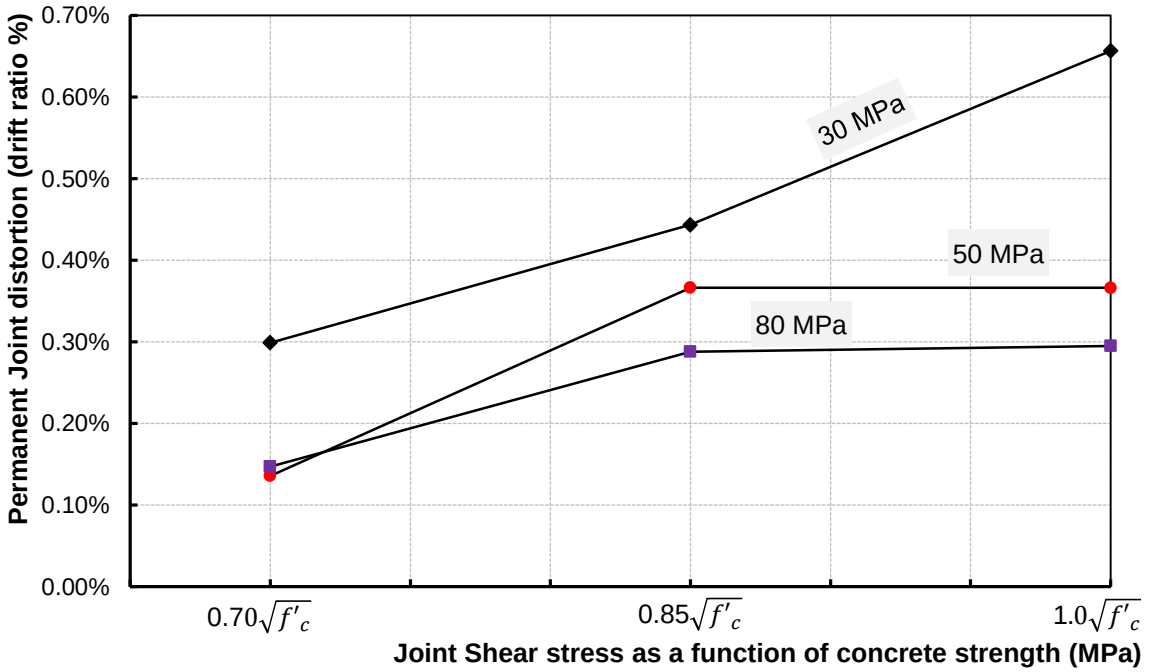

Figure 8.16: Permanent distortion in the joint after sustaining lateral displacement of 4.0% drift ratio

Figure 8.17 shows the column axial capacity after the specimens were subjected to lateral drifts up to 4.0% drift ratio. The figure shows that the axial capacity of the columns significantly dropped as a result of the shear stresses affected the joint. It is shown that the column loses 25% to 30% of its original capacity for specimens with concrete strength of 30 MPa. Furthermore, the loss in the axial capacity was between 45% and 50% in those specimens modeled with higher concrete strength, 50 MPa and 80 MPa. Accordingly, the loss in capacity was higher in those specimens modeled with higher strength concrete. This can be attributed to that higher strength concrete requires higher amount of transverse reinforcement for confinement. The figure also shows that the influence of shear stress in the joint was not significant on the residual axial capacity of the column; however, more experimental research is still required to assess the residual axial capacity of GFRP reinforced concrete columns after surviving a seismic event.

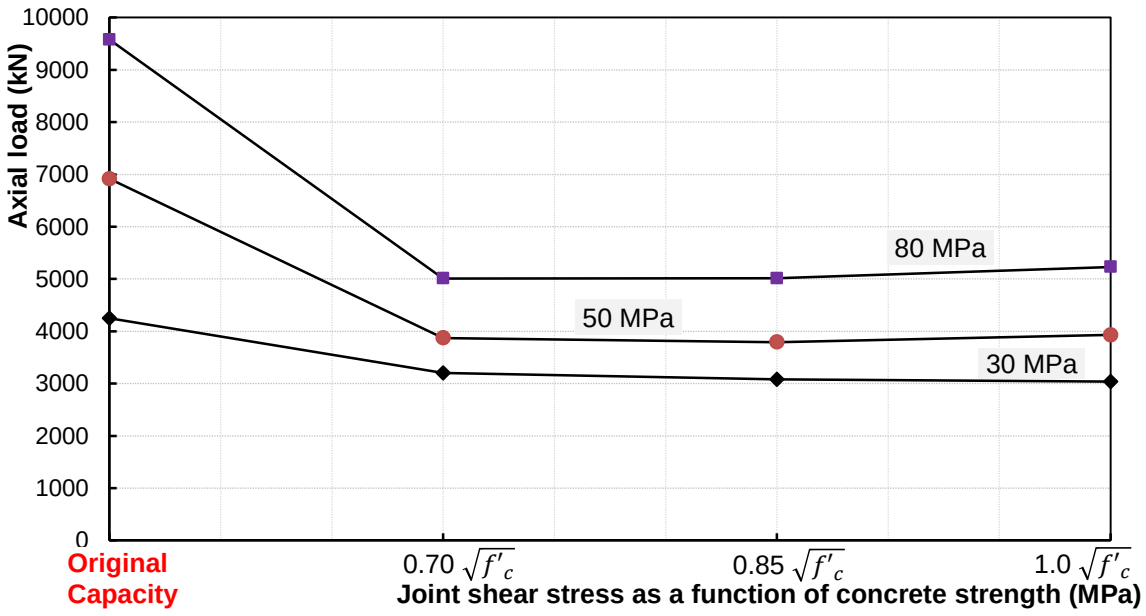

Figure 8.17: Column axial capacity after applying different shear stress level in the joint

CHAPTER 9

EVALUATION OF THE CSA/S806-12 SEISMIC PROVISIONS

9.1 GENERAL

As per the CSA/S806-12, Clause 12.2, it is required that earthquake resistant buildings reinforced with FRPs to be designed by recognizing the mechanical characteristics of FRP that may result in different strength, stiffness, damping, and seismic force resistance characteristics of structures (CSA 2012). These characteristics include lack of ductility, lower modulus of elasticity, higher ultimate strength, and substantially different bond characteristics. In this section, an evaluation of the relevant seismic provisions provided in the Canadian Standard CSA/S806 will be discussed. The general objective of this discussion is to track areas of ambiguity and lack of knowledge related to the use of the GFRP reinforcement in SFRS. The discussion focusses on those clauses related to the seismic design of GFRP-RC moment resisting frames in new construction. Moreover, recommendations and suggestions were proposed for additional provisions that need to be implemented in the CSA/S806 next edition.

9.2 DESIGN REQUIREMENTS REGARDING FAILURE INITIATED BY CONCRETE CRUSHING IN COMPRESSION ZONE FOR ELEMENTS SUBJECTED TO PREDOMINANT FLEXURE, CLAUSE 8.2

As discussed previously in Chapter 6 (Section 6.4.1, Figure 6.12), the highest recorded tensile strains in GFRP bars; 17350, 16570, and 16500 micro-strain, were observed in Specimens II-60-0.85, II-60-0.7, and II-30-0.70, respectively. These recorded strains

were greater than the calculated design values by a range of 7% to 16%. These values represent 90.0% to 95.0% of the ultimate tensile strain of the GFRP longitudinal reinforcement. This observation was in a good agreement with the results of the parametric study in Chapter 8, Section 8.2.1, where those specimens with lower ρ_{frp}/ρ_{bal} exhibited strain values that continued to increase after reaching the maximum lateral resistance until exceeded the ultimate tensile strain of the longitudinal reinforcement in the beam section.

Reaching a strain level that is close or equal to the ultimate tensile strain makes the element vulnerable to the undesired sudden failure by rupture of GFRP bars, which is not always allowed by the CSA/S806-12. The CSA/S806-12, Clause 8.2, requires that all FRP-RC sections shall be designed in such a way that failure of the section is initiated by crushing of the concrete in the compression zone except in cases where the factored resistance of a section is greater than 1.6 times the effect of factored loads. This exception is not realistic in seismic resistant frames where uncertainty of seismic loads is a concern.

On the contrary, the CSA/S806-02 in Clause 8.2 only allows the failure of the section to be initiated by crushing of the concrete in the compression zone. In case of FRP-RC frames under gravity loads, this can be achieved by providing $\rho_{frp}/\rho_{bal} > 1.0$ (where ρ_{frp} is the provided FRP reinforcement ratio and ρ_{bal} is the balanced ratio); however, there is no such requirement that specify how much greater than 1.0 this ratio should be.

Moreover, Series (II) specimens were originally designed according to the CSA/S806-02, Clause 8.2 (at that time CSA/S806-12 was not published) where the ratio ρ_{frp}/ρ_{bal} was larger than 1, as shown in Table 4.4. However, Specimens II-60-0.85, and II-30-0.70 with the lowest ρ_{frp}/ρ_{bal} values (1.42 and 1.5, respectively) exhibited strain values in the longitudinal reinforcement of the beam equal to 90% to 95% of the ultimate tensile strain of the GFRP reinforcement. Accordingly, in moment resisting frames designed to resist seismic forces, it is recommended to set a minimum limit to the ρ_{frp}/ρ_{bal} ratio. Therefore, in light of the experimental and analytical work done in this study, a minimum value of 1.4 can be adopted for GFR-RC element subjected to predominant flexure. This value was also set by the ACI 440.1R-06 (ACI 2006) to guarantee that the failure of the section is controlled by concrete crushing; however, more focused research is still encouraged in this aspect.

9.3 VALUES OF THE DUCTILITY (R_D) AND OVER-STRENGTH-RELATED (R_O) FORCE MODIFICATION FACTORS, CLAUSES 12.4.2.4 AND 12.4.2.5

As per Clause 12.4.2.1 in the CSA/S806-12, the seismic loads for new concrete structures having SFRS that include steel longitudinal and FRP transverse reinforcement, or FRP longitudinal and transverse reinforcement shall be determined in accordance with the relevant provisions of the National Building Code of Canada (*NBC*, 2010) and using the factors specified in Clauses 12.4.2.2 to 12.4.2.5 of the CSA/S806-12. As per the CSA/S806-12, Clause 12.4.2.4 requires that the ductility related factor (R_d) shall be taken equal to 1.0; similar value is assigned for the over-strength-related factor (R_o) in Clause 12.4.2.5.

In general, the values of the (R_d) and (R_o) are obtained from the National building Code of Canada (*NBC*, 2010) - Table 4.1.8.9; however, only the most common structural systems are identified in that table and have been assigned values for (R_d) and (R_o). In case of an SFRS is not specifically identified in that table, then $R_d = R_o = 1.0$ must be used for design. This requirement is based on the assumption that systems that are not described in Table 4.1.8.9 should be designed conservatively (*NBC 2010 Structural Commentaries*, 2010). As a result, FRP-RC seismic force resisting systems designed according to the CSA/S806-12 are not addressed in Table 4.1.8.9 in the NBC 2010 because of the lack of research and experimental data in this field. Therefore, the CSA/S806-12 in Clauses 12.4.2.4 and 12.4.2.5 requires that (R_d) and (R_o) shall be taken equal to 1.0. If it can be demonstrated through testing, research, and analysis that the performance of a structural system is at least equivalent to that of an SFRS listed in Table 4.1.8.9, then Clause 4.1.8.9(5) in the NBC 2010, allows the values for the equivalent listed SFRS to be used.

The most common approach for establishing the appropriate value of (R_d) factor is through experimental testing of prototypes, which simulate the structural system under increasing cyclic reversed deformations until the capacity is reached. The subsequent evaluation of test results and analysis of building configurations incorporating those prototypes is then used to determine the expected building performance and the overall displacement ductility capacity as reported by Mitchell and Paultre (1994) and Rahgozar and Humar (1998). Regarding the over-strength-related factor (R_o), it can be determined based on the research reported by Mitchell et al. (2003).

Caution has to be exercised to ensure that minimum reliable values of the various component factors are used. Some of these factors may be determined from further evaluation of the test results used in the process of determining (R_d) and should be based on assumptions that are compatible with those test results. The (R_o) determined through this process must be comparable to that for the equivalent system listed in Table 4.1.8.9 in the NBC 2010. However, evaluation of the (R_d) and (R_o) factors is out of the scope of this study. Further research is encouraged to determine these factors.

9.4 METHODS OF ANALYSIS AND PROPORTIONING OF STRUCTURAL MEMBERS

The National building code of Canada (NBC 2010) in Clause 4.1.8.7 specifies that the analysis for design of earthquake actions shall be carried out in accordance with the Dynamic Analysis Procedure described in Clause 4.1.8.12; except that, the Equivalent Static force Procedure may be used when some conditions are met. Clause 4.1.8.12 states that the Dynamic Analysis Procedure shall be carried out either by using the Linear Dynamic Analysis (Modal Response Spectrum Method or Numerical Integration Linear Time History Method) or by using the Non-Linear Dynamic Analysis, which requires a detailed study to be performed.

The Linear Dynamic Analysis methods are commonly used in the structural analysis of seismic forces. The structural modelling shall be representative of the structure mass and the stiffness of all elements and shall account for the effect of cracked sections in the SFRS elements as per Clause 4.1.8.3(8) in the NBC 2010. The CSA/A23.3-04 (CSA,

2004) addresses the effect of the cracked sections on the stiffness of steel-RC elements in Clause 21.2.5.2.1. This clause provides reduced section properties of elements that shall be used for the purpose of determining forces and deflections in the SFRS. The values of the effective section property are given as a fraction of the gross section Inertia (I_g). For example, beams are assigned a value of 40% of their (I_g), slab-frame elements are assigned a value of 20% of (I_g), walls and columns are assigned different values based on the level of the axial load applied on them.

On the other hand, the CSA/S806-12 does not address this important analysis criterion in its seismic provisions; this is attributed to the lack of research and experimental data in this field. Research studies investigating the use of GFRP reinforcement in SFRS need to target these areas of ambiguity and lack of knowledge. As discussed before in this study, Chapter 5 – Section 6, the effective stiffness of the cracked beam section was found to be approximately between 25% to 40% of the original stiffness calculated based on the gross inertia of the un-cracked sections. Accordingly, this observation addresses that part related to the effective properties of cracked beam sections in SFRS. However, more research is still required to address this issue for the other structural elements that are part of an SFRS such as walls, columns, coupling beams, and slabs.

9.5 SHEAR RESISTANCE OF EXTERIOR JOINTS IN GFRP-RC MOMENT RESISTING FRAMES

Development of inelastic rotations at the faces of joints connecting the beams and columns in moment resisting frames is associated with strains in the beam flexural

reinforcement anchored in that joint. Consequently, a shear force is generated in the joint. If the joint is not detailed and designed to have adequate capacity against that shear stress, failure of the joint will jeopardize the integrity and stability of the whole structure. Accordingly, design of moment resisting frames cannot be carried out adequately when the shear capacities of the joints are not determined.

Research studies on joints (*Meinheit and Jirsa*, 1977) indicated that shear strength was not significantly influenced by joint transverse reinforcement. Accordingly, the CSA/A23.3-04 set the strength of the joint in steel-RC moment resisting frames as a factor of the compressive strength of the concrete while fulfilling a minimum amount of transverse reinforcement in the joint (Clause 21.5.4). On the other hand, although the CSA/S806-12 allows the use of FRP stirrups in SFRS columns and specifies the amount and spacing of transverse reinforcement that should be provided along the column and through the joint (Clause 12.7.5.2), it surprisingly does not specify the shear capacity of the joint when such amount of transverse reinforcement is provided. Such lack of information does not allow for adequate design to be carried out and subsequently limits the implementation of FRP reinforcement as a non-corrodible sustainable reinforcement in new construction. This is attributed again to the lack of research and experimental data in this field.

One of the main objectives of this study, when started in year 2010, was to address this issue and test the shear capacity of the joints when the amount of transverse reinforcement required by Clause 12.7.1, Equation 12-7, in the CSA/S806-02 (CSA, 2002) is provided. This study started in year 2010 before publishing the CSA/S806-12

which was published by the end of year 2012. Equation 12-7 in the CSA/S806-02 was included in the CSA/S806-12 under Equation 12-4 in Clause 12.7.3.3 with some differences that will be discussed in this section. The equation is given in the CSA/S806-02 as follows:

$$A_{Fh} = 14\, s\, h_c \frac{f_c^{'}}{f_{Fh}} \left(\frac{A_g}{A_c} - 1\right) \frac{\delta}{\sqrt{K_c}} \frac{P_f}{P_{ro}} \qquad \text{[Eq. 9.1]}$$

where; $\frac{P_f}{P_{ro}} \geq 0.2$, $\left(\frac{A_g}{A_c} - 1\right) \geq 0.3$;

$K_c = 0.15 \sqrt{\frac{h_c}{s}\frac{h_c}{s_l}}$ ➔ For rectilinear transverse reinforcement;

A_{Fh}: Area of rectangular FRP hoop reinforcement in each cross-sectional direction;

S: Spacing of transverse reinforcement;

h_c: Cross-sectional dimension of column core;

$f_c^{'}$: Specified compressive strength of concrete;

f_{Fh}: Design stress level in FRP transverse confinement reinforcement which is equal to the smaller of 0.004*E* or ϕ_F * f_{FU}; where (*E*) is the elastic modulus of FRP reinforcement, (ϕ_F) is the resistance factor of FRP reinforcement, and (f_{FU}) is the ultimate tensile strength of the FRP reinforcement;

A_g: Gross area of section;

A_c: Cross-sectional area of the core of a compression member measured to the centreline of the perimeter hoop or spiral;

δ: Design lateral drift ratio which shall not be less than 0.03;

P_f: Factored axial load;

P_{ro}: factored axial load resistance at zero eccentricity;

K_c: Confinement coefficient;

S_l: Spacing of tie legs or the spacing of grid openings in the cross-sectional plane of the column

The CSA/S806-12 utilized the same equation with minor changes in the definition of the terms used in the previous version of this standard (*CSA* 2002) as follows:

(P): is used instead of (P_f), where (P) is the specified axial load;

(P_o): is used instead of (P_{ro}), where (P_o) is the nominal unconfined axial load capacity of column and taken as $\propto_1 f_c^{'}$ (A_g-A_F) for columns with FRP longitudinal reinforcement, where ($f_c^{'}$) is the area of FRP longitudinal reinforcement and ($\propto_1$) is the rectangular stress block parameter;

f_{Fh}: has been re-evaluated to be equal to the smaller of **0.006 *E*** or $\phi_F * f_{FU}$ instead of the smaller of **0.004 *E*** or $\phi_F * f_{FU}$ in the previous version of this standard (CSA 2002);

δ: has been modified as per Clause 12.7.5.2. It is given equal to 0.04 for SFRS subjected to high seismic activity [$I_E F_a S_a(0.2) > 0.75$ as defined in the NBC 2010] and 0.025 for SFRS subjected to lower seismic activity [$I_E F_a S_a(0.2) < 0.75$ as defined in the NBC 2010] instead of 0.03 in the previous version of this standard.

It can be observed that the minimum value of the ratio ($^{P}/_{P_o}$) in the current standard (CSA/S806-12) is kept unchanged and similar to the one given in the previous version (CSA/S806-02). Therefore, it makes no difference to the required area of the transverse reinforcement. Calculation of the ratio between the values of f_{Fh} and δ in the previous version of the standard (0.004*E* and 0.03) and those in the current one (0.006*E* and 0.04), shows that the equation in the CSA/S806-02 is more conservative. Equation 12-7 in the CSA/S806-02 gives an area of transverse reinforcement (A_{Fh}) that is 12.5% higher than the value obtained using its counterpart in the CSA/S806-12, as shown in Equation 9.2 below. Eventually, the difference between the two equations is insignificant; however, it is recommended to follow the conservative side when it is related to the shear capacity of the joint in which failure can jeopardize the integrity of the whole structure.

$$\left[\frac{\delta}{f_{Fh}}\right] \text{ in S806-02} \div \left[\frac{\delta}{f_{Fh}}\right] \text{ in S806-12} = [0.03/0.004] \div [0.04/0.006] = 1.125 \quad \text{[Eq. 9.2]}$$

Test results of Series (II) specimens showed that each two specimens having the same level of shear stress in the joint exhibited the same level of tensile strain in the joint stirrups at the end of the test regardless the drift ratio at which the test was stopped due to the joint failure. This indicates that Equation 12-7 in the CSA-S806-02 accurately proportions the transverse reinforcement in the joint which results in exhibiting the same level of strains in stirrups under the same level of shear stress considering the difference in concrete strength and transverse reinforcement ratio.

With respect to determining the shear capacity of the GFRP-RC joints, test results of Series (II) specimens and the structural evaluation carried out according to the ACI 374.1-05 show that all specimens exhibited satisfactory performance at 4.0% drift ratio except for Specimens II-30-1.0 and II-60-1.0 subjected to high shear stress in the joint ($1.0\sqrt{f'_c}$). The load-drift relationships for these two specimens showed that they were unable to reach the design flexural capacity of the beam and the high shear stress in the joint accelerated strength degradation and failure of the specimens. Also, for both specimens, the cracking pattern in the joint showed excessive damage to the joint core compared to their counterparts with lower shear level in the joint. In addition, the tensile strains developed in the joint transverse reinforcement in Specimens II-30-1.0 and II-60-1.0 exceeded design tensile strength of the stirrups (f_{Fh}) governed by the value of 0.004 *E* (i.e. 4000 micro-strain). The drift component analysis shows that both specimens experienced high levels of joint distortion due to shear deformation in the joint, which resulted in that more than 35% of the sustained drifts were attributed to the distortion occurred in the joint. Therefore, it is evident that GFRP-RC joints cannot sustain a shear stress in the joint equal to $1.0\sqrt{f'_c}$ when Equation 12-7, in the CSA/S806-02 (CSA, 2002) is used to determine the amount of transverse reinforcement in the joint.

Looking into the analysis and behaviour of the two specimens, II-30-0.85 and II-60-0.85, where the joint was subjected to a moderate shear stress ($0.85\sqrt{f'_c}$), it can be observed that both specimens showed satisfactory performance at 4.0% drift ratio. The behaviour of these two specimens can be summarized as follows:

1) Both specimens achieved their flexural design capacity of the beam;
2) Formation of inelastic deformability hinges in the beam section was observed;
3) Concrete deformation and intensity of cracks in the joints at 4.0% drift ratio indicate elastic behaviour of the joint under the specified shear stress;
4) Tensile strain values in the joint transverse reinforcement satisfied the CSA/S806-02 strain limit of 4000 micro-strain as shown in Figures 6.16 (b) and (e);
5) The joint distortion did not exceed 15% of the total drift of the specimens.

All these observations above indicate that the shear capacity of the exterior GFRP-RC joints is $0.85\sqrt{f'_c}$ when Equation 12-7, in the CSA/S806-02 is followed. Further research is still required to address other types of beam-column joints regarding the confinement provided by adjoining members.

9.6 COLUMN-TO-BEAM FLEXURAL STRENGTH RATIO, CLAUSE 12.7.5.1

Formation of plastic hinges in columns during seismic events could lead to instability problems and eventually collapse of the structure. To avoid such problem, the strong column-weak beam concept should be applied in the SFRSs consisting of moment resisting frames. The strong column-weak beam concept allows formation of plastic hinges in beams rather than in columns. This can be achieved by applying a flexural strength ratio greater than one; in other words, the sum of the factored flexural resistances of the column sections framing into a joint, accounting for axial loads, shall exceed the sum of the nominal flexural resistances of the beams framing into the same joint. The CSA/S806-12 adopts this requirement in Clause 12.7.5.1 to avoid formation of plastic

hinges in the columns; however, it does not specify how much greater than 1.0 this value could be.

Looking into the analysis and structural evaluation of Series (II) specimens while considering the elastic linear behaviour of the GFRP reinforcement, Table 6.3 shows the design and the experimental flexural strength ratio for each specimen. The table shows that Specimens II-30-0.85 and II-60-0.85 showed lower experimental flexural strength ratio than the design value. The calculated design flexural strength ratio for Specimens II-30-0.85 and II-60-0.85 was 1.56 and 1.64, respectively. The two specimens achieved higher flexural capacity in the beam and consequently the experimental flexural strength ratio dropped to 1.46 for both specimens, assuming no change in the flexural capacity of the columns. This drop in the flexural strength ratio represents 7% and 11% of the original calculated design flexural strength ratio.

In light of these results, testing a specimen with a design flexure strength ratio that is greater than 1.0 and less than 1.1 could have dropped below 1.0 in the experimental testing allowing for formation of inelastic deformability hinges in the column and collapse under the gravity loads applied to the column. Therefore, it is sought that in the design of FRP-RC SFRS a stringent value higher than 1.0 should be used for the flexural strength ratio. This is required to establish a transition zone between the strong column-weak beam and the strong beam-weak column. Establishing this transition limit will guarantee formation of inelastic deformability hinges in the beams rather than in

columns. The minimum value of 1.4 used in this study for the flexural strength ratio could be used as a guideline until further research is carried out.

CHAPTER 10

CONCLUSIONS AND FUTURE WORK

10.1 SUMMARY

This research study investigated the seismic behaviour of the GFRP-reinforced concrete exterior beam-column joints. The behaviour was studied experimentally using full-scale T-shaped concrete specimens as well as analytically through finite element modelling. In the experimental phase, two series of specimens, (I) and (II), were constructed and tested to failure. Series (I) consisted of four specimens reinforced with GFRP bars and steel stirrups. The main objective of Series (I) was to investigate the anchorage detailing of longitudinal beam reinforcement inside the joint. The main variables in Series (I) specimens were the anchorage type of the beam longitudinal reinforcement (using either bent bars or headed bars) and the reinforcement surface condition (using either deformed/ribbed bars or sand-coated bars). Series (II) consisted of six specimens reinforced with GFRP bars and stirrups. The main objective of Series (II) was to evaluate the shear capacity of the joint. The main variables were the shear stress level in the joint ($0.70\sqrt{f'_c}$, $0.85\sqrt{f'_c}$, and $1.0\sqrt{f'_c}$) and the concrete strength (30 MPa and 60 MPa).

In the analytical phase, a commercial finite element software (ATENA-3D) was used to run a parametric study that investigated the geometry of the joint (presence of lateral beams), axial load on the column, applied shear stresses in the joint, and the concrete strength. The efficiency and accuracy of the finite element modelling was verified against

the experimental results obtained from the experimental phase before conducting the parametric study.

The following sections include the main conclusions drawn from the experimental and analytical phases and future work in this area.

10.2 CONCLUSIONS

In light of the experimental and analytical work carried out in this study, the following conclusions can be drawn.

10.2.1 Conclusions from the Experimental Testing of Series (I) Specimens

1) All specimens exhibited lower resistance in the negative direction of loading (pulling) than that in the other loading direction (pushing), which is common behaviour in cyclic reversed loading due to repetitive tensile-compressive stress cycles of the concrete section. The difference in the resistance values between the two loading directions ranged from 8% to 14%;

2) Both anchorage types (bent bars and headed bars) and reinforcement surface condition had insignificant influence on the energy dissipation up to 4.0% drift ratio. However, specimens with bent bars sustained higher drift ratios, which resulted in higher energy dissipation, yet, at higher drift ratios;

3) Specimens I-H-D and I-H-S reinforced with headed bars exhibited failure due to anchorage slippage at approximately 5.0% drift ratio while Specimens I-B-D and I-D-S did not experience such failure and sustained loading drifts up to 6.0% and 7.0%, respectively. Yet, the anchorage performance of the headed bars was satisfactory and enabled the specimens to pass the 4.0% drift ratio safely without any signs of anchorage slippage failure;

4) The maximum tensile stress resisted by the headed bars was 930 and 620 MPa in Specimens I-H-S and I-H-D, respectively. These values represent 70 and 56% of the ultimate tensile capacity of the bars used in those two specimens, respectively;

5) The reported values of the maximum tensile stresses, 660 and 750 MPa, just before the bent portions in beam longitudinal reinforcement of Specimens I-B-D and I-B-S, respectively, do not represent the maximum anchorage resistance of the 90-degree bent portions. However, these values can be used as a guide for the minimum required anchorage resistance for GFRP bent bars;

6) The maximum tensile stress resisted by the headed bars is 930 and 620 MPa in Specimens I-H-S and I-H-D, respectively. The anchorage performance of sand-coated headed bars outperformed their counterparts with deformed surface by 50% more anchorage capacity. Both headed bars, either with sand-coated or deformed surface, exhibited slippage failure due to failure of anchorage heads by bearing;

10.2.2 Conclusions from the Experimental Testing of Series (II) Specimens

7) Specimens II-30-0.7 and II-60-0.7 exhibited failure after achieving their design lateral resistance and forming inelastic deformability hinges in the beam sections. The failure was due to anchorage slippage of the beam longitudinal headed bars embedded inside the joint. The joints maintained the elastic behaviour with insignificant elastic cracking;

8) Specimens II-30-0.85 and II-60-0.85 showed a stable behaviour while exceeding their design lateral resistance and forming the inelastic deformability hinges in the beam section up to loading drifts of 5.0% and 6.0%, respectively. Thereafter, the joint experienced diagonal shear failure at 6.0% and 7.0%, respectively;

9) Specimens II-30-1.0 and II-60-1.0 recorded the highest lateral load resistance in comparison with their counterparts in Series (II). On the other hand, they were the first specimens to fail. The high shear stress level ($1.0\sqrt{f'_c}$) in the joints of these two specimens accelerated their failure and prevented them from reaching their design lateral resistance and sustaining higher loading drifts. The reported shear failure in the joints raises the demand to limit the shear stress in the joint to avoid such failures which can jeopardize the integrity of the structure;

10) Increasing the concrete strength in specimens II-60-xx compared to their counterparts, specimens II-30-xx, did not significantly increase the lateral resistance capacity. The increase in the lateral capacity was reported to be

approximately not more than 10% at the same loading drift. On the other hand, it increased the sustained drift ratio by approximately 40%;

11) The concrete strength influenced the formation of the inelastic deformability hinges in the beam section. In specimens constructed with normal concrete strength, II-30-xx, the inelastic deformability hinge in the beam took the form of a flat surface with crushed concrete, while in specimens constructed with high concrete strength, II-60-xx, the inelastic deformability hinge was shaped as a V-notch;

12) Specimens II-30-0.70, II-30-0.85, II-60-0.70, and II-60-0.85 exhibited maximum tensile strain in the beam longitudinal reinforcement that was approximately 7.0% to 16.0% higher than the calculated values. Similar behaviour was observed in Series (I) specimens and in the finite element parametric study as well. This is attributed to the elastic-linear behaviour of the GFRP reinforcement associated with the ability of sections to continuously change the compression zone dimensions due to spalling of the concrete cover and/or degradation in concrete strength in order to maintain the flexural resistance while increasing the curvature of the section. Accordingly, it deemed necessary to set a minimum value of the ratio ρ_{frp}/ρ_{bal} to avoid reaching a strain level that is close or equal to the ultimate tensile strain, which makes the element vulnerable to the undesired sudden failure by rupture of GFRP bars;

13) Each two specimens, having the same shear stress level in the joint, exhibited similar level of tensile strain in the joint stirrups at the end of the test regardless the drift ratio at which the test was stopped due to the joint failure. Accordingly, the proposed design procedure successfully proportioned the transverse reinforcement in the joint to reach this result considering the difference in concrete strength;

14) Test results of Specimens II-30-0.85, II-30-1.0, II-60-0.85, and II-60-1.0 showed that reaching a tensile strain of 6000 micro-strain in the stirrups confining the joint resulted in diagonal shear failure in the joint. Accordingly, the stress limit (*0.006*E*) in the CSA/S806-12, Clause 12.7.5.2 which refers back to Clause 12.7.3.3, should be revised;

15) The max tensile strains in the stirrup located in the inelastic deformability hinges in the beam section of all specimens were all below 3000 micro-strain until the end of tests which indicates that no shear failure occurred in the beam section during testing;

16) Although Specimens II-30-1.0 and II-60-1.0 showed the highest stiffness in the early stages of loading, high shear stress in the joint accelerated the stiffness degradation of the specimens to the point that they exhibited lower stiffness at the end of the test compared to their counterparts subjected to lower shear stress in the joint;

17) The calculated values for the relative energy dissipation ratio (β) exhibited by Series (II) specimens are in agreement with the pre-stressed concrete modules reported by Stanton and Mole (1994), and Priestley and Tao (1993). Accordingly, it can be concluded that the behaviour of the specimens with respect to the dissipation of energy is more or less satisfactory and equivalent to the pre-stressed concrete structures; however, steel-RC structures outperform the GFRP-RC structures by approximately 2 to 3 times. Although the lower energy dissipation is considered a disadvantage, on the other hand, it means that the connection regains its original shape after removing the loads, thus requiring minimum amount of repair after surviving such loading event

18) Specimens constructed with normal concrete strength (II-30-xx) experienced higher energy dissipation than their counterparts with high concrete strength (II-60-xx) at the same drift ratio despite of specimens II-60-xx showed higher lateral load resistance than specimens II-30-xx at the same loading drift. This is attributed to the higher ductility of the normal strength concrete compared to high strength concrete, which is more brittle (less ductile). Therefore, high strength concrete needs more confinement;

19) Specimens II-30-1.0 and II-60-1.0 with the highest shear level ($1.0\sqrt{f'_c}$) recorded significant shear distortion in the joint. The shear distortion in the joints reached 46% and 33% of the total drift angle at 4.0% and 5.0% drift ratio for Specimens II-30-1.0 and II-60-1.0, respectively;

20) The evaluation of the anchorage capacity of GFRP headed bars in Specimens II-30-0.70 and II-60-0.70 showed that the bars were able to resist 65% and 74%, respectively, of the ultimate tensile strength of the bars just before failure of the anchorage heads;

21) Two modes of failure in the anchorage heads were observed; the shear stress in the joint influenced these modes of failure. The first mode of failure occurred due to failure in the interface between the bar and the head due to shearing-off of the bar ribs in contact with the head. This mode of failure was observed in those specimens where the joints were subjected to low shear stress ($0.70\sqrt{f'_c}$) and experienced elastic behaviour with no damage until the end of the test. The second mode of failure occurred due to splitting of the anchorage head bearing base in those specimens exhibited shear diagonal failure and significant cracking in the joint by the end of the test;

22) In light of the experimental results in this study, the relevant seismic provisions in the CSA/S806-12 were evaluated and some recommendations were proposed for consideration in the future updates of the CSA/S806-12 as presented in Chapter 9;

10.2.3 Conclusions from the Analytical work and the parametric study

23) It has been verified that the results of the ATENA-3D finite element modelling were in good agreement with the experimental ones. The hysteretic behaviour of the analytical models matched well those of the experimental in trend and lateral

load resistance. ATENA-3D was able to capture the post-failure behaviour of concrete after reaching the maximum lateral resistance. Up to 2.0% drift ratio, the developed strains in the analytical model showed no deviation from the experimental ones. However, at higher drift ratios, the strain values required magnification by 15% more to match the experimental values;

24) Increasing the concrete strength from 30 to 70 MPa increased the sustained lateral load resistance by 36%. Specimens with lower concrete strength developed their maximum lateral resistance earlier than those with higher concrete strength;

25) The tensile strains in the beam longitudinal GFRP reinforcement continued to increase after reaching the design lateral resistance of the specimens. This is in a good agreement with the laboratory testing observations of Series (I) and (II) specimens. This, in turn, supports the demand to have a minimum limit of the ratio ρ_{frp}/ρ_{bal} to avoid sudden rupture of reinforcement in higher drift ratios;

26) The presence of lateral beams influenced the behaviour of the exterior joints. In terms of lateral resistance, specimens with lateral beams showed approximately 10% increase in the maximum lateral load resistance than that of their counterparts without lateral beams;

27) The presence of lateral beams increased the joint confinement and reduced the rate of concrete degradation in the joint. Specimens with lateral beams sustained

prolonged loading drifts while their counterparts with no lateral beams experienced failure at earlier drift ratios;

28) The confinement provided to the joint by the presence of lateral beams increased the shear capacity of the joint and therefore reduced the shear distortion in the joint to the point that it overcame the influence of increasing the concrete strength in the joint. At 4.0% drift ratio, the presence of the lateral beams reduced the shear distortion by 50%, 50%, and 40% in the finite element models of Specimens II-30-1.0, II-50-1.0, and II-80-1.0, respectively;

29) Increasing the axial load level on the column had no influence on the behaviour of the specimens during loading drifts up to 3.0% drift ratio. Thereafter, increasing the axial load level reduced the ability of the specimens to sustain higher drift ratios;

30) Specimens with axial load level higher than 0.3 A_c f'_c experienced drops in their lateral capacity after 4.0% drift ratio. By increasing the axial load over 0.3 A_c f'_c, the models exhibited a drop in the lateral resistance by 10% and 15% up to an axial load level of 0.6 A_c f'_c and 0.8 A_c f'_c , respectively;

31) For better understanding of the influence of the column axial load on the seismic behaviour of beam-column joints, the significance of the column interaction diagram cannot be ignored. The column interaction diagram defines the levels of

axial load through which the mode of failure of the specimen changes. Therefore, research studies investigating the axial-moment interaction of GFRP-RC columns should be encouraged;

32) The finite element modelling of the GFRP-RC column in this study showed that the capacity under pure "concentric" axial loading is approximately equal to 0.85 $A_c\, f'_c$, where (A_c) is the column cross-sectional area and (f'_c) is the concrete strength. These results were in a good agreement with the experimental test results of De Luca et al. (2010) on GFRP-RC columns;

33) The permanent distortion in the joint increased by increasing the shear stress in the joint. However, increasing the concrete strength reduced such permanent distortion in the joint;

34) The shear stress generated in the joint, during the loading drifts applied up to 4.0% drift ratio, was found to reduce the axial capacity of the column by a range of 25 to 50% of its original capacity depending on the concrete strength of the column.

10.3 FUTURE WORK

The findings of this research present useful experimental and analytical data related to the seismic behaviour of GFRP-RC beam-column joints. This study not only proposed recommendations for additional provisions to be implemented in the CSA/S806 future

edition but also tracked areas of ambiguity and lack of knowledge related to the use of the GFRP reinforcement in Seismic Force Resisting System (SFRS). Based on the findings of the current study, the recommended areas for future research include, but not limited to:

1) Evaluation of the ductility-related factor (R_d) and the over-strength-related factor (R_o) required for calculating the seismic loads on SFRS consisting of FRP-RC moment resisting frames and shear walls;

2) Find out the minimum limit required for the ratio ρ_{frp}/ρ_{bal} in GFRP-RC elements subjected to flexure to avoid rupture of longitudinal reinforcement;

3) Develop methods of analysis and proportioning of structural members reinforced with FRPs considering the effective stiffness of the cracked sections of all structural elements forming the SFRS such as walls, beams, columns, coupling beams, and slab frame elements;

4) Study the behaviour of hybrid seismic resistant systems which consist of steel-RC shear walls and GFRP-RC moment resisting frames. It is thought that such combination of systems magnifies the benefits of the two reinforcing materials by limiting the steel corrosion problems using GFRP-RC moment resisting frames as the main structural system to support gravity loads while using the steel-RC shear walls to absorb the seismic energy;

5) Study the bond characteristics of the GFRP bars subjected to cyclic loading including required over-lap splice length of beam longitudinal reinforcement to avoid bar slippage;

6) Analyze the behaviour of GFRP headed bars in joints considering the required embedment length to achieve bar strength, concrete strength, contribution between bearing strength and bond strength, level of confinement in surrounding concrete;

7) Study the influence of the concrete damage in the joint, due to the applied shear stress in the joint, on the axial capacity of the column after surviving a seismic event;

8) The influence of the transverse slabs and beams on the behaviour of FRP-reinforced beam-column connections;

9) Investigate the behaviour of eccentric beam-column joints;

10) Study the behaviour of the interior and the knee beam-column joints under monotonic as well as under seismic loads;

11) Evaluate the shear resistance of beams and columns subjected to seismic loads.

REFERENCES

1- Abdel-Fattah, B. and Wight, J. K. (1987). "Study of Moving Beam Plastic Hinging Zones for Earthquake-Resistant Design of R/C Buildings," *ACI Structural Journal,* 84 (1): 31-39.

2- Abrams, D. P. (1987). "Scale Relations for Reinforced Concrete Beam-Column Joints," *ACI Structural Journal,* 84 (6): 502-512.

3- ACI Committee 318 (2008). "Building Code Requirements for Structural Concrete (ACI 318-08) and Commentary (318R-08)," *American Concrete Institute,* Farmington Hills, Mich., USA.

4- ACI Committee 374 (2005). "Acceptance Criteria for Moment Frames Based on Structural Testing and Commentary (ACI 374.1-05)," *American Concrete Institute,* Farmington Hills, Mich., USA.

5- ACI Committee 440 (2006). "Guide for the Design and Construction of Concrete Reinforced with FRP Bars (ACI 440.1R-06)," *American Concrete Institute,* Farmington Hills, Mich., USA.

6- ACI-ASCE Committee 352 (1976). "Recommendations for Design of Beam-Column Joints in Monotonic Reinforced Concrete Structures," *ACI Journal, proceedings,* 73 (7): 375-393.

7- ACI-ASCE Committee 352 (1985). "Recommendations for Design of Beam-Column joints in Monolithic Reinforced Concrete Structures," *ACI Journal,* 82 (3): 266-283.

8- Ahmed, E., El-Salakawy, E.F. and Benmokrane, B. (2008). "Carbon Fibre Reinforced Polymer Shear Reinforcement for Concrete Members," *CSCE 2008 Annual conference*, Quebec, QC, Canada, 10 p.

9- Ahmed, E., El-Salakawy, E.F. and Benmokrane, B. (2010-a). "Performance Evaluation of GFRP Shear Reinforcement for Concrete Beams," *ACI Structural Journal*, 107 (1): 53-62.

10- Ahmed, E., El-Salakawy, E.F. and Benmokrane, B. (2010-b). "Fibre-Reinforced Polymer (FRP) Composite Shear Reinforcement: Performance Evaluation in Concrete Beams and Code Prediction," *Canadian Journal of Civil Engineering*, 37 (8): 1057-1070.

11- Alsayed, S. H., Al-Salloum, Y. A., Almusallam, T. H., and Amjad, M. A. (1999). "Concrete Columns Reinforced by Glass Fibre Reinforced Polymer Rods," *ACI special publication*, SP-188: 103-112.

12- ASCE 7 Standard (2010). "Minimum design loads for buildings and other structures," ASCE/SEI 7-10, *American Society of Civil Engineers*, Reston, Virginia, USA.

13- Bigaj A.J. (1999). "Structural Dependence of Rotation Capacity of Plastic Hinges in RC Beams and Slabs," *PhD Thesis*, Faculty of Civil Engineering, Delft University of Technology, Delft, Netherlands, 230 pp.

14- Canadian Standards Association (CSA) (1994). "Design of Concrete Structures," CAN/CSA A23.3-94, *Canadian Standards Association*, Rexdale, Ontario, Canada, 199 p.

15- Canadian Standards Association (CSA) (2002). "Design and Construction of Building Components with Fibre-Reinforced Polymers," CAN/CSA S806-02, *Canadian Standards Association*, Rexdale, Ontario, Canada, 177 p.

16- Canadian Standards Association (CSA) (2004). "Design of Concrete Structures," CAN/CSA A23.3-04, *Canadian Standards Association*, Rexdale, Ontario, Canada. 214 p.

17- Canadian Standards Association (CSA) (2006). "Canadian Highway Bridge Design Code," CAN/CSA S6-06, *Canadian Standards Association*, Rexdale, Ontario, Canada, 733 p.

18- Canadian Standards Association (CSA) (2012). "Design and Construction of Building Structures with Fibre-Reinforced Polymers," CAN/CSA S806-12, *Canadian Standards Association*, Rexdale, Ontario, Canada, 187 p.

19- Cervenka, V., and Niewald, J., (2005). "ATENA-FEMAP User's Guide," *Cervenka Consulting Ltd.*, Prague, Czech Republic.

20- Cervenka, V., Jendele, L., and Cervenka, J., (2012). "ATENA Program Documentation Part 1: Theory," *Cervenka Consulting Ltd.*, Prague, Czech Republic.

21- Cheok, G. S.; Stone, W. C. and Nakaki, S. D., (1996). "Simplified Design Procedure for Hybrid Precast Concrete Connections," *NISTIR 5765, NIST*, Gaithersburg, Md., 81 pp.

22- Choo, C. C., Harik, I. E., and Gesund, H. (2006). "Strength of Rectangular Concrete Columns Reinforced With Fibre-Reinforced Polymer Bars," *ACI Structural Journal*, 103 (3): 452-459.

23- Chun, S. C., Lee, S. H., Kang, T. H. K., Oh, B., and Wallace, J. W. (2007). "Mechanical Anchorage in Exterior Beam-Column Joints Subjected to Cyclic Loading," *ACI Structural Journal*, 104 (1): 102-112.

24- Chung, L. and Shah, S.P. (1989). "Effect of Loading Rate on Anchorage Bond and Beam-Column Joints," *ACI Structural Journal*, 86 (2): 132-142.

25- Comité Euro-International du Béton, (1993). "Ceb-Fip Model Code 1990: Design Code," *Thomas Telford Services Ltd, Thomas Telford House*, London, UK.

26- Debaiky, A.S., Nkurunziza, G., Benmokrane, B., and Cousins, P. (2006). "Residual Tensile Properties of GFRP Reinforcing Bars after Loading in Severe Environments," *ASCE Journal of Composites for Construction*, 10 (5):1-11.

27- De Luca, A., Matta, F., and Nanni, A. (2010). "Behavior of Full-Scale Glass Fiber-Reinforced Polymer Reinforced Concrete Columns under Axial Load," *ACI Structural Journal*, 107(5): 589-596.

28- Durrani, A.J., and Wight, J.K. (1985). "Behaviour of Interior Beam-to-Column Connections under Earthquake-Type Loading," *ACI Journal*, 82 (3): 343-349.

29- Ehsani, M. R. and Wight, J. K. (1985-a). "Exterior Reinforced Concrete Beam-to-Column Connections Subjected to Earthquake-Type Loading." *ACI Journal, proceedings*, 82 (4): 492-499.

30- Ehsani, M. R. and Wight, J. K. (1985-b). "Effect of Transverse Beams and Slab on Behaviour of Reinforced Concrete Beam-to-Column Connections." *ACI Journal, proceedings*, 82 (2): 188-195.

31- Ehsani, M. R., and Alameddine, F. (1991). "Design Recommendations for Type 2 High-Strength Reinforced Concrete Connections," *ACI Structural Journal*, 88 (3): 277-291.

32- Ehsani, M. R., Moussa, A. E., and Vallenilla, C. R. (1987). "Comparison of Inelastic Behaviour of Reinforced Ordinary – and High-Strength Concrete Frames," *ACI Structural Journal*, 84 (2): 161-169.

33- El-Ragaby, A., El-Salakawy, E.F., and Benmokrane, B. (2005). "Finite Element Modeling of Concrete Bridge Deck Slabs Reinforced with FRP Bars," *ACI Special Publication*, 230 (52): 915-934.

34- El-Sayed, A. K., El-Salakawy, E.F., and Benmokrane, B. (2007). "Mechanical and Structural Characterization of New Carbon FRP Stirrups for Concrete Members," *Journal of Composites for construction*, ASCE, 11 (4): 352-362.

35- Fischer, G. and Li, V. C. (2003). "Intrinsic Response Control of Moment-Resisting Frames Utilizing Advanced Composite Materials and Structural Elements," *ACI Structural Journal*, 100 (2): 166-176.

36- Fukuyama, H., Masuda, Y., Sonobe, Y., and Tanigaki, M. (1995). "Structural Performances of Concrete Frame Reinforced with FRP Reinforcement," *Proceeding of the 2nd international RILEM Symposium, Non-Metallic (FRP) Reinforcement for Concrete Structures*, Ghent, Belgium, pp. 275-286.

37- Ghobarah, A. and El-Amoury, T. (2005). "Seismic Rehabilitation of Deficient Exterior Concrete Frame Joints," *Journal of Composites for Construction*, ASCE, 11 (5): 408-416.

38- Grira, M. and Saatcioglu, M. (1999). "Reinforced Concrete Columns Confined with Steel or FRP Grids," *Proceedings of the 8th Canadian Conference on Earthquake Engineering*, Vancouver, Canada, pp. 445-450.

39- Hakuto, S., Park, R., and Tanaka, H. (2000). "Seismic Load Tests on Interior and Exterior Beam-Column Joints with Substandard Reinforcing Details," *ACI Structural Journal*, 97 (1): 11-25.

40- Hanson, N.W. and Connor, H.W. (1967). "Seismic Resistance of Reinforced Concrete Beam-Column Joints," *Journal of the structural division, Proceeding of the American society of civil engineers*, 93(ST5): 533-560.

41- Hasaballa, M. H., (2009). "Seismic Behaviour of Exterior GFRP-Reinforced Concrete Beam-Column Joints," *MSc Thesis*, University of Manitoba, Manitoba, Canada, 195 p.

42- Hasaballa, M.H., El-Ragaby, A. and El-Salakawy, E.F. (2011). "Seismic Performance of Exterior Beam–Column Joints Reinforced with Glass Fibre Reinforced Polymer Bars and Stirrups," *Canadian Journal of Civil Engineering*, 38 (10): 1092-1102.

43- Hassan, T., Abdelrahman, A., Tadros, G., and Rizkalla, S. (2000). "Fibre reinforced polymer reinforcing bars for bridge decks," *Canadian Journal of Civil Engineering*, 27 (5): 839-849.

44- Hollaway, L.C. and Head, P.R. (2001). "Advanced Polymer Composites and Polymers in the Civil Infrastructure," *Elsevier Science Ltd.*, Amsterdam, London, New York, Oxford, Paris, Tokyo. 326 p.

45- Hwang, S., Lee, H., Lioa, T., Wang, K., and Tsai, H. (2005). "Role of Hoops on Shear Strength of Reinforced Concrete Beam-Column Joints," *ACI Structural Journal*, 102 (3): 445-453.

46- IBC Standard (2000). "International Building Code (IBC 2000)," *International Code Council*, Inc., Virginia, USA.

47- IBC Standard (2012). "International Building Code (IBC 2012)," *International Code Council*, Inc., Illinois, USA.

48- ISIS Canada. (2007). "Reinforcing Concrete Structures with Fibre Reinforced Polymers - Design Manual No. 3," *ISIS Canada Corporation*, University of Manitoba, Winnipeg, Canada, 103 p.

49- Jaeger, L.G., Tadros, G., and Mufti, A.A. (1995). "Balanced Section, Ductility and Deformability in Concrete with FRP Reinforcement," *Research Report No. 2-1995, The Nova Scotia CAD-CAM Centre*, 29 p.

50- James, R.J., Rashid, Y.R., Cherry, J.L., Chokshi, N., and Tsurumaki, S. (2001). "Analytic Simulation of the Seismic Failure of a Reinforced Concrete Containment Vessel Model," *SMiRT 16*, Washington DC, Paper # 1807, 9p.

51- LI, Jing. (2003). "Effects of Diagonal Steel Bars on Performance of Interior Beam-Column Joints Constructed with High-Strength Concrete," *Ph.D. Thesis*, The University of Hong Kong, Hong Kong.

52- Li, V.C. (1998). "Engineered Cementitious Composites - Tailored Composites through Micromechanical Modeling," *Fiber Reinforced Concrete: Present and the Future*, *Canadian Society for Civil Engineering*, Montreal, Canada, pp. 64-97.

53- Li, Z.J., Balendra, T., Tan, K.H., and Kong K.H. (2005). "Finite Element Modeling of Cyclic Behavior of Shear Wall Structure Retrofitted using GFRP," *ACI Special Publication,* 230 (74): 1305-1324.

54- Mady, M. H. A., (2011). "Seismic Behaviour of Exterior Beam-Column Joints Reinforced with FRP Bars and Stirrups," *PhD Thesis*, University of Manitoba, Manitoba, Canada.

55- Mady, M., El-Ragaby, A., and El-Salakawy, E. (2011). "Seismic Behavior of Beam-Column Joints Reinforced with GFRP Bars and Stirrups," *Journal of Composites for Construction*, ASCE, 15 (6): 875-886.

56- Mallick, P.K. (1988). "Fiber Reinforced Composites – Materials, Manufacturing, and Design," *Marcel Dekker INC.* New York, 469 p.

57- Meinheit, D. F., and Jirsa, J. O., (1977). "Shear Strength of Reinforced Concrete Beam-Column Joints," *Report No. 77-1, Department of Civil Engineering, Structures Research Laboratory*, University of Texas, Austin, TX, USA.

58- Menegotto, M., and Pinto, P. E., (1973). "Method of Analysis for Cyclically Loaded Reinforced Concrete Plane Frames Including Changes in Geometry and Non-Elastic Behavior of Elements Under Combined Normal Force and Bending," *IABSE Symposium*, Resistance and Ultimate Deformability of Structures Acted on by Well-Defined Repeated Loads, Lisbon, Spain.

59- Menetrey, Ph., Walther, R., Zimmerman, Th., Willam, K.J., Regan, P.E. (1997). "Simulation of punching failure in reinforced concrete structures," *Journal of Structural Engineering*, 123 (5)**:** 652-659.

60- Mitchell, D. and Paultre, P. (1994). "Ductility and Overstrength in Seismic Design of Reinforced Concrete Structures," *Canadian Journal of Civil Engineering*, 21 (6): 1049-1060.

61- Mitchell, D., Tremblay, R., Karacabeyli, E., Paultre, P., Saatcioglu, M., and Anderson, D.L. (2003). "Seismic Force Modification Factors for the Proposed 2005 NBCC," *Canadian Journal of Civil Engineering*, 30 (2): 308-327.

62- Mufti, A. A., Onofrei, M., Benmokrane, B., Banthia, N., Boulfiza, M., Newhook, J. P., Bakht, B., Tadros, G. S., and Brett, P. (2007b), "Field study of glass-fibre-reinforced polymer durability in concrete," *Canadian Journal of Civil Engineering*, 34 (3): 355-366.

63- Murty, C.V.R.., Rai, D.C., Bajpai, K.K., and Jain, S.K. (2003). "Effectiveness of Reinforcement Details in Exterior Reinforced Concrete Beam-Column Joints for Earthquake Resistance," *ACI Structural Journal*, 100 (2): 149-156.

64- National Earthquake Hazards Reduction Program (NEHRP) (1997). "NEHRP Recommended Provisions for Seismic Regulations for New Buildings and Other Structures, Part 1," *Federal Emergency Management Agency (FEMA 302*), Washington, D.C., USA, 337 pp.

65- National Earthquake Hazards Reduction Program (NEHRP) (1997). "NEHRP Recommended Provisions for Seismic Regulations for New Buildings and Other Structures, Part 2," *Federal Emergency Management Agency Commentary (FEMA 303*), Washington, D.C., USA, 362 pp.

66- NBC 2010 - Canadian Commission on Building and Fire Codes (2010) "National Building Code of Canada 2010," *National Research Council of Canada*, Ottawa, Ontario, Canada, 1245 p.

67- NBC 2010 Structural Commentaries - Canadian Commission on Building and Fire Codes (2010) "User's Guide - NBC 2010 Structural Commentaries (Part 4 of Division B)," *National Research Council of Canada*, Ottawa, Ontario, Canada, 225 p.

68- NBCC (2005). "National Building Code of Canada," *National Research Council of Canada*, Ottawa, Ontario, Canada, 1167p.

69- Nehdi, M., Shahria Alam, M., Youssef M.A. (2010). "Development of Corrosion-Free Concrete Beam–Column Joint with Adequate Seismic Energy Dissipation," *Engineering Structures*, 32 (9): 2518-2528

70- NZS 3101 (1995). "The Design of Concrete Structures," *Standards New Zealand*, Wellington.

71- Paramanatham, N. (1993). "Investigation of the Behaviour of Concrete Columns Reinforced with Fiber Reinforced Plastic Rebars," *Master of Engineering Science Thesis*, Lamar University, Beaumont, Texas, 75 p.

72- Park, R., and Paulay, T., (1975). "Reinforced Concrete Structures," *John Wiley*, New York, 769 p.

73- Paulay, T., Park, R. and Priestley, M. (1978). "Reinforced Concrete Beam-Column Joints under Seismic Actions." *ACI Journal*, proceedings, 75 (11): 585-593.

74- Priestley, M. J. N., and Tao, J. R., (1993). "Seismic Response of Precast Prestressed Concrete Frames with Partially Debonded Tendons," *PCI Journal*, 38 (1): 58-69.

75- Pultrall Inc. (2014). "V-ROD™, Technical Data Sheets," Available on *http://www.vrod.ca/en/downloads.asp*, Thetford Mines, Quebec, Canada.

76- Rahgozar, M.A., and Humar, J.L, (1998). "Accounting for Overstrength in Seismic Design of Steel Structures," *Canadian Journal of Civil Engineering*, 25 (1): 1-15.

77- Rashid, J.Y.R., Dameron, R.A., and Dowell, R.K. (2000). "Recent Advances in Concrete Material Modeling and Application to the Seismic Evaluation and Retrofit of California Bridges," *12th World Conference on Earthquake Engineering, 12WCEE 2000*, Auckland, New Zealand. 8p.

78- Rashid, Y. R., (1968). "Ultimate Strength Analysis of Pre-stressed Concrete Pressure Vessels," *Nuclear Eng & Design*, 7(4): 334-344.

79- Said, A. M., and Nehdi, M. L. (2004). "Use of FRP for RC Frames in Seismic Zones: Part II. Performance of Steel-Free GFRP-Reinforced Beam-Column Joints," *Applied composite materials*, 11: 227-245.

80- Schoeck Canada Inc. (2014), "Schöck-ComBAR™, Technical Information sheet", Available on *http://www.schoeck.ca*.

81- Seliem, H., Lucier, G., Rizkalla, S., and Zia, P. (2006). "Behavior of Concrete Bridge Decks Reinforced with MMFX Steel," *Solid Mechanics and Its Applications*, Advances in Engineering Structures, Mechanics & Construction, 140: 139-152.

82- Sharbatdar, M. K. (2003). "Concrete Columns and Beams Reinforced with FRP Bars and Grids under Monotonic and Reversed Cyclic Loading," *Ph.D. Thesis*, University of Ottawa, Ottawa, Canada, 371 p.

83- Sharbatdar, M. K., Saatcioglu, M., Benmokrane, B., and El-Salakawy, E. (2007). "Behaviour of FRP Reinforced Concrete Beam-Column Joints under Cyclic

Loading," *3rd International Conference on Durability & Field Applications of Fibre Rein-forced Polymer (FRP) Composites for Construction,* (CDCC-07), Quebec City, Quebec, Canada, pp. 541-548.

84- Shehata, E., Morphy, R., and Rizkalla, S. (2000). "Fibre Reinforced Polymer Shear Reinforcement for Concrete Members: Behaviour and Design Guidelines," *Canadian Journal of Civil Engineering*, 27 (5): 859-872.

85- Sritharan, S. (1998). "Analysis of concrete bridge joints subjected to seismic actions," *PhD Thesis*, Division of Structural Engineering, University of California, San Diego, California, USA.

86- Sritharan, S., Priestley, M.J.N., Seible, F. (2000). "Nonlinear Finite element analyses of concrete bridge joint systems subjected to seismic actions," *Finite Elements in Analysis and Design,* 36 (3-4): 215-233.

87- Stanton, J. F., and Mole, A., (1994). "A Hybrid Precast Prestressed Concrete Frame System," *Fourth Meeting of U.S.-Japan Joint Technical Coordinating Committee on PRESSS*, Tsukuba, Japan, 24 pp.

88- Uang, C.-M., and Maarouf, A. (1993). "Displacement Amplification Factor for Seismic Design Provisions," *Proceedings of Structures Congress*, ASCE, Irvine, California, Vol. 1: 211-216.

89- Uang, C.-M., and Maarouf, A. (1993). "Seismic Displacement Amplification Factor in Uniform Building Code," *SEAONC Research Bulletin Board*, BB93-3, pp. B1-B2.

90- VAN MIER J.G.M. (1986). "Multi-axial Strain-softening of Concrete, Part I: fracture," *Materials and Structures, RILEM*, 19 (111).

91- VECCHIO, F.J., COLLINS, M.P (1986). "Modified Compression-Field Theory for Reinforced Concrete Beams Subjected to Shear," *ACI Journal, Proceedings*, 83 (2): 219-231.

92- Wallace, J. W., McConnell, S. W., Gupta, P., and Cote, P. A., (1998). "Use of Headed Reinforcement in Beam-Column Joints Subjected to Earthquake Loads," *ACI Structural Journal*, 95 (5): 590-606.

93- Xu, J., Nie, J., Hofmayer, C., and Ali, S. (2007). "Finite Element Analysis of JNES/NUPEC Seismic Shear Wall Cyclic and Shaking Table Test Data," *ASME Pressure Vessels and Piping Division Conference, Proceedings of PVP2007*, San Antonio, Texas, U.S.

APPENDIXES

APPENDIX-A

DESIGN OF TEST SPECIMENS

A.1) DESIGN CALCULATIONS OF SPECIMEN I-H-D

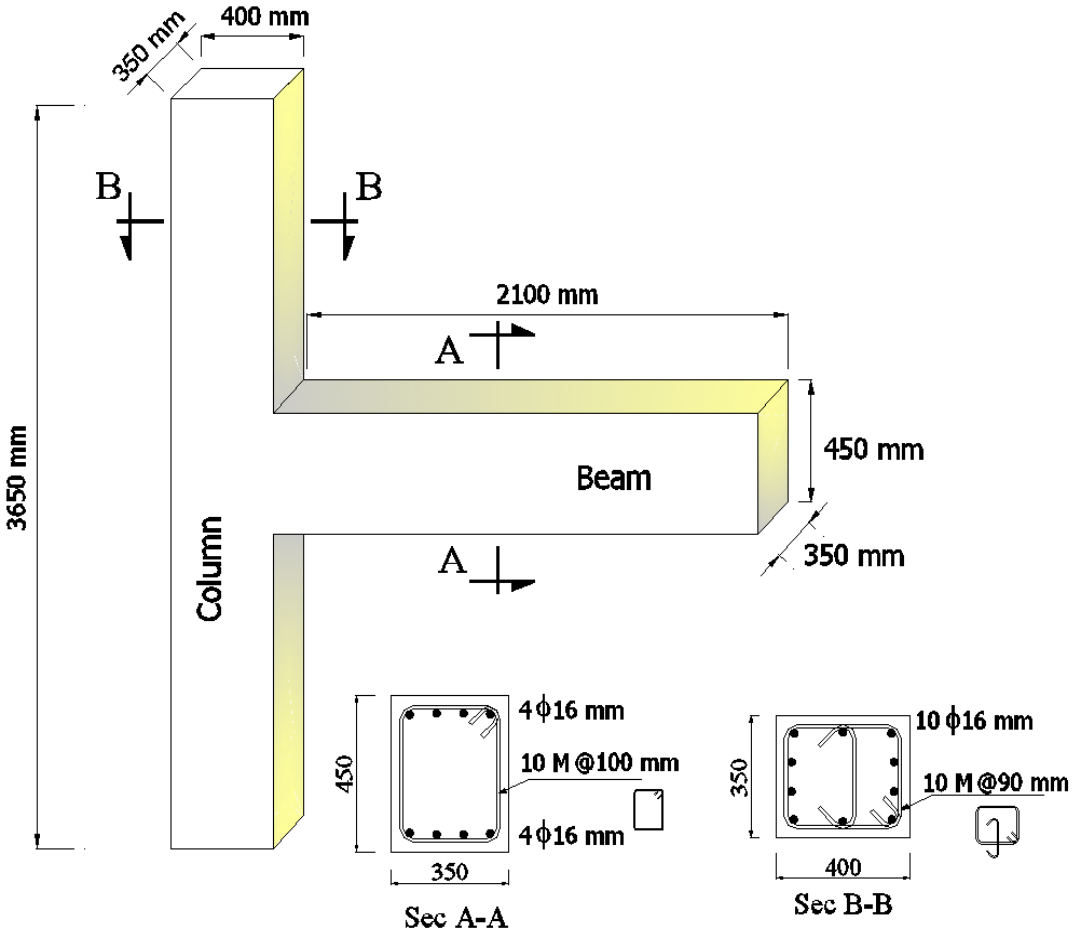

Figure A-1: Specimen I-H-D dimensions and reinforcement

Design of Beam for Flexure:

Materials and Sectional properties:

$f_c^{'} = 30.5\ MPa$ $\phi_c = 1$ $E_c = 4500\sqrt{f_c'} = 4500\sqrt{30.5} = 24852\ MPa$

$\propto_1 = 0.85 - 0.0015 f_c' = 0.804$ $\beta_1 = 0.97 - 0.0025 f_c'$=0.8938

$\varepsilon_{cu} = 0.0035$

Longitudinal reinforcement: GFRP bars

$f_{frp,u} = 1100\ MPa$ $\phi_{frp} = 1$ $E_{frp} = 60.0\ GPa$ $\varepsilon_{frp,u} = 18.33 * 10^{-3}$

$A_{frp} = 4\#16mm = 4 * 200 = 800\ mm^2$

$h = 450\ mm$ $b = 350\ mm$ $d = 400\ mm$

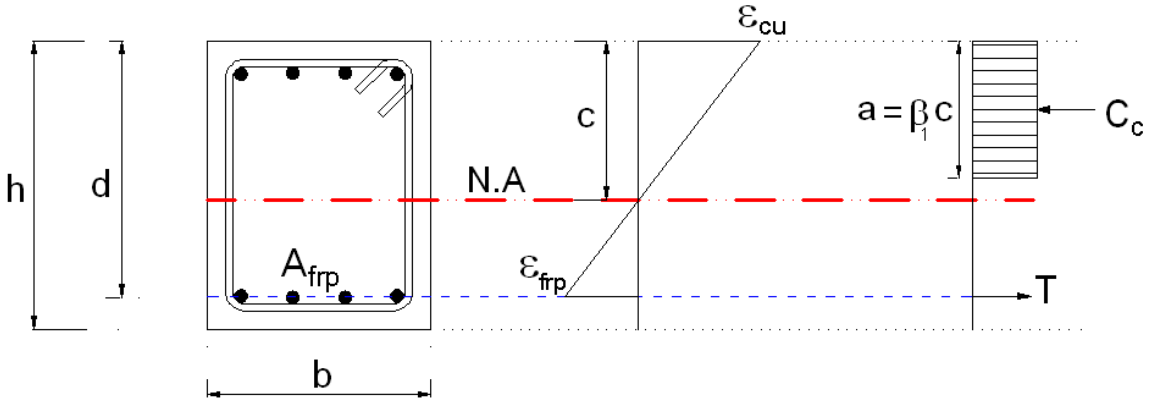

Figure A-2: Compatibility of strains for beam cross section

$$\rho_{frp} = \frac{A_{frp}}{bd} = \frac{800}{400 * 350} = 0.571\%$$

$$\rho_{balance} = \alpha_1 \beta_1 \frac{\phi_c}{\phi_{frp}} \frac{f_c'}{f_{frp,u}} \left(\frac{\varepsilon_{cu}}{\varepsilon_{cu} + \varepsilon_{frp,u}} \right)$$

$$\rho_{balance} = 0.804 * 0.8938 * 1 * \frac{30.5}{1100}\left(\frac{0.0035}{0.0035 + 18.33 * 10^{-3}}\right) = 0.32\%$$

$$\frac{\rho_{frp}}{\rho_{balance}} = 1.78 > 1 \ldots\ldots\ldots\ldots \text{(Compression failure)}$$

From equilibrium and strain compatibility shown in Fig. A-2, the following is calculated;

$$f_{frp} = \frac{1}{2} E_{frp} \varepsilon_{cu} \left[(1 + \frac{4\alpha_1 \beta_1 \phi_c f_c^{'}}{\rho_{frp} \phi_{frp} E_{frp} \varepsilon_{cu}})^{0.5} - 1 \right]$$

$$f_{frp} = 0.5 * 60 * 10^3 * 0.0035 \left[\left(1 + \frac{4 * 0.804 * 0.8938 * 1 * 30.5}{0.00571 * 1 * 60 * 10^3 * 0.0035} \right)^{0.5} - 1 \right]$$

$$= 798.75\ MPa$$

$$a = \beta_1\ c = \left(\phi_{frp}\ A_{frp}\ f_{frp}\right) \div (\alpha_1 \phi_c f_c' b)$$

$$a = (1 * 800 * 799) \div (1 * 0.804 * 30.5 * 350) = 74.43\ mm$$

$$C_c = \alpha_1 \phi_c f_c' \beta_1\ c\ b = 0.804 * 1 * 30.5 * 74.43 * 350 = 638.81\ kN$$

$$T_{frp} = \phi_{frp} A_{frp} f_{frp} = 1 * 800 * 799 = 638.9\ kN$$

Equilibrium is satisfied $T = C_c$

$$M_r = C_c \left(d - \frac{\beta_1 c}{2} \right) = 638.9 * 10^3 \left(400 - \frac{74.43}{2} \right) = 231.8\ kN.m$$

$$\boldsymbol{M_r = 231.8\ kN.m}$$

Design Beam for Shear: *(According to CSA-A23.3-04)*

Shear reinforcement Characteristics: (Steel stirrups)

$f_y = 400\ MPa$ $\varphi_s = 1$ $E_s = 200\ GPa$

$A_v = 2\ legs\ 10M = 2 * 100 = 200\ mm^2$

$Beam\ length\ (l_b) = 2000\ mm$ (from point of load application to column face)

$Column\ height\ (h_c) = 3500\ mm$ (between supports)

$$Effective\ shear\ depth\ (d_v) = larger \begin{cases} 0.9\ \text{d} = 0.9 * 400 = 360\ \text{mm} \\ 0.72\ \text{h} = 0.72 * 450 = 324\ \text{mm} \end{cases}$$

$d_v = 360\ mm$

$$Applied\ shear\ force\ (V_r) = \frac{M_{beam}}{l_b} = \frac{232 * 10^6}{2000} = 116\ kN$$

$V_{r,max} = 0.125\lambda\phi_c f_c' b_w d_v$ Eq. (11-5) - Clause11.3.3- A23.3-04

$V_r = 116\ kN < V_{r,max} = 0.25\lambda\phi_c f_c' b_w d_v = 960.8\ kN$ ..... (OK)

$V_r = V_c + V_s$ Eq. (11-4) - Clause11.3.3- A23.3-04

$V_c = \phi_c \lambda \beta \sqrt{f_c'} b_w d_v$ Eq. (11-6) - Clause11.3.4- A23.3-04

However $\beta = 0$, $\theta = 45°$ ..... as required by Clause 21.3.4.2 (a)- A23.3-04

$\therefore\ V_c = 0, \qquad V_r = V_s$

1- Calculation of required Spacing (S) according to Clause 11.3.5.1

$$V_s = \frac{\phi_s A_v f_y d_v \cot\theta}{S} \qquad \text{Eq. } (11-7)$$

$V_s = V_r = 116\ kN$

$$S = \frac{\phi_s A_v f_y d_v \cot\theta}{V_s} = \frac{1 * 200 * 400 * 360 * \cot 45}{116 * 10^3} = 248\ mm$$

$S = 248\ mm$ ..... (1)

2- Calculation of max. Spacing (S_{max}) according to Clause 11.3.8.3 - A23.3-04 (Maximum spacing of transverse reinforcement)

$0.125\lambda\phi_c f_c' b_w d_v = 0.125 * 1 * 1 * 30.5 * 350 * 360 = 480.4\ kN$

$\because V_r = 116\ kN < 0.125\lambda\phi_c f_c' b_w d_v = 480.4\ kN$

$S_{max} = smaller$
- $0.7\ d_v = 0.7 * 360 = 252$ mm
- 600 mm

$S_{max} = 252\ mm$ ..... (2)

3- Calculation of max. Spacing (S_{max}) according to Clause 11.2.8.2 - A23.3-04

$Min.Shear\ reinforcement\ (A_{v,min}) = 0.06\sqrt{f_c'} * \frac{b_w S}{f_y}$ Eq. (11-1)

Rearranging Eq. (11-1) to be $S_{max} = \frac{A_v\ f_y}{0.06\ b_w\sqrt{f_c'}} = \frac{200*400}{0.06*350\sqrt{30.5}} = 690\ mm$

$S_{max} = 690\ mm$ ..... (3)

4- Calculation of max. Spacing (S_{max}) according to Clause 21.3.3.2 - A23.3-04

$S_{max} = Least\ of$
- $\frac{d}{4} = \frac{400}{4} = 100\ mm$
- Eight times the diameter of the smallest longitudinal bars = 8*16=128 mm
- 24 times the diameter of the hoop bars = 24*11= 264 mm
- 300 mm

$S_{max} = 100\ mm$ ..... (4)

From 1, 2, 3, and 4 ➔ $S_{max} = 100\ mm$

∴ ***Use Stirrups*** **10M @ 100 *mm*** **(Steel stirrups)**

Design of Column for Flexure

- *Construction of Column interaction diagram*

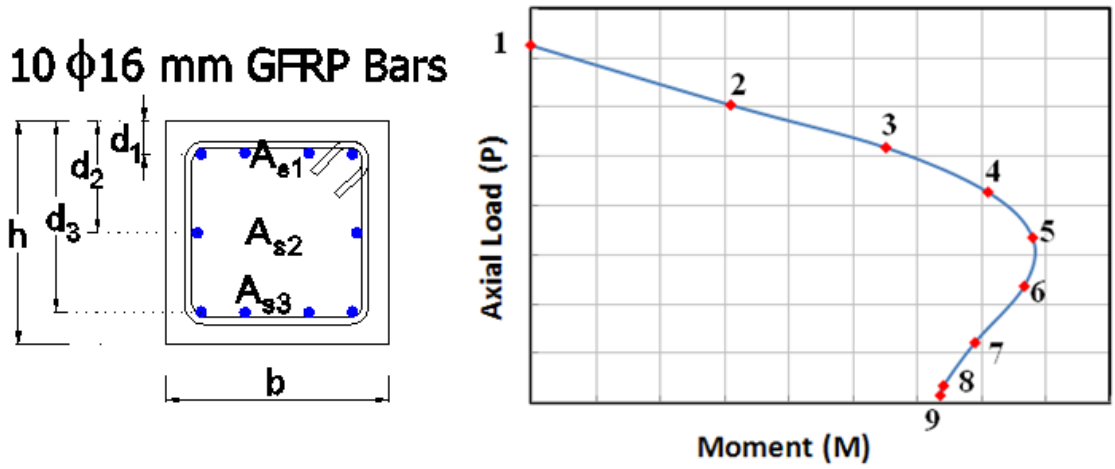

Figure A-3: Calculation points to construct the interaction diagram of column

Materials and Sectional properties:

$f_c^{'} = 30.5\ MPa$ $\phi_c = 1$ $E_c = 4500\sqrt{f_c'} = 4500\sqrt{30.5} = 24.852\ GPa$

$\propto_1 = 0.85 - 0.0015 f_c' = 0.804$ $\beta_1 = 0.97 - 0.0025 f_c' = 0.8938$

$\varepsilon_{cu} = 0.0035$

$f_{frp,u} = 1100\ MPa$ $\phi_{frp} = 1$ $E_{frp} = 60\ GPa$ $\varepsilon_{frp,u} = 18.33 * 10^{-3}$

$A_{f1} = 4\emptyset 16mm = 4 * 200 = 800\ mm^2$ $d_1 = 50\ mm$

$A_{f2} = 2\emptyset 16mm = 2 * 200 = 400\ mm^2$ $d_2 = 200\ mm$

$A_{f3} = 4\emptyset 16mm = 4 * 200 = 800\ mm^2$ $d_3 = 350\ mm$

$h = 400\ mm$ $b = 350\ mm$

$A_{frp} = 10\ \emptyset 16mm = 10 * 200 = 2000\ mm^2$

Calculation of Balanced Reinforcement Required to Avoid Brittle Tension Failure

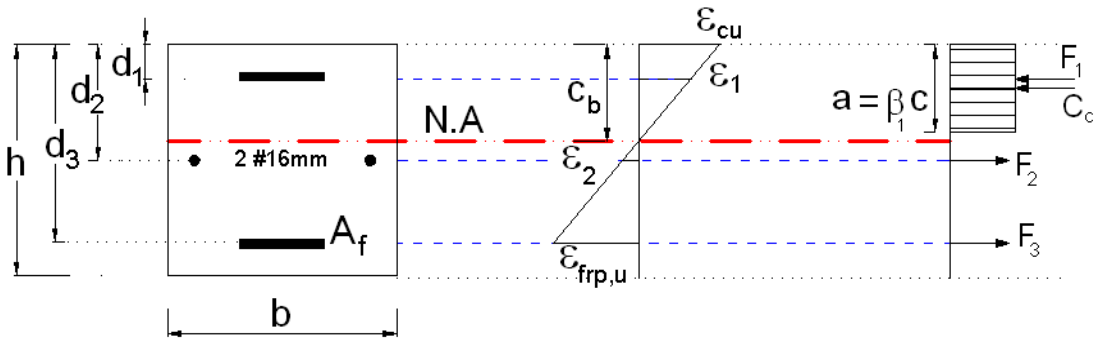

Figure A-4: Calculation for balanced reinforcement area

$$\frac{\varepsilon_{cu}}{c_b} = \frac{\varepsilon_{frp,u}+\varepsilon_{cu}}{d} \rightarrow \therefore c_b = \frac{d*\varepsilon_{cu}}{\varepsilon_{frp,u}+\varepsilon_{cu}} = \frac{0.0035*350}{18.33*10^{-3}+0.0035} = 56.1\ mm$$

$$C_c = \alpha_1 \phi_c f'_c \beta_1\ c_b\ b = 0.804 * 1 * 30.5 * 0.8938 * 56.1 * 350 = 430.35\ kN$$

$$\varepsilon_{2=}\varepsilon_{frp,u}\frac{(d_2 - c_b)}{(d_3 - c_b)} = 18.33 * 10^{-3} * \frac{(200 - 56.1)}{(350 - 56.1)} = 8.98 * 10^{-3}$$

$$F_2 = \phi_{frp} A_{f2} E_{frp} \varepsilon_2 = 1 * 400 * 60 * 10^3 * 8.98 * 10^{-3} = 215.43\ kN$$

Neglecting the contribution of GFRP under compression in flexure strength of the section; $F_1 = 0\ kN$

From equilibrium, $C_c = F_2 + F_3$ ➔ $\therefore F_3 = C_c - F_2 = 430.35 - 215.43 = 214.92\ kN$

$$\therefore A_f = \frac{F_3}{f_{frp,u}} = \frac{214.92 * 10^3}{1100} = 195\ mm^2$$

Available reinforcement area in the column section ($A_{f3} = 4\ \emptyset 16mm = 4 * 200 = 800\ mm^2$) > Required area to avoid brittle tension failure ($A_f = 195\ mm^2$)

(OK- No tensile failure is expected in the column)

Calculations of required points to construct the Column interaction diagram

Point (1): Pure Axial resistance

$P_1 = 0.85 f_c' (A_g - A_{frp}) + 0.002\ E_{fc} A_{frp}$

Assume the contribution of the GFRP longitudinal bars in resisting axial compression is neglected.

$A_{frp} = 10 * 200 = 2000\ mm^2$

$P_1 = 0.85 * 30.5\ (350 * 400 - 2000) = 3577.7\ kN$

$$\therefore \textbf{Point (1):}\ (P_1 = 3577.7\ kN\ ,\ M_r = 0\ kN.m)$$

Point (2): C = 400 mm

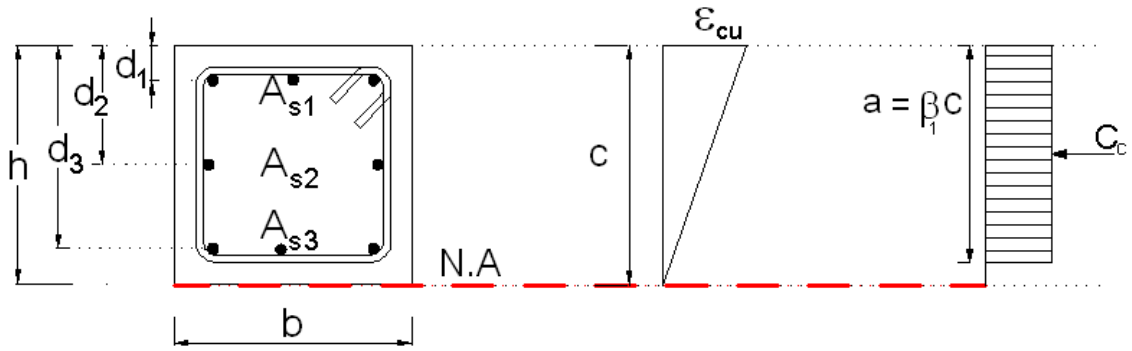

Figure A-5: Compatibility of strains for column cross section ($c = h$)

$C_c = \alpha_1 \phi_c f_c' \beta_1\ c\ b = 0.804 * 1 * 30.5 * 0.8938 * 400 * 350 = 3068.5\ kN$

$P_2 = C_c = 3068.5\ kN$

$M_2 = C_c \left(\frac{h}{2} - \frac{\beta_1 c}{2}\right) = 3068.5 \left(\frac{400}{2} - \frac{0..8938 * 400}{2}\right) = 65.2\ kN.m$

$$\therefore \textbf{Point (2):}\ (P_2 = 3068.5\ kN\ ,\ M_2 = 65.2\ kN.m)$$

Point (3): C = 350 mm

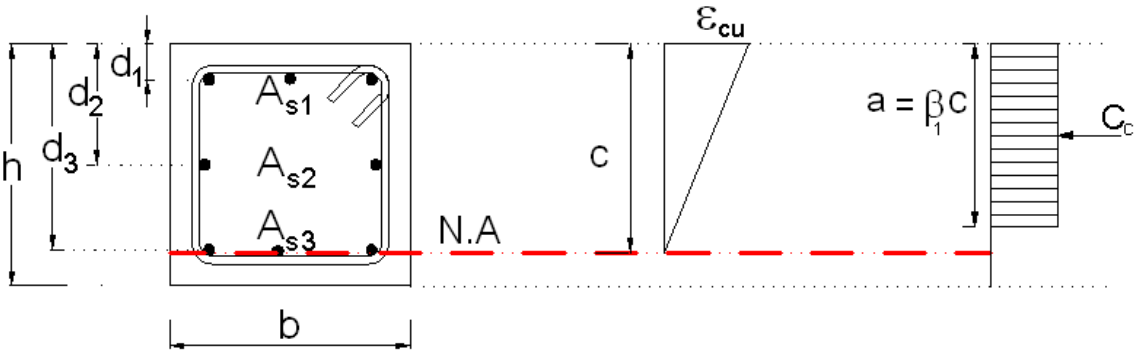

Figure A-6: Compatibility of strains for column cross section ($c = d_3$)

$$C_c = \alpha_1 \phi_c f'_c \beta_1 \, c \, b = 0.804 * 1 * 30.5 * 0.8938 * 350 * 350 = 2685 \, kN$$

$$P_3 = C_c = 2685 \, kN$$

$$M_3 = C_c \left(\frac{h}{2} - \frac{\beta_1 c}{2}\right) = 2685 \left(200 - \frac{0..8938 * 350}{2}\right) = 117 \, kN.m$$

∴ **Point (3):** $(P_3 = 2685 \, kN \, , \; M_3 = 117 \, kN.m)$

Point (4): C = 300 mm

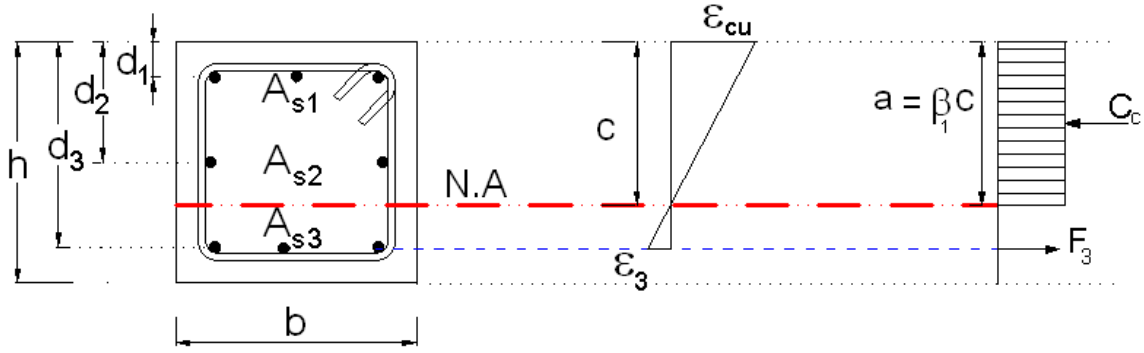

Figure A-7: Compatibility of strains for column cross section ($d_3 > c > h/2$)

$$C_c = \alpha_1 \phi_c f'_c \beta_1 \, c \, b = 0.804 * 1 * 30.5 * 0.8938 * 300 * 350 = 2301.37 \, kN$$

$$\varepsilon_3 = \varepsilon_{cu}\left(\frac{d_3}{c} - 1\right) = 0.0035\left(\frac{350}{300} - 1\right) = 5.833 * 10^{-4}$$

$$F_3 = \phi_f A_{f3} \varepsilon_3 E_{frp} = 1 * 800 * 5.833 * 10^{-4} * 60 * 10^3 = 28\ kN$$

$$P_4 = C_c - F_3 = 2301.37 - 28 = 2273.37\ kN$$

$$M_4 = C_c\left(\frac{h}{2} - \frac{\beta_1 c}{2}\right) + F_3\left(d_3 - \frac{h}{2}\right)$$

$$M_4 = 2301.37\left(200 - \frac{0.8938 * 300}{2}\right) + 28\ (350 - 200) = 155.93\ kN.m$$

∴ **Point (4):** $(P_4 = 2273.4\ kN\ ,\ M_4 = 155.9\ kN.m)$

Point (5): C = 250 mm

$$C_c = \alpha_1 \phi_c f_c' \beta_1\ c\ b = 0.804 * 1 * 30.5 * 0.8938 * 250 * 350 = 1917.8\ kN$$

$$\varepsilon_3 = \varepsilon_{cu}\left(\frac{d_3}{c} - 1\right) = 0.0035\left(\frac{350}{250} - 1\right) = 1.4 * 10^{-3}$$

$$F_3 = \phi_f A_{f3} \varepsilon_3 E_{frp} = 1 * 800 * 1.4 * 10^{-3} * 60 * 10^3 = 67.2\ kN$$

$$P_5 = C_c - F_3 = 1917.8 - 67.2 = 1850.6\ kN$$

$$M_5 = C_c\left(\frac{h}{2} - \frac{\beta_1 c}{2}\right) + F_3\left(d_3 - \frac{h}{2}\right)$$

$$M_5 = 1917.8\left(200 - \frac{0.8938 * 250}{2}\right) + 67.2 * 150 = 179.4\ kN.m$$

∴ **Point (5):** $(P_5 = 1850.6\ kN\ ,\ M_5 = 179.4\ kN.m)$

Point (6): C = 200 mm

$$C_c = \alpha_1 \phi_c f_c' \beta_1\ c\ b = 0.804 * 1 * 30.5 * 0.8938 * 200 * 350 = 1534.24\ kN$$

$$\varepsilon_2 = \varepsilon_{cu}\left(\frac{d_2}{c} - 1\right) = 0.0035\left(\frac{200}{200} - 1\right) = 0$$

$$F_2 = \phi_f A_{f2} \varepsilon_2 E_{frp} = 1 * 400 * 0 * 60 * 10^3 = 0\ kN$$

$$\varepsilon_3 = \varepsilon_{cu}\left(\frac{d_3}{c} - 1\right) = 0.0035\left(\frac{350}{200} - 1\right) = 2.625 * 10^{-3}$$

$$F_3 = \phi_f A_{f3} \varepsilon_3 E_{frp} = 1 * 800 * 2.625 * 10^{-3} * 60 * 10^3 = 126\ kN$$

$$P_6 = C_c - F_3 - F_2 = 1534.24 - 126 - 0 = 1408.24\ kN$$

$$M_6 = C_c\left(\frac{h}{2} - \frac{\beta_1 c}{2}\right) + F_3\left(d_3 - \frac{h}{2}\right) + F_2\left(d_2 - \frac{h}{2}\right)$$

$$M_6 = 1534.24\left(200 - \frac{0.8938 * 200}{2}\right) + 126 * 150 = 188.6\ kN.m$$

∴ **Point (6):** $(P_6 = 1408.2\ kN\ ,\ M_6 = 188.6\ kN.m)$

Point (7): C = 150 mm

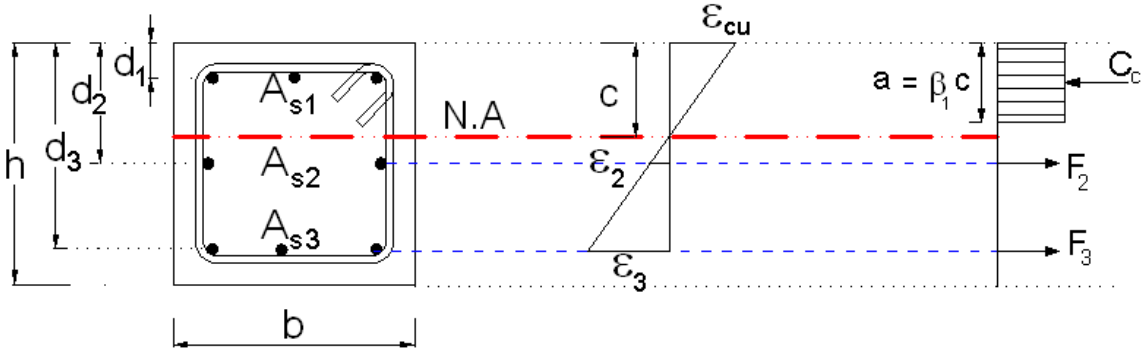

Figure A-8: Compatibility of strains for column cross section ($d_1 < c < h/2$)

$$C_c = \alpha_1 \phi_c f'_c \beta_1\ c\ b = 0.804 * 1 * 30.5 * 0.8938 * 150 * 350 = 1150.7\ kN$$

$$\varepsilon_2 = \varepsilon_{cu}\left(\frac{d_2}{c} - 1\right) = 0.0035\left(\frac{200}{150} - 1\right) = 1.1667 * 10^{-3}$$

$$F_2 = \phi_f A_{f2} \varepsilon_2 E_{frp} = 1 * 400 * 1.1667 * 10^{-3} * 60 * 10^3 = 28\ kN$$

$$\varepsilon_3 = \varepsilon_{cu}\left(\frac{d_3}{c} - 1\right) = 0.0035\left(\frac{350}{150} - 1\right) = 4.667 * 10^{-3}$$

$F_3 = \phi_f A_{f3} \varepsilon_3 E_{frp} = 1 * 800 * 4.667 * 10^{-3} * 60 * 10^3 = 224\ kN$

$P_7 = C_c - F_3 - F_2 = 1150.7 - 224 - 28 = 898.7\ kN$

$M_7 = C_c \left(\frac{h}{2} - \frac{\beta_1 c}{2}\right) + F_3 \left(d_3 - \frac{h}{2}\right) + F_2 \left(d_2 - \frac{h}{2}\right)$

$M_7 = 1150.7 \left(200 - \frac{0.8938 * 150}{2}\right) + 224 * 150 + 28 * 0 = 186.6\ kN.m$

∴ **Point (7):** $(P_7 = 898.7\ kN\ ,\ M_7 = 186.6\ kN.m)$

Point (8): C = 100 mm

$C_c = \alpha_1 \phi_c f_c' \beta_1\ c\ b = 0.804 * 1 * 30.5 * 0.8938 * 100 * 350 = 767.1\ kN$

$\varepsilon_2 = \varepsilon_{cu} \left(\frac{d_2}{c} - 1\right) = 0.0035 \left(\frac{200}{100} - 1\right) = 3.5 * 10^{-3}$

$F_2 = \phi_f A_{f2} \varepsilon_2 E_{frp} = 1 * 400 * 3.5 * 10^{-3} * 60 * 10^3 = 84\ kN$

$\varepsilon_3 = \varepsilon_{cu} \left(\frac{d_3}{c} - 1\right) = 0.0035 \left(\frac{350}{100} - 1\right) = 8.75 * 10^{-3}$

$F_3 = \phi_f A_{f3} \varepsilon_3 E_{frp} = 1 * 800 * 8.75 * 10^{-3} * 60 * 10^3 = 420\ kN$

$P_8 = C_c - F_3 - F_2 = 767.1 - 420 - 84 = 263.1\ kN$

$M_8 = C_c \left(\frac{h}{2} - \frac{\beta_1 c}{2}\right) + F_3 \left(d_3 - \frac{h}{2}\right) + F_2 \left(d_2 - \frac{h}{2}\right)$

$M_8 = 767.1 \left(200 - \frac{0.8938 * 100}{2}\right) + 420 * 150 + 42 * 0 = 182.1\ kN.m$

∴ **Point (8):** $(P_8 = 263.1\ kN\ ,\ M_8 = 182.1\ kN.m)$

Point (9): C = 84 mm

$C_c = \alpha_1 \phi_c f_c' \beta_1\ c\ b = 0.804 * 1 * 30.5 * 0.8938 * 84 * 350 = 645\ kN$

$$\varepsilon_2 = \varepsilon_{cu}\left(\frac{d_2}{c} - 1\right) = 0.0035\left(\frac{200}{84} - 1\right) = 4.833 * 10^{-3}$$

$$F_2 = \phi_f A_{f2} \varepsilon_2 E_{frp} = 1 * 400 * 4.833 * 10^{-3} * 60 * 10^3 = 116\ kN$$

$$\varepsilon_3 = \varepsilon_{cu}\left(\frac{d_3}{c} - 1\right) = 0.0035\left(\frac{350}{84} - 1\right) = 11.0833 * 10^{-3}$$

$$F_3 = \phi_f A_{f3} \varepsilon_3 E_{frp} = 1 * 800 * 11.0833 * 10^{-3} * 60 * 10^3 = 532\ kN$$

$$P_9 = C_c - F_3 - F_2 = 645 - 532 - 116 = -3\ kN$$

$$M_9 = C_c\left(\frac{h}{2} - \frac{\beta_1 c}{2}\right) + F_3\left(d_3 - \frac{h}{2}\right) + F_2\left(d_2 - \frac{h}{2}\right)$$

$$M_9 = 645\left(200 - \frac{0.8938 * 68}{2}\right) + 532 * 150 + 116 * 0 = 189\ kN.m$$

∴ **Point (9):** $(P_9 = -3\ kN\ ,\ M_9 = 189\ kN.m)$`

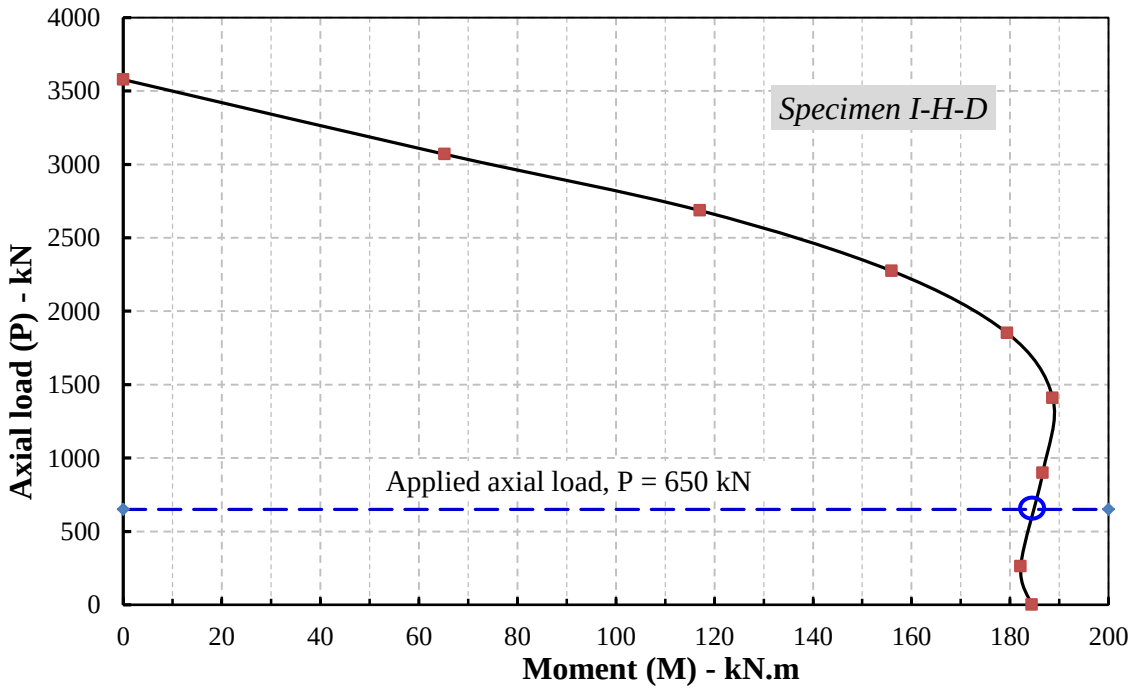

Figure A-9: Calculated column interaction diagram

The Specimen was tested under an axial concentric load at a level equal to 15% A_c * f_c' (i.e. 650 kN). Therefore the flexural capacity of the column cross section at the specified axial load level is equal to 185 kN.m as shown in Figure A-9.

$$Flexure\ strength\ ratio\ (M_R) = \frac{Sum.of\ Column\ nominal\ flexure\ strength}{Beam\ propable\ flexure\ strength}$$

$$\boldsymbol{Flexure\ strength\ ratio\ (M_R) = \frac{2 * 185}{231.8} = 1.59}$$

Design Column for Shear using steel stirrups

(According to CSA-A23.3-04)

Shear reinforcement Characteristics:

$f_y = 400\ MPa \qquad \phi_s = 1 \qquad E_s = 200\ GPa$

$A_v = 2\ legs\ 10M = 2 * 100 = 200\ mm^2$

$Beam\ length\ (l_b) = 2000\ mm \qquad Column\ height\ (h_c) = 3500\ mm$

$Effective\ shear\ depth\ (d_v) = larger$ { 0.9 d $= 0.9 * 350 = 315$ mm ; 0.72 h $= 0.72 * 400 = 288$ mm }

$d_v = 315\ mm$

$Applied\ shear\ force\ (V_f) = \frac{M_{r,beam}}{h_c} = \frac{232 * 10^6}{3500} = 66.3\ kN$

$V_{r,max} = 0.125\lambda\phi_c f_c' b_w d_v$ Eq. (11-5) - Clause11.3.3

$V_{r,max} = 0.125 * 1 * 30.5 * 350 * 315 = 420\ kN$

$V_r = 66.3\ kN < V_{r,max} = 420\ kN$ ..... (OK)

$V_r = V_c + V_s$ Eq. (11-4) - Clause11.3.3

$V_c = \phi_c\lambda\beta\sqrt{f_c'}b_w d_v$ Eq. (11-6) - Clause11.3.4

However $\beta \leq 0.10$ and $\theta \geq 45^\circ$ ..... as specified by Clause 21.4.5.2 (a)

$\varepsilon_x = [\frac{M_f}{d_v} + V_f + 0.5\ N_f] \div 2\ E_s A_s$ Eq. (11-13) - Clause11.3.6.4

Where $M_f = \frac{M_{r,beam}}{2} = \frac{232}{2} = 116$ kN.m

$\varepsilon_x = \left[\frac{116 * 10^6}{315} + 66.3 * 10^3 - 0.5 * 650 * 10^3\right] \div 2 * 60 * 10^3 * 800$

$\varepsilon_x = 1.14 * 10^{-3} < 3 * 10^{-3}$ (OK)

$\beta = \frac{0.4}{(1+1500\varepsilon_x)} * \frac{1300}{(1000+S_{ze})}$ Eq. (11-11) – Clause 11.3.6.4

$Where\ S_{ze} = 300\ mm,\ \ since\ using\ A_v > A_{v,min}$

$$\beta = \frac{0.4}{(1 + 1500 * 1.14 * 10^{-3})} * \frac{1300}{(1000 + 300)} = 0.148 > 0.10$$

β shouldn't exceed 0.10 (Clause 21.4.5.2), therefore take $\beta = 0.1$

$\theta = 29 + 7000\varepsilon_x$ Eq. $(11-12)$ – Clause11.3.6.4

$\theta = 29 + 7000 * 1.14 * 10^{-3} = 37°$

θ shouldn't be less than 45° (Clause 21.4.5.2), therefore take $\theta = 45°$

$\therefore V_c = \phi_c \lambda \beta \sqrt{f_c'} b_w d_v = 1 * 1 * 0.1 \sqrt{30.5} * 350 * 315 = 60.9\ kN$

1- Calculation of required Spacing (S) according to Clause 11.3.5.1

$V_s = V_r - V_c = 66.3 - 60.9 = 5.4\ kN$

$V_s = \frac{\phi_s A_v f_y d_v \cot\theta}{S}$ Eq. $(11-7)$

$S = \frac{\phi_s A_v f_y d_v \cot\theta}{V_s} = \frac{1 * 200 * 400 * 315 * \cot 45}{5.4 * 10\text{^}3} = 4666\ mm$

$S = 4666\ mm$ ..... (A-1)

2- Calculation of max. Spacing (S_{max}) according to Clause 11.3.8.3 (Maximum spacing of transverse reinforcement)

$0.125\lambda\phi_c f_c' b_w d_v = 0.125 * 1 * 1 * 30.5 * 350 * 315 = 420\ kN$

$\because V_r = 66.3\ kN < 0.125\lambda\phi_c f_c' b_w d_v = 420\ kN$

$S_{max} = smaller$ { $0.7\ d_v = 0.7 * 315 = 220$ mm ; 600 mm }

$S_{max} = 220\ mm$ ..... (A-2)

3- Calculation of max. Spacing (S_{max}) according to Clause 11.2.8.2

$Min.Shear\ reinforcement\ (A_{v,min}) = 0.06\sqrt{f_c'}\ \frac{b_w\ S}{f_y}$ Eq. (11-1)

Rearranging Eq. (11-1) to be $S_{max} = \frac{A_v\ f_y}{0.06\ b_w\sqrt{f_c'}} = \frac{200*400}{0.06*350\sqrt{30.5}} = 690\ mm$

$S_{max} = 690\ \ mm$ ..... (A-3)

4- Calculation of max. Spacing (S) according to Clause 21.4.4.2 (b)

$$A_{sh} = larger\ of \begin{cases} 0.2k_n k_p \frac{A_g}{A_{ch}} \frac{f_c'}{f_{yh}} Sh_c & \text{Eq. (21-5)} \\ 0.09 \frac{f_c'}{f_{yh}} Sh_c & \text{Eq. (21-6)} \end{cases}$$

Where

$k_n = n_l/(n_l - 2)$, $k_p = P_f/P_o$

$f_{yh} shall\ not\ be\ taken\ as\ greater\ than\ 500\ MPa$

n_l: Total number of longitudinal bars in the column cross-section that are laterally supported by the corner of hoops or by hooks of seismic crossties. $\therefore In\ our\ case\ \ n_l = 6$

$A_g = 350 * 400 = 140000\ mm^2$

$A_{ch} = (350 - 2 * 30)(400 - 2 * 30) = 98600\ mm^2$

$A_{sh} = 200\ mm^2$, $k_n = 1.5$, $k_p = 0.15$

According to Eq. (21-5), $S = \frac{A_{sh}\ A_{ch}\ f_{yh}}{0.2k_n k_p A_g f_c' h_c} = \frac{200*98600*400}{0.2*1.5*0.15*140000*30.5*340} = 120\ mm$

According to Eq. (21-6), $S = \frac{A_{sh}\ f_{yh}}{0.09 f_c' h_c} = \frac{200*400}{0.09*30.5*340} = 86\ mm$

$S = 86\ \ mm$ ..... (A-4)

5- Calculation of max. Spacing (S_{max}) according to Clause 21.4.4.3

S_{max} = Least of
- One-quarter of the minimum member dimension $= \frac{400}{4} = 100\ mm$
- Six times the diameter of the smallest long. bar $= 6 * 16 = 96\ mm$
- $S_x = 100 + \left(\frac{350 - h_x}{3}\right) = 100 + \left(\frac{350-200}{3}\right) = 150$ mm

$S_{max} = 96\ mm$ ..... (A-5)

From A-1, A-2, A-3, A-4 and A-5

$\therefore\ S_{max} = 86\ mm, which\ can\ be\ considerd\ \approx 90\ mm$

$\therefore$ ***Use Stirrups* 10*M* @ 90 *mm***

Check shear resistance of the joint

According to CSA A23.3-04 - Clause 21.5.4.1 (c).

$Applied\ shear\ on\ the\ joint\ (V_j) = T_{frp} - V_{column}$

$V_{column} = 66.3$ kN

$T_{frp} = Calculated\ tensile\ force\ in\ longitudinal\ beam\ bars\ at\ failure$

$T_{frp} = \phi_{frp} A_{frp} f_{frp} = 1 * 800 * 799 = 638.9\ kN$

$V_j = 638.9 - 66.3 = 572.6\ kN$

$Shear\ capacity\ of\ the\ joint = 1.3\lambda\phi_c\sqrt{f_c'}A_j$ CSA A23.3-04 - Clause 21.5.4.1 (c)

$Shear\ capacity\ of\ the\ joint = 1.3 * 1 * 1 * \sqrt{30.5} * 350 * 400 = 1005\ kN$

$\therefore V_j = 572.6\ kN < Shear\ capacity\ of\ the\ joint = 1005\ kN$.....(OK)

Shear stress $= \frac{V_j}{b * t} = \frac{572.6 * 10^3}{350 * 400} = 4.1\ MPa = 0.74\sqrt{f'_c}$

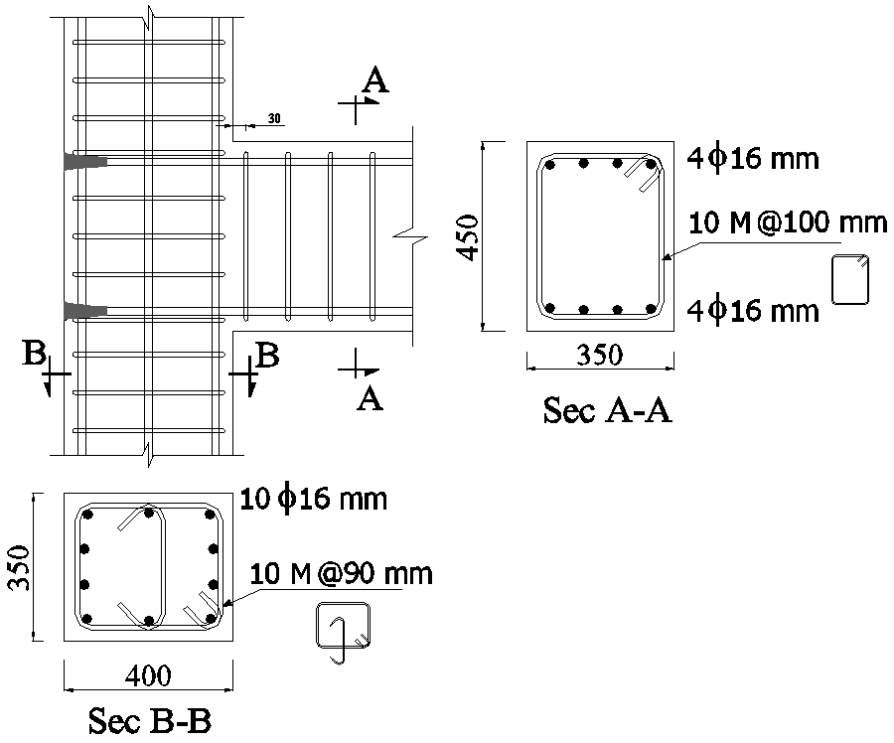

Figure A-10: Reinforcement details of Specimen I-H-D

A.2) DESIGN CALCULATIONS OF SPECIMEN II-30-0.85

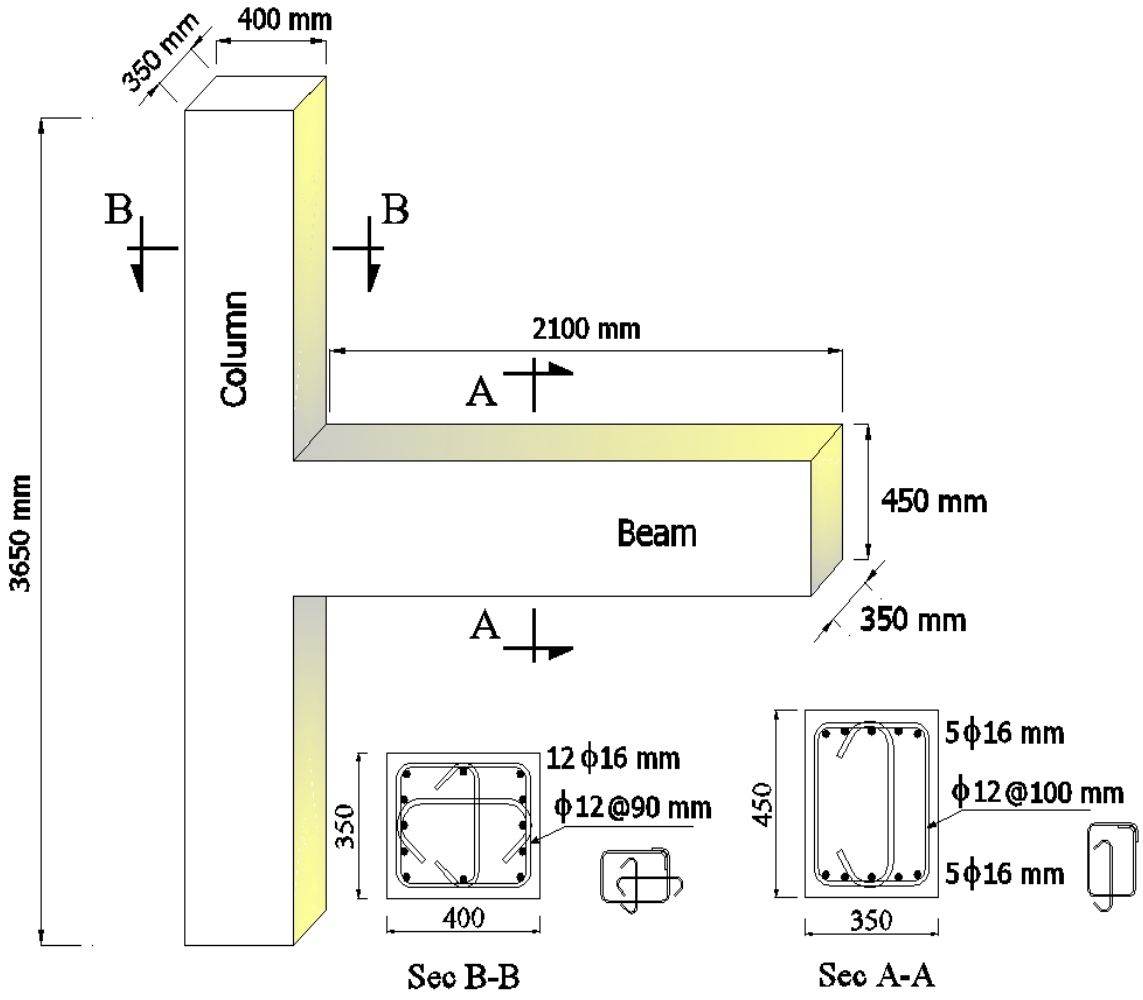

Figure A-11: Specimen II-30-0.85 dimensions and reinforcement

Design Beam for Flexure

Materials and Sectional properties:

$f_c^{'} = 32.6\ MPa$ $\quad \phi_c = 1$ $\quad E_c = 4500\sqrt{f_c'} = 4500\sqrt{32.6} = 25693\ MPa$

$\propto_1 = 0.85 - 0.0015 f_c' = 0.8011$ $\quad \beta_1 = 0.97 - 0.0025 f_c' = 0.8885$

$\varepsilon_{cu} = 0.0035$

Longitudinal reinforcement: GFRP bars

$f_{frp,u} = 1100\ MPa \quad \phi_{frp} = 1 \qquad E_{frp} = 60.0\ GPa \qquad \varepsilon_{frp,u} = 18.33 * 10^{-3}$

$A_{frp} = 5\emptyset 16mm = 5 * 200 = 1000\ mm^2$

$h = 450\ mm \qquad b = 350\ mm \qquad d = 400\ mm$

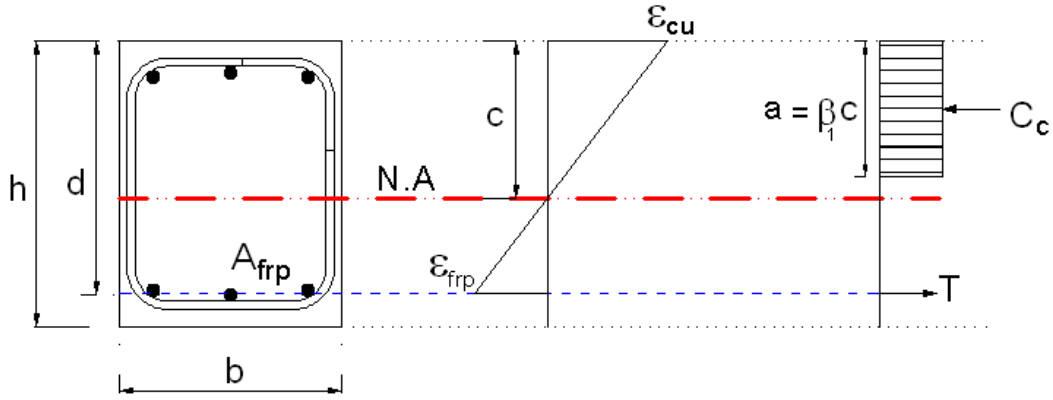

Figure A-12: Compatibility of strains for beam cross section

$$\rho_{frp} = \frac{A_{frp}}{bd} = \frac{1000}{400 * 350} = 0.71\%$$

$$\rho_{balance} = \alpha_1\beta_1 \frac{\phi_c}{\phi_{frp}} \frac{f_c'}{f_{frp,u}} \left(\frac{\varepsilon_{cu}}{\varepsilon_{cu} + \varepsilon_{frp,u}}\right)$$

$$\rho_{balance} = 0801 * 0.889 * 1 * \frac{32.6}{1100}\left(\frac{0.0035}{0.0035 + 18.33 * 10^{-3}}\right) = 0.34\%$$

$$\frac{\rho_{frp}}{\rho_{balance}} = 2.1 > 1 \ldots\ldots\ldots\ldots \text{(Compression failure)}$$

From equilibrium and strain compatibility shown in Fig. A-2, the following is calculated;

$$f_{frp} = \frac{1}{2} E_{frp}\varepsilon_{cu}\left[(1 + \frac{4\alpha_1\beta_1\phi_c f_c'}{\rho_{frp}\phi_{frp}E_{frp}\varepsilon_{cu}})^{0.5} - 1\right]$$

$$f_{frp} = 0.5 * 60 * 10^3 * 0.0035\left[(1 + \frac{4 * 0.801 * 0.889 * 1 * 32.6}{0.0071 * 1 * 60 * 10^3 * 0.0035})^{0.5} - 1\right]$$

$$= 728\ MPa$$

$a = \beta_1\, c = \left(\phi_{frp}\, A_{frp}\, f_{frp}\right) \div (\alpha_1 \phi_c f_c' b)$

$a = (1 * 1000 * 730) \div (1 * 0.801 * 32.6 * 350) = 79.6\, mm$

$C_c = \alpha_1 \phi_c f_c' \beta_1\, c\, b = 0.801 * 1 * 32.6 * 79.6 * 350 = 727.5\, kN$

$T_{frp} = \phi_{frp} A_{frp} f_{frp} = 1 * 1000 * 728 = 728\, kN$

Equilibrium is satisfied $T = C_c$

$M_r = C_c \left(d - \frac{\beta_1 c}{2}\right) = 728 * 10^3 \left(400 - \frac{79.6}{2}\right) = 262.2\, kN.m$

$\boldsymbol{M_r = 262\ kN.m}$

Design Beam for Shear

Shear reinforcement Characteristics: (GFRP stirrups)

$Strength\ of\ straight\ part(f_{v,frp}) = 825\ MPa$ (Assumed to be 75% of the strength of 12.7 mm straight bars; 0.75 * 1100 = 825 MPa)

$\phi_{frp} = 1 \qquad E_{v,frp} = 50\ GPa$

$A_v = 3\ branches\ \#13mm = 3 * 113 = 339\ mm^2$

$l_d/d_e = 8 \qquad r_b/d_e = 4$

$Beam\ length\ (l_b) = 2000\ mm \qquad Column\ height\ (h_c) = 3500\ mm$

$$Design\ Strength\ of\ stirrups\ \left(f_{fh}\right) = least\ of \begin{cases} \left(0.4 + 0.015\frac{l_d}{d_e}\right) f_{v,frp} = 429 MPa \\ \left(0.05\frac{r_b}{d_b} + 0.3\right) f_{v,frp} = 412\ MPa \\ 0.004 E_{v,frp} = 200\ MPa \\ \phi_{frp}\, f_{v,frp} = 825\ MPa \end{cases}$$

$\therefore f_{fh} = 200\ MPa$

$$Applied\ shear\ force\ (V_r) = \frac{M_{beam}}{l_b} = \frac{262 * 10^6}{2000} = 131\ kN$$

According to CSA-S806-02, Clause 8.4.4.4, Eq. (8-8), the shear resistance of a reinforced section subjected to gravity loads should be equal to:

$$V_r = V_c + V_{sf} \leq V_c + 0.6\lambda\phi_C\sqrt{f_c'}b_w d$$

However, the contribution of concrete will be neglected in the design to account for the concrete damage occurs under seismic loading, i.e. $V_c = zero$.

Accordingly, $V_r = V_{sf}$

1- Calculation of the required spacing (S) according to the required min. Reinforcement, According to CSA-S806-02, Clause 8.4.5

$$A_{v,min} = \frac{0.3\sqrt{f_c'}b_w s}{f_{fh}} \qquad \text{Eq. } (8-14)$$

$$Rearranging \text{ Eq. } (8-14) \quad \therefore\ S = \frac{A_v f_{fh}}{0.3\sqrt{f_c'}b_w} = \frac{339 * 200}{0.3\sqrt{32.6} * 350} = 113\ mm$$

$S = 113\ mm$ ..... (B-1)

2- Calculation of max. Spacing (S) required to resist the applied shear force according to CSA-S806-02, Clause 8.4.4.4.

$V_{sf} = V_r = 131\ kN$

$$V_{sf} = \frac{0.4\phi_f A_v f_{fu} d}{S} \qquad \text{Eq. } (8-12)$$

Rearranging Eq. (8-12)

$$\therefore\ S = \frac{0.4\phi_f A_v f_{fu} d}{V_{sf}} = \frac{0.4 * 1 * 339 * 825 * 400}{131 * 10^3} = 341\ mm$$

$S = 341\ mm$ ..... (B-2)

However, the CSA/S806-02 does not provide any provisions for frame members subjected to predominant flexure due to seismic loads and reinforced with GFRP stirrups, therefore Clause 21.3.3.2 at CSA/A23.3-04 was adopted to limit spacing of stirrups.

3- Calculation of max. Spacing (S_{max}) according to CSA/A23.3-04 Clause 21.3.3.2

$S_{max} = Least\ of$ {
- $d/4 = 400/4 = 100\ mm$
- Eight times the diameter of the smallest longitudinal bars =8*16=128 mm
- 24 times the diameter of the hoop bars = 24*13= 312 mm
- 300 mm
}

$S_{max} = 100\ \ mm$ ..... (B-3)

From B-1, B-2, and B-3 ➔ $S_{max} = 100\ \ mm$

$\therefore$ ***Use Stirrups* 3#13*mm* @ 100 *mm***

Design of Column for Flexure

Construction of Column interaction diagram

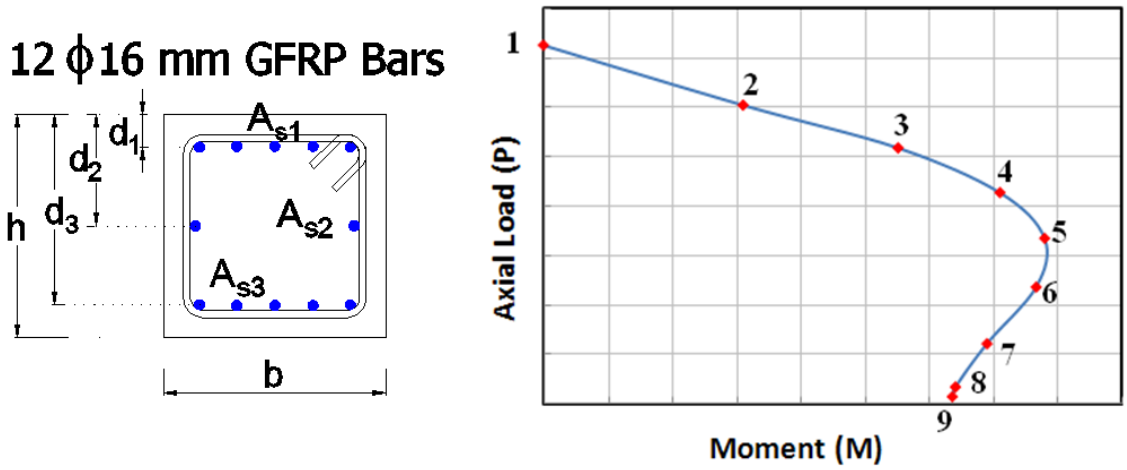

Figure A-13: Calculation points to construct the interaction diagram of column

Materials and Sectional properties:

$f_c^{'} = 32.6\ MPa$ $\phi_c = 1$

$\propto_1 = 0.85 - 0.0015 f_c' = 0.8011$ $\beta_1 = 0.97 - 0.0025 f_c'$=0.8885

$\varepsilon_{cu} = 0.0035$

$f_{frp,u} = 1100\ MPa$ $\phi_{frp} = 1$ $E_{frp} = 60\ GPa$ $\varepsilon_{frp,u} = 18.33 * 10^{-3}$

$A_{f1} = 5\emptyset 16mm = 4 * 200 = 1000\ mm^2$ $d_1 = 50\ mm$

$A_{f2} = 2\emptyset 16mm = 2 * 200 = 400\ mm^2$ $d_2 = 200\ mm$

$A_{f3} = 5\emptyset 16mm = 4 * 200 = 1000\ mm^2$ $d_3 = 350\ mm$

$h = 400\ mm$ $b = 350\ mm$

$A_{frp} = 12\#16mm = 12 * 200 = 2400\ mm^2$

Calculation of Balanced Reinforcement Required to Avoid Brittle Tension Failure

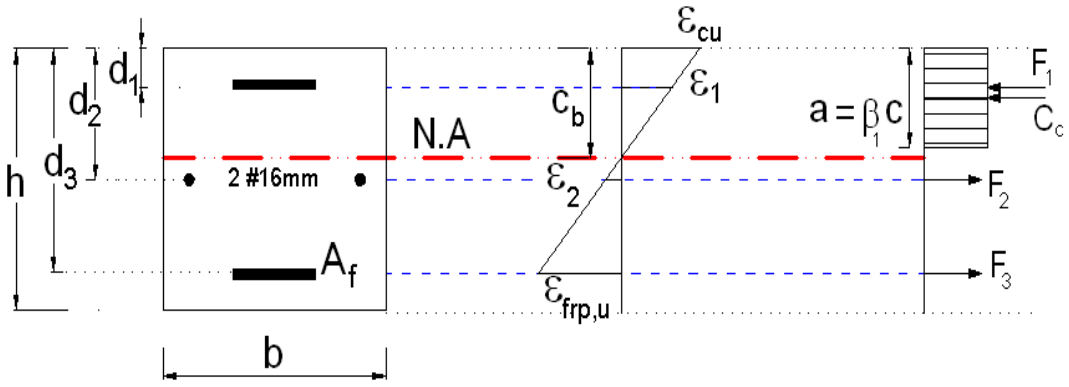

Figure A-14: Calculation for balanced reinforcement area

$$\frac{\varepsilon_{cu}}{c_b} = \frac{\varepsilon_{frp,u}+\varepsilon_{cu}}{d} \rightarrow \therefore c_b = \frac{d*\varepsilon_{cu}}{\varepsilon_{frp,u}+\varepsilon_{cu}} = \frac{0.0035*350}{18.33*10^{-3}+0.0035} = 56.1\ mm$$

$$C_c = \alpha_1 \phi_c f_c' \beta_1\ c_b\ b = 0.8011 * 1 * 32.6 * 0.8885 * 56.1 * 350 = 455.61\ kN$$

$$\varepsilon_{2=}\varepsilon_{frp,u}\frac{(d_2 - c_b)}{(d_3 - c_b)} = 18.33 * 10^{-3} * \frac{(200 - 56.1)}{(350 - 56.1)} = 8.976 * 10^{-3}$$

$$F_2 = \phi_{frp} A_{f2} E_{frp} \varepsilon_2 = 1 * 400 * 60 * 10^3 * 8.97 * 10^{-3} = 215.43\ kN$$

Neglecting the contribution of GFRP under compression in flexure strength of the section; $F_1 = 0\ kN$

From equilibrium, $C_c = F_2 + F_3$ $\rightarrow$ $\therefore F_3 = C_c - F_2 = 455.61 - 215.43 = 240.2\ kN$

$$\therefore A_f = \frac{F_3}{f_{frp,u}} = \frac{240.2 * 10^3}{1100} = 218\ mm^2$$

Available reinforcement area in the column section ($A_{f3} = 5\emptyset 16mm = 5 * 200 = 1000\ mm^2$) > Required area to avoid brittle tension failure ($A_f = 218\ mm^2$)

(OK- No tensile failure is expected in the column)

Calculations of required points to construct the Column interaction diagram

Point (1): Pure Axial resistance

$P_1 = 0.85 f_c' (A_g - A_{frp}) + 0.002\, E_{fc} A_{frp}$

Assume the contribution of the GFRP longitudinal bars in resisting axial compression is neglected.

$A_{frp} = 12 * 200 = 2400\ mm^2$

$P_1 = 0.85 * 32.6\ (350 * 400 - 2400) = 3812.9\ kN$

∴ **Point (1):** $(P_1 = 3812.9\ kN\ ,\ M_r = 0\ kN.m)$

Point (2): C = 400 mm

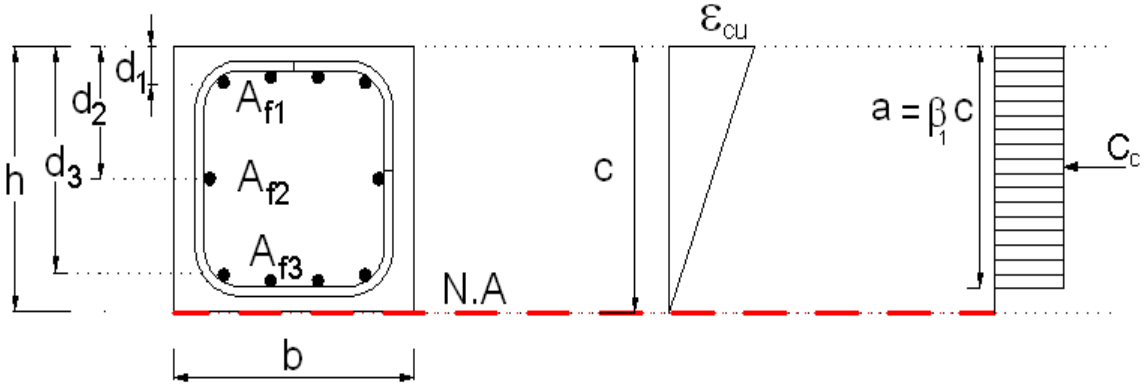

Figure A-15: Compatibility of strains for column cross section ($c = h$)

$C_c = \alpha_1 \phi_c f_c' \beta_1\, c\, b = 0.8011 * 1 * 32.6 * 0.8885 * 400 * 350 = 3248.55\ kN$

$P_2 = C_c = 3248.55\ kN$

$M_2 = C_c \left(\frac{h}{2} - \frac{\beta_1 c}{2}\right) = 3248.55 \left(\frac{400}{2} - \frac{0.8885 * 400}{2}\right) = 80.8\ kN.m$

Point (2): $(P_2 = 3248.6\ kN\ , M_2 = 72.4\ kN.m)$

Point (3): C = 350 mm

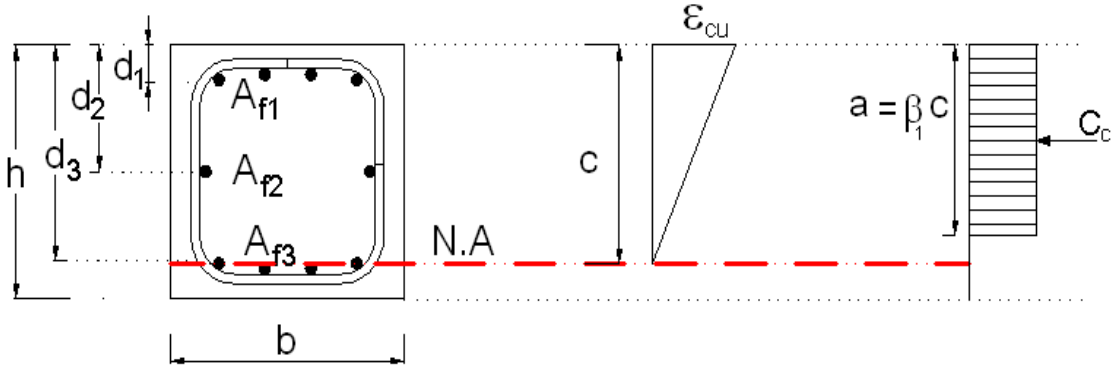

Figure A-16: Compatibility of strains for column cross section ($c = d_3$)

$$C_c = \alpha_1 \phi_c f'_c \beta_1 \, c \, b = 0.8011 * 1 * 32.6 * 0.8885 * 350 * 350 = 2842.5 \, kN$$

$$P_3 = C_c = 2842.5 \, kN$$

$$M_3 = C_c \left(\frac{h}{2} - \frac{\beta_1 c}{2}\right) = 2842.5 \left(200 - \frac{0.8885 * 350}{2}\right) = 126.5 \, kN.m$$

Point (3): ($P_3 = 2842.5 \, kN$, $M_3 = 126.5 \, kN.m$)

Point (4): C = 300 mm

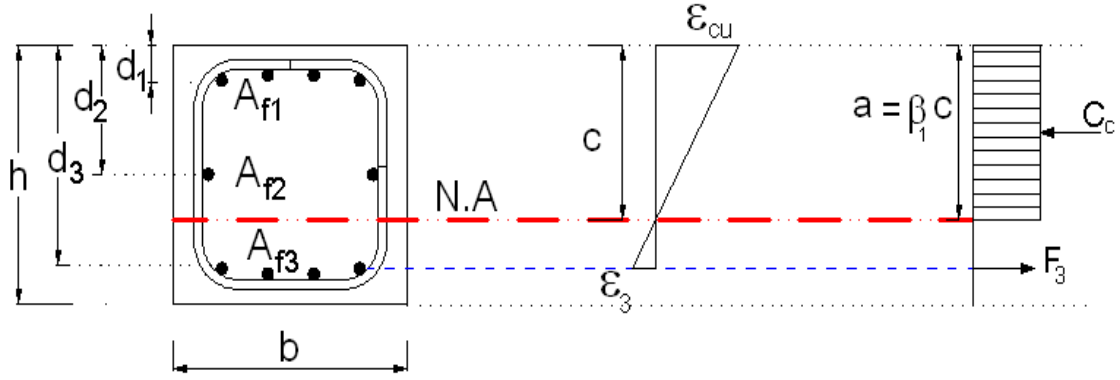

Figure A-17: Compatibility of strains for column cross section ($d_3 > c \geq h/2$)

$$C_c = \alpha_1 \phi_c f_c' \beta_1 \, c \, b = 0.8011 * 1 * 32.6 * 0.8885 * 300 * 350 = 2436.4 \, kN$$

$$\varepsilon_3 = \varepsilon_{cu}\left(\frac{d_3}{c} - 1\right) = 0.0035\left(\frac{350}{300} - 1\right) = 5.833 * 10^{-4}$$

$$F_3 = \phi_f A_{f3} \varepsilon_3 E_{frp} = 1 * 1000 * 5.833 * 10^{-4} * 60 * 10^3 = 35 \, kN$$

$$P_4 = C_c - F_3 = 2436.4 - 35 = 2401.4 \, kN$$

$$M_4 = C_c\left(\frac{h}{2} - \frac{\beta_1 c}{2}\right) + F_3\left(d_3 - \frac{h}{2}\right)$$

$$M_4 = 2436.4\left(200 - \frac{0.8885 * 300}{2}\right) + 35\,(350 - 200) = 167.8 \, kN.m$$

Point (4): ($P_4 = 2401.1 \, kN$, $M_4 = 167.8 \, kN.m$)

Point (5): C = 250 mm

$$C_c = \alpha_1 \phi_c f_c' \beta_1 \, c \, b = 0.8011 * 1 * 32.6 * 0.8885 * 250 * 350 = 2030.3 \, kN$$

$$\varepsilon_3 = \varepsilon_{cu}\left(\frac{d_3}{c} - 1\right) = 0.0035\left(\frac{350}{250} - 1\right) = 1.4 * 10^{-3}$$

$$F_3 = \phi_f A_{f3} \varepsilon_3 E_{frp} = 1 * 1000 * 1.4 * 10^{-3} * 60 * 10^3 = 84 \, kN$$

$$P_5 = C_c - F_3 = 2030.3 - 67.2 = 1946.3 \, kN$$

$$M_5 = C_c\left(\frac{h}{2} - \frac{\beta_1 c}{2}\right) + F_3\left(d_3 - \frac{h}{2}\right)$$

$$M_5 = 2030.3\left(200 - \frac{0.8885 * 250}{2}\right) + 84\,(350 - 200) = 193.2 \, kN.m$$

Point (5): ($P_5 = 2030.3 \, kN$, $M_5 = 193.2 \, kN.m$)

Point (6): C = 200 mm

$$C_c = \alpha_1 \phi_c f_c' \beta_1 \, c \, b = 0.8011 * 1 * 32.6 * 0.8885 * 200 * 350 = 1624.3 \, kN$$

$$\varepsilon_3 = \varepsilon_{cu}\left(\frac{d_3}{c} - 1\right) = 0.0035\left(\frac{350}{200} - 1\right) = 2.625 * 10^{-3}$$

$$F_3 = \phi_f A_{f3} \varepsilon_3 E_{frp} = 1 * 1000 * 2.625 * 10^{-3} * 60 * 10^3 = 157.5\ kN$$

$$P_6 = C_c - F_3 = 1624.3 - 157.5 = 1466.8\ kN$$

$$M_6 = C_c \left(\frac{h}{2} - \frac{\beta_1 c}{2}\right) + F_3 \left(d_3 - \frac{h}{2}\right)$$

$$M_6 = 1624.3 \left(200 - \frac{0.8885 * 200}{2}\right) + 157.5\ (350 - 200) = 204.2\ kN.m$$

Point (6): $(P_6 = 1466.8\ kN\ , M_6 = 204.2\ kN.m)$

Point (7): C = 150 mm

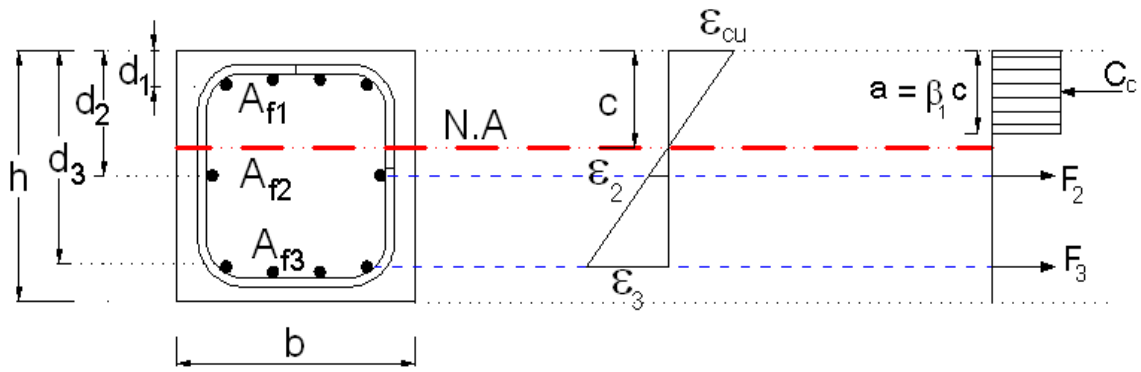

Figure A-18: Compatibility of strains for column cross section ($d_1 < c <$ *h/2*)

$$C_c = \alpha_1 \phi_c f'_c \beta_1\ c\ b = 0.8011 * 1 * 32.6 * 0.8885 * 150 * 350 = 1218.2\ kN$$

$$\varepsilon_2 = \varepsilon_{cu} \left(\frac{d_2}{c} - 1\right) = 0.0035 \left(\frac{200}{150} - 1\right) = 1.167 * 10^{-3}$$

$$F_2 = \phi_f A_{f2} \varepsilon_2 E_{frp} = 1 * 400 * 1.167 * 10^{-3} * 60 * 10^3 = 28\ kN$$

$$\varepsilon_3 = \varepsilon_{cu} \left(\frac{d_3}{c} - 1\right) = 0.0035 \left(\frac{350}{150} - 1\right) = 4.67 * 10^{-3}$$

$$F_3 = \phi_f A_{f3} \varepsilon_3 E_{frp} = 1 * 1000 * 4.67 * 10^{-3} * 60 * 10^3 = 280\ kN$$

$$P_7 = C_c - F_3 - F_2 = 1218.2 - 280 - 28 = 910.2\ kN$$

$$M_7 = C_c\left(\frac{h}{2}-\frac{\beta_1 c}{2}\right)+F_3\left(d_3-\frac{h}{2}\right)+F_2\left(d_2-\frac{h}{2}\right)$$

$$M_7 = 1218.2\left(200-\frac{0.8885*150}{2}\right)+280\ (350-200)+28*0 = 204.5\ kN.m$$

Point (7): ($P_7 = 910.2\ kN$, $M_7 = 204.5\ kN.m$)

Point (8): C = 100 mm

$$C_c = \alpha_1\phi_c f_c'\beta_1\ c\ b = 0.8011*1*32.6*0.8885*100*350 = 812.1\ kN$$

$$\varepsilon_2 = \varepsilon_{cu}\left(\frac{d_2}{c}-1\right) = 0.0035\left(\frac{200}{100}-1\right) = 3.5*10^{-3}$$

$$F_2 = \phi_f A_{f2}\varepsilon_2 E_{frp} = 1*400*3.5*10^{-3}*60*10^3 = 84\ kN$$

$$\varepsilon_3 = \varepsilon_{cu}\left(\frac{d_3}{c}-1\right) = 0.0035\left(\frac{350}{100}-1\right) = 8.75*10^{-3}$$

$$F_3 = \phi_f A_{f3}\varepsilon_3 E_{frp} = 1*1000*8.75*10^{-3}*60*10^3 = 525\ kN$$

$$P_8 = C_c - F_3 - F_2 = 812.1-525-84 = 203.1\ kN$$

$$M_8 = C_c\left(\frac{h}{2}-\frac{\beta_1 c}{2}\right)+F_3\left(d_3-\frac{h}{2}\right)+F_2\left(d_2-\frac{h}{2}\right)$$

$$M_8 = 812.1\left(200-\frac{0.8885*100}{2}\right)+525*150+84*0 = 205.1\ kN.m$$

Point (8): ($P_8 = 203.1\ kN$, $M_8 = 205.1\ kN.m$)

Point (9): C = 89 mm

$$C_c = \alpha_1\phi_c f_c'\beta_1\ c\ b = 0.8011*1*32.6*0.8885*89*350 = 722.8\ kN$$

$$\varepsilon_2 = \varepsilon_{cu}\left(\frac{d_2}{c}-1\right) = 0.0035\left(\frac{200}{89}-1\right) = 4.365*10^{-3}$$

$$F_2 = \phi_f A_{f2}\varepsilon_2 E_{frp} = 1*400*4.365*10^{-3}*60*10^3 = 104.76\ kN$$

$$\varepsilon_3 = \varepsilon_{cu}\left(\frac{d_3}{c} - 1\right) = 0.0035\left(\frac{350}{89} - 1\right) = 10.26 * 10^{-3}$$

$$F_3 = \phi_f A_{f3} \varepsilon_3 E_{frp} = 1 * 1000 * 10.26 * 10^{-3} * 60 * 10^3 = 615.84\ kN$$

$$P_9 = C_c - F_3 - F_2 = 722.8 - 615.84 - 104.76 = 2.2\ kN$$

$$M_9 = C_c\left(\frac{h}{2} - \frac{\beta_1 c}{2}\right) + F_3\left(d_3 - \frac{h}{2}\right) + F_2\left(d_2 - \frac{h}{2}\right)$$

$$M_9 = 722.8\left(200 - \frac{0.8885 * 89}{2}\right) + 615.84 * 150 + 104.76 * 0 = 208.4\ kN.m$$

Point (9): $(P_9 = 2.2\ kN\ , M_9 = 208.4\ kN.m)$

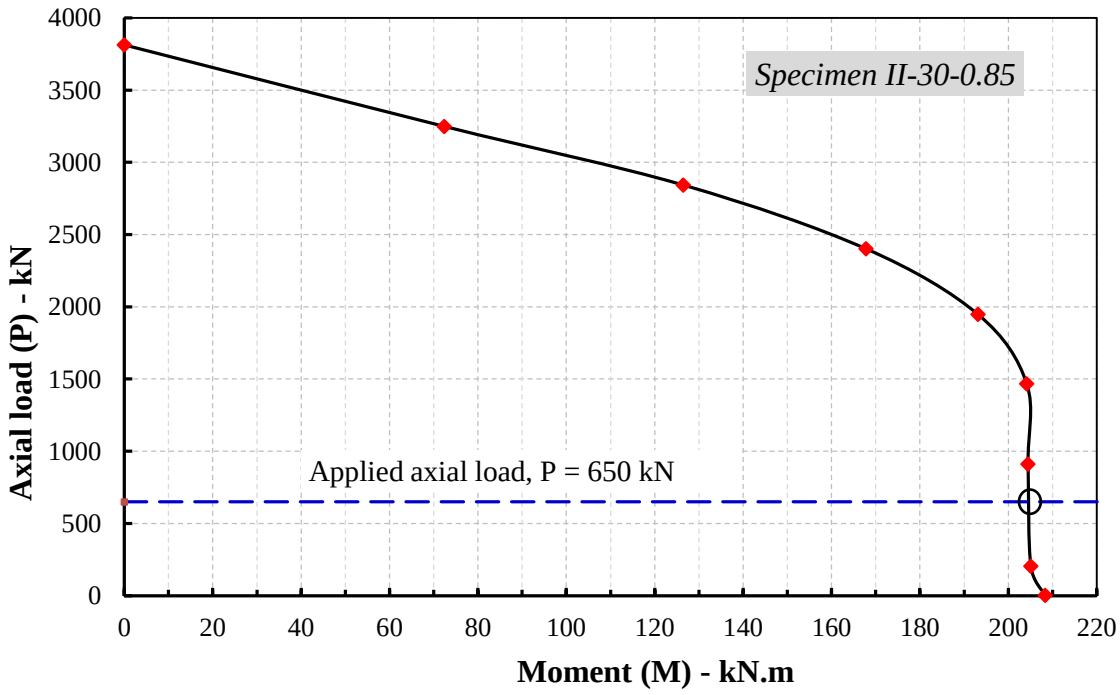

Figure A-19: Calculated column interaction diagram of Specimen II-30-0.85

The Specimen was tested under an axial concentric load at a level equal to approximately 15% of the column axial capacity (i.e. 650 kN). Therefore the flexural capacity of the

column cross section at the specified axial load level is equal to **205 kN.m** as shown in Figure A-19.

$$Flexure\ strength\ ratio\ (M_R) = \frac{Sum.\ of\ Column\ nominal\ flexure\ strength}{Beam\ propable\ flexure\ strength}$$

$$\boldsymbol{Flexure\ strength\ ratio\ (M_R) = \frac{2 * 205}{262} = 1.56}$$

Design of Column for Shear

Shear reinforcement Characteristics: (GFRP stirrups)

$Strength\ of\ straight\ part(f_{v,frp}) = 825\ MPa$ (Assumed to be 75% of the strength of 12.7 mm straight bars; 0.75 * 1100 = 825 MPa)

$\phi_{frp} = 1 \qquad E_{v,frp} = 50\ GPa$

$A_v = 3\ branches\ \#13mm = 3 * 113 = 339\ mm^2$

$l_d/d_e = 8 \qquad r_b/d_e = 4$

$Beam\ length\ (l_b) = 2000\ mm \qquad Column\ height\ (h_c) = 3500\ mm$

$$Design\ Strength\ of\ stirrups\ \left(f_{fh}\right) = least\ of \begin{cases} \left(0.4 + 0.015\frac{l_d}{d_e}\right) f_{v,frp} = 429MPa \\ \left(0.05\frac{r_b}{d_b} + 0.3\right) f_{v,frp} = 413\ MPa \\ 0.004E_{v,frp} = 200\ MPa \\ \phi_{frp}\, f_{v,frp} = 825\ MPa \end{cases}$$

$\therefore f_{fh} = 200\ MPa$

$$Applied\ shear\ force\ (V_r) = \frac{M_{beam}}{l_c} = \frac{262 * 10^6}{3500} = 74.9\ kN$$

$V_r = V_c + V_{sf} \leq V_c + 0.6\lambda\phi_C\sqrt{f_c'}b_w d$ Eq. (8-8) – Clause 8.4.4.4

Assume using min. Shear reinforcement;

$V_c = 0.035\lambda\phi_c(f_c'\rho_w E_f \frac{V_r}{M_f} d)^{1/3} b_w d$ Eq. (8-10) – Clause 8.4.4.4

$\rho_w = \frac{5*200}{350*350} = 8.163 * 10^{-3}$

$M_f = 0.5 * M_{r,beam} = 0.5 * 262 = 131\ kN.m$

$$V_c = 0.035 * 1 * 1\left[32.6 * 8.163 * 10^{-3} * 60 * 10^3 * \frac{74.9 * 10^3}{131 * 10^6} * 350\right]^{1/3} * 350 * 350$$

$V_c = 63.15\ kN$

$V_c\ should\ not\ exceed\ \left[0.2\lambda\phi_c\sqrt{f_c'}b_w d\right] and\ not\ less\ than\ \left[0.1\lambda\phi_c\sqrt{f_c'}b_w d\right]$ ➔

Clause 8.4.4.4

$V_c = 63.15\ kN < 0.2 * 1 * \sqrt{32.6} * 350 * 350 = 139.9\ kN$ ..... (OK)

$V_c = 60\ kN < 0.1 * 1 * \sqrt{32.6} * 350 * 350 = 69.9\ kN$ ..... (Not OK)

$\therefore\ take\ V_c = 69.9\ kN$

1- Calculation of required Spacing (S) according to required minimum transverse reinforcement area, Clause 8.4.5

$$A_{v,min} = \frac{0.3\sqrt{f_c'}b_w s}{f_{fh}} \qquad \text{Eq. } (8-14)$$

$Rearranging$ Eq. $(8-14)$ $\therefore\ S = \dfrac{A_v f_{fh}}{0.3\sqrt{f_c'}b_w} = \dfrac{339 * 200}{0.3\sqrt{32.6} * 350} = 113\ mm$

$S = 113\ mm$ ..... (B-4)

2- Contribution of minimum area of stirrups according to Clause 8.4.4.4.

$V_{sf} = V_r - V_c = 74.9 - 69.9 = 5\ kN \quad (where\ V_c \approx V_r)$

$$V_{sf} = \frac{0.4\phi_f A_v f_{fu} d}{S} \qquad \text{Eq. } (8-12)$$

$$V_{sf} = \frac{0.4 * 1 * 339 * 825 * 350}{113} = 346.5\ kN$$

$Total\ shear\ resistance = V_{sf} + V_c = 346.5 + 69.9 = 416.4\ kN$

$Check\ of\ maximum\ shear\ resistance\ \left(V_{r,max}\right) = V_c + 0.8\lambda\phi_c\sqrt{f_c'}b_w d$

$$V_{r,max} = 69.9 + \frac{0.8 * 1 * 1 * \sqrt{32.6} * 350 * 350}{1000} = 629.4\ kN$$

$\therefore\ V_{sf} + V_c = 416.4\ kN < V_{r,max} = 629.4\ kN$ .....(OK)

$\therefore\ V_{sf} + V_c = 416.4\ kN > V_r = 74.9\ kN$ .....(OK)

3- Calculation of max. Spacing (S_{max}) according to CSA S806-02 Clause 12.7 (Seismic provision)

$$A_{Fh} = 14\ S\ h_c\ \frac{f_c'}{f_{Fh}} \left(\frac{A_g}{A_c} - 1\right) \frac{\delta}{\sqrt{k_c}} * \frac{P_f}{P_{ro}} \qquad \text{Eq. } (12-7)$$

Where;

$h_c = 350 - 2\left(25 + \frac{13}{2}\right) = 287mm$ (Cross-sectional dimension of column core, assuming 25 mm clear concrete cover from the stirrup)

$\delta = 3.0\%$ (Design lateral drift ratio)

$f_c' = 32.6\ MPa$

$f_{Fh} = 200\ MPa$

$A_c = 287 * 337 = 96719\ mm^2$ (Cross-sectional area of the core of a compression member measured to the centreline of the perimeter hoop or spiral)

$A_g = 350 * 400 = 140000\ mm^2$

$where\ \left(\frac{A_g}{A_c} - 1\right) = 0.45\ \geq 0.3 \ldots\ldots\ldots (OK)$

$A_{Fh} = 3 * 113 = 339\ mm^2$ (Total area of rectangular FRP hoop reinforcement in each cross-sectional direction)

$\frac{P_f}{P_{ro}} = 20\%$ (Ratio of the factored axial load to factored axial load resistance at zero eccentricity)

$$Confinement\ \ coefficient\ (k_c) = 0.15 \sqrt{\frac{h_c}{S} * \frac{h_c}{S_1}}$$

$S_1 = \frac{287}{2} = 143.5\ mm$ (Spacing of tie legs or the spacing of grid openings in the cross-sectional plane of the column)

Rearranging Eq. (12-7) to calculate the stirrups spacing (*S*)

$$S = \left[\frac{A_{Fh}}{14h_c} * \frac{f_{Fh}}{f_c'} * \frac{P_{ro}}{P_f} * \frac{1}{\delta} * \left(\frac{A_c}{A_g - A_c}\right)\left(\frac{0.15h_c}{\sqrt{S_1}}\right)^{0.5}\right]^{4/5}$$

Applying in equation above, we get that the maximum spacing $S = 128\ mm$

$S = 112\ mm$ ..... (B-5)

3- Check of maximum Spacing (S_{max}) according to CSA S806-02 Clause 12.7.2

$S_{max} = least\ of$
- 1/4 min. member dimension=$0.25 * 350 = 88$ mm
- $150\ mm$
- 6 times the longitudinal bar diameter =6*16=96 mm
- 48 times the stirrup diameter =48*13=610 mm

$\therefore\ S_{max} = 88\ mm \approx 90mm$ ..... (B-6)

From B-4, B-5, and B-6 ➔ $S_{max} = 90\ mm$

$\therefore$ ***Use Stirrups* 3#13*mm* @ 90 *mm***

Calculation of shear stress in the joint

The CSA S806-02 has no expression to evaluate the joint shear capacity of joints reinforced with FRP stirrups; however, the CSA A23.3-04 does. Consequently, a new expression similar to that in CSA/A23.3-04 - Clause 21.5.4.1 (c) should be developed based on the test results.

$Applied\ shear\ on\ the\ joint\ (V_j) = T_{frp} - V_{column}$

$V_{column} =$ Applied shear force to the column at the joint face

$V_{column} = 74.9$ kN

$T_{frp} = Calculated\ tensile\ force\ in\ longitudinal\ beam\ bars\ at\ failure$

$T_{frp} = \phi_{frp} A_{frp} f_{frp} = 1 * 1000 * 728 = 728\ kN$

$V_j = 728 - 74.9 = 653.1\ kN$

$Shear\ stress\ in\ the\ joint (v_j) = V_j / A_j$

Where A_j = Minimum cross-sectional area within a joint in a plane parallel to the axis of reinforcement generating the shear in the joint

$A_j = 350 * 400 = 140000\ mm^2$

$Shear\ stress\ in\ the\ joint (v_j) = 653.1 * 10^3 / 140000$

$Shear\ stress\ in\ the\ joint (v_j) = \mathbf{4.7}\ MPa = \mathbf{0.82}\sqrt{f'_c}$

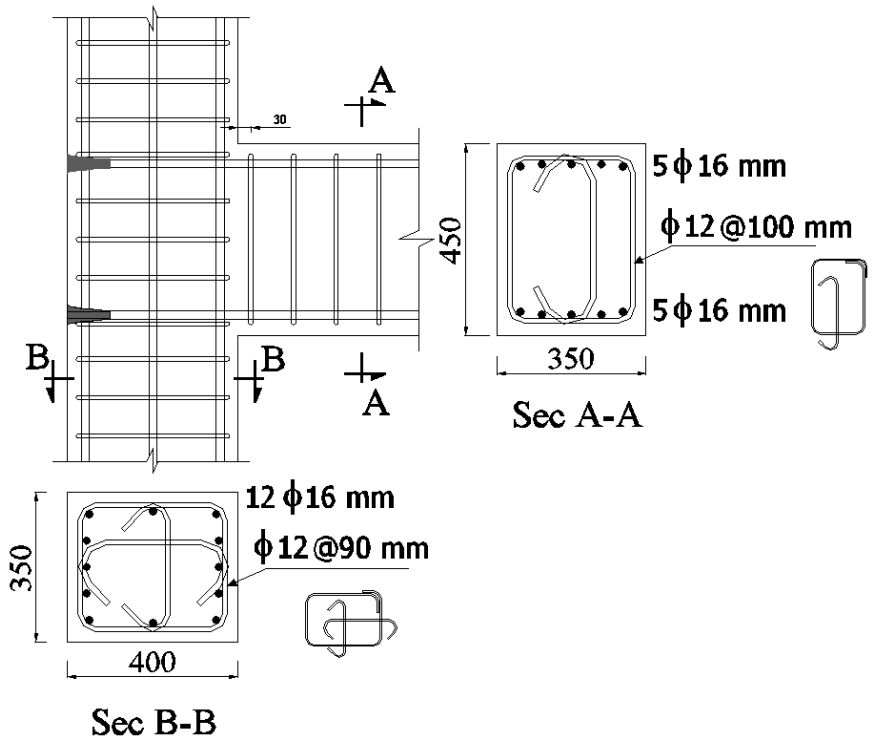

Figure A-20: Reinforcement details of Specimen II-30-0.85

APPENDIX-B

DETAILS AND TEST RESULTS OF SPECIMEN I-B-D0

B.1 INTRODUCTION

This appendix summarizes the details and the experimental results for Specimen I-B-D0. Specimen I-B-D0 was reinforced with longitudinal bent bars that are not long enough to cover the whole length of the beam due to some manufacturing restriction at the time of construction. Therefore, the beam longitudinal reinforcement was spliced within the beam length.

During testing, Specimen I-B-D0 showed no consistency between the lateral load resistances in the reversed loading directions. Therefore it was decided to disregard that specimen and reconstruct it using full-length longer longitudinal bent bars that have been made available at later time. The concrete dimensions and reinforcement details are shown in Figures B-1 and B-2, respectively. Table B-1 summarizes the design characteristics Specimen I-B-D0; the calculated stresses and strength are based on the concrete strength on the day of testing.

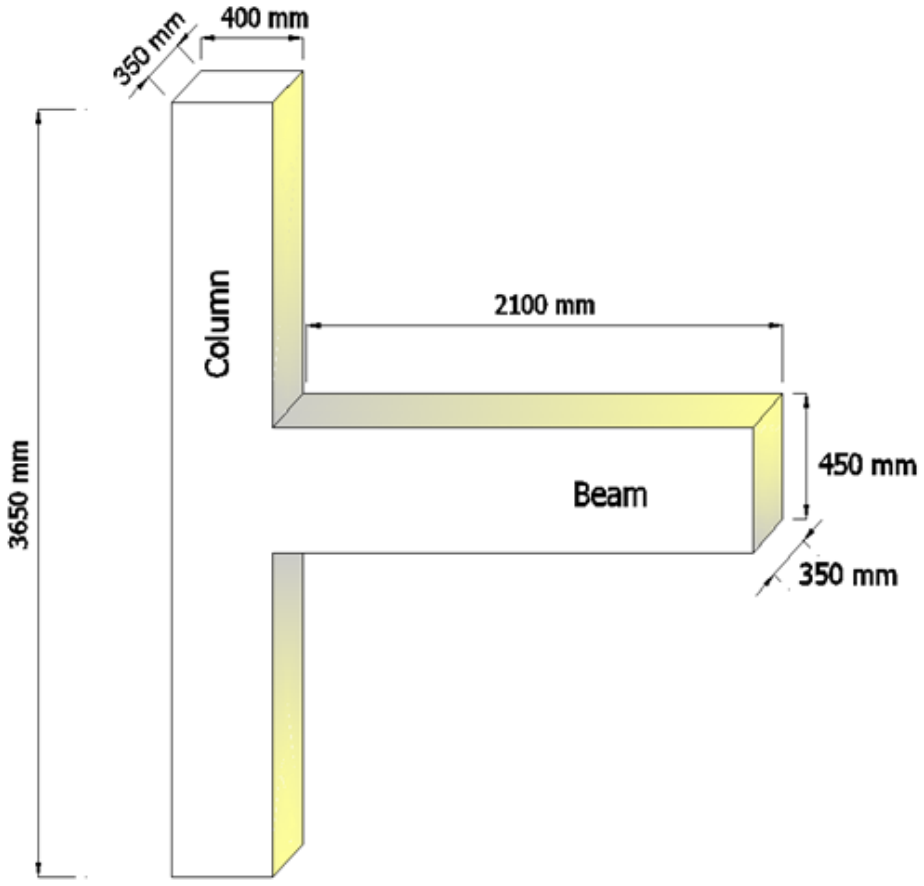

Figure B-1: Concrete dimensions of Specimen I-B-D0

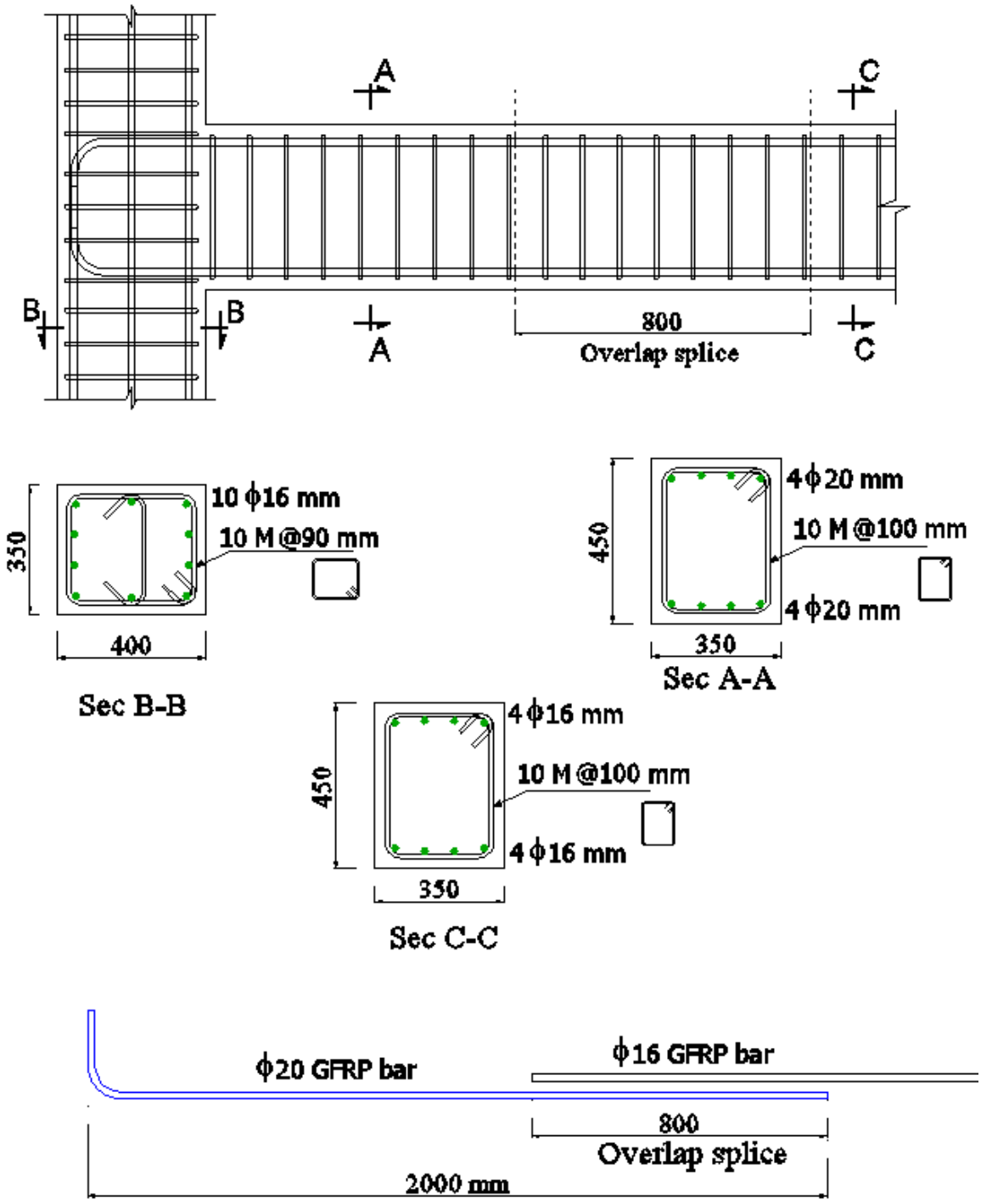

Figure B-2: Reinforcement details of Specimen I-B-D0

Table B-1: Design characteristics of Specimen I-B-D0

	Specimen ID	I-B-D0
Beam	No. of Bars	4 ϕ 20 T&B
	End Anchorage	90-degree hooks
	ρ_{frp}/ρ_{bal}	1.68
	Calculated Bar stress (MPa)	619
	Flexural resistance (kN.m)	268
Column	No. of Bars	10 No. 16
	Applied axial load (kN)	650
	Flexural capacity (kN.m)	202
Overall	Flexural strength ratio	1.47
	Joint shear stress (MPa)	4.76
		$0.82\sqrt{f'_c}$
	Concrete Strength (MPa)	34.1
	Expected Failure mode	Compression failure

B.2 LOAD–LATERAL DRIFT RESPONSE (HYSTERETIC BEHAVIOUR)

Plots of the hysteresis diagrams which represent the relationship between the applied lateral load and the drift ratio of the beam tip are shown in Figure B.3. The measured hysteresis loops demonstrated stable response up to a drift ratio of 1.5%. After a drift

ratio of 2.0%, the specimen showed no increase in flexural resistance in the positive loading direction (i.e. pushing of beam tip) compared to the opposite loading direction which showed increasing flexural resistance up to 5.0% drift ratio. The difference in the flexural resistance between the two loading directions gradually increased with loading until the flexural resistance in the –ve loading direction reached approximately 1.5 times the resistance exhibited in the opposite loading direction. It is thought that this difference in resistance is attributed to the failure in the overlap splice. Also, it should be noted that the specimen was not able to reach the design flexural resistance. The recorded lateral loading values were only 60% and 90% of the calculated flexural resistance in the beam in the +ve and –ve loading directions, respectively, as shown in Figure B-3.

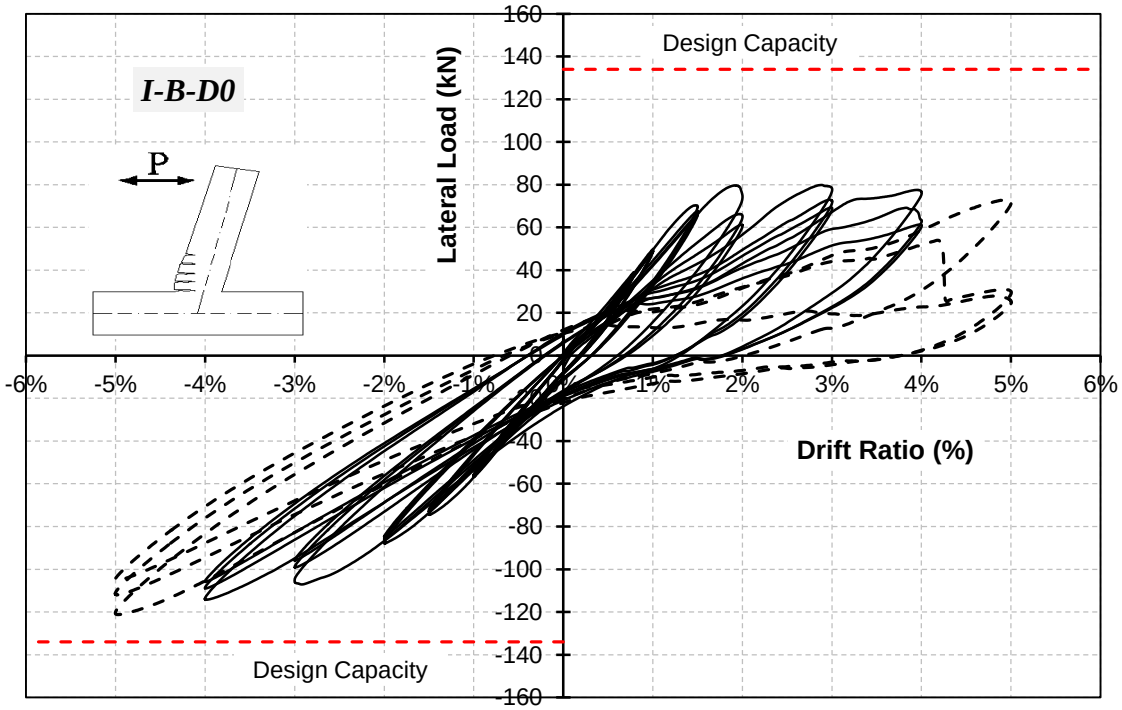

Figure B-3: Load-Lateral Drift relationship for Specimen I-B-D0

B.3 CRACKING PATTERN AND MODE OF FAILURE

Figure B.4 shows the cracking pattern at different loading steps. The specimen had a stable behaviour up to 1.5% drift ratio where flexural cracks were observed in the beam near the column face with no cracking in the joint area as shown in Figures B-4(a) through B-4(c). At 2.0% drift ratio level, the specimen exhibited a difference in flexural resistance between the positive and negative loading direction where the specimen showed no increase in flexural resistance to the positive loading direction.

At 3.0% drift ratio, vertical splitting cracks were observed in the concrete cover of the beam bars which in turn lead to the concrete cover to fall as shown in Figures B-4 (d) through (g). This can be attributed to slippage failure in the overlap splice of the longitudinal reinforcement. The specimen completed the loading step of 5.0% drift ratio; however, the test was stopped since the specimen showed no increase in loading.

(a) 0.8% drift ratio

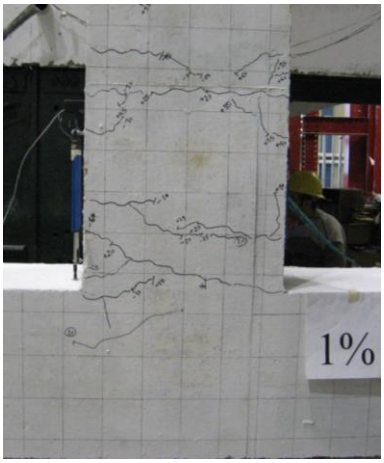

(b) 1.0% drift ratio

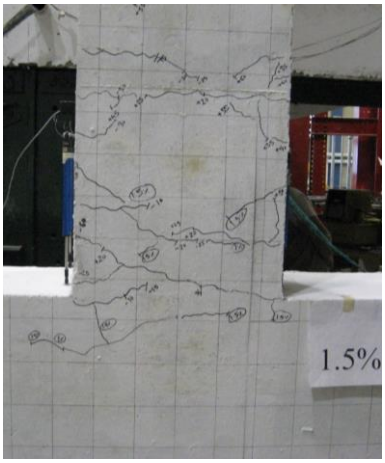

(c) 1.5% drift ratio

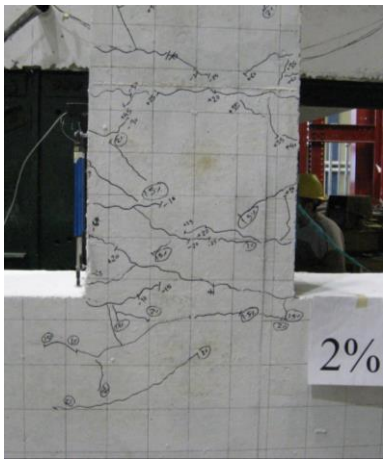

(d) 2.0% drift ratio

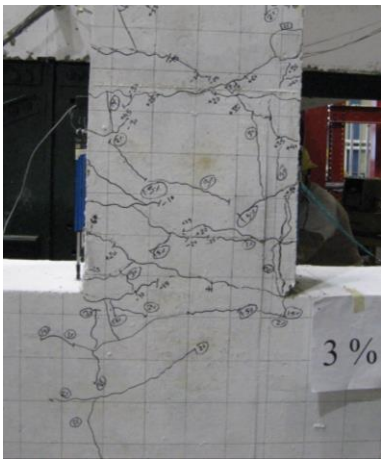

(e) 3.0% drift ratio

(f) 4.0% drift ratio

(g) 5.0% drift ratio

Figure B-4: Cracking progression of Specimen I-B-D0

B.4 LATERAL DRIFT-STRAIN RELATIONSHIP

B.4.1 Developed Strains in Beam Longitudinal Reinforcement

Figure B-5 shows the strain distribution along the beam longitudinal reinforcement in the vicinity of the joint area during the successive loading drifts. For Specimen I-B-D0, the flexural resistance difference between the positive and negative loading direction affected the strain values in both directions as shown in Figure B-5. Figure B-5(a) shows that strain values at 200-mm away from column face are much higher than those on the column face. Moreover, the maximum values of strains were detected at 1.5% drift ratio, and then decreased with the increase of the drift ratio level. On the other hand, Figure B-5(b) shows an acceptable strain profile where strain values on the column face were higher than those away from it.

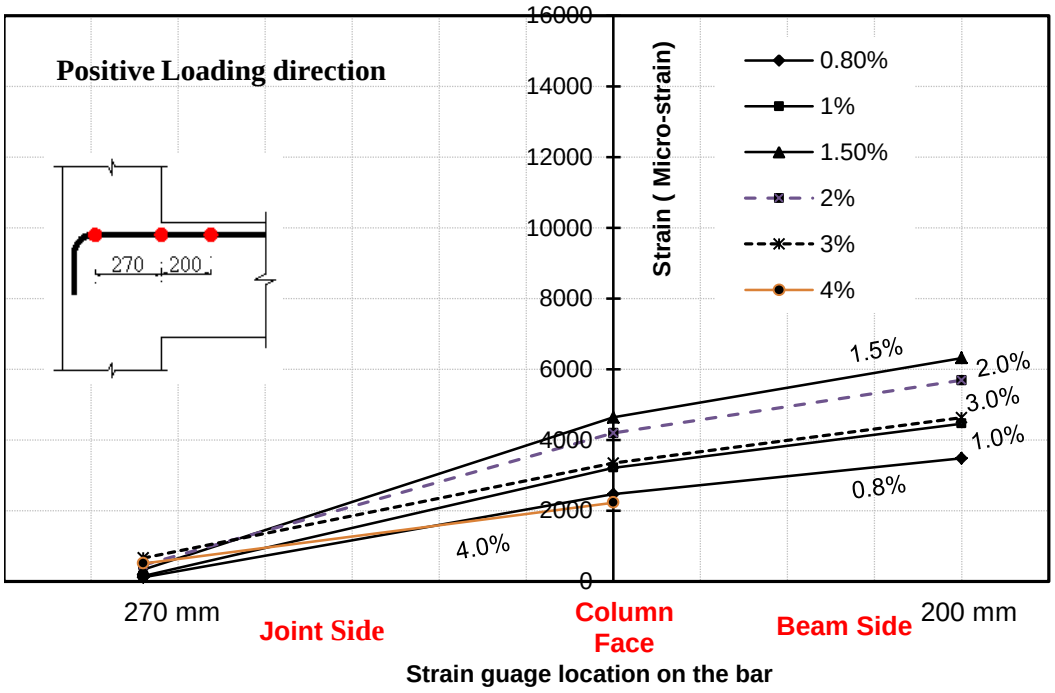

(a) Bars resisting positive loading

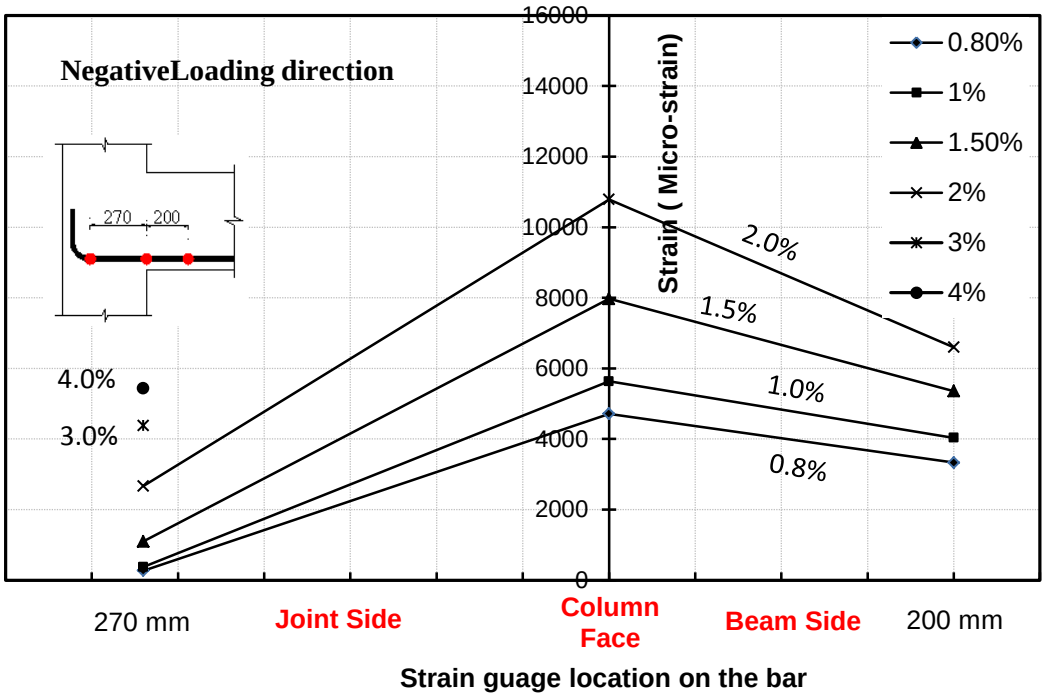

(b) Bars resisting negative loading

Figure B-5: Strain profile on beam longitudinal bars for Specimen I-B-D0

B.4.2 Developed Strains in Beam and Column Transverse Reinforcement

Figure B-6 shows the relationship between the maximum strains developed in the beam stirrups and the drift ratio. Specimen I-B-D0 developed low strain values that didn't exceed 500 micro-strain. To draw the following figures, it should be noted that the reported strain values are those corresponding to loading the specimen in the negative direction (pulling the beam tip).

Figure B-7 shows the relationship between the drift ratio and the maximum measured strain in the joint stirrups.

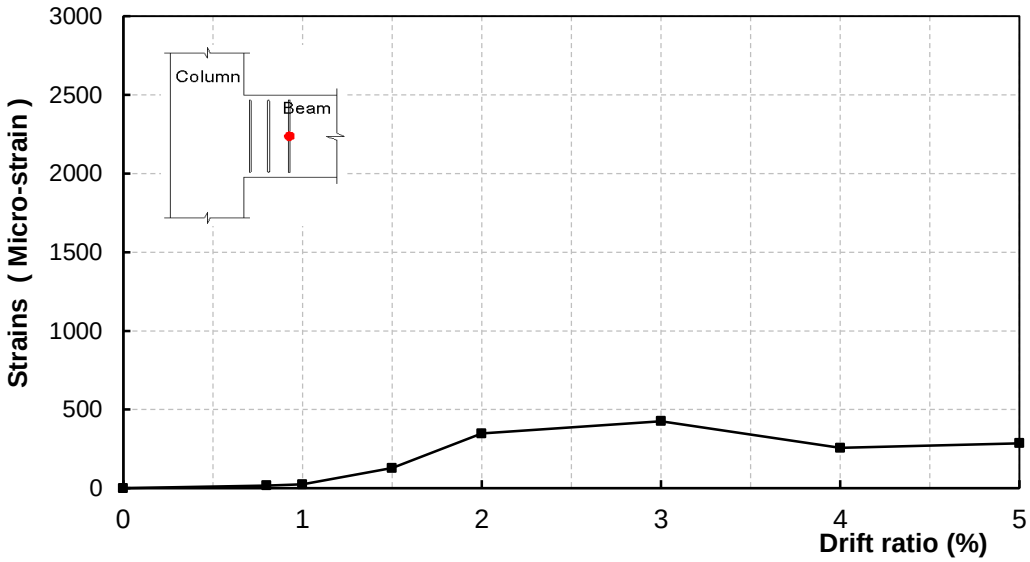

Figure B-6: Maximum strains–drift ratio relationship for beam stirrups

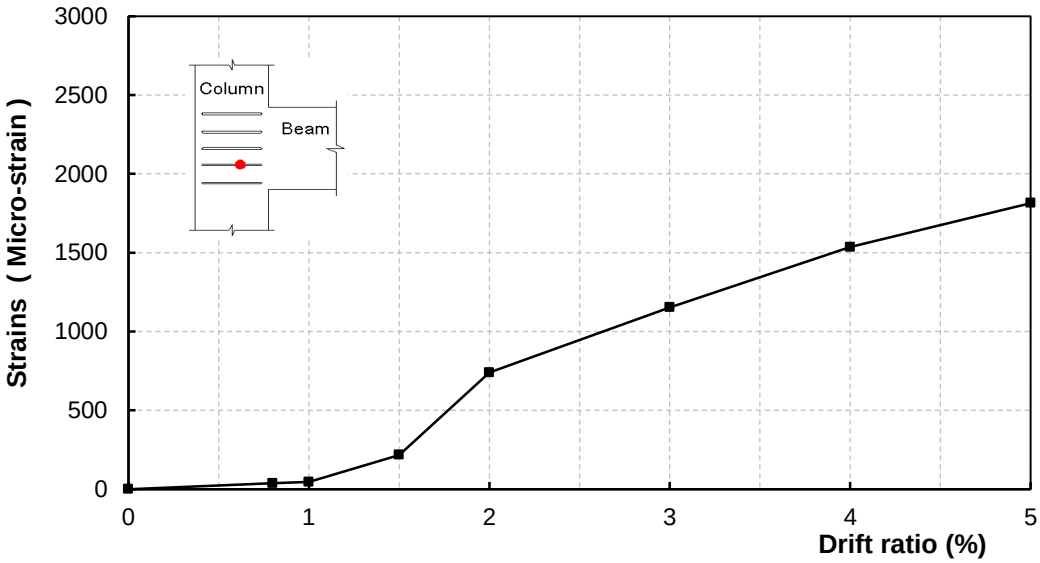

Figure B-7: Maximum strains–drift ratio relationship for joint stirrups

B.4.3 Developed Strains in Column Longitudinal Reinforcement

Figure B-8 shows the relationship between the drift ratio and the maximum strains measured in column longitudinal bars. Specimen I-B-D0 exhibited increase in strains

with a value of 2640 micro-strain at failure. It should be noted that the reported strain values in this figure are those corresponding to loading the specimen in the negative direction (pulling the beam tip).

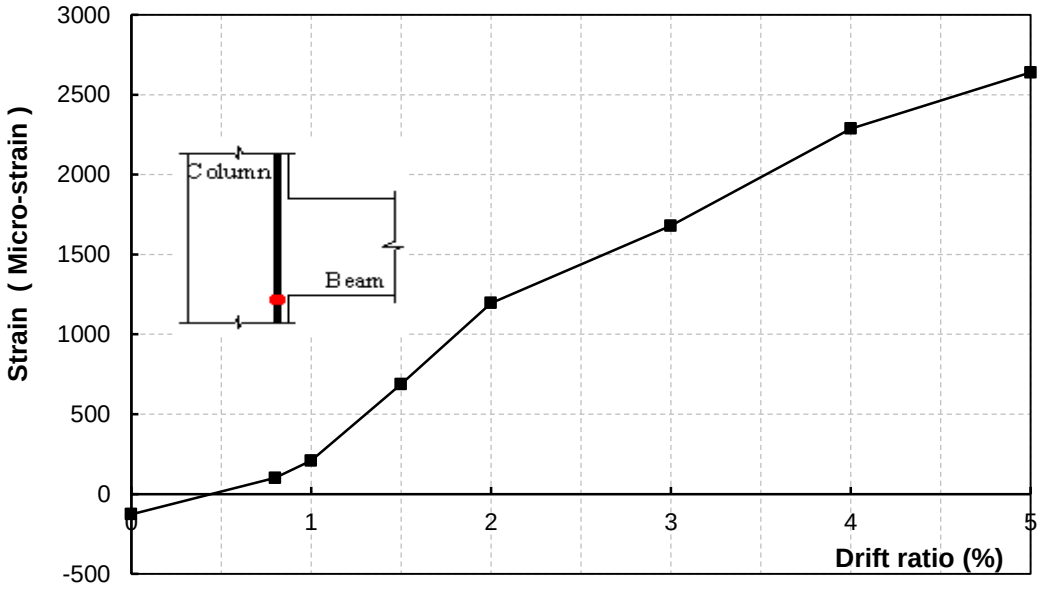

Figure B-8: Maximum strains–drift ratio relationship for column bars